



HAL
open science

Exploration of Internal Anatomy and Morphological Integration in the Skull of Cingulates (Xenarthra, Mammalia) and their Phylogenetic Implications

Kévin Le Verger

► **To cite this version:**

Kévin Le Verger. Exploration of Internal Anatomy and Morphological Integration in the Skull of Cingulates (Xenarthra, Mammalia) and their Phylogenetic Implications. Paleontology. Museum National d'Histoire Naturelle (MNHN), 2021. English. NNT: . tel-03207494

HAL Id: tel-03207494

<https://hal.science/tel-03207494v1>

Submitted on 25 Apr 2021

HAL is a multi-disciplinary open access archive for the deposit and dissemination of scientific research documents, whether they are published or not. The documents may come from teaching and research institutions in France or abroad, or from public or private research centers.

L'archive ouverte pluridisciplinaire **HAL**, est destinée au dépôt et à la diffusion de documents scientifiques de niveau recherche, publiés ou non, émanant des établissements d'enseignement et de recherche français ou étrangers, des laboratoires publics ou privés.



MUSÉUM NATIONAL D'HISTOIRE NATURELLE

ÉCOLE DOCTORALE 227 « SCIENCES DE LA NATURE ET DE L'HOMME :
EVOLUTION ET ECOLOGIE »

DEPARTEMENT « ORIGINES ET ÉVOLUTION »

UMR 7207 CENTRE DE RECHERCHE EN PALEONTOLOGIE – PARIS

Année 2017-2020



THÈSE

Pour obtenir le grade de

Docteur du Muséum national d'Histoire naturelle

Spécialité : **Paléontologie, Systématique Phylogénétique et Morphométrie Géométrique**

Présentée et soutenue publiquement par

Kévin LE VERGER

Exploration of Internal Anatomy and Morphological Integration in the Skull of Cingulates (Xenarthra, Mammalia) and their Phylogenetic Implications

Sous la direction de : Guillaume Billet, MNHN

Soutenue le 22 janvier 2021 devant le JURY composé de :

Mme Isabelle Rouget (Prof., CR2P, Paris)	Examinatrice
Mme Allowen Evin (Chargé de Recherche, ISEM, Montpellier)	Examinatrice
M. Timothy Gaudin (Prof., University of Tennessee, Chattanooga)	Rapporteur
Mme Sophie Montuire (Directrice de Recherche, UB, Dijon)	Rapporteuse
M. Robert J. Asher (Doctor, University of Cambridge, Cambridge)	Examineur
M. Guillaume Billet (M. de Conf. And Curator, CR2P, Paris)	Directeur de thèse
M. Lionel Hautier (Chargé de Recherche, ISEM, Montpellier)	Invité

« Voici encore des arbres et je connais leur rugueux, de l'eau et j'éprouve sa saveur. Ces parfums d'herbe et d'étoiles, la nuit, certains soirs où le cœur se détend, comment nierais-je ce monde dont j'éprouve la puissance et les forces ? Pourtant toute la science de cette terre ne me donnera rien qui puisse m'assurer que ce monde est à moi. Vous me le décrivez et vous m'apprenez à le classer. Vous énumérez ses lois et dans ma soif de savoir je consens qu'elles soient vraies. Vous démontez son mécanisme et mon espoir s'accroît. Au terme dernier, vous m'apprenez que cet univers prestigieux et bariolé se réduit à l'électron. Tout ceci est bon et j'attends que vous continuiez. Mais vous me parlez d'un invisible système planétaire où des électrons gravitent autour d'un noyau. Vous m'expliquez ce monde avec une image. Je reconnais alors que vous en êtes venus à la poésie : je ne connaîtrai jamais. Ai-je le temps de m'en indigner ? Vous avez déjà changé de théorie. Ainsi cette science qui devait tout m'apprendre finit dans l'hypothèse, cette lucidité sombre dans la métaphore, cette incertitude se résout en œuvre d'art. »

Albert Camus. 1942. Le Mythe de Sisyphe, « *Un raisonnement absurde : les murs de l'absurdes* ».

“And here are trees and I know their gnarled surface, water and I feel its taste. These scents of grass and stars at night, certain evenings when the heart relaxes — how shall I negate this world whose power and strength I feel? Yet all the knowledge on earth will give me nothing to assure me that this world is mine. You describe it to me and you teach me to classify it. You enumerate its laws and in my thirst for knowledge I admit that they are true. You take apart its mechanism and my hope increases. At the final stage you teach me that this wondrous and multicolored universe can be reduced to the atom and that the atom itself can be reduced to the electron. All this is good and I wait for you to continue. But you tell me of an invisible planetary system in which electrons gravitate around a nucleus. You explain this world to me with an image. I realize then that you have been reduced to poetry: I shall never know. Have I the time to become indignant? You have already changed theories. So that science that was to teach me everything ends up in a hypothesis, that lucidity founders in metaphor, that uncertainty is resolved in a work of art.”

Albert Camus. 1942. The Myth of Sisyphus, “*An Absurd Reasoning: Absurd Walls*”. Translated from the French by Justin O'Brien (1955).

Acknowledgements

It has been three long years filled with adventures, but what particularly characterizes them is the constant headaches regarding the question of biological variation, which I am sure does not leave the mental health unscathed for those who try to understand it. I could not have completed this work without the unfailing support of several people whom I would like to thank infinitely.

First of all, I would like to thank my PhD supervisor, Guillaume Billet, who guided my research from the beginning to end, yet trusted me in such a way that it allowed me to progress within the exciting world of research. He was always kind and patient. No one could reproach him for being bothered by my pitiful English or my lack of rigor in certain aspects of the writing of draft versions. He always followed a rigorous, pedagogical, and friendly approach towards me while nourishing our discussions and flourishing ideas. Even on a personal note, he was always available to provide advice not related to my PhD. Guillaume, it was an honor to have been at your side during these three years. It is with emotion that I write these lines in the hope that this PhD is only the beginning of a long collaboration. I wish to give you my full gratitude and friendship. I can never thank you enough for everything...

I would also like to thank especially Christian de Muizon, *Directeur de Recherche* at the *Centre de Recherche en Paléontologie – Paris*, who allowed me, with Guillaume, to do this PhD by being my supervisor. Our interactions were rarer, but he was always there when I needed his help. I am very grateful to him.

My thanks also go to Sophie Montuire, *Directrice de Recherche* at the *Université de Bourgogne*, and to Timothy Gaudin, Professor at the University of Tennessee, for agreeing to be the reviewers of my PhD. I would also like to thank Isabelle Rouget, Professor at the *Centre de Recherche en Paléontologie – Paris*, Allowen Evin, *Chargée de Recherche* at the *Institut des Sciences de l'Evolution Montpellier*, and Robert J. Asher, Doctor at the University of Cambridge, for having accepted the invitation to be part of my PhD jury. To have them all on my jury is a great honor.

Within the *Centre de Recherche en Paléontologie – Paris* and more broadly the *Muséum national d'Histoire naturelle* in Paris and at the *Institut des Sciences de l'Evolution Montpellier*, I interacted with many colleagues who allowed me to produce good work. Their help was

ACKNOWLEDGEMENTS

indispensable, and I would like to thank them all. Thank you to Sylvie Crasquin for welcoming me into the paleontology laboratory in unit 7207. Thanks also to Didier Merle, Michel Laurin and Sylvain Charbonnier for always validating my administrative requests. Thank you to Angelina Bastos and Suzy Colas for helping me with all the administrative procedures, particularly for funding and travels. You have always welcomed me and helped me with patience and kindness. Thank you very much. Thanks to Christine Argot, Géraldine Véron and Guillaume Billet for giving me access to the study material. Thanks also to Claire Sagne, Sandra Daillie, Damien Olivier, Maxime Perretta and Vincent Pernègre, who work in the palaeontology collections of the *Museum National d'Histoire Naturelle*, for their help and friendship. Thanks to Julien Barbier for our discussions and for allowing me to share my research with the broader public. Thanks to Jérémie Kazan for our many discussions and for the superb reconstitution of the skull of *Glyptodon*. Thanks to Marta Bellato and Patricia Wils for scanning the *Glyptodon* from the *Muséum national d'Histoire naturelle* in Paris, and to Nathalie Poulet and Florent Goussard for your indispensable help with the 3D processing, as well as for our many discussions and your friendship. They saved me from having to redo the whole process at the mercy of computer whims. Thanks to Renaud Lebrun, from the University of Montpellier, for training me in 3D acquisition and allowing me to use the X-ray microtomograph to scan a large number of specimens. Thanks also for his kindness and his trust. Thanks to the technical teams, Charlène Letenneur, Sophie Fernandez, Colas Bouillet, Lilian Cazes, Yohan Despres, Philippe Loubry, Renaud Vacant and Jean-Charles Zajac for your friendship and help. Our interactions were always very friendly, and I learned a lot from them. Thanks to Marie-Astrid Angel for always helping me to consult the documents in the library of the *Centre de Recherche en Paléontologie – Paris*. Thanks to Maria Lages for her daily welcomes, always with a smile. Finally, many thanks to my office mates, Véronique Barriel, Sandrine Ladevèze, Chloé Olivier, Nathalie Poulet, Claire Sagne, Guillaume Billet, Helder Gomes Rodrigues, Damien Olivier, Maxime Perretta and Vincent Pernègre, who have brightened up these three years with rich discussions and laughs. I would also like to thank the whole team of doctoral missions and my colleagues who accompanied me during my teaching missions.

The PhD is an opportunity to travel and acquire new data. Several people have allowed me to undertake these trips and for this, I would like to thank them. First of all, a huge thank you to Lionel Hautier and Frédéric Delsuc, from the *Institut des Sciences de l'Evolution Montpellier*, for allowing me to use their dataset on several extant armadillos for my PhD. Many thanks to Laureano Gonzalez Ruiz, from the *Universidad Nacional de la Patagonia*, for

ACKNOWLEDGEMENTS

allowing me to use his magnificent dataset composed mainly of fossil armadillos. I would also like to thank Adrienne Stroup and Ken Angielczyk of the Field Museum of Natural History in Chicago and Zhe Xi Luo of the University of Chicago for allowing me to work on a pampathere. Thanks to Eli Amson, from the *Museum für Naturkunde* in Berlin, for scanning several specimens of *Zaedyus* and *Cabassous* and sending them to me for study. Thanks to Pepijn Kamminga, Rob Langelaan and Arjen Speksnijder, from the Naturalis Center Biodiversity in Leiden, for sending me one of the rare juvenile specimens of *Cabassous unicinctus* present in European collections. Thanks to Roberto Portela Miguez, from the Natural History Museum in London, for allowing me to scan several specimens of extant armadillos. Thanks to Eleanor Hoeger, Neil Duncan, and especially Marisa Surovy of the American Museum of Natural History, for allowing me to scan several specimens of *Zaedyus* and *Cabassous*. Thank you also for arranging the shipment of the specimens. Thanks also to Alice Cibois and Manuel Ruedi, from the *Museum d'Histoire Naturelle de Genève*, for allowing me to scan several of their extant armadillo specimens. Many thanks to Daniel Brinkman of the Yale Peabody Museum in New Haven for allowing me to visit their collection. Thanks also for his kindness and exemplary hospitality. Finally, thanks to Soledad De Esteban-Trivigno of the *Institut Català de Paleontologia M. Crusafont* and Chris Klingenberg of the University of Manchester for allowing me to follow a course on integration and modularity in Sabadell which was very useful during this PhD. I would also like to thank Doctoral School 227 of the *Muséum national d'Histoire naturelle* and the *Société des amis du Muséum* for funding a large portion of my data acquisitions.

I would also like to thank my colleagues who are co-authors for the versions of this research published or in preparation, without whom this work would never have seen the light of day. Thanks to Laureano for his kindness, friendship and interesting discussions on the diversity of cingulates. Thank you to Jérémie Bardin and Sylvain Gerber for having worked on the morphological integration with Guillaume and me. Thank you for our many discussions and for your help and support in all our studies. Special thanks to Jérémie who helped me with the R scripts with which I was not at all familiar. Thanks to Eli Amson for his discussions and pertinent remarks. Thanks to Frédéric Delsuc for his very interesting remarks and discussions, especially on the diversity of the extant groups. Huge thanks to Sergio Ferreira-Cardoso and Lionel Hautier. Thank you for your warm welcome in Montpellier, your help with the specimens to be scanned and your very enriching discussions. Many thanks to Sergio and his

ACKNOWLEDGEMENTS

partner Laura for hosting me during my missions. To all of you, I convey my most sincere gratitude and friendship.

My thanks also go to all my other friends and colleagues in Paris, Montpellier, Fribourg and other places. From students to retirees, in and out of science, while I cannot mention everyone by name, I would like to thank them all for their unfailing friendship, passionate discussions, help and support for the various aspects of my PhD and personal life. Thank you to them for being faithful companions during these three years of my life and for believing in me.

Special thanks to Sandrine Ladevèze and Floréal Solé. It has been five years since we crossed paths on the winding university roads that lead students to meet their supervisors. And since then, a deep friendship has linked us. I thank them for helping me whenever they could, for their friendship, for their proofreading and for the projects they have involved me in, which have never ceased to multiply. The latter have notably allowed me not to sink completely into the subject of my PhD, but also to grow intellectually through other studies.

I would like to thank my roommates, who are my lifelong friends. It has been a privilege for me to spend a large part of these three years with them. There were ups and downs. It is not always easy to share one's daily life. But they were always there through the worst and the best times. I will be eternally grateful to them for that. Thank you, Lionel and Maxime. I would like to thank especially Maxime, who allowed me to use his computer during the lockdown thus saving my PhD.

I would like to thank my father, mother, brother, and sister. Without them, I would not be where I am today. They never questioned my professional choices, trying at all costs to bring the best to our family. Despite all the difficulties, they are an immense support to me. I thank them from the bottom of my heart.

Finally, my gratitude goes to Olivia, my partner. Without her, none of this would have been possible. She was always by my side, no matter what it cost, helping me with all the events of my life, both personal and professional. Her patience, kindness, and love were a solid foundation for me. Even if life has separated us geographically, multiplying emotions tenfold, she was always close to me. Olivia, I will never find the words to tell you how grateful I am to you. Thank you so much.

Table of Contents

INTRODUCTION.....11

CHAPTER 1: CINGULATA, A CASE STUDY IN MAMMALIAN PHYLOGENY

1.1 Extant and extinct diversity of Cingulata

1.1.1 *Who are the Cingulata?*.....15

1.1.2 *What about past diversity?*.....17

1.1.3 *The Special Case of Glyptodonts*.....21

1.2 Systematics and phylogenetic issues on cingulates

1.2.1 *The place of Xenarthra in mammals*.....23

1.2.2 *Systematics and phylogenetics of the Cingulata*.....23

1.2.3 *The special case of the Glyptodonts*.....27

1.3 Anatomy and Covariation Patterns on the Cingulate Skull: State of the Art

1.3.1 *External and Internal Anatomy in Cingulata*.....29

1.3.2 *Morphology, phylogeny, and covariation pattern in the cingulate skull*.....30

CHAPTER 2: NEW INSIGHTS FROM INTERNAL ANATOMY

Section 2. Comparative anatomy and phylogenetic contribution of internal cranial structures in extant armadillos and extinct glyptodonts (*Xenarthra*, *Cingulata*)

2.1 Introduction.....36

2.2 Materials and methods.....38

2.2.1 *Sampling*38

2.2.2 *Selected regions of interest and anatomical nomenclature*.....38

2.2.3 *Virtual reconstruction of the selected regions*41

2.2.4 *Measurements*.....42

2.2.5 *Reconstructing evolutionary scenarios for intracranial traits*.....42

2.2.6 *Institutional Abbreviations*.....44

2.3 Results – anatomical description and comparison.....44

2.3.1 *Teeth and Alveolar Cavities – Orientation, Curvature and Height*.....44

2.3.2 *Cranial Canals*.....50

2.3.3 *Inclination of the cranial roof*.....65

2.4 Discussion.....66

CHAPTER 3: CRANIAL ALLOMETRY IN CINGULATA

Section	3.1	<i>Ontogenetic and static allometry in the skull and cranial units of nine-banded armadillos (Cingulata: Dasypodidae: Dasypus novemcinctus)</i>	
3.1.1	Introduction		78
3.1.2	Material and methods		80
3.1.2.1	<i>Sampling</i>		80
3.1.2.2	<i>Geometric morphometrics</i>		81
3.1.2.3	<i>Determination of ontogenetic stages</i>		84
3.1.2.4	<i>Ontogenetic and static allometry</i>		84
3.1.2.5	<i>Common allometry among morphotypes</i>		86
3.1.2.6	<i>Common allometry between ontogenetic stages</i>		86
3.1.3	Results		87
3.1.3.1	<i>Allometry and geography</i>		87
3.1.3.2	<i>Allometric variations on the entire skull (ES)</i>		89
3.1.3.3	<i>Allometric variations studied bone by bone (3B)</i>		90
3.1.3.4	<i>Allometry at different stages</i>		99
3.1.3.5	<i>Size variation per OBU and allometry</i>		102
3.1.4	Discussion		102
3.1.4.1	<i>Allometric and geographical interaction</i>		102
3.1.4.2	<i>Main allometric variations</i>		103
3.1.4.3	<i>Heterogeneity of cranial allometry in space and time</i>		106
Section	3.2	<i>Comparative study of cranial allometry in Cingulata</i>	
3.2.1	Introduction		110
3.2.2	Material & methods		112
3.2.2.1	<i>Intraspecific Sampling</i>		112
3.2.2.2	<i>Interspecific Sampling</i>		113
3.2.2.3	<i>Correction of taphonomic deformations</i>		114
3.2.2.4	<i>Geometric Morphometrics</i>		114
3.2.2.5	<i>Determination of ontogenetic stages</i>		116
3.2.2.6	<i>Phylogenetically-informed analyses</i>		117
3.2.2.7	<i>Allometric analyses</i>		117
3.2.3	Results		118
3.2.3.1	<i>Allometric variations in the intraspecific samples</i>		118
3.2.3.1.1	<i>Allometric variations on the entire skull (ES) in <i>Zaedyus pichiy</i></i>		118
3.2.3.1.2	<i>Allometric variations on the entire skull (ES) in <i>Cabassous</i> datasets</i>		121
3.2.3.1.3	<i>Allometric variations studied Bone By Bone (3B) in <i>Zaedyus</i> and <i>Cabassous</i></i>		123
3.2.3.2	<i>Allometric variations in the interspecific datasets</i>		144
3.2.3.2.1	<i>Allometric variations on the entire skull (ES) at the evolutionary level</i>		144
3.2.3.2.2	<i>Allometric variations studied Bone By Bone (3B) at the evolutionary level</i>		149
3.2.4	Discussion		161
3.2.4.1	<i>Common allometric pattern in Entire Skull (ES)</i>		161
3.2.4.2	<i>Allometric proportions of cranial shape variation in Cingulata</i>		165
3.2.4.3	<i>Common Allometric Pattern in Cranial Units</i>		166
3.2.4.4	<i>Improvement and perspectives</i>		167

CHAPTER 4: EXPLORATION OF CRANIAL COVARIATION PATTERN IN CINGULATA

Section	4.1	<i>An exploration of the strongest covariations among cranial distances in Cingulata</i>	
4.1.1	Introduction		171
4.1.2	Material and methods		173
4.1.2.1	<i>Biological sample</i>		173
4.1.2.2	<i>Geometric morphometrics</i>		174
4.1.2.3	<i>Size standardization</i>		174
4.1.2.4	<i>Selection of pairs of correlated standardized distances</i>		175
4.1.3	Results		177
4.1.3.1	<i>Selected pairs of correlated S-distances and R-distances common to all three species (DZC)</i>		177
4.1.3.2	<i>Selected pairs of correlated S-distances and R-distances common to Zaedyus and Cabassous (ZC)</i>		186
4.1.3.3	<i>Testing the selected pairs of correlated distances at the evolutionary level</i>		191
4.1.4	Discussion		198
4.1.4.1	<i>Methodological considerations</i>		198
4.1.4.2	<i>Shared cranial covariations in cingulates</i>		198
Section	4.2	<i>Cranial modularity in Cingulata</i>	
4.2.1	Introduction		204
4.2.2	Material & Methods		205
4.2.2.1	<i>Biological sample</i>		205
4.2.2.2	<i>Geometric morphometrics</i>		205
4.2.2.3	<i>Analyses of modularity</i>		206
4.2.3.1	Results		207
4.2.3.1.1	<i>Number of modules</i>		207
4.2.3.1.2	<i>Modular mapping in the three armadillo species</i>		209
4.2.4	Discussion		212
Section	4.3	<i>3D Cranial Shape Variation in Cingulata</i>	
4.3.1	Introduction		215
4.3.2	Material & Methods		216
4.3.2.1	<i>Biological sample</i>		216
4.3.2.2	<i>Correction of taphonomic deformations</i>		217
4.3.2.3	<i>Geometric morphometrics</i>		217
4.3.2.4	<i>Phylogenetic considerations</i>		217
4.3.2.5	<i>Shape variation</i>		218
4.3.3	Results		219
4.3.3.1	<i>Only extant species</i>		220
4.3.3.2	<i>Extant and Fossils Best Sample</i>		222
4.3.3.3	<i>Intramodular Morphological variation</i>		222

TABLE OF CONTENTS

CHAPTER 5: GENERAL DISCUSSION AND CONCLUSION

5.	General Discussion and Conclusion	231
5.1	<i>Limitation of taxonomic data and sampling</i>	231
5.2	<i>Potential implications of internal anatomy and morphological integration on morphological matrices in cingulates</i>	235
5.3	<i>Complexity of morphological variation, limitations, and prospects</i>	251
REFERENCES		258
APPENDICES		283
ABSTRACT		395

INTRODUCTION

Morphological variation is a pervasive biological phenomenon, which has long inspired naturalists and led them to propose classifications of organisms based on observed similarities and differences. From [Linnæus \(1758\)](#) to the present day, biologists have never ceased to study the patterns produced by this variation and the processes that are its source. However, the more we examine morphological variation, the more we discover its extreme complexity. In recent decades, the use of morphological variation as a source of traits for phylogenetic analyses has been strongly questioned, despite the primacy of these data for the study of extinct taxa inaccessible to molecular analyses ([Wiens, 2004](#); [Asher *et al.*, 2008](#); [Springer *et al.*, 2008](#)). This primacy of morphological data for reconstructing relationships of extinct forms is hampered by critical assessments of its performance, particularly for analyses of interordinal relationships within placental mammals ([Scotland *et al.*, 2003](#); [Springer *et al.*, 2008, 2013](#)). This observation is in line with the fact that many studies have called for an improvement of our phylogenetic methods using morphology (*e.g.*, [Dávalos *et al.*, 2014](#); [Goswami *et al.*, 2014](#); [Billet *et al.*, 2015a](#); [Harrison & Larsson, 2015](#); [Lee & Palci, 2015](#); [Pyron, 2015](#); [Wright *et al.*, 2016](#); [Bardin *et al.*, 2017](#); [Billet & Bardin, 2019](#)). Efforts towards that goal must include a broader exploration of patterns of morphological variation and a better identification of the covariation among traits, as frequently underlined by these studies.

Cingulates are a group of placental mammals that belong to the superorder Xenarthra together with anteaters and sloths. The Cingulata includes the extant armadillos and extinct taxa such as glyptodonts. This clade represents an ideal case study for the exploration of morphological variation in a phylogenetic context. Their modest extant diversity permits a detailed exploration of the entire group, whereas their past diversity, exhibiting cranial shapes very unusual in mammals ([Superina & Loughry, 2015](#)), offers a wide range of investigations. The major interest of this group for the subject treated in the present work lies in the lack of congruence between phylogenetic analyses using morphological versus molecular data (not at all level). The recent incorporation of a glyptodont's mitogenome in molecular analyses has clearly revealed these incongruences ([Delsuc *et al.*, 2016](#); [Mitchell *et al.*, 2016](#)). In this context, we propose to explore patterns of morphological variation of the skull within the Cingulata

using different perspectives and to discuss the possible impact of our findings on the phylogenetic reconstructions proposed for the group.

In a first step ([Chapter 1](#)), we introduce the Cingulata group by specifying the state of the art concerning their taxonomic diversity and by summarizing all the existing hypotheses on their phylogenetic relationships. This overview enables us to highlight the lack of consensus among these hypotheses, and to underline gaps in our morphological knowledge of the group, especially with regard to internal anatomy and integration patterns (= tendency of traits to covary) of the skull. We show that an exploration of these two aspects will be useful to complete morphological matrices used in phylogenetic analysis but also to better understand the existing covariations among several anatomical structures and characters that can mislead morphological phylogenetics.

Our work starts with an in-depth study of the internal anatomy of the skull of the Cingulata, demonstrating that these poorly known structures can deliver new phylogenetic information ([Chapter 2](#)). This exploration allows us to complement our existing anatomical knowledge of the skull of cingulates and to highlight new characters, which can be incorporated to the existing matrices, with a signal focused on the position of the glyptodonts. We discuss the evolutionary scenarios corresponding to these new characters and their congruence with current phylogenetic hypotheses concerning the group.

The next part of our work explores the morphological integration of the cingulate skull in two steps ([Chapters 3 & 4](#)). We first focus on one of the most powerful factors responsible for morphological integration known in mammals, allometry, in order to target cranial covariation patterns related to size variation ([Chapter 3](#)). Our work on this aspect starts with an exploratory approach on one of the best sampled cingulate species, the nine-banded armadillo (*Dasypus novemcinctus* [Linnaeus, 1758](#)). It enables us to identify allometric patterns in this species at two scales – the entire skull and cranial subunits – and at two levels of integration – the static and ontogenetic levels. Based on this exploratory study, we test the existence of similar allometric patterns in two other extant and distantly related species of cingulates with the same approach. All these patterns are then compared to an evolutionary analysis of allometry gathering most extant cingulate species and most of the emblematic fossil groups (with a focus on glyptodonts). This comparison makes it possible to determine if certain allometric patterns detected at the species level were at play during the evolution of cingulates.

This last analysis highlights several covariations between the size and shape of the skull that seem to be present across the whole group.

The second step in our investigation of morphological integration is represented by an in-depth study of the strongest covariations among cranial linear distances in the three armadillo species initially sampled for allometry (Chapter 4). Our selective exploration of pairs of covarying distances highlight strong cranial correlations not detected in our previous study on allometry. The patterns obtained in the three species are then analyzed at the evolutionary level to identify whether these covariations were also present in the morphological evolution of the group. This new approach was then complemented by an analysis of cranial modularity without *a priori* about the possible modules in the three armadillo species – modularity “*exists if integration is concentrated within certain parts or regions of a structure, the modules, but is relatively weak between these modules*” (Klingenberg, 2014: pp. 2). This analysis reveals a partitioning of the integration into three anteroposteriorly distributed modules of the skull. In a complementary way, we carry out the very first exploration of the variations of cingulate cranial shape at the evolutionary level, using the modules detected at the preceding step, which allows us to cover a larger scope of potential covariations.

Finally, the implications of these studies are briefly discussed in a general conclusion (Chapter 5) regarding the already existing phylogenetic hypotheses and the cranial characters used in the matrices. Our results on cranial integration are compared with existing matrices and phylogenetic analyses in order to identify possible groups of traits that may covary and to discuss their impact on the phylogenetic reconstruction within the group. This exploratory work emphasizes the necessity to better understand the complexity of morphological variation in order to make progress in our phylogenetic investigations of extinct taxa.

CHAPTER 1

Cingulata, a Case Study in Mammalian Phylogeny

« Tous les tatous sont originaires de l'Amérique ; ils étaient inconnus avant la découverte du nouveau monde, les anciens n'en ont jamais fait mention ».

Buffon. 1753. Quadrupède. Tome IV: p. 115.

“All armadillos originate from America; they were unknown before the discovery of the new world, the ancients never mentioned them”.

Buffon. 1753. Quadrupède. Tome IV: p. 115. Translated.

1.1 Extant and extinct diversity of Cingulata

1.1.1 Who are the Cingulata?

The Cingulata, which comprise all extant armadillos and a rich fossil diversity, correspond to one of the 21 orders of placental mammal (Wilson *et al.*, 2018). In Latin, this term means "*the girdled ones*", which emphasizes the main characteristic of the group, *i.e.* the presence of a bony carapace made of osteoderms covering the head, body and tail (most often mobile), a unique feature within mammals (McDonald, 2003). Earlier classifications grouped cingulates with sloths, anteaters, pangolins, and aardvarks in the super-order Edentata based on their reduction in dental complexity (Cuvier, 1798; see Gunnell & Rose, 2008 for a summary of the group). It is only at the end of the 19th century, following an earlier suggestion by Flower (1882), that armadillos were gathered within the same group with sloths and anteaters: the Xenarthra Cope, 1889 (etymology: strange articulation). The monophyly of the Xenarthra is still supported today, and they constitute one of the four major clades of extant placental mammals (Zachos, 2020; see Section 1.2).

The extant Cingulata are composed of 21 extant species of armadillos grouped in nine genera and two families (Gardner, 2005; McDonough & Loughry, 2018; Superina & Abba, 2018) (Figure 1). Traditionally, all extant species were included in the same family: the Dasypodidae (*e.g.*, Simpson, 1945). Recent molecular studies incorporating extinct glyptodonts, and the accompanying newly proposed phylogenies, have questioned the existence of a single family, leading Delsuc *et al.* (2016) to define two families for the extant diversity of armadillos: the Dasypodidae including the clade Dasypodinae (Figure 1) and the Chlamyphoridae including the other three extant clades Euphractinae, Chlamyphorinae and Tolypeutinae (Figure 1)¹.

¹ In their discussion Gaudin & Lyon (2017) explain that this proposition is not the most consistent with what is known about fossil diversity. They propose to raise all sub-families to the family level for greater consistency. Here, we will follow the nomenclature of Delsuc *et al.* (2016) to facilitate comparisons between molecular and morpho-anatomical analyses and not to confuse discussions regarding previous works. Because of this choice, the fossil families will be readjusted to the subfamily rank if they are included within the Dasypodidae or Chlamyphoridae, as advocated by Delsuc *et al.* (2016).

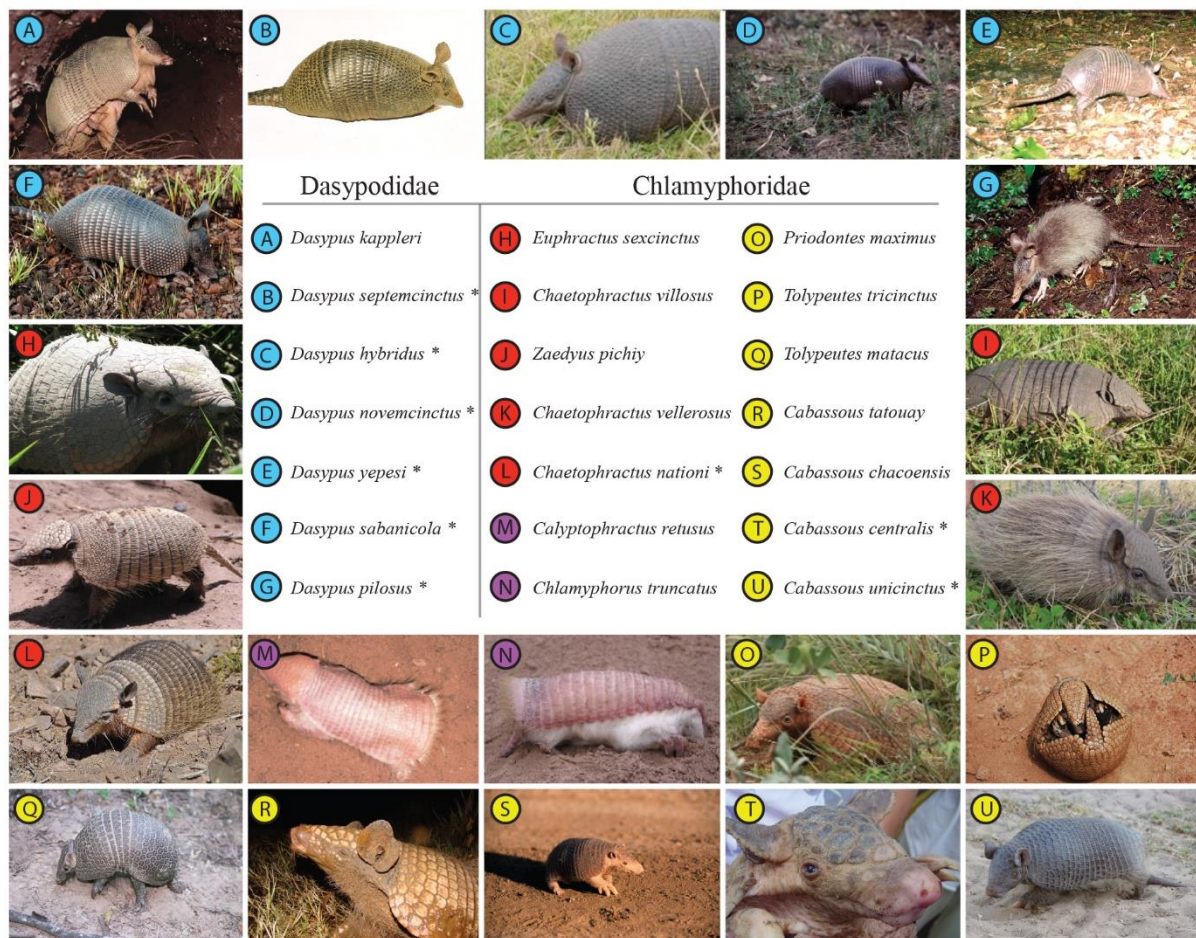


Figure 1. Mosaic of extant cingulate species with details of their taxonomic affiliation based on recent molecular analyses (Delsuc *et al.*, 2016; Gibb *et al.*, 2016; Mitchell *et al.*, 2016). The family Dasypodidae contains 7 extant species all attributed to the clade Dasypodinae (in blue). The family Chlamyphoridae contains 14 extant species distributed within three clades: Euphractinae (in red); Chlamyphorinae (in purple) and Tolypeutinae (in yellow). The colors chosen follow Mitchell *et al.* (2016), as for the rest of the manuscript. Specimens marked with an asterisk (*) correspond to species whose status is currently under discussion (see Chapter 3 & Supporting Information 1). The photographs are from the International Union for Conservation of Nature (= IUCN) website except for *C. nationi* from Mount Salvation Salton Sea (© Carol Milligan) and *D. kappleri* from Aya-Cuero *et al.* (2019).

Extant cingulates are omnivorous or insectivorous (see Gaudin & Croft, 2015) but also include some more specialized species such as the myrmecophagous giant armadillo – *Priodontes maximus* Kerr, 1792 (Desbiez *et al.*, 2020). Their weight varies between a few hundred grams (*Calyptophractus retusus* Burmeister, 1863) to about fifty kilos (*Priodontes maximus*). Together with other xenarthrans, armadillos most likely originated in South America (Vizcaíno & Loughry, 2008; see more specifically Aguiar & Fonseca, 2008, for extant species) and most of their subsequent evolution took place on this continent (the so-called "Splendid Isolation" of Simpson, 1980). Due to their long endemic evolution in South America and their unique characters (*e.g.*, bony carapace), they are often regarded as morphologically exotic in comparison to Old World placental mammals (Superina & Loughry, 2015). It is only with the

formation of the Isthmus of Panama, about 2.8 Ma, that one can find remains of cingulates outside the South American continent (Gilette & Ray, 1981; Carranza-Castañeda & Miller, 2004; Zurita *et al.*, 2011). Today, only one species of armadillo is present much further in the north, as far as the United States, due to its northern migration that began 200 years ago – the nine-banded armadillo, *Dasypus novemcinctus* (Taulman & Robbins, 1996). Although they currently represent the most diverse group within the xenarthrans, extant armadillos only represent a reduced portion of the great past diversity of cingulates.

1.1.2 What about past diversity?

The first xenarthran remains date back to approximately 55 Ma and correspond to osteoderm fragments and postcranial remains from Itaborai, Brazil (Bergqvist *et al.*, 2004; Gaudin & Croft, 2015). To date, there are almost 200 described genera referred to Xenarthra in the fossil record, a large proportion of which belong to the Cingulata (more than 100; McKenna & Bell, 1997) probably due to a preservational bias in favor of osteodermal remains. Traditionally (*e.g.*, Simpson, 1945), most extant and extinct Cingulata were classified in two different families, marking a strong dichotomy in their morphological appearance: the Dasypodidae and the extinct Glyptodontidae (Figures 2, 3 & 4 – see below for their updated systematics; and see Figure 1 and Section 1.2). The Glyptodontidae (= Glyptodontinae in our manuscript; see below) included the extinct glyptodonts (Figure 2D), a group of large cingulates defined by Owen (1839) whose name means "engraved tooth" (see Section 1.1.3 for their characteristic) (Fericola, 2008). The Dasypodidae included extant taxa and extinct forms (Figure 2B) closer to armadillos than glyptodonts in the old nomenclature. An additional extinct family of uncertain taxonomic affinities was the Peltephilidae (Figure 2A). Several extinct clades belong to the Cingulata, such as the enigmatic Pachyarmatheriinae and Palaeopeltinae (Fericola *et al.*, 2017). The extinct Pamphateriinae (Figure 2C) were first considered to belong to the Dasypodidae (Simpson, 1930) although Paula Couto (1954) proposed that this sub-family be raised to the family level. They are now considered to be very closely related to glyptodonts (Patterson & Pascual, 1972; Gaudin & Wible, 2006; Billet *et al.*, 2011; Gaudin & Lyon, 2017). Pamphateres and glyptodonts are considered herbivores (Vizcaíno *et al.*, 2006, 2012a) whereas most other fossil taxa tend to have a diet similar to modern forms, except for *Macroeuphractus Ameghino, 1887* for which a carnivorous diet is assumed (Vizcaíno & De Iuliis, 2003). The pamphateres and glyptodonts also stand out from other cingulates due to their larger body mass,

which could reach up to 250 kg and over 2 tons respectively (Vizcaíno *et al.*, 2011; Vizcaíno *et al.*, 2012a; Delsuc *et al.*, 2016).

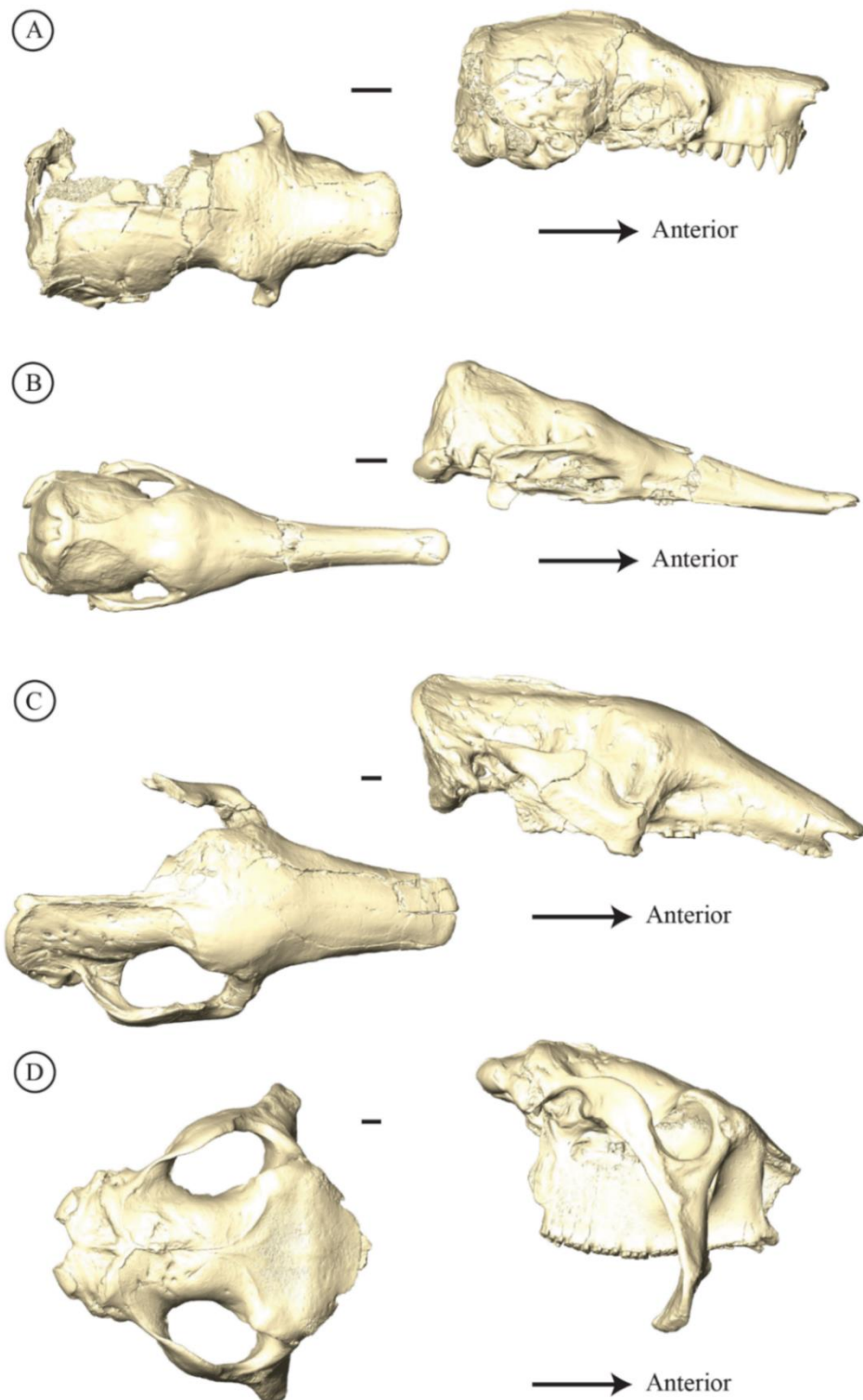


Figure 2. 3D model plate illustrating the skulls of extinct specimens of different families of living and extinct Cingulata. A) *Peltephilus pumilus* Ameghino, 1887 (Miocene, Santacrucian SALMA – peltephilid). B) *Stegotherium tauberi* Ameghino, 1887 (Santacrucian – dasypodine). C) *Vassallia maxima* Castellanos, 1946 (Miocene/Pliocene, Montehermosan SALMA – pamphathere). D) *Glyptodon* sp. Owen, 1839 (Pleistocene, Lujanian SALMA – glyptodont). Scale = 2 cm.

Cingulates were mainly represented by osteoderms in the South American fossil record and the oldest sub-complete skulls for most groups date back to the Oligocene at best (Figure 3 – Gaudin & Croft, 2015). Among the oldest cingulate cranial remains, an incomplete portion of caudal cranium is known for *Utaetus buccatus* Ameghino, 1902 (Simpson, 1948), of uncertain phylogenetic affinities, from the Middle Eocene of Patagonia (Barrancan subage – Gaudin & Croft, 2015). Partial cranial remains of cingulates were also documented from the middle Eocene of northern Argentina (Vacan subage – Herrera *et al.*, 2017) and from the early Oligocene of Chile (Tinguirirican subage – Carlini *et al.*, 2009) (Figure 3). More complete skulls were reported from the Upper Oligocene Beds of Salla, Bolivia, for the tolypeutines (*Kuntinaru boliviensis* Billet, Hautier, Muizon & Valentin, 2011) and peltephilids (Shockey & Vlachos, 2017). As regards glyptodonts, the earliest well-preserved cranial remains are known from the early Miocene of the Santa Cruz Formation in Argentina *i.e.* more than 20 Ma later than the first partial skull of dasypodines (Figure 3). These correspond to well-preserved complete skulls (Scott, 1903) (Figure 4A-D). The 16-17 Ma old Santa Cruz Formation, which also delivered complete skulls for other cingulate taxa, probably provided one of the most complete glimpses into the past evolutionary history of cingulates, both anatomically and taxonomically (González-Ruiz, 2010; Vizcaíno *et al.*, 2012b). Finally, the oldest skulls of pampatheres date from the middle Miocene (De Iuliis & Edmund, 2002; Gaudin & Croft, 2015; Gaudin & Lyon, 2017). For the pachyarmatheres, only the postcranial remains and osteoderms are known, dating back to the middle Miocene period (Madden *et al.*, 1997; Cozzuol, 2006; Laurito & Valerio, 2012; Fernicola *et al.*, 2017). For palaeopeltines, their taxonomic validity is much debated and, to our knowledge, this group is not represented by available cranial remains but only by a multitude of osteodermal remains that could not be assigned to other families (pers. com. Laureano González-Ruiz). A skull was described by Kraglievich & Rivas (1951) but has been lost since.

Although the earliest remains are relatively rare for most of these fossil groups, late Miocene through Pleistocene remains are particularly abundant in comparison (except for peltephilids). All these fossil specimens testify to the existence of a great past diversity for the Cingulata. This taxonomic diversity is accompanied by a great variety of cranial shapes ranging from the elongated snout of the small dasypodines (*e.g.*, Figure 2B) to the giant cubical skulls of Pleistocene glyptodonts (*e.g.*, Figures 2D & 4E).

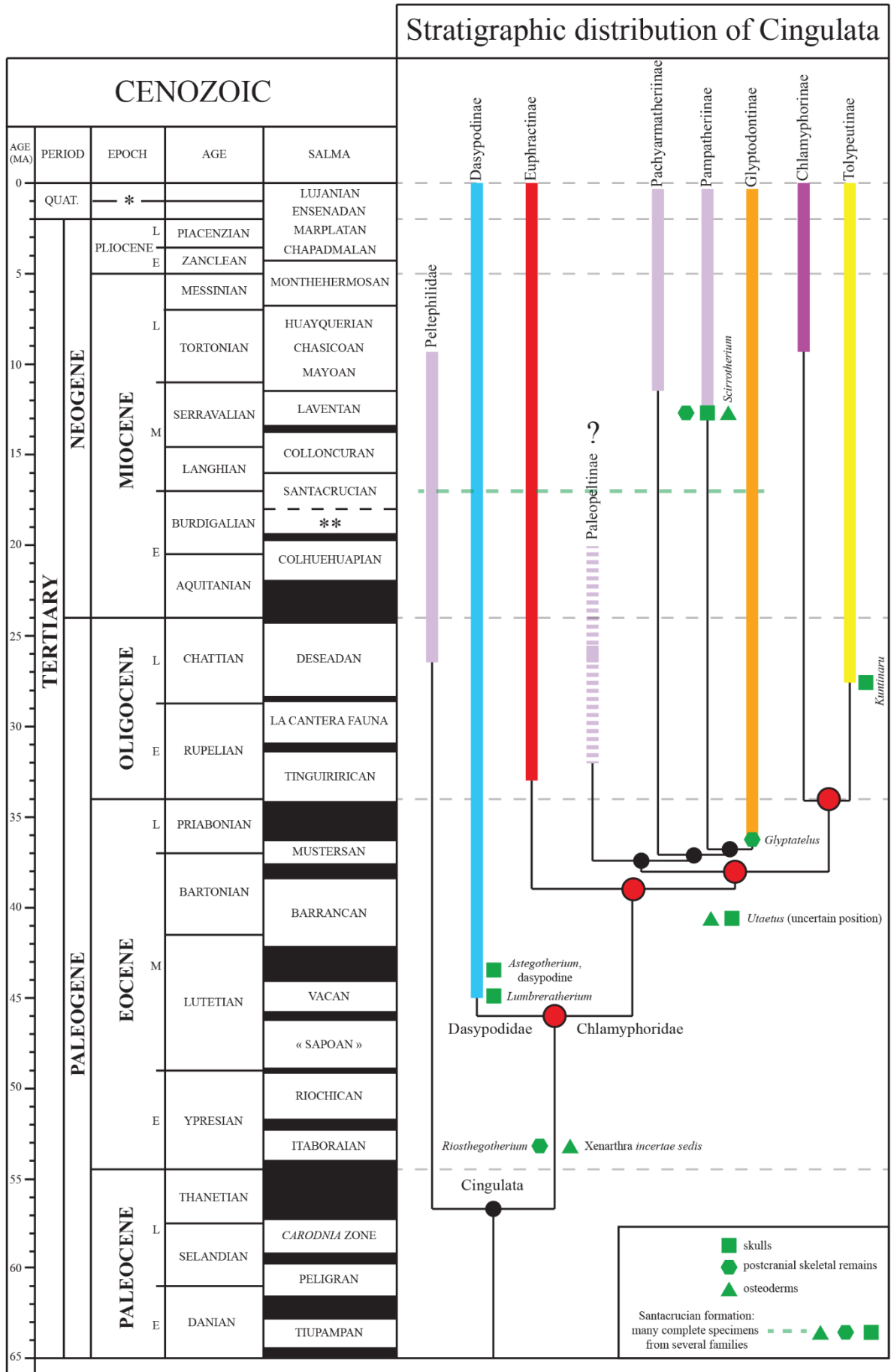


Figure 3. Temporal distribution of each major group inspired by Gaudin & Croft (2015) with Cenozoic SALMAs (= South American Land Mammal Ages - based on Woodburne *et al.*, 2014) and indication of earliest remains for each quoted group (inspired by Gaudin & Croft, 2015). The phylogenetic relationships are based on recent molecular analyses (Delsuc *et al.*, 2016; Mitchell *et al.*, 2016) to which have been added the potential phylogenetic positions of each fossil taxa (peltephilids and pampatheres from Gaudin & Wible, 2006; Billet *et al.*, 2011; Gaudin & Lyon, 2017; pachyarmatheres from Fernicola *et al.*, 2017; palaeopeltines from Perea *et al.*, 2014). The stratigraphic distribution is based on the oldest occurrences for each group (Pascual *et al.*, 1996; Edmund & Theodor, 1997; Carlini *et al.*, 2009; Billet *et al.*, 2011; Fernicola *et al.*, 2017; Herrera *et al.*, 2017; Shockey & Vlachos, 2017; Barasoain *et al.*, 2020). The red nodes correspond to the molecular dating of Delsuc *et al.* (2016). Those in black are not dated. The taxonomic nomenclature used corresponds to the proposition of Delsuc *et al.* (2016). The taxonomic level of fossil taxa has been adapted accordingly. For more details on this nomenclature see Section 1.2. Abbreviations: Quat., Quaternary. Symbols: *, Pleistocene then Holocene; **, *Notohippus* zone.

1.1.3 *The Special Case of Glyptodonts*

Glyptodonts are a group of large herbivorous cingulates whose body mass varied from 80 kg at the end of the lower Miocene up to several tons for the last representatives of the Pleistocene (Vizcaíno *et al.*, 2011). Glyptodont remains are very abundant in the fossil record of South America during the Cenozoic (from the late Eocene onwards) but also in southern North America during the Pleistocene (Gillette & Ray, 1981). Glyptodonts have several autapomorphic characters including a thickened essentially immobile dorsal carapace, a variable number of tri-lobed teeth, elephantine limbs, and a telescopic chewing apparatus under the skull (Hoffstetter, 1958; Fariña & Vizcaíno, 2001; Fernicola, 2008). Their first representative, *Glyptatelus* Ameghino, 1897, is documented by osteoderms from the middle/late Eocene of Patagonia in Argentina (Scillato-Yané, 1976), which could be compatible with molecular estimates for their origin (35 ± 3 Ma – Delsuc *et al.*, 2016). Glyptodonts survived until the beginning of the Holocene in South America (Messineo & Politis, 2009) (Figure 3).

As noted above, no complete glyptodont skull is known from the Paleogene. The Santa Cruz Formation of Patagonia yielded the earliest well-preserved glyptodont crania, all of modest size (Figure 4A-D). Many remains were discovered for later glyptodonts increasing the diversity of the group to more than 65 genera (McKenna & Bell, 1997) and showing a trend towards gigantism and graviportal limbs (Vizcaíno & Bargo, 1998; Soibelzon *et al.*, 2010; Cione *et al.*, 2015; Mitchell *et al.*, 2016) (Figure 4). Although all glyptodonts have a distinctive cranial shape relative to other cingulates (*i.e.*, "broad, deep and almost cubical skull", Scott, 1903: pp. 5), comparisons among glyptodont specimens from the lower Miocene and more recent taxa show strong differences in many respects (*e.g.*, Scott, 1903), which warrants further

study. Moreover, because of their very distinctive anatomy, the phylogenetic position of glyptodonts within Cingulata has been heavily debated (see below).

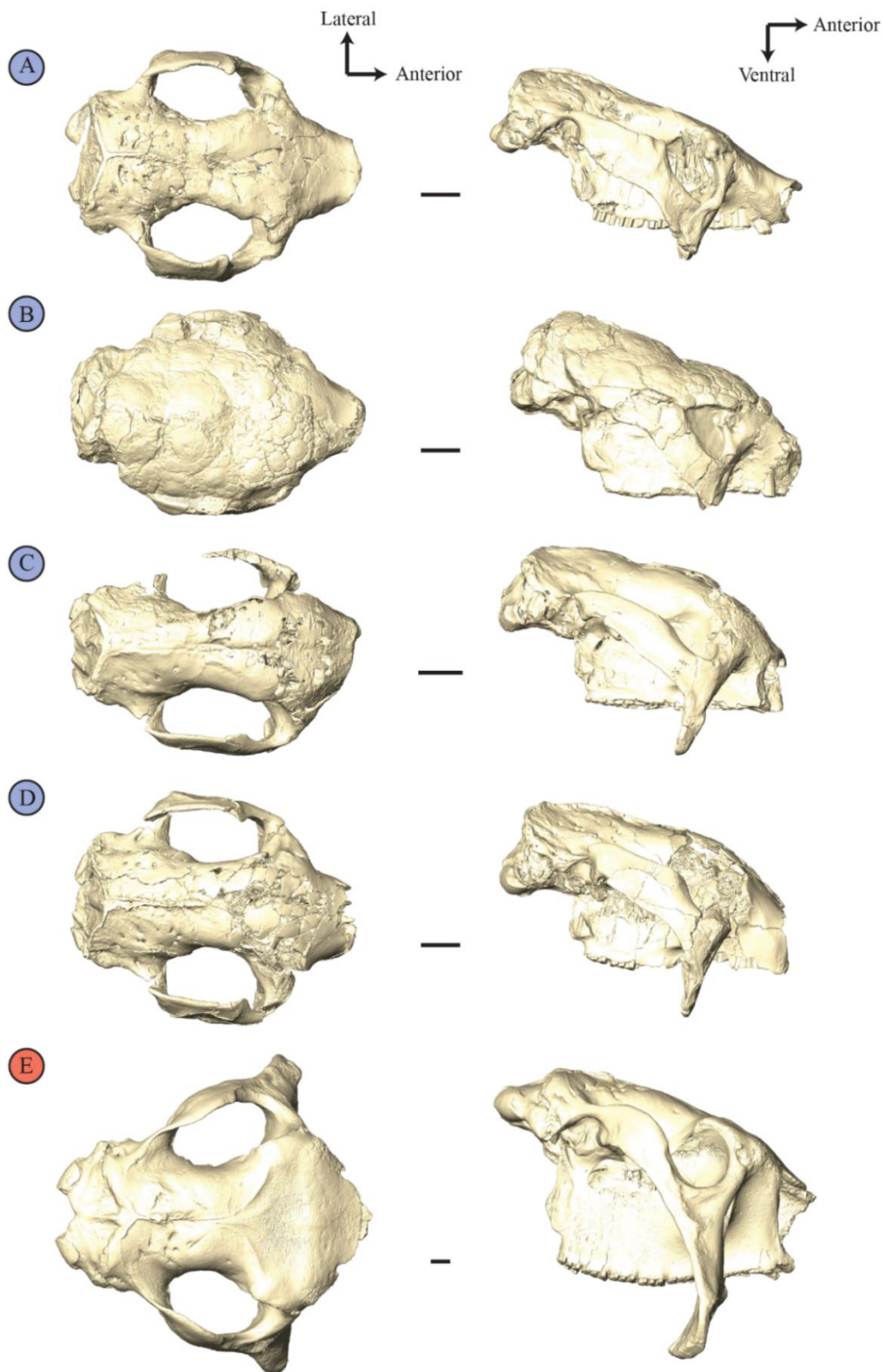


Figure 4. 3D model plate illustrating the skulls of extinct specimens of different families of Cingulata. A) *Eucinepeltus complicatus* Ameghino, 1891 (Miocene, Santacrucian SALMA). B) “*Cochlops*” *debilis* Ameghino, 1891 (Santacrucian). C) “*Metopotoxus*” *anceps* Scott, 1903 (Santacrucian). D) *Propalaeohoplophorus minus* Ameghino, 1891 (Santacrucian). E) *Glyptodon* sp. (Pleistocene, Lujanian SALMA). Scale = 2 cm.

1.2 Systematics and phylogenetic issues on cingulates

1.2.1 *The place of Xenarthra in mammals*

Xenarthrans are nearly unanimously regarded as one of the four major clades of extant placental mammals today (e.g., Upham *et al.*, 2019; Zachos, 2020). It is the only one that is strongly supported by both molecular and morpho-anatomical data (discussed for Afrotheria - see Sánchez-Villagra *et al.*, 2007). Uncertainties remain regarding their exact position in the placental tree (Figure 5) and their date of origin (Zachos, 2020). There are 3 hypotheses regarding their relationship with the other three primary groups of placentals (= Afrotheria, Euarchontoglires, and Laurasiatheria) (Figure 5).

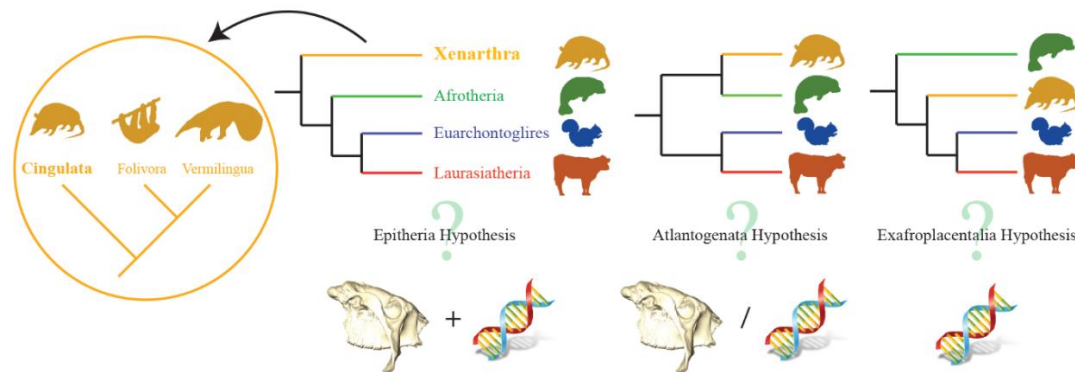


Figure 5. Illustration of the three current hypotheses concerning the relations between the 4 major placental clades: Xenarthra (= Cingulata, Folivora, Vermilingua); Afrotheria (= Proboscidea, Sirenia, Hyracoidea, Tubulidentata, Macroscelidea, Afrosoricida); Euarchontoglires (= Scandentia, Primates, Dermoptera, Rodentia, Lagomorpha); Laurasiatheria (= (Eu-)Lipotyphla, Chiroptera, Pholidota, Carnivora, (Cet-)Artiodactyla, Perissodactyla). The Epitheria hypothesis is the least broadly supported (e.g., O’Leary *et al.*, 2013 – phenomic and genomic data). The Atlantogenata and Exafroplacentalia hypotheses are more clearly supported by molecular analyses (e.g., Romiguier *et al.*, 2013; Tarver *et al.*, 2016 – for morphological data see Halliday *et al.*, 2017). In recent years, Atlantogenata hypothesis is favored (Tarver *et al.*, 2016; Esselstyn *et al.*, 2017; Zachos & Asher, 2018; Upham *et al.*, 2019). For a more extensive discussion of these hypotheses refer to Foley *et al.* (2016) and Zachos (2020).

1.2.2 *Systematics and phylogenetics of the Cingulata*

As for most taxa, our knowledge of the taxonomic composition of Cingulata and their phylogenetic relationships has changed through time. From the end of the 19th century to the present day, many hypotheses have been put forward about the relationships within and among extant and extinct cingulate groups. It was long difficult to find a strong signal and hence consensus on many aspects of the cingulate systematics and phylogeny before the advent of molecular phylogenetics.

The monophyly of the clades Dasypodinae and Chlamyphorinae has never been seriously questioned (Figure 6). However, this is not the case for the Tolypeutinae and Euphractinae for which some morpho-anatomical analyses questioned their monophyly as well as the relationships among their members (Engelmann, 1985; Gaudin & Wible, 2006 – Figure 6A, C), including in a recent contribution (Herrera *et al.*, 2017 – Figure 6F). In 2006, Abrantes & Bergqvist (Figure 6B) published a phylogenetic analysis based on postcranial material that supported a clade grouping dasypodines and tolypeutines and another one grouping chlamyphorines and euphractines (Figure 6B). In the same year, Gaudin & Wible (2006) performed an analysis based on craniodental characters grouping chlamyphorines and a paraphyletic version of euphractines; the tolypeutines were also paraphyletic in their study (Figure 6C). When their analysis was performed only on extant taxa, they recovered a monophyletic Euphractinae but not Tolypeutinae (Gaudin & Wible, 2006). Finally, Billet *et al.* (2011) revised the matrix of Gaudin & Wible (2006). Their results supported the monophyly of extant clades while still supporting a closer relationship between chlamyphorines and euphractines (Figure 6D). On the other hand, when their analysis was performed only on extant taxa, the monophyly of euphractines and tolypeutines was not confirmed (Figure S1). In summary, morpho-anatomical analyses did not provide clear support to the 4 extant clades and to their relationships as recovered in molecular analyses (Delsuc *et al.*, 2012, 2016; Abba *et al.*, 2015; Gibb *et al.*, 2016; Mitchell *et al.*, 2016 – Figure 6G, H).

Molecular analyses have brought to light additional questions about the diversity and systematics of extant cingulates. They have indicated that several species initially recognized on a morphological basis may in fact be considered a single species, such as *Chaetophractus nationi* Thomas, 1894 and *Chaetophractus vellerosus* Gray, 1865 [a proposition now confirmed by morpho-anatomical and molecular analyses within the euphractines (see Abba *et al.*, 2015) – for more details see Supporting Information 1]. A similar situation may exist between *Cabassous unicinctus* Linnæus, 1758 and *Cabassous centralis* Miller, 1899, (for more details see Supporting Information 1). Molecular analyses have also detected cases in which one species may actually correspond to a species complex, such as in the nine-banded armadillo (Huchon *et al.*, 1999; Gibb *et al.*, 2016; Arteaga *et al.*, 2020), *Dasypus novemcinctus*, which previously represented the extant armadillo species with the largest geographic distribution (McBee & Baker, 1982). Morpho-anatomical analyses have subsequently provided additional evidence for this novel hypothesis in nine-banded armadillos (Billet *et al.*, 2017; Hautier *et al.*, 2017; Feijó *et al.*, 2018, 2019). Many of these issues still need further work and clarification. This demonstrates that the systematics of extant cingulates is not yet fully understood. As

regards extinct cingulates, a large number of fossil specimens have been reported as potentially pertaining to the one of the extant clades (dasypodines, tolpeutines, euphractines, chlamyphorines) based on recent phylogenetic analyses using morphology (e.g., [Carlini et al., 2009](#); [Billet et al., 2011](#); [Herrera et al., 2017](#); [Barasoain et al., 2020](#)). However, an even greater number of extinct taxa have been associated with or included within the extinct glyptodonts (see below). Following the proposal of [Delsuc et al. \(2016\)](#) (see above), the systematics of Cingulata at the subfamily level could be represented as follows (the taxa not treated by these authors are defined at an adapted taxonomic rank and indicated by *):

CINGULATA

- Peltephilidae †
- Dasypodidae
 - Dasypodinae
- Chlamyphoridae
 - Euphractinae
 - *Palaeopeltinae? †
 - *Pachyarmatheriinae †
 - *Pampatheriinae †
 - Glyptodontinae †
 - Chlamyphorinae
 - Tolpeutinae

It is now generally accepted that peltephilids, with their very peculiar skull and dentition, represent the earliest-diverging family among cingulates (e.g., [Gaudin & Wible, 2006](#); [Shockey & Vlachos, 2017](#)) ([Figure 3](#)). Although they are poorly documented (see above), historical records concerning palaeopeltines consider them as potential distant relatives of the glyptodonts, or at least as members of the Cingulata ([Kraglievich & Rivas, 1951](#)). Pachyarmatheriinae is a clade proposed by [Fericola et al. \(2017\)](#) based on the results of a phylogenetic analysis using cranial and postcranial characters (whereas no skull is known in this family), and which links the genus *Pachyarmatherium* [Downing & White, 1995](#) and the genus *Neoglyptatelus* [Carlini, Vizcaíno & Scillato-Yané, 1997](#). The latter belonged to Glyptatelineae which were previously considered as the earliest diverging group of glyptodonts ([Carlini et al., 1997](#)). Therefore, like palaeopeltines, the pachyarmatheres might be closely related to glyptodonts ([Figure 3](#)). The same applies to pampatheres, which were either considered to be the ancestor of the glyptodonts ([Patterson & Pascual, 1972](#)) or their closest relatives (e.g., [Gaudin & Wible, 2006](#); [Billet et al., 2011](#)). Therefore, apart from the fossils attributed to the extant clades and the peltephilids, many systematic issues regarding extinct cingulates may revolve around the history of the glyptodonts.

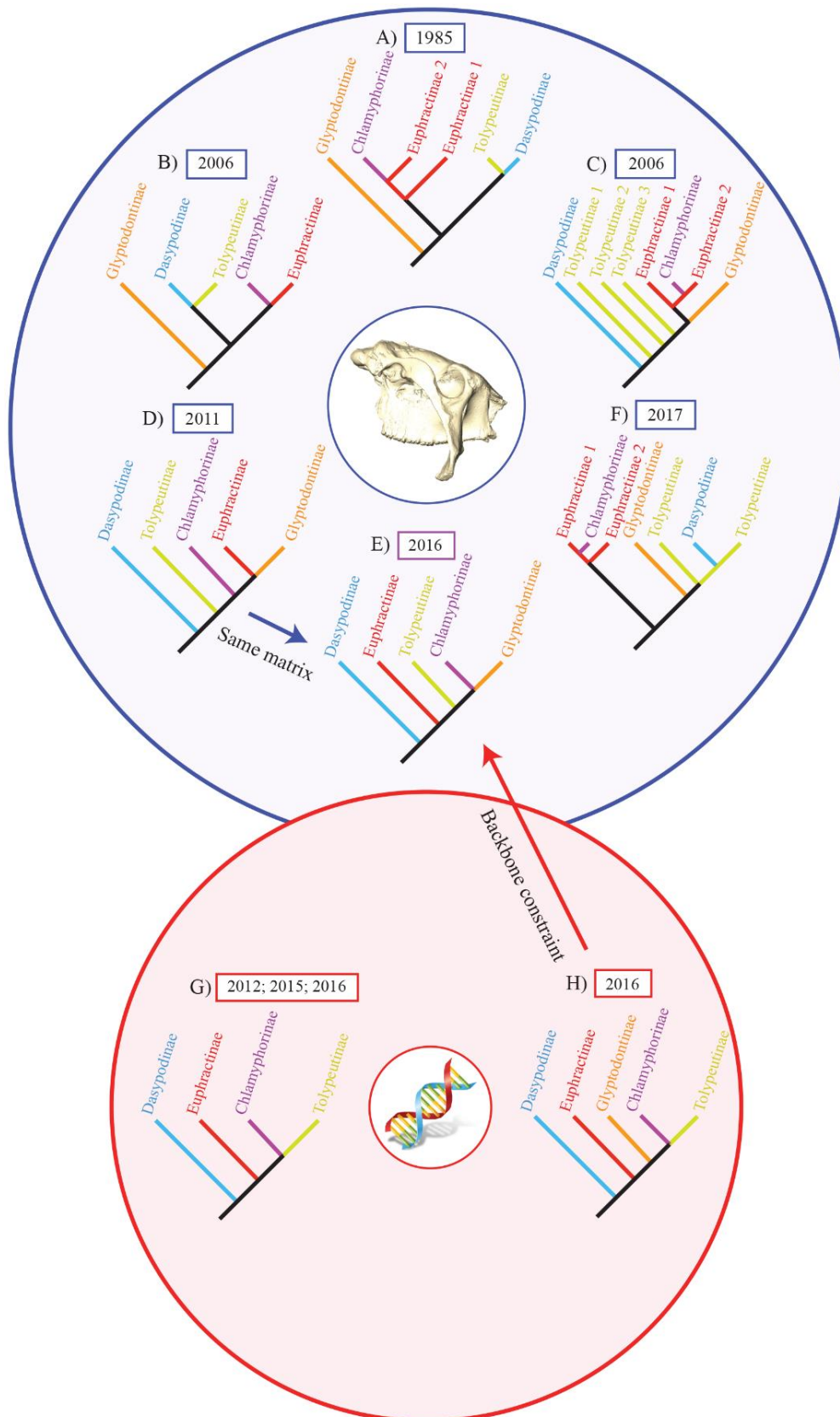


Figure 6. Summary of the molecular (red circle) and morpho-anatomical (blue circle) phylogenetic analyses for Cingulata (only including all extant clades). When present, non-glyptodont fossil taxa were pruned from the original cladograms. A) [Engelmann \(1985\)](#). B) [Abrantes & Bergqvist \(2006\)](#). C) [Gaudin & Wible \(2006\)](#). D) [Billet *et al.* \(2011\)](#). E) [Mitchell *et al.* \(2016\)](#). F) [Herrera *et al.* \(2017\)](#). G) [Delsuc *et al.* \(2012\)](#); [Abba *et al.* \(2015\)](#); [Gibb *et al.* \(2016\)](#). (H) [Delsuc *et al.* \(2016\)](#); [Mitchell *et al.* \(2016\)](#).

1.2.3 *The special case of the Glyptodonts*

The position of the glyptodonts has been debated for a long time since the first cranial description of glyptodont remains by Owen (1839). Both Owen (1839) and Huxley (1864) described the cranial anatomy in the genus *Glyptodon*, but their work was not oriented toward comparison with other cingulates, but rather with giant extinct sloths. Flower (1882) was one of the first to compare the glyptodonts with other armadillos, which he saw as their direct descendants. Ameghino (1884, 1889) then proposed an opposite scenario, with glyptodonts nested within armadillos, since he regarded the great dental and cranial complexity of the former (Owen, 1839) as evidence of derived characters. He also regarded their rigid carapace as a derived character as opposed to a mobile carapace. This proposition was discussed by other authors underlining the very specialized cranial anatomy of glyptodonts (Burmeister, 1874; Carlini & Zurita, 2010; Fariña *et al.*, 2013). A potential solution to the position of glyptodonts within Cingulata was provided by Scott (1903: pp. 103-104), who explained that "... the Santa Cruz glyptodonts [Figure 4] are decidedly more primitive than those of later epochs, and to a certain extent they bridge over the gap between the glyptodonts and the armadillos, for the primitive features are, for the most part, points of resemblance to the latter group". Following these observations, Ameghino's hypothesis (1884, 1889) (glyptodonts in an apical position among cingulates) was supported by many authors throughout the 20th century (Castellanos, 1932, 1959; Hoffstetter, 1958; Patterson & Pascual, 1972 – see Fericola (2008) for a brief review). The work of Abrantes & Bergqvist (2006) constitutes an exception, as they defined glyptodonts as an outgroup to armadillos and pampatheres *a priori* in their phylogenetic analysis of cingulates (Figure 6B). While the Ameghino hypothesis remains the consensus view today (*e.g.*, Gaudin & Wible, 2006; Fericola, 2008; Porpino *et al.*, 2010; Delsuc *et al.*, 2016; Fericola *et al.*, 2017; but see Engelmann, 1985), the exact position of glyptodonts within cingulates has long been a hard question to answer. Phylogenetic analyses based on morphology have delivered contradictory results (Figure 6). The earliest phylogenetic analyses of the group found glyptodonts to be closely related to Eutatini (*Proeutatus* Ameghino, 1891 and *Eutatus* Ameghino, 1887 – extinct armadillos generally linked to euphractines (Scillato-Yané, 1980, 1982; McKenna & Bell, 1997; Scillato-Yané *et al.*, 2010)) and to form with the pampatheres the sister group to extant cingulates (*e.g.*, Engelmann, 1985 – Figure 6A). More recent analyses using morphology favored instead a close relationship of glyptodonts with *Proeutatus* but not with *Eutatus*, in a nested position within extant armadillos (Gaudin & Wible, 2006; Billet *et al.*, 2011). These studies also suggested that glyptodonts are more closely related to euphractines

and chlamyphorines than to other extant armadillos (Figure 6C, D). The most recent analysis proposed a position of glyptodonts as a sister group to a clade formed by dasypodines and tolyteutines (Herrera *et al.*, 2017 – Figure 6F). As with the extant clades, morpho-anatomical analyses have struggled to reach a consensus view on the position of the glyptodonts.

The advent of molecular analyses first challenged the previous phylogenetic hypotheses on extant cingulates based on morpho-anatomy (*e.g.*, Delsuc *et al.*, 2002, 2003). In 2016, two teams succeeded in extracting and analyzing mitochondrial DNA of one of the last representatives of glyptodonts: *Doedicurus* Burmeister, 1874 (Delsuc *et al.*, 2016; Mitchell *et al.*, 2016). This new data resulted in a completely new hypothesis: glyptodonts were recovered as the sister group of a clade formed by the extant chlamyphorines and tolyteutines (Delsuc *et al.*, 2016; Mitchell *et al.*, 2016 – Figure 6H). These results differed considerably from the various hypotheses proposed by morphological phylogenetics. Interestingly, Mitchell *et al.* (2016) demonstrated that by using the same morphological matrix as Billet *et al.* (2011) but applying a molecular backbone constraint, the analysis revealed several morphological characters that supported a close relationship between glyptodonts and chlamyphorines (in agreement with comments by Delsuc *et al.*, 2016) (Mitchell *et al.*, 2016 – Figure 6E), but not with tolyteutines.

In conclusion, in addition to being debated among morphologists, the position of glyptodonts represents a major conflict between morpho-anatomical and molecular analyses. This situation encourages us to assess whether a revision of morphological evidence can help to resolve these conflicts. In particular, such a re-evaluation could consist of *i*) examining poorly known anatomical regions in order to collect a wider spectrum of characters, and, *ii*) having a closer look at patterns of morphological covariation to see if they can affect phylogenetic analyses of the group.

1.3 Anatomy and Covariation Patterns on the Cingulate Skull: State of the Art

1.3.1 *External and Internal Anatomy in Cingulata*

Cranial and postcranial skeletal anatomy are already well known for many groups within the Cingulata, representing one of the most intensively investigated topics for the group (Superina *et al.*, 2013). This is particularly the case for glyptodonts, which have been the subject of numerous anatomical descriptions and discussions for more than 150 years, especially regarding the skull (*e.g.*, Owen, 1839; Scott, 1903; González-Ruiz, 2010). Yet, many aspects of the internal cranial anatomy remain poorly known in the group although recent works have shown that internal cranial anatomy in the Cingulata could provide new phylogenetic information. This includes the study of the inner ear in extant xenarthrans (Billet *et al.*, 2015a); the study of the paranasal sinuses and the narial region, which has led to the discovery of synapomorphies in Pleistocene glyptodonts (Zurita *et al.*, 2011; Fericola *et al.*, 2012); or the study of morphological similarities of the brain endocast in extinct and extant Cingulata species, including glyptodonts (Tambusso & Fariña, 2015a; Tambusso & Fariña, 2015b). Apart from these, there are still many understudied aspects of the internal cranial anatomy that could potentially provide phylogenetic insight into the origins of glyptodonts. These include internal cranial canals which are rarely described or discussed beyond the presence/absence of their external foramina (but see the descriptive work on *Euphractus sexcinctus* Linnæus, 1758 by Wible & Gaudin, 2004) although they may be of real systematic interest (*e.g.*, in turtles – Albrecht, 1967, 1976; Gaffney, 1979; Rollot *et al.*, *in press*; or in therapsids – Araujo *et al.*, 2017). The morphological variation of the internal part of the dentition, hidden within dental alveoli, is also poorly known in the group. Tooth roots can extend very high in the snout in glyptodonts (*e.g.*, González-Ruiz *et al.*, 2020) and this root height may be much lower in other groups (*e.g.*, *Dasypus* – Ciancio *et al.*, 2012). More studies are needed to investigate these aspects. Figure 7 provides an overview of some internal cranial regions that remain to be explored in glyptodonts and in other cingulates. Added to our knowledge of external anatomy, the scrutiny of new internal structural features would allow us to have a more complete view of the cranial anatomy of glyptodonts. The greater the completeness of our anatomical knowledge, the more potential characters could be defined and used for morphological phylogenetics to

search for the origin of glyptodonts among cingulates. These poorly studied anatomical structures will be explored in [Chapter 2](#).

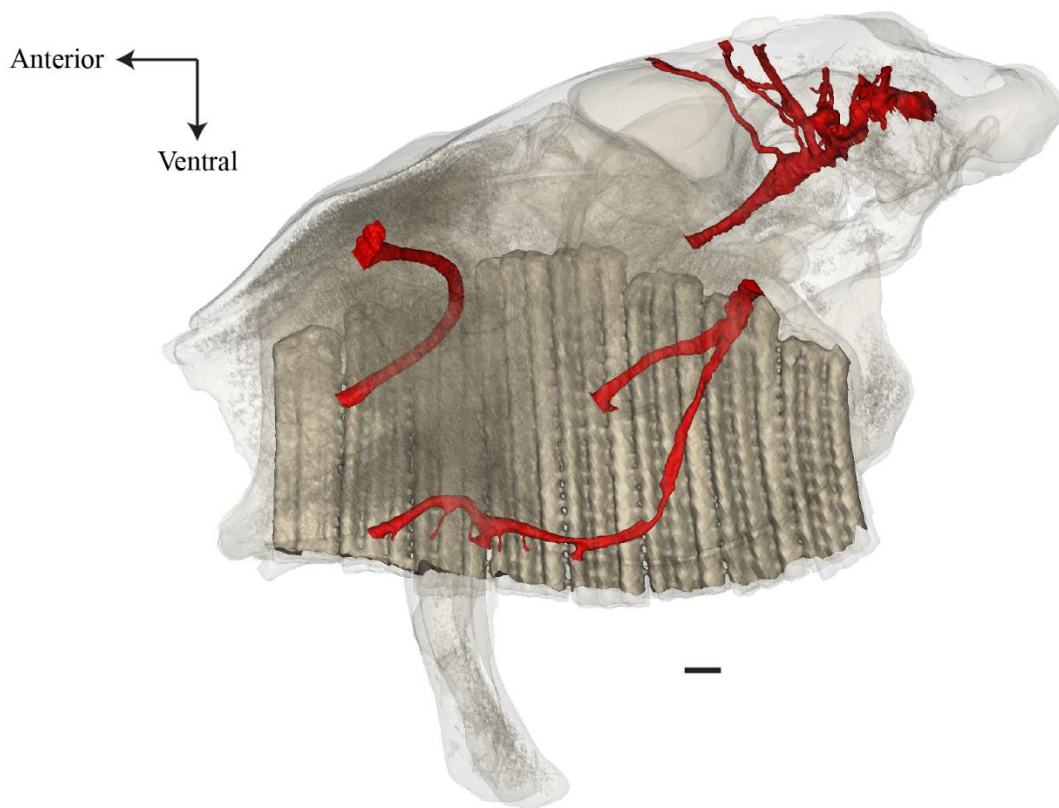


Figure 7. Transparent 3D model of a skull of *Glyptodon* sp. (MNHN.PAM.760) in lateral view with poorly studied internal structures of interest poorly studied in glyptodonts and other cingulates highlighted. The elements studied in this work correspond to the dental alveolar cavities (in grey) and some of the main vascular or nervous canals internal to the skull (in red). Scale = 1 cm. See [Chapter 2](#).

1.3.2 *Morphology, phylogeny, and covariation pattern in the cingulate skull*

Despite numerous studies on the evolutionary history of cingulates, disagreements and uncertainties remain regarding several systematic issues, as noted above (see [Section 1.2](#)). The number of hypotheses is particularly high among phylogenies based on morphological data, especially for glyptodonts ([Engelmann, 1985](#); [Abrantes & Bergqvist, 2006](#); [Gaudin & Wible, 2006](#); [Billet *et al.*, 2011](#); [Herrera *et al.*, 2017](#)). Conversely, molecular studies provided more stable results on the group ([Delsuc *et al.*, 2002, 2003, 2012, 2016](#); [Abba *et al.*, 2015](#); [Gibb *et al.*, 2016](#); [Mitchell *et al.*, 2016](#)) but they are restricted in terms of access to data for extinct taxa. The oldest reconstituted nuclear DNA for extinct mammals is around 1.7 Ma ([Cappellini *et al.*, 2018](#)), but proteomics extended this limit beyond one million years by reconstructing several protein sequences recovered from fossil mammal teeth (the oldest of which are 1.8 million years

in age (Warren, 2019)) which can be exploited for phylogenetic analyses (Warren, 2019). As glyptodonts have recently disappeared, teams have been able to reconstruct mitochondrial DNA sequences of one of their last representatives (Delsuc *et al.*, 2016; Mitchell *et al.*, 2016). However, the history of cingulates goes back at least to the beginning of the Eocene, and the history of glyptodonts at least to the late Eocene (Figure 3). Consequently, a large part of the history of cingulates cannot be covered by the molecular data alone, which confers a prime importance to morphological data for reconstructing their evolutionary history.

This observation is obviously not unique to cingulates and over the last twenty years, the primacy of morphological data to phylogenetically place those extinct taxa inaccessible to molecular analysis has been widely recognized (Wiens, 2004; Asher *et al.*, 2008; Springer *et al.*, 2008). Fossils and their morphology are of prime importance for the reconstruction of evolutionary scenarios and for evolutionary biology in general because of the crucial contribution of their historical information. Although the analysis of fossils can yield congruence between molecular and morphological analyses (*e.g.*, Morlon *et al.*, 2011; Legg *et al.*, 2013), phylogenetic analyses including extinct of cingulates did not reach a high level of agreement with molecular studies (see Section 1.2).

Strong criticism of the use of morphological data for phylogenetic analyses has been expressed by several authors in the last decades (*e.g.*, Scotland *et al.*, 2003; Springer *et al.*, 2008, 2013). For instance, they underlined the frequent ambiguity in the definition of the morphological characters and the difficulty posed by correlated homoplasy among morphological characters. It is certainly true that the usefulness of fossils and morphological data for reconstructing evolutionary scenarios is complicated by the complexity of extracting the phylogenetic signal contained in morphological variation. In line with this observation, many studies have called for an improvement of our approaches and methods, which logically includes a better modeling of morphological variation (Dávalos *et al.*, 2014; Goswami *et al.*, 2014; Billet *et al.*, 2015a; Harrison & Larsson, 2015; Lee & Palci, 2015; Pyron, 2015; Wright *et al.*, 2016; Bardin *et al.*, 2017; Billet & Bardin, 2019). However, morphological variation is a very complex matter (Hallgrímsson & Hall, 2005) and designing adapted models of morphological evolution is therefore extremely challenging.

A limiting factor for the modeling of morphological variation corresponds first and foremost to a lack of knowledge of the nature and scope morphological variation in general

(Hallgrímsson & Hall, 2005). One of the major problems lies in the degree of integration between two morphological traits, which often remains unexplored or neglected (Emerson & Hastings, 1998). The concept of morphological integration is defined as “*the tendency of different traits to vary jointly, in a coordinated manner, throughout a morphological structure or even a whole organism*” (Klingenberg, 2014: pp. 2). A strong integration thus signals a dependence between morphological traits. It is now well-known that dependence between characters in a matrix can be a major source of misleading data in phylogenetic analyses (*e.g.*, Wilkinson, 1995; Emerson & Hastings, 1998; Goswami & Polly, 2010a; Goswami *et al.*, 2014; Guillerme & Brazeau, 2018). Morphological integration may thus have a deleterious effect on morphological phylogenetics whose methods presuppose independence between characters (Felsenstein, 1973; Kluge, 1989; Emerson & Hastings, 1998; O’Keefe & Wagner, 2001; Lewis, 2001; Felsenstein, 2004). Examples of highly covarying characters used in phylogenetics may be found among serial homologues which correspond to repeated structures sharing a large proportion of their genetic architecture and developmental trajectory (*e.g.*, Young & Hallgrímsson, 2005). Teeth count as serial homologues and their serial variation is sometimes scored as multiple separated traits on successive loci in mammalian phylogenetics (*e.g.*, Wesley & Hunt, 2005; O’Leary *et al.*, 2013). This approach can be problematic as repeated characters on successive teeth can show a high degree of integration in mammals and may thus mislead phylogenetic analyses (Naylor & Adams, 2001; Billet & Bardin, 2019). A high degree of integration may also be found in the skull or other anatomical regions (*e.g.*, Olson & Miller, 1958; Cheverud, 1982a; Hallgrímsson *et al.*, 2007; Goswami & Finarelli, 2016) and thus a better knowledge of patterns of covariation in general is a prerequisite towards an improvement in our morphological matrices and models of character evolution (Billet & Bardin, 2019).

As discussed above, morphological variation is extremely complex. In addition to having determinants that might be multiple and interconnected, variation is a pervasive phenomenon at all levels of the biological hierarchy (Hallgrímsson & Hall, 2005). The same is certainly true for morphological integration, which can be studied at various levels (Klingenberg, 2014). Morphological integration can occur at the static level (within one species and ontogenetic stage), at the ontogenetic level (across developmental stages within one species), and at the evolutionary level (among several species) (Figure 8). A main goal of comparative studies scrutinizing morphological integration at various levels is to investigate whether we can identify common covariation patterns within one or several species, and how constrained these patterns are (*e.g.*, Pélabon *et al.*, 2013). Therefore, such studies can serve as

a basis for screening morphological data matrices in search of characters that could relate to common covariation patterns and thus be potentially misleading in phylogenetic analyses (i.e., condition of the character independence – see above).

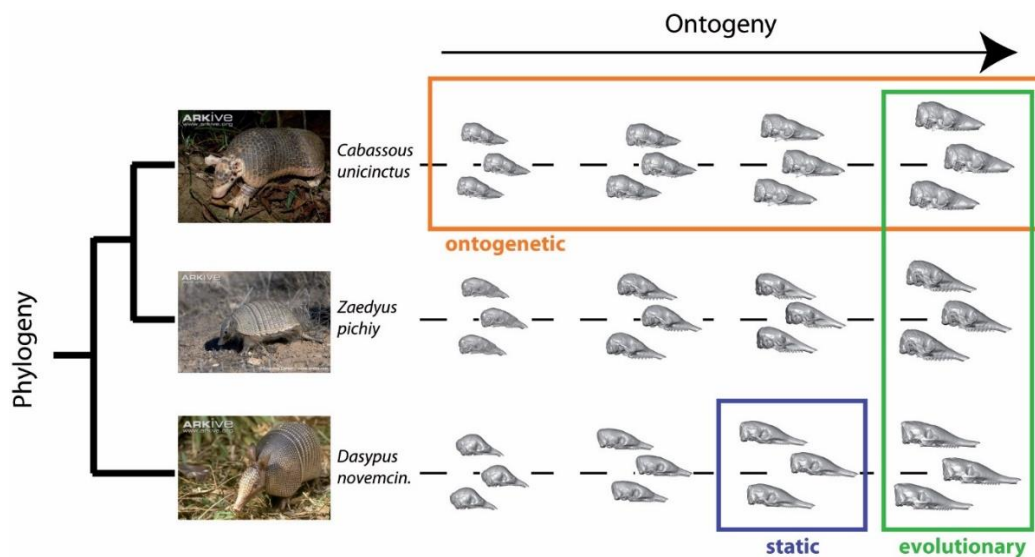


Figure 8. Examples of ontogenetic, static, and evolutionary levels of variation in three species of armadillos. The ontogenetic level concerns variation across developmental stages within one species. The static level is variation within one species and stage. The evolutionary level focuses on variation among species at any given stage (= interspecific) (Klingenberg, 2014). Abbreviation: *novemcin.*, *novemcinctus*.

Despite the great number of studies on morphological integration in recent years, cranial covariation patterns in Cingulata remain poorly known. Some studies have focused on the covariation of specific cranial distances with a size variable (e.g., Moeller, 1968) or on covariations among shape variables in the inner ear region (e.g., inner ear – Billet *et al.*, 2015a) using mainly adult specimens of extant species. A few studies based on extant and fossil species have also explored the covariation between cranial shape and functional aspects such as diet (e.g., Vizcaíno *et al.*, 2004; in glyptodont – Fariña & Vizcaíno, 2001). In addition, Hubbe *et al.* (2016) analyzed the structure of phenotypic variance-covariance matrices based on 18 cranial linear distances within 7 genera of extant armadillos, in order to test whether such matrices in extant taxa can be used as surrogates for extinct ones. Their study, however, did not provide a detailed account of the covarying distances in the cingulate skull. Beside morphological integration, there are also few studies evaluating cranial shape variation in cingulates using 3D data (through almost none that incorporate fossils). Cranial shape variation has been analyzed among species of euphractines (Abba *et al.*, 2015) and among several species of the genus *Dasypus* Linnæus, 1758 together with a preliminary report on allometric patterns (Hautier *et al.*, 2017; Feijó *et al.*, 2018). Overall, there remain few detailed accounts of patterns of

covariation among cranial traits in cingulates, whether at the evolutionary level, or at the ontogenetic or static levels. We explore these aspects in detail in [Chapter 3](#) and [Chapter 4](#).

CHAPTER 2

New Insights from Internal Anatomy

« Fais d'abord l'anatomie de l'aile, puis celle des plumes sans plumes, puis celles des plumes avec les plumes ».

Leonard de Vinci.

“First do the anatomy of the wing, then the anatomy of the featherless pen, then the anatomy of the feathered pen”.

Leonard de Vinci.

2. Comparative anatomy and phylogenetic contribution of internal cranial structures in extant armadillos and extinct glyptodonts (Xenarthra, Cingulata)

ABSTRACT

The evolutionary history of the Cingulata, as for many groups, remains a highly debated topic to this day, particularly for one of their most emblematic representatives: the glyptodonts. There is no consensus among morphological and molecular phylogenies relative to their position within Cingulata. As demonstrated by recent works, the study of the internal anatomy constitutes a promising path for enriching morphological matrices for the phylogenetic study of armadillos. However, internal cranial anatomy remains under-studied in the Cingulata. Here we explored and compared the anatomy of intracranial osseous canals and cavities in a diverse sample of extant and extinct cingulates, including the earliest well-preserved glyptodont crania. The virtual 3D reconstruction (using X-ray microtomography) of selected canals and cavities related to cranial vascularization, innervation or tooth insertion allowed us to compare the locations, trajectories and shape of these structures and to discuss their potential interest for cingulate systematics. We tentatively reconstructed evolutionary scenarios for eight selected traits on these structures, in which glyptodonts often showed a greater resemblance to pampatheres, to the genus *Proeutatus* and/or to chlamyphorines. This latter pattern was partly congruent with recent molecular hypotheses, but more research is needed on these resemblances and on the potential effects of development and allometry on the observed variations. Overall, these comparisons have enabled us to highlight new anatomical variation that may be of great interest to further explore the evolutionary history of cingulates and the origins of glyptodonts on a morphological basis.

2.1 Introduction

The peculiar morphology of xenarthrans, which include armadillos (Cingulata), sloths (Folivora) and anteaters (Vermilingua), has aroused the curiosity of anatomists since the end of the 18th century (Cuvier, 1798). Compared to other mammals, the sum of their unique characteristics has led them to be considered by some earlier workers the most unusual mammals (Vizcaíno & Loughbry, 2008; for a summary see Superina & Loughry, 2015). Cingulates represent the only known mammals with a carapace, which contains a variable number of mobile bands and is formed by a mosaic of osteoderms covering the head, body and tail (Vizcaíno & Loughry, 2008). Cingulates include extant and extinct armadillos, among them the four extant clades Dasypodinae, Euphractinae, Tolypeutinae, and Chlamyphorinae, as well as the extinct glyptodonts, a group of herbivorous and large bodied mammals appearing in the late Eocene and disappearing at the beginning of the Holocene (Delsuc *et al.*, 2016; see also Gaudin & Lyon, 2017 for an alternative classification). The phylogenetic position of glyptodonts within Cingulata is particularly difficult to resolve based on morphological data because of their highly specialized anatomy and the large morphological gap separating them from extant armadillos (Burmeister, 1874; Carlini & Zurita, 2010; Fariña *et al.*, 2013). This difficulty was recently emphasized by ancient DNA studies showing that phylogenetic analyses of their mitogenomes support a position for glyptodonts at odds with that proposed in prior morphological studies (Engelmann, 1985; Gaudin & Wible, 2006; Billet *et al.*, 2011; Delsuc *et al.*, 2016; Mitchell *et al.*, 2016; Herrera *et al.*, 2017).

While it has long been accepted that glyptodonts were closely related to extant armadillos (Huxley, 1864), their exact relationships with the latter were never clearly resolved on the basis morphological data. Flower (1882) initially proposed that glyptodonts were the ancestors of extant armadillos but Ameghino (1884, 1889) disputed this hypothesis, arguing that their great dental and postcranial complexity, as described by Owen (1839) was evidence of their derived nature. The nested position of glyptodonts among extant armadillos has been supported by many authors since then, including by recent phylogenetic analyses using morphological data (Castellanos, 1932, 1959; Hoffstetter, 1958; Patterson & Pascual, 1972; see Fericola (2008) for a brief review of the history of the group; Gaudin & Wible, 2006; Billet *et al.*, 2011; Herrera *et al.*, 2017). However, the consensus stops here. Engelmann (1985) proposed a close relationship of glyptodonts with the extinct Eutatini (*Proeutatus* and *Eutatus*) and pampatheres, whereas the analysis of Gaudin & Wible (2006) retrieved glyptodonts in an apical position nested within a large clade gathering euphractines, chlamyphorines, the extinct

pamphateres and some extinct eutatines. A similar hypothesis was also supported by other studies, but with much variation in the composition of this large apical clade (Fericola, 2008; Porpino *et al.*, 2010; Billet *et al.*, 2011; Fericola *et al.*, 2017; Herrera *et al.*, 2017). Most of these studies, however, unvaryingly proposed a close relationship between the extinct giant pamphateres and glyptodonts, in agreement with Patterson & Pascual (1972). Thanks to the progress made in ancient DNA studies and the recent extinction of glyptodonts – at the beginning of the Holocene (Messineo & Politis, 2009) – the complete mitochondrial genome of the late diverging glyptodont *Doedicurus* could be successfully assembled, which gave rise to a completely new phylogenetic hypothesis (Delsuc *et al.*, 2016; Mitchell *et al.*, 2016). Based on analyses of their mitogenomes, glyptodonts are nested within extant armadillos and represent the sister group of a clade formed by chlamyphorines and tolpeutines (Delsuc *et al.*, 2016; Mitchell *et al.*, 2016). Although analyses of morphological matrices using a molecular backbone constraint can detect morphological characters congruent with the molecular pattern (Mitchell *et al.*, 2016), the high level of disagreement between the two data partitions still calls into question the phylogenetic signal provided by morphological matrices on cingulates.

External cranial and postcranial skeletal anatomy are already well known for many groups within Cingulata, but the internal cranial anatomy remains understudied. However, its study has already provided data of systematic interest for both the extant and extinct xenarthran diversity (Zurita *et al.*, 2011; Fericola *et al.*, 2012; Billet *et al.*, 2015a; Tambusso & Fariña, 2015a; Tambusso & Fariña, 2015b; Billet *et al.*, 2017; Boscaini *et al.*, 2018; Boscaini *et al.*, 2020). Intracranial osseous canals provide important pathways for innervation and vascularization of the head (Evans & de Lahunta, 2012). The diversity and phylogenetic signal of their intracranial trajectories are poorly known, as these hidden structures are rarely described in mammals in general, including xenarthrans (*e.g.*, Wible & Gaudin, 2004). In contrast, their external openings on the skull are often described and scored in phylogenetic matrices (*e.g.*, 37/131 of cranial characters – Gaudin & Wible, 2006).

Here we present a comparative investigation of intracranial osseous canals and cavities in a diverse sample of extant and extinct cingulates, including the earliest well-preserved glyptodont crania, using X-ray microtomography. The 3D virtual reconstruction of selected canals and cavities related to cranial vascularization, innervation or tooth insertion enabled us to compare the locations, trajectories and shape of each homologous structure and discuss their potential interest for cingulate systematics. We tentatively reconstructed the evolutionary history of these traits using a molecularly constrained phylogeny, and we discuss the potential effects of development and allometry on their variation. These comparisons, combined with

information obtained from the literature, allowed us to propose new potential characters that may be used to further explore the origins of glyptodonts within cingulates on a morphological basis.

2.2 Materials and methods

2.2.1 Sampling

We examined the skulls of 33 extant and extinct xenarthran specimens. Two specimens belonging to the Pilosa (sloths and anteaters) were chosen as outgroups. The remaining 31 skulls belonged to Cingulata (Table 1). This sample included specimens representing the 9 extant genera, as well as three small developmental series in phylogenetically distant species (*Cabassous unicinctus*, *Dasybus novemcinctus*, *Zaedyus pichiy*), with the aim of better understanding the ontogenetic variation of the selected anatomical structures. The cingulate specimens also included 14 specimens belonging to fossil species, among them six glyptodonts (Table 1). This sample covered more than 40 million years of cingulate evolutionary history and includes all the major cingulate clades. The small number of well-preserved fossil specimens did not allow us to evaluate intraspecific variation, as we were unable to perform measurements on more than 1 or 2 specimens per species (Table S1). Species identification was based on collection data, geographical origin, cranial anatomy, and the literature on cingulate taxonomy (e.g., Scott, 1903; McBee & Baker, 1982; Wetzel, 1985; Gaudin & Wible, 2006; Wetzel *et al.*, 2007; Hayssen, 2014a; Abba *et al.*, 2015; Carlini *et al.*, 2016; Gaudin & Lyon, 2017; Smith & Owen, 2017). Digital data of all specimens were acquired using X-ray micro-computed tomography (μ CT). Specimens were scanned on X-ray tomography imagery platforms at the American Museum of Natural History (New York, USA); the *Museum national d'Histoire naturelle* (France) in Paris (AST-RX platform), the University of Montpellier (France) and the *Museum für Naturkunde* (ZMB) in Berlin (Germany). Three-dimensional reconstructions of the selected structures were performed using stacks of digital μ CT images with MIMICS v. 21.0 software (3D Medical Image Processing Software, Materialize, Leuven, Belgium). The visualization of 3D models was also conducted with AVIZO v. 9.7.0 software (Visualization Sciences Group, Burlington, MA, USA).

2.2.2 Selected regions of interest and anatomical nomenclature

We selected several osseous anatomical complexes in the internal cranial anatomy of cingulates that are poorly known and of interest for this study such as dental alveoli and several

specific intraosseous canals. The latter mostly correspond to vascular pathways and/or the courses of cranial nerves involved in the innervation of various cranial areas: the nasolacrimal canal, the palatine canal, the sphenopalatine canal, the canal for the frontal diploic vein, the transverse canal, the orbitotemporal canal, the canal for the capsuloparietal emissary vein and the posttemporal canal.

Except for *Dasypus*, which represents a special case (see [Ciancio et al., 2012](#)), the homologies in the dental row between the different species of Cingulata are not known mainly because of the drastic reduction in dental complexity ([Vizcaíno, 2009](#)). For glyptodonts, previous studies conventionally designated the whole set of teeth as molariform but without further precision (*e.g.*, [González-Ruiz et al., 2015](#)). We therefore chose to use a positional nomenclature and to designate separately the teeth housed in the premaxillary (Pt) from the molariform teeth (Mf) borne by the maxillary (see [Herrera et al., 2017](#) for a different nomenclature).

Only those intracranial canals whose sampled variation appeared to bear clear systematic information were selected in this work ([Figure 9](#)). Non-selected canals generally showed asymmetric and intraspecific variation (*e.g.*, hypoglossal canal; trajectory of the internal carotid artery – see [Patterson et al., 1989](#); [Gaudin, 1995](#)) or provided no new data (*e.g.*, infraorbital canal) with respect to what was already described or scored for the systematics of the group ([Wible & Gaudin, 2004](#); [Gaudin & Wible, 2006](#); [Gaudin & Lyon, 2017](#)). Other non-selected canals were rarely visible in all specimens (often due to taphonomy – not in place and/or obscured by a hard and dense matrix) and were therefore difficult to compare. Specimens that presented a canal that was too incomplete are not described in the relevant section. For the identification and nomenclature of the selected intracranial canals, our study used previous work describing intracranial anatomy in cingulates and eutherians in general ([Thewissen 1989](#); [Wible, 1993](#); [Gaudin, 2004](#); [Wible & Gaudin 2004](#); [Evans & de Lahunta, 2012](#); [Muizon et al., 2015](#); [Gaudin & Lyon, 2017](#)). We have indicated for each selected region of interest: the variation of these regions during ontogeny, a synthetic comparison among specimens, and the formalization of potential discrete or continuous characters to highlight potential evolutionary scenarios to be mapped onto the tree of cingulates. The formalization of new characters was performed based on observations that were stable among glyptodonts and were shared with some non-glyptodonts cingulates, so that they could provide pertinent information when investigating glyptodont origins.

CHAPTER 2: NEW INSIGHTS FROM INTERNAL ANATOMY

Table 1. List of specimens.

Family/Clade	Species	Institutional number	Locality	Period	Age range	Reference
Bradypodidae	<i>Bradypus tridactylus</i>	MNHN ZM-MO-1999-1065	French Guiana; Petit saut rive droite	Extant	0	Linnaeus, 1758
Myrmecophagidae	<i>Tamandua tetradactyla</i>	NHM 3-7-7-135	Brazil; Mato Grosso; Chapada	Extant	0	Linnaeus, 1758
Peltephilidae	<i>Peltephilus pumilus</i> †	YPM-PU 15391	Argentina; Santa Cruz formation; Coy inlet	Santacrucian	17.5-16.3	Ameghino, 1887
Dasypodidae	<i>Utaetus buccatus</i> †	AMNH 28668	Argentina; Gran Barranca	Barrancan	41.6-39.0	Ameghino, 1902
Dasypodinae	<i>Dasypus novemcinctus</i> *	AMNH 33150	Colombia; Quindui; Salento	Extant	0	Linnaeus, 1758
Dasypodinae	<i>Dasypus novemcinctus</i> **	AMNH 133261	Brazil; Goias; Anapolis	Extant	0	Linnaeus, 1758
Dasypodinae	<i>Dasypus novemcinctus</i> ***	AMNH 133328	Brazil; Mato Grosso do Sul; Maracaju	Extant	0	Linnaeus, 1758
Dasypodinae	<i>Dasypus novemcinctus</i> ****	AMNH 255866	Bolivia; Beni; Cercado	Extant	0	Linnaeus, 1758
Dasypodidae	<i>Stegotherium tauberi</i> †	YPM-PU 15565	Argentina; Santa Cruz formation	Santacrucian	17.5-16.3	Ameghino, 1887
Euphractinae	<i>Prozaedyus exilis</i> †	YPM-PU 15579	Argentina; Santa Cruz formation; Kilik Aike	Santacrucian	17.5-16.3	Ameghino, 1887
Euphractinae	<i>Prozaedyus proximus</i> †	YPM-PU 15567	Argentina; Santa Cruz formation; Coy inlet	Santacrucian	17.5-16.3	Ameghino, 1887
Euphractinae	<i>Euphractus sexcinctus</i>	AMNH 133304	Brazil; Goias; Anapolis	Extant	0	Linnaeus, 1758
Euphractinae	<i>Chaetophractus villosus</i>	AMNH 173546	South America - No more precision	Extant	0	Desmarest, 1804
Euphractinae	<i>Zaedyus pichiy</i> *	ZMB 49039	Argentina; Oso Marino	Extant	0	Desmarest, 1804
Euphractinae	<i>Zaedyus pichiy</i> **	MHNG 1627.053	Argentina; Chubut; Punta Ninfas	Extant	0	Desmarest, 1804
Euphractinae	<i>Zaedyus pichiy</i> ***	MHNG 1276.076	Argentina; Chubut; Fofó Cahuel	Extant	0	Desmarest, 1804
Euphractinae	<i>Zaedyus pichiy</i> ****	FMNH 23810	Argentina; Chubut	Extant	0	Desmarest, 1804
Euphractinae	<i>Doellotatus</i> sp. †	UF 260533	Argentina; Santa Cruz formation; Quebrada Honda	Santacrucian	17.5-16.3	Bordas, 1932
Tolypeutinae	<i>Cabassous unicinctus</i> **	NBC 26326.B	Suriname	Extant	0	Linnaeus, 1758
Tolypeutinae	<i>Cabassous unicinctus</i> ***	AMNH 133386	Brazil; Mato Grosso do Sul; Maracaju	Extant	0	Linnaeus, 1758
Tolypeutinae	<i>Cabassous unicinctus</i> ****	MNHN 1999-1044	French Guiana	Extant	0	Linnaeus, 1758
Tolypeutinae	<i>Tolypeutes matacus</i>	FMNH 28345	Brazil; Mato Grosso; Descalvado	Extant	0	Desmarest, 1804
Tolypeutinae	<i>Priodontes maximus</i>	AMNH 208104	Zoo - No more precision	Extant	0	Kerr, 1792
Chlamyphorinae	<i>Chlamyphorus truncatus</i>	AMNH 5487	Argentina; Mendoza	Extant	0	Harlan, 1825
Chlamyphorinae	<i>Calyptophractus retusus</i>	NMNH 283134	Bolivia; Santa Cruz	Extant	0	Burmeister, 1863
Chlamyphoridae	<i>Proeutatus lagena</i> †	YPM-PU 15613	Argentina; Santa Cruz formation	Santacrucian	17.5-16.3	Ameghino, 1887
Pampatheriinae	<i>Vassallia maxima</i> †	FMNH P14424	Argentina; Catamarca; Corral Quemado	Montehermosan	6.8-4.0	Castellanos, 1946
Glyptodontinae	" <i>Metopotoxus</i> " <i>anceps</i> †	YPM-PU 15612	Argentina; Santa Cruz formation; Lago Pueyrredón	Santacrucian	17.5-16.3	Scott, 1903
Glyptodontinae	<i>Propalaeohoplophorus minus</i> †	AMNH 9197	Argentina; Santa Cruz formation; Corriegen Kaik	Santacrucian	17.5-16.3	Ameghino, 1891
Glyptodontinae	" <i>Cochlops</i> " <i>debilis</i> †	YPM-PU 15592	Argentina; Santa Cruz formation; Guer Aike	Santacrucian	17.5-16.3	Ameghino, 1891
Glyptodontinae	<i>Eucinepeltus complicatus</i> †	AMNH 9248	Argentina; Santa Cruz formation; Kilik Aike Norte	Santacrucian	17.5-16.3	Ameghino, 1891
Glyptodontinae	<i>Glyptodon</i> sp. †	MNHN PAM-759	Argentina; Buenos Aires	Pleistocene	3.0-0.011	Owen, 1839
Glyptodontinae	<i>Glyptodon</i> sp. †	MNHN PAM-760	Argentina; Buenos Aires	Pleistocene	3.0-0.011	Owen, 1839

† extinct species; * perinatal stage; ** juvenile; *** subadult; **** adult.

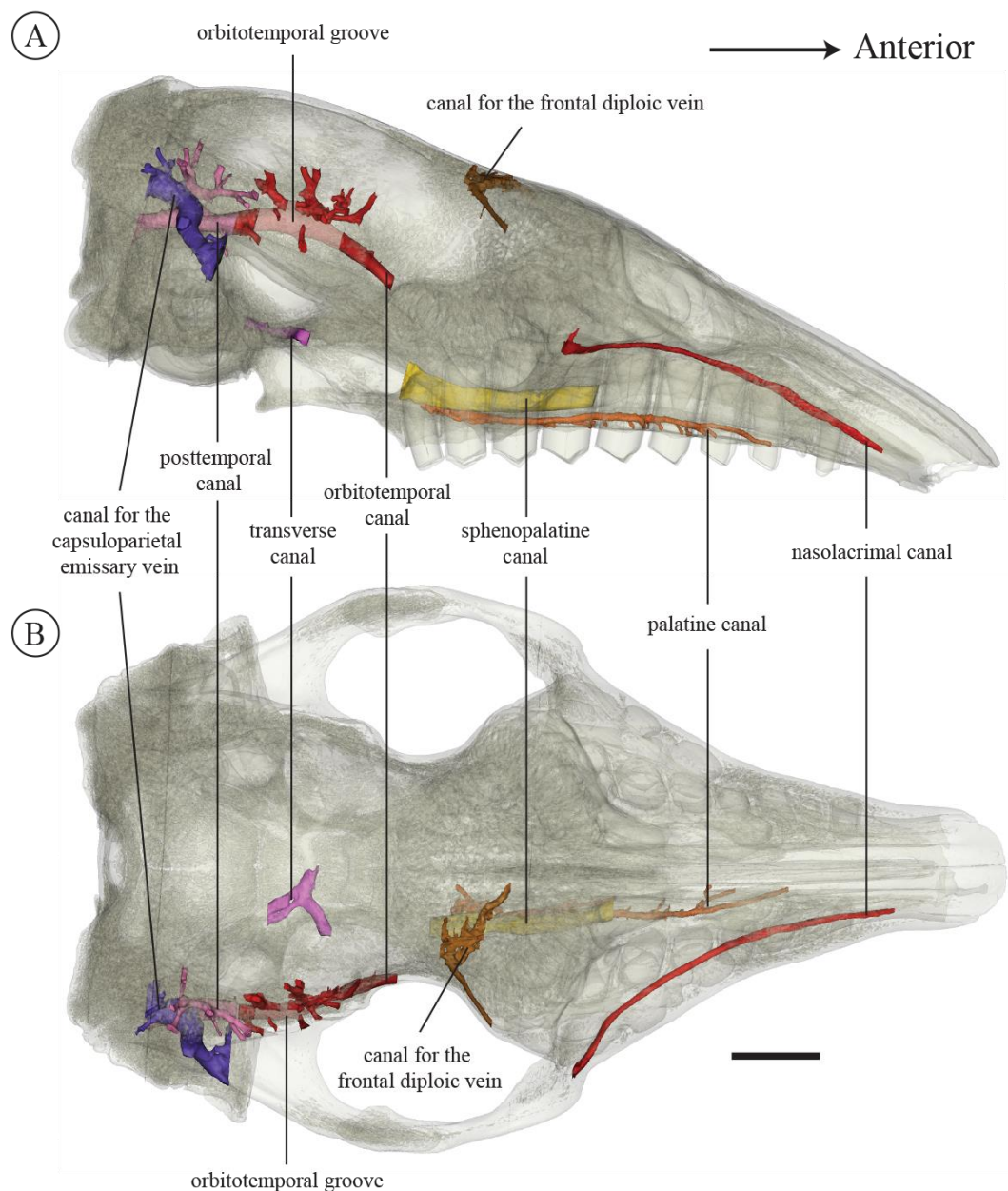


Figure 9. Illustration of the selected internal canals on the transparent cranium of *Euphractus sexcinctus* AMNH 133304 in right lateral (A) and ventral (B) views. Scale = 1 cm.

2.2.3 Virtual reconstruction of the selected regions

Teeth were absent for many specimens, but they were reconstructed when present. When present, the most dorsal part of the teeth did not always fill the whole alveolar cavity, leaving a void between the roof of the alveolar cavity and the dorsal edge of the tooth. Because we selected the internal orientation and curvature of the whole dental row for study, the reconstruction of alveoli was preferred over the modelling of teeth, which were sometimes absent for our specimens. In some cases, the distinction between the limit of the alveolar wall,

the tooth and the sediment were not identifiable. In this case we modelled only the distinguishable structures to allow comparison (*e.g.*, *Doellotatus* sp. in [Figure 10](#)).

A canal corresponds to a duct completely enclosed in one or more bones, and which usually provides passageway to vessels and/or nerves. In some cases, a canal may not be continuously enclosed by bone, and thus turns into a groove for part of its course (*e.g.*, orbitotemporal canal). In such a case, we have reconstructed the course of the groove in a manner similarly to that of a canal, but we illustrated the areas corresponding to the groove with increased transparency. In some cases, two canals were confluent in such a way that it was no longer possible to distinguish which part of the duct corresponds to the passage of which vessel or nerve. These regions of confluence were specified in each of our reconstructions by a shaded area (*e.g.*, posttemporal canal and canal for the capsuloparietal emissary vein). Most selected canals were continuous with external or internal foramina. [Figure S2](#) shows the location of each of these foramina in *Euphractus sexcinctus*.

2.2.4 Measurements

A few specific measurements were taken for comparison where quantification seemed to offer a better account of the observed variation than a qualitative description. Skull length, height and width were measured to calculate the geometric mean of each specimen (= geometric mean, an estimator of the size of a specimen defined by the cubic root of the product of the three variables ([Claude, 2008](#))). The geometric mean was log transformed to facilitate graphing of the data ([Claude, 2008](#)). Several other cranial measurements were selected, and their variation was compared to that of the geometric mean in our sample ([Table S2](#) and [Figure S3](#)). These measurements were selected in order to quantify the following aspects that appeared interesting to us after our anatomical observations: 1) the relative height of the dental row (*i.e.*, GDRH/GSH = the ratio between the greatest dental row height and the greatest skull height); 2) the angle between the straight line marked by the ventral most point of the tentorial process and the dorsal most point of the annular ridge (see [Wible & Spaulding, 2013](#)) and the horizontal anteroposterior axis defined here by the straight line between the mesial edge of the first tooth and the distal edge of the last tooth in sagittal view to compare the internal vault inclination (IVI) among taxa. These measurements are further explained and summarized in [Figure S3](#); they were taken using the linear distance and angle tools of MIMICS v. 21.0 software.

2.2.5 *Reconstructing evolutionary scenarios for intracranial traits*

In order to visualize possible evolutionary scenarios for the discrete and continuous intracranial traits defined based on our observations, we reconstructed a cladogram focused on the taxa in our sample by performing a parsimony analysis using PAUP v. 4.0a167 (Swofford, 2002). We used the morphological matrix of Billet *et al.* (2011) (largely based on that of Gaudin & Wible, 2006), which we limited to the genera in our sample (*Utaetus buccatus* was also removed due to an overly large amount of missing data). The initial matrix included all the genera of our sample except for one extant genus (*Calyptophractus*), along with four fossil genera: three Santacrucian glyptodonts (“*Cochlops*”, *Eucinepeltus*, and “*Metopotoxus*”) and one Pleistocene glyptodont (*Glyptodon*). We therefore scored these fossil taxa based on our CT-scanned specimens and added them to the analysis. After this stage, the matrix included 22 taxa scored for 125 characters (Supporting information 2). We performed the same analysis as Billet *et al.* (2011), with a heuristic search involving 1000 random addition replicates, with 27 morphological characters treated as ordered and treating taxa with multiple states as polymorphic (Supporting information 2). Following the recent molecular works of Delsuc *et al.* (2016) and Mitchell *et al.* (2016), we enforced a backbone constraint similar to that of Mitchell *et al.* (2016). Because this resulted in an unusual position for *Proeutatus lagena* (*i.e.*, as the sister group of euphractines), contrary to its usual placement close to the glyptodonts in morphological analyses (Engelmann, 1985; Gaudin & Wible, 2006; Billet *et al.*, 2011; Herrera *et al.*, 2017), we added a constraint on this taxon to assign it a priori to a position close to glyptodonts (Figure S4A). By using this approach, our aim was only to obtain a more consensual topology, based on recent morphological and molecular analyses, in order to discuss the relevance of our characters. This study is not intended to produce a new phylogenetic analysis. The strict consensus of the most parsimonious trees (with two polytomies – extant euphractines and glyptodont except for “*Metopotoxus*” *anceps*) obtained was then used to calculate branch lengths in order to explore evolutionary scenarios for our qualitative and quantitative observations over the entire topology of the tree. The strict consensus was used as a baseline cladogram (Figure S4B – the strict consensus of the same analysis without constraint is illustrated in Figure S4C for indication). As the optimization options of the analysis can affect the length of the branches, we have chosen to favor the hypothesis of convergence (= DELTRAN) rather than reversion because they have been regarded as more likely (Wake *et al.*, 2011). For the reconstruction of evolutionary scenarios for intracranial discrete or continuous traits, one needs to complete missing data ($n = 5$ on 8 characters) and resolve polytomies. For the latter, we used the *multi2di* function of the *ape* package of R (Paradis & Schliep, 2019). The

function resolves polytomies by adding one or several additional node(s) and corresponding branch(es) of length 0. The duplicate nodes thus have the same values, allowing the removal of duplicates *a posteriori*. In order to facilitate the visualization of the evolutionary scenarios on the tree, we have rendered the tree ultrametric using the *force.ultrametric* function of the *phytools* package of R (Revell, 2012). For the discrete traits, the missing data (*i.e.*, 1 taxon for characters 1 and 2 (not applicable), 7 taxa for character 4; 1 taxon for character 5 – see results) were completed according to their ancestor node optimization. In case of optimization uncertainties, we also favored convergences for the same reason mentioned previously (Wake *et al.*, 2011). The reconstruction and mapping of ancestral states was performed using stochastic mapping with a symmetric condition matrix (*i.e.*, one for which all transformation rates are considered equivalent; see Bollback, 2006; Revell, 2012). This analysis was performed using the *make.simmap* function of the *phytools* package of R, with which we produced 100 simulations for each character. For continuous traits, missing data (*i.e.*, 2 taxa for the character 8) were estimated using an approach combining the use of multiple imputations with procrustean superimposition of principal component analysis results (Clavel *et al.*, 2014) with the *estim* function of the *mvMORPH* package of R (Clavel *et al.*, 2015). Then, the reconstruction of the ancestral states was performed using maximum likelihood using the *contMap* function of the *phytools* package of R (Revell, 2012).

2.2.6 Institutional Abbreviations

AMNH, American Museum of Natural History, New York, USA; **FMNH**, Field Museum of Natural History, Chicago, USA; **MHNG**, *Muséum d'Histoire Naturelle de Genève*, Genève, Switzerland; **MNHN**, *Muséum National d'Histoire Naturelle, Zoologie et Anatomie comparée collections (ZM)*, *Mammifères et Oiseaux collections (MO)*, fossil mammal collections, Pampean (**F.PAM**), Paris, France; **NBC**, Naturalis Biodiversity Center, Leiden, Holland; **NHM**, Natural History Museum, London, ; **NMNH**, National Museum of Natural History, Smithsonian Institution, Washington, DC, USA; **UF**, University of Florida, Gainesville, USA; **YPM-PU**, Princeton University collection housed at Peabody Museum, Yale University, USA; **ZMB**, *Museum für Naturkunde*, Berlin, Germany.

2.3 RESULTS – ANATOMICAL DESCRIPTION AND COMPARISON

2.3.1 Teeth and Alveolar Cavities – Orientation, Curvature and Height

The three species sampled intraspecifically do not show any ontogenetic variation in the orientation and curvature of the teeth compared to the pattern observed in adults (see below). In *Dasypus* and *Zaedyus* the relative height of teeth shows an increase from the youngest to the oldest specimens, suggesting an increase in height during ontogeny (Figure 11). In *Cabassous*, which possess a reduced dentition, no clear ontogenetic trend has been observed (Figure 11).

Height--The relative height of the alveolar cavities distinguishes specimens with reduced teeth such as *Dasypus*, *Stegotherium*, *Cabassous* and *Priodontes*, from other cingulate species, some of which may even show extremely enlarged teeth, as is the case in glyptodonts (Figure 10, Table S2).

In taxa with reduced teeth, the height of the alveolar cavity in lateral view is practically the same for all teeth (Figure 10). In the other taxa, the dorsal profile of the dental row in lateral view is curved (dorsal convexity): teeth gradually increase in height backward until the middle of the dental series and then gradually decrease in height posteriorly. The most dorsal point is reached in the middle of the dental row (at the level of Mf5 in dental rows containing 7-10 Mf – unfunctional supernumerary teeth are not considered) in *Chaetophractus* (at Mf5/Mf9), *Euphractus* (at Mf5/Mf9), *Doellotatus* (at Mf5/Mf9-10) and *Tolypeutes* (at 5Mf/Mf9) and more anteriorly in *Peltephilus* (at Mf2/Mf7), and *Proeutatus* (at 4Mf/Mf9). In *Bradypus*, this dorsal point is attained more anteriorly (at Mf2/Mf5). It is reached more posteriorly in *Zaedyus* (at Mf5/Mf8), *Prozaedyus* (at Mf5/Mf8), *Vassallia* (at Mf6/Mf9), chlamyphorines (at Mf6/Mf8) and most glyptodonts (at Mf5-6/Mf8). In addition, the GDRH/GSH ratio, which express the relative dental height according to the skull height, seems to be correlated to the body size ($R^2 = 0.5363$; $P\text{-value} = 9.42\text{E-}06$), showing that large-sized taxa have relatively taller dentitions. This is reminiscent of the increase in height of the dental row during ontogeny in *Dasypus* and *Zaedyus*. The largest species in the sample, glyptodonts and *Vassallia*, do indeed show a strongly elevated dentition in relation to the skull depth (Figure 12). This is also the case in *Peltephilus*, for which the height of the skull is particularly low in relation to its length. Although they are small (*i.e.*, $\text{GSL} < 43\text{mm}$) and despite the allometric trends noted in *Dasypus* and *Zaedyus*, chlamyphorines show a tooth height comparable in proportion to the larger-sized *Chaetophractus*, *Proeutatus* and *Euphractus* (Figure 12). Relative tooth height is lower in *Tolypeutes*, *Zaedyus*, *Prozaedyus*, and *Cabassous*, and extremely low in specimens with dental reduction - *Dasypus*, *Stegotherium*, and *Priodontes* (Figure 12).

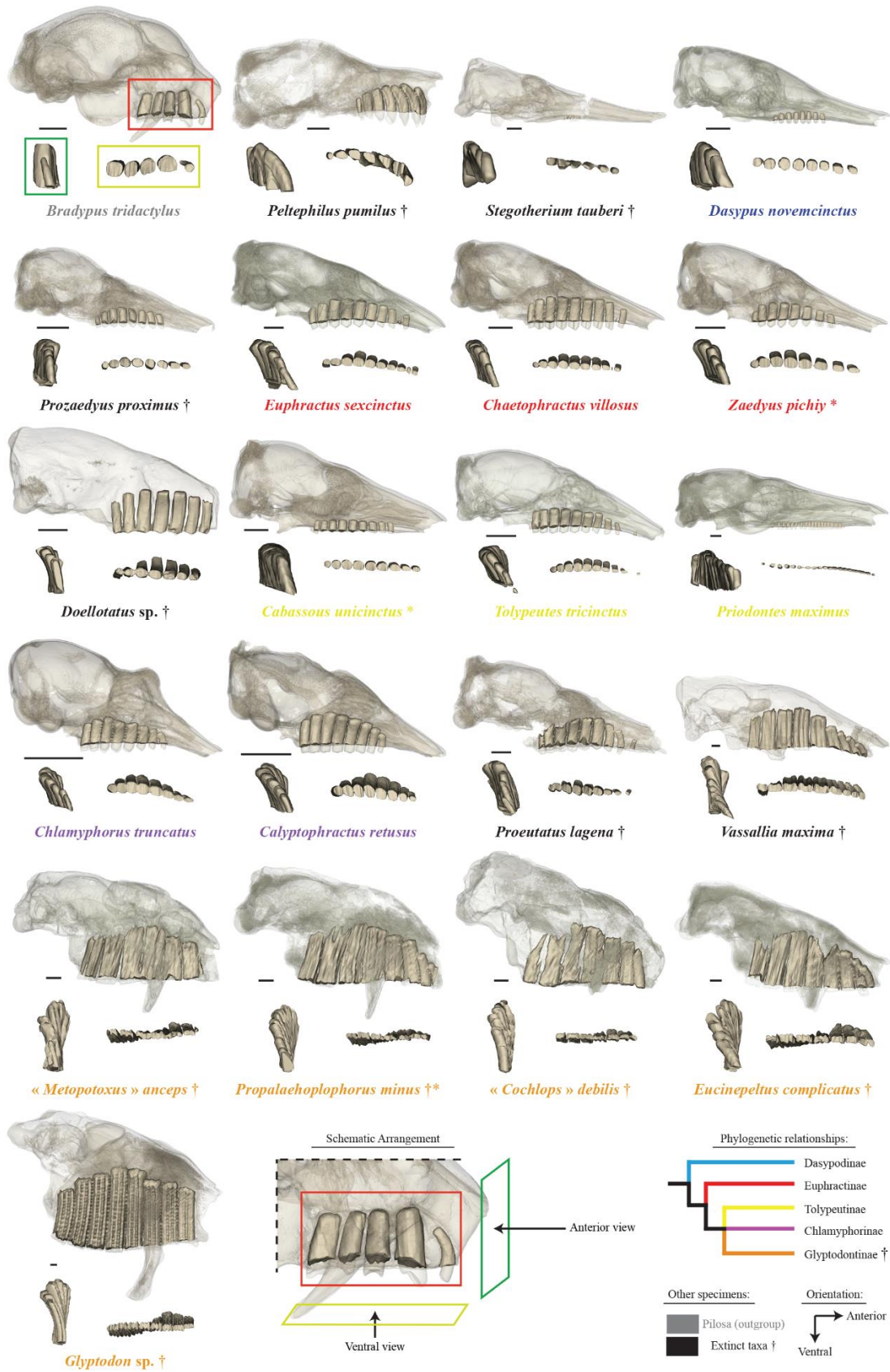


Figure 10. Diversity of the dental alveolar cavities in our cingulate sample in lateral (red square), ventral (yellow square) and anterior (green square) view. Skulls are reconstructed with transparency to leave the cavities apparent. Colors of species names refer to their attribution at the subfamilial level according to molecular analyses (lower right panel); extinct species not allocated to one of these clades are shown in black. † represents an extinct taxon. Scale = 1 cm.

Curvature & Orientation--As visible in anterior and ventral views (Figure 10), taxa with reduced teeth and *Peltephilus* exhibit a rather homogenous curvature and orientation of teeth along the dental row while most cingulates show gradual changes in these aspects anteroposteriorly. In most cingulates, anterior teeth are tilted lingually, *i.e.* tilted with a medially offset apex, while most posterior teeth often tilt labially. The tilt of posterior teeth is often much less pronounced than for anterior teeth. Similarly, taxa that show curved crowns generally show anterior teeth with an inward curvature (lingual convexity) which can be strongest in the middle of the dental row, while the two posteriormost teeth often show a lesser degree of inward curvature or even an outward curvature (labial convexity). A strong inward curvature of anterior teeth is observed in *Peltephilus*, *Doellotatus*, *Tolypeutes*, *Vassallia*, chlamyphorines, and glyptodonts in our sample, whereas other taxa show straighter crowns, and an outward curvature is observed in *Dasypus*. In lateral view, the first tooth (Mf1; P1 for *Dasypus*) or teeth show a mesial curvature (mesial convexity) and a mesially offset apex in *Bradypus*, *Peltephilus*, *Proeutatus*, *Vassallia*, *Propalaehoplophorus* and *Eucinepeltus*. Mf1 is also tilted with a mesially offset apex in *Prozaedyus*. Finally, the two to three posteriormost teeth are distinctly tilted with a distally offset apex in *Bradypus* and glyptodonts. Most other loci and taxa exhibit a nearly vertical orientation of teeth in lateral view.

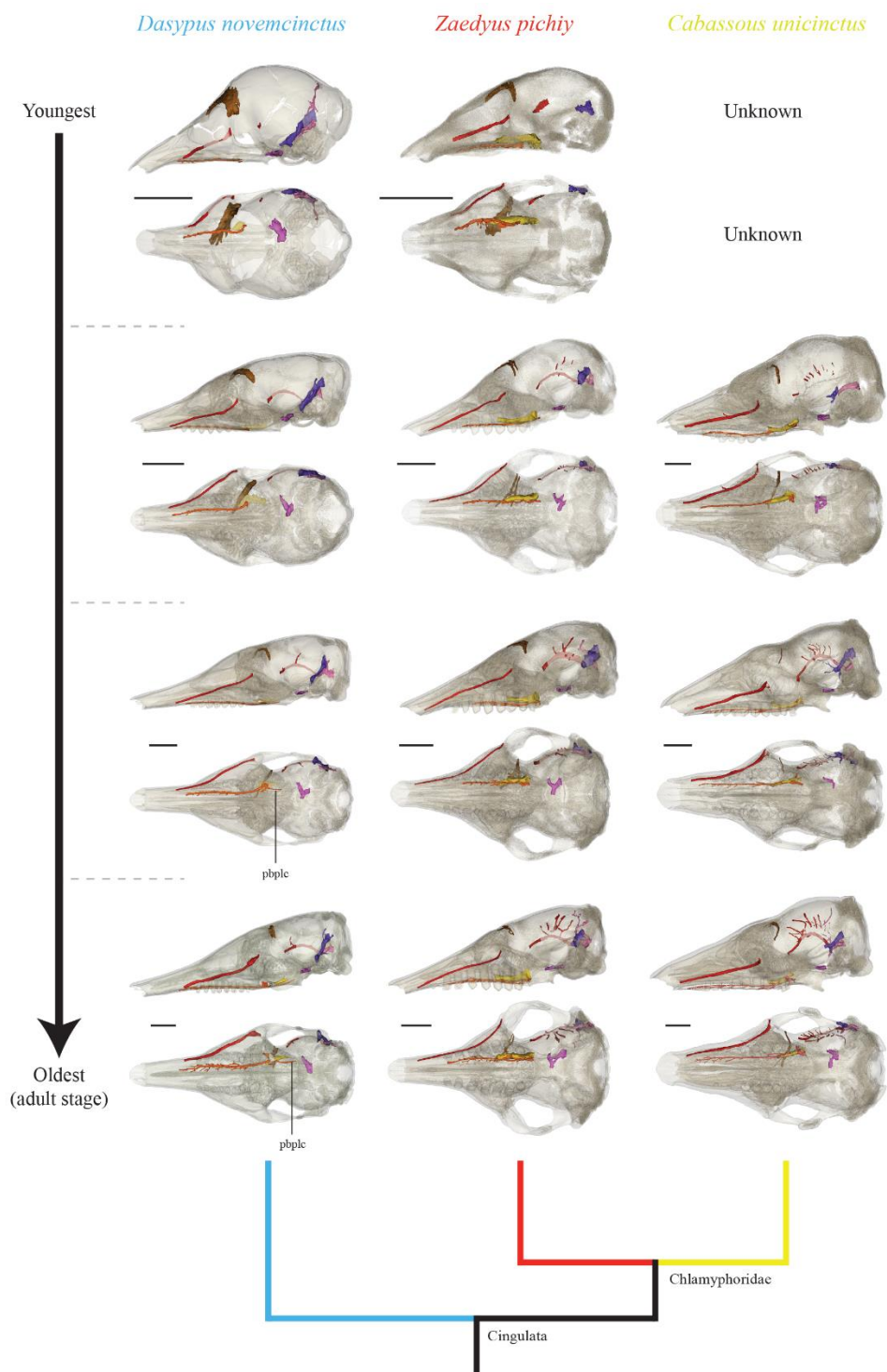


Figure 11. Ontogenetic variation of internal canals selected in this study viewed on transparent skulls in each developmental series (*Dasytus*, *Zaedyus* and *Cabassous*). Note that early postnatal stages for *Cabassous* are not documented in our sample. See [Chapter 3](#) for the determination of stages. Phylogenetic relationships are indicated with colors following [Figure S4](#). The color of canals follows that of [Figure 9](#). Abbreviations: **pbplc**, posterior branch of the palatine canal. Scale = 1 cm.

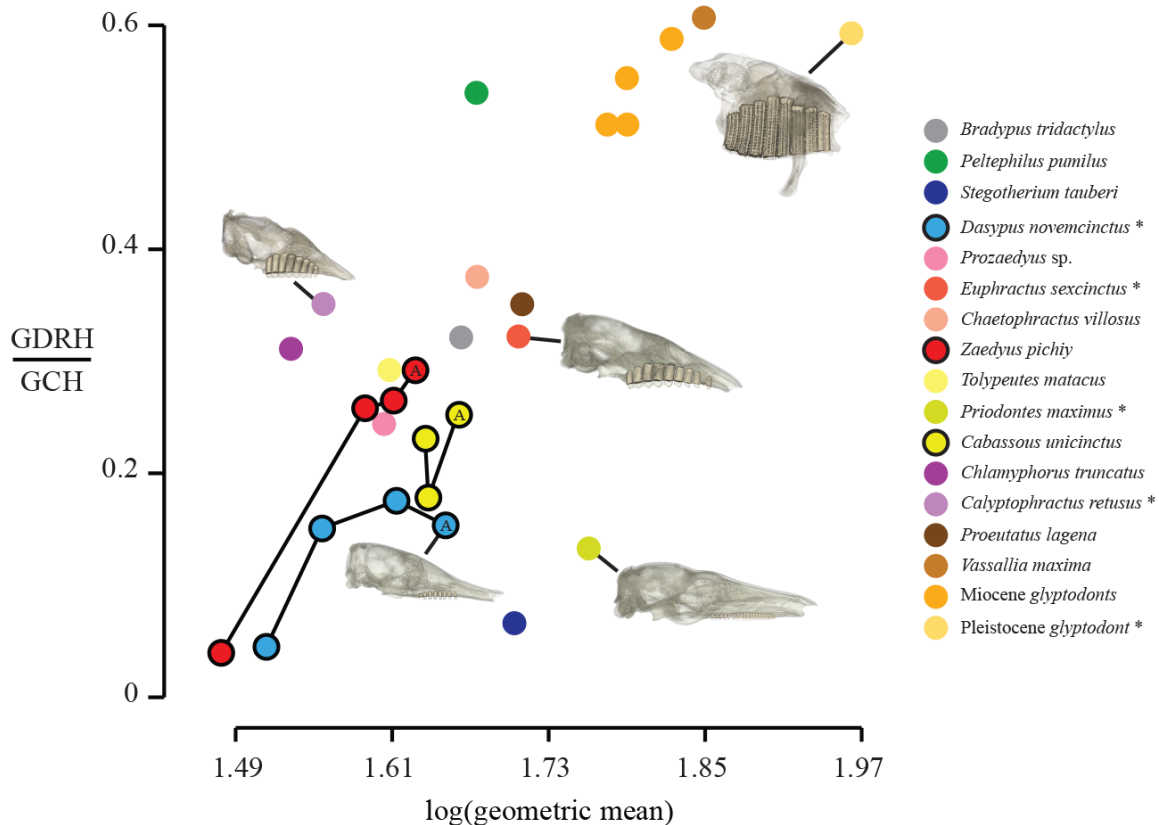


Figure 12. Distribution of the ratio of greatest dental row height (GDRH) to greatest skull height (GSH) with respect to cranial size (= $\log(\text{geometric mean})$); see [Material & Methods](#). For each of the three developmental series, A, symbolizes the adult specimen. Skulls of specimens marked with an asterisk are illustrated in the graph. Scale = 1 cm.

Based on these observations, we propose scrutinizing evolutionary scenarios for the following two characters of the dentition (see [Table 2](#)).

Character 1 (discrete - unordered): Position of the most dorsal point of the dorsal convexity of the tooth row.

State (0): Toothrow not dorsally convex.

State (1): Anterior to middle of the tooth row.

State (2): At the middle of the tooth row.

State (3): Posterior to middle of the tooth row.

Character 2 (discrete - unordered): Curvature of anterior teeth in anterior view.

State (0): Inward curvature.

State (1): Straight.

State (2): Outward curvature.

CHAPTER 2: NEW INSIGHTS FROM INTERNAL ANATOMY

Table 2. Data matrix with character scores for each genus. Character 1 and 7 are discrete and character 8 is continuous (see text). Symbols: -, not applicable; ?, missing data.

Taxa	Character 1	Character 2	Character 3	Character 4	Character 5	Character 6	Character 7	Character 8
<i>Bradypus</i>	1	1	0	0	2	0	0	3.66
<i>Tamandua</i>	-	-	0	0	0	0	0	11.06
<i>Peltephilus</i> †	1	0	0	1	2	1	1	-4.85
<i>Dasypus</i>	0	2	1	1	0	1	1	17.73
<i>Stegotherium</i> †	0	1	1	1	2	1	1	20.83
<i>Prozaedyus</i> †	3	1	?	?	0	1	1	?
<i>Doellotatus</i> †	2	0	?	?	?	1	1	8.08
<i>Euphractus</i>	2	1	1	1	0	1	1	6.58
<i>Chaetophractus</i>	2	1	1	1	0	1	1	3.96
<i>Zaedyus</i>	3	1	1	1	0	1	1	1.67
<i>Chlamyphorus</i>	3	0	1	2	2	1	1	18.29
<i>Calyptophractus</i>	3	0	1	2	2	2	2	11.68
<i>Cabassous</i>	0	1	1	1	0	1	2	8.57
<i>Tolypeutes</i>	2	0	1	1	2	1	2	-1.04
<i>Priodontes</i>	0	1	1	1	0	0	2	-2.11
<i>Proeutatus</i> †	1	1	0	?	1	2	1	17.92
<i>Vassallia</i> †	3	0	0	?	1	1	2	0.08
<i>Propalaehoplophorus</i> †	3	0	0	?	1	2	2	18.56
“ <i>Metopotoxus</i> ” †	3	0	0	?	1	2	2	19.45
“ <i>Cochlops</i> ” †	3	0	0	2	1	2	2	21.2
<i>Eucinepeltus</i> †	3	0	0	?	1	2	2	?
<i>Glyptodon</i> †	3	0	0	2	2	2	2	35.84

† extinct species.

2.3.2 *Cranial Canals**Frontal Diploic Vein canal*

The course of this canal is entirely within the frontal bone. It opens externally at one or exceptionally two foramina located in the orbitotemporal fossa, slightly ventral to the most dorsal part of the orbital margin (Figure S2). This canal conveys the frontal diploic vein, an emissary of the dorsal cerebral vein/dorsal sagittal sinus or a vein issuing from the frontal diploë (Thewissen 1989; Wible & Gaudin, 2004; Evans & de Lahunta, 2012; Muizon *et al.*, 2015).

In early ontogeny, the canal of the frontal diploic vein is initially extremely thick in youngest specimens of *Dasypus* (see also Billet *et al.*, 2017) and *Zaedyus* and occupies a large part of the frontal bone (Figure 11). Its relative diameter is considerably reduced in older specimens of *Dasypus* and *Zaedyus* with no change in its curved trajectory in *Zaedyus* but becoming more strictly transverse in the adult stage in *Dasypus* (Figure 11). In *Cabassous*, it remains fairly similar from juvenile to adult stages in our sample (Figure 11).

In our adult sample, the canal is relatively straight, very thin, oriented posteromedially in dorsal view and without ramifications or only one small branch in *Bradypus* and *Utaetus* (Figure 13, Figure S5). In *Tamandua*, *Peltephilus*, *Stegotherium*, *Dasypus*, *Euphractus*, *Priodontes* and *Cabassous*, its overall course is transverse but with a posterior bend or convexity of varying degree (Figure 13). Ramifications and a posterior convexity are also found in *Prozaedyus*, *Chaetophractus*, *Zaedyus* and *Proeutatus*, but the overall course of their canal is more anteromedially oriented, as is also observed in *Priodontes*, *Stegotherium* and *Cabassous* (Figure 13). The same orientation is found in *Doellotatus* (incomplete), except that the course of the canal is completely straight and has no ramifications (Figure 13). *Tolypeutes*, on the other hand, shows a very peculiar course with a forked structure in dorsal view (Figure 13). The canal is merged with diploë in chlamyphorines but its presence is observable in *Calyptophractus* in which it has a straight and anteromedially oriented trajectory (Figure 13). This canal was not observed in all the glyptodonts sampled or in *Vassallia*. However, Gaudin (2004) notes the presence of this canal in glyptodonts and Gaudin & Lyon (2017) mention it in pampatheres. For the last group, there was a possible confusion with the anterior opening of the orbitotemporal canal (Figure S6). We suspect a taphonomic bias for some specimens (*e.g.*, some

Santacrucian glyptodonts) and call for a deeper study of this canal in cingulates before its variation can be scored.

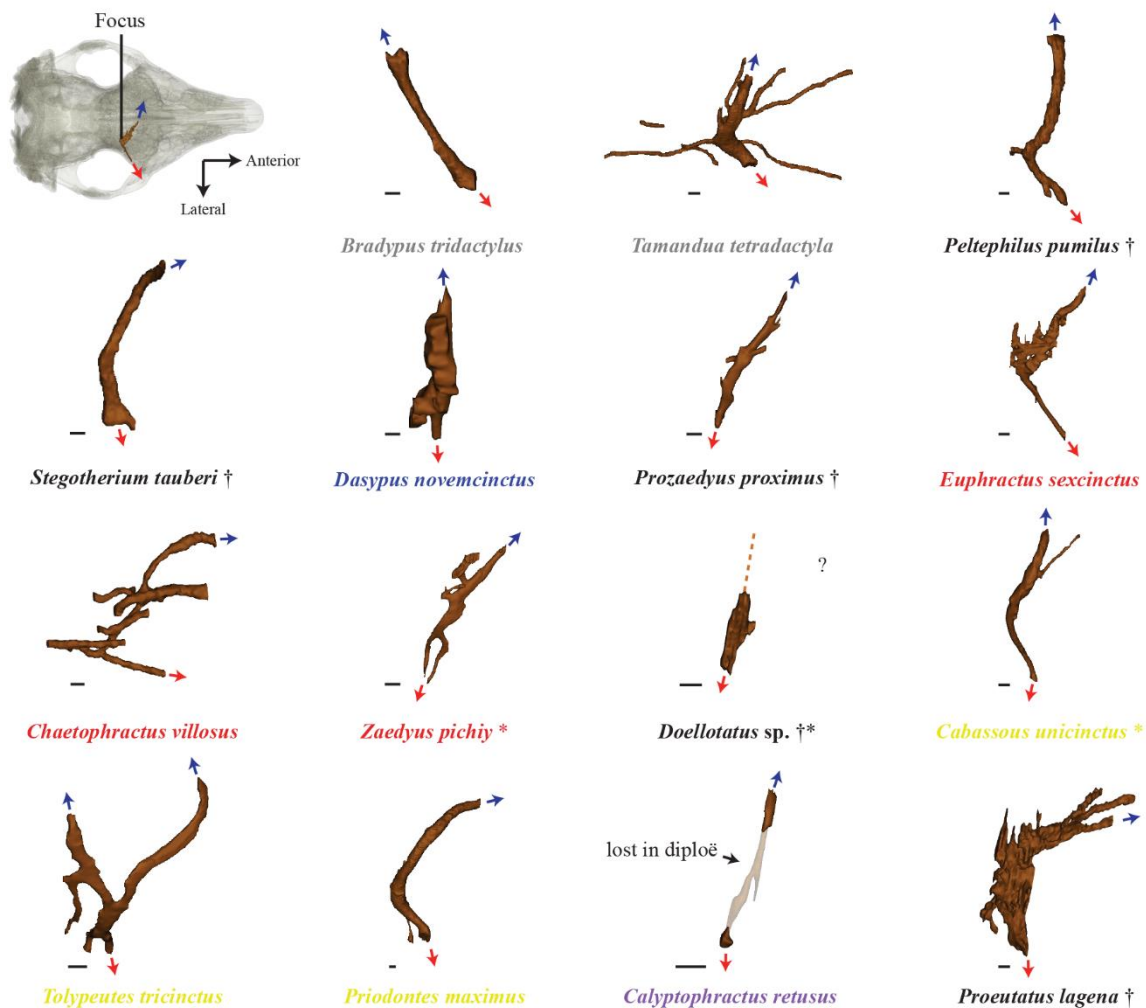


Figure 13. Interspecific variation of the canal for the frontal diploic vein in our sample, all illustrated in dorsal view. Red arrows mark the main external opening of the canal. Blue arrows mark the main internal path of the canal on the cranial midline. Colors of species names follow Figure 10. Scale = 1 mm.

Nasolacrimal Canal

The nasolacrimal canal originates posteriorly at the anterior orbital edge with the lacrimal foramen (Figures 9 & S2). It runs anteriorly within the lacrimal and the maxillary bones in its most posteriormost portion. More anteriorly, the canal is located between the inner wall of the maxillary and turbinates. It opens anteriorly (in front of the tooth row, except in *Peltephilus*) and ventromedially into the nasal cavity (Figures S2E & S7). This canal allows the

transmission of fluids from the lacrimal sac to the nasal cavity and is potentially accompanied by a vein in *Euphractus* (Wible & Gaudin, 2004).

The course of the nasolacrimal canal barely changes during ontogeny in our sample (Figure 11). Its length changes, and follows the lengthening of the snout that accompanies the growth of the cranium (Chapter 3). In addition, *Cabassous* and, to a lesser degree, the adult stage of *Zaedyus* show a more medial orientation of the course of the nasolacrimal canal in its most posterior part which differs slightly from *Dasybus* and other stages of *Zaedyus*, where it runs more parallel to the external surface of the skull (Figure 11).

The position of the nasolacrimal canal and lacrimal foramen varies among taxa, although this feature was not scored in previous matrices (e.g., Gaudin & Wible, 2006). The lacrimal foramen is particularly high relative to the orbital edge (closer to the most dorsal point of the orbit than to the jugal bone in lateral view) in chlamyphorines, *Proeutatus* and glyptodonts (Figure 14). The trajectory of the nasolacrimal canal is strongly sigmoid in *Tamandua* (Figure 14). In *Bradypus*, *Peltephilus*, *Proeutatus*, *Chaetophractus*, and *Euphractus*, the course of the nasolacrimal canal is slightly convex dorsally (Figure 14). The curvature is much pronounced in *Vassallia* in the posterior half of its course as it passes above the tooth row (Figure 14). In dasypodines, *Prozaedyus*, *Zaedyus*, tolyteutines, and chlamyphorines, the nasolacrimal canal is relatively straight or it bears a slight ventral convexity in its posterior part (Figure 14). In glyptodonts, the canal runs ventromedially and not anteriorly from the lacrimal foramen (Figures 14 & 15), and curves strongly inward anteriorly when approaching the sagittal plane of the skull (Figures 14 & 15).

Whereas glyptodonts appear to show a unique condition in the course of their nasolacrimal canal, the anterior opening of this canal is located halfway up in their nasal cavity as in *Bradypus*, *Tamandua*, *Peltephilus*, *Doellotatus*, *Proeutatus* and *Vassallia*. In comparison, this opening is closer to the palate in other specimens (Figure 14). This variation can be scored in the following character (see Table 2).

Character 3 (discrete - unordered): Opening of the nasolacrimal canal in nasal cavity.

State (0): Halfway up in the nasal cavity.

State (1): Ventral in the nasal cavity, close to the palate.

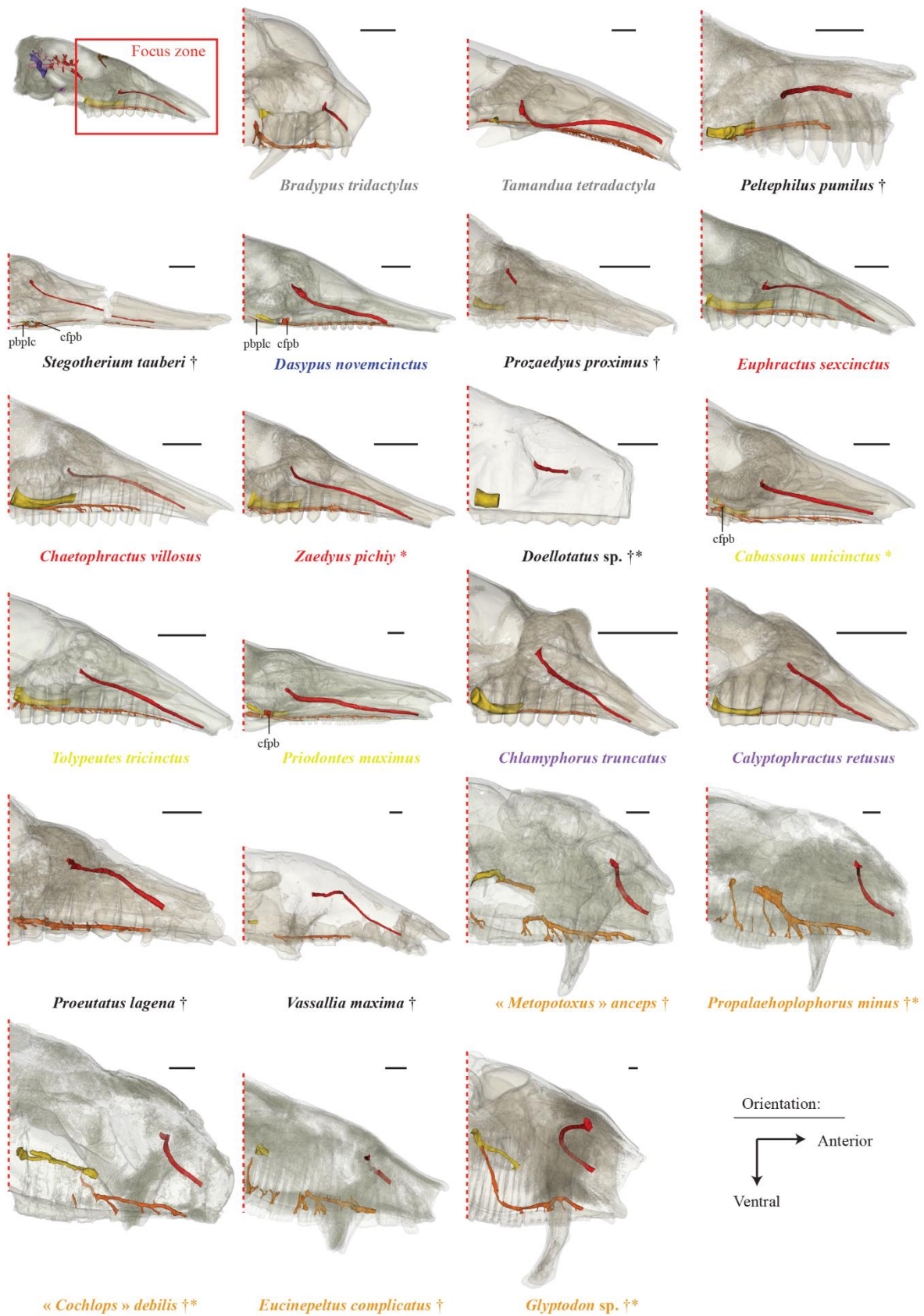


Figure 14. Interspecific variation in our sample of the reconstructed nasolacrimal (= red), sphenopalatine (= yellow) and palatine (= orange) canals shown in lateral view. Skulls are reconstructed with transparency. Colors of species names follow Figure 10. Abbreviations: **cfpb**, caudal foramen for palatine canal branch; **pbplc**, posterior branch of palatine canal. Scale = 1 cm.

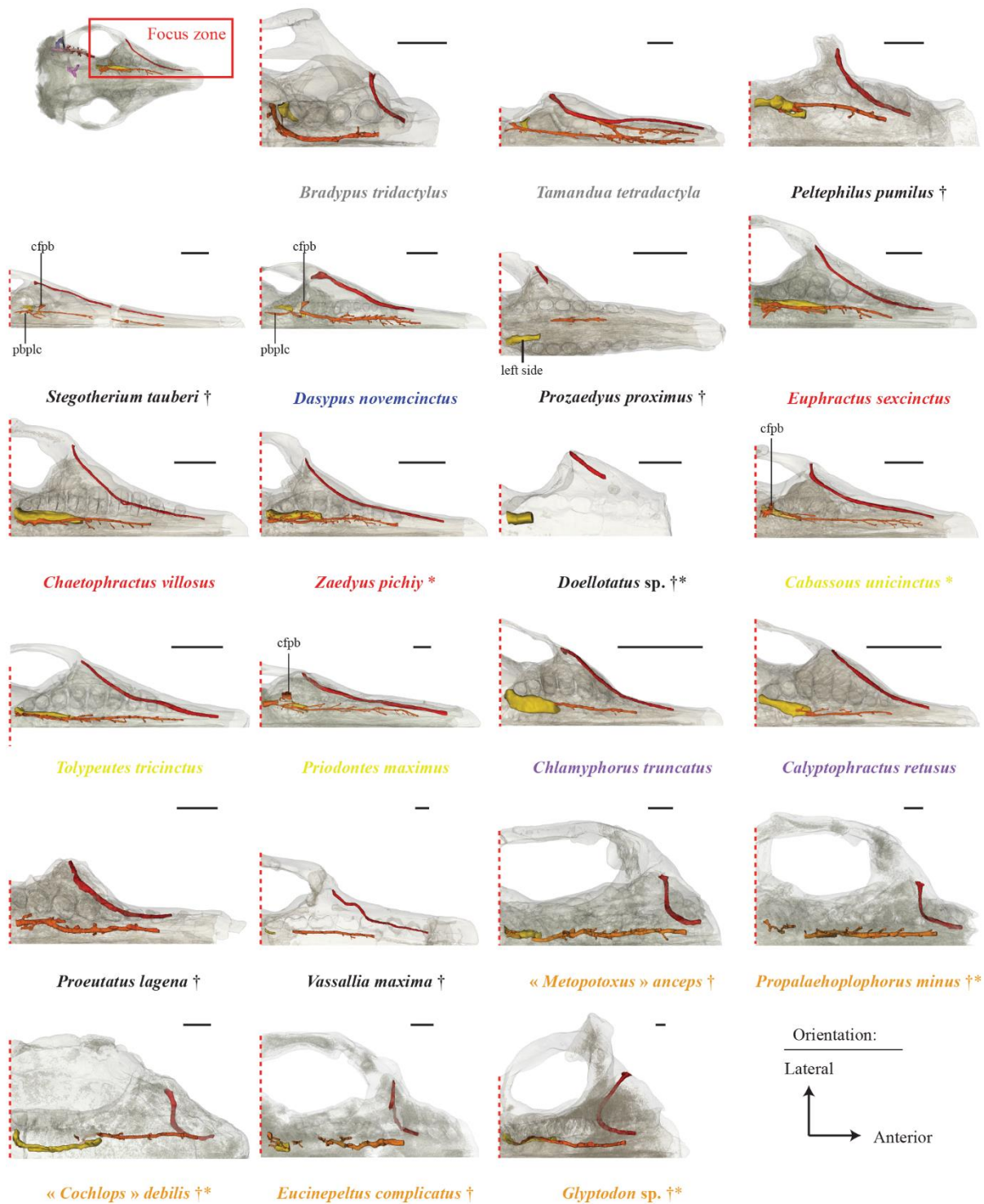


Figure 15. Interspecific variation in our sample of the reconstructed nasolacrimal (= red), sphenopalatine (= yellow) and palatine (= orange) canals shown in ventral view. Skulls are reconstructed with transparency. Colors of species names follow [Figure 10](#). Abbreviations: **cfpb**, caudal foramen for palatine canal branch; **pbplc**, posterior branch of palatine canal. Scale = 1 cm.

Palatine and Sphenopalatine Canals

Two large canals are enclosed within the maxillary and palatine bones forming the hard palate in cingulates: the palatine canal and the sphenopalatine canal (Wible & Gaudin, 2004). The palatine canal is generally thinner, longer than and positioned medial to the sphenopalatine canal. The palatine canal transmits the major and minor palatine nerve, artery, and vein in *Euphractus* (Wible & Gaudin, 2004). This canal opens externally at the caudal palatine foramen posteriorly and at the multiple foramina scattered throughout the hard palate (both in the palatine and maxillary) anteriorly (Figure S2). The sphenopalatine canal, which is often very wide in cingulates, transmits the caudal nasal nerve and the sphenopalatine artery and vein (Wible & Gaudin, 2004). The sphenopalatine canal opens anteriorly in the nasal cavity and posteriorly in the pterygopalatine fossa just posterior to the dental row and close to or confluent with the caudal palatine foramen (Wible & Gaudin, 2004; Figure S2). The palatine canal and sphenopalatine canal are confluent in part of their posterior course in many of the species in our sample.

The palatine canal and sphenopalatine canal vary little during ontogeny within the three species of our ontogenetic series (Figure 11). The branch of the palatine canal posterior to its region of confluence with the sphenopalatine canal in *Dasypus* and *Cabassous* appears in the subadult (or intermediate) stage and elongates further in the adult stage (Figure 11). In the youngest specimen of *Zaedyus*, the sphenopalatine canal is much wider relative to skull size than in later stages, and there is no region of confluence with the palatine canal (Figure 11). In the youngest *Dasypus* specimen, the sphenopalatine canal is absent. It is present only as a wide groove in the youngest to subadult stages, but is completely enclosed in the adult stage of *Dasypus* in our sample (Figure 11).

In our adult sample, the shape and trajectory of the palatine canal does not vary much among species (Figures 14 & 15). In glyptodonts, the palatine canal strongly ascends posteriorly (starting from Mf6) (Figure 14) and forms a groove running along the inner wall of the nasopharyngeal canal (Figure S8). In other cingulates, the palatine canal does not show such an ascending trajectory posteriorly. The sphenopalatine canal, which is thicker than the palatine canal, features a relatively straight trajectory in lateral view in *Peltephilus*, dasypodines, *Prozaedyus*, *Euphractus*, *Zaedyus*, *Doellotatus* and “*Cochlops*”, whereas it shows a strong ventral curvature in *Chaetophractus*, tolypeutines, chlamyphorines and *Glyptodon* (Figure 14).

It should be further noted that the dorsal position of the sphenopalatine canal relative to the nasopharyngeal canal is a feature shared by *Vassallia* and *Glyptodon* (Figure S9). In *Bradypus* and *Tamandua*, the palatine canal does not contact the sphenopalatine canal (Figures 14 & 15). The two canals are in contact in a small region of confluence in the dasypodines whereas the palatine canal becomes completely confluent with the sphenopalatine canal, and sometimes accompanied by ventrally oriented auxiliary branches of the palatine canal, in *Peltephilus*, tolypeutines, chlamyphorines and *Glyptodon* (Figures 14 & 15). In euphractines, the confluence between the sphenopalatine canal and the palatine canal is not as clear-cut as in the above-cited cingulates (Figures 14 & 15). The palatine canal of euphractines runs ventrally along the sphenopalatine canal in the same figure 8-shaped canal while being completely conjoined only in their most posterior part and at their posterior opening (Figures 14 & 15). The extent of this confluence is highly variable in *Euphractus* according to Wible & Gaudin (2004), and in other cingulates as well (Gaudin & Wible, 2006 – character 71). We observed the same variation as Gaudin & Wible (2006) concerning the extent of this confluence in the vicinity of the posterior opening of the sphenopalatine canal for all the taxa in our sample. Several branches may emerge from this region of confluence (Figures 14 & 15), some of which present an interesting pattern. One branch opens externally from the caudal foramen of the palatine canal in dasypodines, *Cabassous* and *Priodontes* (Figures 14 & 15). A second branch extends posteriorly into the hard palate, before disappearing in the bone diploe in dasypodines. In *Euphractus*, *Zaedyus*, *Cabassous* and *Priodontes*, two or more branches extend posteriorly into the hard palate, but they open in the nasopharyngeal canal (Figures 14 & 15). Several other ramifications of the palatine canal are present in our sample, but it remains to be determined how variable these are at the intraspecific level with a dataset larger than that of Table S1.

Based on the observation of these two canals, we proposed to scrutinize evolutionary scenarios for the following character (see Table 2).

Character 4 (discrete - unordered): Sphenopalatine and palatine canal connection.

State (0): No contact.

State (1): Partial contact, with palatine canal running ventrally along the sphenopalatine canal and producing posterior branches.

State (2): Complete fusion.

Transverse Canal

When present, the transverse canal is marked externally by a foramen positioned anteroventrally to or within the foramen ovale in the alisphenoid (Figure S2). This canal crosses the cranium transversally at the level of the basisphenoid and transmits a large vein issued from the cavernous sinus (Sánchez-Villagra & Wible, 2002; Wible & Gaudin, 2004). Often, one or more branches originate from this canal and extend posteriorly towards the lateral edge of the basisphenoid to join the inferior petrosal sinus (Wible & Gaudin, 2004).

The transverse canal appears early in *Dasypus* and varies little during ontogeny. Although, in *Zaedyus* and *Cabassous*, the connection between the transverse canal and the posterior branch extending towards the inferior petrosal sinus varies in both series, we have not observed a clear ontogenetic pattern of variation in our three species (Figure 11).

In *Bradypus*, *Peltephilus*, *Stegotherium*, *Doellotatus*, *Tolypeutes* and *Glyptodon*, there is no transverse canal, or it is not detectable (scored as present in *Doellotatus* and *Stegotherium*, variable in *Tolypeutes* by Gaudin & Wible, 2006 – character 111). Chlamyphorines have a transverse canal foramen opening directly within the braincase, and thus there is a very short canal that does not cross the midline of the cranium. *Tamandua* stands out in having a thin lateral part of the transverse canal which is not comparable to the condition in Cingulata (Figure 16). In *Utaetus* (Figure S5), *Dasypus*, euphractines, *Prozaedyus*, *Cabassous* and *Priodontes*, the branch starting from the transverse canal foramen is oriented posteromedially in ventral view (Figure 16). In the Santacrucian glyptodonts, it is medially oriented (Figure 16). In *Vassallia* it is anteromedially oriented (Figure 16). This lateral branch of the transverse canal splits into a branch that crosses the midline in the basisphenoid bone and a branch that joins the inferior petrosal sinus (except in *Utaetus* (Figure S5) where the branch extends dorsolaterally to open into the roof of the basisphenoid) (Figure 16). In *Proeutatus*, this bifurcation occurs much closer to the transverse canal foramen than in other taxa (Figure 16). It is relatively more medial in euphractines, *Prozaedyus*, *Cabassous* and *Priodontes* (Figure 16). In *Tamandua*, *Dasypus*, *Vassallia* and Santacrucian glyptodonts, this bifurcation is closer to the sagittal plane than to the foramen (Figure 16). The transverse medial branch is anteromedially oriented in ventral view in *Proeutatus*, *Cabassous* and *Prozaedyus*, whereas it is medially oriented in the

other taxa (Figure 16). Our specimens of *Tamandua*, euphractines (not complete in *Chaetophractus*) and *Priodontes* show an additional branch connecting the transverse medial branch to the posterior branch reaching the inferior petrosal sinus (Figure 16). In *Vassallia* and the Santacrucian glyptodonts, the posterior branch reaching the inferior petrosal sinus is much thinner than the rest of the canal, in contrast to the other taxa, in which the whole canal exhibits a relatively homogeneous width (Figure 16).

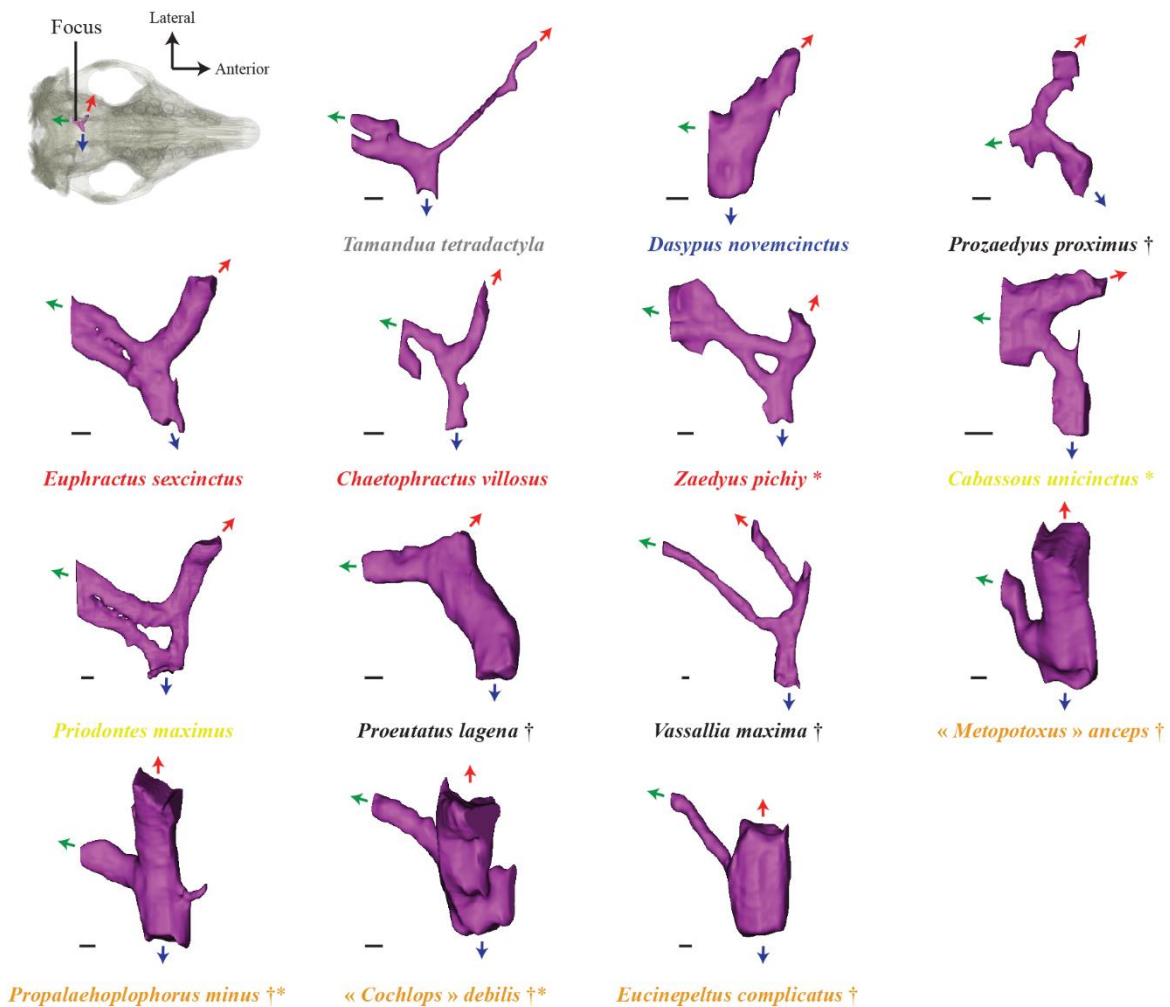


Figure 16. Interspecific variation of the transverse canal in ventral view in our sample. Red arrows mark the main external opening of the canal. Blue arrows mark the branch crossing the midline. Green arrows mark the main posterior branch which connects to the inferior petrosal sinus (see text). Colors of species names follow Figure 10. Scale = 1 mm.

Based on these observations of the transverse canal, we propose to scrutinize evolutionary scenarios for the following character (see [Table 2](#)).

Character 5 (discrete - unordered): Orientation of the branch starting from the transverse canal foramen.

State (0): Posteromedial.

State (1): Medial or anteromedial.

State (2): No canal.

Orbitotemporal and Posttemporal Canals

Within the braincase, the orbitotemporal canal provides passageway to the rostral extension of the *ramus superior* of the stapedia artery, or orbitotemporal artery (giving rise to the *ramus supraorbitalis* in the orbital region), and a few small veins ([Wible & Gaudin, 2004](#)) whereas the more posterior posttemporal canal transmits the *arteria diploëtica magna* and the large *vena diploëtica magna* ([Wible & Gaudin, 2004](#)). These two canals can give rise to the arterial and venous *rami temporales* along the lateral wall of the braincase which exit via numerous foramina on the cranial roof to irrigate the *temporalis* muscle ([Wible & Gaudin, 2004](#); [Figure S2](#)). The posttemporal canal is connected posteriorly to an external groove in the petro-occipital region marking the passage of the occipital artery ([Wible & Gaudin, 2004](#); [Figure S2](#)). From there, the posttemporal canal extends forward as a canal enclosed between the petrosal and squamosal (or only in the squamosal) and oriented mostly horizontally. More anteriorly, past the petrosal, the posttemporal canal is connected to the orbitotemporal canal, which runs further anteriorly within or on the inner surface of the lateral braincase wall of the braincase (formed by the squamosal, frontal and sometimes the parietal). The delimitation between the two canals generally occurs where the canal for the *ramus superior* joins them ([Muizon et al., 2015](#)). However, we were only able to observe a canal possibly transmitting the *ramus superior* in *Tolypeutes* ([Figure S10](#)), but not in the other specimens. Consequently, we followed the suggestion of [Wible & Gaudin \(2004\)](#), who separate the two canals at the level of the postglenoid foramen. In some taxa, the orbitotemporal canal is not completely enclosed for parts of its length, and appears instead as a groove on the internal wall of the braincase. The anterior opening of the orbitotemporal canal is located in the orbitotemporal region, just posteroventral to the postorbital constriction ([Figure S2](#); [Wible & Gaudin, 2004](#); = cranioorbital foramen in [Gaudin & Wible, 2006](#); see also [Muizon et al. \(2015\)](#) for multiple illustrations of these canals in another placental taxon).

The orbitotemporal canal only appears as a short canal near the orbitotemporal region in the youngest specimens of all three species, whereas the canal (or groove) is clearly visible for its entire length in later stages (Figure 11). The connections of the orbitotemporal canal with canals for the numerous *rami temporales* occur in the two last stages in both *Zaedyus* and *Cabassous* (Figure 11). The posttemporal canal is already well formed in the youngest specimen of *Dasybus* and hardly changes during ontogeny (Figure 11). In *Zaedyus*, the posttemporal canal is not enclosed in the youngest stage. In *Cabassous*, the posttemporal canal is present in the youngest stage sampled, but it expands anteriorly during the two subsequent stages (Figure 11).

In our adult sample, *Bradypus*, *Tamandua*, euphractines, *Vassallia* and glyptodonts possess a posttemporal canal emerging at the center of the occiput in lateral view and at the level of the jugular foramen (Figure 17). In *Peltephilus*, it originates more ventrally, even with the most dorsal margin of the occipital condyles in lateral view (Figure 17). In dasypodines, tolypeutines and chlamyphorines, the posterior extremity of the canal is at an intermediate height (Figure 17). Apart from the position of the posterior opening of this canal (= posttemporal foramen of Wible & Gaudin, 2004), we were unable to determine any systematically significant variation regarding its direction, length, or width.

In *Bradypus* and *Tamandua*, the orbitotemporal canal does not reach the orbitotemporal region (Figures 17 & 18). It reaches the orbitotemporal region in all the cingulates in our sample except for *Priodontes* (Figures 17 & 18). Gaudin & Wible (2006) mention the absence of the anterior opening of the orbitotemporal canal in *Priodontes* (character 78), but also in *Chlamyphorus* and *Vassallia* for which we observe a clear opening in the orbitotemporal region (Figure 17). In *Bradypus*, *Tamandua* and *Peltephilus*, this canal bears a ventral curvature (strong in *Peltephilus*), whereas its trajectory exhibits a more or less strong dorsal curvature in all the other taxa (Figure 17). In *Utaetus* (Figure S5), *Peltephilus*, *Dasybus*, *Prozaedyus*, euphractines, *Cabassous*, *Tolypeutes*, chlamyphorines, *Proeutatus* and Santacrucian glyptodonts, the orbitotemporal canal becomes a groove on the internal lateral wall of the braincase before being enclosed again as a canal close to its external anterior opening (Figure 17). In *Calyptophractus*, *Proeutatus* and glyptodonts, the anterior half of the orbitotemporal canal displays a pronounced downward trajectory, and its anterior opening is located lower than its posterior connection with the posttemporal canal (Figure 17). *Calyptophractus* stands out, however, in having two branches that connect the orbitotemporal and posttemporal canals (Figure 17). A large region of confluence between the orbitotemporal and posttemporal canals and the canal for the capsuloparietal emissary vein is identified in *Tamandua*, *Peltephilus*, *Stegotherium*, *Dasybus*, *Chaetophractus*, *Priodontes*, *Vassallia* and the glyptodonts (and potentially also in *Proeutatus*

but the orbitotemporal canal is not distinct in this region; [Figures 17 & 18](#)). This confluent region is reminiscent of the petrosquamosal fossa in *Alcidedorbignya* ([Muizon et al., 2015](#)). The orbitotemporal and posttemporal canals connect with the *rami temporales* through multiple small canals whose number remains quite variable at the intraspecific level. However, a high density of *rami temporales* for the orbitotemporal canal is particularly noticeable in euphractines, *Cabassous*, *Calyptophractus* and glyptodonts ([Figure 17](#)). This density is coded by [Gaudin & Wible \(2006\)](#), who counted the number of foramina for *rami temporales* in the temporal fossa of parietal (0, equal to or less than five; 1, greater than five – character 97). In their matrix, almost all cingulates are coded as having more than 5 foramina. The variations in the density of the canals for the *rami temporales* observed in our study call for further investigation of these structures, which could potentially carry an interesting phylogenetic signal among cingulates.

Based on these observations of the orbitotemporal canal, we propose to scrutinize evolutionary scenarios for the following character (see [Table 2](#)).

Character 6 (discrete - unordered): Downward trajectory of the orbitotemporal canal.

State (0): Canal does not reach the orbitotemporal region.

State (1): The anterior part of the canal has a slight downward trajectory ending at the same or almost the same height as its origin from the posttemporal canal.

State (2): The canal has a strong downward anterior trajectory, and its anterior opening is much lower than its posterior connection to the posttemporal canal.

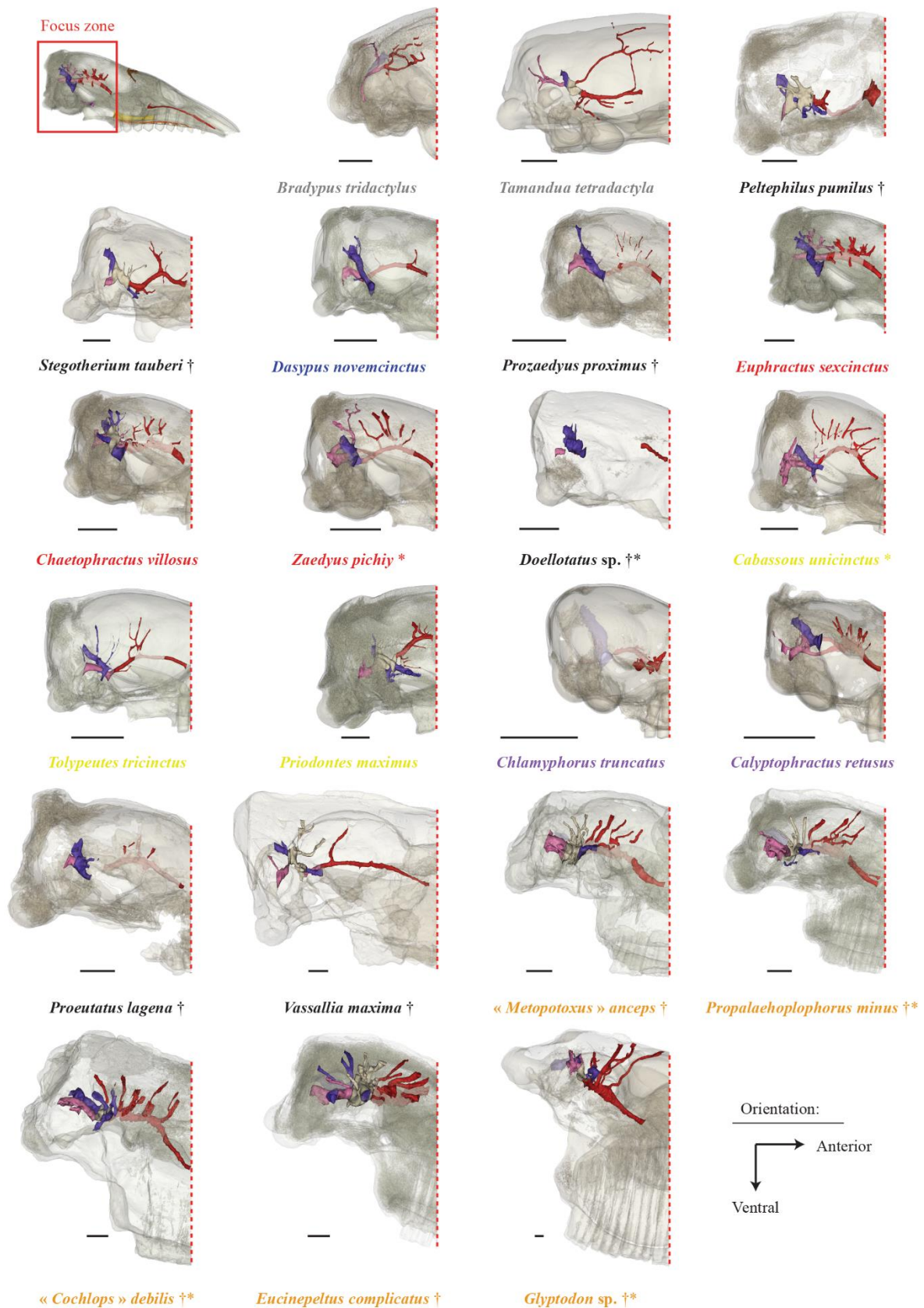


Figure 17. Interspecific variation in our sample of the orbitotemporal (= red), posttemporal (= pink) and capsuloparietal emissary vein (= blue) canals shown in lateral view. Caudal part of the skull is transparent. Parts of the canals showing transparency symbolize a groove instead of a fully enclosed canal. Colors of species names follow Figure 10. Scale = 1 cm.

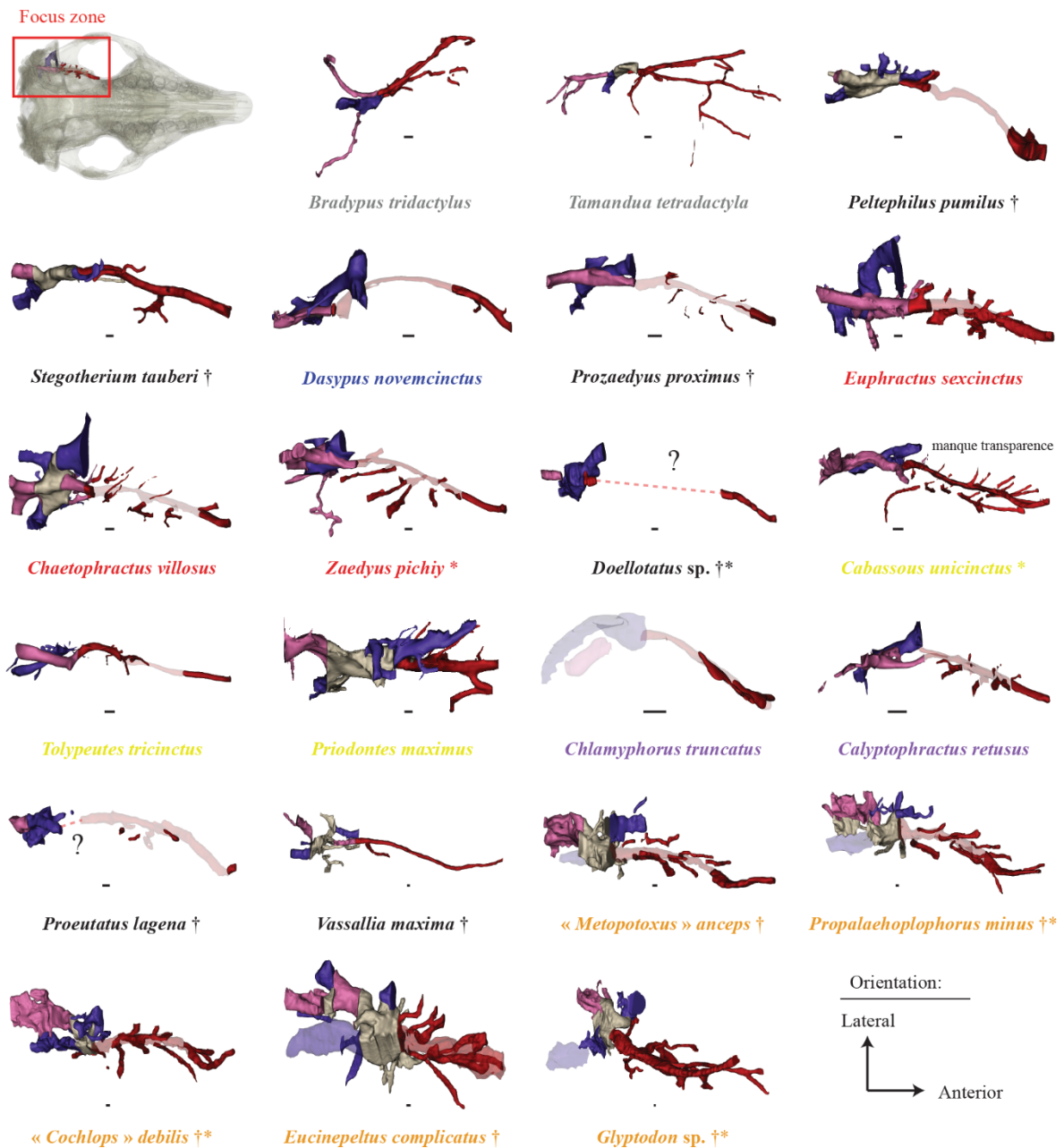


Figure 18. Interspecific variation in our sample of the orbitotemporal (= red), posttemporal (= pink) and capsuloparietal emissary vein (= blue) canals shown in ventral view. Transparent parts of the canals indicate a groove instead of a fully enclosed canal. Colors of species names follow Figure 10. Scale = 1 mm.

Canal of the Capsuloparietal Emissary Vein

The canal for the capsuloparietal emissary vein opens anteroventrally at the postglenoid and suprameatal foramina, and connects to the groove for the transverse sinus posterodorsally (Wible, 1993; Muizon *et al.*, 2015). From the cranial roof, the transverse sinus runs posterovertrally in a wide groove excavated in the inner surface of the parietal and extends

anteroventrally within a canal formed by the petrosal medially and the squamosal laterally. This canal opens externally through the suprameatal foramen, the postglenoid foramen and accessory foramina at the posterior base of the zygomatic arch (e.g., Wible & Gaudin, 2004; Figure S2). It transmits the capsuloparietal emissary vein (= retroarticular vein in *Canis* (Evans & de Lahunta, 2012); postglenoid vein in *Cynocephalus* (Wible, 1993) and *Dasypus* (Wible, 2010)). In our sample, this canal is often partly confluent with the posttemporal and orbitotemporal canal in its posterodorsal portion (Figure S11).

The canal for the capsuloparietal emissary vein is already well formed in the youngest specimen of *Dasypus* and hardly changes during ontogeny, except that it becomes relatively thinner (Figure 11). In *Zaedyus*, it is only partly formed in the youngest specimen, and its trajectory is better marked in older stages (Figure 11). In the youngest *Cabassous*, this canal is noticeably short and only marked in its most ventral part (glenoid region). It is only in older stages that the canal elongates posterodorsally (Figure 11).

The canal is absent and the passage of the vein is only indicated by a groove in *Bradypus*, *Chlamyphorus* and *Utaetus* (maybe due to the absence of the petrosal in the *Utaetus* specimen illustrated on Figure S5). The groove is very wide in the latter two (Figure 17). In *Utaetus*, several *rami temporales* open into the cranial roof, and the groove becomes a short canal opening into the glenoid region (Figure S5). The canal of the capsuloparietal emissary vein opens through the postglenoid foramen and potentially in the suprameatal foramen as well (see *rami temporales* opening in the squamosal whose number varies in our intraspecific sampling (Table S1)) in *Peltephilus*, euphractines, *Prozaedyus*, *Doellotatus*, *Proeutatus*, chlamyphorines, *Vassallia* and the glyptodonts (as notably scored for the glenoid region by Gaudin & Wible, 2006 – character 119; Figures 17 & 18). In tolyteutines, the canal always opens by a suprameatal foramen with a well-marked branch, whereas its opening via the postglenoid foramen may sometimes be absent, as we have occasionally observed the absence of a postglenoid foramen in our intraspecific sample of *Cabassous unicinctus* (Table S1). For all our taxa except *Bradypus*, the canal extends anteroventrally the cranial roof (Figure 17). However, its inclination varies considerably from one species to another. It is steeply inclined in dasypodines, slightly less so in euphractines, *Prozaedyus*, *Doellotatus* and *Proeutatus*, and much less so in tolyteutines, *Calyptophractus*, *Vassallia* and glyptodonts (Figure 17). The canal is sinuous in *Euphractus* and *Chaetophractus*. In glyptodonts, the canal even has an almost anteroposterior orientation near its anterior opening (Figures 17 & 18). The canal (or groove)

for the capsuloparietal emissary vein reaches a region of confluence (= petrosquamosal fossa, Muizon *et al.*, 2015) with the other canals of the braincase in *Tamandua*, *Peltephilus*, dasypodines (particularly thin in *Dasypus*), *Chaetophractus*, *Priodontes*, *Vassallia* and glyptodonts (Figures 17 & 18). For the other taxa, the canal for the capsuloparietal emissary vein is only adjacent to the other canals (Figures 17 & 18 – see Figure S11 for an illustration of the different cases in our sample). The variation in length and thickness of this canal does not provide clear systematic information. A relatively short canal is present in *Tamandua*, *Zaedyus*, *Doellotatus* and *Proeutatus* compared with dasypodines (Figure 17). Chlamyphorines and *Zaedyus* show a relatively thicker canal, as compared with the very thin canal in *Vassallia*. The fact that small taxa have a relatively thicker canal is reminiscent of young specimens of *Dasypus* as compared to older and larger specimens of the same species (Figure 11) and suggest a potential allometric pattern.

Based on these observations, we propose to scrutinize evolutionary scenarios for the following character related to the anterolateral extremity of the canal (see Table 2).

Character 7 (discrete - unordered): Canal of the capsuloparietal emissary vein inclination in lateral view.

State (0): Anterodorsal orientation or canal very short.

State (1): Inclination anteroventral from the posterior opening to the anterior opening.

State (2): Less anteroventrally inclined, with an almost anteroposterior orientation close to the anterior opening.

2.3.3 Inclination of the cranial roof

Digital study of the braincase of our sample enabled observation of notable variations in the internal vault inclination (= IVI) relative to the anteroposterior axis of the cranium. The values of the IVI angle show an interesting pattern in our sample that does not correlate ($R^2 = 0.1768$; P -value = 0.3246) with size (Figure 19). Whereas *Glyptodon* is distinguished from the other cingulates by an exceedingly high inclination combined with a large size, the large-sized *Vassallia* has a very low cranial roof inclination (Figure 19). Miocene glyptodonts, *Proeutatus*, *Stegotherium*, *Chlamyphorus* and the adult specimen of *Dasypus* are also characterized by high inclinations (Figure 19). The juvenile *Cabassous* also displays a strong inclination, which decreases with age whereas the inclination increases with age in *Dasypus* (Figure 19). *Calyptophractus* shows an intermediate cranial roof inclination (Figure 19). The outgroups,

Cabassous (adult) and euphractines exhibit low values, and the remaining tolypeutines and *Peltephilus* are even characterized by a negative tilting of IVI (Figure 19).

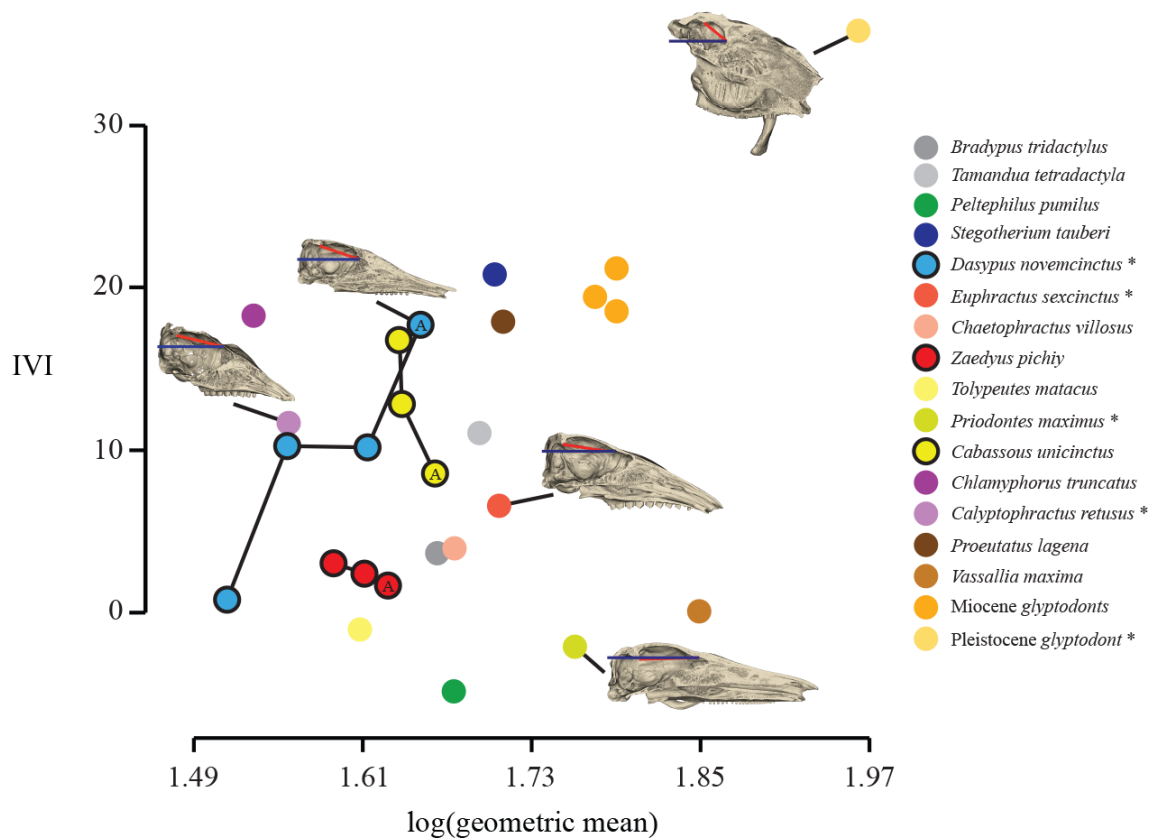


Figure 19. Distribution of the internal vault inclination (IVI) with respect to cranial size (= log(geometric mean)) in our sample. For the three developmental series, A symbolizes the adult specimen. Specimens marked with an asterisk are illustrated by cranial reconstructions in sagittal view in the graph. Scale = 1 cm.

We propose to treat the IVI as a continuous character to scrutinize evolutionary scenarios (see Table 2).

Character 8 (continuous): Internal Vault Inclination.

2.4 DISCUSSION

Due to their very unusual anatomy, even within the Cingulata, the phylogenetic placement of glyptodonts has been long debated (Burmeister, 1874; Scott, 1903; Carlini & Zurita, 2010; Fariña *et al.*, 2013). Recent molecular analyses have proposed a new hypothesis (*i.e.*, as sister group of the clade tolypeutines + chlamyphorines – Delsuc *et al.*, 2016; Mitchell *et al.*, 2016) at odds with the multiple hypotheses based on morphological analyses (Engelmann, 1985; Gaudin & Wible, 2006; Billet *et al.*, 2011; Herrera *et al.*, 2017). The recent investigation of the internal anatomy in the *Dasybus novemcinctus* species complex (Billet *et al.*, 2017) underlined the potential phylogenetic signal hidden in the internal cranial structures of cingulates. Comparative studies on the paranasal sinuses and on brain endocasts of cingulates have been performed, but could not provide consistent information on the placement of glyptodonts within the Cingulata (Zurita *et al.*, 2011; Fernicola *et al.*, 2012; Tambusso & Fariña, 2015a). Our comparative study complements these previous efforts by adding the analysis of the dental alveolar cavities (previously only explored in the glyptodont genus *Eucinepeltus* – González-Ruiz *et al.*, 2020) and of various canals involved in the vascularization and innervation of the skull (see Wible & Gaudin, 2004). Based on an extensive sample of extant and extinct cingulates, our survey enabled us to describe many new aspects of the internal cranial anatomy in the group, and to propose 8 potential characters with helpful phylogenetic information to aid in determining the placement of glyptodonts within Cingulata.

The anatomical variation of the dental alveolar cavities in cingulates comprises many aspects including the height, curvature, and orientation of teeth, along with their number and distribution on the rostrum (Vizcaíno, 2009). Among our observations, we have proposed two characters with potential bearing on the affinities of glyptodonts. The first corresponds to the position of the most dorsal point of these cavities in lateral view (character 1). The dorsal margins of the alveoli for a dorsally convex line for the whole dental row in most cingulates, except in taxa with reduced teeth. This point is situated posteriorly (*i.e.*, at Mf5-6) in glyptodonts, pampatheres, chlamyphorines, *Prozaedyus* and *Zaedyus* in our sample. The distribution of this character would be congruent with the hypothesis of a close relationship between glyptodonts and pampatheres, as suggested by many previous authors (Patterson & Pascual, 1972; Gaudin & Wible, 2006; Billet *et al.*, 2011; Herrera *et al.*, 2017), but also supports the clade formed by the latter two with chlamyphorines, as proposed by the morphological

analysis of Mitchell *et al.* (2016) constrained by the molecular backbone (Figure 20). On the other hand, *Proeutatus*, generally considered to be a close relative of the clade glyptodonts + pampatheres (Engelmann, 1985; Gaudin & Wible, 2006; Billet *et al.*, 2011; Gaudin & Lyon, 2017), has its most dorsal point situated much further anteriorly (*i.e.*, *ca.* Mf1-3).

The second character derived from dental alveolar cavities corresponds to the curvature of the anterior teeth in anterior view (character 2). As for character 1, chlamyphorines and pampatheres resemble glyptodonts in this aspect, exhibiting an inward curvature. *Tolypeutes*, *Doellotatus* and *Peltephilus* also show a similar condition (Figure 20). As shown by the reconstructed evolutionary scenario (Figure 20), this character could still support the morphological hypothesis of Mitchell *et al.* (2016) of a close relationship between glyptodonts and chlamyphorines. The distribution of this character on the baseline cladogram shows some homoplasy, however, with the condition in *Proeutatus* contrasting with that of glyptodonts, while the early diverging *Peltephilus* resemble the latter (Figure 20). Another point of interest concerning the variation of dental alveolar cavities is the potential allometric pattern identified by the correlation between the relative height of the dental row and skull size (Figure 12). This needs to be analyzed further, but if confirmed, such an allometric pattern pertaining to the relative height of the dentition may be closely related to the variation in shape of the rostrum. Extremely high teeth, if not strongly curved, should occupy a large dorsoventral space and would thus require a relatively high rostrum. This hypothesis is reinforced by the existence of a common allometric pattern in mammals corresponding to the relative elongation of the snout as size increases (Cardini & Polly, 2013; Cardini, 2019). However, we do not know whether allometry could affect the variation of the two aforementioned alveolar cavity characters, but the resemblance of small taxa (*i.e.*, chlamyphorines) and large taxa (*i.e.*, glyptodonts and pampatheres) seems to argue against this. In any case, our study brings to light interesting new variation regarding the upper tooth roots/alveolar cavities of cingulates, which have in the past been compared to one another on the basis of their number, the presence/absence of teeth in the premaxillary, tooth wear, histology, and the orientation of the long axis of the teeth relative to the long axis of the dental row (characters 1, 3 to 8 – Gaudin & Wible, 2006 ; see discussion for glyptodonts regarding these characters – Scott, 1903; Ferigolo, 1985; González-Ruiz *et al.*, 2015).

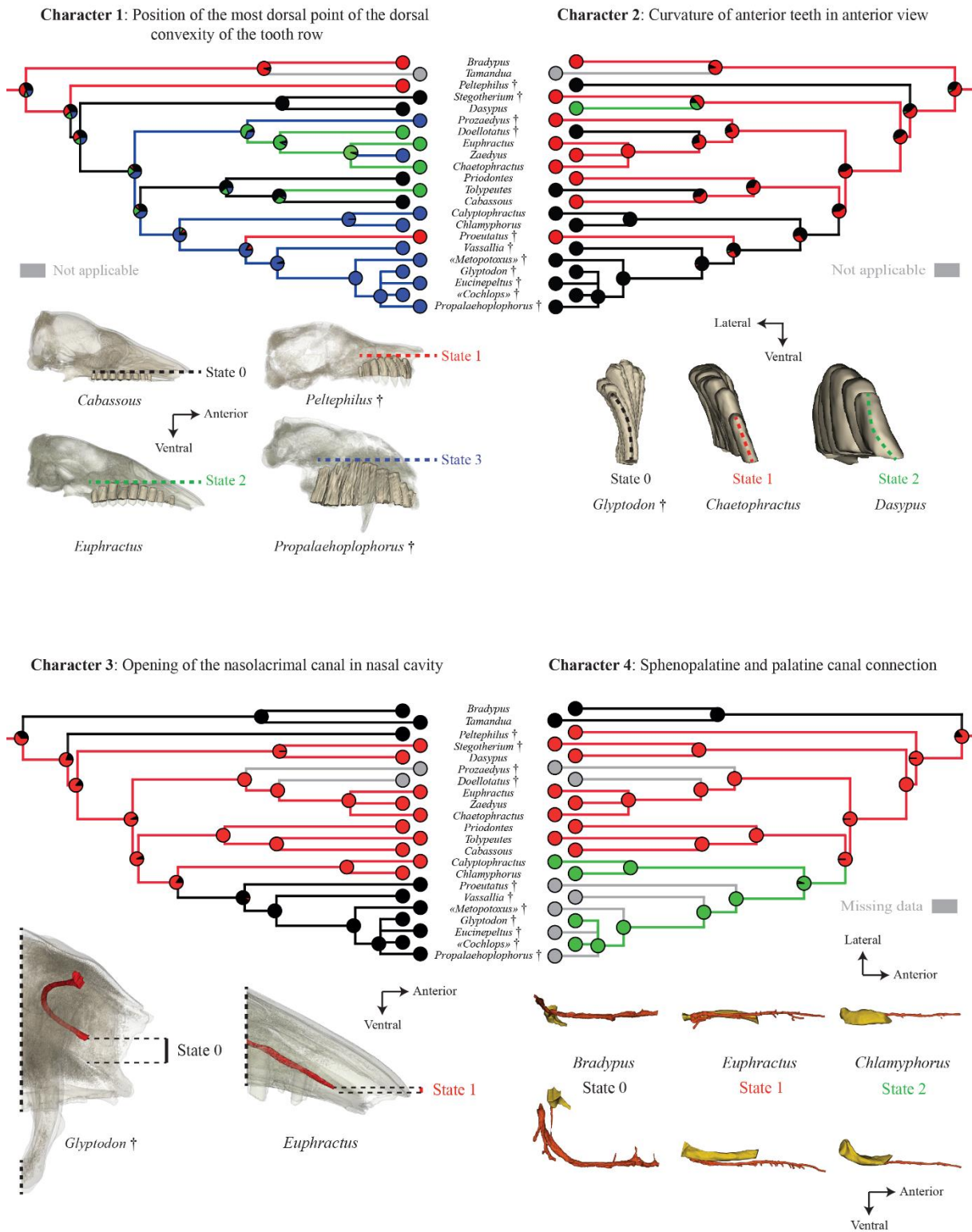


Figure 20. Reconstructed evolutionary scenarios for the endocranial characters 1 – 4 plotted on the reference cladogram with ancestral state estimation for internal nodes (see [Material & Methods, Supporting information 2](#) and [Figure S4](#)). Each character is illustrated, and the relationship between color and coding is indicated within the figure itself. † represents extinct genera. Scale = 1 cm.

Our initial observations point towards a resemblance between glyptodonts, chlamyphorines and pampatheres on the overall spatial organization of the alveolar cavities, which would be partly compatible with molecular results (Delsuc *et al.*, 2016; Mitchell *et al.*, 2016). However, we believe further information could be gained by more detailed quantified analyses of shape to more fully reflect the complex spatial variation of the dental alveolar cavities.

Our analysis of selected intracranial canals described various aspects of their variation, which were unknown in cingulates until now. Furthermore, it enabled us to propose five characters, that provide potentially significant phylogenetic information. This analysis also demonstrated the need to further examine the variation of several structures (*e.g.*, canal of the frontal diploic vein).

Both the trajectory and position of the nasolacrimal canal vary within the sample. A trajectory that is first directed medially at its posterior opening (*i.e.*, the lacrimal foramen) represents a unique characteristic of glyptodonts within the Cingulata (Figures 14 & 15). The most informative feature on this canal regarding the relationships of glyptodonts with other cingulates is the relative height of its anterior opening within the nasal cavity (character 3 – Figure 20). In most cingulates, this opening is positioned ventrally in the nasal cavity, close to the hard palate, whereas in glyptodonts it is near the vertical midpoint of the cavity. The distribution of this character on the baseline cladogram supports the node linking the glyptodonts, pampatheres and *Proeutatus* (Figure 20), as in several previous morphological analyses (Engelmann, 1985; Gaudin & Wible, 2006; Billet *et al.*, 2011; Gaudin & Lyon, 2017).

The course and connection between the sphenopalatine canal and the palatine canal is characterized by a complex pattern which is very peculiar in glyptodonts (Figures S8 & S9). The degree of fusion between the two canals was variable within our sample. Because of taphonomic issues, only “*Cochlops*” and *Glyptodon* allowed us to observe a fusion of the two canals in glyptodonts. However, this fusion was also present as in the chlamyphorines. The uncertain condition in pampatheres and *Proeutatus* does not allow us to draw clear conclusions (character 4 – Figure 20), but the distribution of this character on the baseline cladogram could be congruent with the morphological hypothesis of Mitchell *et al.* (2016) (Figure 20). However, caution is warranted, because the confluence between the sphenopalatine foramen and the caudal palatine foramen is known to exhibit substantial intraspecific variation in several taxa

(see character 71, [Gaudin & Wible, 2006](#)) including *Euphractus* ([Wible & Gaudin, 2004](#)). In addition, the condition in pampatheres needs further investigation, since a caudal palatine foramen has been identified in the floor of the sphenopalatine canal in *Holmesina* ([Gaudin & Lyon, 2017](#)). Our study also reveals a strong resemblance between pampatheres and glyptodonts, which share a dorsal position of the sphenopalatine canal in relation to the nasopharyngeal canal ([Figure S9](#)). This feature could have been coded as a character, but an investigation of potential allometry for this trait is required before coding this trait.

The course, orientation and connections of the transverse canal also vary in our sample. We were unable to identify this canal in *Glyptodon*, *Tolypeutes* and chlamyphorines, as well as *Bradypus*, *Peltephilus* and *Stegotherium*. Its presence in the Santacrucian glyptodonts, pampatheres, *Proeutatus* and many other cingulates suggests that it has been lost in *Glyptodon*. Apart from this potential loss, the distribution on the baseline cladogram of the character corresponding to the orientation of the branch directly connected to the transverse canal foramen may support the common morphological hypothesis of a close relationship among glyptodonts, pampatheres, and *Proeutatus* (character 5 – [Figure 21](#); see also [Engelmann, 1985](#); [Gaudin & Wible, 2006](#); [Billet et al., 2011](#); [Gaudin & Lyon, 2017](#)). Moreover, our work is congruent with the matrix of [Gaudin & Wible \(2006\)](#) regarding the presence/absence of the transverse canal foramen for most taxa (character 111) with the exceptions of *Stegotherium* (coded as present in [Gaudin & Wible, 2006](#)), *Tamandua* (coded as absent in [Gaudin & Wible, 2006](#)), and *Doellotatus*. In the case of the latter, the specimen available for our study was poorly preserved for this character (coded as present in [Gaudin & Wible, 2006](#)). Our study also allows us to confirm the hypothesis of [Wible & Gaudin \(2004\)](#), which suggested that the canal crosses the midline of the skull in *Euphractus sexcinctus*. In their fetuses, they did not observe this transverse pattern, and doubted whether it existed in adult specimens ([Wible & Gaudin, 2004](#)). We can confirm this pattern in our specimen ([Figure 16](#)). This well-known circulation pattern in several marsupials is much less clear in placentals, for which the occurrence of a foramen for the transverse canal (often without knowing whether it crosses the skull midline) is most often interpreted as a case of convergence ([Sánchez-Villagra & Wible, 2002](#)). In addition, our analysis of the youngest specimen of *Zaedyus* also suggests that the transverse canal is not formed in young euphractine individuals, according with the observations of [Wible & Gaudin \(2004\)](#). However, in young dasypodines, we clearly observe this feature ([Figure 11](#)). For a large majority of taxa in our sample, we can confirm that a transverse canal crossing the midline is present in cingulates.

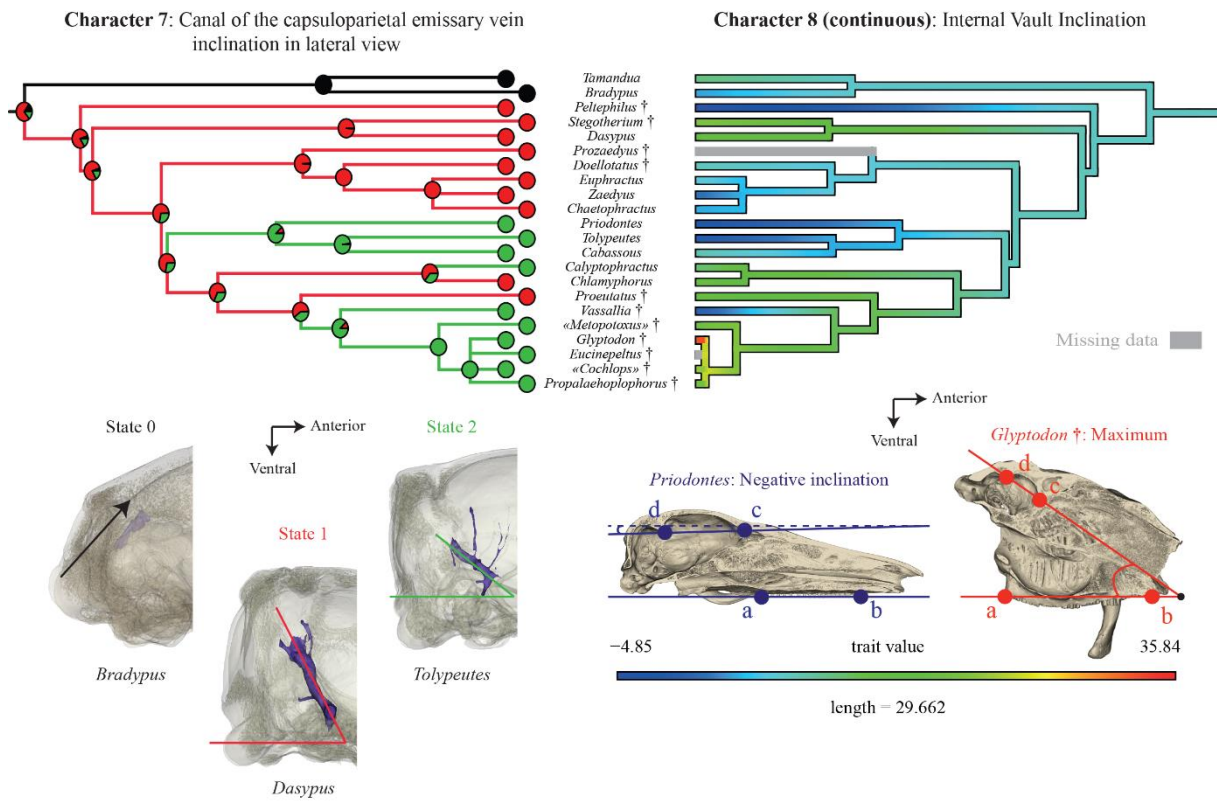
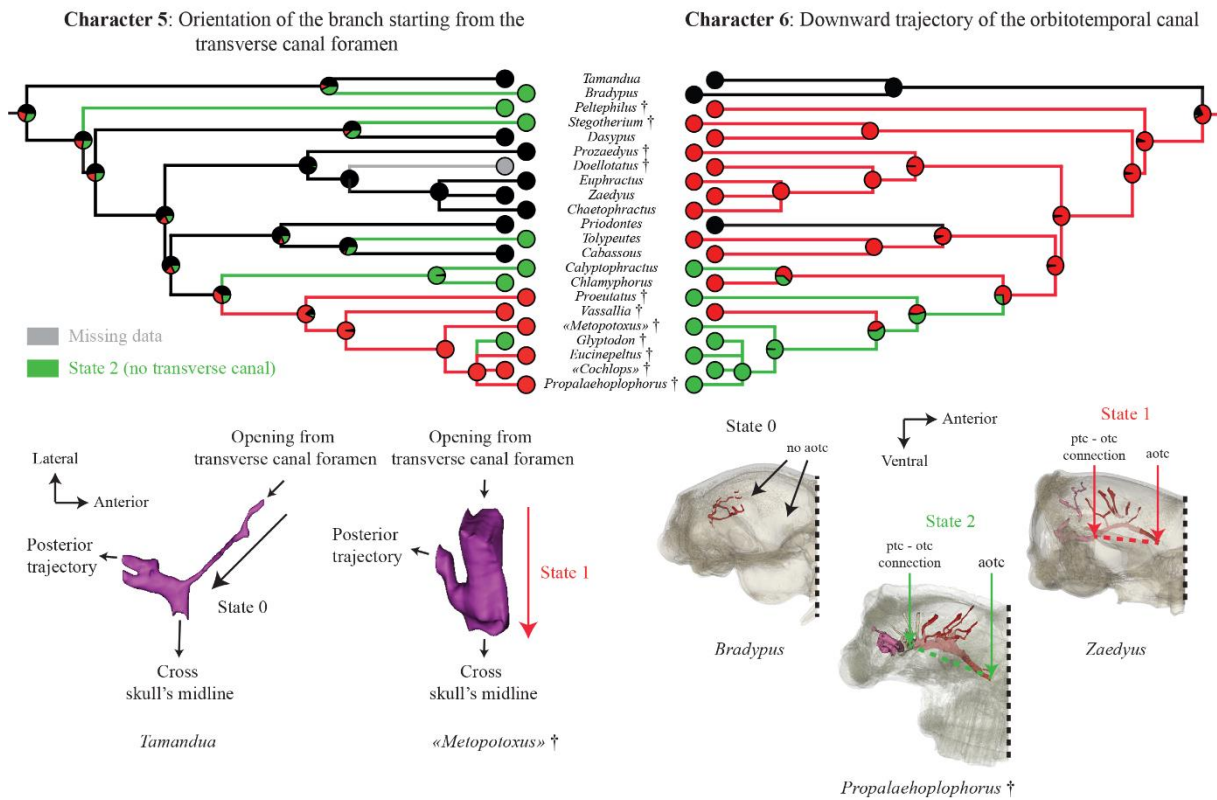


Figure 21. Reconstructed evolutionary scenarios for the endocranial characters 5-8 plotted on the reference cladogram with ancestral state estimation for internal nodes (see [Material & Methods, Supporting information 2](#) and [Figure S4](#)). Each character is illustrated and the relationship between color and coding is explained within the figure. † represents extinct genera. For character 8 (= IVI), the angle between the anteroposterior axis of the cranium (defined by the line connecting the most posterior (a) and anterior (b) edges of the tooth row) and the straight line connecting the most dorsal point of the annular ridge (c) and the most ventral point of the tentorial process (d). Scale = 1 cm.

The distribution on the baseline cladogram of the character corresponding to the anterior course of the orbitotemporal canal also provided interesting information (character 6 – [Figure 21](#)). *Calyptophractus*, *Proeutatus* and glyptodonts share a strong downward trajectory of this canal, with an anterior opening located much lower in lateral view than its posterior connection of the orbitotemporal canal to the posttemporal canal. The evolutionary scenario for this character is, however, unclear for glyptodonts and their close allies, and homoplasy seem to be present ([Figure 21](#)). Our study also highlights the presence of a foramen for the anterior opening of the orbitotemporal canal in all cingulates except *Priodontes* whereas this foramen was scored as absent in *Vassallia* and *Chlamyphorus* in [Gaudin & Wible \(2006, character 78\)](#), and is often unknown for other cingulate taxa. Based on our observation, there is no doubt that the canal opens in the orbitotemporal region in *Vassallia*, while this opening is described as absent in *Holmesina floridanus* ([Gaudin & Lyon, 2017](#)). The opposite discrepancy exists regarding the foramen for the frontal diploic vein, absent in *Vassallia* and described as present in *Holmesina floridanus* by [Gaudin & Lyon \(2017\)](#). As these two foramina are usually located relatively close to each other in the orbitotemporal region (bearing many foramina), we suggest that misidentifications may have occurred between the opening of these two canals, if they are presents, and ethmoidal foramina ([Figure S6](#)). The only way to confirm this hypothesis would be to scan [Gaudin & Lyon's \(2017\)](#) specimens of *Holmesina floridanus*.

Another character we investigated concerned the inclination of the canal for the capsuloparietal emissary vein in lateral view (character 7 – [Figure 21](#)). All tolypeutines, *Calyptophractus*, *Vassallia* and glyptodonts share a less steep inclination than that observed in other cingulates, with a part close to the anterior opening oriented almost directly anterior direction. The distribution of this character could provide support for the molecular hypothesis of a closer relationship of the glyptodonts with chlamyphorines and tolypeutines ([Delsuc et al., 2016; Mitchell et al., 2016; Figure 21](#)). However, the condition is reversed in *Chlamyphorus* and *Proeutatus*, creating homoplasy that casts doubt on the evolution of this trait. The trajectory of this canal has never been scored in prior phylogenetic analyses of the Cingulata. In the literature, only two characters have been scored that indirectly concern this canal, characters

119 and 120 of Gaudin & Wible (2006), related to the presence/absence of the postglenoid foramen and suprameatal foramen, respectively. These characters deliver contrasting grouping among cingulates (Gaudin & Wible, 2006).

Finally, the internal inclination of the cranial vault relative to the anteroposterior axis of the cranium also helps identify some cingulate taxa that may resemble glyptodonts in this regard (character 8; Figure 21). The distribution of this quantitative trait on the baseline cladogram indicates that the glyptodonts, *Proeutatus*, *Chlamyphorus*, *Calyptophractus* and Dasypodinae exhibit a strong angle, whereas *Vassallia* possesses a very weak angle. The variation of this trait was not explained by allometry in our sample. A highly inclined vault may have been evolved independently in the dasypodines and in glyptodonts and their allies. Its distribution could provide support for a relationship between glyptodonts, *Proeutatus* and chlamyphorines to the exclusion of pampatheres or they may have undergone a reversal (Figure 21). The vault inclination in these taxa seems to be partly congruent with the distribution of a character proposed by Billet *et al.* (2011) and discussed by Delsuc *et al.* (2016), *i.e.*, the dorsal position of the ventral surface of the auditory region relative to the palate (character 78 – Billet *et al.*, 2011). This is a characteristic of glyptodonts, pampatheres, Eutatini and chlamyphorines in Billet *et al.*'s (2011) analysis. The potential relationship of these two aspects of the braincase should be tested in future studies.

In conclusion, our investigation of the cranial canals and alveolar cavities highlighted several endocranial characters that support a resemblance of glyptodonts with chlamyphorines, *Proeutatus* and pampatheres. Except for character 7, our investigation did not bring to light new, and strong resemblances between glyptodonts and tolpeutines that would support their close relationship as suggested by molecular studies (Delsuc *et al.*, 2016; Mitchell *et al.*, 2016). In short, our study of internal anatomy lends further credence to recent reports of a greater morphological resemblance between glyptodonts and chlamyphorines than tolpeutines (Delsuc *et al.*, 2016; Mitchell *et al.*, 2016). These results are reinforced by the low statistical support for the chlamyphorines + tolpeutines relationship relative to other clades in molecular analyses of cingulate phylogeny (Delsuc *et al.*, 2016; Mitchell *et al.*, 2016).

The congruence of these new internal characters with past morphological phylogenetic analyses of the group is difficult to evaluate since the results of the latter have been rather unstable (e.g., Engelmann, 1985; Gaudin & Wible, 2006; Billet *et al.*, 2011). However, a close resemblance of glyptodonts to the eutatine *Proeutatus* and the pampatheres is also supported by several

characters in our study, which would be congruent with several recent phylogenetic hypotheses based on morphological data (Engelmann, 1985; Gaudin & Wible, 2006; Billet *et al.*, 2011; Gaudin & Lyon, 2017). However, even if our study shows similarities among chlamyphorines, pampatheres, glyptodonts, and *Proeutatus*, new analyses are needed that incorporate this new data before firmer phylogenetic conclusions can be reached. Our study provides a non-exhaustive account of internal canals of the skull, but internal structures still need to be studied to select new characters in particular for endocranial traits that we briefly describe but do not explore in detail. This is notably the case of the canal for the frontal diploic vein or the relative position of the sphenopalatine canal in relation with the nasopharyngeal canal, whose patterns of variation remain unclear at the moment. Another promising way forward was also revealed by our developmental series in which *Cabassous* varies in a manner different from that of *Zaedyus* and *Dasypus* as far as the inclination of the cranial roof is concerned (Figure 19). A better exploration of the developmental series with more specimens per species and more developmental series could provide a better understanding of the covariation patterns, especially since their trajectories can be coded for phylogenetic analyses (*e.g.*, Bardin *et al.*, 2017). Further studies are also needed to better understand the patterns of variation of the internal characters highlighted here, which in some respects may be affected by allometry as we have highlighted for alveolar cavities and the canal for the capsuloparietal emissary vein.

CHAPTER 3

Cranial Allometry in Cingulata

« [...] les patrons allométriques de la variation sont si répandus dans la nature qu'ils expliquent souvent des variations d'une ampleur surprenante, tant au sein des populations qu'entre les espèces. ».

Hallgrímsson *et al.*, 2019, Translated.

“[...] allometric patterns of variation are so pervasive in nature, often accounting for surprising magnitudes of variation both within populations and among species.”.

Hallgrímsson *et al.*, 2019.

3.1 Ontogenetic and static allometry in the skull and cranial units of nine-banded armadillos (Cingulata: Dasypodidae: *Dasypus novemcinctus*)

ABSTRACT

A large part of extant and past mammalian morphological diversity is related to variation in size through allometric effects. Previous studies suggested that craniofacial allometry is the dominant pattern underlying mammalian skull shape variation, but cranial allometries were rarely characterized within cranial units such as individual bones. Here, we used 3D geometric morphometric methods to study allometric patterns of the whole skull (global) and of cranial units (local) in a postnatal developmental series of nine-banded armadillos (*Dasypus novemcinctus* ssp.). Analyses were conducted at the ontogenetic and static levels, and for successive developmental stages. Our results support craniofacial allometry as the global pattern along with more local allometric trends, such as the relative posterior elongation of the infraorbital canal, the tooth row reduction on the maxillary, and the marked development of nuchal crests on the supraoccipital with increasing skull size. Our study also reports allometric proportions of shape variation varying substantially among cranial units and across ontogenetic stages. The multi-scale approach advocated here allowed unveiling previously unnoticed allometric variations, indicating an untapped complexity of cranial allometric patterns to further explain mammalian morphological evolution.

Le Verger K, Hautier L, Bardin J, Gerber S, Delsuc F, Billet G. 2020. Ontogenetic and static allometry in the skull and cranial units of nine-banded armadillos (Cingulata: Dasypodidae: *Dasypus novemcinctus*). *Biological Journal of the Linnean Society* 131: 673-698 p.

3.1.1 INTRODUCTION

Variation in size is a major component of tetrapod evolution and diversity. Among them, mammals developed a wide range of body sizes since the onset of the Cenozoic era (Smith *et al.*, 2010), with multiple independent events of size increase (Baker *et al.*, 2015; Bokma *et al.*, 2016). The extant mammalian diversity extends over eight orders of magnitude in size (Price & Hopkins, 2015), and this variation has accompanied ecological diversification (Sibly & Brown, 2007; Price & Hopkins, 2015). This size variation was also accompanied with major allometric trends during the course of mammalian evolution, particularly on the skull. Recent studies suggested that craniofacial allometry, *i.e.* larger faces relative to the rest of the skull in larger individuals, is a general evolutionary trend of morphological change in placentals, and possibly in other groups of vertebrates (Cardini & Polly, 2013; Cardini, 2019a; Linde-Medina, 2016). Craniofacial allometry is also observable intraspecifically in developmental series of extant mammals (Cardini & Polly, 2013) but is absent in early diverging amniotes and in stem-mammals such as cynodonts (Hoffman & Rowe, 2018). This shows that the craniofacial allometry might represent a mammal-specific trend at both the evolutionary and ontogenetic levels. Other common allometric aspects previously suggested in the mammalian skull, and generally based on bivariate analyses, include the negative allometry of middle-ear ossicles relative to the skull dimensions (*e.g.*, Nummela, 1995), the negative allometry of the inner ear relative to the petrosal (Billet *et al.*, 2015a), and more generally the negative allometry of sense organs relative to other skull parts (*e.g.*, Sánchez-Villagra, 2012).

Many recent studies analyzed cranial allometry in mammalian species using 3D geometric morphometrics methods (GMM) in relation to functional morphology, phylogeny or cranial integration (Marroig & Cheverud, 2004; Slater & Van Valkenburgh, 2009; Hautier *et al.*, 2017; Cardini, 2019a). Most of these GMM studies considered the entire skull, and only a few of them touched upon this concept using an atomistic approach, *i.e.* focusing on more specific anatomical regions. Although it lacks the 3D approach of GMM, the use of linear distances showed on several instances that large cranial regions display different allometries relative to the entire skull (Slijper, 1962; Monteiro *et al.*, 1999; Ross & Metzger, 2004; Marroig & Cheverud, 2004). These studies have highlighted complex allometric trends on the mammalian skull, which are likely determined by multiple and interacting developmental processes (Hallgrímsson *et al.*, 2019). In fact, much

remains to be discovered about these complex morphological patterns especially in the way that allometric growth differentially affects the various parts of the skull and induces cranial shape changes during ontogeny.

Armadillos have been poorly studied regarding allometry despite the fact that the group experienced a spectacular body mass increase in some lineages, especially in glyptodonts (Delsuc *et al.*, 2016). The smallest armadillo species do not exceed 0.115 kg while some glyptodonts weighed more than 2,000 kg (Superina & Abba, 2018; Vizcaíno *et al.*, 2012). Size was generally treated separately from other biological traits in taxonomic or evolutionary contributions on this group (*e.g.*, Wetzel & Mondolfi, 1979), while other studies addressed allometry in the postcranial skeleton of armadillos from the functional, metabolic or physiological viewpoints (*e.g.*, Frappell *et al.*, 1998; Vizcaíno & Milne, 2002; Costa *et al.*, 2019). However, Cardini (2019) demonstrated that extant armadillos exhibit a craniofacial evolutionary allometry similar to that of other placental mammals, a trend also detected in a comparative investigation of allometric variations between several armadillo genera (Moeller, 1968) and in two more detailed studies on euphractines (Abba *et al.*, 2015) and dasypodines (Hautier *et al.*, 2017). Apart from craniofacial allometry, no other quantitative analysis of cranial allometry exists for armadillos and no cranial shape change related to size was described in the group.

Our study focuses on describing ontogenetic and static allometric patterns in the skull of the most common, best studied, and widely distributed extant cingulate: the nine-banded armadillo (*Dasypus novemcinctus* ssp. Linnæus, 1758). Being distributed on the two American continents, this taxon can be split in as much as four different geographical morphotypes, some or all of which may represent distinct species or subspecies: Southern, Central, Northern, and Guianan (Billet *et al.*, 2017; Hautier *et al.*, 2017), as also suggested by molecular studies based on mitochondrial markers (Huchon *et al.*, 1999; Gibb *et al.*, 2016; Feijó *et al.*, 2018, 2019; Arteaga *et al.*, 2020). Based on a large sample covering three of these four morphotypes, our study aims at understanding how allometric variation is distributed in their skull and seeks to further characterize the covariation between shape and size across different cranial units, while controlling for potential effects of geography. More precisely, we analyzed allometry in: i) the entire skull, and ii) virtually isolated cranial units, looking at both ontogenetic and static allometry. We report heterogeneous cranial allometric patterns in time and space and discuss potential underlying processes.

3.1.2 MATERIAL AND METHODS

3.1.2.1 Sampling

We sampled 96 cranial specimens stored in the collections of the *Muséum national d'Histoire naturelle* (MNHN, *collections Zoologie et Anatomie comparée, Mammifères et Oiseaux*) in Paris (France), the Natural History Museum (BMNH) in London (UK), the Museum of Natural Science of the Louisiana State University (LSU) in Baton Rouge (USA), the American Museum of Natural History (AMNH) in New York (USA), the National Museum of Natural History (NMNH) in Washington (USA) and the *Muséum d'Histoire Naturelle* in Geneva (MHNG, Switzerland) (see [Table S3](#) for a complete list of specimens). The sample is largely similar to that of [Hautier et al. \(2017\)](#), although some specimens could not be considered here, as they were too incomplete for the proposed set of landmarks (see below). We also added new specimens to complete the ontogenetic series (details available in [Table S3](#)). In order to minimize phylogenetic effects, we did not include specimens belonging to the “Guianan morphotype” ([Hautier et al., 2017](#); [Billet et al., 2017](#)) as recent morpho-anatomical and molecular studies considered it to be clearly distinct from other *D. novemcinctus* populations, and to likely represent a new species ([Huchon et al., 1999](#); [Gibb et al., 2016](#); [Billet et al., 2017](#); [Hautier et al., 2017](#); [Feijó et al., 2018, 2019](#); [Arteaga et al., 2020](#)). These studies have also shown that other morphotypes recognizable within *D. novemcinctus* may represent sub-species or even distinct species, hence our use of *D. novemcinctus* ssp. to refer to this potential species complex. Pending more definite conclusions on these aspects, the northern, central, and southern morphotypes were included together in our study and their distribution systematically scrutinized within the allometric analyses. In addition, all analyses of ontogenetic allometry were performed on two different datasets for comparison: on the whole sample and on the best-sampled morphotype only (*i.e.* southern; $n = 48$). Finally, potential differences between allometric trajectories among morphotypes were also tested. No specimen belonging to the hairy long-nosed armadillo (*Dasypus pilosus*) was included in the study as it is very divergent morphologically, although recent molecular studies have shown that this species may also be part of the *Dasypus novemcinctus* ssp. complex ([Gibb et al., 2016](#); [Feijó et al., 2019](#)).

3.1.2.2 Geometric morphometrics

Digital data were acquired using X-ray μ CT facilities at the University of Montpellier (France), at the Natural History Museum (BMNH), and at the AST-RX platform of the *Muséum national d'Histoire naturelle* (MNHN). Image stacks were improved in contrast, rotated, cropped, and reduced to 8 bits using the ImageJ software (Schneider *et al.*, 2012). Three-dimensional reconstruction and visualization of the skulls and of the virtually isolated bones were performed using stacks of digital images with MIMICS v. 21.0 software (3D Medical Image Processing Software, Materialize, Leuven, Belgium). Cranial shapes were quantified with 131 anatomical landmarks (Figure 22 and Table 3, 4, S4) placed on the exported 3D models using AVIZO v. 9.7.0 software (Visualization Sciences Group, Burlington, MA, USA). The landmarks corresponding to external cranial structures were based on well-established landmark sets from previous studies on mammalian taxa (Goswami & Finarelli, 2016; Hautier *et al.*, 2017), and new landmarks were added on internal structures. Landmarks were selected to provide a good overall representation of skull shape, isolated bones, and characters traditionally used in cingulate phylogenetic analyses of the group (Gaudin & Wible, 2006; Billet *et al.*, 2011). The last criterion was set for future studies aiming at integrating knowledge on allometry and covariation patterns for the construction of phylogenetic characters. All landmarks were positioned on suture contacts or at the maximum of curvature, or extreme points of bony processes, fossae or foramina except for landmark #131 (Figure 22), which corresponds to the dorsal projection of the most posterior point of the frontal sinuses (see Billet *et al.*, 2017) on the midline in dorsal view (it was landmarked with the transparency option in Avizo). This point was added to the landmark set in order to include an anatomical landmark on the large dorsal exposure of the frontal bone. We then performed a generalized Procrustes analysis (Rohlf & Slice, 1990) using function *gpagen* in the R package *geomorph* version 3.1.0 (Adams *et al.*, 2019), and intra-individual asymmetries (Klingenberg *et al.*, 2002) were removed using the function *symmetrize* in the R package *Morpho* version 2.6 (Schlager, 2017). When some landmarks were missing on one side of the skull, their position was estimated using the function *fixLMmirror* in the *Morpho* R package (see Table S5). The logarithm of the centroid size was used as a size variable for the different cranial structures.

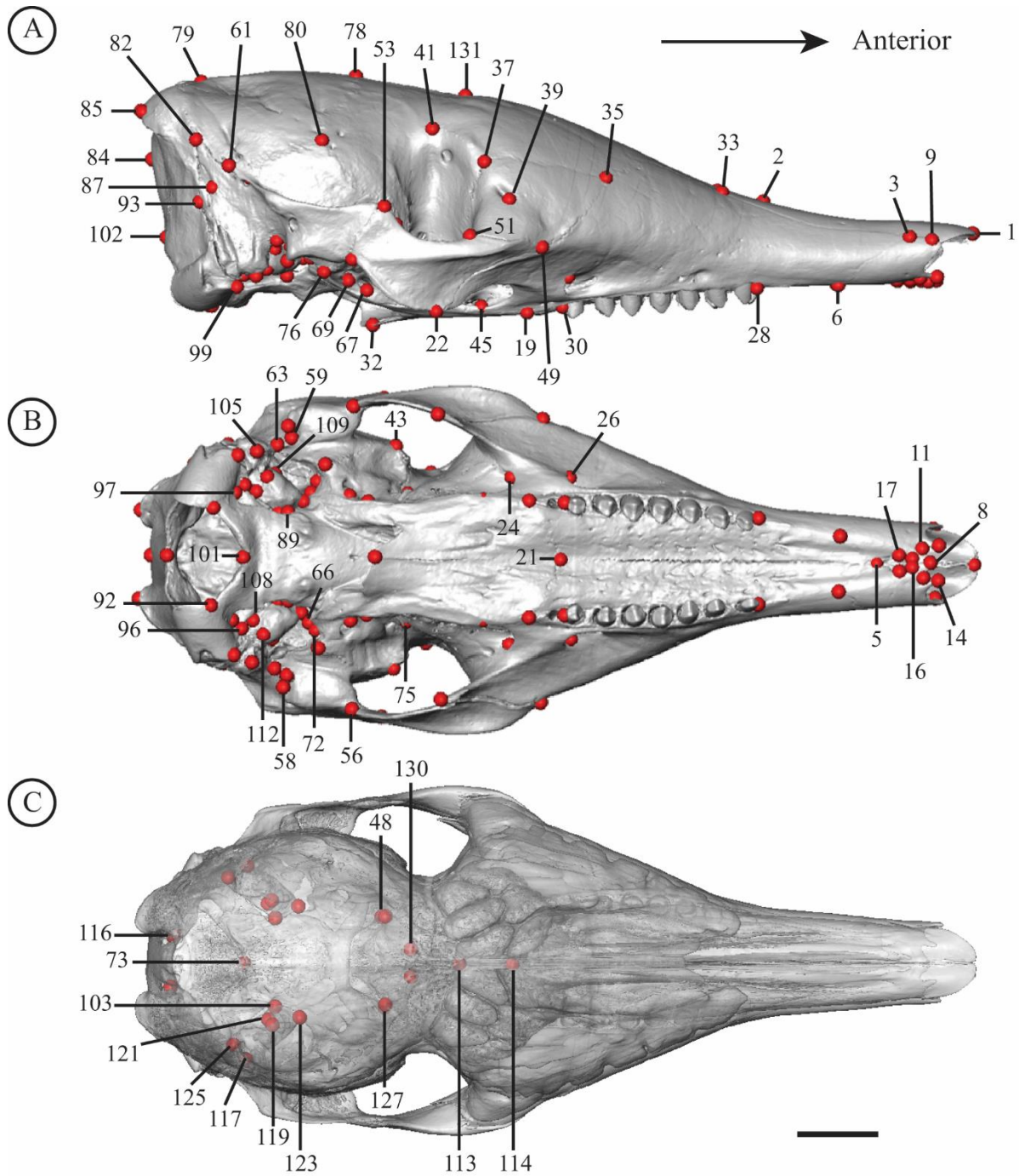


Figure 22. Landmarks digitized on the skull of *Dasyus novemcinctus* (MNHN.CG.2006-565). Lateral (A), ventral (B), and dorsal (C) views. The skull in dorsal view is shown with bone transparency (25%). Scale-bar = 1 cm. List of landmarks can be found in Table 3 and Table 4.

CHAPTER 3: Cranial allometry in Cingulata

Table 3. Definition of external landmarks. * Suture exoccipital/supraoccipital marks by a bulge in adult.

Number	Definition
1	Most anterodorsal point of the internasal suture
2	Intersection between internasal suture and frontal bone
3-4	Triple contact point between premaxillary/maxillary/nasal
5	Intersection between midline and premaxillary/ maxillary suture
6-7	Most posterior point of the premaxillary/maxillary suture on the palate
8	Most anterior point of the premaxillary midline suture
9-10	Most anterior point of the premaxillary/nasal suture
11-12	Maximum curvature point between #8 and the anterior process of the premaxillary
13-14	Most anterior point of the premaxillary anterior process
15-16	Most anterior point of incisive foramen in strict ventral view
17-18	Most posterior point of incisive foramen in strict ventral view
19	Intersection between palatine/maxillary suture and the palate midline
20-21	Intersection between maxillary/palatine suture and lateral edge of palate
22-23	Intersection between jugal/maxillary suture and ventral edge of zygomatic arch
24-25	Most dorsal point of the maxillary foramen
26-27	Most dorsal point of the infraorbital foramen
28-29	Most anterior point of the alveolar margin of the premolar tooth row
30-31	Most posterior point of the alveolus margin of the premolar tooth row
32	Most posterior point of the palatine midline
33-34	Triple contact point between frontal/maxillary/nasal
35-36	Triple contact point between lacrimal/maxillary/frontal
37-38	Intersection between the lacrimal/frontal suture and the anterior orbital edge
39-40	Anteroventral margin of the lacrimal foramen
41-42	Most dorsomedial point of the orbit (<i>i.e.</i> , minimal interorbital length)
43-44	Triple contact point between squamosal/frontal/alisphenoid
45-46	Most anteroventral point of caudal palatine foramen (in lateral view)
47-48	Most anteroventral point of the sphenorbitaire fissure
49-50	Triple contact point between maxillary/jugal/lacrimal
51-52	Intersection between anterior orbital edge and jugal/lacrimal suture
53-54	Most dorsal point of the jugal/squamosal suture
55-56	Most ventral point of the jugal/squamosal suture
57-58	Most ventral point of the postglenoid process
59-60	Most posterodorsal point of the postglenoid foramen
61-62	Most posterodorsal point of the zygomatic ridge of the squamosal
63-64	Most dorsal point of the external acoustic meatus on squamosal (in lateral view)
65-66	Most posterior point of the small alisphenoid process delimitating the carotid notch laterally
67-68	Most anteroventral point of the transverse canal foramen
69-70	Most anteroventral point of the foramen ovale
71-72	Most posterior point of the alisphenoid/squamosal suture in front of pyriform fenestra
74-75	Most anterodorsal point of the optic foramen
76-77	Ventral tip of entoglenoid process
78	Intersection between frontal/parietal suture and the midline
79	Intersection between parietal/supraoccipital suture and the midline
80-81	Triple contact point between the frontal/squamosal/parietal
82-83	Triple contact point between the parietal/squamosal/supraoccipital
84	Most distal point of the supraoccipital on the midline (occipital face)
85-86	Most posterior point of the nuchal process of the supraoccipital
87-88	Most anterodorsal point of the sulcus for the occipital artery
89-90	Most lateral point of basioccipital/basisphenoid suture
91-92	Intersection between the anteromedial edge of occipital condyle and foramen magnum
93-94	Triple contact point between the supraoccipital/exoccipital/petrosal*
95-96	Most posterolateral point of the jugular foramen
97-98	Most posterolateral point of the hypoglossal foramen
99-100	Most anterolateral point of the occipital condyle (in ventral view)
101	Most anteroventral point of the foramen magnum
102	Most posterodorsal point of the foramen magnum
103-104	Most medial point of promontorium of petrosal in ventral view
105-106	Most anteroventral point of mastoid process (= paroccipital process of petrosal)
107-108	Most ventral point of external aperture of cochlear canaliculus
109-110	Most anterior point of the fenestra vestibuli
111-112	Most anteroventral point of the external apertur of cochlear fossula

CHAPTER 3: Cranial allometry in Cingulata

Table 4. Definition of internal landmarks. * Landmark removed in 3B analyses. ** Projected landmark.

Number	Definition
73	Anteroventral tip of the tentorial process on the midline
113	Dorsal intersection of annular ridge and midline
114*	Dorsal intersection between cribriform plate and median septum posterior to the latter
115-116	Maximum curvature point of the lateral occipital ridge in caudal cerebral fossa
117-118	Most dorsal point of the petrosal on the level of the crista tentoria transversally
119-120	Most anteromedial point of the foramen acusticum superius
121-122	Most anteromedial point of the foramen acusticum inferius
123-124	Most anterior point of epitympanic wing of petrosal
125-126	Maximum curvature point in the ventromedial area of the fossa subarcuata
127-128	Most dorsal point of the internal posterior aperture of the optic canal
129-130	Most ventromedial point on the annular ridge lateral to posterior median septum
131**	Dorsal projection of the most posterior point of the frontal sinuses in the midline

3.1.2.3 Determination of ontogenetic stages

The determination of the developmental stage of each specimen was based on dental eruption, cranial ossification, and cranial length. Except for size, these variables were each composed of various discrete observations scored numerically. The scored observations were then averaged to be compiled in a dental eruption index and a cranial ossification index. The observations on dental eruption were made on CT-images and on 3D reconstructions of the skulls and corresponded to the number of teeth present, as well as their class and generation. Based on our observations of the upper dentition, we defined five dental stages. Concerning the ossification, only bones whose suture closure vary along our ontogenetic series were scored. The cranial length value (LTC – measure taken between landmarks #1 and #84) used for this analysis was directly sourced from the work of [Hautier et al. \(2017\)](#). The combination of these three variables allowed confirming the ontogenetic separation of specimens in five stages. Some specimens could not be allocated to a particular stage because they preserved no teeth. In this case, these specimens were not included in the analyses where information on ontogenetic stage was needed (see [Supporting Information 3, Figures S12, S13 & S14, Table S6 & S7](#) for details of the protocol and results concerning the determination of ontogenetic stages).

3.1.2.4 Ontogenetic and static allometry

Only complete specimens (n = 76, [Table S3](#)) were included in the analyses of allometry performed on the entire skull (ES). The ES Procrustes alignment was realized on the entire set of cranial landmarks, including both sides of the skull. For the ES analysis of ontogenetic allometry, the whole sample corresponds to 76 specimens with 48 specimens belonging to the "Southern group", 11 specimens to the "Central group", and 17 specimens to the "Northern group" as defined

CHAPTER 3: Cranial allometry in Cingulata

by Hautier *et al.* (2017) and Billet *et al.* (2017). Only adult specimens were considered in the ES analysis of static allometry (*i.e.*, 51 specimens in total, with 35 from the Southern, five from the Central, and 11 from the Northern groups).

Under the Bone-By-Bone (3B) approach, the analyzed objects corresponded to a virtually isolated bone or group of bones that we defined in this study as Operational Bone Units (OBUs). We used the same samples for both the ES and 3B analyses of allometry ($n = 76$ for ontogenetic allometry; $n = 51$ for static allometry). Each 3B Procrustes alignment was realized on a reduced set of landmarks corresponding to the OBU under consideration. The allometric component in the shape variation of OBUs was analyzed using the skull centroid size as a measure of size. We performed the 3B analyses only on the left cranial side, which was more complete in most cases. These 3B analyses were only performed on one side since many paired bones were not contiguous and to avoid taking into account symmetrized structures (see above). For the 3B analyses, 13 OBUs were defined, including 11 single bones: premaxillary (pmx); maxillary (mx); nasal (na); frontal (fr); lacrimal (lac); jugal (ju); palatine (pal); parietal (pa); squamosal (sq); supraoccipital (so); petrosal (pe). Two OBUs corresponding to bone complexes (alisphenoid-orbitosphenoid-pterygoid-basisphenoid, as-os-pt-bs; basioccipital-exoccipital, bo-eo) were also defined as some of their bony components (alisphenoid-orbitosphenoid; basioccipital-exoccipital) were often fused in adults, and because only OBUs represented by more than three landmarks could be considered. In the whole landmark dataset, only landmark #114 was not included in the 3B approach as it could not be associated with any of the 13 OBUs.

For both the ES and 3B analyses of allometry, we performed a multivariate regression of Procrustes shape coordinates (Izenman, 2013) on size (Log Centroid Size) using the function *procD.lm* of the R package *geomorph*. The R^2 (coefficient of determination) of these analyses represents the percentage of the total shape variation explained by the independent variable, here size (Goodall, 1991; Klingenberg & McIntyre, 1998; Drake & Klingenberg, 2008). We referred to this percentage as the “allometric proportion of the total shape variation”. We assessed the statistical significance of the regressions against the null hypothesis of isometric variation using permutation tests with 10,000 iterations (Good, 2000). We also present the values for the R^2 of non-significant regressions (at $p\text{-value} > 0.05$) and comment them cautiously following recent recommendations by Dushoff *et al.* (2019).

3.1.2.5 Common allometry among morphotypes

For the ES approach, differences in allometric trajectories among morphotypes at the ontogenetic and static levels were investigated. For this analysis, we performed a HOS (Homogeneity of Slope Test) using a Procrustes ANOVA (Goodall, 1991) for morphotypes, size, and interaction between both variables (Collyer & Adams, 2013). The HOS performs statistical assessment of the terms in the model using Procrustes distances among specimens, rather than explained covariance matrices among variables, which is equivalent to distance-based ANOVA designs (Anderson, 2001). The HOS calculates the amount of shape variation explained by size, computes the allometric slopes for each category of the independent variable, and quantifies the influence of a given factor on the shape variation. Statistical significance was evaluated with a residual randomization permutation procedure with 10,000 iterations (Collyer *et al.*, 2015). If the null hypothesis of HOS (= parallel slopes) is rejected, then morphotypes differ in their patterns of allometric growth. The HOS analysis was conducted using the *procD.allometry* function of the *geomorph* package version 3.0.7 (Adams *et al.*, 2018). More precisely, these analyses were performed to identify the interaction between geographic distribution (morphotypes) and allometry on shape variation by including pairwise comparisons between groups (distribution) to assess significant differences of both the direction (angles) and magnitude (amount of change in shape with size) of allometric trajectories. The pairwise comparisons were performed with *advanced.procD.lm* from the *geomorph* package version 3.0.7. When trajectories significantly differed between morphotypes, allometric patterns were analyzed both within the whole sample and within the southern morphotype subsample only.

3.1.2.6 Common allometry between ontogenetic stages

Multivariate regressions of shape on the logarithm of the skull centroid size were also performed for the different ontogenetic stages determined (see Results) in order to compare the allometric proportions between stages for a given OBU. We then tested the allometric differences between each ontogenetic stage for a given OBU. This preliminary investigation could not be conducted within particular morphotypes because their sampling per ontogenetic stage for each was too low. For this analysis, we also performed a HOS test using a Procrustes ANOVA on each OBU for ontogenetic stage, size, and interaction between both variables. In order to reduce biases linked to sample size, we calculated the angles of each slope for a given OBU versus the horizontal

axis to test whether the different ontogenetic stages for a given OBU share a common allometry (see [Klingenberg, 2016](#)). The ratio between the OBU relative size and its average for a given ontogenetic stage was also calculated for each stage and for the entire sample in order to analyze the growth dynamics of the OBU.

3.1.3 RESULTS

3.1.3.1 Allometry and geography

The regression of shape on log centroid size in our ontogenetic series of *D. novemcinctus* ssp. accounts for 27.62% of the total shape variation (p -value < 0.0001, [Figure 23](#); [Figure S15](#)). The geographical distribution explains 16.64% of the total shape variation (p -value < 0.0001, [Figure S15](#)). At the ontogenetic level, the morphotypes show a slight difference in their allometric trajectory attesting to an interaction between geography and allometry on shape variation during ontogeny ([Figure S15](#)). However, this effect seems to be minimal (3.16 %; [Figure S15](#)). The HOS test pairwise comparisons of ontogenetic allometric trajectories suggests no difference between the Central and Southern morphotypes, but a significant difference between the latter two and the Northern morphotype. These results should be taken with caution as the p -value is very close to the statistical significance threshold in the comparison between the Central and Southern morphotypes (p -value = 0.0515) and the difference revealed with the Northern morphotype may be due to the lack of specimens as young as for the other two morphotypes. Because these results suggest that the ontogenetic allometries may slightly differ among morphotypes, the allometric shape changes during ontogeny were analyzed both within the whole sample (see below) and within the Southern morphotype subsample ([Figure S16](#)).

The regression of shape on the logarithm of the centroid size in our adult sample of *D. novemcinctus* ssp. accounts for only 6.31% of the total shape variation (p -value < 0.0001, [Figure 23](#); [Figure S15](#)). The effect of geographical distribution is proportionally higher, expressing 22.81% of the total shape variation (p -value < 0.0001, [Figure S15](#)). At the static level, the morphotypes share a common allometric trajectory and no interaction between geography and allometry is statistically supported, although the p -value is close to the significance threshold (p -value = 0.0619). It should also be noted that the central morphotype has relatively low sample size ([Figure S15](#)). The HOS test pairwise comparisons of static allometric trajectories suggests no

CHAPTER 3: Cranial allometry in Cingulata

difference between each morphotype. Because these results suggest that the static allometries are similar among morphotypes, the allometric shape changes at the adult stage were analyzed within the whole sample only (see below).

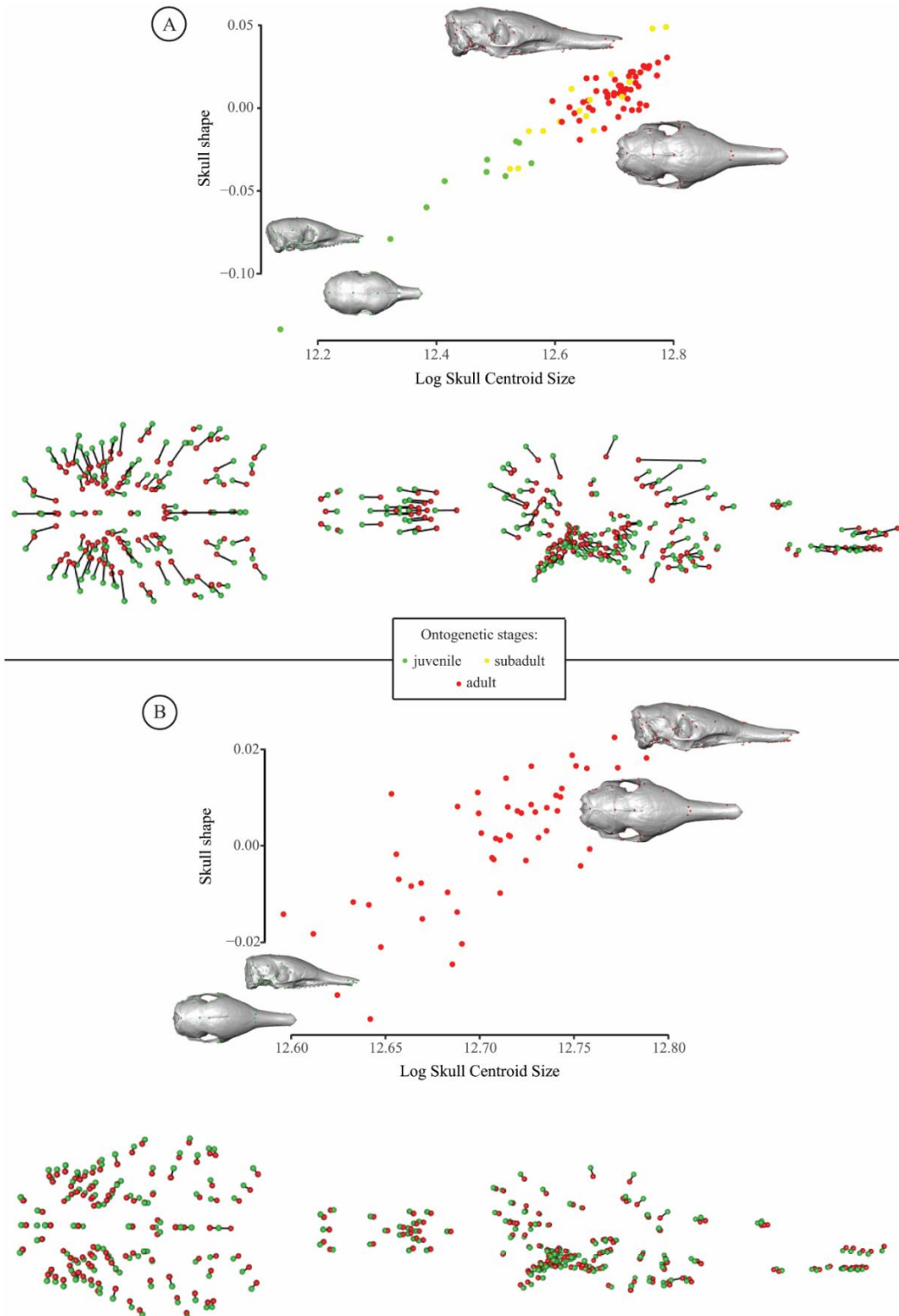


Figure 23. Ontogenetic and static allometry on the entire skull (ES) of nine-banded armadillos. Ontogenetic stages are represented with different colors (juvenile = green; subadult = yellow; adult = red; see text for more detail). For graphical display, we used the projected regression scores of the shape data to represent shape variation related to changes in log centroid size (Adams *et al.*, 2013). Shape changes were visualized as vectors from the minimal shape (green) to the maximal shape (red) of the shape regression scores corresponding to the projection of the data points in shape space on to an axis in the direction of the regression vector (see Drake & Klingenberg, 2008). A. Multivariate regression of skull shape on log skull centroid size at the ontogenetic level, representing 27.62% of the total shape variation. B. Same analysis, at the static level (6.31% of total shape variation) (see text).

3.1.3.2 Allometric variations on the entire skull (ES)

Ontogenetic allometry

Three main regional trends of skull allometric variation can be recognized in our ontogenetic series. Adult cranial proportions clearly differed from juvenile ones in the relative size of the snout and zygomatic arches compared to the braincase (Figure 23A; Table S8). The snout undergoes an anteroposterior elongation with size increase. This elongation is bidirectional (one directed anteriorly and the other posteriorly) and has different magnitudes of variation depending on the landmarks considered. Most of the landmarks of the anterior tip of the snout (#1; #3-20) and the ones delineating the posterior end of the premolar row (#29-30), show an anterior displacement relative to other landmarks during growth. On the other hand, most landmarks of the snout posterior to the premaxillary and nasal display a posterior directed elongation relative to the other landmarks. In addition to this elongation, the posterior end of the snout (*i.e.*, delimited anteriorly by the most anterior point of the zygomatic arches) narrows in larger specimens, especially at the level of the infra-orbital and maxillary foramina. The zygomatic arches extend more ventrally and the temporal fenestra widen considerably as the size increases, as expressed by the vectors associated to landmarks #22-23 and #51-52, and by the increase of the postorbital constriction (#41-42). In the posterior half of the skull, most of landmark displacements are directed towards the center of the braincase. During ontogeny, the proportions of the neurocranium decreases relative to the rest of the skull due to allometric growth. More local allometric changes are also highlighted: the landmark located at the posterior edge of the frontal sinuses (#131) is particularly distinctive for its strong relative posterior displacement. The dental row is relatively shorter in larger specimens, with an anterior displacement of the posterior portion of the dental row (#29-30) while the anterior portion varies very slightly (#27-28). The analysis of the ES

ontogenetic allometry in the southern morphotype revealed remarkably similar shape changes to the ones described above (Figure S16).

Static allometry

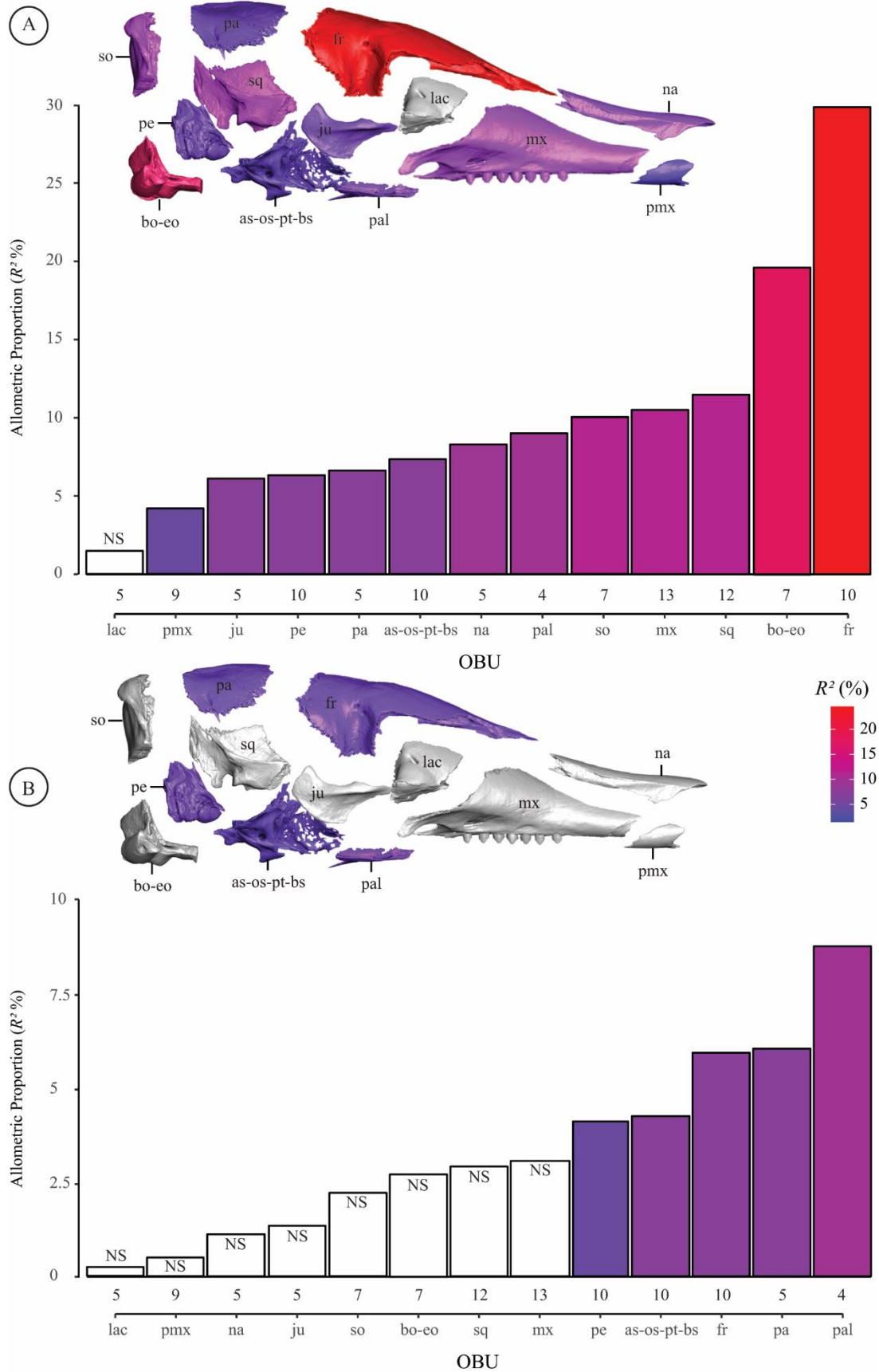
An increase in size, at the static level, is only associated with minor shape variations of the skull (Figure 23B; Table S8), similar to the pattern detected with the ontogenetic analyses of allometry, albeit to a lesser degree and with some variations specific to this level (see below). The most anterior part of the nasal bone shows a relative anterior displacement, just like the W-shaped processes in front of the premaxillary (as defined by landmarks #8; #11-14; Figure 22). The rest of the face shows a relative narrowing as size increases. The shape changes of the zygomatic arches (slightly increasing width) are less strong than in the ontogenetic allometry analyses. The reduction in the relative proportions of the braincase is more pronounced for landmarks located on the cranial roof (frontal and parietal midline landmarks (#113; #114; #131)) and the zygomatic-pterygoid region. The anterior border of the orbit widens as the post-orbital constriction becomes stronger with size. Strikingly, the landmark located on the maxillary-palatine suture (#21) strongly moves forward in comparison to other surrounding landmarks as size increases, much more than in the ontogenetic analysis. A very strong anterior (#19-21; #45-46) and weak posterior (#32) relative elongation of the palatine is detected at the static level. For all other landmarks, the allometric changes appear very weak when compared to their changes in the analysis of ontogenetic allometry.

3.1.3.3 *Allometric variations studied bone by bone (3B)*

Comparison between OBUs

We observe differences in the proportions of allometric shape variation between different OBUs both at the ontogenetic and static levels. In both cases (Figure 24), the regression of shape on size shows no statistical support for the lacrimal (Figure 24; Table 5; Figures S17 & S18). This is not the case for other OBUs, for which at least the analyses at the ontogenetic level show a significant allometric effect.

CHAPTER 3: Cranial allometry in Cingulata



CHAPTER 3: Cranial allometry in Cingulata

Figure 24. Bar graphs showing the allometric proportions (R^2) of each cranial unit's (OBU) total shape variation under the 3B approach (see text), at the ontogenetic (A) and static (B) levels. Allometric proportions are shown with the log skull centroid size taken as a size variable. On the virtually dislocated skull (in right lateral view), the allometric proportions are reported in corresponding colors. White bars indicate a statistically unsupported (NS) allometry for a given OBU (at p value > 0.05). Abbreviations of OBUs: as-os-pt-bs, alisphenoid-orbitosphenoid-pterygoid-basisphenoid complex; bo-eo, basioccipital-exoccipital complex; fr, frontal; ju, jugal; lac, lacrimal; mx, maxillary; na, nasal; pa, parietal; pal, palatine; pe, petrosal; pmx, premaxillary; so, supraoccipital; sq, squamosal.

At the ontogenetic level, the premaxillary has the lowest proportion of shape variation explained by size of all OBUs (lacrimal excluded; [Figure 24A](#) & [Table 5](#)). The jugal, petrosal, parietal, as-os-pt-bs OBU, nasal, palatine have a proportion of shape variation explained by size varying between 5% and 10% ([Figure 24A](#) & [Table 5](#)). The maxillary, supraoccipital and squamosal show allometric proportions between 10% and 12% ([Figure 24A](#) & [Table 5](#)). Finally, the last two OBUs showing the highest proportion of variation explained by size at the ontogenetic level are the bo-eo OBU and the frontal, the latter with more than twice the proportion values found in the other OBUs ([Figure 24A](#) & [Table 5](#)). At the static level, the allometric proportion is much lower than at the ontogenetic level for most OBUs. Only five OBUs show a statistically well-supported allometric effect at this level. Among them, the petrosal and the as-os-pt-bs OBU show an allometric proportion lower than 5% ([Figure 24B](#) & [Table 5](#)). The frontal shows a drastic reduction in its allometric proportion (5.96%) ([Figure 24B](#) & [Table 5](#)). Finally, the parietal and palatine have an allometric proportion almost equivalent to that obtained at the ontogenetic level – for the palatine, it is even higher to that of the entire skull ([Figure 24B](#) & [Table 5](#)).

All descriptions of the allometric shape changes below describe the maximal shapes as compared to the minimal shapes per OBU at the ontogenetic level. This was done only for the OBUs whose allometric variation is statistically well-supported (p -value < 0.05). Only landmarks on the left side of the skull are mentioned (see [Table 3](#) and [Table 4](#) for their symmetrical landmark/counterparts). The same analyses were performed using the Southern morphotype only. We obtained very similar results ([Figure S16](#)) as the ones described hereafter for the entire dataset. The only notable differences are generally in the norm (*i.e.*, lesser) of the vectors and not in their direction. The results and shape changes explained by size for the static level on the whole sample are illustrated in [Figure S19](#) and those changes that differ from the ontogenetic level are described in [Supporting Information 4](#).

CHAPTER 3: Cranial allometry in Cingulata

Table 5. Results of the multivariate regression for ES and 3B with log skull centroid size at the ontogenetic and static levels. Index: a, slope coefficient; Intercept; R^2 , allometric proportion of shape variation; p -value, significance following the permutation test. The shaded lines correspond to the tests with a non-significant p -value (> 0.05).

	Log Skull Centroid Size							
	Ontogenetic Level				Static Level			
	a	intercept	R^2	p -value	a	intercept	R^2	p -value
Entire Skull	0.2273	-2.8776	0.27618	0.0001	0.2307	-2.9312	0.06311	0.0001
Premaxillary	2.6620	-6.7570	0.04242	0.0054	2.3270	-5.9140	0.00558	0.9774
Maxillary	2.5780	-6.5430	0.10665	0.0001	3.2890	-8.3600	0.03148	0.1040
Nasal	1.6900	-4.2890	0.08368	0.0004	1.4820	-3.7670	0.01127	0.6700
Frontal	5.2690	-13.376	0.29873	0.0001	5.1750	-13.155	0.05965	0.0200
Lacrimal	1.8680	-4.7420	0.01568	0.2802	2.4230	-6.1600	0.00429	0.9425
Jugal	3.2730	-8.3090	0.06006	0.0015	3.7490	-9.5290	0.01476	0.5640
Palatine	4.0190	-10.202	0.09004	0.0006	9.7290	-24.730	0.08829	0.0053
Parietal	2.2530	-5.7180	0.06661	0.0005	5.1620	-13.121	0.06036	0.0120
Squamosal	3.7480	-9.5130	0.11490	0.0001	4.6370	-11.787	0.03084	0.0875
As-Os-Pt-Bs	3.8850	-9.8610	0.07351	0.0001	7.4030	-18.819	0.04347	0.0178
Supraoccipital	3.5370	-8.9790	0.10031	0.0001	4.0930	-10.405	0.02223	0.3164
Bo-Eo	4.7010	-11.933	0.19612	0.0001	4.0220	-10.223	0.02801	0.1756
Petrosal	2.6430	-6.7100	0.06281	0.0001	5.5540	-14.119	0.04270	0.0242

Alisphenoid-Orbitosphenoid-Pterygoid-Basisphenoid complex (Figure 25.A1-A3)

When the skull size increases, the foramen ovale (#70) shows very little variation, while the transverse canal foramen (#68) takes a more medial position. The pterygoid wings (#66) are more extended posteriorly. The optical foramen is located more dorsolaterally (#75). Internally, the most lateral point of the dorsal transverse ridge (#130), which delimits the ethmoidal fossa anteriorly, is more laterally positioned. Finally, the contact between the frontal, the squamosal, and the alisphenoid (#44) is located much more anteromedially.

Basioccipital-Exoccipital complex (Figure 25.B1-B3)

As size increases, the basioccipital becomes mediolaterally wider (#90). The concavity that constitutes the posterior part of the jugular foramen is less marked (#96). The occipital condyles are relatively larger and more anterolaterally oriented (#92; #100). The foramen magnum (#92; #101) is relatively narrower mediolaterally, its ventral portion being more ventral. The exoccipital meets the supraoccipital much further dorsoanteriorly (#94).

Frontal (Figure 25.C1-C3)

The allometric changes mainly involve the posterior development of the frontal sinuses (#131), the deepening of the post-orbital constriction (#42), and a more posteroventral location of the ventral intersection of the annular ridge and cribriform plate (#113). While the frontal sinuses are poorly developed in the juvenile stage, they extend much farther posteriorly in older specimens (see also Billet *et al.*, 2017). The anterior part of the frontal extends further anteriorly in larger individuals (#2; #34; #36) while its posterior part is relatively shortened anteroposteriorly and compressed dorsoventrally, as expressed by the landmarks #44, #78, and #81. Finally, the anterior edge of the orbit is placed only slightly more medially (#38).

Jugal (Figure 25.D1-D3)

Two main allometric trends can be recognized for the jugal. Its anterior part, in contact with the lacrimal and the maxillary (#50), shows a relative shortening as size increases. The second trend corresponds to a dorsoventral increase of the zygomatic arch (#23; #54; #56), which is stronger in its anteroventral and posterodorsal parts.

Maxillary (Figure 25.E1-E3)

From the juvenile stage to the adult stage, the maxillary shows a relative anterior elongation as shown by the landmarks in contact with the premaxillary (#4; #5; #7), especially ventrally at the level of the midline. The landmarks in contact with the palatine (#19; #21) are shifted anterodorsally and the dorsal part of the snout (#34; #36) more posteroventrally. While the maxillary is bulging in its dorsal mid-part in juveniles, it is much shorter dorsoventrally in larger specimens, as marked by the landmark in contact with the nasal and the frontal (#34). Large specimens also display a proportionally reduced dental row (#29; #31). The zygomatic process of the maxillary shows a more ventrolateral position (#23). Finally, the relative length of the infraorbital canal varies strongly from juveniles to adults, the maxillary foramen being more posterior in larger specimens, as expressed by the landmark #25.

CHAPTER 3: Cranial allometry in Cingulata

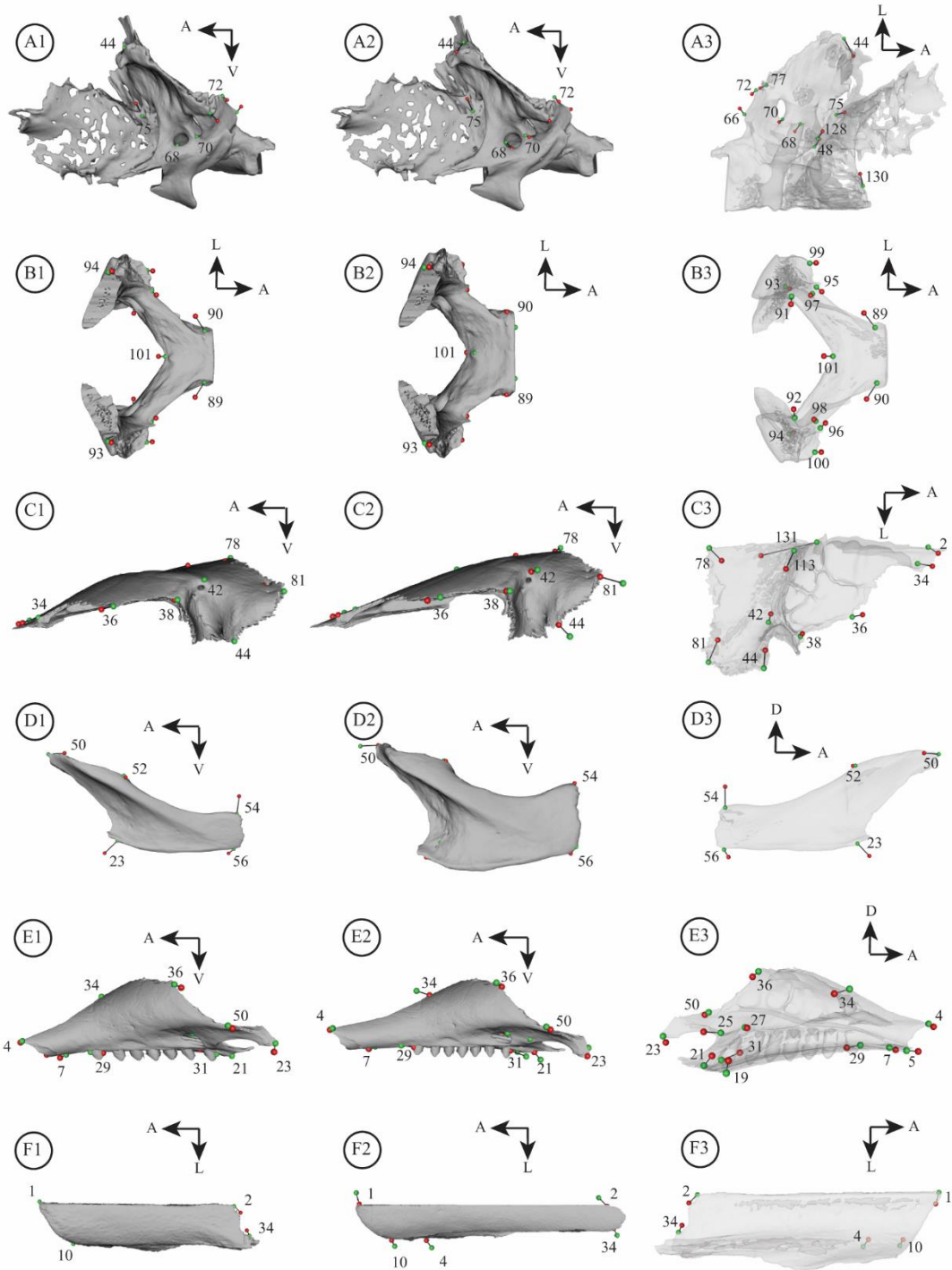
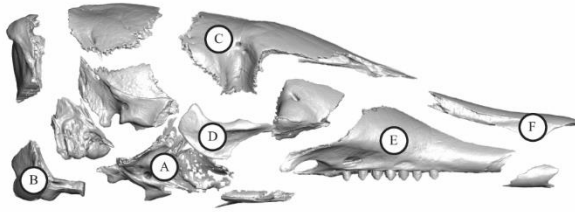


Figure 25. Vector representation of the allometric shape changes detected for a given cranial unit (OBU), represented between its minimal (green – smaller centroid size) and maximal (red – larger centroid size) shape (see [Figure 23](#)). Results of the analysis performed at the ontogenetic level, and with the log skull centroid size taken as the size variable (see text). For each OBU, the changes are shown in three subsections organized horizontally: 1, vectors from minimal to maximal shape with minimal OBU shape; 2, same as 1) with maximal OBU shape; 3, minimal OBU shape in transparency with vectors. A) alisphenoid-orbitosphenoid-pterygoid-basisphenoid complex; A1-A2, lateral view; A3, dorsal view. B) basioccipital-exoccipital complex; B1-B2, dorsal view; B3, ventral view. C) frontal; C1-C2, lateral view; C3, ventral view. D) jugal; D1-D2, lateral view; D3, medial view. E) maxillary; E1-E2, lateral view; E3, medial view. F) nasal; F1-F2, dorsal view; F3, ventral view. Landmark numbers and orientation arrows were added for more readability as well as the overall representation of the unpaired bone (basioccipital). Abbreviations: A, anterior; D, dorsal; L, lateral; V, ventral.

Nasal (Figure 25.F1-F3)

The nasal is relatively narrower mediolaterally in larger specimens with a much more pronounced internal curvature. Only the landmarks in contact with the premaxillary (#4; #10) show a slight anterior elongation in the medial part of the bone.

Palatine (Figure 26.G1-G3)

The palatine becomes relatively more elongated anteroposteriorly and narrower mediolaterally as size increases. This elongation is particularly visible between the anterolateral edge of the palatine and the caudal palatine foramen that became more distant from one another as size increases (#19; #21; #46).

Parietal (Figure 26.H1-H3)

The parietal is slightly more elongated anteroposteriorly and narrower mediolaterally in larger specimens (#78; #79; #81; #83). The tentorial process forms a higher ventrally-directed crest as size increases (#73).

Petrosal (Figure 26.I1-I3)

On the promontorium, size has little effect on shape variation except at the anterior and medial borders, which are slightly more reduced as size increases (#104; #124). In larger specimens, the mastoid process (#106) is much more pronounced ventrally, the dorsal tip of the crista petrosa (#118) is more anterodorsal, and the bottom of the fossa subarcuata shows a relatively more posterior position (#126).

CHAPTER 3: Cranial allometry in Cingulata

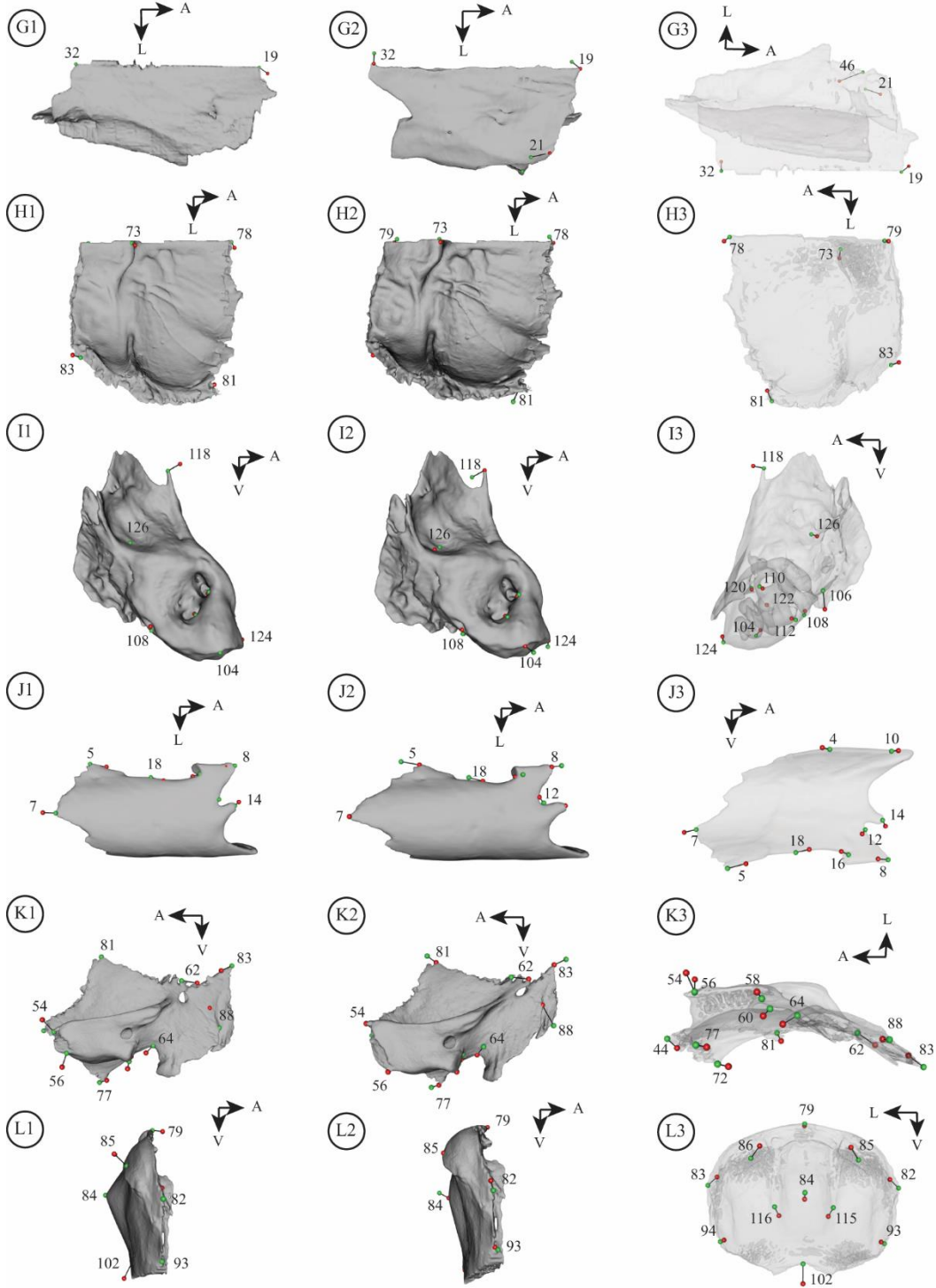
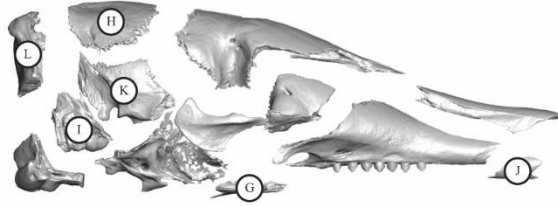


Figure 26. Vector representation of the allometric shape changes detected for a given cranial unit (OBU), represented between its minimal (green – smaller centroid size) and maximal (red – larger centroid size) shapes (see [Figure 23](#)). Results of the analysis performed at the ontogenetic level, and with the log skull centroid size taken as the size variable (see text). For each OBU, the changes are shown in three subsections organized horizontally: 1, vectors from minimal to maximal shape with minimal OBU shape; 2, same as 1) with maximal OBU shape; 3, minimal OBU shape in transparency with vectors. G) palatine; G1-G2, ventral view; G3, dorsal view. H) parietal; H1-H2, ventral view; H3, dorsal view. I) petrosal; I1-I2, medial view; I3, lateral view. J) premaxillary; J1-J2, ventral view; J3, medial view. K) squamosal; K1-K2, lateral view; K3, ventral view. L) supraoccipital; L1-L2, lateral view; L3, occipital view. Landmark numbers and orientation arrows were added for more readability as well as the overall representation of the unpaired bone (supraoccipital). Abbreviations: A, anterior; L, lateral; V, ventral.

Premaxillary (Figure 26.J1-J3)

The premaxillary is slightly more elongated dorsally in larger specimens while the situation is more complex ventrally. Medially, the premaxillary shortens (#5; #8) while it elongates laterally (#7; #14). The W-shaped process located in the anterior part of the bone ([Figure 22](#)) is more pronounced laterally with a deeper curvature (#12) and longer processes (#14). However, the W-shaped process is less sharp medially as its midline point is positioned more posteriorly (#8). The incisive foramen becomes relatively shorter anteroposteriorly mainly due to the anterior displacement of the most posterior point of these foramina (#18).

Squamosal (Figure 26.K1-K3)

The relative allometric reduction of the braincase is also visible on the dorsal edge of the squamosal of larger specimens (#81; #83). As for the jugal, we observe a dorsoventral increase of the zygomatic process of the squamosal (#54; #56). The posterior root of the zygomatic arch (#62) is also relatively more posterior. The posterior opening of the posttemporal canal ([Gaudin & Wible, 2006](#)) is more dorsal in larger specimens (#88). The postglenoid process (#58) is more pronounced anterolaterally and the postglenoid foramen (#60) is positioned slightly more medially. Therefore, the postglenoid process and postglenoid foramen are relatively more distant from one another on larger skulls. The sulcus for the external acoustic meatus (#64) is shallower and positioned more medially in larger specimens. Finally, the most posteroventral point between the alisphenoid and squamosal (#72) and the tip of the entoglenoid (#77) are shifted posteriorly.

Supraoccipital (Figure 26.L1-L3)

The increase in size is accompanied by a slight lateromedial narrowing (#83) and a dorsoventral elongation (#102) of the supraoccipital. The processes of the nuchal crests undergo a

strong posteromedial development in larger specimens (#86). The external occipital crest (#84) is less prominent. In the inner part of the supraoccipital, the lateral occipital vertical ridges (#116) are more developed in the anterior part of the caudal cerebral fossa.

3.1.3.4 *Allometry at different stages*

The allometric proportion of shape variation varies between the juvenile, subadult, and adult stages for a given OBU and for the entire skull in the whole sample (Figure 27A; Table 6; Table S9). For the entire skull, the allometric proportion decreases from juvenile to adult stages. In the 3B approach, the stage with the highest allometric proportion of shape variation varies from one OBU to another. The juvenile stage shows the highest allometric proportion for the maxillary, the frontal, the basioccipital-exoccipital complex, and the petrosal (Figure 27A; Table 6; Table S9). Allometric effects are often not statistically supported in older stages for these OBUs, as exemplified by the bo-eo OBU that only shows a strongly supported allometric effect at the juvenile stage. The allometric proportion of the maxillary shape variation in juveniles is only slightly higher than that retrieved at the subadult stage. The subadult stage shows the highest allometric proportion for the premaxillary, lacrimal, jugal, palatine, parietal, squamosal, and supraoccipital (Figure 27A; Table 6; Table S9). Allometric effects are statistically supported only at the subadult stage for the lacrimal, jugal, premaxillary, squamosal, and supraoccipital among these OBUs. The allometric proportion of shape variation is generally very low at the adult stage. The frontal, palatine, parietal, as-os-pt-bs OBU, and petrosal all display allometry at this stage (Figure 27A; Table 6; Table S9). The nasal bone is the only OBU that shows no stage with a supported static allometry. Stages with the highest allometric proportion for a given OBU generally show a higher slope (Table 6). Thus, the subadult stage is usually characterized by the highest slope coefficients for most OBUs. The comparison of the angles of each regression slope with respect to the horizontal axis shows that several OBU stages may share a common allometry (Figure S20, Table 6, Table S9-S10). By cross-checking these results with the statistical support values obtained for the allometric analyses of a given OBU at a given stage (Table 6 and Figure 27A), we find that only the juvenile and subadult stages of the maxillary (for which the angles are negative) and the juvenile and adult stages of the petrosal show a common allometry in our sample. This analysis also reveals a significantly different allometric effect between the subadult and adult stages of the palatine and parietal. (Figure S20, Table 6, Table S9-10).

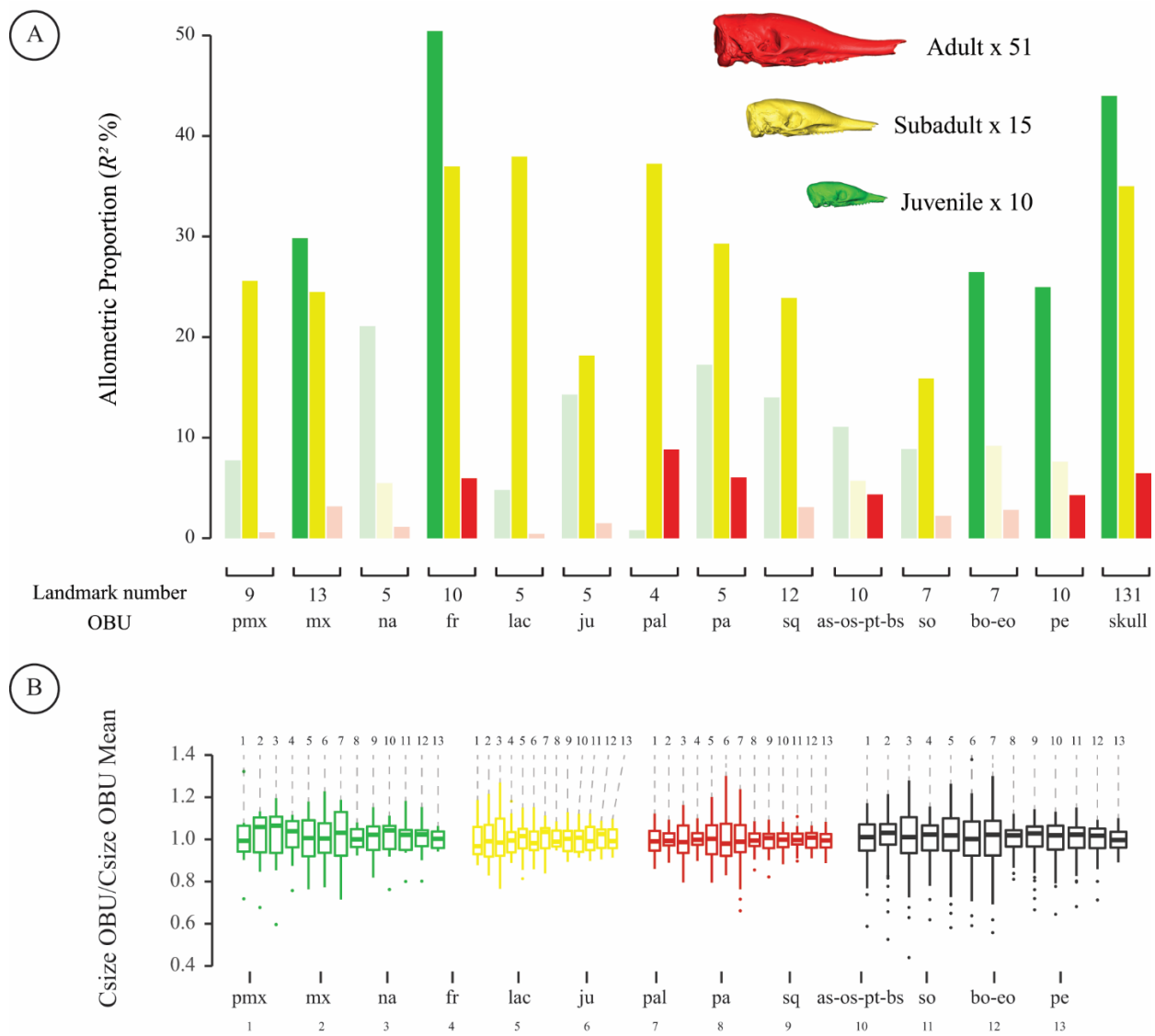


Figure 27. Allometry and growth pattern per cranial unit (OBU) and per postnatal ontogenetic stage. A) Bar graph showing the allometric proportions of shape variation per OBU and ontogenetic stage (see text). Bars with transparency indicate a statistically unsupported allometry for a given OBU and stage (at p -value > 0.05) (see Table 6). B) Boxplot showing the variation of size for each OBU relative to its mean per stage (green, juvenile; yellow, subadult; red, adult), and for the whole sample (in black), as measured by the following ratio for every specimen: log OBU centroid size / mean log OBU centroid size at a given stage. Abbreviations of OBUs: as-os-pt-bs, alisphenoid-orbitosphenoid-pterygoid-basisphenoid complex; bo-eo, basioccipital-exoccipital complex; fr, frontal; ju, jugal; lac, lacrimal; mx, maxillary; na, nasal; pa, parietal; pal, palatine; pe, petrosal; pmx, premaxillary; so, supraoccipital; sq, squamosal.

CHAPTER 3: Cranial allometry in Cingulata

Table 6. Results of the multivariate regression for ES and 3B with log skull centroid size for each ontogenetic stage. Index: *a*, slope coefficient; Intercept; α^* , angle of the slope with the horizontal axis in the common allometry analyses; R^2 , allometric proportion of the shape variation; *p-value*, significance following the permutation test. The shaded lines correspond to the tests with a non-significant *p-value* (> 0.05).

	Log Skull Centroid Size														
	Juvenile (N = 10)					Subadult (N = 15)					Adult (N = 51)				
	a	intercept	α^*	R^2	<i>p-value</i>	a	intercept	α^*	R^2	<i>p-value</i>	a	Intercept	α^*	R^2	<i>p-value</i>
Entire Skull	0.2842	-3.5343	36.35	0.45026	0.0005	0.3612	-4.5690	40.39	0.34846	0.0002	0.2307	-2.9312	23.09	0.06311	0.0002
Premaxillary	3.5220	-8.8770	40.02	0.07737	0.7393	9.8730	-25.054	40.29	0.25597	0.0016	2.3270	-5.9140	40.13	0.00558	0.9774
Maxillary	3.7910	-9.5550	-39.72	0.29837	0.0053	5.9980	-15.219	-39.18	0.24496	0.0008	3.2890	-8.3600	-15.61	0.03148	0.1040
Nasal	2.8210	-7.1110	-29.81	0.21065	0.1068	1.5110	-3.8350	-29.88	0.05470	0.5587	1.4820	-3.7670	-29.84	0.01127	0.6700
Frontal	6.1710	-15.554	36.87	0.50433	0.0005	8.1520	-20.687	41.51	0.36966	0.0004	5.1750	-13.155	23.50	0.05965	0.0200
Lacrimal	2.5470	-6.4210	0.990	0.04779	0.8327	15.430	-39.150	61.83	0.37951	0.0023	2.4230	-6.1600	-7.180	0.00429	0.9425
Jugal	4.6950	-11.835	37.47	0.14280	0.2647	9.5180	-24.153	37.90	0.18160	0.0394	3.7490	-9.5290	37.41	0.01476	0.5640
Palatine	0.8950	-2.2564	2.570	0.00776	0.9931	12.390	-31.450	23.58	0.37248	0.0031	9.7290	-24.730	-65.62	0.08829	0.0053
Parietal	3.2760	-8.2570	14.13	0.17248	0.1762	6.8370	-17.348	61.72	0.29289	0.0014	5.1620	-13.121	-56.18	0.06036	0.0120
Squamosal	3.7980	-9.5740	29.92	0.13981	0.2253	7.7990	-19.791	50.64	0.23893	0.0006	4.6370	-11.787	27.04	0.03084	0.0875
As-Os-Pt-Bs	4.0700	-10.260	27.29	0.11073	0.4488	4.5870	-11.639	27.35	0.05703	0.6605	7.4030	-18.819	27.66	0.04347	0.0178
Supraoccipital	2.7750	-6.9940	31.53	0.08856	0.5530	6.2200	-15.780	31.48	0.15893	0.0421	4.0930	-10.405	31.40	0.02223	0.3164
Bo-Eo	4.3580	-10.986	28.50	0.26473	0.0124	4.0810	-10.356	28.77	0.09176	0.2475	4.0220	-10.223	28.64	0.02801	0.1756
Petrosal	4.4010	-11.093	39.49	0.24980	0.0071	4.1190	-10.452	39.61	0.07592	0.3881	5.5540	-14.119	39.45	0.04270	0.0242

3.1.3.5 Size variation per OBU and allometry

The variation in size of an OBU relative to its mean size is different from one OBU to another and among ontogenetic stages (Figure 27B). At the juvenile stage, the OBUs with the largest size variations from their mean are the maxillary, nasal, lacrimal, jugal, palatine, squamosal, supraoccipital, and bo-*eo* OBUs. At the subadult level, OBUs with the largest variation in size constitute the anterior part of the snout (*i.e.*, premaxillary, maxillary, and nasal). In the adult stage, the OBUs with the greatest variation in size from their mean correspond to the lacrimal, jugal, and palatine. Finally, over the entire sample and stages, the size variation of an OBU compared to its average size enables us to sort the OBUs into two categories: those with a large size range (*i.e.*, premaxillary, maxillary, nasal, frontal, lacrimal, jugal, and palatine) and those with a small size range (*i.e.*, parietal, squamosal, as-os-pt-bs OBU, supraoccipital, bo-*eo* OBU, and petrosal) (Figure 27B). These patterns of size variation do not reflect the allometric proportions per OBU and per stage. However, the two size categories clearly separate an anterior from a posterior block of OBUs, which recall the allometric pattern detected on the entire skull (Figure 23 and see Discussion).

3.1.4 DISCUSSION

3.1.4.1 Allometric and geographical interaction

In mammals with a wide geographical distribution, such as the Pan-American nine-banded armadillos, allometric patterns can vary with geography and across environments (*e.g.*, Meloro *et al.* 2014; Bubadué *et al.* 2015; Ferreira-Cardoso *et al.*, 2019). Recent work on nine-banded armadillos has shown that variation in cranial shape had an important geographic imprint in this widely distributed species (Hautier *et al.*, 2017). In conjunction with evidence from internal anatomy and molecular data, these observations suggested the existence of four morphotypes (Southern, Central, Northern and Guianan) that potentially correspond to different species or subspecies (Huchon *et al.*, 1999; Gibb *et al.*, 2016; Billet *et al.*, 2017; Hautier *et al.*, 2017; Feijó *et al.*, 2018, 2019; Arteaga *et al.*, 2020). Regarding allometry, our results show that the percentage of variation in skull shape due to the interaction between geography and size is weak at the ontogenetic level ($R^2 = 3.16\%$ - Figure S15) and statistically unsupported at the static level. The slight difference in ontogenetic allometric trajectories among morphotypes of *D. novemcinctus*

ssp. must be considered cautiously as it may be due to insufficient juvenile samplings in the Northern morphotype. A weak relationship between geography and allometry was also described in subspecies of the widespread Eurasian red squirrel (Marr & MacLeod, 2019), for which subtle and continuous mandibular shape changes were retrieved.

Our comparison of allometric patterns between the whole sample and the Southern morphotype in nine banded armadillos further demonstrates that overall cranial allometric patterns are well conserved within this potential species complex. While ecological factors such as diet can influence allometric patterns (Wilson, 2013), the distinction suggested by Smith & Redford (1990) between Central and South American populations (feeding more on termites and ants) and North American populations (more omnivorous) questions the influence of diet on allometric variation. But, the weak link between geography and allometry in nine-banded armadillos also suggests that there is no clear influence of diet on overall cranial allometric patterns either.

3.1.4.2 *Main allometric variations*

Entire Skull approach

Allometry was recognized as an important component of mammalian skull variation, often accounting for about a third of the cranial variation at intra- and interspecific levels in mammals (Frost *et al.*, 2003; Hallgrímsson *et al.*, 2009; Cassini, 2013; Hallgrímsson *et al.*, 2015). Nine-banded armadillos are no exception with nearly 28% of the total cranial shape variation explained by size at the ontogenetic level. The two major ontogenetic allometric trends detected here were the relative snout elongation and the reduction of braincase proportions, which is reminiscent of previous results dealing with mammalian species (Drake & Klingenberg, 2008; Moyano *et al.*, 2018; Heck *et al.*, 2019). This pattern, often designated as craniofacial allometry, was also detected at the evolutionary level in many groups of mammals (Cardini & Polly, 2013; Cardini *et al.*, 2015; Tamagnini *et al.*, 2017). Cardini (2019) proposed that craniofacial allometry could represent a much widespread pattern of vertebrate morphological evolution.

In nine-banded armadillos, our analysis highlights some important additional allometric patterns on the entire skull, which could be summarized as follows:

- (i) The elongation of the snout is accompanied by a relative dorsoventral flattening and a lateromedial narrowing. At the intraspecific level, previous studies have also characterized a similar narrowing (*e.g.*, [Segura & Prevosti, 2012](#)) or flattening (*e.g.*, [Ferreira-Cardoso *et al.*, 2019](#)) of the snout.
- (ii) When size increases and the snout elongates, the length of the dental row (excluding the M1; see [Material and Methods](#)) shortens relatively to the entire skull at both the ontogenetic and static levels ([Figure 23](#)), which might suggest that its size does not increase much during ontogeny. Several species belonging to the genus *Dasypus* stand out among extant armadillos in showing dental replacement of most of their cheek teeth ([Ciancio *et al.*, 2012](#)). Further research is needed to establish whether this allometric reduction of the dental row proportion is specific to nine-banded armadillos or more widespread in other xenarthran species. It is indeed worth noting that this variation is known to be reversed in other mammals such as pronghorns ([Moyano *et al.*, 2020](#)), zokors ([Kang *et al.*, 2020](#)) or howler monkeys ([Meloro *et al.*, 2014](#)) in which the relative length of the upper dental row increases relative to the length of the skull.
- (iii) The orbitotemporal region shows a relative widening as the size increases, with a deeper postorbital constriction, a dorsoventally higher zygomatic arch and a wider temporal fenestra. An allometric relationship between these two parts of the orbitotemporal region has already been described in a canid species ([Segura & Prevosti, 2012](#)) while in horses the opposite variation is observed ([Heck *et al.*, 2019](#)). It was noted that the effect of allometry throughout the orbitotemporal region is highly contrasted at the evolutionary level within mammalian groups, which is probably due to the functional relationship between the masticatory muscles and normal oculomotor function ([Heesy, 2005](#)).
- (iv) Much of the allometric shape changes found at the static level were already detected with clearly higher proportions at the ontogenetic level, except for the parietal and palatine bones ([Figure 28A](#)). The high proportion of static allometry for these two bones suggests that much of their size-related shape variation occurs late during ontogeny ([Figure 27A](#)), exhibits high phenotypic plasticity or is subject to high selective pressure ([Pélabon *et al.*, 2013](#)). This result is particularly interesting in the

case of long-nosed armadillos as their palatal region bears several diagnostic traits for the genus *Dasypus* (Feijó & Cordeiro-Estrela, 2016). It would be worth performing the same analyses in other *Dasypus* species to see if this allometric pattern is conserved within dasypodines and how it relates to the diagnostic features used to distinguish species (Feijó *et al.*, 2019).

Bone-By-Bone (3B) approach and the complexity of cranial allometry

Most studies on cranial allometry involved analyses of covariation between local cranial distances and the skull length (*e.g.*, Goswami & Prochel, 2007; Wilson, 2011; Wilson, 2013; Wilson, 2018), or multivariate regressions over a set of cranial landmarks (GMM data) using a whole-skull Procrustes alignment (*e.g.*, Monteiro *et al.*, 1999; Cardini & O’Higgins, 2005; Heck *et al.*, 2019; *this study*). A few studies, however, detailed allometric patterns on specific regions of the skull with the use of linear distances (*e.g.*, Billet *et al.*, 2015a). Our 3B analysis may represent a novel approach, to our knowledge, as it uses geometric morphometrics to pinpoint and compare allometric variations at a smaller anatomical scale, such as individual bones, while changing the referential for the Procrustes alignment. Such an approach enabled us to detect previously unnoticed allometric variations and to reveal an untapped complexity of allometric patterns. The scrutiny of different spatial scales has important implications for studies on morphological integration and modularity, because growth patterns and allometry are essential factors for morphological integration (Porto *et al.*, 2013; Klingenberg, 2013; Mitteroecker *et al.*, 2020). Such detailed characterization of shape variation linked to size should also help towards a better knowledge and more appropriate treatment of correlated characters in morphological phylogenetics (Billet & Bardin, 2019).

The differences in allometric variation found in specific regions of the skull, with the entire skull (ES) and 3B approaches at the ontogenetic and static levels, show that the whole cranial allometric variation results from a complex superimposition of different allometric patterns expressed at different times and locations. At the ontogenetic level, our 3B analyses enabled to highlight major cranial allometric variations for most cranial units (OBUs; see [Material & Methods](#)), which differ from the ones retrieved using the ES. For instance, a size-related dorsoventral elongation and mediolateral shortening of the supraoccipital was detected with the

3B approach but not with the ES analyses (Figure 23, Figure 26.L1-L3). These results partly agree with the bivariate analyses of Goswami & Prochel (2007), which showed that the width of the supraoccipital followed an isometric growth in the common European mole (*Talpa europaea* Linnæus, 1758) while its height displayed positive allometry. Our 3B analyses also highlighted that the processes of the nuchal crests undergo a strong posteromedial development as size increases. Obviously, different allometric patterns could potentially be detected when considering different scales (*e.g.*, focus on the basicranium region instead of a given bone).

3.1.4.3 Heterogeneity of cranial allometry in space and time

Our study shows that the degree of allometric shape variation is not homogeneously distributed among the skull bones of nine-banded armadillos. Our 3B analyses most particularly revealed that the allometric proportions of shape variation are regionalized. Cranial units displaying the highest allometric proportions are not necessarily located close to one another (Figure 24). The relation with cranial size differs between OBUs, which is in line with bivariate analyses demonstrating that most distances measured on mammalian skulls follow different allometric trends (*e.g.*, Abdala *et al.*, 2001; Marroig & Cheverud, 2004; Goswami & Prochel, 2007; Wilson, 2011; Segura & Prevosti, 2012; Moyano *et al.*, 2018). This heterogeneity of allometric proportions per cranial unit could not be explained by the variation in size during ontogeny (see Results and Figures 27A-B & 28A). Similarly, both the prenatal skull ossification sequence (Figure 28B – see Hautier *et al.*, 2011) and the embryonic origin of each bone (Figure 28C – see Piekarski *et al.*, 2014) could not explain the differences in allometric proportions observed. Slight methodological artefacts (*e.g.*, number of landmarks per object) and the multiplicity of developmental and genetic processes at stake during local cranial morphogenesis (Hallgrímsson *et al.*, 2019) may explain the heterogeneous pattern found in our study. In addition, the proportion of total shape variation of each cranial unit explained by an independent variable, here size, may also depend on how much other variables (*e.g.*, environment) explain total shape variation and how these overlap with size.

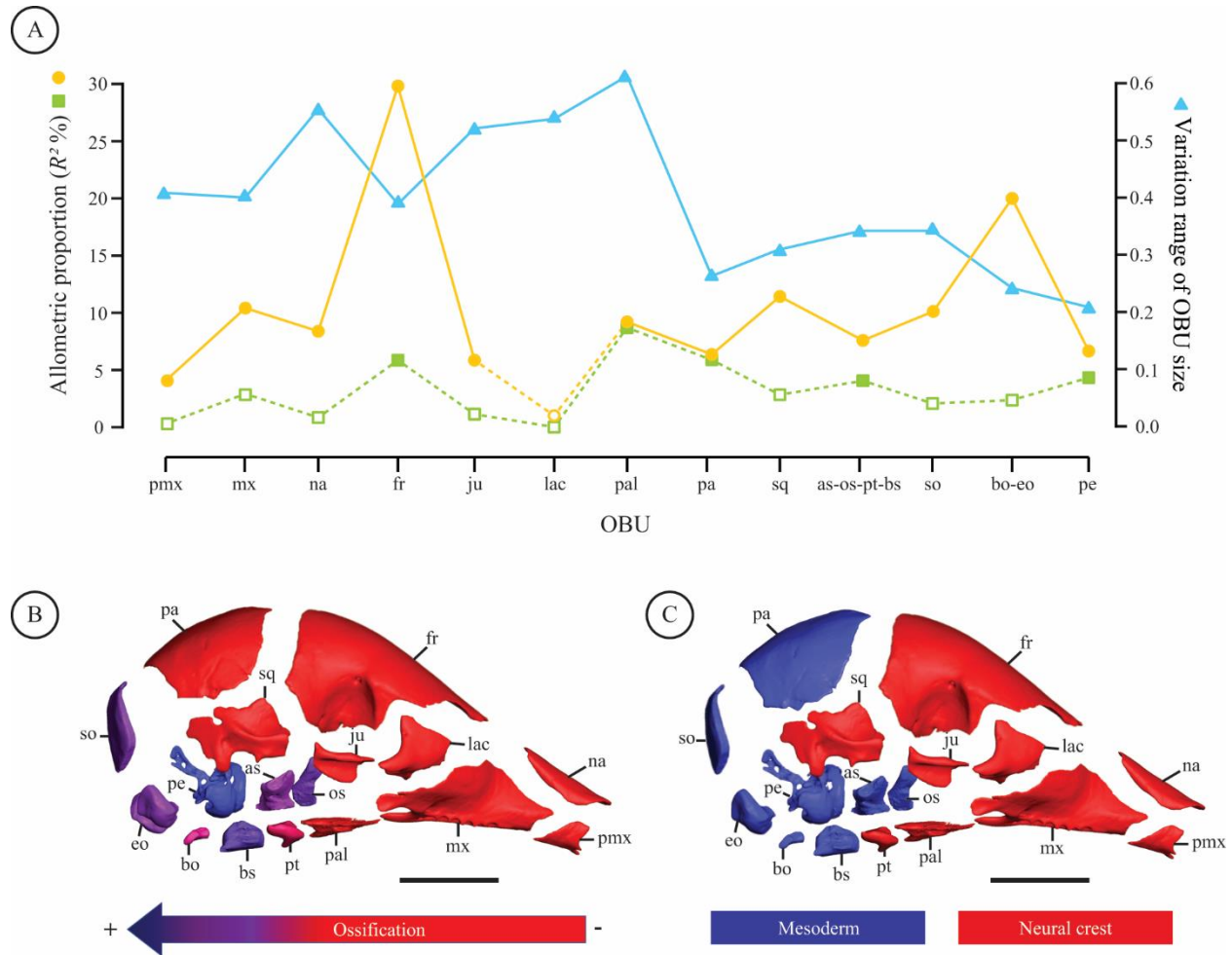


Figure 28. Comparison between the allometric proportion of shape variation, the variation in size and developmental characteristics for each cranial unit treated in this paper (see [Discussion](#)). A) Allometric proportions at ontogenetic (light orange circles) and static (light green squares) levels (unfilled figures correspond to non-supported allometric effects, see text) and variation range of each OBU’s size around its mean (light blue triangles). The latter is calculated as the interval between the first and third quartile of the ratio used in [Figure 27B](#), for the whole sample. B) Ossification chain according to [Hautier et al. \(2011\)](#). C) Distribution of embryonic origin of each bone according to [Piekarski et al. \(2014\)](#). Abbreviations: as-os-pt-bs, alisphenoid-orbitosphenoid-pterygoid-basisphenoid complex; bo-eo, basioccipital-exoccipital complex; fr, frontal; ju, jugal; lac, lacrimal; mx, maxillary; na, nasal; pa, parietal; pal, palatine; pe, petrosal; pmx, premaxillary; so, supraoccipital; sq, squamosal. Scale-bar = 1 cm.

We demonstrated that cranial units located in the anterior half of the skull vary more in size during postnatal development than those in the posterior half ([Figures 27B & 28A](#) – see [Segura & Prevosti, 2012](#) for another example in Canidae). This result echoes the ontogenetic pattern of allometric variation of the entire skull where a clear separation could be made between the snout and braincase ([Figure 23](#)). In contrast to the mosaic distribution of allometric proportions, such a division of the skull into two parts (or modules) is more congruent with the skull ossification

sequence and the embryonic origin of each bone (with the exclusion of the squamosal) (Figure 28).

Considering several ontogenetic stages contribute to a better understanding of the relative influences of the various developmental periods to the observed allometric patterns (Klingenberg & Zimmermann, 1992; Mitteroecker *et al.*, 2013). Although preliminary, and pending confirmation for each morphotype, our results show that the allometric proportion of shape variation regularly decreases with age for the entire skull, as well as for most cranial units (Figure 27A), as could be expected for mammals (finite growth). However, the allometric proportions over time differ between cranial units as illustrated by OBUs having higher allometric proportions at the juvenile stage than at other stages (maxillary, frontal, bo-*eo* OBU and petrosal), and OBUs displaying higher or better supported allometric proportions in subadults and adults than in juveniles (palatine and parietal) (Figure 27A). We thus characterized a partition across developmental stages in each cranial unit, superimposed to the partition in the allometric proportion of shape variation among cranial bones. This heterogeneity of cranial allometry in time and space in nine-banded armadillos strongly suggests the existence of a complex modular architecture. Such modularity might facilitate the evolvability of the phenotype and be a prerequisite for heterochronic evolutionary changes, which are often local and mosaic (Mitteroecker *et al.*, 2004; Gerber & Hopkins, 2011).

Several authors (Zumpano & Richtsmeier, 2003; Goswami & Prochel, 2007; Sardi *et al.*, 2007; Wilson, 2011) have shown that birth may constitute a clear-cut transition in the growth dynamics of several cranial units in rodents and primates, especially for the cranial roof. Since nine-banded armadillos are precocial (Derrickson, 1992; Krmpotic *et al.*, 2012), much of the allometric variation patterns found in our postnatal sample may also be expressed prenatally (Zelditch *et al.*, 2003; Wilson, 2018), a hypothesis that could be tested on a sample including fetuses. These analyses of allometric patterns could also be performed in different armadillo species, at both the intraspecific and interspecific levels, to see how allometric patterns are comparable between species and whether they are maintained at an evolutionary scale (*e.g.*, Gerber *et al.*, 2008; Esquerré *et al.*, 2017; Wilson, 2018).

3.2 Comparative study of cranial allometry in Cingulata

ABSTRACT

Allometry represents a pervasive pattern in morphological evolution. Recognition of a common allometric pattern across species requires comparative studies because analyses of size-related shape changes within a species are not sufficient to infer allometric patterns within other species or in an entire clade. Here, we used 3D geometric morphometric methods to study allometric patterns of the entire skull and cranial units at the ontogenetic and static levels in two phylogenetically distant armadillo species in the genera *Cabassous* and *Zaedyus*, which we compare to the armadillo *Dasypus novemcinctus* (Section 3.1) to identify common patterns of covariation. We then compare these intraspecific patterns to an evolutionary analysis of allometry, gathering most extant cingulate species and most of the emblematic fossil groups (with a focus on glyptodonts), using the same approach. Our results reveal a widespread craniofacial allometry, *i.e.*, relative skull lengthening and reduction of braincase proportions as size increases, in all cingulates. Our study also demonstrates that an increase in skull size in cingulates is generally accompanied by a relatively greater postorbital constriction, more protruding nuchal crests, broader temporal fossae, and a flatter cranial roof. The analyses conducted on cranial subunits show that widespread allometric patterns are also found more locally, such as for the relative position of the hypoglossal foramen, the proportions of the foramen magnum, and the protrusion of the posterior root of the zygomatic arch and of the mastoid process. This analysis also highlights an effect of size on shape variation for internal cranial structures, with a shallower fossa subarcuata and a thickening of the frontal bone resulting from size increases. These results evidence strong and widespread allometric patterns affecting cranial shape variation in cingulates, and represent a solid basis for the establishment of a mapping of strong covariation patterns to be discussed with respect to morphological characters employed in phylogenetic analysis.

3.2.1 INTRODUCTION

Variation in size constitutes a major determinant for variation in many biological traits. Studies have shown that the size-related changes of traits, called allometry, indeed represent a pervasive pattern in morphological evolution (Gould, 1966; Hallgrímsson *et al.*, 2019). However, the variation of this pattern, within and among species, remains poorly known for many taxa. Recognition of a common allometric pattern among species requires the production of comparative studies. Allometric variation may indeed differ between closely related species (*e.g.*, Frost *et al.*, 2003), and thus analyses of size-related shape changes within one species are not sufficient to infer allometric patterns within other species or within an entire clade. Allometry constitutes a complex and highly polygenic phenomenon (Zelditch *et al.*, 2003; Klingenberg, 2010; Pélabon *et al.*, 2014; Hallgrímsson *et al.*, 2019). Various factors (*e.g.*, ecology) may influence size variation and thus indirectly impact morphological variation through allometric processes in several species (*e.g.*, Esquerré *et al.*, 2017). In turn, size variation may be a driving force behind an evolutionary trend or a constraint in morphological variation (Gould, 1989; Sidlauskas, 2008; Klingenberg & Marugán-Lobón, 2013; Klingenberg, 2016). Allometric trajectories or patterns can therefore be biological traits under selection (Adams & Nistri, 2010; Klingenberg 2010; Urošević *et al.* 2013; Porto *et al.*, 2013; Giannini, 2014). Yet, the evolutionary mechanisms responsible for changes in allometric trajectories remain poorly understood. Allometry is expressed at various levels of the biological hierarchy and comparative studies can thus adopt complementary approaches to gain a global understanding of its variation within a group (Klingenberg, 1996).

A first approach is to analyze allometric patterns and trajectories at the intraspecific level in several species and to compare them (Strauss & Altig, 1992; Zelditch *et al.* 2003; Adams & Nistri 2010; Frédérix & Sheets, 2010; Piras *et al.* 2011; Urošević *et al.* 2013; Esquerré *et al.*, 2017; Wilson, 2018; Ferreira-Cardoso *et al.*, 2019; Simons & Frost, 2020). This comparison of intraspecific patterns allows a determination of whether the integration between size and shape is expressed in the same way in several taxa that are closely related. Looking at several intraspecific levels of variation (*i.e.*, static or ontogenetic) also makes it possible to compare allometric patterns across various ontogenetic stages (see Pélabon *et al.*, 2013). Many studies have used these approaches, providing evidence of both widespread intraspecific allometric patterns shared among

several species (*e.g.*, [Shea, 1983, 1985](#); [Ferreira-Cardoso *et al.*, 2019](#)) as well as diverging patterns among close relatives (*e.g.*, [Weston, 2003](#)). Several authors have argued that allometric trajectories within species are biological traits under selection and can promote a greater diversity of shape ([Frankino *et al.*, 2005](#); [Adams & Nistri, 2010](#); [Wilson & Sánchez-Villagra, 2010](#); [Klingenberg 2010](#); [Urošević *et al.*, 2013](#); [Porto *et al.*, 2013](#); [Giannini, 2014](#); [Esquerré *et al.*, 2017](#)). Further studies are needed perhaps confirm this claim, however.

A second and complementary approach consists of analyzing allometric patterns at the evolutionary level (among species) to test whether evolutionary changes in shape in a group could be related with variation in size ([Klingenberg & Marugán-Lobón, 2013](#) and citation therein). This approach can highlight widespread evolutionary patterns, as is the case for the craniofacial evolutionary allometry (CREA) hypothesis in mammals, which postulates that larger mammals show a relatively longer snout combined with a relatively reduced braincase ([Cardini & Polly, 2013](#); [Cardini *et al.*, 2015](#); [Tamagnini *et al.*, 2017](#); [Cardini, 2019a](#); [Marcy *et al.*, 2020](#); [Section 3.1](#)). There is much interest in comparing the patterns obtained by these two approaches (intraspecific and evolutionary), especially because it can provide information on the origin of the variation observed ([Klingenberg, 2014](#)). For example, a correspondence between the evolutionary level and the static level is most often interpreted as the result of neutral selection by drift ([Weaver *et al.*, 2007](#); [Smith, 2011](#)), whereas correspondences between the ontogenetic level and the evolutionary level may also imply differential timing of growth ([Cheverud, 1982b](#); [Gonzalez *et al.*, 2011](#)). In addition, the combination of both approaches is useful, because studies looking for correlations at the evolutionary level alone can be fooled by singular evolutionary events ([Uyeda *et al.*, 2018](#)), and intraspecific studies alone do not inform about among-species patterns. By relating the allometric patterns at both levels, it is possible to show whether size-related shape changes observable during the ontogeny of species are the same as those detected in the morphological evolution of the group. This is important since a similarity between these two levels of variation can lend further weight to a newly detected evolutionary allometry (such as for CREA; [Cardini & Polly, 2013](#)), especially in the case of unreplicated evolutionary events.

Cingulates represent a clade of extant placental mammals in which allometry remains poorly studied. Regarding the skull, a few studies have provided brief accounts on the evolutionary allometry within a clade such as [Hautier *et al.* \(2017\)](#) and [Feijó *et al.* \(2018\)](#) for dasypodines and

Abba *et al.* (2015) for euphractines. Our detailed study of ontogenetic and static allometry for the entire skull as well as cranial subunits in the nine-banded armadillo has provided the first in-depth investigation of cranial allometric patterns within a cingulate species (Section 3.1). To date, there has been neither a detailed analysis of cranial allometric patterns in other cingulate species, nor an analysis of cranial evolutionary allometry among cingulates that would encompass extant and fossil forms, including the giant-sized glyptodonts.

In this work, following on our previous study (Section 3.1), we first tested the hypothesis that the allometric patterns detected in *Dasypus novemcinctus* are similarly present in two other series of phylogenetically distant armadillo species, *Zaedyus pichiy* and *Cabassous unicinctus/centralis*. Second, we tested the existence of the same allometric pattern at the evolutionary level in a dataset incorporating almost all the extant species and a rich diversity of fossil specimens, including the large-sized glyptodonts and pampatheres. To test these hypotheses, we used 3D geometric morphometrics methods to test for allometric patterns of the whole skull (global) and of cranial subunits (local) both within and among species. The comparison of the allometric patterns obtained at various levels enabled us to highlight size-related shape changes that to be seen present both within and among cingulates species, and which represent common trends of morphological variation induced by variation in size in the group.

3.2.2 MATERIAL & METHODS

3.2.2.1 Intraspecific Sampling

We sampled 43 skulls of *Zaedyus pichiy* (Table S11), a species belonging to the Euphractinae (see Section 1.1), and 27 skulls belonging to either *Cabassous unicinctus* or *Cabassous centralis* (Table S11), two species belonging to the Tolypeutinae (see Section 1.1). There is considerable doubt about the distinction between these two species of *Cabassous* which are not weakly divergent morphologically and only weakly differentiated based on molecular evidence (Wetzel & Wetzel, 1980; Wetzel, 1985; Hayssen, 2014; Gibb *et al.*, 2016; Supporting Information 1). The only way to differentiate them is by their geographic origin, as *C. centralis* has a geographic range in Central America and northwesternmost South America (Hayssen *et al.*, 2013) whereas *C. unicinctus* occupies much of the remainder of northern South America east of

the mountains (Hayssen, 2014a). Unfortunately, the geographic origin of each specimen was not always known. Our investigation of the shape variation in our sample of these two species revealed no clear differences based on cranial shape, and for this reason, we used both species in the same data set (for more details refer to [Supporting Information 1](#)). However, our investigation highlighted an unexpected divergence in cranial shape between *Cabassous unicinctus* specimens from northern the Amazon basin and *Cabassous unicinctus* specimens from the southern Amazon ([Supporting Information 1](#)). Consequently, we divided the *Cabassous* data into two sets. The first one is the largest and, containing 27 specimens including both northern and southern specimens. We refer to this dataset as *CabassousNS*. The second dataset corresponds only to the northern specimens, and contains 21 specimens. We refer to this dataset as *CabassousN* (results for this dataset will be illustrated in supplementary data only). The material studied is stored in several museum collections, as indicated in [Table S11](#).

3.2.2.2 Interspecific Sampling

Our sampling for the evolutionary analysis of allometry includes 27 specimens of which 6 belong to extinct species and 21 correspond to extant species ([Table S12](#)). The sample covers all extant armadillo genera and almost all species (17/21 – [Gibb et al., 2016](#)). Morphotypes representing possibly distinct specific entities for species complexes are also included in the dataset for *Dasypus novemcinctus* ([Section 3.1](#)) and *Cabassous unicinctus* ([Supporting Information 1](#)). Our evolutionary sample covers a large diversity of cranial shapes in cingulates including the Santacrucian glyptodont “*Metopotoxus*” *anceps*, the Pleistocene glyptodont *Glyptodon* sp., the early diverging armadillo *Peltephilus pumilus* ([Shockey & Vlachos, 2017](#)), as well as the pampathere *Vassallia maxima*, and the dasypodine *Stegotherium tauberi*. We built three datasets that represent different combinations within this total sample. The first dataset consists of all specimens with the exclusion of *Proeutatus lagena*, which is less well-preserved than the other specimens. This dataset maximizes the number of landmarks ($n_{\text{landmark}} = 100$) over that of species ($n_{\text{specimen}} = 26$) and is thus called Dataset-Lmax. The second dataset includes only the extant species, which are less disparate concerning their cranial shapes ($n_{\text{landmark}} = 114$; $n_{\text{specimen}} = 21$). It is thus called DatasetExt. The third dataset includes all specimens, including *Proeutatus lagena*, which several authors suspect to be closely related to glyptodonts and pampatheres ([Engelmann, 1985](#); [Gaudin & Wible, 2006](#); [Billet et al., 2011](#); [Gaudin & Lyon, 2017](#)). This dataset maximizes

the number of taxa ($n_{\text{specimen}} = 27$) over that of landmarks ($n_{\text{landmark}} = 90$) and is called Dataset-Tmax. The results for this dataset will be illustrated in supplementary data only. The material examined in this portion of the study is stored in several museum collections, as indicated in [Table S12](#).

3.2.2.3 Correction of taphonomic deformations

Three fossil specimens presented obvious cranial deformations that limited our landmark acquisition, and which could not be directly compensated for by missing data estimates (*e.g.*, symmetrization requires minimally the presence of a landmark on both sides of an object). Using the software Cinema 4D (Maxon, release 23), we arbitrarily retrodeformed the cranial meshes of “*Metopotoxus*” *anceps* (YPM-VPPU 15612), *Proeutatus lagena* (YPM-VPPU 15613) and *Stegotherium tauberi* (YPM-VPPU 15565) to reduce the deformation due to taphonomic effect. In order to keep these arbitrary corrections to a minimum, we only applied deformations when they concerned areas directly on the midline axis of the skull or when at least one of the two sides (right or left) was in place and undeformed. In the glyptodont “*Metopotoxus*” *anceps*, we corrected a slight uniform right lateral tilt of 9.33%, and we moved the left part of the skull back in line with the right part that remained in place. In *Proeutatus lagena*, we realigned the midline to the anterior part of the frontal bone where it was offset to the right. Then we reoriented the rostrum, which was tilted slightly to the right, to match the midline. Finally, we realigned the left posterior edge of the skull, which was slightly offset from the right part. In *Stegotherium tauberi*, a break separated the front part of the rostrum from the rest of the face on our specimen. A very slight shift of 0.022 cm to the right was applied to correct for this break, in accordance with the midline of the part of the face that remained in place. These few retrodeformations are all illustrated with the specimens before and after deformation in [Figures S21, S22 & S23](#). Although not ideal, the shape variation that could be induced by the arbitrary component of these (slight) corrections have been shown to be negligible in comparison to interspecific variation of cranial shape in other groups ([Gomes Rodrigues *et al.*, 2018](#)). Here, it concerned few taxa, the variations due to these deformations were relatively minor, and the high diversity of cranial shape in our interspecific sample largely exceeded these variations.

3.2.2.4 Geometric Morphometrics

Specimens for both the intraspecific and interspecific samples were scanned on X-ray microtomography imagery platforms at the American Museum of Natural History (New York, USA); the *Muséum national d'Histoire naturelle* (France) in Paris (AST-RX platform), the University of Montpellier (France) and the *Museum für Naturkunde* (ZMB) in Berlin (Germany). Three-dimensional reconstruction and visualization of the skulls and of the virtually isolated bones were performed using stacks of digital images with MIMICS v. 21.0 software (3D Medical Image Processing Software, Materialize, Leuven, Belgium). Image stacks were improved in contrast, rotated, cropped, and reduced to 8 bits using the ImageJ software (Schneider *et al.*, 2012). Cranial shapes were quantified with a maximum of 114 anatomical landmarks (see [Figure S24](#) for an illustration of the landmarks employed for each dataset, [Table S13](#) for the landmark definitions, with two modifications to adapt the definitions to the interspecific datasets (#28-#29; #39-#40), and [Table S14](#) for landmark coordinates for all specimens) placed on the exported 3D models using AVIZO v. 9.7.0 software (Visualization Sciences Group, Burlington, MA, USA).

For the intraspecific sample, 17 landmarks were removed from the original dataset used for *Dasypus novemcinctus* ([Section 3.1](#)), because they could not be placed on the skulls of *Zaedyx pichiy*, *CabassousNS* and *CabassousN* (homologous structures were absent or not observable; [Tables S15 & S16](#)). The remaining 114 landmarks were initially defined for the analyses concerning the *Dasypus novemcinctus* complex ([Section 3.1](#); [Table S13](#)). The reduction of the landmark set was neither problematic for the analyses of the whole skull and nor for those of cranial bone subunits. None of the previously defined Operational Bone Units in the skull (OBU; see [Section 3.1](#)) included less than 4 landmarks after the reduction of the landmark dataset, thus keeping all OBUs available for analysis as explained in [Section 3.1](#).

For the interspecific sample, only DatasetExt retained all 114 landmarks. Dataset-Lmax was composed of 100 landmarks, and Dataset-Tmax included 90 landmarks ([Figure S24](#)). For the Bone-By-Bone analyses (3B; see [Section 3.1](#)), the reduction in the number of landmarks was at times problematic, since it forced us to discard several bone units with too few landmarks ($n < 4$ or 5; see below). The composition of the landmark sample for each dataset and their attribution to each OBU is shown in [Tables S15 & S16](#). Most of the missing landmarks for the Dataset-Lmax and Dataset-Tmax concerned points in the anterior part of the skull. The jugal and palatine, which had only 3 landmarks remaining in these datasets, could not be analyzed. This is also the case for

the premaxillary and nasal, which each retained 4 landmarks but with some extreme points missing, precluding a comparison with other analyses (e.g., the most anterodorsal point of the internasal suture #1– [Table S16](#)). Following the methodology explained in [Section 3.1](#), we performed a generalized Procrustes analysis ([Rohlf & Slice, 1990](#)) using the function *gpagen* in the R package *geomorph* version 3.1.0 ([Adams et al., 2019](#)). Intra-individual asymmetries ([Klingenberg et al., 2002](#)) were removed using the function *symmetrize* in the R package *Morpho* version 2.6 ([Schlager, 2017](#)). When some landmarks were missing on one side of the skull, their position was estimated using the function *fixLMmirror* in the *Morpho* R package (this represented 0.04% of the intraspecific datasets – [Table S17](#), and 0.07% of the interspecific datasets – [Table S18](#)). Missing landmarks on the skull midline or landmarks missing on both sides were estimated in intraspecific datasets with the function *estimate.missing* in the R package *geomorph* version 3.3.1 ([Adams et al., 2020](#)) (represented 0.01% - [Table S17](#)). In the interspecific datasets, the missing midline landmarks could not be estimated because the shape of the skull is too different among specimens at the evolutionary level. These landmarks therefore had to be removed, which led to the construction of the three different datasets. The logarithm of the centroid size of the skull was used as a size variable in all analyses.

3.2.2.5 Determination of ontogenetic stages

For each intraspecific dataset within *Cabassous* and *Zaedyus*, we subdivided the sample into different age classes (ontogenetic stages) that enabled us to study allometric patterns at the ontogenetic and static levels (see [Section 3.1](#)). For *Dasypus novemcinctus*, we recognized three ontogenetic stages – juvenile, subadult, and adult – based on the dental eruption stage, the level of ossification of the skull and its total length ([Section 3.1](#)). For *Zaedyus* and *Cabassous*, the datasets are too small to allow analyses at each ontogenetic stage as in *Dasypus novemcinctus*, but we still mention these stages in our results as useful information. Because members of the genus *Cabassous* and *Zaedyus* only have one dental generation (the possession of two dental generations seems to be restricted to *Dasypus* – [Ciancio et al., 2012](#)), dental eruption could not be used to determine ontogenetic stage. For these taxa, we used the degree of ossification of the basicranium following the criteria of [Hubbe et al. \(2016\)](#), who consider as adults only those armadillo specimens in which both the supraoccipital-exoccipital, basioccipital-basisphenoid and basioccipital-exoccipital contacts are completely closed (bones fused). Following these criteria,

we considered as strictly adult the specimens having these three contacts completely fused in *Cabassous* and *Zaedyus*. Conversely, a specimen with completely unfused supraoccipital-exoccipital contact was considered juvenile and specimens with intermediate degrees of ossification for these three sutures were attributed to the subadult stage. In summary, sampling for the ontogenetic level contains three ontogenetic stages (*Zaedyus pichiy* = 43; *Cabassous*NS = 27; *Cabassous*S = 21) whereas the static level corresponds to a subset of this sample consisting only of adult specimens (*Zaedyus pichiy* = 23; *Cabassous*NS = 16; *Cabassous*S = 14). A complete account of the observations for these criteria and attributions to ontogenetic stages for each specimen can be found in [Table S19](#) (see [Supporting information 1](#) for more detail).

3.2.2.6 Phylogenetically-informed analyses

At the evolutionary level, it is necessary to consider the phylogenetic structure of the data ([Klingenberg & Marugán-Lobón, 2013](#)) because phylogeny can be a confounding variable altering the independence of the data ([Pagel, 1994](#)). It is therefore necessary to integrate a dated tree into our analyses to control for phylogenetic constraints. For extant species, several molecular works have already produced dated trees, and even included a Pleistocene glyptodont ([Delsuc *et al.*, 2016](#); [Mitchell *et al.*, 2016](#)). However, these did not include any other fossil taxa. We have therefore used the more complete consensus tree and branch lengths obtained in [Chapter 2](#) (see [Figure S4](#)) for our analyses here. Species that were not coded for [Chapter 2](#) were duplicated with the same branch lengths as other representatives of their genus that were already present in the matrix (*e.g.*, *Dasypus*). Since the three datasets had a different taxonomic composition, we adapted each baseline tree by removing taxa to be discarded while keeping the branch lengths ([Figure S25](#)) with the *drop.tip* function of the R *ape* package ([Paradis & Schliep, 2019](#)).

3.2.2.7 Allometric analyses

To quantify the covariance between cranial shape and size, we used the same approach as for the ontogenetic and static level ([Section 3.1](#) and above). The entire skull (ES) Procrustes alignment was realized on the entire set of cranial landmarks, including both sides of the skull. Under the Bone-By-Bone (3B) approach (see [Section 3.1](#)), the analyzed objects corresponded to the same virtually isolated bone or group of bones that we defined in the study of *D. novemcinctus* as Operational Bone Units (OBUs). We used the same specimens for the 3B analyses as for the ES

approach. Each 3B Procrustes alignment was realized on a reduced set of landmarks corresponding to the OBU under consideration, with a slight difference in the number of landmarks compared to [Section 3.1](#) (see [Tables S15 & S16](#)). We performed the 3B analyses only on the left side of the cranium, which was more complete in most cases. The allometric component in the shape variation of OBUs and of the entire skull was analyzed using the skull centroid size as a measure of size ([Monteiro, 1999](#)). For intraspecific datasets, for both the ES and 3B analyses of allometry, we performed a multivariate regression of Procrustes shape coordinates ([Izenman, 2013](#)) on the log centroid size using the function *procD.lm* of the R package *geomorph*. For the evolutionary level, we performed a phylogenetic regression (Phylogenetic Generalized Least Squares using our baseline trees – PGLS - [Rohlf, 2001](#); [Klingenberg & Marugán-Lobón, 2013](#); [Adams & Collyer, 2018](#)) for Procrustes shape variables on the log centroid size using the function *procD.pgls* of the R package *geomorph*. We also produced the same analysis without considering the phylogeny, to evaluate its effect on the regressions obtained, using the same function as for the intraspecific datasets. The same statistical approach (*i.e.*, Procrustes ANOVA for Procrustes shape variables with permutation procedure) as the method used for *Dasypus novemcinctus* ([Section 3.1](#)) was used for the analysis of intraspecific datasets and evolutionary datasets. For the intraspecific datasets and for the DatasetExt, the variations were represented from the minimum to the maximum shape by vectors on deformed meshes. For the Dataset-Lmax and the Dataset-Tmax, the variations from the minimum to the maximum shape was too extreme to allow the use of mesh deformations. They were instead represented by wireframes representing the minimum and maximum shapes.

3.2.3 RESULTS

3.2.3.1 Allometric variations in the intraspecific samples

3.2.3.1.1 Allometric variations on the entire skull (ES) in *Zaedyus pichiy*

Ontogenetic allometry

The regression of shape on log centroid size in our ontogenetic series of *Z. pichiy* accounts for 7.732% of the total shape variation (p -value < 0.0002, [Figure 29A](#); [Table 7](#)). The major cranial

allometric variations mainly concern a relative flattening of the cranial roof, and a slight reduction of the braincase proportions from juvenile to adult specimens. This trend is mainly shown by a relatively more ventral position of the frontal in contact with the parietal as size increases, a more medial position of the landmarks of the alisphenoid (#41-42; #45-46) and a stronger postorbital constriction (#39-40). In addition, the intersection between the most dorsal point of the annular ridge and the midline (#97), as well as the dorsal intersection between the cribriform plate and the median septum posterior to the latter (#98) show a relatively more ventral (and posterior) position, like landmarks on the frontal (#66), in larger specimens. Conversely, the contact between the parietal and the supraoccipital (#67) takes a more posterior position as the size increases, giving the entire skull a more elongated and flattened aspect. This allometric variation is accompanied by relatively more salient nuchal crest processes posteriorly (#73-74). More anteriorly, a strong allometric variation is detected for several midline landmarks such as the contact between the maxillary and palatine (#17), between the nasal and frontal (#2) and between the premaxillary and maxillary (#5). These all move relatively forward in larger specimens. We note that the whole snout follows the same trend, but to a lesser degree, except for the triple premaxillary - nasal - maxillary contact (#3-4). This suggests a snout elongation that appears to be very unequally expressed among the landmarks in this region. Among the minor allometric variations, we can note a relatively more anterior position of the mastoid process (#89-90), a narrowing of the face at the triple contact among lacrimal-maxillary-frontal (#33-34) and a slight lateral widening of the zygomatic arches (#20-21; #49-54) when size increases.

Static allometry

The regression of shape on log centroid size in our adult specimens of *Z. pichiy* accounts for 9.369% of the total shape variation (p -value < 0.0066, [Figure 29B](#); [Table 7](#)). In this species, the allometric proportion of shape variation is higher at the static level than at the ontogenetic level. However, the allometric variations are more or less the same. We can note as a difference a relative reduction of the allometric variation with respect to landmarks on the alisphenoid (#41-42; #45-46), postorbital constriction (#39-40) and zygomatic arch (#20-21; #49-54). A directional shift also affects the processes of the nuchal crests (#73-74) which are shifted posteromedially relative to other landmarks as size increases. The dorsal intersection of the annular ridge and

midline (#97) no longer follows the relatively more ventral position of the frontal (#66), when size increases, but rather takes a more posterior position from the smallest to the largest specimen. Among the other differences with the ontogenetic analysis, we also note that the most posterodorsal point of the zygomatic ridge of the squamosal (#55-56) is located relatively more anteroventrally as size increases. Overall, most of the allometric variations impacting the snout at the ontogenetic level are present at the static level.

The distribution of *Zaedyus pichiy* specimens in the morphospace of the regression of shape on size reveals a clear gap between the smallest and largest specimens, a pattern that is somewhat hidden by the presence of subadult specimens at the ontogenetic level (Figure 29). The existence of this gap has already been highlighted during the selection of the sample prior to this study (see Supporting Information 1 and General Discussion & Conclusion) and suggests the existence of distinct subspecific entities or sexual dimorphism differentiated by size and shape in our sample for this species (General Discussion & Conclusion).

3.2.3.1.2. Allometric variations on the entire skull (ES) in Cabassous datasets

Ontogenetic allometry

The regression of shape on log centroid size in our ontogenetic series of *CabassousNS* accounts for 6.597% of the total shape variation (p -value = 0.0471, Figure 30; Table 8) whereas it is higher for *CabassousN* (8.798%, p -value = 0.0131, Figure S16; Table S20). The major allometric variations concern most of the regions discussed in *Zaedyus pichiy*, especially at the ontogenetic level. The cranial roof is similarly impacted with a more ventral position of the frontal midline landmarks and the dorsal edge of the cribriform plate (#66, #97, #98) as size increases. The processes of the nuchal crests extend farther posteriorly (#73-74) and the contact between the parietal and supraoccipital is in a relatively more posterior position (#67) in larger specimens. The postorbital constriction is also much more marked (#39-40) in larger specimens, but the zygomatic arches do not widen, in contrast to *Zaedyus* (#20-21; #49-54).

CHAPTER 3: Cranial allometry in Cingulata

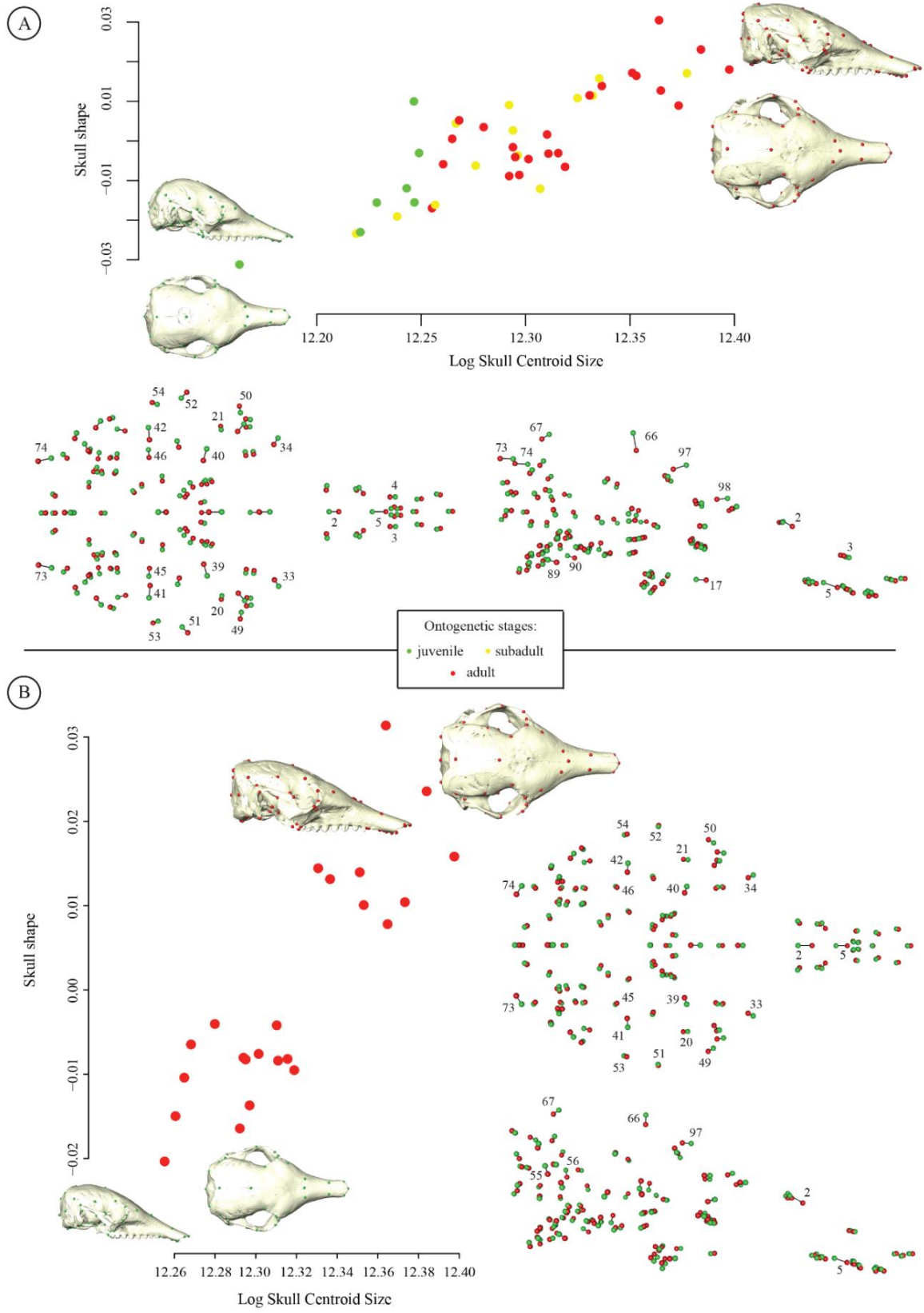


Figure 29. Ontogenetic and static allometry on the entire skull (ES) of *Zaedyus pichiy*. Ontogenetic stages are represented with different colors (juvenile = green; subadult = yellow; adult = red; see text for more detail). For graphical display, we used the projected regression scores of the shape data to represent shape variation related to changes in log skull centroid size (Adams *et al.*, 2013). Shape changes were visualized as vectors from the minimal shape (green) to the maximal shape (red) of the shape regression scores corresponding to the projection of the data points in shape space on to an axis in the direction of the regression vector (see Drake & Klingenberg, 2008). A. Multivariate regression of skull shape on log skull centroid size at the ontogenetic level, representing 7.73% of the total shape variation. B. Same analysis, at the static level (9.37% of total shape variation) (see text).

A slight reduction of the neurocranium is indicated by the more medial position of the contact between the alisphenoid, the squamosal and the frontal (#41-42) but also with the contact between the squamosal, the parietal and the frontal (#68-69). Finally, the vectors of most snout landmarks (#1; #3-16) indicate a slight elongation of this region directed anteriorly, as size increases. In addition, some allometric variations are new compared to *Zaedyus pichiy*. As size increases, the tentorial process elongates more ventrally (#63). The parietal, squamosal and supraoccipital contact also shifts dorsomedially (#70-71), and the contact between the frontal and nasal (#2; #31-32) on the snout moves posteriorly, unlike most landmarks of the front of the snout that shift anteriorly. The contact between the maxillary and palatine on the midline (#17) also migrates posteriorly in larger specimens, contrary to *Zaedyus pichiy*. The optic foramen is located relatively more anterolateral (#64-65), and the infraorbital foramen more posteroventrally (#24-25) in larger specimens. There is no difference in the allometric patterns detected between both *Cabassous* datasets, except for the higher vector norm in *CabassousNS*.

Static allometry

We detect no significant correlation between skull shape and size at the static level for *Cabassous* datasets (*CabassousNS*, p -value = 0.2197; *CabassousN*, p -value = 0.0859). However, caution is required when interpreting this result because the number of individuals is relatively small in the static datasets. The different composition of the two datasets ([Supporting Information 1](#)) also seem to play a role in the difference in p -value between *CabassousNS* and *CabassousS*.

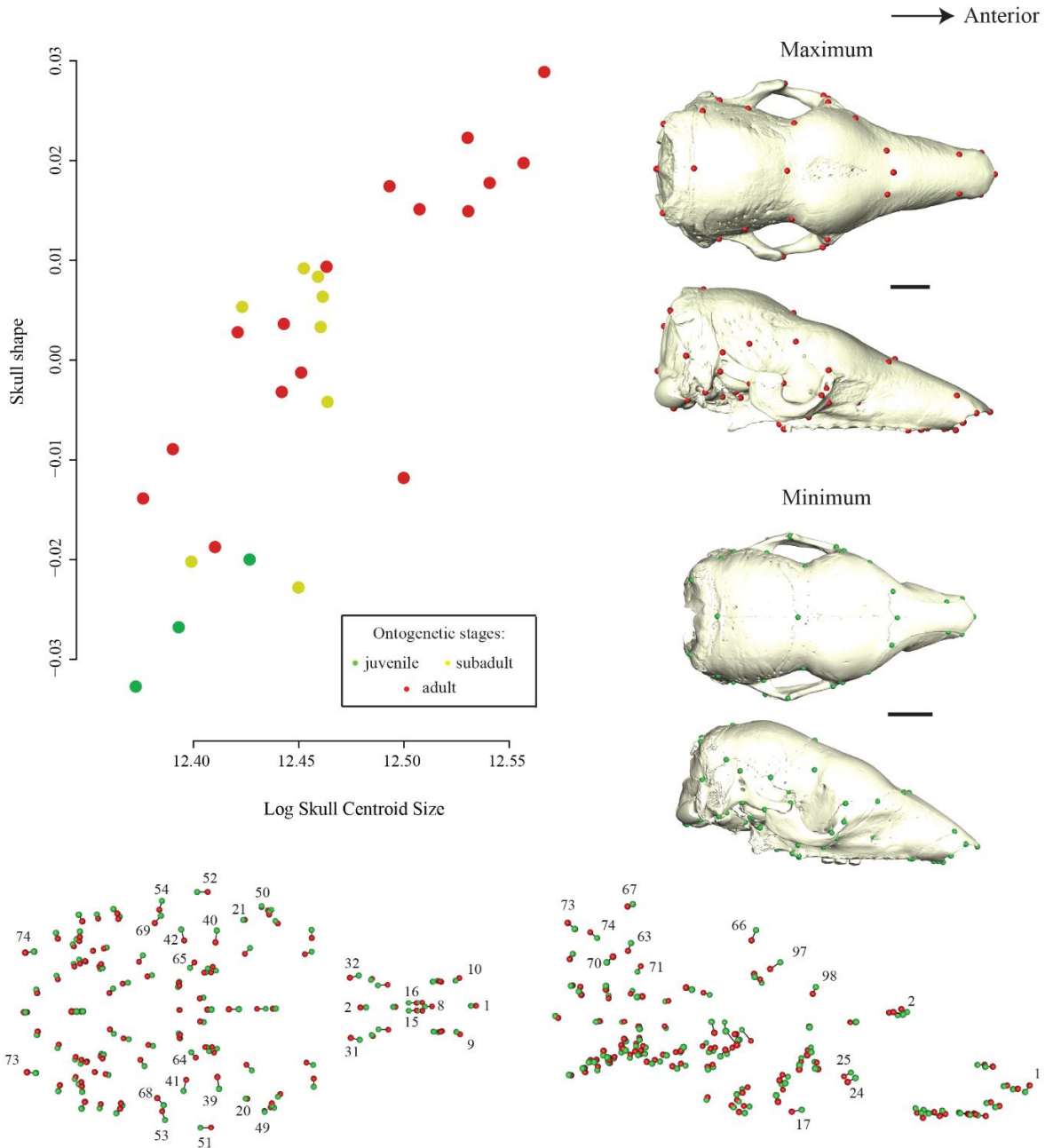


Figure 30. Ontogenetic allometry on the entire skull (ES) of *CabassousNS*. Ontogenetic stages are represented with different colors (juvenile = green; subadult = yellow; adult = red; see text for more detail). For graphical display, we used the projected regression scores of the shape data to represent shape variation related to changes in log skull centroid size (Adams *et al.*, 2013). Shape changes were visualized as vectors from the minimal shape (green) to the maximal shape (red) of the shape regression scores corresponding to the projection of the data points in shape space on to an axis in the direction of the regression vector (see Drake & Klingenberg, 2008). Multivariate regression of skull shape on log skull centroid size at the ontogenetic level represented 6.60% of the total shape variation.

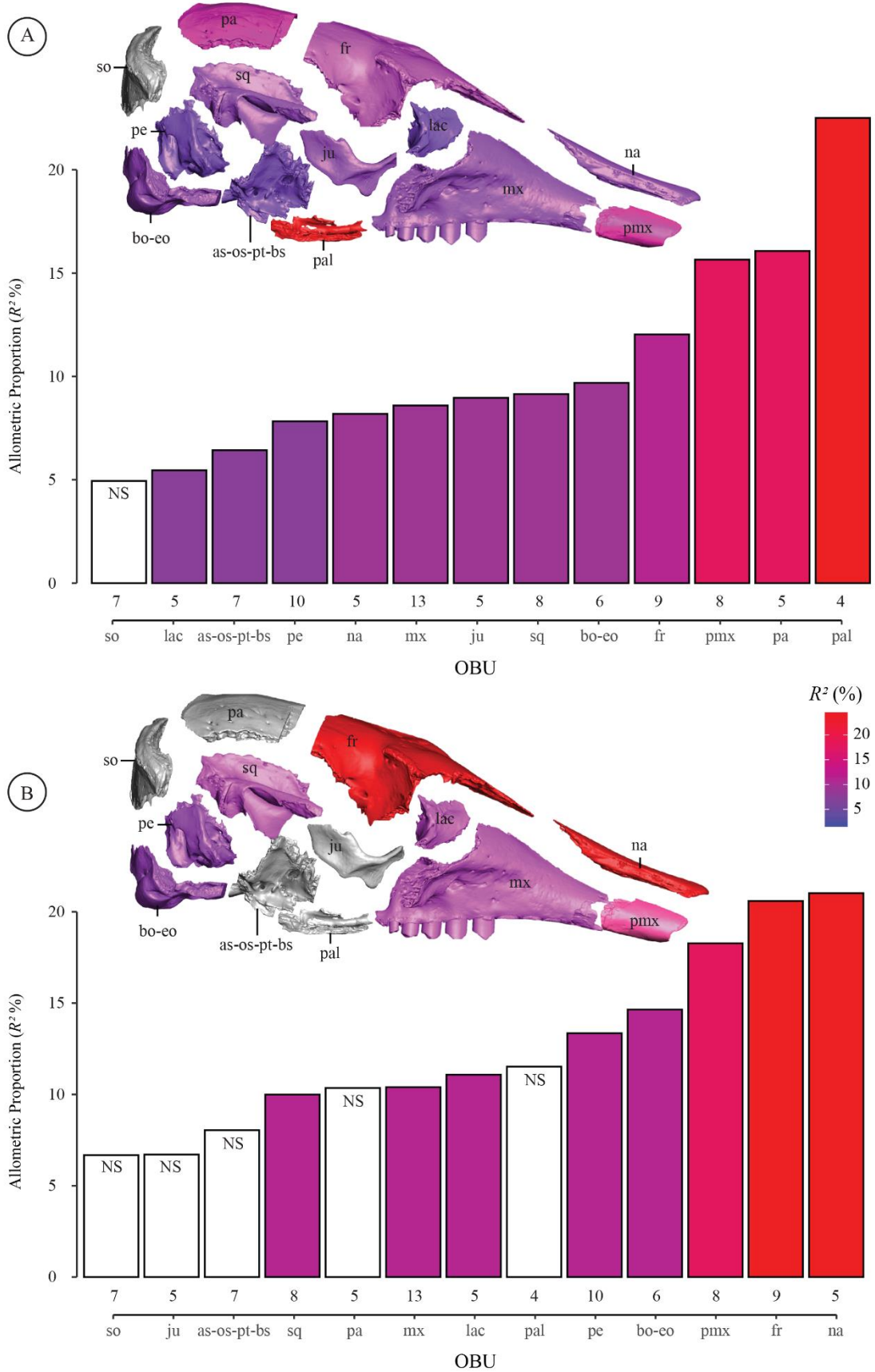
3.2.3.1.3. Allometric variations studied Bone By Bone (3B) in *Zaedyus* and *Cabassous*

Comparison between OBUs

In *Zaedyus pichiy*, we observe differences in the proportions of allometric shape variation among different OBUs both at the ontogenetic and static levels. At both levels (Figure 31), the regression of shape on size shows no statistical significance for the supraoccipital (Figure 31; Table 7). This is not the case for other OBUs, for which at least the analyses at the ontogenetic level show a significant allometric effect.

At the ontogenetic level, the lacrimal has the lowest proportion of shape variation explained by size of all OBUs (supraoccipital excluded; Figure 31A; Table 7). The proportion of shape variation explained by size ranges between 5% and 10% for the as-os-pt-bs, petrosal, nasal, maxillary, jugal, squamosal and bo-eo OBUs (Figure 31A; Table 7). The frontal shows a slightly higher allometric proportion, at 12% (Figure 31A; Table 7). The premaxillary and parietal have an even higher allometric proportion, ranging between 15% and 20% (Figure 31A; Table 7). The OBU showing the highest proportion of variation explained by size at the ontogenetic level is the palatine, at more than 22% (Figure 31A; Table 7). At the static level, 4 OBUs in addition to the supraoccipital no longer show a significant allometric component in their shape variation (Figure 31B; Table 7) – jugal, as-os-pt-bs OBU, parietal and palatine. The absence of allometric variation at the static level for the palatine and parietal is in stark contrast to the strong allometric component of their shape variation at the ontogenetic level (Figure 31). In increasing order, the squamosal, maxillary, lacrimal, petrosal and bo-eo OBU show a proportion of the variation in shape explained by size ranging between 10% and 15% (Figure 31B; Table 7). The allometric proportion of the premaxillary is comparable to that obtained at the ontogenetic level, whereas the frontal and nasal show a much higher allometric proportion, exceeding 20% (Figure 31B; Table 7).

CHAPTER 3: Cranial allometry in Cingulata



CHAPTER 3: Cranial allometry in Cingulata

Figure 31. Bar graphs showing the allometric proportions (R^2) of each cranial unit's (OBU) total shape variation under the 3B approach (see text), at the ontogenetic (A) and static (B) levels in *Zaedyus pichi*. Allometric proportions are shown with the log of skull centroid size taken as a size variable. On the virtually dislocated skull (in right lateral view), the allometric proportions are reported in corresponding colors. White bars indicate a statistically unsupported (NS) allometry for a given OBU (with a p -value > 0.05). Abbreviations of OBUs: as-os-pt-bs, alisphenoid-orbitosphenoid-pterygoid-basisphenoid complex; bo-eo, basioccipital-exoccipital complex; fr, frontal; ju, jugal; lac, lacrimal; mx, maxillary; na, nasal; pa, parietal; pal, palatine; pe, petrosal; pmx, premaxillary; so, supraoccipital; sq, squamosal.

In *CabassousNS*, we also observe differences in the proportions of allometric shape variation between different OBUs both at the ontogenetic and static levels. At both levels ([Figure 32](#)), the regression of shape on size shows no statistical support for the lacrimal, premaxillary, bo-eo, nasal, supraoccipital, maxillary, parietal and palatine OBUs ([Figure 32](#); [Table 8](#)). *CabassousN* differs at this point from the larger data set for the parietal which is statistically supported at the ontogenetic level (= 11.705%; [Figure S27](#); [Table S20](#)). In *CabassousNS*, the frontal, squamosal and petrosal have a proportion of shape variation explained by size ranging between 5% and 10% at the ontogenetic level ([Figure 32A](#); [Table 8](#)). The allometric proportion of the jugal is slightly higher, reaching 11.74% ([Figure 32A](#); [Table 8](#)). The highest proportion of shape variation explained by size corresponds to the as-os-pt-bs OBU, at 19% ([Figure 32A](#); [Table 8](#)). At the static level, only the petrosal and as-os-pt-bs OBU show a significant allometric component of their shape variation with proportions above the ontogenetic level (respectively 15.20% and 25.22%, [Figure 32](#); [Table 8](#)). *CabassousN* differs at this point from the larger dataset as the jugal and nasal are also statistically supported at the 18.43% and 26.44% level, respectively ([Figure S27](#); [Table S20](#)).

CHAPTER 3: Cranial allometry in Cingulata

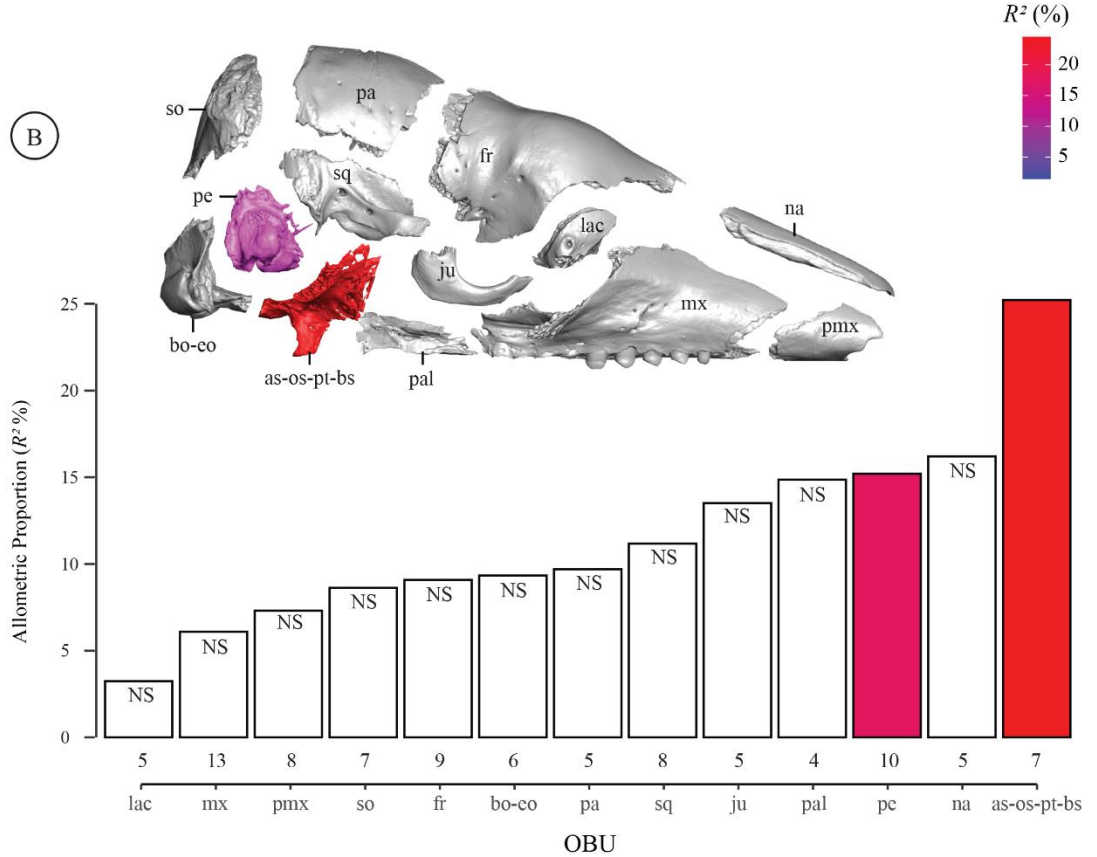
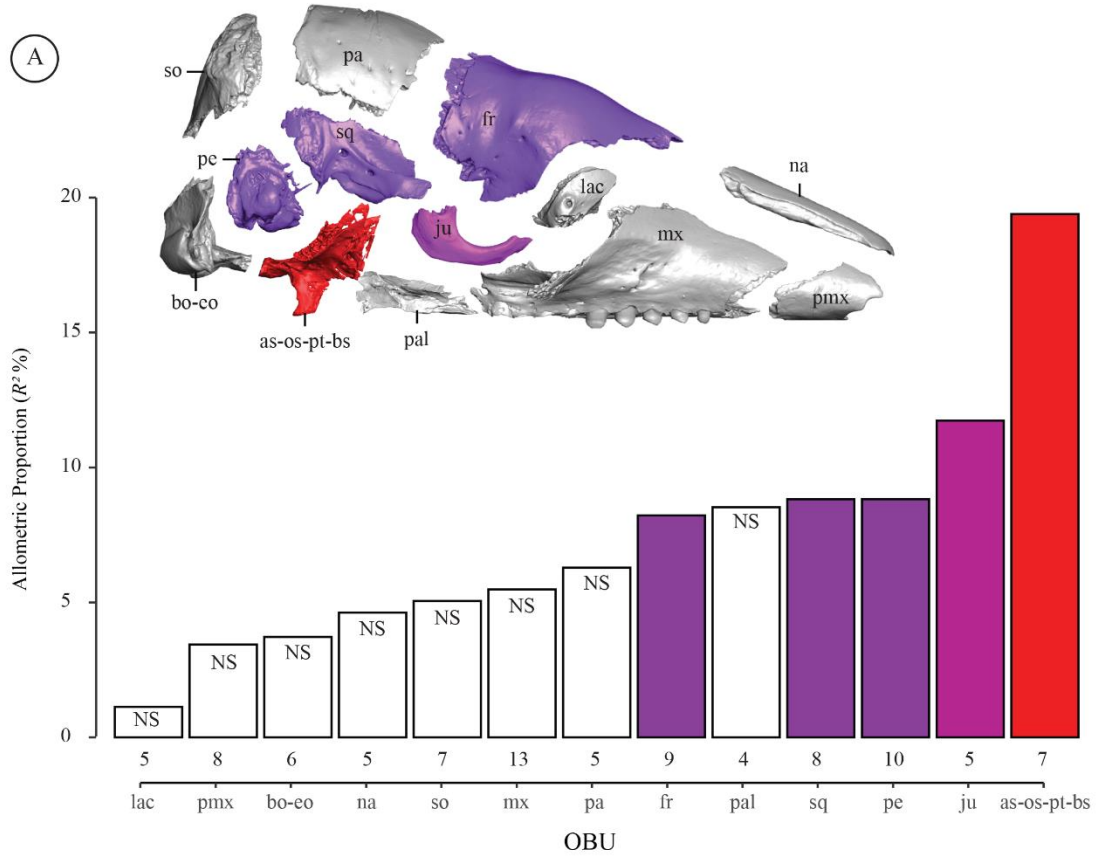


Figure 32. Bar graphs showing the allometric proportions (R^2) of each cranial unit's (OBU) total shape variation under the 3B approach (see text), at the ontogenetic (A) and static (B) levels in *CabassousNS*. Allometric proportions are shown with the log of skull centroid size taken as size variable. On the virtually dislocated skull (in right lateral view), the allometric proportions are reported in corresponding colors. White bars indicate a statistically unsupported (NS) allometry for a given OBU (with a p -value > 0.05). Abbreviations of OBUs: as-os-pt-bs, alisphenoid-orbitosphenoid-pterygoid-basisphenoid complex; bo-eo, basioccipital-exoccipital complex; fr, frontal; ju, jugal; lac, lacrimal; mx, maxillary; na, nasal; pa, parietal; pal, palatine; pe, petrosal; pmx, premaxillary; so, supraoccipital; sq, squamosal.

Allometric variation within OBUs

All descriptions of the allometric shape changes below describe the maximal shapes as compared to the minimal shapes in individual OBUs, but only those OBUs whose allometric variations were statistically significant (p -value < 0.05). Only landmarks on the left side of the skull are discussed. The results and shape changes explained by size for *CabassousN* at the ontogenetic level are not described below (except when different from *CabassousNS*), but are illustrated in supplementary data. This is also the case for the static level (see below).

Alisphenoid-Orbitosphenoid-Pterygoid-Basisphenoid complex

In *Zaedyus pichiy* (Figure 33), when size increases, the anterolateral edge of the alisphenoid in contact with the frontal and squamosal extends relatively more anterolaterally (#42) while the foramen ovale is more posteromedial (#60). The region bearing the sphenorbital fissure and the optic foramen is located slightly more anteromedial (#46; #65). The internal opening of the optic canal (#112) assumes a more anterolateral position as size increases, produces a reduction in the relative length of the canal. The most ventromedial point on the annular ridge lateral to posterior median septum (#114) shows the greatest allometric variation, with a more posterolateral position as size increases. At the static level, the allometric variation of this OBU is not statistically significant but the p -value is close to the significance threshold (Table 7).

CHAPTER 3: Cranial allometry in Cingulata

Table 7. Results of the multivariate regression for ES and 3B with log skull centroid size at the ontogenetic and static levels in *Zaedyus pichiy*. Index: a, slope coefficient; b, intercept; Df, degrees of freedom; F, Fisher-test; MS, mean square; N, sample size; P, *p-value*, significance following the permutation test; R^2 , allometric proportion of shape variation; SS, sum of squares; Z, Z-test. The shaded lines correspond to the tests with a non-significant *p-value* (> 0.05).

<i>Zaedyus pichiy</i>										
Ontogenetic level										
	N	Df	SS	MS	R2	F	Z	P	a	b
Entire Skull	43	42	0.005664	0.0056638	0.07732	3.4358	4.2609	0.0002	0.2279	-2.8025
Premaxillary	43	42	0.07228	0.07228	0.1565	7.6068	3.4665	0.0001	0.8142	-10.0116
Maxillary	43	42	0.011603	0.0116027	0.08591	3.8531	3.4369	0.0007	0.3262	-4.0112
Nasal	43	42	0.018739	0.018739	0.08187	3.6562	1.7275	0.0374	0.4146	-5.0976
Frontal	43	42	0.026446	0.0264461	0.12029	5.6064	3.2375	0.0008	0.4925	-6.0558
Lacrimal	43	42	0.02892	0.028917	0.05457	2.3666	1.6309	0.041	0.515	-6.332
Jugal	43	42	0.024745	0.0247455	0.08969	4.0396	2.5877	0.001	0.4764	-5.8579
Palatine	43	42	0.07353	0.073526	0.22511	11.911	2.9973	0.0002	0.8212	-10.0975
Parietal	43	42	0.03742	0.03742	0.16069	7.8497	3.0991	0.0001	0.5858	-7.2035
Squamosal	43	42	0.03593	0.035926	0.09148	4.1283	3.2912	0.0002	0.574	-7.058
As-Os-Pt-BS	43	42	0.02453	0.0245275	0.06435	2.8198	2.1397	0.0132	0.4743	-5.832
Supraoccipital	43	42	0.02725	0.027246	0.04944	2.1324	1.5898	0.0533	0.4999	-6.1467
Bo-Eo	43	42	0.021376	0.0213761	0.0969	4.3991	2.944	0.0005	0.4428	-5.4445
Petrosal	43	42	0.03381	0.033815	0.07829	3.4828	2.9193	0.0011	0.5569	-6.8477
Static level										
	N	Df	SS	MS	R2	F	Z	P	a	b
Entire Skull	23	22	0.003186	0.0031864	0.09369	2.171	2.6005	0.0066	0.2916	-3.592
Premaxillary	23	22	0.044522	0.044522	0.18274	4.6957	2.5147	0.0046	1.09	-13.43
Maxillary	23	22	0.00658	0.0065802	0.10395	2.4363	2.2571	0.0162	0.4191	-5.162
Nasal	23	22	0.019532	0.0195324	0.2102	5.5891	2.1173	0.0129	0.722	-8.893
Frontal	23	22	0.022633	0.022633	0.20588	5.4445	3.0799	0.0006	0.7772	-9.5733
Lacrimal	23	22	0.021984	0.0219842	0.11079	2.6165	1.7958	0.0227	0.766	-9.435
Jugal	23	22	0.008264	0.0082635	0.06704	1.5091	0.94584	0.1763	0.4696	-5.7847
Palatine	23	22	0.01663	0.0166303	0.11519	2.734	1.4436	0.0768	0.6662	-8.2063
Parietal	23	22	0.011271	0.0112708	0.1035	2.4245	1.4867	0.0651	0.5484	-6.7557
Squamosal	23	22	0.019251	0.0192512	0.09987	2.3299	2.0271	0.0204	0.7168	-8.8292
As-Os-Pt-BS	23	22	0.014352	0.0143518	0.08039	1.8357	1.4037	0.0677	0.6189	-7.6234
Supraoccipital	23	22	0.016417	0.016417	0.0668	1.5032	0.90453	0.1862	0.6619	-8.1534
Bo-Eo	23	22	0.016452	0.0164522	0.14644	3.6028	2.3628	0.0028	0.6626	-8.1622
Petrosal	23	22	0.029284	0.0292841	0.13351	3.2356	2.7029	0.0034	0.884	-10.89

In the two *Cabassous* datasets (Figures 34, 35, S28 & S29), both at the ontogenetic and static levels, the entire OBU is particularly impacted by allometric variation except for the sphenorbital fissure (#46). As size increases, the anterolateral edge of the alisphenoid in contact

with the frontal and squamosal (#42) takes a much more anteromedial position. The internal and external opening of the optic canal (#65; #112) extend concurrently in an anterolateral direction, but to a greater extent for the external opening (at the ontogenetic level), thereby increasing the length of the canal. The ventral edge of the foramen ovale (#60) is located relatively more posterolateral in larger specimens, whereas the most posterior point of the alisphenoid/squamosal suture in front of pyriform fenestra (#62) is situated further posteromedially. Finally, the most ventromedial point on the annular ridge lateral to the posterior median septum (#114) moves slightly more posteromedially as size increases, which reduces the relative thickness of the annular ridge.

Basioccipital-Exoccipital complex

In *Zaedyus pichiy*, at the ontogenetic and static levels (Figures 33 & 36), the allometric variation of this OBU is relatively weak. When size increases, the major variations are concentrated on the occipital condyles, with a slightly more anteromedial position of the intersection between the anteromedial edge of the occipital condyle and foramen magnum (#76) and of the most anterolateral point of the occipital condyle (#84). The most anteroventral point of the foramen magnum is also located slightly more posterior as size increases, which, together with the variation of landmarks #75-76, makes the foramen magnum relatively smaller. In addition, the hypoglossal foramen (#82) takes a relatively more posterolateral position as size increases. The rest of the points hardly vary at all. An allometric variation for this OBU is not supported statistically for the *Cabassous* datasets (Tables 8 & S20).

Frontal

In *Zaedyus pichiy*, at the ontogenetic level and at the static level (Figures 33 & 36), when size increases, the major allometric variations mainly concern regions of the frontal close to the midline. The anterior extremity in contact with the nasal (#2; #32) shows an anteriorly directed elongation, whereas the intersection between the frontoparietal suture and the midline (#66) and the dorsal intersection of annular ridge and midline (#97) become closer to one another. These allometric variations are accompanied by a slightly more pronounced and more posteriorly situated postorbital constriction (#40) in larger specimens, and a narrowing of the frontal shown by the greater proximity of the contact between the frontal and the parietal (#66) with the landmarks

CHAPTER 3: Cranial allometry in Cingulata

defining the triple frontal - parietal - squamosal contact (#69) and the triple frontal - squamosal - alisphenoid contact (#42).

Table 8. Results of the multivariate regression for ES and 3B with log skull centroid size at the ontogenetic and static levels in *CabassousNS*. Index: a, slope coefficient; b, intercept; Df, degrees of freedom; F, Fisher-test; MS, mean square; N, sample size; P, p-value, significance following the permutation test; R², allometric proportion of shape variation; SS, sum of squares; Z, Z-test. The shaded lines correspond to the tests with a non-significant *p*-value (> 0.05).

<i>CabassousNS</i>										
Ontogenetic level										
	N	Df	SS	MS	R2	F	Z	P	a	b
Entire Skull	27	26	0.004687	0.0046872	0.06597	1.7656	1.8452	0.0471	0.2465	-3.0713
Premaxillary	27	26	0.0167	0.016697	0.03441	0.8909	0.09613	0.4596	0.4653	-5.7969
Maxillary	27	26	0.010518	0.010518	0.05484	1.4505	1.003	0.156	0.3693	-4.6007
Nasal	27	26	0.006004	0.0060045	0.04627	1.213	0.58906	0.2808	0.279	-3.476
Frontal	27	26	0.01306	0.0130605	0.08221	2.2393	1.9446	0.0192	0.4115	-5.1268
Lacrimal	27	26	0.0096	0.009596	0.01134	0.2868	-1.0435	0.851	0.3527	-4.3945
Jugal	27	26	0.036643	0.036643	0.1174	3.3255	2.044	0.017	0.6893	-8.5874
Palatine	27	26	0.021219	0.0212185	0.08525	2.3298	1.3296	0.0745	0.5245	-6.5347
Parietal	27	26	0.010159	0.010159	0.0629	1.6781	1.1056	0.1224	0.3629	-4.5216
Squamosal	27	26	0.03343	0.033433	0.08821	2.4185	1.9003	0.0315	0.6584	-8.2028
As-Os-Pt-BS	27	26	0.10189	0.101891	0.19386	6.0122	3.2709	0.0003	1.149	-14.32
Supraoccipital	27	26	0.015361	0.015361	0.05055	1.331	0.75444	0.2349	0.4463	-5.56
Bo-Eo	27	26	0.005198	0.0051979	0.03722	0.9664	0.15091	0.4674	0.2596	-3.2343
Petrosal	27	26	0.023394	0.0233936	0.08823	2.4192	2.11	0.0144	0.5507	-6.8615
Static level										
	N	Df	SS	MS	R2	F	Z	P	a	b
Entire Skull	16	15	0.00303	0.0030299	0.07933	1.2063	0.76511	0.2197	0.236	-2.945
Premaxillary	16	15	0.021173	0.021173	0.07305	1.1033	0.44206	0.3368	0.6239	-7.784
Maxillary	16	15	0.006214	0.0062136	0.06092	0.9081	0.0075874	0.5154	0.338	-4.217
Nasal	16	15	0.010764	0.0107643	0.16205	2.7074	1.5919	0.0626	0.4449	-5.5502
Frontal	16	15	0.007495	0.0074948	0.09078	1.3979	0.93413	0.1731	0.3712	-4.6312
Lacrimal	16	15	0.01207	0.012074	0.0324	0.4688	-0.6026	0.7327	0.4711	-5.8781
Jugal	16	15	0.021148	0.0211479	0.1351	2.1869	1.4151	0.0745	0.6235	-7.7794
Palatine	16	15	0.025065	0.025065	0.14857	2.4429	1.374	0.0704	0.6788	-8.4692
Parietal	16	15	0.00962	0.0096202	0.09693	1.5027	0.88191	0.1895	0.4205	-5.2469
Squamosal	16	15	0.020567	0.020567	0.11179	1.762	1.2473	0.1056	0.6149	-7.6718
As-Os-Pt-BS	16	15	0.073603	0.073603	0.25219	4.7214	2.6495	0.0045	1.163	-14.513
Supraoccipital	16	15	0.015893	0.015893	0.08621	1.3209	0.70717	0.2476	0.5405	-6.744
Bo-Eo	16	15	0.007614	0.0076139	0.09337	1.4419	0.95901	0.1621	0.3741	-4.6678
Petrosal	16	15	0.024154	0.0241536	0.15201	2.5097	2.2297	0.0087	0.6664	-8.3139

In *Cabassous* datasets, at the ontogenetic level (Figures 34 & S28), the directions of the allometric variations for several points differ from the observations made in *Zaedyus* except for the two most posterior landmarks on the midline (#66; #97), which also suggest a slight posterior narrowing of the frontal bone as size increases. As size increases, there is no elongation of the anterior extremity of the frontal (#2; #32). The anterior edge in contact with the lacrimal is situated more anterolaterally (#34; #36). The postorbital constriction is also more pronounced in larger specimens, as in *Zaedyus*, but it is only slightly shifted posteriorly (#40). Finally, the slight posterior narrowing of the frontal is not due to a more medial position of the posterolateral edges of the OBU (#42; #69). Instead, there is a relative lengthening in the posterolateral border of the frontal from the smallest to the largest specimens. An allometric variation for this OBU is not supported at the static level for the *Cabassous* datasets (Tables 8 & S20).

Lacrimal

In *Zaedyus pichiy*, at the ontogenetic level (Figure 33), the variation in shape due to size seem to concern most landmarks on the lacrimal to a similar extent. The anteroventral margin of the lacrimal foramen (#38) and the triple contact point of the lacrimal - maxillary - frontal (#34) are both located relatively more posterior as size increases. Conversely, the triple contact point of the maxillary - jugal - lacrimal (#48) takes a more anterior position and the intersection between the lacrimal/frontal suture and the anterior orbital edge (#36) extends anterodorsally. The position of the intersection between the anterior orbital edge and jugal/lacrimal suture (#50) seems relatively unimpacted by the increase in size. Overall, these changes suggest that the lacrimal bone becomes relatively shorter in its lateroventral part in larger specimens, and that the distance between the lacrimal foramen and the posterodorsal edge of the bone on the orbital rim increases. At the static level (Figure 36), the increase in size is no longer accompanied by a strong change in the position of the triple contact point between maxillary – lacrimal – frontal (#34). Otherwise, allometric variations at this level differ only for the intersection between the anterior orbital edge and the jugal/lacrimal suture (#50), which takes a relatively more posterior position, and for the intersection between the lacrimal/frontal suture and the anterior orbital edge (#36), which extends more anteriorly as size increases. An allometric variation for this OBU is not significantly supported for the *Cabassous* datasets (Tables 8 & S20).

CHAPTER 3: Cranial allometry in Cingulata

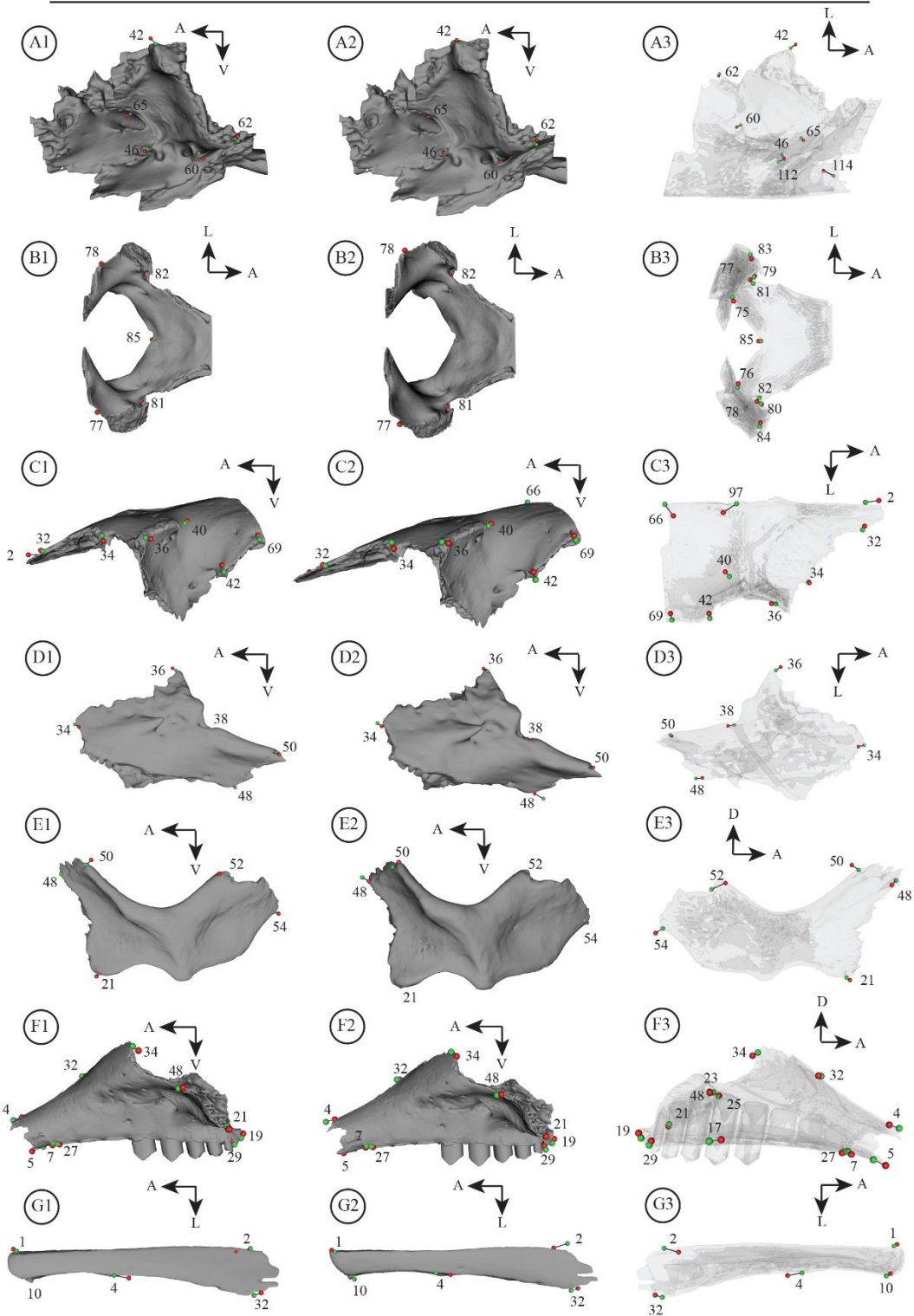
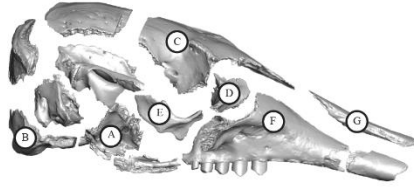


Figure 33. Vector representation of the allometric shape changes detected for a given cranial unit (OBU) in *Zaedyus*, represented between its minimal (green – smaller centroid size) and maximal (red – larger centroid size) shape (see [Figure 29](#)). Results of the analysis performed at the ontogenetic level, and with the log skull centroid size taken as the size variable (see text). For each OBU, the changes are shown in three subsections organized horizontally: 1, vectors from minimal to maximal shape with minimal OBU shape; 2, same as 1) with maximal OBU shape; 3, minimal OBU shape in transparency with vectors. A) alisphenoid-orbitosphenoid-pterygoid-basisphenoid complex; A1-A2, lateral view; A3, dorsal view. B) basioccipital-exoccipital complex; B1-B2, dorsal view; B3, ventral view. C) frontal; C1-C2, lateral view; C3, ventral view. D) lacrimal; D1-D2, lateral view; D3, medial view. E) jugal; E1-E2, lateral view; E3, medial view. F) maxillary; F1-F2, lateral view; F3, medial view. G) nasal; G1-2, dorsal view; G3, ventral view. Landmark numbers and orientation arrows were added for more readability, as well as to produce an overall representation of the unpaired basioccipital. Abbreviations: A, anterior; D, dorsal; L, lateral; V, ventral.

Jugal

In *Zaedyus pichiy*, at the ontogenetic level ([Figure 33](#)), the major allometric variations of the jugal concern its posterior edges in contact with the squamosal (#52; #54) and an anterior landmark corresponding to its intersection with the orbital edge and lacrimal. When size increases, the dorsal (#52) and ventral (#54) contact with the squamosal move away from each other, resulting in an increase in depth of the zygomatic arch. To a lesser extent, the increase in size also results in a more posterodorsal position of the intersection between the anterior orbital edge and the jugal – lacrimal suture (#50). We also note that the contact with the lacrimal and maxillary (#48) is relatively more posteroventral, which reduces the relative length of the anterior extremity of the jugal. All these allometric changes suggest that the jugal becomes relatively shorter and higher in larger specimens. Finally, the intersection between the jugal – maxillary suture and the ventral edge of the zygomatic arch (#21) takes a slightly more anteroventral position as size increases. At the static level, allometric variation for this OBU is not significantly supported for this species ([Table 7](#)).

In *CabassousNS*, at the ontogenetic level ([Figure 34](#)), we also detect allometric variation leading to a relative enlargement of the posterior part of the jugal on the zygomatic arch, with its dorsal extremity being shifted more anteriorly and its ventral extremity shifted posteroventrally as size increases (#52; #54). It can also be noted that, as size increases, the intersection between the anterior orbital edge and the jugal/lacrimal suture (#50) and the intersection between the jugal - maxillary suture and the ventral edge of the zygomatic arch (#21) take a slightly more posterior position. In addition, the contact with the lacrimal and maxillary (#48) extends more anterodorsally, causing a slight elongation of the anterior extremity of the jugal as size increases. At the static level, allometric variation for this OBU is nearly significant but is not supported, for *CabassousNS* ([Table 8](#)).

CHAPTER 3: Cranial allometry in Cingulata

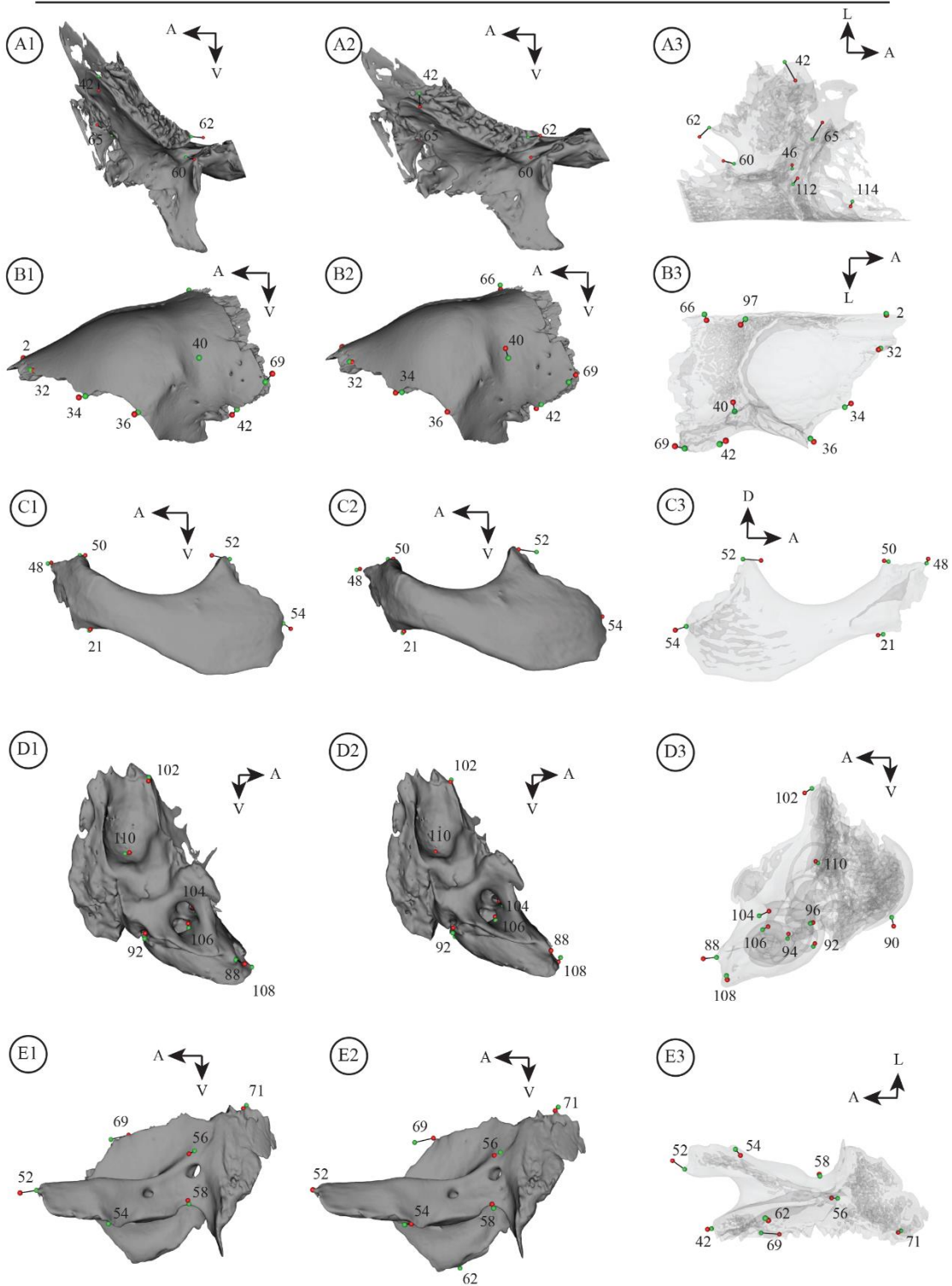
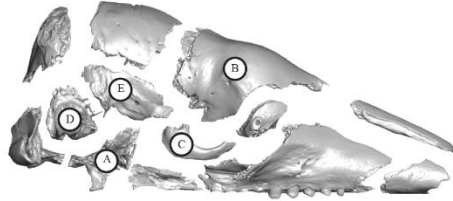


Figure 34. Vector representation of the allometric shape changes detected for a given cranial unit (OBU) in *CabassousNS*, represented between its minimal (green – smaller centroid size) and maximal (red – larger centroid size) shape (see [Figure 29](#)). Results of the analysis performed at the ontogenetic level, and with the log skull centroid size taken as the size variable (see text). For each OBU, the changes are shown in three subsections organized horizontally: 1, vectors from minimal to maximal shape with minimal OBU shape; 2, same as 1) with maximal OBU shape; 3, minimal OBU shape in transparency with vectors. A) alisphenoid-orbitosphenoid-pterygoid-basisphenoid complex; A1-A2, lateral view; A3, dorsal view. B) frontal; B1-B2, lateral view; B3, ventral view. C) jugal; C1-C2, lateral view; C3, medial view. D) petrosal; D1-D2, medial view; D3, lateral view. E) squamosal; E1-E2, lateral view; E3, ventral view. Landmark numbers and orientation arrows were added for more readability. Abbreviations: A, anterior; D, dorsal; L, lateral; V, ventral.

In *CabassousN*, at the ontogenetic and static level ([Figures S28 & S29](#)), we observe the same general allometric variations as in *CabassousNS*, except for the intersection between the jugal/maxillary suture and the ventral edge of zygomatic arch (#21) which assumes a more dorsal position, and for the contact with the lacrimal and maxillary (#48), which exhibits a more posteroventral position as size increases. As for *Zaedyus*, most of these changes suggest a relatively higher (and/or broader) and shorter jugal bone as size increases.

Maxillary

In *Zaedyus pichiy*, at the ontogenetic level ([Figure 33](#)), the maxillary shows an anterior elongation of the anteroventral portion that contacts the premaxillary on the palate (#5) in larger specimens, whereas its anterodorsal contacts the premaxillary and the nasal is shifted in the opposite direction (#4). One of the strongest allometric variations in this OBU corresponds to its midline contact with the palatine (#17), which takes on a more anterior position in larger specimens, similar to its ventral contact with the premaxillary (#5). The most posterior point of the premaxillary – maxillary suture on the palate (#7) is located relatively more anteromedial in larger specimens, although this variation is weak. The dorsal part in contact with the frontal and lacrimal (#34) is situated more posteroventral, whereas its posteroventral part close to the posterior edge of the dental row (#19; #29) is located slightly further dorsally as size increases. The combination of these two allometric variations suggest a slight reduction in the posterior height of the bone in larger specimens. In addition, the most anterior point of the alveolar margin of the dental row (#27) is located a little more posterior in larger specimens. The position of the landmarks in contact with the zygomatic arch (#21; #48) and the contact with the nasal and frontal (#32) hardly vary with size at all. The same allometric variations are detected at the static level ([Figure 36](#)) except for a much less anterior position of the midline contact with the palatine (#17)

CHAPTER 3: Cranial allometry in Cingulata

in larger specimens. An allometric variation for this OBU is not significantly supported for the *Cabassous* datasets (Tables 8 & S20).

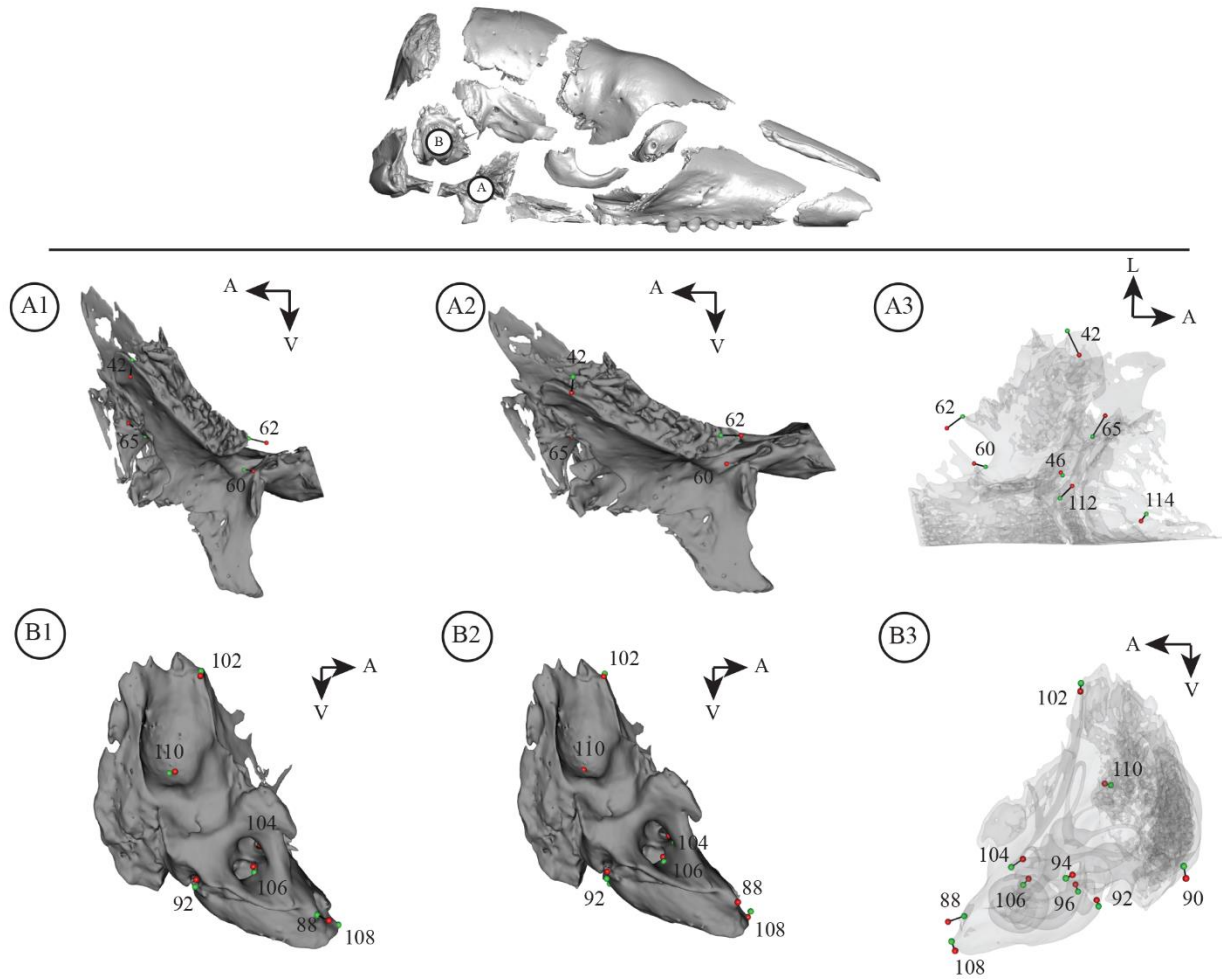


Figure 35. Vector representation of the allometric shape changes detected for a given cranial unit (OBU) in *Cabassous*NS, represented between its minimal (green – smaller centroid size) and maximal (red – larger centroid size) shape (see Figure 29). Results of the analysis performed at the static level, and with the log skull centroid size taken as the size variable (see text). For each OBU, the changes are shown in three subsections organized horizontally: 1, vectors from minimal to maximal shape with minimal OBU shape; 2, same as 1) with maximal OBU shape; 3, minimal OBU shape in transparency with vectors. A) alisphenoid-orbitosphenoid-pterygoid-basisphenoid complex; A1-A2, lateral view; A3, dorsal view. B) petrosal; B1-B2, medial view; B3, lateral view. Landmark numbers and orientation arrows were added for more readability. Abbreviations: A, anterior; L, lateral; V, ventral.

Nasal

In *Zaedyus pichiy*, at the ontogenetic and static levels (Figures 33 & 37), the landmarks on the anterior part of the nasal (#1; #10) are relatively more anteromedial in position as size increases. The contact with the maxillary and premaxillary (#4) move much further posteriorly as size increases, which indicates that a larger portion of the nasal is in contact with the premaxillary in larger specimens. More posteriorly, the part of the nasal contacting the frontal (#2) near the midline takes a more anterior position as size increases, whereas the posterolateral edge in contact with the frontal and maxillary (#32) elongates in a posteromedial direction. The combination of these two trends indicates an elongation of the frontal process of the nasal posterolaterally as size increases and a deeper nasal process of the frontal between the nasal bones. This pattern is congruent with the results found for the frontal bone (see above).

Only *Cabassous*N at the static level (Figure S29) shows statistically supported allometric variation for this OBU (Tables 8 & S20), although it is nearly significant at this same level in *Cabassous*NS. When size increases, the allometric variations are very different from that found for *Zaedyus pichiy*. The landmarks on the anterior part of the nasal assume a more posterior position (#1; #10) in larger specimens. The contact of the nasal with the premaxillary and maxillary (#4) takes a much more anterior position as size increases which indicates that a smaller portion of the nasal is in contact with the premaxillary in larger specimens, in contrast to the pattern found in *Zaedyus*. Finally, the frontal process of the nasal (#32) extends slightly more posterolaterally in larger specimens, as in *Zaedyus*, whereas the position of the landmark marking the nasal contact with the frontal at the midline level (#2) hardly varies.

Palatine

At the ontogenetic level (Figure 38), the palatine in *Zaedyus pichiy* is relatively more elongated anteroposteriorly (#17; #30) and narrower mediolaterally (#21; #44; #17; #30) as size increases. This elongation is coupled with a reduction in the width of the bone from the juvenile to the adult stage. This is particularly marked at the intersection between maxillary/palatine suture and the lateral edge of palate (#21) and caudal palatine foramen (#44). Allometric variation for this OBU is not significantly supported for the *Cabassous* datasets and for *Zaedyus pichiy* at the static level, but the *p-values* are close to the significance threshold (Tables 7, 8 & S20).

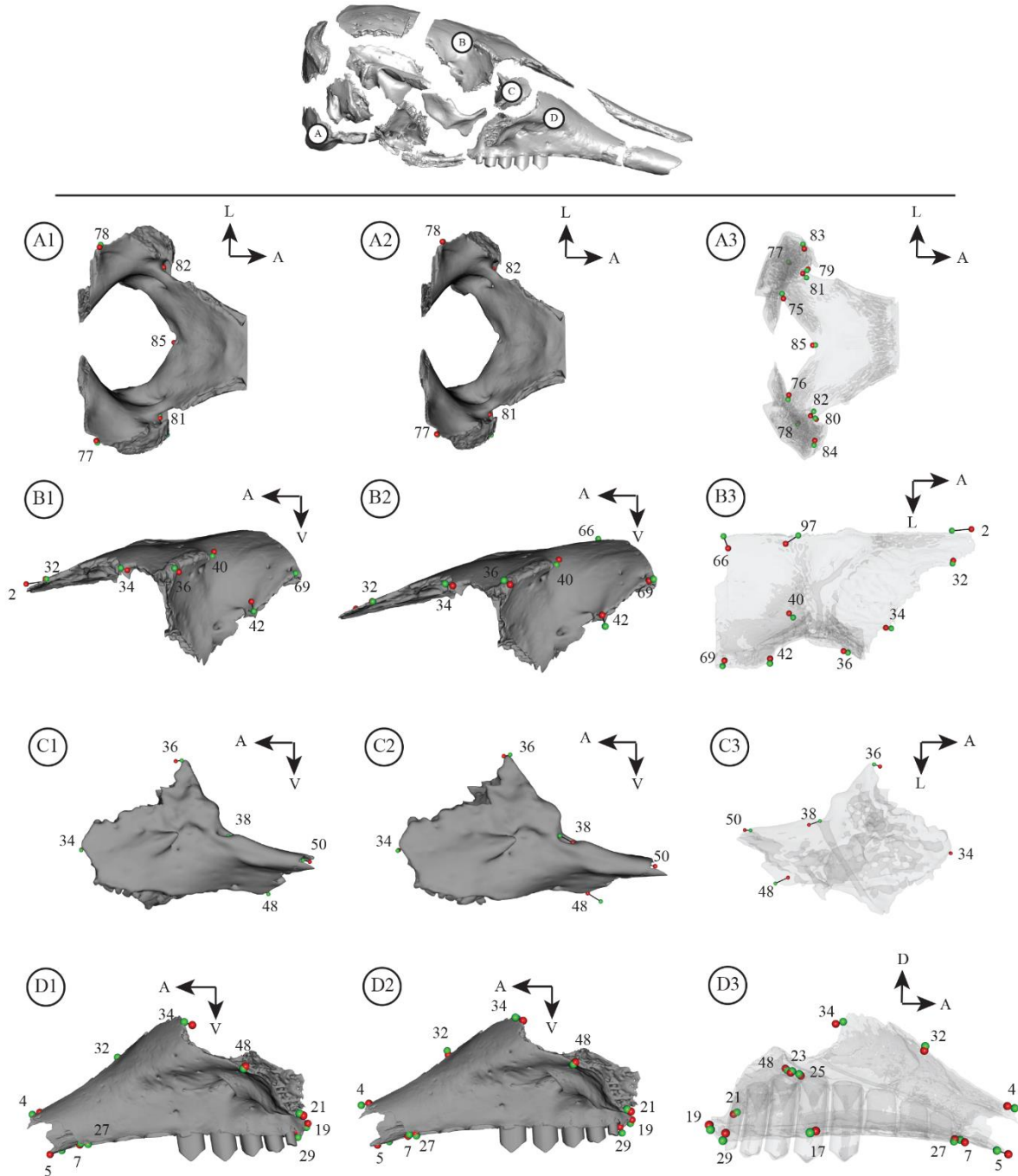


Figure 36. Vector representation of the allometric shape changes detected for a given cranial unit (OBU) in *Zaedyus*, represented between its minimal (green – smaller centroid size) and maximal (red – larger centroid size) shape (see [Figure 29](#)). Results of the analysis performed at the static level, and with the log skull centroid size taken as the size variable (see text). For each OBU, the changes are shown in three subsections organized horizontally: 1, vectors from minimal to maximal shape with minimal OBU shape; 2, same as 1) with maximal OBU shape; 3, minimal OBU shape in transparency with vectors. A) basioccipital-exoccipital complex; A1-A2, dorsal view; A3, ventral view. B) frontal; B1-B2, lateral view; B3, ventral view. C) lacrimal; C1-C2, lateral view; C3, medial view. D) maxillary; D1-D2, lateral view; D3, medial view. Landmark numbers and orientation arrows were added for more readability as well as the overall representation of the unpaired bone (basioccipital). Abbreviations: A, anterior; D, dorsal; L, lateral; V, ventral.

Parietal

In *Zaedyus pichiy* (Figure 38), the parietal is more elongated anteroposteriorly and narrower mediolaterally (especially in its anterior part) as size increases through ontogeny (#66; #67; #69; #71). The tentorial process varies little except for a slightly more posterior position of its ventralmost point (#63) as size increases. At the static level, the allometric variation of this OBU is not statistically supported but the *p-value* is close to the significance threshold (Table 7). Only *Cabassous*N exhibits statistically supported allometric variation over the course of ontogeny for this OBU (Tables 8 & S20). The pattern obtained (Figure S28) is similar to that of *Zaedyus pichiy* except that the length of the lateral part of the bone in contact with the squamosal reduces as size increases (#69; #71), and the tentorial process forms a more ventrally directed crest (#63). It should be noted that in *Dasypus novemcinctus* and *Cabassous* spp. the tentorial process is completely formed by the parietal, whereas in *Zaedyus pichiy*, its anterior half is formed by the parietal and its posterior half is formed by the supraoccipital.

Petrosal

In *Zaedyus pichiy*, the allometric variations of the petrosal are approximately the same between the static and ontogenetic levels (Figures 37 & 38). When size increases, the mastoid process (#90) lengthens ventrally, the depression marking the fossa subarcuata (#110) is shallower, the most dorsal point of the petrosal, located at the transverse level of the crista tentoria transversally (#102), assumes a more anteroventral position, whereas the most ventral point of external aperture of the cochlear canaliculus (#92) is positioned further dorsal. In contrast, the most anteroventral point of the external aperture of the cochlear fossula (#96) shows almost no variation. The most medial point of promontorium of the petrosal in ventral view (#88) extends farther anteriorly, and the most anterior point of epitympanic wing of the petrosal (#108) takes a relatively more dorsal position in larger specimens. In addition, the most anteromedial point of the foramen acusticum superius (#104) and the most anteromedial point of the foramen acusticum inferius (#106) are very slightly closer to one another in larger specimens.

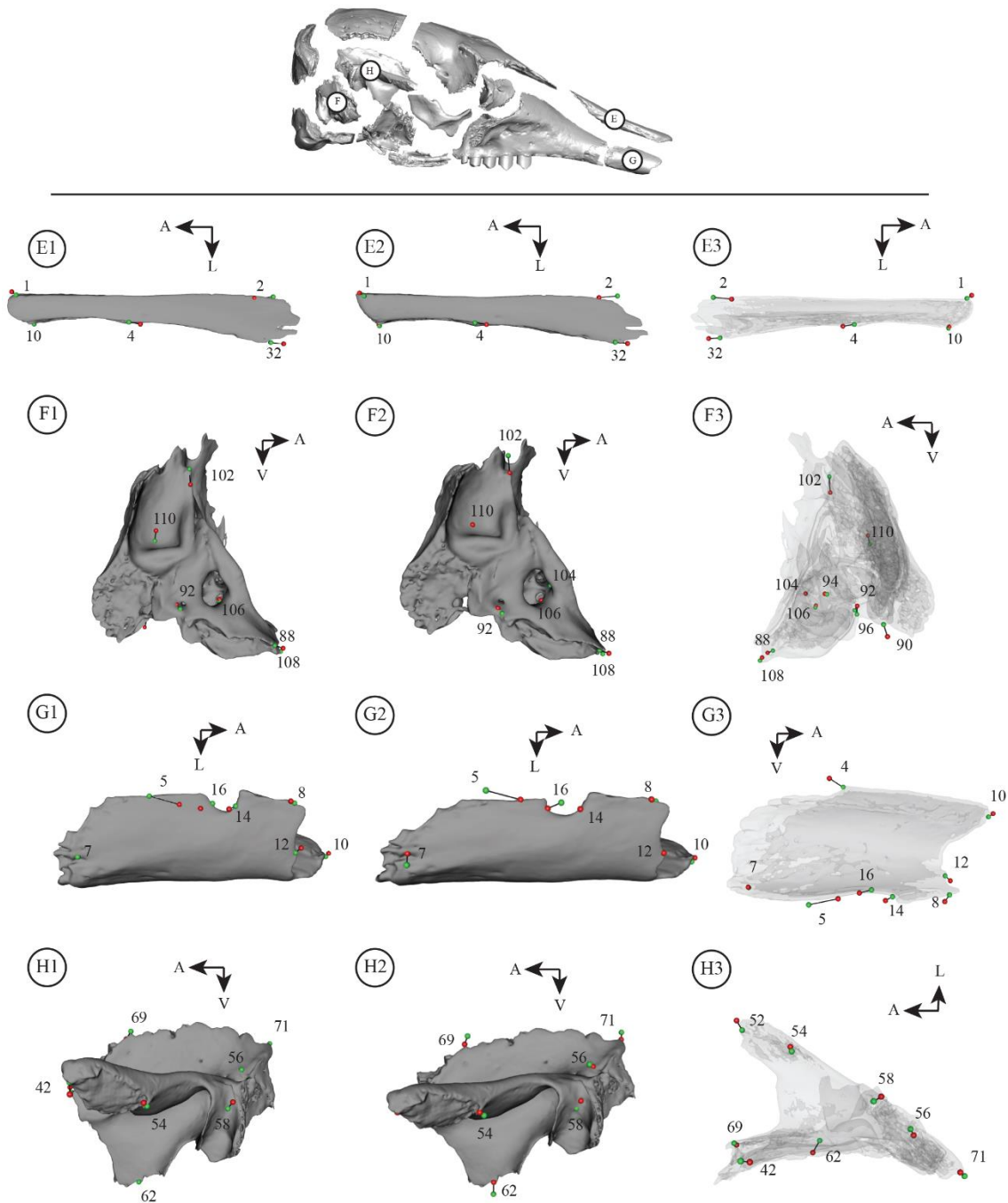


Figure 37. (continued from [Figure 36](#)). Vector representation of the allometric shape changes detected for a given cranial unit (OBU) in *Zaedyus*, represented between its minimal (green – smaller centroid size) and maximal (red – larger centroid size) shape (see [Figure 29](#)). Results of the analysis performed at the static level, and with the log centroid size taken as the size variable (see text). For each OBU, the changes are shown in three subsections organized horizontally: 1, vectors from minimal to maximal shape with minimal OBU shape; 2, same as 1) with maximal OBU shape; 3, minimal OBU shape in transparency with vectors. E) nasal; E1-E2, dorsal view; E3, ventral view. F) petrosal; F1-F2, medial view; F3, lateral view. G) premaxillary; G1-G2, ventral view; G3, medial view. H) squamosal; H1-H2, lateral view; H3, ventral view. Landmark numbers and orientation arrows were added for more readability. Abbreviations: A, anterior; L, lateral; V, ventral.

In *Cabassous*, the allometric variations are the same among the two datasets and the ontogenetic and static levels of analysis (Figures 34, 35, S28 & S29). The results only partly resemble those of *Zaedyus pichiy*. When size increases, in comparison with *Zaedyus*, the ventral elongation of the mastoid process (#90) is less strong, although the depression marking the fossa subarcuata (#110) is also shallower. The most dorsal point of the petrosal on the transverse level of the crista tentoria (#102) takes a relatively more ventral position, while the most ventral point of external aperture of cochlear canaliculus (#92) and the most anteroventral point of the external aperture of cochlear fossula (#96) is situated more dorsally. In addition, the most anteromedial point of the foramen acusticum superius (#104), the most anteromedial point of the foramen acusticum inferius (#106) and the most anterior point of the fenestra vestibuli (#94) are more posterodorsal in larger specimens. Finally, the most medial point of the promontorium of the petrosal in ventral view (#88) extends much farther anteriorly and the most anterior point of the epitympanic wing of petrosal (#108) is relatively more ventral, as size increases.

Premaxillary

In *Zaedyus pichiy* (Figure 38), the greatest ontogenetic allometric variation is concentrated on the palatal contact between the premaxillary and maxillary (#5), which extends farther anteriorly, and the triple premaxillary - maxillary - nasal contact, which extends farther posteriorly (#4) in larger specimens. As size increases, the anterior edge of the premaxillary on the midline (#8) also occupies a more ventral position, the most anterior point of the premaxillary anterior process (#12) extends farther anteroventrally and the most anterior part of the suture between the nasal and premaxillary (#10) is situated further anterior. The most posterior point of the premaxillary – maxillary suture on the palate (#7) assumes a more medial position showing a relative reduction in the posterior width of the premaxillary in larger specimens. Finally, the posterior point of the incisive foramen in ventral view (#16) exhibits a more posterolateral position, whereas the most anterior point of the incisive foramen in strict ventral view (#14) hardly varies. This variation in the posterior edge of the incisive foramen results in their relative enlargement in larger specimens. At the static level, when size increases, similar allometric variations are observed, except for the enlargement of the incisive foramen (#14; #16) (Figure 37). Allometric variation for this OBU is not significantly supported for the *Cabassous* datasets (Tables 8 & S20).

CHAPTER 3: Cranial allometry in Cingulata

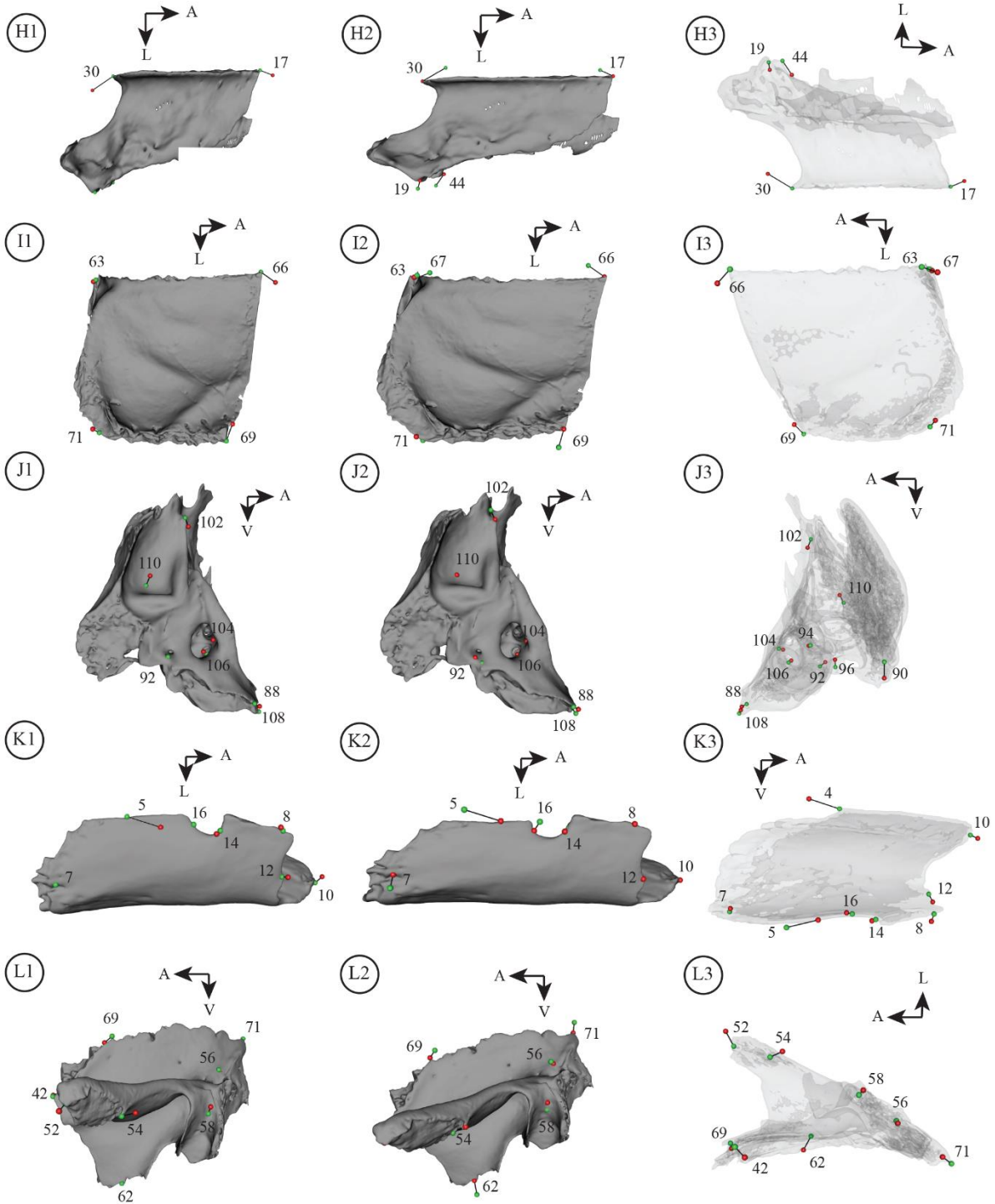
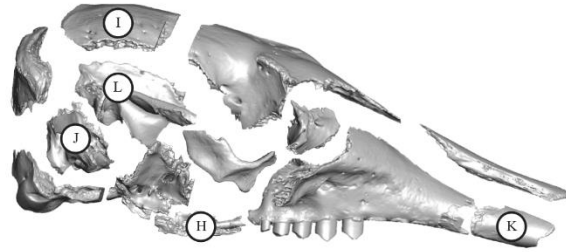


Figure 38. (continued from [Figure 33](#)). Vector representation of the allometric shape changes detected for a given cranial unit (OBU) in *Zaedyus*, represented between its minimal (green – smaller centroid size) and maximal (red – larger centroid size) shape (see [Figure 29](#)). Results of the analysis performed at the ontogenetic level, and with the log skull centroid size taken as the size variable (see text). For each OBU, the changes are shown in three subsections organized horizontally: 1, vectors from minimal to maximal shape with minimal OBU shape; 2, same as 1) with maximal OBU shape; 3, minimal OBU shape in transparency with vectors. H) palatine; H1-H2, ventral view; H3, dorsal view. I) parietal; I1-I2, ventral view; I3, dorsal view. J) petrosal; J1-J2, medial view; J3, lateral view. K) premaxillary; K1-K2, ventral view; K3, medial view. L) squamosal; L1-L2, lateral view; L3, ventral view. Landmark numbers and orientation arrows were added for more readability. Abbreviations: A, anterior; L, lateral; V, ventral.

Squamosal

In *Zaedyus pichiy* ([Figure 38](#)), the most dorsal contact between the jugal and squamosal extends farther anterolaterally (#52) whereas the ventral contact between the two bones extends farther posterolaterally (#54) when size increases through ontogeny (as observed on the jugal bone; see above). The most posterodorsal point of the zygomatic ridge of the squamosal (#56) takes a slightly more posteroventromedial position as size increases, whereas the most dorsal point of the external acoustic meatus on squamosal (#58) is situated more dorsolaterally. In addition, the triple contact point between the parietal – squamosal – supraoccipital (#71) is located further anteroventral whereas the contact with the alisphenoid and frontal (#42) and the contact with the parietal and frontal (#69) assume a more medial position, reflecting the ontogenetic reduction in size of the neurocranium. In ventral view, the most posterior point of the alisphenoid/squamosal suture in front of pyriform fenestra (#62) is also relatively more medial in larger specimens. Overall, larger specimens thus show a greater distance separating landmarks on the zygomatic arch (#52, #54) from the landmarks on the lateral wall of the braincase (#42, #62, #69), in the anterior half of the bone. This suggests more laterally protruding zygomatic arches in larger specimens, as detected in the ES analyses (see above). At the static level, the allometric variations are nearly identical but with much lower norms for the vectors ([Figure 37](#)).

For the *Cabassous* datasets ([Figures 34 & S28](#)), the ontogenetic allometric variations are slightly less marked than for *Zaedyus pichiy*. The main differences with the latter concern the relatively more posteromedial position of the ventral contact between squamosal and jugal (#54), the more posteromedial position of the triple frontal-parietal-squamosal contact (#69) and a slightly more posterior position of the most posterior point on the alisphenoid/squamosal suture in front of the pyriform fenestra (#62) in larger specimens. There is also no ontogenetic increase in the distance separating landmarks on the zygomatic arch (#52, #54) from the landmarks on the lateral wall of the braincase (#42, #62, #69), in the anterior half of the bone, in contrast to the

pattern in *Zaedyus*. Allometric variation for this OBU is not significantly supported for the *Cabassous* datasets at the static level, but the *p-value* is close to the significance threshold for the *CabassousN* dataset (Tables 8 & S20).

3.2.3.2 Allometric variations in the interspecific datasets

3.2.3.2.1 Allometric variations on the entire skull (ES) at the evolutionary level

The phylogenetic regression of shape on log centroid size in our DatasetExt accounts for 20.66% of the total shape variation (*p-value* = 0.0008, Figure 39; Table 9). Dasypodines follow an allometric trend quite dissimilar from the other clades, showing a greater variation in shape with increasing size (Figure 39). From the smallest to the largest of the extant armadillo species, three trends are very strongly marked, as evidenced by high vector norms. The snout displays a strong anterior elongation with size increase, as indicated by many landmarks of the snout, including the dental row, that assume a more anterior position (#1; #3-16; #18-19; #26-29). In contrast, the intersection between the maxillopalatine suture and the midline (#17) varies only slightly. The lengthening of the snout is also accompanied by a relative reduction in its height particularly well marked by the contact between the interfrontal and the internasal sutures on the midline and the triple contact point between nasal - maxillary - frontal that assumes a more ventral position (#2; #31-32). The face also exhibits a mediolateral narrowing of the snout in its posterior part (#24-27; #31-34). The lateral parts of the orbit that connect with the anterior end of the zygomatic arches occupy a much more posterior position (#20-21; #37-38; #47-50) which constitutes a second indication of facial lengthening. This posterior displacement of the anterior zygomatic arches reduces the relative length of the zygoma. The postorbital constriction is also located in a much more posterior position in larger specimens, and also slightly narrower transversely (#39-40). The landmarks on the roof and lateral wall of the braincase almost all shift convergently towards the center of the braincase which indicates its relative reduction as size increases. The posterior part of the cranial vault (defined in this study as the part of the cranial roof protecting the brain) does not strictly follow this trend. The midline contact between the supraoccipital and the parietal (#67) assumes a more posteroventral position, as does the supraoccipital - parietal - squamosal triple

contact (#70-71), indicating a decrease in depth of the posterior part of the vault in relation to the rest of the braincase as size increases.

Contrary to the general trend of an allometric reduction in the size of the braincase, the processes of the nuchal crests (#73-74) extend further posteromedioventrally as size increases, and thus protrude further posteriorly. Finally, the most medial point of the promontorium of the petrosal (#87-88) is shifted more lateral in larger specimens contrasting with the general shrinking of the surrounding braincase elements. This variation indicates that the promontorium of the petrosal becomes more distant from the midline of basicranium in larger specimens. The distribution of specimens with respect to the regression line shows a clear distinction between the dasypodids located above the line and the chlamyphorids located below the regression line (Figure 39).

CHAPTER 3: Cranial allometry in Cingulata

Table 9. Results of the phylogenetic regression for ES and 3B with log skull centroid size at the evolutionary level in DatasetExt. Index: a, slope coefficient; b, intercept; Df, degrees of freedom; F, Fisher-test; MS, mean square; N, sample size; P, p-value, significance following the permutation test; R², allometric proportion of shape variation; SS, sum of squares; Z, Z-test. The shaded lines correspond to the tests with a non-significant *p-value* (> 0.05).

	DatasetExt																			
	With phylogenetic correction									Without phylogenetic correction										
	N	Df	SS	MS	R2	F	Z	P	a	b	N	Df	SS	MS	R2	F	Z	P	a	b
Entire Skull	21	20	0.012966	0.0129665	0.20666	4.9493	3.4998	0.0008	0.0125	-0.1565	21	20	0.06719	0.067193	0.18719	4.3758	2.3742	0.0103	0.178	-2.23
Premaxillary	21	20	0.013417	0.013417	0.05754	1.1601	0.52361	0.3174	0.004975	-0.062309	21	20	0.03762	0.037618	0.03958	0.7831	-0.061462	0.534	0.1332	-1.6684
Maxillary	21	20	0.013333	0.013333	0.09742	2.0508	1.6793	0.0473	0.01592	-0.19942	21	20	0.11655	0.116552	0.11817	2.5462	1.5222	0.0799	0.2345	-2.9367
Nasal	21	20	0.001726	0.0017261	0.02733	0.5339	-0.52278	0.7121	0.001522	-0.019059	21	20	0.03568	0.03568	0.09503	1.9952	1.1491	0.1286	0.1297	-1.6248
Frontal	21	20	0.020507	0.0205066	0.19747	4.6751	3.0704	0.0015	0.01118	-0.14002	21	20	0.03434	0.034344	0.06611	1.345	0.74271	0.2274	0.1273	-1.5941
Lacrimal	21	20	0.0134	0.013399	0.02891	0.5657	-0.38893	0.6506	0.01035	-0.12958	21	20	0.09487	0.094868	0.08821	1.8381	1.2101	0.099	0.2116	-2.6494
Jugal	21	20	0.012809	0.012809	0.04824	0.963	0.26292	0.4016	-0.004458	0.055831	21	20	0.04307	0.04307	0.05601	1.1273	0.47204	0.3314	0.1425	-1.7852
Palatine	21	20	0.039987	0.039987	0.15348	3.4449	1.684	0.0336	0.07202	-0.90192	21	20	0.41403	0.41403	0.18033	4.1801	1.7066	0.0346	0.442	-5.535
Parietal	21	20	0.009333	0.0093328	0.08075	1.6691	1.0305	0.143	0.008161	-0.10221	21	20	0.04211	0.042113	0.08227	1.7032	1.0291	0.1552	0.141	-1.765
Squamosal	21	20	0.019611	0.0196112	0.0967	2.0341	1.7482	0.0343	0.01313	-0.16444	21	20	0.07234	0.072343	0.077	1.585	1.0241	0.1572	0.1847	-2.3136
As-Os-Pt-BS	21	20	0.03549	0.03549	0.09459	1.985	1.3125	0.097	0.04096	-0.51294	21	20	0.21793	0.217931	0.20222	4.8162	2.7289	0.0003	0.3206	-4.0156
Supraoccipital	21	20	0.028419	0.0284194	0.16076	3.6395	2.6716	0.0005	0.0143	-0.1791	21	20	0.05192	0.05192	0.07333	1.5035	0.92309	0.1785	0.1565	-1.96
Bo-Eo	21	20	0.011857	0.011857	0.13824	3.0479	2.2474	0.004	0.01094	-0.13696	21	20	0.035615	0.035615	0.17068	3.9104	2.7612	0.0003	0.1296	-1.6234
Petrosal	21	20	0.021752	0.0217523	0.11375	2.4387	2.1206	0.0127	0.02388	-0.29912	21	20	0.13427	0.13427	0.14995	3.3518	2.1794	0.0119	0.2517	-3.152

Table 10. Results of the phylogenetic regression for ES and 3B with log skull centroid size at the evolutionary level in Dataset-Lmax. Index: a, slope coefficient; b, intercept; Df, degrees of freedom; F, Fisher-test; MS, mean square; N, sample size; P, p-value, significance following the permutation test; R², allometric proportion of shape variation; SS, sum of squares; Z, Z-test. The shaded lines correspond to the tests with a non-significant *p-value* (> 0.05).

	Dataset-Lmax																			
	With phylogenetic correction									Without phylogenetic correction										
	N	Df	SS	MS	R2	F	Z	P	a	b	N	Df	SS	MS	R2	F	Z	P	a	b
Entire Skull	26	25	0.013565	0.0135651	0.16081	4.599	3.5601	0.0007	0.003741	-0.046893	26	25	0.12504	0.125037	0.16775	4.8375	2.7696	0.0029	0.1485	-1.8619
Premaxillary	-	-	-	-	-	-	-	-	-	-	-	-	-	-	-	-	-	-	-	-
Maxillary	26	25	0.01133	0.01133	0.06318	1.61186	1.1995	0.1159	0.02032	-0.25475	26	25	0.23169	0.231691	0.10632	2.8553	1.7249	0.0496	0.2022	-2.5345
Nasal	-	-	-	-	-	-	-	-	-	-	-	-	-	-	-	-	-	-	-	-
Frontal	26	25	0.013605	0.0136046	0.13871	3.8652	2.9501	0.0008	0.006618	-0.082961	26	25	0.15953	0.159526	0.17195	4.9839	2.6064	0.0044	0.1678	-2.1031
Lacrimal	26	25	0.00985	0.0098514	0.0199	0.4872	-0.61769	0.7359	0.01483	-0.18589	26	25	0.15317	0.153172	0.08529	2.2379	1.4821	0.0558	0.1644	-2.0608
Jugal	-	-	-	-	-	-	-	-	-	-	-	-	-	-	-	-	-	-	-	-
Palatine	-	-	-	-	-	-	-	-	-	-	-	-	-	-	-	-	-	-	-	-
Parietal	26	25	0.007451	0.0074505	0.05899	1.5046	0.86486	0.1963	0.003891	-0.048775	26	25	0.13618	0.13618	0.17817	5.2032	2.5905	0.0014	0.155	-1.943
Squamosal	26	25	0.016618	0.0166181	0.08328	2.1802	1.5405	0.0608	0.008719	-0.109299	26	25	0.14339	0.143385	0.11745	3.194	2.1636	0.0086	0.1591	-1.9939
As-Os-Pt-BS	26	25	0.04484	0.044843	0.10648	2.8601	1.9127	0.0286	-0.005635	0.070633	26	25	0.44255	0.44255	0.2318	7.242	3.5235	0.0001	0.2794	-3.5029
Supraoccipital	26	25	0.024315	0.0243149	0.12654	3.4769	2.6366	0.001	-0.003859	0.048381	26	25	0.10876	0.108758	0.09859	2.625	1.8596	0.028	0.1385	-1.7365
Bo-Eo	26	25	0.018716	0.018716	0.19429	5.7873	3.0249	0.0001	0.00474	-0.05942	26	25	0.156	0.155999	0.34637	12.718	3.751	0.0001	0.1659	-2.0797
Petrosal	26	25	0.03121	0.0312096	0.14332	4.0151	3.1577	0.0002	0.002614	-0.032767	26	25	0.35848	0.35848	0.26251	8.5427	3.6983	0.0001	0.2515	-3.1526

The phylogenetic regression of shape on log centroid size in our Dataset-Lmax accounts for 16.81% of the total shape variation (p -value = 0.0007, [Figure 40](#); [Table 10](#)). Clearly, *Peltephilus* appears as an outlier in this analysis. Several patterns of allometric variation are consistent with that of the DatasetExt. As size increases, the snout shows a strong relative lengthening, but also a relative increase rather than a decrease in height (#2; #3-4; #6-7; #9-12; #17; #18-19; #26-29; #31-32). The relative lengthening of the snout is also evidenced by the strong posterior extension of the midline apex of the postpalatal notch and of the maxillary foramen (#22-23; #30), although the position of the infraorbital foramen hardly varies (#24-25). The anterior edge of the orbit and zygomatic arch also exhibits a much more posterior position in larger specimens, in addition to being slightly more laterally situated (#20-21; #35-38; #47-50). The postorbital constriction (#39-40) is shifted in the same direction as most of the other points in the orbitotemporal region, narrowing by converging towards the center of the braincase, which shows a relative reduction in its proportions. The cranial vault is much lower in larger species with a more posteroventral position of the intersections between the frontoparietal and the parietal/supraoccipital sutures and the midline (#66-67) in larger specimens. The two internal points defined by the dorsal intersection of annular ridge and midline (#97), and the dorsal intersection between the cribriform plate and the median septum posterior to the latter (#98) are strongly shifted posteroventrally, becoming located almost at the same level as the most posterodorsal point of the foramen magnum (#86). It thus indicates increase in depth of the large space between these points (#97-98) and the dorsal edge of the frontal (#31, #66). However, neither *Zaedyus pichiy* nor *Cabassous unicinctus* have frontal sinuses ([Billet et al., 2017](#)). Compared to the DatasetExt, the posterior processes of the nuchal crest (#73-74) extend even further posteromedioventrally and become even more prominent.

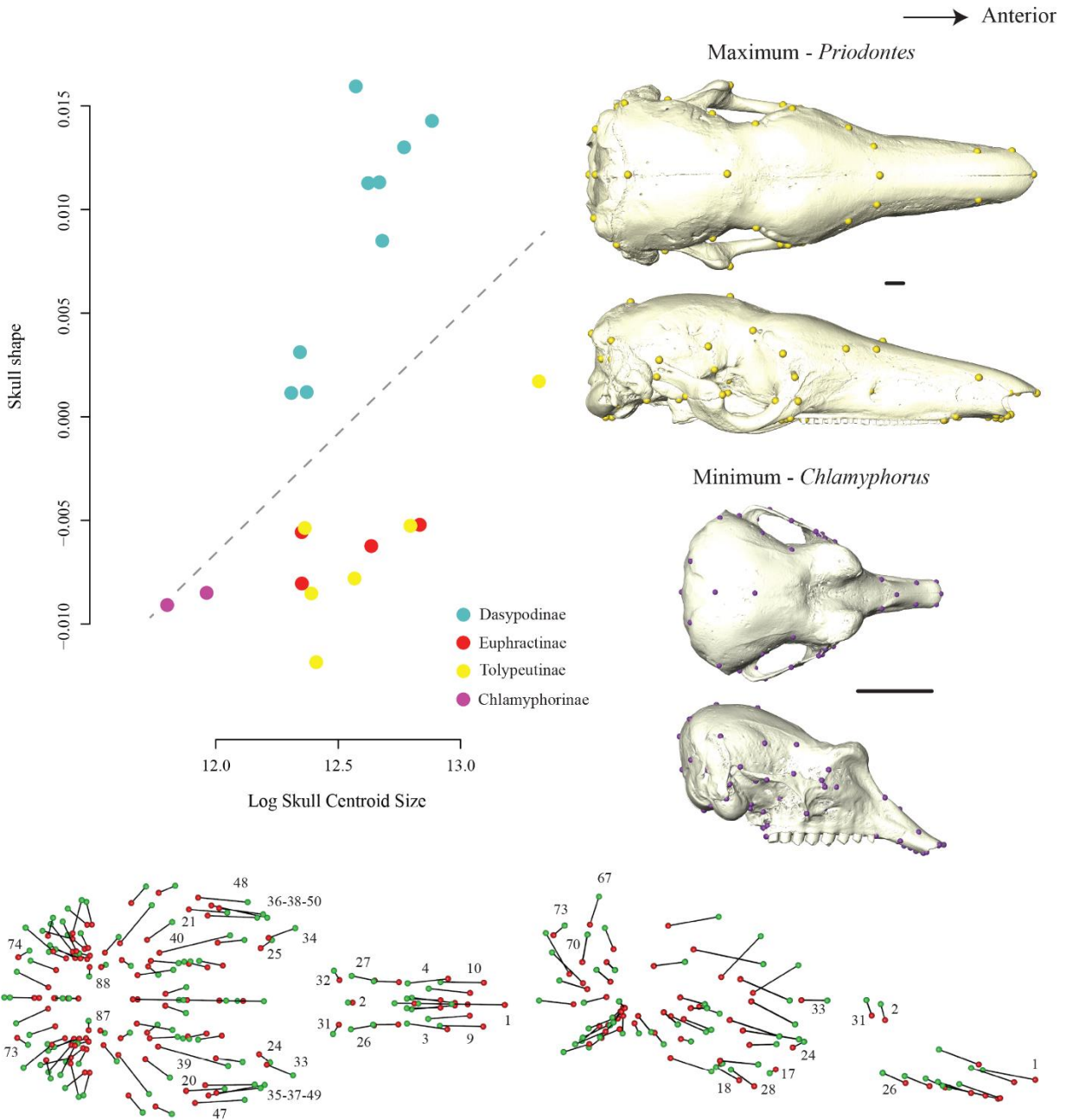


Figure 39. Evolutionary allometry on the entire skull (ES) of DatasetExt. Clades are represented with different colors. For graphical display, we used the projected regression scores of the shape data to represent shape variation related to changes in log centroid size (Adams *et al.*, 2013). Shape changes were visualized as vectors from the minimal shape (green) to the maximal shape (red) of the shape regression scores corresponding to the projection of the data points in shape space on to an axis in the direction of the regression vector (see Drake & Klingenberg, 2008). Phylogenetic regression of skull shape on log skull centroid size of DatasetExt, represented 20.66% of the total shape variation.

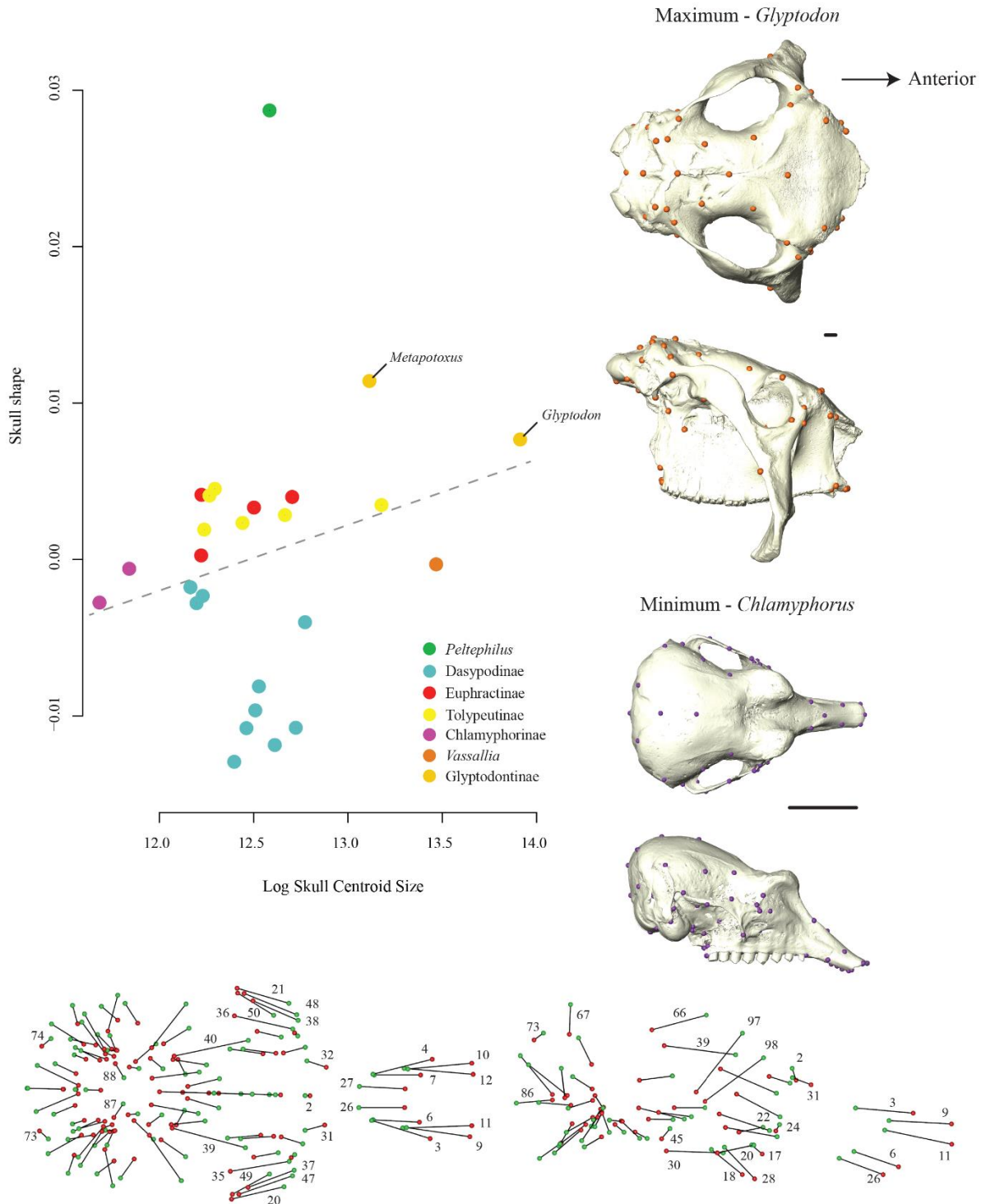


Figure 40. Evolutionary allometry on the entire skull (ES) of Dataset-Lmax. Clades and fossils taxa are represented with different colors. For graphical display, we used the projected regression scores of the shape data to represent shape variation related to changes in log centroid size (Adams *et al.*, 2013). Shape changes were visualized as vectors from the minimal shape (green) to the maximal shape (red) of the shape regression scores corresponding to the projection of the data points in shape space on to an axis in the direction of the regression vector (see Drake & Klingenberg, 2008). Phylogenetic regression of skull shape on log skull centroid size of Dataset-Lmax, represented 16.81% of the total shape variation.

The most medial point of the promontorium of petrosal (#87-88) is situated further lateral but also further posteriorly and thus becomes more distant from the basicranium midline in larger specimens in Dataset-Lmax. Together with other landmarks on the petrosal, this also indicates a relative reduction in the proportions of the promontorium of the petrosal. Finally, contrary to previous analyses, the sphenorbital fissure (#45-46) does not follow the general reduction in the size of the braincase, but rather shows a more posteroventral position in larger specimens.

The same dichotomy (dasypodids vs chlamyphorids) is obtained in DatasetExt and Dataset-Lmax regarding the position of species with respect to the regression line (Figure 40). As regards extinct taxa, *Peltephilus* is a clear outlier and seems to present a cranial shape very different from the other cingulates with regard to the size. Glyptodonts are located above the regression line, as the extant chlamyphorids. *Vassallia* is located below the regression line along with the dasypodids (Figure 40).

The same analysis on the Dataset-Tmax results in a slightly lower allometric proportion ($R^2 = 13.62\%$; $p\text{-value} = 0.0001$ – Figure S30, Table S21) and nearly the same allometric patterns (Figure S36). It provides no further information about allometric variation. However, the position of the specimens in relation to the regression line changes strongly with the addition of *Proeutatus*, and no longer provides a clear distinction between the dasypodids and chlamyphorids. The chlamyphorines are located under the regression line, along with *Glyptodon*, *Vassallia* and most of the dasypodines (Figure S30).

3.2.3.2.2 Allometric variations studied Bone By Bone (3B) at the evolutionary level

Comparison between OBUs

In the DatasetExt, we observe differences in the proportions of allometric shape variation among different OBUs (Figure 41A). The phylogenetic regression of shape on size shows no statistical support for the nasal, lacrimal, jugal, premaxillary, parietal and as-os-pt-bs OBUs (Figure 41A; Table 9), but does reveal a significant allometric effect for the other OBUs. The squamosal and maxillary have the lowest proportion of shape variation explained by size of all OBUs (almost 10%; Figure 41A; Table 9). The petrosal and bo-eo OBUs have a proportion of

shape variation explained by size ranging between 10% and 15% (Figure 41A; Table 9). The palatine and supraoccipital show a higher allometric proportion, ranging between 15% and 20% (Figure 41A; Table 9). The OBU showing the highest proportion of variation explained by size is the frontal, at 19.75% (Figure 41A; Table 9). Without the phylogenetic correction, the regression of the shape on the size shows significant allometric variations only for the palatine, as-os-pt-bs, bo-eo and petrosal OBUs. The allometric proportions are in all cases higher without than with the phylogenetic correction (Table 9).

In the Dataset-Lmax, the premaxillary, nasal, jugal and palatine OBUs could not be analyzed due to an insufficient number of landmarks. For the other OBUs, we also observe differences in the proportions of allometric shape variation (Figure 41B; Table 10). The phylogenetic regression of shape on size shows no statistical support for allometry in the lacrimal, parietal, maxillary and squamosal (Figure 41B; Table 10). In contrast, the as-os-pt-bs, supraoccipital, frontal and petrosal OBUs have a significant proportion of shape variation explained by size, ranging between 10% and 15% (Figure 41B; Table 10). The OBU showing the highest proportion of variation explained by size is the bo-eo OBU, at 18.72% (Figure 41B; Table 10). Without the phylogenetic correction, the regression of shape on size shows significant allometric variations for all OBUs except for the lacrimal, with allometric proportions always higher than with the phylogenetic correction, except for the as-os-pt-bs OBU (Table 10). In the Dataset-Tmax, the proportion of shape variation explained by size are very similar, although a little higher, to those presented here for the Dataset-Lmax (Figure S31, Table S21).

Allometric variation within OBUs

All descriptions of the allometric shape changes below describe the minimal shapes as compared to the maximal shapes per OBU (DatasetExt, Figure 42; Dataset-Lmax, Figures 43 & 44). This is discussed only in the OBUs whose allometric variation was statistically supported (p -value < 0.05) in the phylogenetic regressions. Only landmarks on the left side of the skull are mentioned. The results and shape changes explained by size for the Dataset-Tmax are not described below (except when different from the Dataset-Lmax) but are illustrated in Figures S32 & S33. To clarify, the taxa representing the minimum size for all datasets are chlamyphorines. The

CHAPTER 3: Cranial allometry in Cingulata

maximum size is represented by *Priodontes* for DatasetExt and by *Glyptodon* for Dataset-Lmax and Dataset-Tmax.

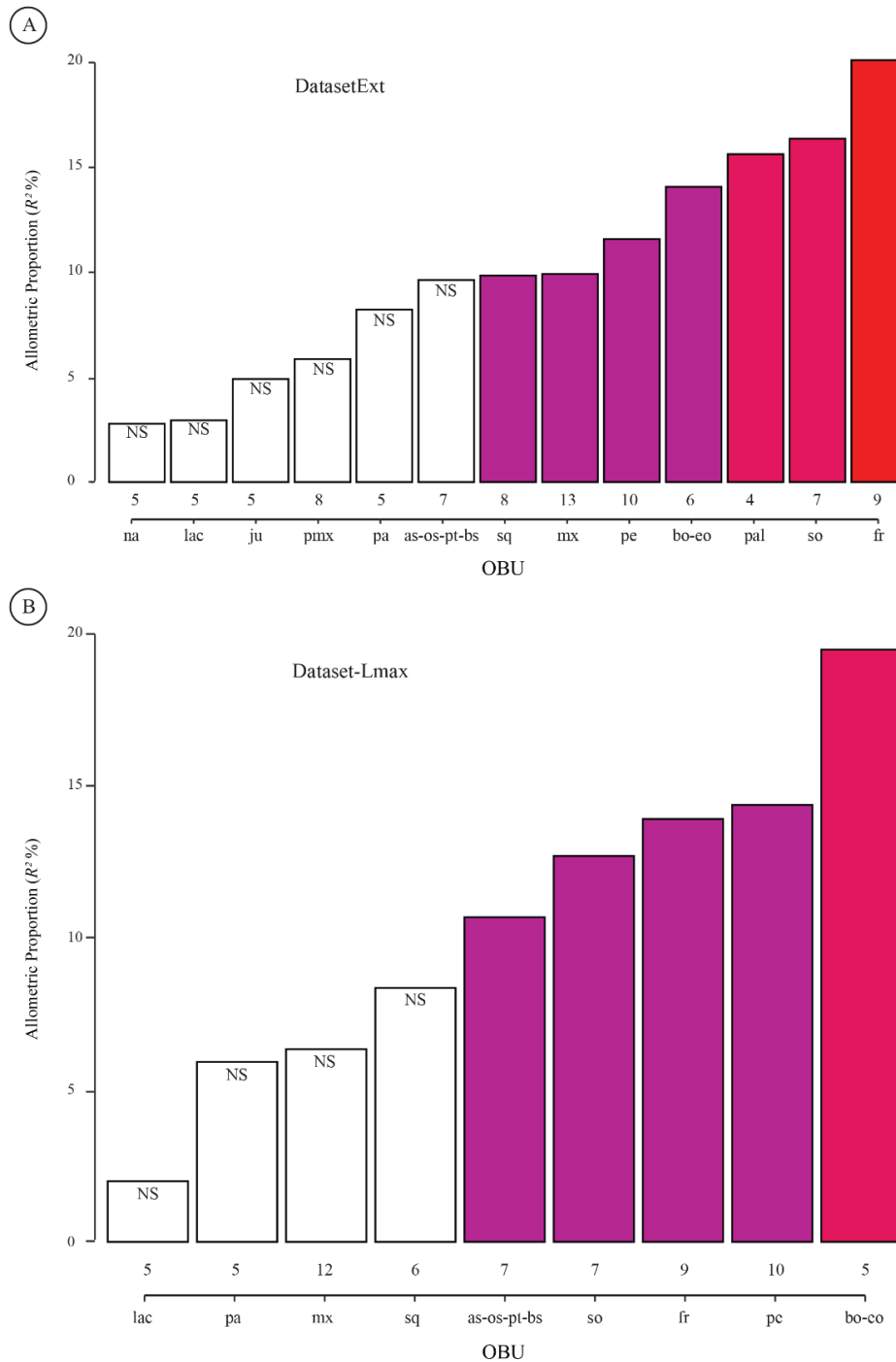


Figure 41. Bar graphs showing the allometric proportions (R^2) of each cranial unit's (OBU) total shape variation under the 3B approach (see text) for both evolutionary datasets. Allometric proportions are shown with the log skull centroid size taken as size variable. White bars indicate a statistically unsupported (NS) allometry for a given OBU (at p -value > 0.05). Abbreviations of OBUs: as-os-pt-bs, alisphenoid-orbitosphenoid-pterygoid-basisphenoid complex; bo-eo, basioccipital-exoccipital complex; fr, frontal; ju, jugal; lac, lacrimal; mx, maxillary; na, nasal; pa, parietal; pal, palatine; pe, petrosal; pmx, premaxillary; so, supraoccipital; sq, squamosal.

Alisphenoid-Orbitosphenoid-Pterygoid-Basisphenoid complex

In the DatasetExt, there is no statistically supported allometric variation for this OBU (Table 9).

In the Dataset-Lmax (Figures 43 & 44), as size increases, the most posterior point of the alisphenoid/squamosal suture in front of the pyriform fenestra (#62) and the most anteroventral point of the foramen ovale (#60) are shifted anteriorly, but also dorsally for the former and ventrally for the latter (Figures 43 & 44). Together with the variation of more anterior landmarks (#65, optic canal – Figures 43 & 44), this indicates an anteroposterior shortening of the ventral portion of the alisphenoid, which is accompanied by an increase in height of its posterolateral portion. The most anteroventral point of the sphenorbital fissure (#46) occupies a much more anteroventral position in larger specimens. The most dorsal point of the internal posterior aperture of the optic canal (#112) and the most ventromedial point on the annular ring lateral to posterior median septum (114) move away from each other, resulting in an anteroposterior elongation of the sphenoidal jugum (Wible & Spaulding, 2013). The triple contact point between squamosal - frontal - alisphenoid (#42) takes a slightly more posteromedial position as size increases. Finally, the most anterodorsal point of the optic foramen (#65) moves to a more posteroventrolateral position and a greater separation from the much posterodorsally shifted internal posterior aperture of the optic canal (#112). This indicates a relative lengthening and reorientation (more dorsoventral) of the optic canal in larger specimens. Overall, the combined variation of most landmarks shows a strong increase in height of the as-os-pt-bs OBU as size increases (#62; #112; #114 shift dorsally; #42; #46; #60 shift ventrally).

The Dataset-Tmax shows the same allometric variations (Figures S32 & S33).

CHAPTER 3: Cranial allometry in Cingulata

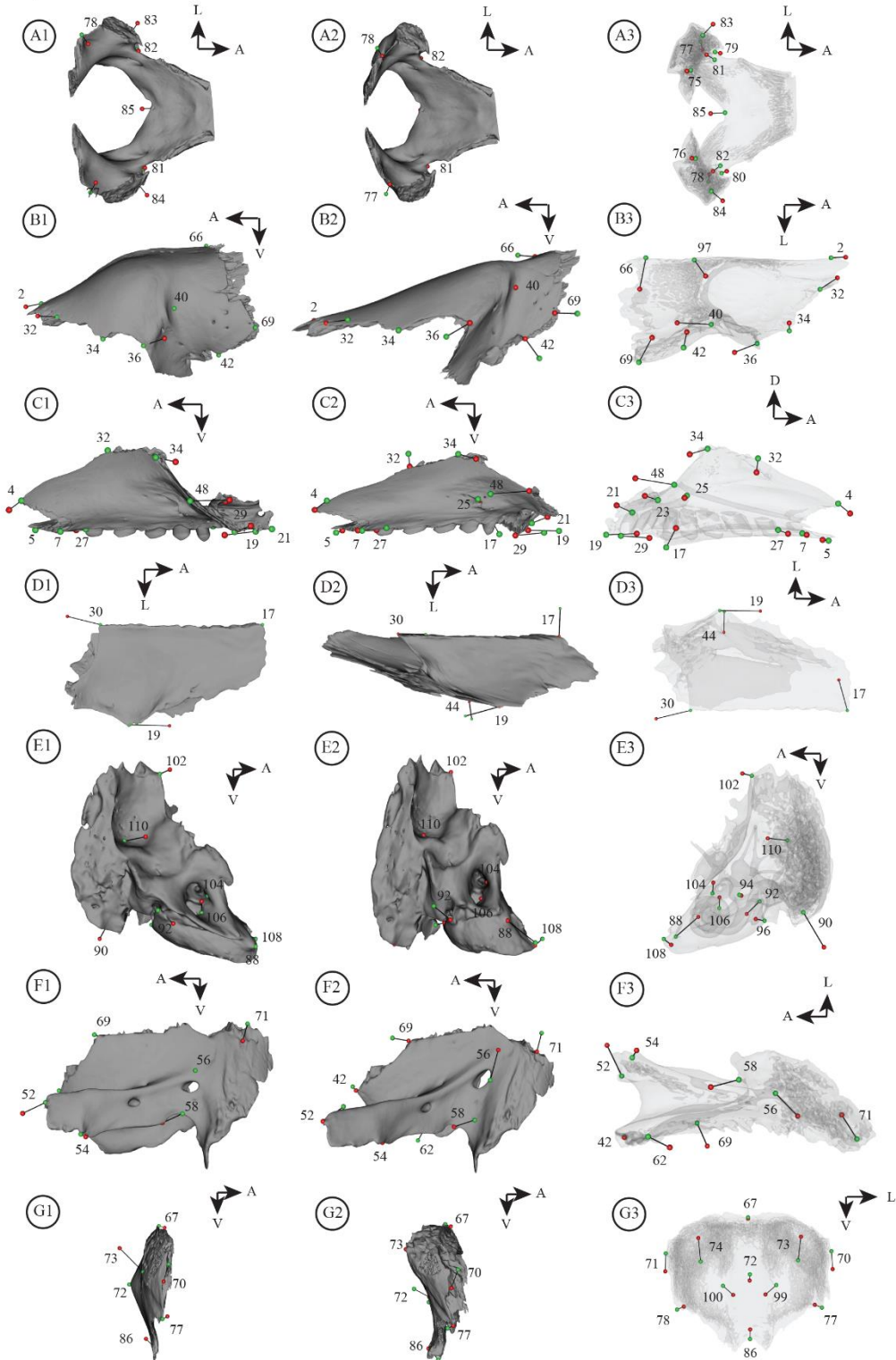
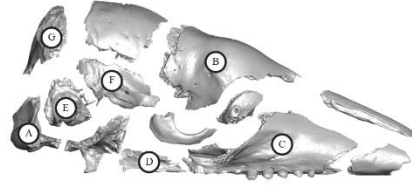


Figure 42. Vector representation of the allometric shape changes detected for a given cranial unit (OBU) in DatasetExt, represented between its minimal (green – smaller centroid size) and maximal (red – larger centroid size) shape (see Figure 29). Results of the analysis performed at the evolutionary level, and with the log skull centroid size taken as the size variable (see text). For each OBU, the changes are shown in three subsections organized horizontally: 1, vectors from minimal to maximal shape with minimal OBU shape; 2, same as 1) with maximal OBU shape; 3, minimal OBU shape in transparency with vectors. A) basioccipital-exoccipital complex; A1-A2, dorsal view; A3, ventral view. B) frontal; B1-B2, lateral view; B3, ventral view. C) maxillary; C1-C2, lateral view; C3, medial view. D) palatine; D1-D2, ventral view; D3, dorsal view. E) petrosal; E1-E2, medial view; E3, lateral view. F) squamosal; F1-F2, lateral view; F3, ventral view. G) supraoccipital; G1-G2, lateral view; G3, occipital view. Landmark numbers and orientation arrows were added for more readability as well as the overall representation of the unpaired bone (basioccipital, supraoccipital). For the facilitation of meshes deformation, we selected *Cabassous* rather than *Dasyus* or *Zaedyus* to represent allometric variation because this genus has a shape closer to the consensus shape across all cingulates in our analysis. Abbreviations: A, anterior; D, dorsal; L, lateral; V, ventral.

Basioccipital-Exoccipital complex

In the DatasetExt (Figure 42), as size increases, the intersection between the anteromedial edge of the occipital condyle and foramen magnum (#76) hardly varies in position while the most anteroventral point of the foramen magnum (#85) is shifted posteriorly. The combination of these two allometric variations suggests a relative reduction in the sagittal diameter of the foramen magnum as size increases. The most anterolateral point of the occipital condyle (#84) extends more anterolaterally, which indicates a relative broadening of the occipital condyle with increasing size. The most posterolateral point of the jugular foramen (#80) is slightly shifted anteromedially, whereas the most posterolateral point of the hypoglossal foramen (#82) is relatively more posterolateral in larger specimens. The combination of these two allometric variations suggests a relative widening of the portion of the exoccipital separating the two foramina. Finally, the triple contact point between the supraoccipital - exoccipital - petrosal (#78) has a slightly more anteromedial position as size increases.

In the Dataset-Lmax (Figures 43 & 44), some differences are observed with the previous dataset. From the smallest to the largest specimen, the intersection between the anteromedial edge of occipital condyle and foramen magnum (#76) assumes a more posteromedial and ventral position, which indicates a slight narrowing of the width of the foramen magnum. The triple contact point between the supraoccipital - exoccipital - petrosal (#78) is more medioventral, which indicates a relative reduction in the height of the exoccipital. The most anterolateral point of the occipital condyle (#84), hardly varies being only slightly more anterolateral in larger specimens. The most posterolateral point of the jugular foramen (#80) takes a more anterolateral and dorsal position while the most posterolateral point of the hypoglossal foramen (#82) is shifted posteromedially.

CHAPTER 3: Cranial allometry in Cingulata

The Dataset-Tmax shows the same allometric variations (Figures S32 & S33) as the Dataset-Lmax.

Frontal

In the DatasetExt (Figure 42), from the smallest to the largest specimen, the triple contact point between the frontal - squamosal - parietal (#69) and the triple contact point between squamosal - frontal - alisphenoid (#42) take a relatively more anteromedial position. This is also the case for the dorsal intersection of annular ridge and midline (#97), which also moves ventrally. The intersection between the frontal - parietal suture and the midline (#66) is more posteromedial in larger specimens. The combination of these allometric variations suggests a strong relative narrowing of the posterior half of the frontal. As size increases, the intersection between the internasal suture and the frontal bone (#2) is located more anteriorly and the triple contact point between frontal - maxillary - nasal (#32) has a more anteromedial position. The triple contact point between lacrimal - maxillary - frontal (#34) is shifted only slightly medially. The intersection between the lacrimal - frontal suture and the anterior orbital edge (#36) is located more posterolateral. The combination of these allometric variations (#2; #32; #36) suggests a relative lengthening of the anterior half of the frontal. Finally, the most dorsomedial point of the postorbital constriction (#40) is more posterior and slightly more medial in larger specimens. The combination of this change with that of landmark #36 suggests a slightly deeper postorbital constriction in larger specimens.

In the Dataset-Lmax (Figures 43 & 44), from the smallest to the largest specimen, most allometric variations are similar to those observed for the DatasetExt. The dorsal intersection of annular ridge and midline (#97) takes a more ventral position in larger specimens than in the DatasetExt.

The Dataset-Tmax shows the same allometric variations (Figures S32 & S33) as the two other datasets.

CHAPTER 3: Cranial allometry in Cingulata

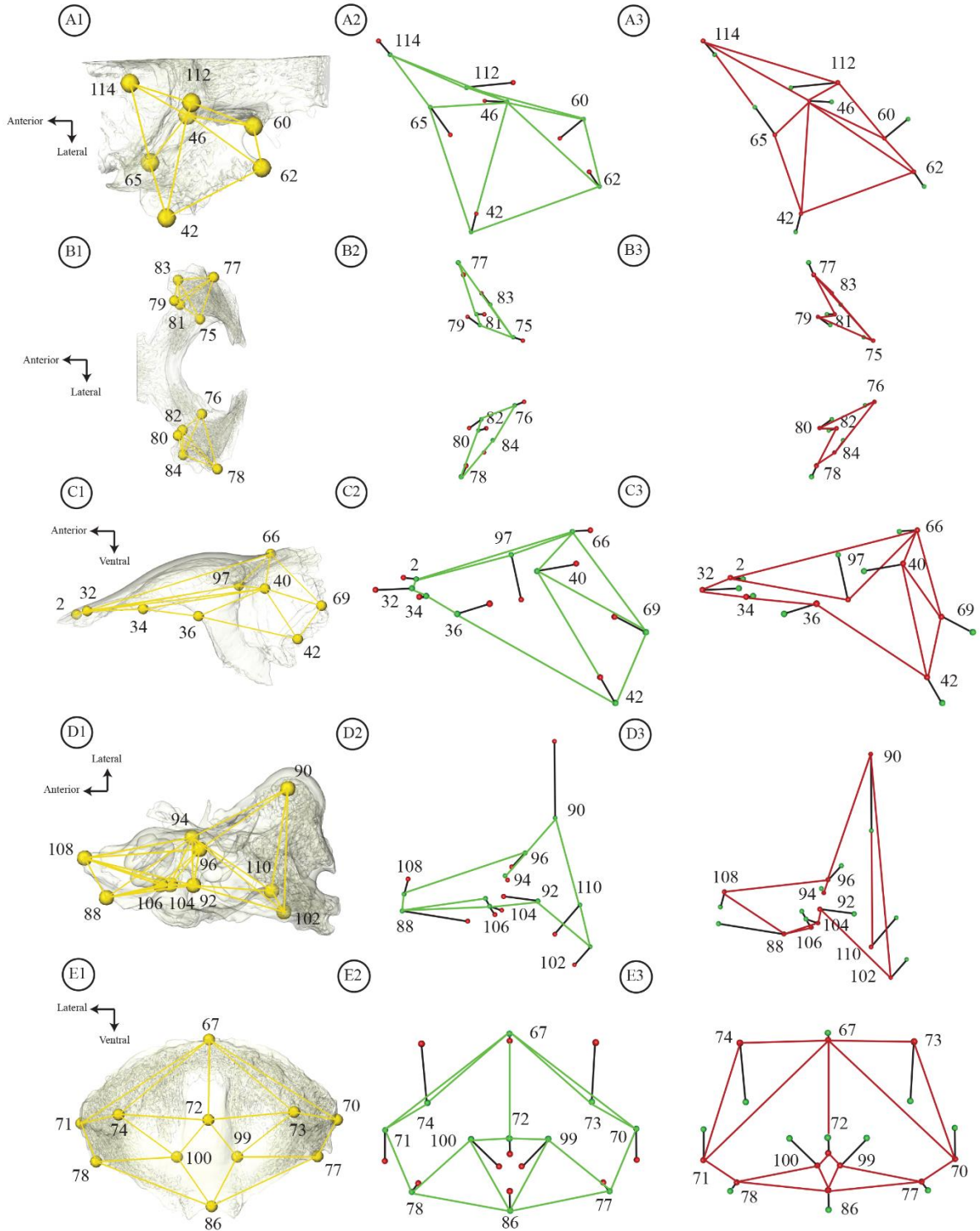
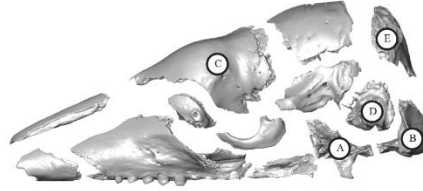


Figure 43. Vector representation of the allometric shape changes detected for a given cranial unit (OBU) in Dataset-Lmax, represented between its minimal (green – smaller centroid size) and maximal (red – larger centroid size) shape (see [Figure 29](#)). Results of the analysis performed at the evolutionary level, and with the log skull centroid size taken as the size variable (see text). Each OBU is defined in three subsections organized horizontally: 1, landmarks and wireframe on an OBU of *Cabassous* used as a reference as in [Figure 42](#); 2, vectors with a wireframe representing the minimal OBU shape; 3, vectors with a wireframe representing the maximal OBU shape. A1-A3, alisphenoid-orbitosphenoid-pterygoid-basisphenoid complex in dorsal view. B1-B3, basioccipital-exoccipital complex in dorsal view. C1-C3, frontal in lateral view. D1-D3, petrosal in ventral view. E1-E3, supraoccipital in occipital view. Landmark numbers and orientation arrows were added for more readability as well as to provide overall representations of the unpaired bones, *i.e.*, basioccipital, supraoccipital.

Maxillary

In the DatasetExt ([Figure 42](#)), from the smallest to the largest specimen, the triple contact point between premaxillary - maxillary - nasal (#4) assumes a more anteroventral position. The most anterior point of the alveolar margin of the dental row (#27) extends farther anteriorly as do the intersection between maxillary/palatal suture and lateral edge of palate (#19) and the most posterior point of the alveolar margin of the dental row (#29). In larger specimens, the intersection between jugal - maxillary suture and ventral edge of zygomatic arch (#21), the most dorsal point of the maxillary foramen (#23) and the triple contact point between maxillary - jugal - lacrimal (#48) are shifted posteriorly. This is also the case for the triple contact point between lacrimal - maxillary - frontal (#34), but with a slightly more ventral displacement. Overall, the combination of these allometric variations with the triple contact point between premaxillary - maxillary - nasal (#4) suggests a relative anteroposterior lengthening of the upper half of the maxillary. It also shows a relatively more posterior position of the area of the maxillary foramen and anterior root of the zygomatic (where it contacts the jugal bone), while the dental row reduces in relative length and is shifted forward. As size increased, the intersection between palatal - maxillary suture and the palate midline (#17) has a more anterodorsal position, which suggests that the maxillary contribution to the hard palate is reduced in its posteromedial part. The triple contact point between frontal - maxillary - nasal (#32) shows a more ventral position, which, when combined with the variation of landmarks #34 and #4, indicates a relative reduction of the maxillary height in larger specimens.

An allometric variation for this OBU is not significantly supported for the Dataset-Lmax and Dataset-Tmax ([Tables 10 & S21](#)).

CHAPTER 3: Cranial allometry in Cingulata

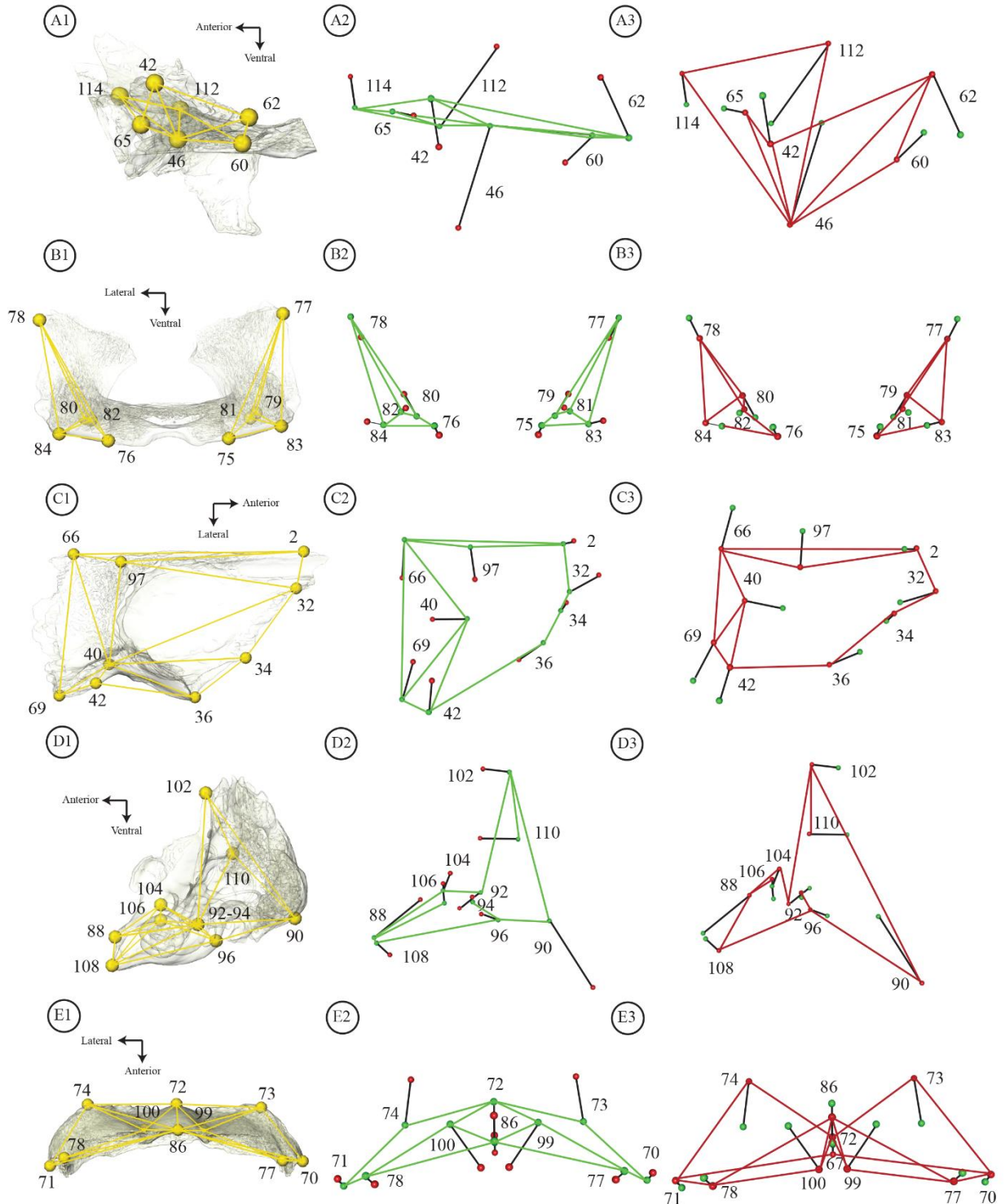
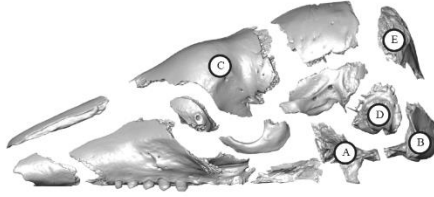


Figure 44. (continued from **Figure 43**). Vector representation of the allometric shape changes detected for a given cranial unit (OBU) in Dataset-Lmax, represented between its minimal (green – smaller centroid size) and maximal (red – larger centroid size) shape (see **Figure 29**). Results of the analysis performed at the evolutionary level, and with the log skull centroid size taken as the size variable (see text). Each OBU is defined in three subsections organized horizontally: 1, landmarks and wireframe on an OBU of *Cabassous* used as a reference as in **Figure 42**; 2, vectors with a wireframe representing the minimal OBU shape; 3, vectors with a wireframe representing the maximal OBU shape. A1-A3, alisphenoid-orbitosphenoid-pterygoid-basisphenoid complex in lateral view. B1-B3, basioccipital-exoccipital complex in occipital view. C1-C3, frontal in ventral view. D1-D3, petrosal in lateral view. E1-E3, supraoccipital in ventral view. Landmark numbers and orientation arrows were added for more readability as well as the overall representation of the unpaired bone (basioccipital, supraoccipital).

Palatine

In the DatasetExt (**Figure 42**), from the smallest to the largest specimen, the intersection between palatal - maxillary suture and the palate midline (#17) is shifted laterally while the most anteroventral point of caudal palatine foramen (#44) is more medial. This indicates a relative narrowing of the palatine in larger specimens. The intersection between maxillary - palatine suture and lateral edge of palate (#19) moves anteriorly, whereas the most posterior point of the palatine midline (#30) extends more posteriorly in larger specimens. This indicates a relative anteroposterior elongation of the palatine on the midline, and an anterior shift of the lateral part of its suture with the maxillary on the palate.

An allometric variation for this OBU is not significantly supported for the Dataset-Lmax and Dataset-Tmax (**Tables 10 & S21**).

Petrosal

In the DatasetExt (**Figure 42**), the most anteroventral point of the mastoid process (#90) shows the strongest allometric variation and extends much further posteroventrally in larger specimens. The most dorsal point of the petrosal on the transverse level of the crista tentoria (#102) is slightly shifted anterodorsally. The maximum point of curvature in the ventromedial area of the fossa subarcuata (#110) moves to a more anteromedial position, which creates a shallower fossa subarcuata. The most ventral point of the external aperture of the cochlear canaliculus (#92) is also located more anterior and dorsal in larger specimens. The position of the most anteroventral point of the external aperture of cochlear fossula (#96) converges towards the latter, taking a more anterior position. Therefore, this indicates that the external aperture of the cochlear fossula and the aperture of the cochlear canaliculus are relatively closer to one another in larger specimens. The most anteromedial point of the foramen acusticum superius (#104) and the most anteromedial point

of the foramen acusticum inferius (#106) are shifted dorsomedially, which indicates a relative thickening of the pars cochlearis of the petrosal. The most medial point of the promontorium in ventral view (#88) occupying a much more posterodorsal position, while the most anterior point of the petrosal's epitympanic wing (#108) is only slightly shifted posteroventrally and laterally.

The Dataset-Lmax (Figures 43 & 44) and the Dataset-Tmax show essentially the same allometric variations (Figure S32 & S33) as DatasetExt.

Squamosal

In the DatasetExt (Figure 42), from the smallest to the largest specimen, the triple contact point between the parietal - squamosal - supraoccipital (#71) takes a more ventral position, whereas the triple contact point between the frontal - squamosal - parietal (#69) is located relatively more posteriorly. The most posterodorsal point of the zygomatic ridge of the squamosal (#56) is shifted dorsally, and the most dorsal point of the external acoustic meatus (#58) is located more anteroventrally in larger specimens. The combination of these allometric variations makes the posterior root of the zygomatic arch much wider and higher in larger specimens. Allometric variation in the zygomatic process of the squamosal occurs primarily at the most dorsal point of the jugal - squamosal suture (#52), which extends much further anteriorly as size increases. Together with the variation of other landmarks, this indicates that the squamosal portion of the zygomatic arch is more elongated in larger specimens. Finally, the most posterior point of the alisphenoid - squamosal suture in front of the pyriform fenestra (#62) assumes a more anterior and medial position in larger specimens. The ventral view (Figure 42) also clearly shows a greater distance separating landmarks on the zygomatic arch (#52, #54) from those on the sidewall of the braincase (#42, #62, #69), in the anterior half of the bone. This indicates that the zygomatic arch protrudes further laterally in larger specimens.

An allometric variation for this OBU is not significantly supported for the Dataset-Lmax and Dataset-Tmax (Tables 10 & S21; although it is near the significance threshold in the former).

Supraoccipital

In the DatasetExt (Figure 42), from the smallest to the largest specimen, the most posterior point of the nuchal process of the supraoccipital (#74) shows the greatest allometric variation, as it is extended much further posterodorsally than other landmarks. The point of maximum curvature

of the lateral occipital ridge in the caudal cerebral fossa (#100) has a relatively more medioventral position in larger specimens. The triple contact point between the parietal - squamosal - supraoccipital (#71) is located relatively more ventrally, described above for the squamosal. The triple contact point between the supraoccipital - exoccipital - petrosal (#78) is positioned slightly more dorsomedial and the most posterodorsal point of the foramen magnum (#86) more posterodorsal in larger specimens. The combination of these two allometric variations indicates a reduction in the proportions of the ventral part of the supraoccipital as size increases.

The Dataset-Lmax (Figures 43 & 44) and the Dataset-Tmax show the same allometric variations (Figures S32 & S33) as the DatasetExt.

3.2.4 DISCUSSION

3.2.4.1 *Common allometric pattern in Entire Skull (ES)*

Our comparative study of allometric patterns at the ontogenetic and static levels in *Zaedyus* and *Cabassous* coupled with the analysis of evolutionary allometry across Cingulata, revealed several patterns shared with those described previously in *Dasypus* (Section 3.1). The strongest allometric variation over the entire skull corresponded to relative lengthening of the snout associated with a reduction in the proportions of the braincase (Table 11). This pattern was very strongly marked in *Dasypus*, whereas in *Zaedyus* and *Cabassous*, it appeared to be much weaker but still present. Relative lengthening of the snout and reduction of braincase proportions were also found as an allometric variation at the evolutionary level across our three datasets despite the presence of taxa with anteriorly shifted orbits on the snout, such as glyptodonts. Our study thus showed that this widespread pattern, described in the literature as craniofacial evolutionary allometry (CREA), is not only found in *Dasypus* (Section 3.1) but is pervasive among cingulates. This pattern may be stronger in *Dasypus*, with its more dramatically elongated snout (Hautier *et al.*, 2017; Section 3.1) but it is clearly expressed in the morphological diversity of cingulates as a whole, which suggests a deep origin for this pattern.

CHAPTER 3: Cranial allometry in Cingulata

Table 11. Summary of common allometric variations at different levels and in different datasets at the ES and 3B level as size increases (versus Log Skull Centroid Size – see text).

Common pattern		Common Allometric Pattern With Size Increase (relative to Log Skull Centroid Size)	
		Entire Skull (ES)	Bone-By-Bone (3B)
Static - Ontogenetic - Evolutionary level	All datasets	<p>i) Anterior snout lengthening. ii) Stronger postorbital constriction iii) Reduction of braincase proportion. iiiii) More protruding nuchal crest processes. iiiiii) Enlargement between zygomatic arches and postorbital constriction iiiiii) Relative flattening of the cranial roof.</p>	<p>Bo-Eo: i) hypoglossal foramen located relatively more posterior; ii) relative reduction of foramen magnum (not in <i>Cabassous</i>).</p> <p>Frontal: i) more posterior and stronger postorbital constriction; ii) greater separation between the annular ridge and frontal roof.</p> <p>Petrosal: i) more protruding mastoid process; ii) shallower fossa subarcuata (not in <i>Dasyopus</i>).</p> <p>Squamosal: i) more protruding zygomatic arch laterally (not in <i>Cabassous</i>).</p>
	Without fossils	<p>i) Posterior snout narrowing.</p>	<p>Maxillary (without <i>Cabassous</i>): i) reduction in height.</p> <p>Palatine (without <i>Cabassous</i>): i) anteroposterior elongation on the midline and mediolateral narrowing.</p>
Static - Ontogenetic level	Only DZC	<p>i) Widening of the zygomatic arch.</p>	<p>Jugal: i) shortening and increase in height.</p> <p>Parietal: i) anteroposterior elongation and mediolateral narrowing.</p> <p>Squamosal: i) more posterior position of the posterior root of the zygomatic arches.</p>
	Only ZC	<p>i) More medial position of braincase anterolateral edge.</p>	<p>Jugal: i) more posterior position of the orbital edge.</p> <p>Nasal: i) frontal process of the nasal elongated posteriorly.</p>
Evolutionary level	<p>DatasetExt Dataset-Lmax Dataset-Tmax</p>	<p>i) More posterior position of the anterior edge of the orbit and zygomatic arches. ii) More lateral position of the promontorium of the petrosal indicating its greater separation from the midline of the basicranium.</p>	<p>-----</p>

CHAPTER 3: Cranial allometry in Cingulata

Several studies have shown that CREA is a global allometric pattern present in several mammalian groups (Cardini & Polly, 2013; Cardini *et al.*, 2015; Tamagnini *et al.*, 2017; Cardini, 2019a; Macey *et al.*, 2020). Cardini (2019a) even suggested that this is an allometric pattern common to all mammals and perhaps even all vertebrates. Cardini (2019a) also showed that armadillos in his sample had a relatively low craniofacial allometry compared to other mammals, even though this sample included species belonging to *Dasypus*.

Craniofacial allometry was not the only common pattern detected on the entire skull among our cingulate species (Table 11). Allometric variation also included a postorbital constriction in larger specimens at all the levels studied in cingulates (Table 11). This allometric variation was also quite common and found in many other mammals (*e.g.*, Frost *et al.*, 2003; Flores *et al.*, 2006; Segura & Prevosti, 2012; Moyano *et al.*, 2017) although not in all groups (*e.g.*, equids: Heck *et al.*, 2019). Allometry was correlated with a greater development of the temporalis muscle in large specimens of *Dasyurus* (Flores *et al.*, 2010) and *Puma concolor* (Giannini *et al.*, 2010) both of which also exhibited a greater postorbital constriction as size increased. This hypothesis requires further research in armadillos, since this muscle does not reach the postorbital constriction in *Dasypus* but it does in *Euphractus* (Smith & Redford, 1990), a closer relative of *Zaedyus*. We also detected a relative flattening of the cranial roof (Table 11) with larger size, which is probably associated with craniofacial allometry (*e.g.*, Ferreira-Cardoso *et al.*, 2019). This flattening is accompanied by an enlarging space separating the internal landmarks on the frontal (#97, #98) from the dorsal edge of this bone (#31, #66) at the intraspecific level in *Cabassous*, in *Dasypus*, and, above all, at the evolutionary level (Table 11). This was also detected in 3B analyses focused on the frontal bone. We previously suggested that this allometric thickening of the frontal in *Dasypus* was linked to the development of frontal sinuses during ontogeny (Billet *et al.*, 2017; Section 3.1). This hypothesis is consistent with the pattern found at the evolutionary level because the smallest cingulates such as chlamyphorines do not possess frontal sinuses (Smith & Owen, 2017; Le Verger, pers. Obs., 2020) whereas larger forms such as some dasypodines and glyptodonts have strongly developed frontal sinuses (Fericola *et al.*, 2012; Billet *et al.*, 2017). Several studies have suggested a relationship between an increase in size and the presence or extension of sinuses in many mammals (Weidenreich, 1941; Zollikofer *et al.*, 2008; Farke, 2010;

CHAPTER 3: Cranial allometry in Cingulata

Curtis *et al.*, 2015; Krentzel & Angielczyk, 2016; Sharp & Rich, 2016; Billet *et al.*, 2017; Boscaini *et al.*, 2018; 2020).

Finally, we detected an elongation of the nuchal crests with increasing cranial size both within and among species (Table 11; Section 3.1). A greater protrusion of these crests in larger specimens was also an allometric pattern frequently found in other mammals at both intraspecific and evolutionary levels (Frost *et al.*, 2003; Flores *et al.*, 2006; Moyano *et al.*, 2017). This region of the occiput serves as an area of insertion for several neck muscles (*e.g.*, *recti capitis dorsalis major* and *minor*, *semispinalis capitis*; Barone, 2000; Evans & de Lahunta, 2012), which control the flexibility of the neck for head movements (Evans & de Lahunta, 2012). The stronger development of these crests in large specimens could increase the surface of insertion for these muscles to compensate for the increase in head mass. Dissections in extant Cingulata will be necessary to test this hypothesis.

In addition, we detected a relative narrowing of the snout in its posterior part in larger specimens in the evolutionary dataset including only extant species (Table 11). This pattern is relatively common in mammals (*e.g.*, in canids: Drake & Klingenberg, 2008; Segura & Prevosti, 2012). An allometric widening of the zygomatic arches relative to the rest of the skull and a greater distance from the zygomatic arches to the postorbital constriction was also recovered in our intraspecific analyses and in the evolutionary DatasetL-max (Table 11). This allometric variation is known in several other mammals (Cardini & O'Higgins, 2005; Cardini *et al.*, 2015; Tamagnini *et al.*, 2017) and may be linked to the CREA pattern even though such a linkage has not yet been demonstrated. Finally, the commonly observed allometric reduction in braincase proportions in larger specimens was more strongly localized on the anterolateral edges of the braincase in our intraspecific series of *Zaedyus* and *Cabassous* (Table 11).

We also noted two allometric variations in the ES analyses that were only found at the evolutionary level, but were common to all three evolutionary datasets (Table 11). The first corresponded to a much more posterior position of the anterior edge of the orbit and anterior zygomatic arches, which seemed to accompany the snout lengthening in larger specimens (Table 11). This is congruent with the morphology of *Priodontes* or *Vassallia*, but not with that of the large-sized glyptodonts, which possess an anteriorly shifted orbit and who thus depart from this allometric trend among cingulates. The second allometric variation corresponds to a relatively more lateral position of the promontorium of the petrosal, indicating its greater separation from

the midline of the basicranium in larger specimens. According to the matrix of [Billet *et al.*, \(2011\)](#) (character 90), large taxa (glyptodonts, pampatheres) no longer present a contact between the promontorium of the petrosal and the lateral edge of the basicranium. A patent basicochlear fissure is also present in *Dasypus* and *Stegotherium* (see [Wible, 2010](#); [Gaudin and Lyon, 2017](#) – also in *Priodontes*, see [Patterson *et al.*, 1989](#)). This is congruent with a putative negative allometry of the petrosal bone relative to skull size among placentals ([Billet *et al.*, 2015b](#)), which further contributes to the presence of the medial cavity between the petrosal and basicranium in larger species. More research is on allometric variation of the auditory region is needed to test this hypothesis.

3.2.4.2 Allometric proportions of cranial shape variation in Cingulata

The proportions of shape variation for the entire skull explained by allometry were very unequal when comparing all the analyses. *Dasypus* showed the highest proportion with almost 28% at the ontogenetic level ([Section 3.1](#)). At the static level, it exhibited values closer to those of *Zaedyus* at both levels and *Cabassous* at the ontogenetic level, *i.e.* between 5% and 10% ([Section 3.1](#)). The allometric proportion of shape variation resulting from the evolutionary analyses were higher, approaching 20%. Compared to intraspecific values for other mammals, *Cabassous* and *Zaedyus* showed a particularly low allometric proportion of cranial shape variation, whereas *Dasypus* was closer to values typical for mammals ([Frost *et al.*, 2003](#); [Hallgrímsson *et al.*, 2009, 2015](#)). The proportions of allometric variation at the evolutionary level are particularly variable according to the group of mammals studied (although a majority shows proportions between 10% and 30% ([Cassini, 2013](#))).

As regards cranial units, the allometric proportions of shape variation for each OBU were very different among the different data sets and different levels of analysis, as was the case in our previous study of *Dasypus* ([Section 3.1](#)). Only the petrosal showed statistically significant supported allometric variation in all analyses and, except for *Cabassous* at the static level, this was also the case for the frontal. The frontal often showed strong allometric variations in previous studies at the ES level (*e.g.*, [Hautier *et al.*, 2017](#); [Ferreira-Cardoso *et al.*, 2019](#); [Section 3.1](#)). To our knowledge, few studies have performed allometric analyses on virtually isolated bone units (our 3B approach), but we note, for example, that in the regionalized allometric analyses of [Gonzalez *et al.* \(2011\)](#) in humans, the face and vault showed stronger allometric variations than the basicranium.

In our analyses, it is also worth noting that the palatine and parietal, which showed strong allometry at the static level in *Dasypus* (Section 3.1), also exhibit a high proportion of allometric variation in *Zaedyus* at the ontogenetic level and, for the palatine, in the evolutionary analyses as well (in extant species only). In addition, *Cabassous* consistently showed a lower allometric proportion of shape variation in the ES analyses, and significant allometric variation was supported for fewer cranial units in this taxon, which suggests an lower overall level of cranial allometry. However, the as-os-pt-bs was the OBU with the highest allometric proportions in *Cabassous*, and it clearly exceeded values found for this OBU in *Zaedyus* and *Dasypus*. A significant allometric variation for this OBU at the evolutionary level was only recovered in the dataset incorporating glyptodonts.

3.2.4.3 Common Allometric Pattern in Cranial Units

Through the different levels of analysis, our study allowed us to detect several allometric patterns on virtually isolated cranial units within intraspecific series in *Dasypus* (Section 3.1), *Cabassous* and *Zaedyus*, and among cingulate species in our evolutionary analysis. Allometric variations common to several intraspecific and evolutionary levels of analyses were found for the bo-eo, frontal, petrosal and squamosal OBUs (Table 11). This comes as no surprise, as these OBUs were often among those with the highest allometric proportions in most of our analyses (Figures 31, 32 & 41; and Section 3.1). As size increased, all cingulates exhibited a more posterolateral position of the hypoglossal foramen on the basioccipital-exoccipital (bo-eo) unit, both within and among species. Similarly, the foramen magnum was reduced in size as the size of the skull increased, a tendency also known in squamates (Monteiro & Abe, 1997). On the frontal, the postorbital constriction was more pronounced and more posteriorly located, and a greater distance separated the annular ridge from the frontal roof dorsoventrally in larger specimens. These last two variations were also detected in part at the ES level. On the petrosal, the mastoid process (= paroccipital process of petrosal in Wible & Gaudin (2004)) elongated with increasing skull size. The mastoid process of the petrosal in armadillos serves the site of origin for the digastric muscle involved in the mandibular movement (Wible & Gaudin, 2004). A larger area of attachment may be associated with larger and stronger digastric muscles in larger specimens. At the evolutionary level, this pattern may be related to the specialized herbivory seen in the largest cingulates

(pamphathères, glyptodonts) (Vizcaíno *et al.*, 2004). As for the nuchal crests, dissection in extant cingulates could help to better explain this pattern.

Cingulates also shared a shallower fossa subarcuata on the petrosal with increasing skull size. Because of negative allometry of the inner ear labyrinth compared with the surrounding petrosal bone, Billet *et al.* (2015b) have questioned whether the reduced size of the anterior semicircular canal (ASC) in large taxa could constrain the shape of the fossa subarcuata (this fossa being circumscribed by the ASC in many mammals). Our study is congruent with this idea, given that large specimens in our sample often have a shallower fossa subarcuata.

Our study also allows us to identify allometric patterns common to our intraspecific series and that are only found in the evolutionary sample that excludes fossil specimens. We detected several common allometric variations among *Dasypus*, *Zaedyus* and DatasetExt with respect to the maxillary and palatine (Table 5). With increasing skull size, the dorsoventral height of the maxillary was reduced. We also noted a relative reduction of the maxillary tooth row length at the evolutionary level and in *Dasypus* (Section 3.1). This allometric pattern was originally proposed in armadillos by Moeller (1968). However, the pattern does not hold in *Zaedyus* and *Cabassous*, nor at the evolutionary level when including fossils, which means that it does not represent a clear trend in the group. We also detected a general narrowing of the palatine and its elongation on the midline.

Leaving aside the evolutionary, we also detected common patterns of intraspecific allometry among *Dasypus*, *Zaedyus* and *Cabassous*. These concerned the jugal, the parietal and the squamosal (Table 11). The jugal became relatively shorter and deeper in larger specimens over the course of ontogeny. The parietal was more elongated anteroposteriorly and narrower mediolaterally with increasing skull size in the ontogenetic analyses. On the squamosal, the posterior root of the zygomatic arches assumed a more posterior position in larger specimens at both the ontogenetic and static level (less clear in *Cabassous*).

Finally, our study also allowed us to detect common allometric patterns in the jugal and nasal of *Zaedyus* and *Cabassous* (Table 11). The all edge of the jugal moved posteriorly in older, larger individuals. The frontal process of the nasal was elongated at both the ontogenetic and static levels.

3.2.4.4 *Improvement and perspectives*

One limitation of our analysis is the poor sampling in *Cabassous* compared to the other two species analyzed at both the ontogenetic and static levels. Better sampling for this taxon might potentially reveal allometric patterns that were not supported statistically in our study, especially where *p-values* were close to the significance threshold. The minimum sample size needed for the study of allometry is not clear in the literature (Cobb & O'Higgins, 2004; Cardini & Elton, 2007; Brown & Vavrek, 2015), but it is certain that a larger sample size is desirable. However, improving the sampling for this taxon would require more research on the differences that exist between the northern and southern populations of *Cabassous unicinctus* (Supporting Information 1). In addition, improving the alpha taxonomy of the other two species would also enhance future allometric studies (Section 3.1; Supporting Information 1).

At a more inclusive taxonomic level, it would be interesting to compare the ontogenetic allometric trajectories among the different extant and extinct clades of Cingulata at the evolutionary level (Klingenberg, 2016; Esquerré *et al.*, 2017; Wilson, 2018). Clearly, our results often suggested different allometric trends, especially for dasypodids with respect to chlamyphorids, at the evolutionary level (Figures 39 & 40). In the present study, *Peltephilus* appears as a highly divergent specimen in terms of its relationship between shape and size in comparison with other cingulates, and future studies may want to test evolutionary allometric patterns in the group without this taxon.

Allometric analyses at the evolutionary level could also be compared to dietary habits among cingulates. Recently, the study by Hennekam *et al.* (2020) revealed that the increase in size of island giants in dormice was accompanied by novel feeding adaptations. Adding this dimension to our evolutionary analyses would be relevant because the giant fossil forms in Cingulata such as pampatheres and glyptodonts are herbivorous, as is the divergent armadillo *Peltephilus* (Vizcaíno & Fariña, 1997; Vizcaíno *et al.*, 2004).

A last perspective relates to Procrustes superimposition and the interpretation of the shape variations obtained that cannot be unambiguously attributed to individual landmarks (Klingenberg, 2020). We have described the variations reconstructed for each landmark relative to the other landmarks, from which we tried to infer more general information on shape changes. A possible complementary approach would involve the use of linear distances to explore further covariation patterns in the skull of cingulates.

CHAPTER 4

Exploration of Cranial Covariation Patterns in Cingulata

« « *Quand quelqu'un cherche* », dit Siddhartha, « *il arrive facilement que ses yeux ne voient que ce qu'il cherche, et il est capable de ne rien trouver, de ne rien recevoir parce qu'il ne pense toujours qu'à la chose qu'il cherche, parce qu'il a un but, parce qu'il est obsédé par son but. Chercher signifie : avoir un but. Mais trouver signifie : être libre, être ouvert, ne pas avoir de but.* ». ».

Hermann Hesse. 1922. Siddhartha. Translated.

“ ‘*When someone seeks,*’ said Siddhartha, ‘*then it easily happens that his eyes see only the thing that he seeks, and he is able to find nothing, to take in nothing because he always thinks only about the thing he is seeking, because he has one goal, because he is obsessed with his goal. Seeking means: having a goal. But finding means: being free, being open, having no goal.*’ ”.

Hermann Hesse. 1922. Siddhartha.

4.1 An exploration of the strongest covariations among cranial distances in Cingulata

ABSTRACT

Morphological integration, the trend for anatomical traits to covary, is a concept that has been intensively explored in recent decades, particularly as it relates to the skull of mammals. A detailed knowledge of morphological integration patterns represents an essential need for morphological phylogenetics, which rely on the independence of the characters analyzed. Towards that aim, it is necessary to analyze integration at several levels (static, ontogenetic, evolutionary) and on several anatomical scales (*e.g.*, entire skull, individual cranial bones) to gain a global understanding of the cranial covariations that can be shared within and among species. In this study, we explored cranial covariation patterns among pairs of interlandmark distances at the static and ontogenetic levels within three developmental series of phylogenetically distant extant armadillo species belonging to the genera *Dasypus*, *Zaedyus*, and *Cabassous*. We first described a selection of pairs of strongly correlated cranial distances shared by the three species. We showed that, apart from a strong impact of craniofacial allometry, the coordinated variations evidenced by our selection of strongly correlated cranial distances are concentrated around the anterior root of the zygomatic arch, the braincase, the mesocranium and the auditory region. Second, we tested whether the pairs selected within armadillo species are also represent correlated at the evolutionary level (*i.e.*, among species), using a rich sample of extinct and extant cingulate species. Statistically significant evolutionary correlations were again localized to the area around the anterior root of zygomatic arch, a region particularly rich in muscular insertions for mastication and often coded as multiple independent characters in phylogenetic analyses of cingulates. The coordinated variations detected by our exploration of cranial covariation patterns within armadillo species can help to highlight groups of potentially non-independent characters in phylogenetic matrices.

Le Verger K, Ferreira-Cardoso F, Gerber S, Hautier L, Delsuc F, Amson E, Ladevèze S, Bardin J, Billet G. *Article In Preparation.*

4.1.1 INTRODUCTION

Morphological integration is the tendency of traits to covary within a morphological structure or in an entire organism (Klingenberg, 2014). Since its modern definition in 1958, the concept of morphological integration (Olson & Miller, 1958) has been extensively studied in evolutionary biology, with renewed interest in the last few decades (*e.g.*, Cheverud, 1982a; Wagner & Altenberg, 1996; Klingenberg, 2008; Goswami & Polly, 2010b; Wagner *et al.*, 2007; Klingenberg, 2010; Klingenberg, 2014). Morphological integration, intimately connected to the concept of modularity (see Section 4.2), can be expressed at different biological levels, such as intraspecific (ontogenetic, static) and interspecific (evolutionary) levels (Klingenberg, 2014; Klingenberg, 2016). A promising way to gain a global understanding of morphological integration in a given clade is to analyze the covariation patterns at static and ontogenetic levels (*e.g.*, Mitteroecker *et al.*, 2005; Bulygina *et al.*, 2006; Freidline *et al.*, 2015; Chinga & Pérez, 2016; Goswami & Finarelli, 2016; Klenovšek & Jojić, 2016) and see how these align with patterns of evolutionary integration (Klingenberg, 2014). Several studies have explored and compared patterns of morphological integration at these three different levels in plants (*e.g.*, Armbruster, 1991; Armbruster & Gobeille, 2004; Klingenberg *et al.*, 2012) and animals (*e.g.*, Klingenberg & Zaklan, 2000; Mitteroecker *et al.*, 2005; Monteiro *et al.*, 2005; Drake & Klingenberg, 2010; Urošević *et al.*, 2019).

The study of integration patterns in the vertebrate skull has drawn particular attention (*e.g.*, Felice & Goswami, 2018; Parsons *et al.*, 2018; Watanabe *et al.*, 2019; Bardua *et al.*, 2019, 2020; Bon *et al.*, 2020; Felice *et al.*, 2019, 2020). Mammals have been the target of an extensive array of studies on cranial integration and modularity, especially focused on the functional and developmental determinants of covariance (*e.g.*, Bolker, 2000; Klingenberg, 2005; Monteiro *et al.*, 2005; Klingenberg, 2008; Goswami & Polly, 2010b; Makedonska *et al.*, 2012; Santana & Lofgren, 2013; Goswami & Finarelli, 2016; Heck *et al.*, 2019; Churchill *et al.*, 2019). Most of these studies generally analyzed integration and modularity at a global scale, but more rarely explore local aspects such as the covariation between two traits in a given cranial region (*e.g.*, Cheverud, 1982a; Percival *et al.*, 2018). Such local covariations could be analyzed directly between landmarks or among interlandmark distances (Cheverud, 1982a; Goswami, 2006; Zelditch *et al.*, 2009; Goswami & Finarelli, 2016), although misleading effects of the Procrustes superimposition on the

CHAPTER 4: Exploration of Cranial Covariation Pattern in Cingulata

former are possible (Cardini, 2019b). Irrespective of the method used, the characterization of covariation patterns among traits is crucial for a more comprehensive understanding of morphological variation in the skull of mammals (Monteiro *et al.* 2005; Mitteroecker & Bookstein, 2008; Porto *et al.*, 2009; Marroig *et al.*, 2009; Jamniczky & Hallgrímsson 2011; Klingenberg & Marugán-Lobón, 2013; Billet *et al.*, 2015a; Percival *et al.*, 2018). A detailed knowledge of cranial covariation patterns also represents an essential need for morphological phylogenetic analyses (Goswami *et al.*, 2014; Billet & Bardin, 2019), which rely on the independence of characters during matrix construction (Felsenstein, 1973; Wilkinson, 1995; Emerson & Hastings, 1998; Felsenstein, 2004; Goswami & Polly, 2010a; Guillaume & Brazeau, 2018). Although this knowledge is key to building morphology-based phylogenies, collecting correlation data for every single pair of characters in a large number of taxa seems unrealistic (Goswami & Polly, 2010a, 2010b; Goswami *et al.*, 2014). Modularity analyses could constitute an initial step towards the incorporation of character independence models (Goswami *et al.*, 2014), but they do not provide a detailed picture of trait covariation patterns.

Xenarthra represent one of the four major clades of extant placental mammals (Zachos, 2020). Within it, the Cingulata include the extant armadillos and extinct glyptodonts and pampatheres (Gaudin & Croft, 2015). Patterns of morphological integration in the skull of cingulates are poorly known, except for a few studies on allometry (*e.g.*, Chapter 3) and covariance structure (*e.g.*, Hubbe *et al.*, 2016; Porto *et al.*, 2009, 2013). Previous morphology-based phylogenetic studies lack consensus regarding the relationships within Cingulata (Engelmann, 1985; Abrantes & Bergqvist, 2006; Gaudin & Wible, 2006; Billet *et al.*, 2011; Herrera *et al.*, 2017), with tree topologies that conflict in various ways with recent molecular results (Delsuc *et al.*, 2012, 2016; Abba *et al.*, 2015; Gibb *et al.*, 2016; Mitchell *et al.*, 2016).

In this study, we present a novel approach to explore cranial covariation patterns at the ontogenetic and static levels, using three growth series from phylogenetically distant extant armadillo species, and at the evolutionary level, using a large extant and extinct diversity of armadillos and their kin. Our two-step approach consists of intraspecific analyses of covariation between interlandmark distances (1) followed by the testing of these covariations at the evolutionary level (2). To our knowledge, this represents the first in-depth (though non-exhaustive) exploration of the strongest cranial covariations present on the mammalian skull at different levels.

CHAPTER 4: Exploration of Cranial Covariation Pattern in Cingulata

The comparison of the patterns found within each of the three species in our sample enables us to highlight shared intraspecific covariation patterns and test if these were also expressed during the morphological evolution of the group, particularly in its most diversified family (*i.e.*, Chlamyphoridae). Based on a landmark sample partly corresponding to traits used in cladistic matrices, our aim is to further explore cranial covariation patterns to provide important information about the degree of independence of these traits before their potential implications for phylogenetic matrices can be evaluated.

4.1.2 MATERIAL AND METHODS

4.1.2.1 Biological sample

We sampled 118 skulls corresponding to four extant species belonging to three out of four extant clades recognized within the order Cingulata (see below). The material studied is a re-composition of the specimens used in [Chapter 3](#) (see [Table S22](#) for a complete list of specimens – for *Dasypus novemcinctus*, we selected only the southern morphotype (SM) to ensure that we remain at an intraspecific level). Our sample includes four species, with two species gathered into the same series. Each series is divided into a dataset for the ontogenetic level (juvenile to adult – see [Chapter 3](#) for ontogenetic determination) and for the static level (adult stages only): *Dasypus novemcinctus*. ($n_{\text{ontogenetic}} = 48$, $n_{\text{static}} = 33$; Southern morphotype, [Huchon et al., 1999](#); [Gibb et al., 2016](#); [Billet et al., 2017](#); [Hautier et al., 2017](#); [Feijó et al. 2018, 2019](#); [Arteaga et al., 2020](#)); *Zaedyus pichiy* ($n_{\text{ontogenetic}} = 43$, $n_{\text{static}} = 23$); *Cabassous unicinctus* and *Cabassous centralis* (see below). Our sample of *Cabassous* contains specimens identified as *Cabassous unicinctus* ($n = 15$) and *Cabassous centralis* ($n = 4$) based on geographical data, and several specimens that could not be unambiguously attributed to one of these two species ($n = 8$), which are weakly divergent morphologically and only weakly differentiated on a molecular basis ([Hayssen, 2014](#); [Gibb et al., 2016](#); [Supporting Information 1](#)) as explained in [Section 3.2](#). As in [Section 3.2](#), we have produced two datasets for *Cabassous*. The first dataset is referred as *CabassousN* ($n_{\text{ontogenetic}} = 21$; $n_{\text{static}} = 14$). The second dataset is referred as *CabassousNS* ($n_{\text{ontogenetic}} = 27$; $n_{\text{static}} = 16$). Results for the larger dataset *CabassousNS* are presented in the main text of the present work while results for the dataset *CabassousN* are presented in the supplementary data for each analysis. In order to preserve a maximum number of landmarks for the investigation of the pairs of selected distances at the

CHAPTER 4: Exploration of Cranial Covariation Pattern in Cingulata

evolutionary level, we favored the Dataset-Lmax also used for the evolutionary allometry analysis (refer to [Section 3.2](#)). It allowed a compromise between keeping the maximum number of landmarks and including a large panel of extant taxa and fossils (at least one pampathere, and one Santacrucian and one Pleistocene glyptodont).

4.1.2.2. Geometric morphometrics

Digital data were acquired using X-ray μ CT facilities at the MRI-ISEM facility platform of the University of Montpellier (France), at the American Museum of Natural History (AMNH, NYC, US), at the AST-RX platform of the *Muséum national d'Histoire naturelle* (MNHN, Paris, France), and the CT-lab of the *Museum für Naturkunde* (Mfn, Berlin, Germany). Image stacks were improved in contrast, rotated, cropped, and reduced to 8 bits to facilitate the 3D specimen acquisition using the ImageJ software ([Schneider et al., 2012](#)). Three-dimensional reconstruction and visualization of the skulls were performed using modified stacks of digital images with MIMICS v. 21.0 software (3D Medical Image Processing Software, Materialize, Leuven, Belgium). Cranial shapes were quantified with the 114 anatomical landmarks used in [Section 3.2](#) and placed on the exported 3D models using AVIZO v. 9.7.0 software (Visualization Sciences Group, Burlington, MA, USA). The same corrections as in [Section 3.2](#) have been made in this section regarding the consideration of asymmetry. Analyses at the evolutionary level have been performed on the Dataset-Lmax, which is described in [Section 3.2](#).

4.1.2.3. Size standardization

Size can significantly affect the analysis of covariation patterns among linear measurements, especially at the ontogenetic level. We used the log shape ratio approach to isolate the shape and size components from our set of linear measurements ([Mosimann, 1970](#); [Claude, 2008, 2013](#)). First, the set of interlandmark distances was calculated for each specimen and the geometric mean of all these measurements was used to define its size (*geosize*; [Claude, 2008](#)), using the following equation:

$$geosize = \sqrt[N]{\prod_{i=1}^N Di}$$

The geometric mean of a specimen thus corresponds to the N th root of the product of all the distances (D) of a specimen where N is defined by the number of possible distances for a given set of landmarks ($= n$) such that $N = \frac{n(n-1)}{2}$. Unfortunately, for large datasets, the product of the set of distances reaches numbers far too high for classical computers to compute their root. Therefore, the order of the equation was changed in the following manner as initially proposed by [Claude \(2008\)](#):

$$geosize = \prod_{i=1}^N \sqrt[N]{D_i}$$

The overall calculation is the same, but the sequence changes so that the size of N no longer becomes an obstacle to the computation of the geometric mean. For the computation of the log shape ratios, we then divided each interlandmark distance (Dx) by the geometric mean (Gy) of the specimen ([Claude, 2008](#)) – the logarithm of this ratio ($\log (Dx/Gy)$) was then used in subsequent analyses.

4.1.2.4 Selection of pairs of correlated standardized distances

We explored the existence of significant correlations between pairs of standardized interlandmark distances (computed as log shape ratios and named S-distances hereafter) in each dataset of *Dasybus*, *Zaedyus* and *Cabassous*, in order to detect the strongest correlations. For each data set ($n = 114$ landmarks), the number N of interlandmark S-distances obtained was equivalent to 6441, which means more than 20 million of pairs of distances ($= \frac{N(N-1)}{2}$). First, we produced matrices of interlandmark distances for each specimen and we selected only one half of the skull (left side) to reduce the number of variables. After standardization with the log shape ratio (see above), we used the following criteria and levels of thresholding for statistical parameters to select the strongest correlations among the large number of pairs of S-distances in each dataset. First, we excluded pairs of S-distances with shared landmarks because their correlation can be partly induced by the variation of only one of their three defining landmarks, and thus due not only to a coordinated variation of several landmarks. Second, for each dataset, we calculated the correlation coefficient r for each remaining pair of S-distances ($\log (Dx/Gy)$) and we arbitrarily selected the pairs of S-distances with $|r| > 0.71$ (*i.e.*, square of the correlation coefficient (R^2) > 0.5). This thresholding enabled us to achieve a compromise between the need to reduce of the number of

CHAPTER 4: Exploration of Cranial Covariation Pattern in Cingulata

pairs to be analyzed, and the desire to explore a wide spectrum of the strongest covariations. Third, we performed analyses of standardized major axis regression (= SMA; [Warton & Weber, 2002](#); [Warton et al., 2006](#); [Warton et al., 2012](#)) on these selected pairs, thus assuming the absence of an independent variable. We selected only the pairs of S-distances whose correlation was significantly statistically supported ($p\text{-value} < 0.05$). At the end of this selection process, the SMA regressions of each supported pair of S-distances were compared among the three species, and only shared correlations were retained for description (*i.e.*, correlation supported in *Dasybus*, *Zaedyus* and at least one dataset for *Cabassous* = DZC comparison). We also retained for the description the correlations only shared by the more closely related *Zaedyus* and *Cabassous* (at least one dataset) (= ZC comparison). We used this rationale because our aim was to retain only intraspecific correlations shared among species, which was more interesting for phylogenetic purposes (see [General Discussion & Conclusion](#)). Among these, we discarded pairs that included S-distances that were closely parallel or overlapping, because they may not signal a coordinated change in shape (*e.g.*, pairs related to skull lengthening; [Figure S34](#)) and were thus not deemed most informative for the purposes of our study. Pairs with contrasting signal among species (*e.g.*, positive vs negative correlation) were also not retained for description because they do not induce the same anatomical variation. We also discarded pairs that signaled an increase in the length of the snout relative to a decrease in the proportions of the neurocranium, as it is a pattern corresponding to the craniofacial allometry already well-known in mammals and now in cingulates as well ([Cardini, 2019a](#); [Chapter 3](#); [Figure S34](#)). Finally, because many linear S-distances were in part parallel and overlapping, several selected pairs were redundant, *i.e.* they highlighted the same anatomical information in terms of cranial covariation. In such cases, only one pair was then chosen for description, and the redundant pairs were summarized in [Table 12](#) and listed in [Tables S23-S26](#). The correlation among the pairs of S-distances selected for description was subsequently scrutinized among the corresponding raw distances (R-distances) in order to evaluate the allometric or isometric nature of the covariation (since the standardization of S-distances affects the values of the slopes)². These analyses were performed at the ontogenetic and static levels. Finally, we analyzed the selected pairs with the same analyses at the evolutionary level,

² If growing at the same pace, smaller distances will be found to increase faster than larger distances when standardized using the skull size.

considering both S-distances and R-distances. The R script used is available in [Supporting information 5](#).

4.1.3 RESULTS

The total number of pairs of correlated S-distances above our threshold criteria is shown in [Figure S44](#) for each species at the ontogenetic and static level.

4.1.3.1 *Selected pairs of correlated S-distances and R-distances common to all three species (DZC)*

Ontogenetic level

According to our selection criteria, 1558 pairs of correlated S-distances on the skull are common to all three species ([Table S27](#)). The set of pairs signaling a skull lengthening or craniofacial allometry correspond to 98% of these pairs ([Figure S34](#); [Table S27](#)). Among the remaining selected pairs (= 38, [Table S23](#)), several carry the same kind of anatomical information (see below) and all essentially involve the braincase while the face lacks any of these selected pairs. After carefully checking for redundancy among pairs, most of the anatomical information carried by the 38 selected pairs can be tentatively summarized by the 3 pairs presented in [Figure 45](#) and [Tables 12 & 13](#) and briefly described below (similar pairs at other levels or the number of redundant pairs are listed in [Table 12](#)).

The pair n°1 shows a coordinated variation between the S-distance from the triple contact alisphenoid - squamosal - frontal (#42) to the intersection between the frontoparietal suture and the midline (#66), and the S-distance between the triple contact frontal - parietal - squamosal (#69) and the most dorsal point of the annular ridge (#97) ([Figure 45](#)). The scrutiny of the correlation between the corresponding R-distances suggests a more rapid horizontal (#69-97) than dorsoventral (#42-66) growth of the front of the braincase in *Zaedyus* and *Cabassous*, whereas the opposite is the case in *Dasybus* ([Table 14](#)). Overall, it suggests a coordinated variation of the oblique height of the anterior part of the braincase with its subhorizontal dimensions, terminating

CHAPTER 4: Exploration of Cranial Covariation Pattern in Cingulata

at the annular ridge dorsoanteriorly. Several other pairs of S-distances express similar covariation in the dorsorostral part of the braincase (Table 12, Table S23). This coordinated variation is also supported by other pairs found at the ontogenetic and static levels in the ZC analyses below (Table 12, Table S23).

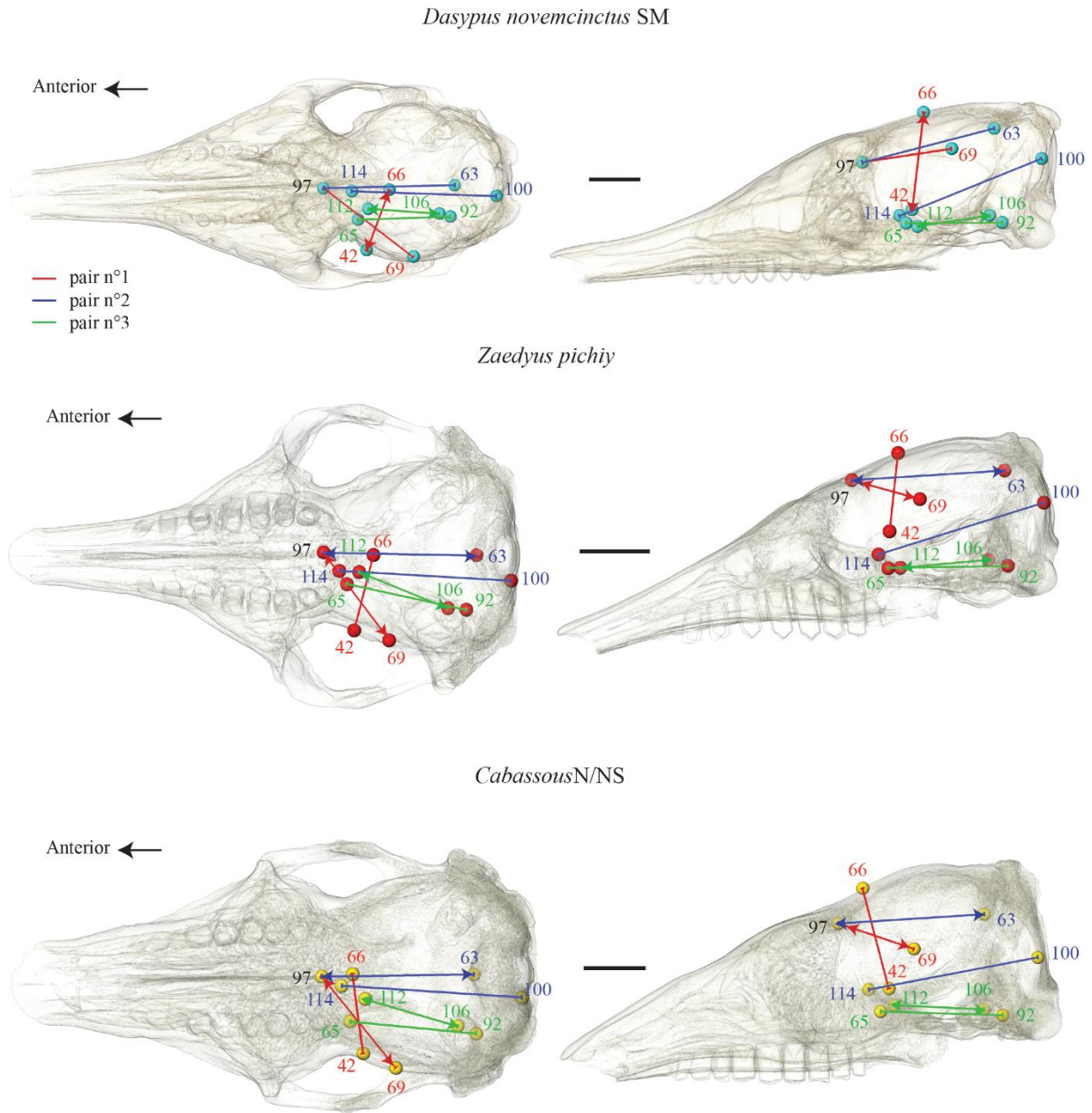


Figure 45. Selected pairs of correlated distances at the ontogenetic level common to the 3 species (= DZC) (see text). Pairs of distances are represented simultaneously on a transparent skull for each species in dorsal and lateral view. Each distance pair is numbered in relation to Table 13 and the colors distinguish the different pairs. Covarying distances ending with bars are isometric. Pairs in which one of the two distances has arrows pointing towards the landmarks are allometric, the distance with arrows being the one increasing the fastest (see Table 14). Scale = 1 cm.

CHAPTER 4: Exploration of Cranial Covariation Pattern in Cingulata

Table 12. Summary of the anatomical information provided by the selected pairs at the ontogenetic and static level for DZC and ZC (Tables 13 & 14) and their concordance with the evolutionary level (Table 15) (see text). Numbered pairs are described in the text. Pairs not described but presenting similar information are indicated by an asterisk (*) and are detailed in Tables S27-S30. Abbreviations: Allom., allometric; intrasp., intraspecific level; Isom., isometric; onto., ontogenetic.

Anatomical Variation	<i>Dasypus - Zaedyus - Cabassous</i> (DZC)		<i>Zaedyus - Cabassous</i> (ZC)		Dataset-Lmax
	Ontogenetic level	Static level	Ontogenetic level	Static level	Evolutionary level
Coordinated variation of the height of the anterior part of the braincase with its subhorizontal dimensions	42-66/69-97 (Pair 1) + 4*	-----	10* (DZC onto.)	18* (DZC onto.)	Allom. similar to <i>Dasypus</i>
Coordinated variation of the height of the anterior part of the braincase compared to the rest of the braincase	-----	-----	60-66/97-112 (Pair 8) + 3* 94-97/66-114 (Pair 9) + 9*	28* (ZC onto.)	8: Allom. similar to <i>Dasypus</i> 9: non-significant
Faster (or isometric) anteroposterior growth of the dorsal part of the braincase (vault) compared to more ventral parts of the middle and caudal cranial fossae.	63-97/100-114 (Pair 2) + 12*	2* (DZC onto.)	-----	-----	Isom. similar to <i>Dasypus</i> & <i>Cabassous</i>
Reduction in relative length and more transverse orientation of the optic canal as it becomes more distant from the basicranium	65-92/106-112 (Pair 3) + 19*	2* (DZC onto.)	75* (DZC onto.)	18* (DZC onto.)	Isom. not similar to intrasp.
Coordinated variation of distances linking the orbital edge and anterior root of the zygomatic arch to the auditory region	-----	38-80/50-92 (Pair 4) + 3*	-----	5* (DZC static)	Isom. similar to <i>Zaedyus</i> & <i>Cabassous</i>
Faster growth of the distance between the anteroventral root of the zygomatic arch and the auditory region than of the distance between the orbital edge and the auditory region	-----	50-94/21-108 (Pair 5)	-----	-----	Allom. similar to intrasp.
Faster growth in width between the posterolateral edge of the palate and the ventral base of the zygomatic arch than between the central part of the palate and the anterodorsal edge of the zygomatic arch	-----	-----	-----	19-21/17-48 (Pair 10) + 4*	Allom. similar to intrasp.
Faster growth of the mesocranium than of the ventral part of the braincase.	-----	-----	19-78/29-90 (Pair 6) + 2*	19-60/29-92 (Pair 11) + 5*	6: Allom. similar to <i>Dasypus</i> & <i>Zaedyus</i> 11: Allom. similar to <i>Zaedyus</i> & <i>Cabassous</i>
Coordinated variation of distances linking the zygomatic arch and cranial roof in the vicinity of the orbit	-----	-----	21-97/48-98 (Pair 7)	-----	Allom. similar to intrasp.
Faster growth of the distance between the posterolateral edge of the palate and the maxillary foramen than of the more dorsal distance contained between the anterior edge of the orbit and the posteromedial edge of the palate	-----	-----	-----	19-23/30-38 (Pair 12) + 1*	Allom. similar to intrasp.

CHAPTER 4: Exploration of Cranial Covariation Pattern in Cingulata

The pair n°2 shows a coordinated variation between the S-distance from the most ventral point of the tentorial process (#63) to landmark #97 and the S-distance between the maximum curvature point of the lateral occipital ridge in the caudal cerebral fossa (#100) and the most ventromedial point on the annular ridge lateral to the posterior median septum (#114). Scrutiny of the correlation between the corresponding R-distances suggests a faster anteroposterior growth of the dorsal part of the vault compared to that of the oblique ventral axis of the middle and caudal cranial fossae in *Cabassous* and *Zaedyus*, whereas *Dasybus* shows an isometrically coordinated variation (Wible & Spaulding, 2013; Figure 45; Table 14). Several other pairs express similar covariation in the analysis of S-distances, almost always involving the dorsal and ventral edges of the annular ridge (Table 12, Table S23). Overall, it suggests that the dorsal part of the annular ridge moves away from the occiput (tentorial process) at a quicker pace than the ventral part of the annular ridge in chlamyphorids. This coordinated variation is also supported by two pairs at the *DZC* static level (Table 12, Tables S23 – S24).

The pair n°3 shows a coordinated variation between the most anterodorsal point of the optic foramen (#65) and the most ventral point of the external aperture of cochlear canaliculus (#92) and the most anteromedial point of the foramen acusticum inferius (#106) with the most dorsal point of the internal posterior aperture of the optic canal (#112). Scrutiny of the correlation between the corresponding R-distances suggests a faster growth of the distance linking the internal posterior aperture of the optic canal to the petrosal than of the distance linking the same bone with the anterior external opening of the same canal (Figure 45; Table 14 – potential isometry in *Dasybus*). An examination of the extreme specimens of each species reveals that, when the two S-distances grow relative to the geometric mean of the skull, the posterior internal opening of the optic canal takes a more anterior and lateral position than its external opening and the overall course of the optic canal reorients slightly more transversely (Figure S36). In other words, this suggests that as the optic canal becomes more distant from the basicranium, reduces its length and assumes a more transverse orientation (Figure S36). This coordinated variation is supported by several selected pairs in this analysis, but also at the *DZC* static level and at the *ZC* ontogenetic and static levels for in which other adjacent landmarks of the optical canal may also be involved (*e.g.*, n°46 – sphenorbital fissure; Table 12, Tables S23-S26).

CHAPTER 4: Exploration of Cranial Covariation Pattern in Cingulata

Table 13. Summary statistics of the standard major axis regression (SMA) for the pairs of correlated **S-distances** selected for description at the ontogenetic (*) and static level (**), common to the 3 species (= *DZC*) or between only *Zaedyus* and *Cabassous* (= *ZC*). Each distance is indicated by the landmarks (L) that define it. Results are shaded when they are below the threshold levels. The numbering of pairs follows the text and [Figures 45-48](#). *, ontogenetic level; **, static level.

Pair	Distance 1 (x)		Distance 2 (y)		S-Distances								
					<i>Dasyopus novemcinctus</i> SM		<i>Zaedyus pichiy</i>		<i>Cabassous</i> N		<i>Cabassous</i> NS		
	n°	L1	L2	L3	L4	<i>R</i> ²	<i>P</i> -value	<i>R</i> ²	<i>P</i> -value	<i>R</i> ²	<i>P</i> -value	<i>R</i> ²	<i>P</i> -value
DZC*	1	42	66	69	97	0.5925	1.6090E-10	0.7084	1.5524E-12	0.6220	2.1576E-05	0.3337	1.6000E-03
	2	63	97	100	114	0.6306	1.6369E-11	0.6144	5.0876E-10	0.6278	1.8534E-05	0.5052	3.2540E-05
	3	65	92	106	112	0.5238	6.1424E-09	0.7921	1.4333E-15	0.7111	1.5809E-06	0.7200	2.2482E-08
DZC**	4	38	80	50	92	0.5256	1.8227E-06	0.6462	3.8268E-06	0.5901	1.3000E-03	0.6052	4.0000E-04
	5	50	94	21	108	0.5546	6.6934E-07	0.6266	6.8182E-06	0.4264	1.1300E-02	0.5131	1.8000E-03
ZC*	6	19	78	29	90	0.0020	7.6009E-01	0.5243	4.0681E-08	0.5711	7.4288E-05	0.3374	1.4879E-03
	7	21	97	48	98	0.1385	9.1841E-03	0.5084	8.0897E-08	0.5246	2.0494E-04	0.6345	6.6669E-07
	8	60	66	97	112	0.3701	4.4930E-06	0.5977	1.2312E-09	0.6094	2.9705E-05	0.6474	4.2177E-07
	9	94	97	66	114	0.1362	9.8357E-03	0.5054	9.2036E-08	0.5345	1.6633E-04	0.5831	3.5945E-06
ZC**	10	19	21	17	48	0.0799	1.1077E-01	0.5096	1.3051E-04	0.5380	2.8310E-03	0.6323	2.3159E-04
	11	19	60	29	92	0.1004	7.2379E-02	0.6766	1.4575E-06	0.6179	8.5759E-04	0.6809	8.3218E-05
	12	19	23	30	38	0.1679	1.7873E-02	0.5566	4.3695E-05	0.5569	2.1729E-03	0.4577	0.0040013

CHAPTER 4: Exploration of Cranial Covariation Pattern in Cingulata

Table 14. Summary statistics of the standard major axis regression (SMA) for the pairs of correlated log(**R-distances**) selected for description at the ontogenetic (*) and static level (***) for each species (and both *Cabassous* datasets). Each distance is indicated by the landmarks (L) that define it. The lower and upper limit of the slope are estimated with the construction of a confidence interval of 95%. The R^2 and the P -value are indicated but not discussed. The numbering of pairs follows the text and [Figures 45-48](#).

R-Distances									
Pair	Distance 1 (x)		Distance 2 (y)		<i>Dasyus novemcinctus</i> SM				
	L1	L2	L3	L4	R^2	P -value	Slope	Slope Inferior	Slope Superior
1*	42	66	69	97	0.6988	1.43E-13	0.7351	0.6250	0.8645
2*	63	97	100	114	0.6900	2.79E-13	1.0006	0.8488	1.1795
3*	65	92	106	112	0.8386	2.22E-16	1.0794	0.9584	1.2158
4**	38	80	50	92	0.8456	4.10E-14	1.2713	1.1014	1.4675
5**	50	94	21	108	0.7617	3.59E-11	1.0689	0.8947	1.2770
6*	19	78	29	90	0.9202	2.22E-16	1.1794	1.0847	1.2825
7*	21	97	48	98	0.8059	2.22E-16	1.0063	0.8833	1.1465
8*	60	66	97	112	0.6149	4.32E-11	0.7567	0.6300	0.9087
9*	94	97	66	114	0.6529	3.87E-12	1.3658	1.1477	1.6253
10**	19	21	17	48	0.3509	2.81E-04	0.4996	0.3734	0.6683
11**	19	60	29	92	0.6422	2.11E-08	0.9730	0.7829	1.2093
12**	19	23	30	38	0.4275	3.68E-05	0.7558	0.5749	0.9938

Pair	Distance 1 (x)		Distance 2 (y)		<i>Zaedyus pichiy</i>				
	L1	L2	L3	L4	R^2	P -value	Slope	Slope Inferior	Slope Superior
1*	42	66	69	97	0.5578	8.84E-09	1.1732	0.9527	1.4448
2*	63	97	100	114	0.6808	1.01E-11	0.8186	0.6856	0.9774
3*	65	92	106	112	0.9222	2.22E-16	1.2314	1.1278	1.3445
4**	38	80	50	92	0.8803	3.80E-11	1.1179	0.9561	1.3071
5**	50	94	21	108	0.7281	2.29E-07	1.2083	0.9558	1.5276
6*	19	78	29	90	0.6794	1.11E-11	1.2324	1.0319	1.4720
7*	21	97	48	98	0.7592	2.99E-14	1.0357	0.8877	1.2083
8*	60	66	97	112	0.4623	5.31E-07	1.2781	1.0162	1.6074
9*	94	97	66	114	0.1267	1.91E-02	1.4209	1.0625	1.9002
10**	19	21	17	48	0.6377	4.93E-06	0.7606	0.5807	0.9962
11**	19	60	29	92	0.5231	9.64E-05	0.6387	0.4692	0.8695
12**	19	23	30	38	0.6082	1.15E-05	0.5192	0.3922	0.6872

Pair	Distance 1 (x)		Distance 2 (y)		<i>Cabassous</i> N				
	L1	L2	L3	L4	R^2	P -value	Slope	Slope Inferior	Slope Superior
1*	42	66	69	97	0.7678	1.92E-07	1.1148	0.8864	1.4022
2*	63	97	100	114	0.7022	2.13E-06	0.8850	0.6830	1.1468
3*	65	92	106	112	0.7993	4.72E-08	1.3800	1.1147	1.7084
4**	38	80	50	92	0.9555	1.79E-09	1.0193	0.8930	1.1636
5**	50	94	21	108	0.9213	5.56E-08	1.2165	1.0206	1.4499
6*	19	78	29	90	0.7609	2.55E-07	1.0243	0.8116	1.2927
7*	21	97	48	98	0.8087	2.98E-08	1.0224	0.8300	1.2594
8*	60	66	97	112	0.6703	5.70E-06	0.9690	0.7380	1.2723
9*	94	97	66	114	0.3546	4.39E-03	1.2623	0.8660	1.8400
10**	19	21	17	48	0.8444	3.44E-06	0.9324	0.7293	1.1920
11**	19	60	29	92	0.8635	1.55E-06	0.9187	0.7297	1.1566
12**	19	23	30	38	0.4364	1.01E-02	0.5531	0.3505	0.8728

CHAPTER 4: Exploration of Cranial Covariation Pattern in Cingulata

Table 14. Continued.

Pair n°	Distance 1 (x)		Distance 2 (y)		R-Distances				
	L1	L2	L3	L4	<i>Cabassous</i> NS				
					<i>R</i> ²	<i>P</i> -value	Slope	Slope Inferior	Slope Superior
1*	42	66	69	97	0.4868	5.23E-05	1.2537	0.9372	1.6772
2*	63	97	100	114	0.6668	2.05E-07	0.8467	0.6690	1.0716
3*	65	92	106	112	0.7679	2.10E-09	1.3699	1.1248	1.6685
4**	38	80	50	92	0.9515	1.34E-10	1.0464	0.9226	1.1867
5**	50	94	21	108	0.9296	1.85E-09	1.2060	1.0365	1.4033
6*	19	78	29	90	0.6573	2.94E-07	1.0356	0.8156	1.3151
7*	21	97	48	98	0.7085	3.77E-08	1.1595	0.9299	1.4457
8*	60	66	97	112	0.5371	1.38E-05	1.3974	1.0596	1.8429
9*	94	97	66	114	0.4071	3.43E-04	1.3705	1.0031	1.8725
10**	19	21	17	48	0.8774	9.24E-08	0.9272	0.7595	1.1317
11**	19	60	29	92	0.7817	5.50E-06	0.7929	0.6085	1.0332
12**	19	23	30	38	0.3869	1.01E-02	0.5881	0.3806	0.9085

Static level

According to our selection criteria, 1670 pairs of correlated S-distances on the skull are common to all three species at the static level (Table S28). When excluding pairs corresponding to skull lengthening, craniofacial allometry and poorly informative variation (= 99% of pairs; see Material & Methods), there remain only nine selected pairs (Table S24). These pairs essentially involve the anterior part of the zygomatic arches, the ventral part of the orbitotemporal region, and the auditory region. Four correspond to anatomical variations already discussed at the ontogenetic level regarding the optic canal and the middle and caudal crania fossae (Table 12, Tables S23 & S24). For the remaining five pairs, most of the anatomical information they carry can be summarized by the two pairs presented in Figure 46 and Tables 12 & 13 and discussed below.

The pair n°4 shows coordinated variation between the S-distance from the anteroventral margin of the lacrimal foramen (#38) to the most posterolateral point of the jugular foramen (#80) and the S-distance between the intersection between anterior orbital edge and jugal/lacrimal suture (#50) and the most ventral point of the external aperture of the cochlear canaliculus (#92). Scrutiny of the correlation between the corresponding R-distances suggests a more rapid growth of the distance connected to the jugal-lacrimal suture than of the distance connected to the more dorsal lacrimal foramen, especially in *Dasypus* and *Zaedyus*, whereas in *Cabassous* this coordinated variation is very close to isometry (Figure 46, Table 14). Overall, it suggests a faster growth of the distance connected to the more ventral part of the anterior orbital edge compared to its more dorsal

CHAPTER 4: Exploration of Cranial Covariation Pattern in Cingulata

part in a direction opposite the auditory region in *Dasypus* and *Zaedyus*. Three other pairs express similar covariation with S-distances (Table 12, Table S24). In complementary fashion, the pair n°5 shows a coordinated variation between the S-distance from the landmark #50 to the most anterior point of the fenestra vestibuli (#94) and the S-distance linking the intersection between jugal/maxillary suture and anteroventral base of the zygomatic arch (#21) and the most anterior point of the epitympanic wing of the petrosal (#108). Scrutiny of the correlation between the corresponding R-distances suggests a more rapid growth of the distance connected to the anteroventral base of the zygomatic arch in comparison to that connected to its anterodorsal margin (lacrima-jugal suture) especially in *Zaedyus* and *Cabassous* (Table 14).

Taken together, the pairs 4 and 5 therefore suggest, at least in *Zaedyus*, a more rapid increase of the distances connected to the ventral parts of the anterior root of the zygomatic arch and orbital edge, as compared to those connected to their respective dorsal parts, in a direction opposite the auditory region. To better understand this, we checked the relative positions of the relevant landmarks in extreme specimens for this covariation (Figures S37 – S38). For both pairs, the points in the auditory region move very slightly in relation to each other in all three species (Figure S37 – S38), which suggests that it is the variation of the landmarks in front of the zygomatic arch which may drive these correlations. For pair n°4, the more ventral landmark on the anterior root of the zygomatic arch is shifted relatively more anteriorly than the more dorsal one in specimens with maximal values of S-distances (Figure S37). For pair n°5, the more ventral landmark seems to be shifted more ventrally in *Dasypus* and *Zaedyus*, but not *Cabassous* (Figure S38). This coordinated variation is also supported by other pairs found at the static levels in the ZC analyses below (Table 12, Table S26).

CHAPTER 4: Exploration of Cranial Covariation Pattern in Cingulata

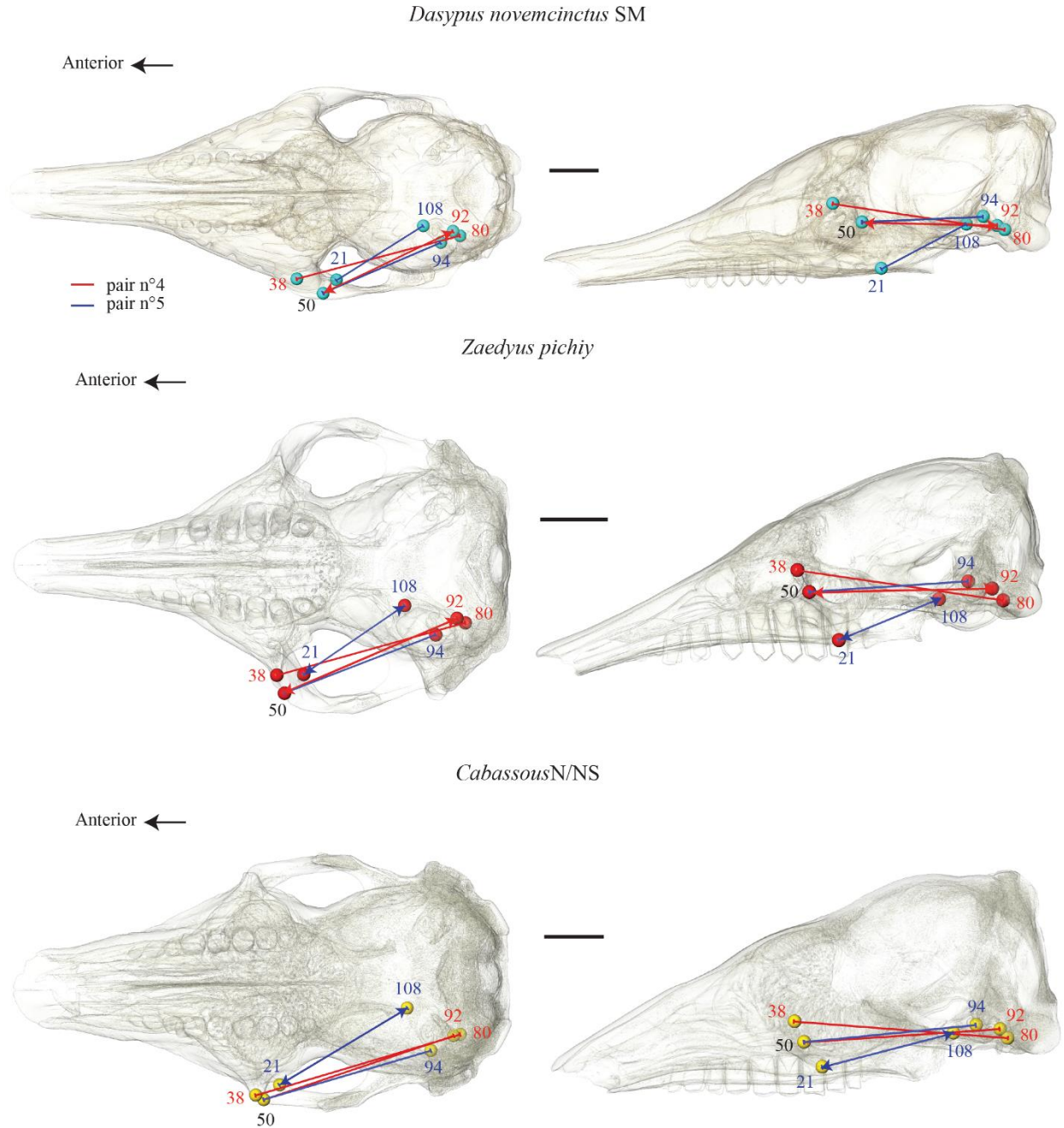


Figure 46. Selected pairs of correlated distances at the static level common to the 3 species (= DZC) (see text). Pairs of distances are represented simultaneously on a transparent skull for each species in dorsal and lateral view. Each distance pair is numbered in relation to [Table 13](#) and the colors distinguish the different pairs. Covarying distances ending with bars are isometric. Pairs in which one of the two distances has arrows pointing towards the landmarks are allometric, the distance with arrows being the one increasing the fastest (see [Table 14](#)). Scale = 1 cm.

4.1.3.2 Selected pairs of correlated S-distances and R-distances common to *Zaedyus* and *Cabassous* (ZC)

Ontogenetic level

According to our threshold criteria, 197 pairs of correlated S-distances on the skull are common to the two species (Table S27). When excluding pairs corresponding to skull lengthening, craniofacial allometry and poorly informative variation (= 48% of pairs), the remaining selected pairs number 103 (Table S25). Most of these pairs concern the orbitotemporal region and connect the posterior half of the snout, the anterior part of the zygomatic arch and several regions of the braincase. Of these, 85 are redundant with anatomical variation presented for *DZC*. For the other pairs, most of the anatomical information they carry can be summarized by the four covariations presented in Figure 47 and Tables 12 & 13.

Pair n°6 shows coordinated variation between the S-distance from the intersection between maxillary/palatine suture and lateral edge of palate (#19) and the triple contact point between the supraoccipital/exoccipital/petrosal (#78) and the S-distance between the most posterior point of the alveolar margin of the tooth row (#29) and the most anteroventral point of mastoid process (#90). Scrutiny of the correlation between the corresponding R-distances suggests that the mesocranium (portion of the skull base between the palate and ear region; Wible *et al.*, 2009) grows at a faster pace than the ventral part of the braincase in *Zaedyus*, whereas *Cabassous* exhibits isometric growth (Table 14). Two other pairs express similar S-distance covariation (Table 12, Table S25). This coordinated variation of these S-distances is far from being statistically supported in *Dasypus*, but with R-distances the trend is similar to *Zaedyus* (Tables 12 & 14).

Pair n°7 shows coordinated variation between the S-distance from the intersection between jugal/maxillary suture and ventral edge of zygomatic arch (#21) and the dorsal intersection of annular ridge and midline (#97) and the S-distance between the triple contact point between maxillary/jugal/lacrimal (#48) with the dorsal intersection between cribriform plate and median septum posterior to the latter (#98). Scrutiny of the correlation between the corresponding R-distances suggests isometric growth of the cranium in the dorsomedial-ventrolateral direction at

CHAPTER 4: Exploration of Cranial Covariation Pattern in Cingulata

the level of the anterior edge of the orbit, and more posteriorly at the level of the midlength of the orbit and most ventral point of the zygomatic arch (Table 14; but possibly allometric in *Cabassous*NS). In other words, this pair suggests coordinated isometric growth for distances linking the zygomatic arch and cranial roof in the vicinity of the orbit. This coordinated variation is significantly supported but with a poor correlation between S-distances in *Dasypus* (Table 13), which also exhibits an isometric relation of R-distances (Table 14).

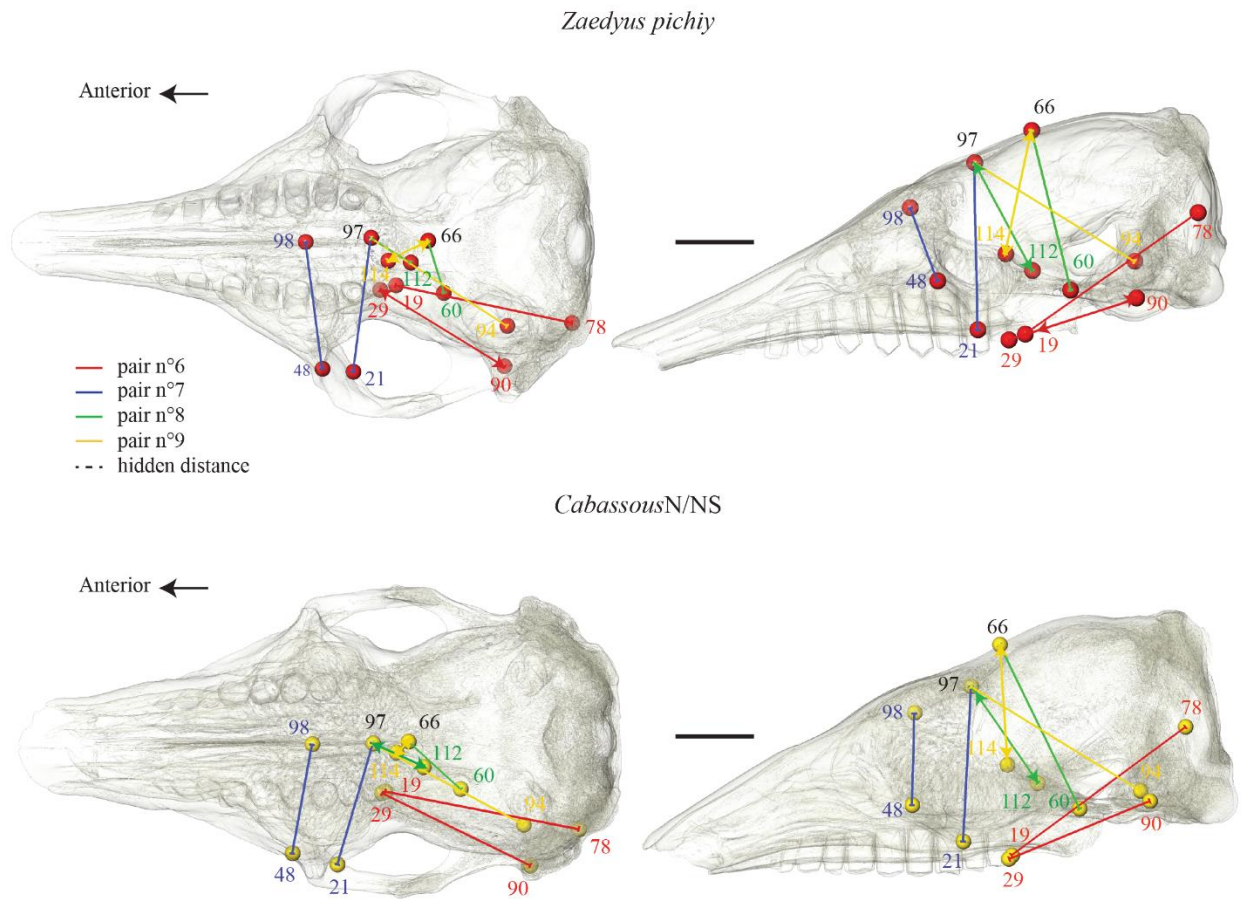


Figure 47. Selected pairs of correlated distances at the ontogenetic level common to the 2 species (= ZC) (see text). Pairs of distances are represented simultaneously on a transparent skull for each species in dorsal and lateral view. Each distance pair is numbered in relation to Table 13 and the colors distinguish the different pairs. Covarying distances ending with bars are isometric. Pairs in which one of the two distances has arrows pointing towards the landmarks are allometric, the distance with arrows being the one increasing the fastest (see Table 14). Scale = 1 cm.

Pair n°8 shows coordinated variation between the S-distance from the most anteroventral point of the foramen ovale (#60) and the intersection between frontal/parietal suture and the midline (#66) and the S-distance between landmark #97 and the most dorsal point of the internal

CHAPTER 4: Exploration of Cranial Covariation Pattern in Cingulata

posterior aperture of the optic canal (#112). Scrutiny of the correlation between the corresponding R-distances suggests a faster growth of the anterior part of the braincase height just posterior to the orbit than its height at the level of the foramen ovale posteriorly (Table 14; but not in *Cabassous*N). Three other pairs express similar covariation among S-distances (Table 12, Table S25). It is also well-supported in *Dasypus*, with a moderate fit to the regression line (Table 13). With R-distances, *Dasypus* shows an opposite allometric trend to that of *Cabassous* and *Zaedyus* (Table 14). A complementary pattern is provided by pair n°9, which shows coordinated variation between the S-distance from the most anterior point of the fenestra vestibuli (#94) and landmark #97 and the S-distance between landmark #66 and the most ventromedial point on the annular ridge lateral to posterior median septum (#114). Scrutiny of the correlation between the corresponding R-distances suggests a faster growth of the height of the braincase just posterior to the olfactory bulbs than the oblique diameter of the braincase from the annular ridge to the auditory region (Table 14). This coordinated variation is significantly supported but with a poor correlation between S-distances in *Dasypus*, which shows the same allometric trend with R-distances (Tables 13 & 14). The two pairs described above, and their associated pairs suggest a faster growth in height of the anterior part of the braincase compared to the rest of the braincase in *Cabassous* and *Zaedyus*. Nine other pairs express similar covariation with S-distances (Table 12, Table S25). Many coordinated variations concern this anatomical region and show the same information at the static level in ZC analysis (= 28 pairs are concerned, Table 12).

Static level

According to our threshold criteria, 403 pairs of correlated S-distances on the skull are common to the two species (Table S28). When excluding pairs corresponding to skull lengthening, craniofacial allometry and poorly informative variation (= 79% of pairs), the remaining selected pairs number 82. Most of the covarying linear S-distances concern the posterior edge of the palatal region and connect the posterior half of the snout, the anterior part of the zygomatic arch, the orbitotemporal region and several regions of the braincase. Of these, 69 are redundant with anatomical variation presented for *DZC* and for the ontogenetic level of *ZC*. For the other pairs, most of the anatomical information they carry can be summarized by the three covariations presented in Figure 48 and Tables 12 & 13.

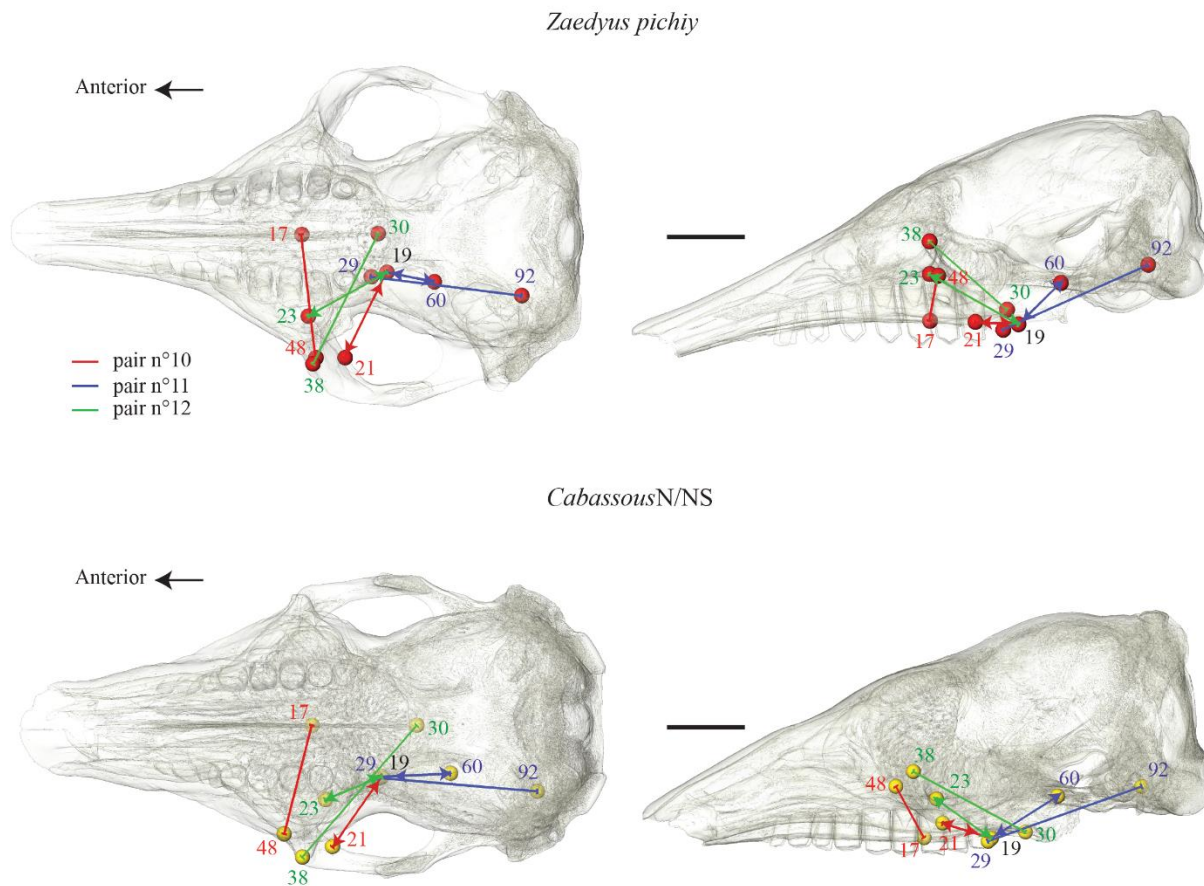


Figure 48. Selected pairs of correlated distances at the static level common to the 2 species (= ZC) (see text). Pairs of distances are represented simultaneously on a transparent skull for each species in dorsal and lateral view. Each distance pair is numbered in relation to [Table 13](#) and the colors distinguish the different pairs. Covarying distances ending with bars are isometric. Pairs in which one of the two distances has arrows pointing towards the landmarks are allometric, the distance with arrows being the one increasing the fastest (see [Table 14](#)). Scale = 1 cm.

Pair n°10 shows coordinated variation between the S-distance from the intersection between maxillary/palatine suture and lateral edge of palate (#19) and the intersection between jugal/maxillary suture and ventral edge of zygomatic arch (#21) and the S-distance between the intersection between palatine/maxillary suture and the palate midline (#17) and the triple contact point between maxillary/jugal/lacrimal (#48). Scrutiny of the correlation between the corresponding R-distances suggests a more rapid growth in width between the posterolateral edge of the palate and the ventral base of the zygomatic arch than between the central part of the palate and the anterodorsal edge of the zygomatic arch ([Figure 48](#), [Table 14](#)). This is particularly true for

CHAPTER 4: Exploration of Cranial Covariation Pattern in Cingulata

Zaedyus, less so for *Cabassous* which is closer to isometry for this selected pair with R-Distances. Four other pairs express similar S-distance covariation (Table 12, Table S26). This allometric variation is not significant in *Dasypus* (Table 13).

Pair n°11 shows coordinated variation between the S-distance from the landmark #19 and the most anteroventral point of the foramen ovale (#60) and the S-distance between the most posterior point of the alveolar margin of the tooth row (#29) and the most ventral point of the external aperture of cochlear canaliculus (#92). Scrutiny of the correlation between the corresponding R-distances suggests a more rapid growth of the mesocranium (length and/or height of the entopterygoid process) than of the distance linking the basicranium to the posterior edge of the palate (Figure 48). Five other pairs express similar covariation with S-distances (Table 12, Table S26). This allometric variation is complementary to the pair n°6 found at the ZC ontogenetic level (Table 12; Figure 48). This allometric variation approaches but is not significant in *Dasypus* and shows isometry with R-distances (Tables 13 & 14).

Pair n°12 shows coordinated variation between the S-distance from the landmark #19 and the most dorsal point of the maxillary foramen (#23) and the S-distance between the most posterior median point of the palatine (#30) and the anteroventral margin of the lacrimal foramen (#38). Scrutiny of the correlation between the corresponding R-distances suggests a much faster growth of the region between the posterolateral edge of the palate and the maxillary foramen than of the larger and more dorsal area contained between the anterior edge of the orbit and the posteromedial edge of the palate (Table 14). Another pair shows similar covariation with S-distances (Table 12, Table S26). This allometric variation is significantly supported but with a poor correlation between S-distances in *Dasypus*, and R-distances shows the same allometric variation as in *Cabassous* and *Zaedyus* (Tables 13 & 14).

4.1.3.3 Testing the selected pairs of correlated distances at the evolutionary level

The analysis at the evolutionary level allowed us to test whether the pairs of correlated S-distances selected at the intraspecific level were also correlated at the evolutionary level among cingulates (Table 15, Figure 49 & Figure S39). Pairs n°1, 8 and 12 are below the threshold criterions used at the intraspecific levels, and there is no statistically supported correlation for pair n°9 (Table 15). All other pairs are strongly supported at this level. In addition to the slopes provided by the R-distances, the distribution of species in plots of S-distances is described to see if it can provide additional information on the variation of these distances at the evolutionary level.

The R-distances for pair n°1 show a more rapid growth of the oblique height of front of the braincase than its subhorizontal dimensions as observed in *Dasypus* (Table 15). The distribution of species in the morphospace shows low S-distances for glyptodonts, *Vassallia* and euphractines, whereas *Peltephilus*, dasypodines, and some tolypeutines and chlamyphorines show the highest S-distances (Figure 49). The allometric variation observed for the R-distances suggests that the oblique height of the anterior part of the braincase is relatively larger compared to its subhorizontal dimensions in larger taxa.

The R-distances for pair n°2 show isometrically coordinated variation of the dorsal part of the vault with that of the oblique ventral axis of the middle and caudal cranial fossae (Table 15). The distribution of the species with S-distances does not show any particular pattern except for *Glyptodon*, which possesses a relatively small braincase anteroposteriorly compared to other cingulates (Figure 49).

The R-distances for pair n°3 show isometrically coordinated variation of the distance linking the internal posterior aperture of the optic canal to the petrosal with the distance linking the same bone with the anterior external opening of the same canal (Table 15). The distribution of species with S-distances shows that euphractines, *Peltephilus* and some tolypeutines have the highest values and thus an optic canal relatively distant from the basicranium, whereas some dasypodines and glyptodonts have the lowest S-distances (Figure 49).

CHAPTER 4: Exploration of Cranial Covariation Pattern in Cingulata

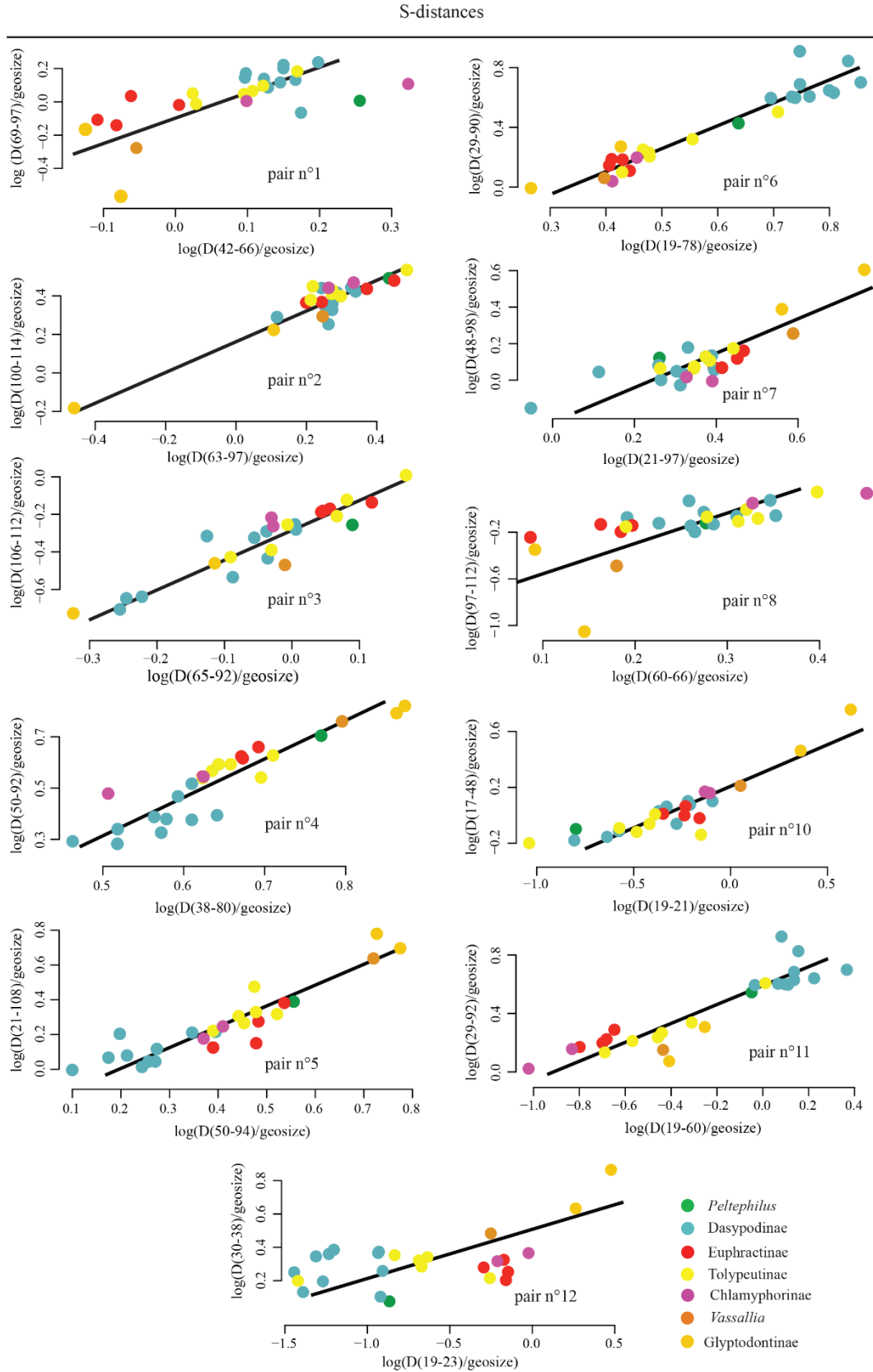


Figure 49. SMA plot of S-distances pairs selected (see [Material & Methods](#)) for the evolutionary level.

CHAPTER 4: Exploration of Cranial Covariation Pattern in Cingulata

The R-distances for pair n°4 show an isometrically coordinated variation of the distance connected to the jugal-lacrimal suture with the distance connected to the more dorsal lacrimal foramen as obtained above in *Cabassous* at the static level (Table 15). The distribution of species in the morphospace seem to closely parallel size proportions among cingulates, with chlamyphorines and dasypodines showing the lowest S-distances, and large fossil taxa having the highest S-distances (Figure 49). This indicates that large taxa have an anterior root of the zygomatic arch relatively more distant from the basicranium than small taxa.

The R-distances for pair n°5 show a more rapid growth of the distance connected to the anteroventral base of the zygomatic arch (jugal/maxillary suture) in comparison to that connected to its anterodorsal margin (lacrimal-jugal suture) as observed at the intraspecific level (Table 15). The distribution of species in the morphospace shows that large species have the highest S-distances, and dasypodines the smallest (Figure 49). This indicates that large species have an anterior root of the zygomatic arch relatively more distant from the petrosal than dasypodines. The allometric variation observed for the R-distances suggests, in turn, that the distance (#21-108) connected to the anteroventral base of the zygomatic arch is relatively larger compared to distance #50-94 in larger taxa. This difference is clearly visible among the species with the shortest S-distances (dasypodines – Figure 49) and those with the highest (the glyptodonts – Figure 49) (Figure 50). In large species, such as glyptodonts, the anteroventral base of their zygomatic arch is shifted more ventrally, with a long descending process of the maxillary and a slightly more dorsal position of the most anterior point of the epitympanic wing of the petrosal (#108), which may, at least partly, explain the observed allometric pattern.

The R-distances for pair n°6 show that the distance on the mesocranium (*i.e.*, #19-78) increases at a faster pace than that on the ventral part of the braincase (Table 15). The distribution of species in the morphospace shows a relatively clear distinction between the dasypodines presenting the highest S-distances and *Peltephilus*, the tolypeutine *Priodontes*, and the chlamyphorines characterized by the lowest S-distances (Figure 49). This indicates that dasypodines have a relatively elongated palatal region posterior to the tooth row. The allometric variation observed for the R-distances suggests, in turn, that the distance focused on the mesocranium (*i.e.*, #19-78) is relatively larger compared to the distance on the ventral part of the braincase (*i.e.*, #29-90) in larger taxa.

CHAPTER 4: Exploration of Cranial Covariation Pattern in Cingulata

Table 15. Summary statistics of the standard major axis regression (SMA) for the pairs of correlated log(R-distances) and S-distances selected for description at the evolutionary level (with Dataset-Lmax). Each distance is indicated by the landmarks that define it. The lower and upper limit of the slope are estimated with the construction of a confidence interval of 95%. The R^2 and the P -value for R-distances are indicated but not discussed. The numbering of pairs follows the text and [Figures 45-48](#). Abbreviations: Inf., inferior; L, landmark; Sup., superior.

Pair	Evolutionary level - Dataset-Lmax										
	Distance 1 (x)		Distance 2 (y)		S-Distances		R-Distances				
	L1	L2	L3	L4	R^2	P -value	R^2	P -value	Slope	Slope Inf.	Slope Sup.
1	42	66	69	97	0.4394	2.24E-04	0.9181	1.52E-14	0.8453	0.7496	0.9534
2	63	97	100	114	0.8682	4.70E-12	0.9708	2.22E-16	1.0076	0.9377	1.0828
3	65	92	106	112	0.8612	8.79E-12	0.9598	2.22E-16	0.9655	0.8874	1.0504
4	38	80	50	92	0.8271	1.26E-10	0.9842	2.22E-16	1.0346	0.9813	1.0907
5	50	94	21	108	0.8402	4.84E-11	0.9894	2.22E-16	1.0909	1.0447	1.1391
6	19	78	29	90	0.9093	5.19E-14	0.9546	2.22E-16	1.0902	0.9967	1.1924
7	21	97	48	98	0.7009	9.70E-08	0.9805	2.22E-16	1.0407	0.9814	1.1037
8	60	66	97	112	0.4203	3.41E-04	0.8584	1.12E-11	0.7023	0.5998	0.8224
9	94	97	66	114	0.0783	0.16601	0.7329	2.45E-08	1.0009	0.8064	1.2423
10	19	21	17	48	0.7953	9.67E-10	0.9347	9.89E-16	0.8876	0.7972	0.9883
11	19	60	29	92	0.8254	1.41E-10	0.9490	2.22E-16	0.7932	0.7213	0.8723
12	19	23	30	38	0.3123	3.00E-04	0.6894	1.54E-07	0.7054	0.5590	0.8902

The R-distances for pair n°7 show isometric growth between the distances linking the zygomatic arch and cranial roof in the vicinity of the orbit, as observed at the intraspecific level ([Table 15](#)). The distribution of species in the morphospace does not reveal major differences among the clades, except that the lowest values are found in some dasypodines and the highest values are found in glyptodonts and *Vassalia* ([Figure 49](#)).

The R-distances for pair n°8 show a slower growth in height of the anterior part of the braincase just posterior to the orbit than its height posteriorly, at the level of the foramen ovale as observed in *Dasypus* but in contrast to the pattern in *Cabassous* and *Zaedyus* ([Table 15](#)). The distribution of species in the morphospace shows that chlamyphorines and some tolypeutines and dasypodines have the highest S-distances, and thus a relatively high braincase, whereas euphractines, *Vassallia* and glyptodonts have the lowest S-distances ([Figure 49](#)). *Glyptodon* stands out with a particularly low #97-112 S-distance, and thus a very low anterior height of the braincase. The allometric variation observed for the R-distances suggests, in turn, that the anterior height of the braincase (#97-112) is relatively smaller compared to the more posterior height (#60-66) in large taxa. *Glyptodon* deviates from this trend towards even smaller proportions for the anterior height of the braincase.

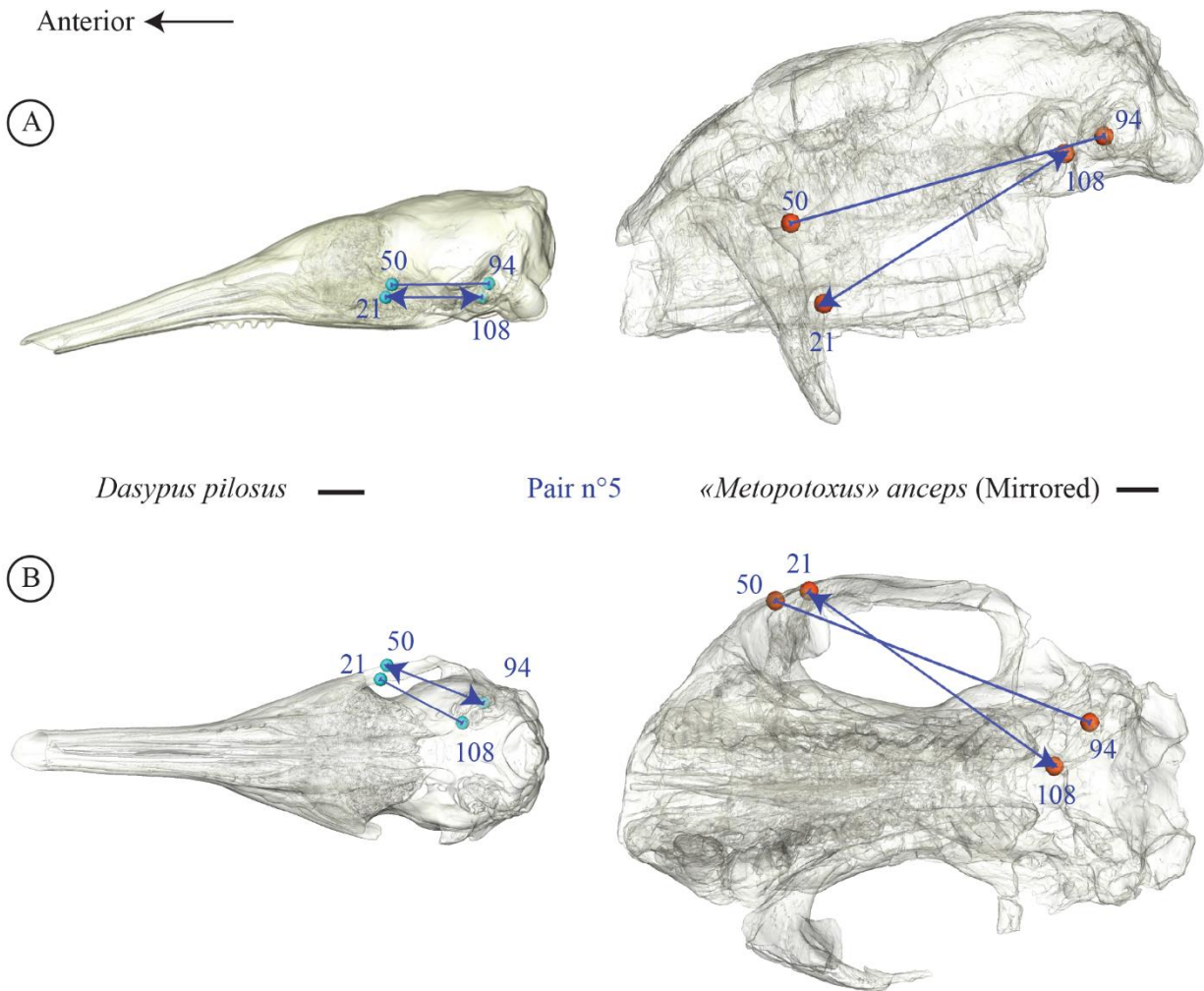


Figure 50. Selected pairs of correlated distances n°5 at the evolutionary level (see text). Pairs of distances are represented simultaneously on a transparent skull for minimal and maximal S-distances (Figure 49). A, lateral view. B, ventral view. Each distance pair is numbered in relation to Table 13. Covarying distances ending with bars are isometric. Pairs in which one of the two distances has arrows pointing towards the landmarks are allometric, the distance with arrows being the one increasing the fastest (see Table 15). Scale = 1 cm.

The R-distances for pair n°10 show a more rapid growth in width between the posterolateral edge of the palate and the ventral base of the zygomatic arch than between the more central part of the palate and the anterodorsal edge of the zygomatic arch, as observed at the intraspecific level (Table 15). The distribution of species in the morphospace reveal much higher S-distances in glyptodonts, *Vassallia* and chlamyphorines (Figure 49), which have a relatively large area between their palate and anterior root of zygomatic arch. The allometric variation observed for the R-distances suggests, in turn, that the width between the posterolateral edge of the palate and the ventral base of the zygomatic arch is relatively larger compared to the width

CHAPTER 4: Exploration of Cranial Covariation Pattern in Cingulata

between the more central part of the palate and the anterodorsal edge of the zygomatic arch in larger taxa (Figure 51). However, chalmyphorines show values close to those of glyptodonts which also suggests a strong phylogenetic signal (Figure 49).

The R-distances for pair n°11 show a more rapid anteroposterior growth of the mesocranium than of the distance linking the basicranium to the posterior edge of the palate, as observed for *Cabassous* and *Zaedyus* at the intraspecific level (Table 15). The distribution of species in the morphospace is similar to that of pair n°6 (see above) (Table 15). Likewise, the allometric variation observed for the R-distances suggests, in turn, that the distance focused on the mesocranium (#29-92) is relatively larger compared to the distance from the palate to the basicranium in larger taxa, which is similar to the condition in pair n°6.

Finally, the R-distances for pair n°12 show a much faster growth of the distance between the posterolateral edge of the palate and the maxillary foramen than of the distance between the anterior edge of the orbit and the posteromedial edge of the palate, as observed at the intraspecific level (Table 15, Figure 51). The distribution of species in the morphospace shows a clustering of dasypodines, *Peltephilus* and most tolypeutines at low values of S-distances, whereas the highest S-distances are found in glyptodonts, *Vassallia*, chlamyphorines and euphractines, which therefore have a relatively large area between their posterior palate and their orbit and maxillary foramen (Figure 49). This is in part reminiscent with the variation seen in pair n°10 (see above). The allometric variation observed for the R-distances suggests, in turn, that the distance between the posterolateral edge of the palate and the maxillary foramen is relatively larger compared to the distance between the anterior edge of the orbit and the posteromedial edge of the palate in larger taxa, as shown in Figure 51.

CHAPTER 4: Exploration of Cranial Covariation Pattern in Cingulata

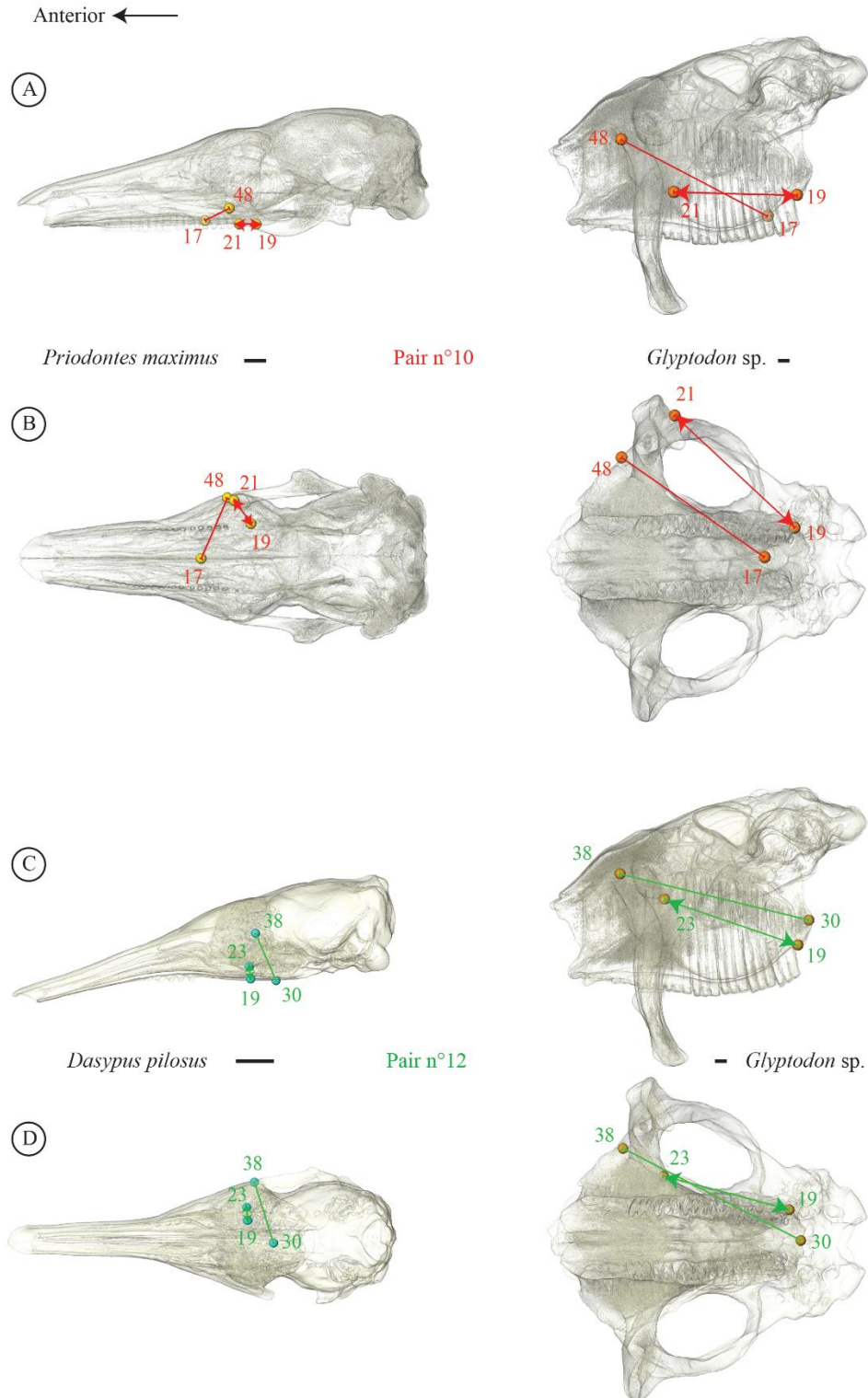


Figure 51. Selected pairs of correlated distances (n°10 and 12) at the evolutionary level (see text). Pairs of distances are represented simultaneously on a transparent skull for minimal and maximal S-distances (Figure 49). A & C, lateral view. B & D, ventral view. Each distance pair is numbered in relation to Table 13. Covarying distances ending with bars are isometric. Pairs in which one of the two distances has arrows pointing towards the landmarks are allometric, the distance with arrows being the one increasing the fastest (see Table 15). Scale = 1 cm.

4.1.4 DISCUSSION

4.1.4.1 *Methodological considerations*

The exceedingly large amount of data resulting from the exploration of correlations among interlandmark distances led us to define threshold criteria in the selection process of correlated S-distance pairs. Our study was thus non-exhaustive and focused on the strongest correlations, using threshold values that revealed readily detectable, widespread and strong cranial covariations within Cingulata. Future studies may want to lower these thresholds in order to uncover a larger proportion of correlations among cranial distances in the group. In the future, this approach could probably be automated with higher computing power, which would make it possible to process data more rapidly and cover as many pairs as possible. They might also take into account the effect of the phylogeny using phylogenetic comparative methods when searching for covariations at the evolutionary level (Klingenberg & Marugán-Lobón, 2013; see also a comment on this method and our approach in the introduction of Section 3.2).

In addition, other avenues of research to explore morphological integration in detail could include the use of methods of geometric morphometrics such as Partial Least Squares (2Block – PLS; *e.g.*, Bookstein *et al.*, 2003; Klingenberg *et al.*, 2003; Monteiro *et al.*, 2005; Klingenberg & Marugán-Lobón, 2013; Barbeito-Andrés *et al.*, 2016), which could be valuable in understanding the shape changes linked to a covariation when two covarying blocks have been pre-identified. This approach would be particularly relevant to shed light on the anatomical covariations indicated by our selected pairs. In several cases, such as for pair n°12, the interpretation of the anatomical changes causing the two distances to covary remains difficult. For a PLS analysis of pair n°12, one could try various constructions of two blocks of landmarks spanning over the anterior root of the zygomatic arch and the posterior edges of the palate to understand further the covariation detected, both within and among species.

4.1.4.2 *Shared cranial covariations in cingulates*

Our exploratory approach revealed that extant species of armadillos in our sample share a variety of intraspecific, strongly correlated intracranial distances, most of which were also significantly supported at the evolutionary level. Most of these correlations have an allometric component and some are partially consistent with our results on cranial allometry. For example,

CHAPTER 4: Exploration of Cranial Covariation Pattern in Cingulata

pair n°10 (Figures 48 & 51) involves a strong mediolateral enlargement of the ventral part of the temporal fossa in larger specimens, which is partially consistent with the greater separation between the zygomatic arches and postorbital constriction in larger specimens in our exploration of cranial allometry (Chapter 3). Almost all the pairs of correlated distances selected for description here locate exclusively in the posterior half of the cranium, whereas statistically supported pairs with at least one distance on the anterior part of the face (landmarks 1-16) all relate to craniofacial allometry (Chapter 3); *i.e.*, they always involve one distance on the face and one on the neurocranium. In other words, there was no intrafacial pair of correlated S-distances detected above our selection criteria. A possible explanation for this result is that craniofacial allometry could constrain the morphological variation of the whole face so strongly (*e.g.*, Cardini & Polly, 2013; Ledevin & Koyabu, 2019; Monson, 2020) that it reduces the possibility of having other strong covariation patterns on the face (Cardini & Polly, 2013). We can also assume that the whole face can present strong covariations controlled by the diet/function (see below). An alternative or complementary explanation is given by Cheverud (1982a) who revealed that the facial units he detected on the skull of rhesus macaque are not genetically independent but complementary, contrary to neurocranial units, which are more independent. This relationship of genetic dependence in the face could further explain why a single strong covariation pattern (craniofacial allometry) is obtained for facial pairs, whereas the regions of the neurocranium were more susceptible to vary and covary in different combinations and directions due to their relative genetic independence. In addition, bones of the face are impacted by developmental processes, such as neural crest migration, neural crest patterning, facial outgrowth and fusion, earlier than bones of the neurocranium in ontogeny (*i.e.*, during prenatal growth; Hallgrímsson *et al.*, 2009), possibly because they ossify first (Hautier *et al.*, 2011). It is possible that patterns of covariation due to early developmental processes on the face are expressed in young armadillos, but are subsequently hidden in more mature specimens by the superimposition of other overarching patterns such as craniofacial allometry. This hypothesis could be verified in armadillos with an analysis of prenatal specimens. Most importantly, it is also possible that pairs of correlated distances on the face could be found just below the threshold criteria in our sample. Therefore, whether there is an underrepresentation of pairs of covarying distances on the face in armadillos should be carefully examined with lower threshold criteria.

CHAPTER 4: Exploration of Cranial Covariation Pattern in Cingulata

Based on our selection criteria, our study described twelve selected pairs of correlated distances at the intraspecific level, that are shared among three distantly related species of armadillos (Table 12). When tested at the evolutionary level, only one of these pairs (pair n°9) no longer presents a statistically supported correlation between distances (Table 15). This pair corresponds to a covariation shared only at the ontogenetic level among our three series (and only weakly so in *Dasypus*), thus suggesting a common ontogenetic origin behind this pattern (Bookstein *et al.*, 2003; Klingenberg, 2014). It is possible that this pattern is expressed at the intraspecific level in all cingulate species, but this hypothesis could only be confirmed by comparing intraspecific series for more species. The strong statistical support for the remaining eleven pairs at both the intraspecific and evolutionary levels highlight more pervasive covariation patterns in cingulates. However, among these eleven pairs, seven do not show similar trends (*e.g.*, isometry vs allometry) within and among species (Table 12). The stability of the four remaining pairs, which each showed comparable covariation trends at the intraspecific and evolutionary levels (Table 1), highlights the pervasiveness of these covariations in cingulates.

Our aim was to search for common covariation patterns among cingulates to address the issue of dependence among cranial traits at a later stage. Therefore, the four selected pairs (n°5, 7, 10 & 12 – Figures 50 & 51) showing the same covariations in all cingulates at all levels (Table 12) are of great interest in this regard. These pairs mainly cover the region of the zygomatic arch, the orbital region, the auditory region and the posterior part of the palate (Table 12, Figures 50 & 51). Although this requires further analysis, several of these pairs (n°5, 10, 12) seem to suggest a relatively fast growth of distances linked to the anteroventral area of the zygomatic arch (including the maxillary foramen) as size increases (Table 12). This region often undergoes strong allometric variation in mammals (*e.g.*, Cardini & Polly, 2013; Ferreira-Cardoso *et al.*, 2019). More broadly, the concentration of most of these pairs in the zygomatic, posterior palatal and mesocranial regions also echoes the zygomatic-pterygoid module initially identified in carnivores (Goswami, 2006). This region constitutes a source of phylogenetic characters within cingulates (*e.g.*, characters 84 – 86 in Gaudin & Wible, 2006) as well as the posterior part of the palate (*e.g.*, characters 56 – 59 in Gaudin & Wible, 2006; but also Fariña & Vizcaíno, 2001). In particular, strong morphological changes are observed in these regions in fossil forms such as glyptodonts (Scott, 1903; Figures 50 & 51), some of which may related to the selected pairs (see below).

CHAPTER 4: Exploration of Cranial Covariation Pattern in Cingulata

In view of these results, it is a complex matter to clearly assign one or more origins for these covariation patterns. These regions are impacted by several developmental processes that overlap during the life of an organism (Hallgrímsson *et al.*, 2009). The anterior root of the zygomatic arch is part of the masticatory apparatus and interacts with the musculature in connection with the jaw, particularly during development (Hallgrímsson *et al.*, 2009). In armadillos, few studies have dealt with the development of the cranial musculature. The few existing ones show the attachment of the *m. masseter* on the ventromedial surface of the zygomatic arch in embryos (Edgeworth, 1923) and a larger area of insertion in adults on the ventral part of the zygomatic arch (especially the anterior root) of the *m. nasolabialis* (Figure 52) and *m. masseter* (Figure 52) in *Dasypus* and *Euphractus* (Smith & Redford, 1990). Dissection of a *Dasypus* skull in a study in progress also shows the strong interaction between the *m. nasolabialis* and *masseter* with the anterior root of the zygomatic arch (Hautier *et al.*, *in prep* – Figure 52). In any case, we can hypothesize an association between our covariation patterns in this region and the insertion surfaces of the masticatory muscles. A putatively increasing muscle mass in this region as size increases could explain modifications in the shape of the ventromedial surface of the zygomatic arch, as muscles and bones have been shown to often covary (e.g., Cornette *et al.*, 2015; Fabre *et al.*, 2018). Further research is of course needed to test this hypothesis.

The strong integration between the distances of pairs n°5, 7, 10 & 12 could then be partly functional if related to muscle ontogeny and function because "*it is intuitive that changes in such systems [i.e., associations between parts interacting in some functional context – e.g., upper and lower jaws], and the coordination among parts within them, are likely to have significant fitness consequences*" (Klingenberg, 2014: pp. 4). Some studies argue for a correspondence between developmental and functional integration (Cheverud, 1984; Wagner & Altenberg, 1996), although if such a correspondence exists, testing it is difficult if not impossible (Klingenberg, 2014). In our case, the potential functional and/or developmental integration for pairs n°5, 7, 10 & 12 is also evolutionary, attesting to a conservation of covariation patterns in all cingulates.

In a phylogenetic context, our study makes it possible to identify patterns preserved at different levels of the evolutionary history of Cingulata and thus to target potentially non-independent morphological characters, which should be avoided in phylogenetic analyses (Emerson & Hastings, 1998; Felsenstein, 2004; Goswami & Polly, 2010a; Guillerme & Brazeau,

2018). Our work clearly identifies integration patterns common to cingulates and forms a first basis for dealing with these aspects.

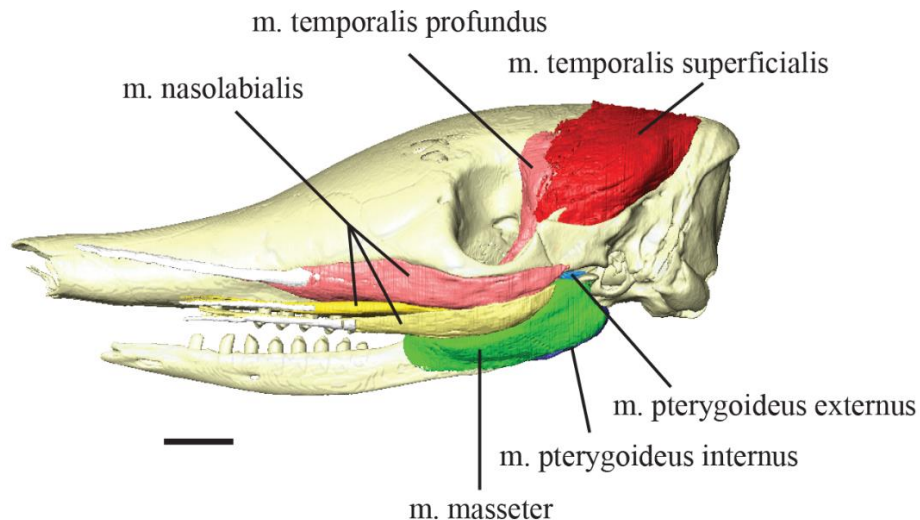


Figure 52. 3D reconstruction of masticatory muscle and tendons of insertion of *Dasypus* using dice-CT (courtesy of L. Hautier). Skull and left mandible in left lateral view. Abbreviation: m., musculus. Scale = 1 cm.

For instance, as mentioned above, several of these pairs suggest a relatively rapid growth of distances linked to the anteroventral area of the zygomatic arch (including maxillary foramen) as size increases. This calls to mind the presences of a descending process of the zygomatic arch known in glyptodonts to form a large ventrally directed apophysis (character 86 – [Gaudin & Wible, 2006](#); [Scott, 1903](#)) (see [General Discussion & Conclusion](#)). In addition, pampatheres also have a large process in the anterior part of the zygomatic arch ([Gaudin & Lyon, 2017](#)) while *Euphractus* exhibits a smaller boss ([Wible & Gaudin, 2004](#)). This descending process is also found in sloths, in which its broad development provides a large insertion surface for masticatory muscles (*m. masseter superficialis* & *m. masseter profundus* – [Naples, 1985](#)). It is possible that the same muscle configuration was present in glyptodonts (see [Gillette & Ray, 1981, Figure 96](#)), suggesting that these covariation patterns common to all cingulates are also common to all xenarthrans. As noted above, dissections of extant xenarthrans are now needed to investigate these questions further and test for a link between the development of the descending process, muscle mass, mastication patterns and cranial size.

The novel approach used in this study to search for integration patterns present at various levels of morphological variation in cingulates allowed to highlighted novel cranial covariations

CHAPTER 4: Exploration of Cranial Covariation Pattern in Cingulata

within the group. It opens new avenues for research on cranial covariations in the group and their relation to muscular anatomy, cranial development and allometry, as well as their implications for phylogenetic matrices (see [Section 5](#)). In order to deepen our knowledge of cranial integration in cingulates, we can also complement the present study on local covariations (pairs of correlated distances) with broader analyses of global covariation pattern (see [next sections](#)).

4.2 Cranial modularity in Cingulata

ABSTRACT

The assumption of a regionalization of morphological integration in the skull has been extensively tested in mammals, giving rise to a plethora of modular hypotheses. Most studies use confirmatory approaches that require the definition of potential modules prior to testing, while exploratory approaches tend to address this problem instead by searching for the most likely modular model in the data. We propose to use one of these exploratory approaches to determine the most probable modular pattern in cingulates, which represent one of the few large mammalian groups unexplored for this question. We performed an approach using Euclidean Distance Matrix Analysis (EDMA) to identify potential patterns of cranial modularity in the three phylogenetically distant armadillo genera *Cabassous*, *Zaedyus* and *Dasypus* at the ontogenetic and static levels. This approach is complementary to our previous analyses of cranial integration and allows us to test whether there is a regionalization of the latter common to all three species and thus potentially to all cingulates. Our results show that the most probable modular pattern with our approach corresponds to an anteroposterior partitioning of the skull (for the ontogenetic and static level) into three modules in *Zaedyus* and *Cabassous*: face, orbit-neurocranium, and vault-basicranium. *Dasypus* shows an additional module corresponding to a parceling of the face module. After a brief discussion of the known modular patterns in mammals, we suggest that the additional module in *Dasypus* is potentially due to extreme snout elongation in this genus.

4.2.1 INTRODUCTION

Modularity is a concept derived from morphological integration which stipulates that organisms or structures can be divided into strongly integrated sets of traits, *i.e.*, modules, that present a relatively weak integration between them (Klingenberg, 2014). This assumption is based on the idea that there are functional or developmental anatomical regions (*e.g.*, the facial region) that are more integrated within themselves than with the rest of a structure (*i.e.*, the rest of the skull) (Olson & Miller, 1958; Cheverud, 1995; Hallgrímsson *et al.*, 2004, 2007; Willmore *et al.*, 2006). In recent decades, many studies have tested hypotheses of modularity in vertebrates (*e.g.*, Felice & Goswami, 2018; Parsons *et al.*, 2018; Watanabe *et al.*, 2019; Bardua *et al.*, 2019, 2020; Bon *et al.*, 2020; Felice *et al.*, 2019, 2020), especially in mammals, in which these concepts and methods have been initiated (*e.g.*, Bolker, 2000; Klingenberg, 2005; Monteiro *et al.*, 2005; Klingenberg, 2008; Goswami & Polly, 2010b; Makedonska *et al.*, 2012; Santana & Lofgren, 2013; Goswami & Finarelli, 2016; Heck *et al.*, 2019; Churchill *et al.*, 2019). This has produced a multitude of modular hypotheses.

A large majority of past studies used *a priori* hypotheses of modules to test whether integration is stronger within these modules than between them. For example, one of the most frequently tested hypotheses corresponds to the two-modules face/neurocranium hypothesis which is particularly well-supported by developmental arguments (*e.g.*, Urošević *et al.*, 2019). This confirmatory approach has gained weight recently with the development of methods to compare the supports for different modular models (*e.g.*, Goswami & Finarelli, 2016). However, this approach requires the formulation of modular hypotheses prior to testing, whereas an organism could be constituted of any combination of modules organized hierarchically (Hallgrímsson *et al.*, 2009). Therefore, the confirmatory approach only tests a reduced number of modular models among the many possible ones. Exploratory approaches tend to reduce this problem, since they do not require *a priori* hypotheses, but seek the most probable modular pattern in the data (*e.g.*, Suzuki, 2013; Parr *et al.*, 2016). Among these approaches, a method developed by Cheverud (1982a) makes it possible to explore the most probable modular pattern based on linear distances (Goswami, 2006; Zelditch *et al.*, 2009). It is the only method of this kind that does not use Procrustes superimposition. This is important, since this superimposition used in geometric

CHAPTER 4: Exploration of Cranial Covariation Pattern in Cingulata

morphometrics may spuriously alter the degree of morphological integration among landmarks and affect the exploration of modularity (Cardini, 2019b; Goswami *et al.*, 2019; Cardini, 2020).

Cranial modularity in Xenarthra is unexplored since, to our knowledge, there exists no analysis searching for modular patterns in the skull of any xenarthran species. Some studies analyzed cranial covariance structures among the Cingulata, but without specifically testing for the existence of cranial modules within the group (*e.g.*, Hubbe *et al.*, 2016; Porto *et al.*, 2009, 2013). In the context of this PhD dissertation, the exploration of cranial modularity within cingulates represents a complementary approach to our previous analyses on cranial integration and enables us to test whether there is a regionalization of the latter.

In this section, we use the exploratory approach of Cheverud (1982a) based on an Euclidean Distance Matrix Analysis (EDMA) to identify potential patterns of cranial modularity. We perform this analysis at the static and ontogenetic levels, following Klingenberg (2014), in the three developmental series of *Cabassous*, *Zaedyus* and *Dasybus* used in previous sections of this thesis. In order to test whether the modular patterns obtained are common to all three species, and thus potentially to all cingulates. This study provides new elements that can improve understanding of the structure of cranial integration in cingulates, and allows comparisons to patterns known in other mammals.

4.2.2 MATERIAL & METHODS

4.2.2.1 Biological sample

The selected sampling corresponds exactly to that of Section 4.1 for *Dasybus*, *Zaedyus* and *Cabassous* (2 datasets), for both the ontogenetic and static levels. Please refer to Section 4.1 for more details.

4.2.2.2 Geometric morphometrics

As for sampling, the acquisition of 3D models and landmarks as well as the corrections applied to them are identical to those described in the Section 4.1. Please refer to this previous section for more details.

4.2.2.3 Analyses of modularity

We analyzed cranial modularity for each of the datasets mentioned above for *Dasypus*, *Zaedyus* and *Cabassous*. We favored an approach using interlandmark linear distances to maintain consistency with the detailed analysis of the strongest covariations (Section 4.1). Despite their great potential for modularity studies (Goswami & Finarelli, 2016; Goswami *et al.*, 2019), 3D geometric morphometric approaches were not used here for consistency's sake and to avoid transformation effects on raw data such as Procrustes superimposition, which may cause artifacts in the intensity of a correlation (Cardini, 2019b; Cardini, 2020) or may affect the landmark variance (*e.g.*, Richtsmeier *et al.*, 2002; but see also Goswami & Polly, 2010b). We performed an Euclidean Distance Matrix Analysis (EDMA) to detect modular pattern of the skull in the four intraspecific datasets. This method uses interlandmark distance matrices and compares each of the distances to the average of all distances of a set of objects (here all skulls of one species) in order to construct a calculation of mean shape (see details in Lele & Richtsmeier, 1991). Once this mean configuration was obtained, we computed the variance-covariance matrix (Claude, 2008). At this stage, some landmarks that were too close in 3D space could produce distances that were too small and induced missing data in the mean shape (Lele & Richtsmeier, 1991; Claude, 2008). Such landmarks ($n=8$) were removed from the analysis bringing our total landmark number to 106 (see Figure S40 for an illustration of the landmarks removed in the modular search). We constructed an interlandmark distance correlation matrix and then used the eigenvalues and eigenvectors from a principal component analysis (PCA) to obtain the interlandmark distance loadings (only those of the components with positive eigenvalues) which were then used as coordinates (Cheverud, 1982a). We then performed a hierarchical clustering using the Ward method (see Ward, 1963; Murtagh & Legendre, 2014). The graphical visualization of a dendrogram alone does not allow the definition of a preferred number of clusters without *a priori* information (Tibshirani *et al.*, 2001). Many approaches have been proposed to estimate the number of clusters (Gordon, 1999), and we opted here for a three-step approach. First, we used the gap statistic (= Gapk) on the distance loadings to evaluate the quality of a clustering measure in comparison with an appropriate null reference distribution of the data (Tibshirani *et al.*, 2001). This index was measured for each cluster number hypothesis (= K) which we increased arbitrarily up to 20, because the number of relevant modules retrieved for mammals never exceeded this number (*e.g.*, Churchill *et al.*, 2019). This estimates the cluster optimal number, which is graphically translated by a slope break. More

precisely, this optimal number is the K value for which the logarithm of the pooled within-cluster sum of squares around the cluster means ($= \log(W_k)$) becomes much lower than its reference curve (Tibshirani *et al.*, 2001). Second, the robustness of the K value was tested using a clustering method based on parameterized finite Gaussian mixture models (Scrucca *et al.*, 2016). For this, we imposed the number of mixture components as a function of the K value obtained with the gap statistic. The analysis then assigned each landmark to a module (*e.g.*, Terray *et al.*, 2020). If the K is stable, then the allocation agrees with the distance tree obtained with the Ward clustering method. Third, once the number of clusters was fixed, we evaluated their stability by resampling the data using bootstraps (see Hennig, 2007). This step enabled us to estimate the average similarities between the original cluster and the clusters produced by resampling. We arbitrarily considered a cluster to be well-supported when it yielded bootstrap values greater than 80%. The analysis was performed at the ontogenetic and static levels. The R script is incorporated in the same script for Section 4.1 which is available in Supporting Information 5.

4.2.3.1 RESULTS

4.2.3.1.1 Number of modules

The statistically stable module number determined with the EDMA varies among the three species but not among levels and datasets within each species (Figures 53, S41). In *Dasyopus novemcinctus*, the slope break for Gapk corresponded to four modules ($K = 4$), while three modules were detected for *Zaedyus pichiy* and for the *Cabassous* datasets ($K = 3$) (Figures 53, S41). *D. novemcinctus* also differed from the other two species with a second slope break at $K = 8$ (Figure 53). However, the eight modules obtained were not statistically supported by bootstrapping, although a face/neurocranium modular pattern was statistically supported (Figures S42 – S45). The four modules hypothesis of *D. novemcinctus* and the three modules of the two other species were consistent with the trees obtained with Mclust and were all statistically supported by bootstrapping (Figures S42 – S45, Table S29), with the sole exception of *D. novemcinctus*, which has a bootstrap of 78% for its third module (orbitotemporal region) at both ontogenetic and static levels (Figures S42 – S45).

CHAPTER 4: Exploration of Cranial Covariation Pattern in Cingulata

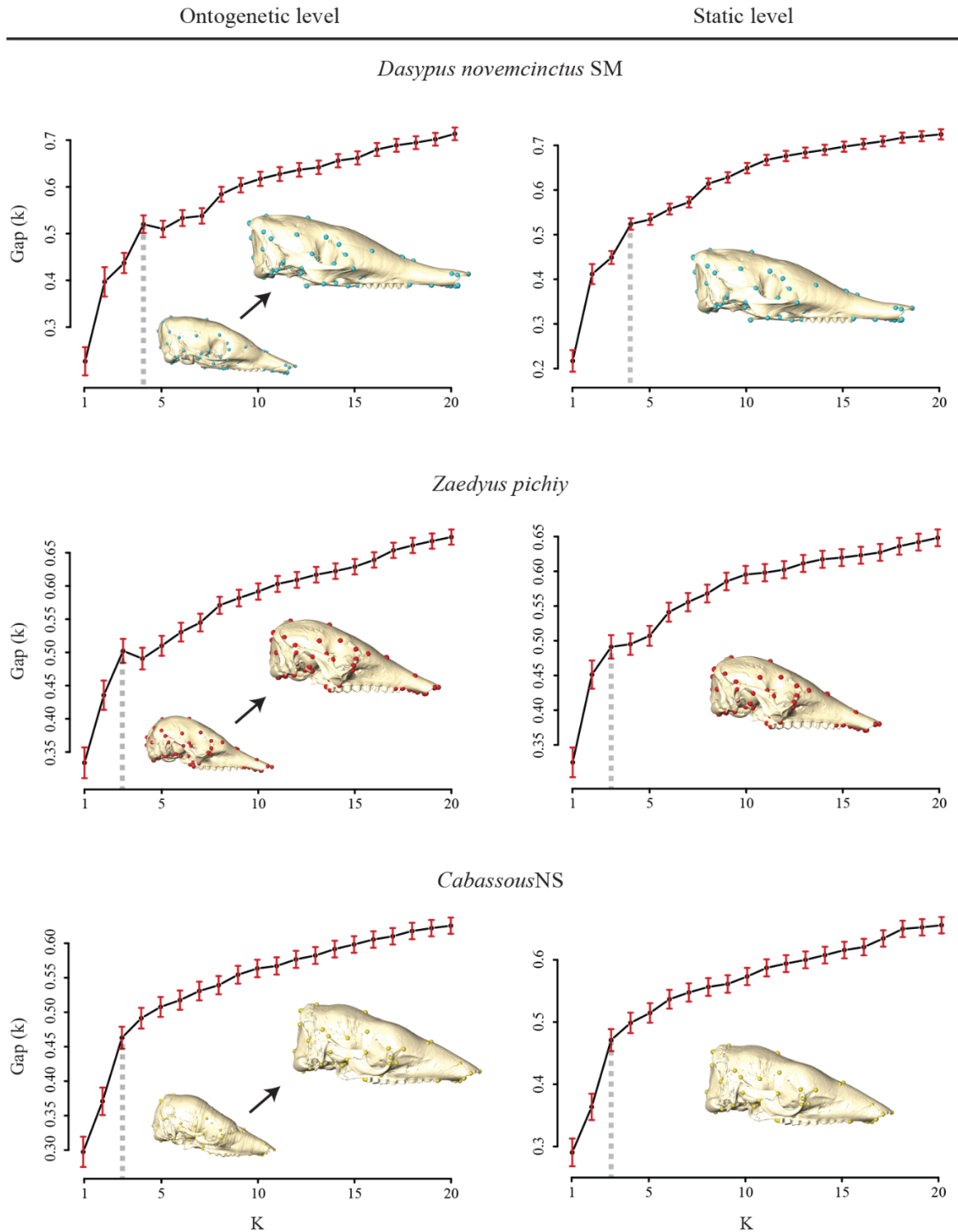
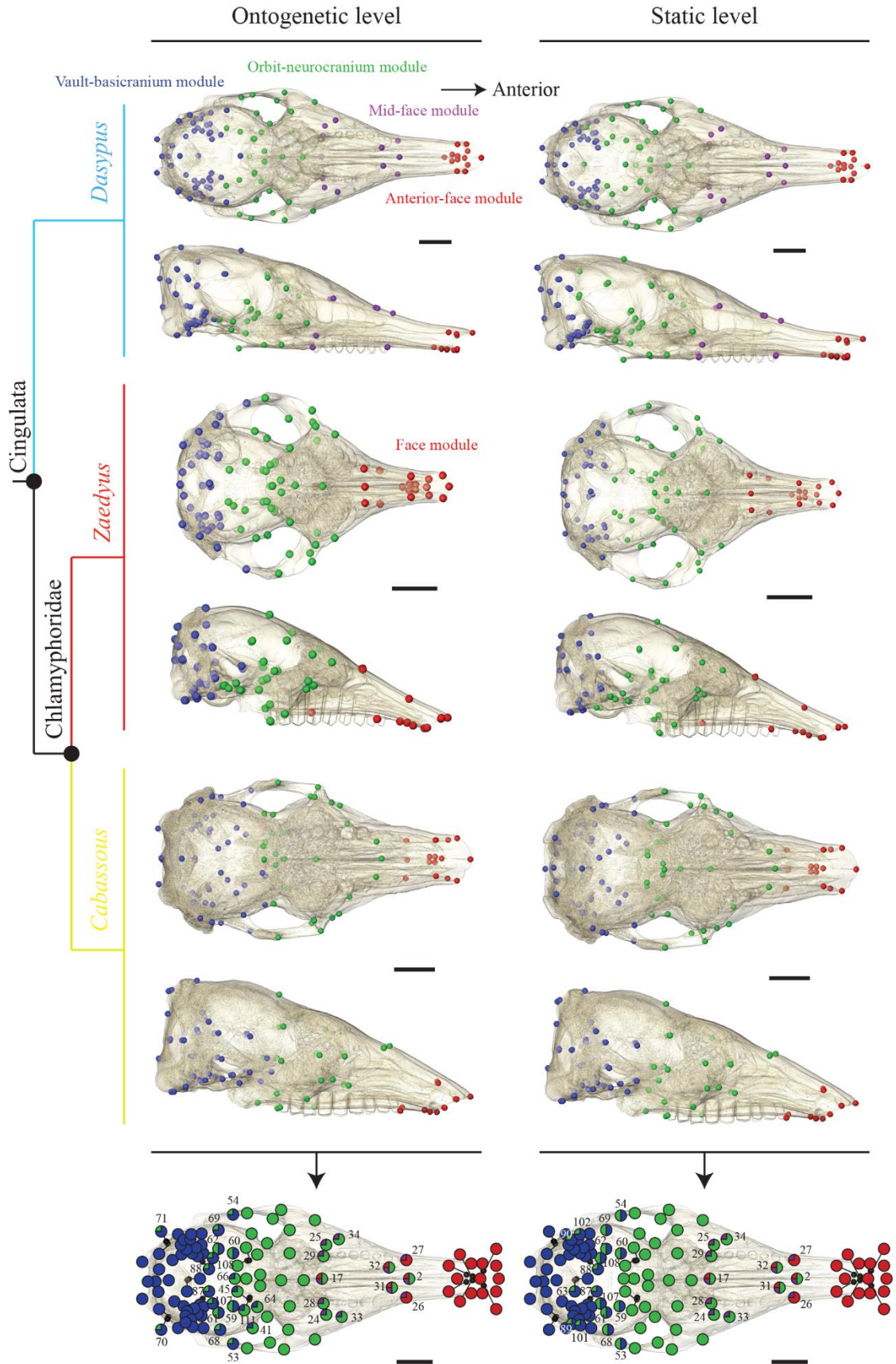


Figure 53. Selection of the number of stable modules using the gap statistic for each species at the ontogenetic level (represented by a juvenile and an adult specimen in lateral view, with landmarks) and at the static level (represented by an adult only). The slope break showing the number of statistically stable modules (see text), is marked by a dotted grey line.

4.2.3.1.2 Modular mapping in the three armadillo species

At the ontogenetic level, the four modules detected in *Dasypus novemcinctus* separate the cranium in four anteroposterior regions which correspond to the front of the snout (anterior-face module), the rest of the snout and the teeth-bearing part of the palatal region (mid-face module), the orbitotemporal region and the most anteroventral part of the neurocranium (orbit-neurocranium module), and the rest of the neurocranium (vault-basicranium module) (Figure 54; Figure S44). In *Zaedyus pichiy*, the anterior-face and mid-face module of *Dasypus* are largely gathered into a single face module (Figure 54; Figure S44). It extends over most of the snout, whereas the face module in the *Cabassous* datasets remains restricted to the front of the snout and resembles more the anterior-face module in *Dasypus* (Figure 54; Figures S44 & S46). In the *Cabassous* datasets, most of the mid-face module of *Dasypus* is therefore gathered into a single module with the orbit-neurocranium module of *Dasypus*, thus making up a larger mid-cranium module than in the other species and datasets (Figure 54; Figures S44 & S46). The parcelling of the face module in *D. novemcinctus* corresponds to the greatest difference between the three species (Figure 54; Figures S44 & S46). *Zaedyus* and *Cabassous* also differ from *Dasypus* regarding the orbit-neurocranium and vault-basicranium modules, as they exhibit: *i*) a slight posterodorsal extension of the orbit-neurocranium module which covers part of the vault; and, *ii*) an anteroventral extension of the vault-basicranium module which covers the posterodorsal part of the zygomatic arches (Figure 54; Figures S44 & S46). Finally, contrary to *Dasypus* and *Zaedyus*, the *Cabassous* datasets do not show a posteroventral extension of the orbit-neurocranium module around the most anteroventral part of the neurocranium, which results in a vault-basicranium module almost entirely covering the caudal cranium in the *Cabassous* datasets (Figure 54; Figures S44 & S46). In the *CabassousNS*, a slight asymmetry of modularity was detected for four landmarks (#41; #45; #64 & #111) located at the level of the alisphenoid and the optic canal (attributed to orbit-neurocranium module on the left side, and vault-basicranium module on the right) (Figure 54; Figure S44). It is probably due to the strong variation of these points in several individuals within *CabassousNS*. Figure 54 summarizes the distribution of landmarks in each module among all species and datasets.

CHAPTER 4: Exploration of Cranial Covariation Pattern in Cingulata



CHAPTER 4: Exploration of Cranial Covariation Pattern in Cingulata

Figure 54. Top: mapping of the modules obtained for each species in dorsal and lateral view (only *Cabassous*NS is represented, see [Figure S59](#) for *Cabassous*N) at the ontogenetic, and static levels. Phylogenetic relationships between the three species are indicated based on molecular and morphological studies ([Billet et al., 2011](#), [Delsuc et al., 2016](#), [Gibb et al., 2016](#) - colors follow [Mitchell et al., 2016](#)). Bottom: concatenation of the distribution of each landmark in each module between the three species as a percentage represented by diagrams (considering both *Cabassous* datasets) is provided, mapped onto a skull of *Dasyus novemcinctus* in dorsal view. The number of every landmark that is shared by several modules is indicated. In red, face/anterior-face module; in purple, mid-face module; in green, orbit-neurocranium module; in blue, vault-basicranium module. Scale = 1 cm.

Most landmarks are consistently found in the same modules among the three species ([Table S30](#)), with the least stable landmarks corresponding to the areas of contact between modules, such as the contact between the frontal and nasal bones, the most posterior part of the snout and the region connecting the first half of the neurocranium to the posterior part of the orbitotemporal region ([Figure 54](#); [Table S30](#)).

The static level differs from the ontogenetic level in *D. novemcinctus* by a larger posterodorsal extension of the orbit-neurocranium module similar to that retrieved in *Z. pichiy* and *Cabassous* datasets at the ontogenetic level ([Figure 54](#); [Figures S44](#), [S45](#) & [S46](#)). This module thus becomes the largest at this level in this species, and covers all of the anterior half of the neurocranium. In *Zaedyus pichiy*, the vault-basicranium module is no longer present on the zygomatic arches and is replaced there by the orbit-neurocranium module, which then completely encompasses these structures (landmarks #51 & #52) ([Figure 54](#); [Figure S45](#)). For *Cabassous*, the two datasets exhibit the same modular distribution at the static level, with only a few changes compared to the ontogenetic level ([Figure 54](#); [Figures S45](#) & [S46](#)). There is no asymmetry of modules at this level. The posterior extension of the orbit-neurocranium module is weaker at the static level in *Cabassous*N than in the ontogenetic level, with the transfer of the landmark connecting the parietal, supraoccipital and squamosal (landmarks #70 & #71) from the orbit-neurocranium module to the vault-basicranium module ([Figure 54](#); [Figure S46](#)). The summarized distribution of landmarks among the three species at the static level shows that the least stable landmarks correspond to the contact between the nasal and frontal and the contact between orbit-neurocranium and vault-basicranium modules, which is largely similar to the patterns observed at the ontogenetic level ([Figure 54](#), [Table S46](#)).

4.2.4 DISCUSSION

Cranial modularity hypotheses have flourished in the literature over the last thirty years. Studies either tested several *a priori* hypotheses of modularity on the basis of functional or developmental arguments (*e.g.*, Hallgrímsson *et al.*, 2004; Willmore *et al.*, 2006) or searched for modular patterns without *a priori* assumptions (Cheverud, 1982a; Goswami, 2006; Zelditch *et al.*, 2009). Mammals have been the subject of these investigations without *a priori* assumptions, with more attention paid to primates, rodents, and carnivorans (see Klingenberg, 2013). The most commonly supported patterns range from 2 modules (face/neurocranium – Drake & Klingenberg, 2010) to about 10 modules distributed across the skull (*e.g.*, Parr *et al.*, 2016; Churchill *et al.*, 2019). Using interlandmark distances, we detected 3 anteroposteriorly distributed modules both at ontogenetic and static levels in *Cabassous* and *Zaedyus* (face, orbit-neurocranium and vault-basicranium), with *Dasypus* showing an additional parcellation of the face module into an anterior-face module and a mid-face module. The anteroposterior distribution of modularity in these taxa stands out regarding previously supported hypotheses, which most often suppose a division of the placental skull into six modules distributed in various directions (*e.g.*, Cheverud, 1995; Goswami, 2006; Goswami & Finarelli, 2016). However, our results also strongly support a major division into two larger modules corresponding to the face/neurocranium complex (*i.e.*, first two branches of the distance tree – Figures S44 & S45). The addition of a third, or even a fourth module, corresponds closely to several empirical hypotheses of the distribution of integration in mammalian skulls (Cheverud, 1982a; Hallgrímsson *et al.*, 2007), that recognize the rostrum, neurocranium and basicranium as separate modules (*e.g.*, Del Castillo *et al.*, 2017), although the neurocranium and basicranium are each partly separated within our two posterior modules (orbit-neurocranium and vault-basicranium modules). This partition gives us a first global view on the distribution of morphological integration on the skull of three cingulate species and highlights above all the particularity of *Dasypus* compared to the two others, with its two modules on the face.

Long-nosed armadillos (*Dasypus*) exhibit a strong craniofacial allometry (Hautier *et al.*, 2017; Section 3.1), which is also supported by the high proportion of selected pairs of correlated S-distances that were related to this pattern at the ontogenetic level (Section 4.1). Our previous results on cranial allometry have also suggested a weaker craniofacial allometry in *Cabassous* and

Zaedyus compared to *Dasypus* (Section 3.2). We therefore hypothesize that the additional module in *Dasypus* is due to a stronger craniofacial allometry. It is already well known that size is a powerful integrating factor and could affect modular distribution especially at the ontogenetic level (Mitteroecker & Bookstein, 2007; Klingenberg, 2013; Porto *et al.*, 2013). It would be interesting to test this hypothesis further in different ontogenetic stages in long-nosed armadillos as the number of modules may also vary during ontogeny (*e.g.*, Zelditch, 2005; Hallgrímsson *et al.*, 2009; Gonzalez *et al.*, 2011; Klenovšek, 2014; Klenovšek & Jojić, 2016). However, at the static level, the distribution of modules barely changes relative to the ontogenetic level and the two modules on the face are still supported in *Dasypus*. This stability of modular architectures throughout ontogeny is consistent with the results of a previous study on Japanese macaques (Goswami & Finarelli, 2016) and other primates (Ackermann, 2005).

The difference in facial patterns observed between *Dasypus* and the other two armadillo species in our sample could be the result of other developmental factors as well, in addition to a stronger craniofacial allometry. For instance, potential explanations can be explored in the proliferation rates and patterns of cells and chondrocytes of the face and sphenothmoidal synchondrosis, which show differences between taxa of different snout shapes (Smith *et al.*, 2017; Camacho *et al.*, 2020). These are only lines of reasoning, but it is clear that a good way to further explore these differences lies in the study of these developmental processes which remains understudied in armadillos (Loughry *et al.*, 2015). In any case, the existence of two modules on the face in *Dasypus*, with an anterior face module and a mid-face module, is consistent with the results of several studies on modularity which highlight a strong relationship between naso-frontal landmarks and landmarks in a molar-palate area. These studies have shown that the naso-frontal landmarks and the molar landmarks may constitute an individual module (Cheverud, 1982a; Goswami, 2006; Parr *et al.*, 2016; Churchill *et al.*, 2019), which would closely resemble our mid-face module in *Dasypus*.

A next step for this work would be to compare our modular hypothesis to existing mammalian modular models using a confirmatory approach (*e.g.*, Goswami & Finarelli, 2016). The addition of such an analysis will allow us to further evaluate the robustness of our modular hypotheses and draw comparisons between cingulates, the most diverse group of Xenarthra, and other mammals.

4.3 3D Cranial Shape Variation in Cingulata

ABSTRACT

Morphological variation impacts the shape in different coordinated manners. 3D geometric morphometrics (GMM) is a widely used method that allows quantification of shape differences between objects using landmark coordinates. A few studies have quantified variations in skull shape in cingulates, but never on the whole diversity within the clade using 3D coordinates. This kind of study is desirable to document variations in cranial shape at the evolutionary level in the group, and to uncover a wider range of potential covariations. We investigate the cranial shape diversity of cingulate species with 3D GMM using Principal Component Analysis. We explore seven evolutionary datasets incorporating a large diversity of extant and fossil cingulates. These seven datasets correspond to analyses on the entire skull and on the modules defined in the preceding section. The detected variations in shape are reminiscent of several allometric variations detected in previous sections of this thesis, but also demonstrate additional shape changes that occurred in the group.

4.3.1 INTRODUCTION

Morphological variation is a complex phenomenon affecting the shape of an organism in multiple directions. Quantification of morphological variation can be performed using several complementary approaches ranging from the analysis of shape of an anatomical object such as the skull (Klingenberg & Marugán-Lobón, 2013) to the scrutiny of the relationship between two shape variables (*e.g.*, Cheverud, 1982a), the correlation of shape with an external factor (*e.g.*, diet, geographical distribution – Nogueira *et al.*, 2009; Cáceres *et al.*, 2014) or with a variable such as size, for investigating allometry (Klingenberg, 2016). 3D geometric morphometrics is a much-used method that allows quantification of morphological differences between objects using landmark coordinates (Adams *et al.*, 2004; Zelditch *et al.*, 2012). Compared to linear distances, it offers the advantage of quantifying more components of shape variation, especially by enabling the use of three-dimensional data.

Several studies have quantified shape variation in cingulates using linear distances on the skull (or mandible) within (Squarcia *et al.*, 1993; Squarcia & Casanave, 1999; Squarcia *et al.*, 1999; Squarcia *et al.*, 2006; Squarcia *et al.*, 2009) or among armadillo species (Squarcia *et al.*, 2007; Sidorkewicz & Casanave, 2012, 2013; Hubbe *et al.*, 2016). Shape variation in the group has also been addressed with linear distances on postcranial material (Vizcaíno & Fariña, 1996; Vizcaíno *et al.*, 1999; Vizcaíno & Milne, 2002; Vizcaíno *et al.*, 2003; Vizcaíno *et al.*, 2006; De Esteban Trivigno *et al.*, 2008; Galliari *et al.*, 2010) and even on the shape of cells (Polini *et al.*, 1999; Codón *et al.*, 2001; Sousa *et al.*, 2013).

The first analyses of geometric morphometrics (GMM) on armadillos used two-dimensional landmarks to characterize morphological variation of skull by comparing the patterns of a few extant and fossil specimens (Vizcaíno & Bargo, 1998; Vizcaíno *et al.*, 1998; De Iuliis *et al.*, 2000; Vizcaíno & De Iuliis, 2003; Vizcaíno *et al.*, 2004). More recently, 2D GMM was used to analyze morphological variation of the postcranial material (Oliver *et al.*, 2016; Acuña *et al.*, 2017) or cranial (or mandibular) variation in relation to different factors such as geography, environment or diet (Serrano-Fochs *et al.*, 2015; Magnus *et al.*, 2018).

A more powerful way to characterize shape variation involves the use of 3-dimensional landmarks (Rohlf & Marcus, 1993). In cingulates, 3D GMM studies were performed either on postcranial material (Milne *et al.*, 2009; Milne & O'Higgins, 2012; Milne *et al.*, 2012), cranial

CHAPTER 4: Exploration of Cranial Covariation Pattern in Cingulata

shape within a clade (Abba *et al.*, 2015; Feijó & Cordeira-Estrela, 2016; Hautier *et al.*, 2017; Feijó *et al.*, 2018; Feijó *et al.*, 2020; Section 3.1) or on selected cranial regions (*e.g.*, inner ear; Billet *et al.*, 2015a; Coutier *et al.*, 2017). To our knowledge, no analysis of the shape of the cingulate skull using 3-dimensional landmarks has been performed on the whole diversity of the group.

In this PhD dissertation, we first explored the variations in cranial shape correlated with size in cingulates (Chapter 3). We then tried to detect the strongest covariations between interlandmark distances (SubChapter 4.1) and, finally, we explored for the first time cranial modular patterns (SubChapter 4.2). However, an analysis of 3-dimensional shape variation among cingulate species is missing. This type of analysis can provide a useful overview of variational patterns in the group, as well as clues on potential covariations at the evolutionary level. Here, we investigate this variation using 3D GMM on the skull of multiple cingulate species, and employing a Principal Component Analysis (Jolicoeur & Mosimann, 1960) to analyse shape variation. This method enables coverage of a large proportion of the shape variation in order to identify potential covariation patterns, because a strong covariance between traits could be correlated with differences in shape variance (Young, 2006). We apply this method on seven evolutionary datasets incorporating a large diversity of extant and fossil cingulates. We analyze shape variation both for the entire skull, but also for the modules detected in the previous section. We briefly describe the main variations obtained from these datasets and discuss these results in the general discussion and conclusion of this PhD dissertation, as it provides avenues for future research on the group.

4.3.2. Material & Methods

4.3.2.1. *Biological sample*

Our sampling for this study was split into seven evolutionary datasets with an aim at incorporating alternatively a maximum number of taxa or a maximum number of landmarks. Among these datasets, three correspond to those used for the analysis of allometry at the evolutionary level (see Section 3.2): DatasetExt, Dataset-Lmax and Dataset-Tmax. A fourth dataset was added to incorporate a maximum number of glyptodonts (referred to as dataset-G hereafter), which lowered the number of landmarks ($n_{\text{taxa}} = 29$; $n_{\text{landmark}} = 60$ – Tables S31 & S32). Three additional datasets were created to analyze the morphological variation within the three modules (referred to as Dataset-M-face; Dataset-M-orbit-neurocranium; Dataset-M-vault-

CHAPTER 4: Exploration of Cranial Covariation Pattern in Cingulata

basicranium) delineated in the preceding section (Section 4.2). Only stable landmarks have been preserved in the composition of these module datasets (see Section 4.2). The taxonomic composition for each dataset is given in Table S31. The taxa added with respect to Section 3.2 are *Propalaehoplophorus minus*, *Eucinepeltus complicatus* and “*Cochlops*” *debilis* (see Chapter 1), which are all Santacrucian glyptodonts.

4.3.2.2 Correction of taphonomic deformations

As for some specimens in Section 3.2, we applied a retrodeformation on the “*Cochlops*” *debilis* specimen. We followed the same method rigorously. We corrected a slight uniform ventral displacement of skull height on the left lateral region of the skull, to match the right lateral part of the skull that is undistorted. This correction is shown in Figure S47.

4.3.2.3 Geometric morphometrics

The acquisition of 3D models and landmarks, as well as the corrections made to them, follow the methodology described in Section 4.1. Please refer to this section for more details. The landmark composition for each dataset is given in Table S32. For *Propalaehoplophorus minus*, *Eucinepeltus complicatus* and “*Cochlops*” *debilis*, the landmark coordinates are available in Table S33, and details about their missing and symmetrized landmark, are given in Table S34.

4.3.2.4 Phylogenetic considerations

To investigate whether the morphometric data contains a phylogenetic signal, we used the multivariate K_{mult} -statistic, which estimates the phylogenetic signal present in the symmetrized Procrustes coordinates for each dataset (Adams, 2014). This was calculated using the function *physignal* of the R *geomorph* package (Adams *et al.*, 2020), with 10,000 permutations to determine the significance. A K_{mult} close to 1 means that the taxa are phenotypically similar, as expected under Brownian motion (Adams, 2014). A K_{mult} greater than 1 means that the taxa are phenotypically more similar than expected by the model, and a K_{mult} less than 1 means that the taxa are phenotypically less similar than expected by Brownian motion (Adams, 2014). The value of the phylogenetic signal served here as an indication of the possible phylogenetic patterning of

the data. It was complemented by the representation of the phylogenetic tree used in the [Section 3.2](#) in the morphospace (*i.e.*, baseline cladogram used in previous chapter – see below and [Figure S4](#)). This same tree was used for the computation of the K_{mult} statistics. We adapted each baseline tree by removing taxa to be discarded while keeping the branch lengths (refer to [Material & Methods – Section 3.2](#)).

Because our goal was to analyze the overall cranial shape variation, we kept all aspects responsible for the shape changes in our analyses. Therefore, no correction was made regarding the effect of phylogeny or allometry. This approach was also favored because this kind of correction in general shape analyses is still strongly debated in the literature (*e.g.*, [Klingenberg, 2016](#); [Uyeda *et al.*, 2018](#)).

4.3.2.5. Shape variation

To investigate major shape variations in the datasets we used a principal component analysis (PCA) ([Jolliffe, 2002](#)) using the *gm.prcomp* function of the *geomorph* R package ([Adams *et al.*, 2019](#)). For each dataset, the corresponding phylogenetic tree was incorporated into the morphospace to illustrate possible phylogenetic relationships. We decided to present only the variations contained in the first two axes (generally representing more than 50% of the total variance). These shape variations were illustrated by vectors representing the minimum and maximum shape of each axis. Using the distance matrix from the principal component scores, we performed neighbor-joining tree estimations ([Saitou & Nei, 1987](#)) of the total variance, using the function *nj* in the *ape* R package v.5.3 ([Paradis & Schliep, 2019](#)). This phenetic analysis considers the overall dissimilarities between all the specimens and makes comparisons between them to build a tree that summarizes overall morphological distances among specimens.

4.3.3 Results

For each dataset, we describe here the main variations of the minimum to maximum shapes observed on the two main axes of PCA. Then we report on the proximity of clusters (*i.e.*, clade and fossil taxa) in the morphological space on these first two axes, which is complemented by the Neighbor Joining tree.

4.3.3.1 *Only extant species*

For the DatasetExt, the first two axes of the PCA account for 73.86% of the total variance (Figure 55). K_{mult} is low (= 0.17072; p -value = 0.0001) which means that the taxa are phenotypically significantly less similar than expected with Brownian motion, assuming a high level of homoplasy. The first axis accounts for almost half of the total variance (60.62%). From the minimal shape (most negative value) to the maximal shape (most positive value) along this axis, we observe that: *i*) almost all landmarks move away from the center of the braincase showing a relative increase in the proportions of neurocranium also affecting part of the face (Figure 55); and, *ii*) the snout is shortened with an increase in its height (#2; #3-4; #31-32) and width (#31-32) accompanied by a strong reduction of tooth row length from its posterior edge (#28-29) and an anterior elongation of the palatine (#18-19). The shape variation along this first axis distinguishes most chlamyphorids (except for the large-sized tolypeutine *Priodontes*) from the long-nosed dasypodids, which plot at negative values. For the second axis (explaining 13.24% of total variance), the anterior part of the snout shows a dorsoventral and mediolateral enlargement at positive values (#2; #3-4; #9-12; #31-32). The premaxillary is elongated anteroposteriorly especially at its posterior ventral end (#5-7). The dental row is also relatively more elongated anteriorly (#26-29) and the posterior part of the palate is less ventrally positioned (#18-19; #28-29; #30). The orbit is strongly displaced anteroventrally position (#35-40; #47-50). The parietal extends more anteriorly (#66-67). The orbitotemporal region narrows mediolaterally (#41-42; #45-46; #64-65; #111-112). The posterior part of the zygomatic arch and the anterior part of the basicranium take a more posteromedial position while the rest of the basicranium takes a more posterior position (Figure 55). Finally, the tentorial process is displaced further anteriorly (#63) and the nuchal crests extend more ventrolaterally (#73-74). These shape changes are driven largely by *Priodontes*, which plots at high PC2 values, as opposed to chlamyphorines at negative values. All dasypodids, euphractines and other tolypeutines are clustered at median values.

On the PC1-2 morphospace, a slight overlap is detected between the tolypeutines and the euphractines (Figure 55). In contrast, the Neighbor Joining (NJ) tree (computed on 100% of the variance) shows a closer resemblance between chlamyphorines and euphractines (Figure 55). Dasypodines are well differentiated from other armadillos on the NJ tree, as are most tolypeutines (Figure 55).

CHAPTER 4: Exploration of Cranial Covariation Pattern in Cingulata

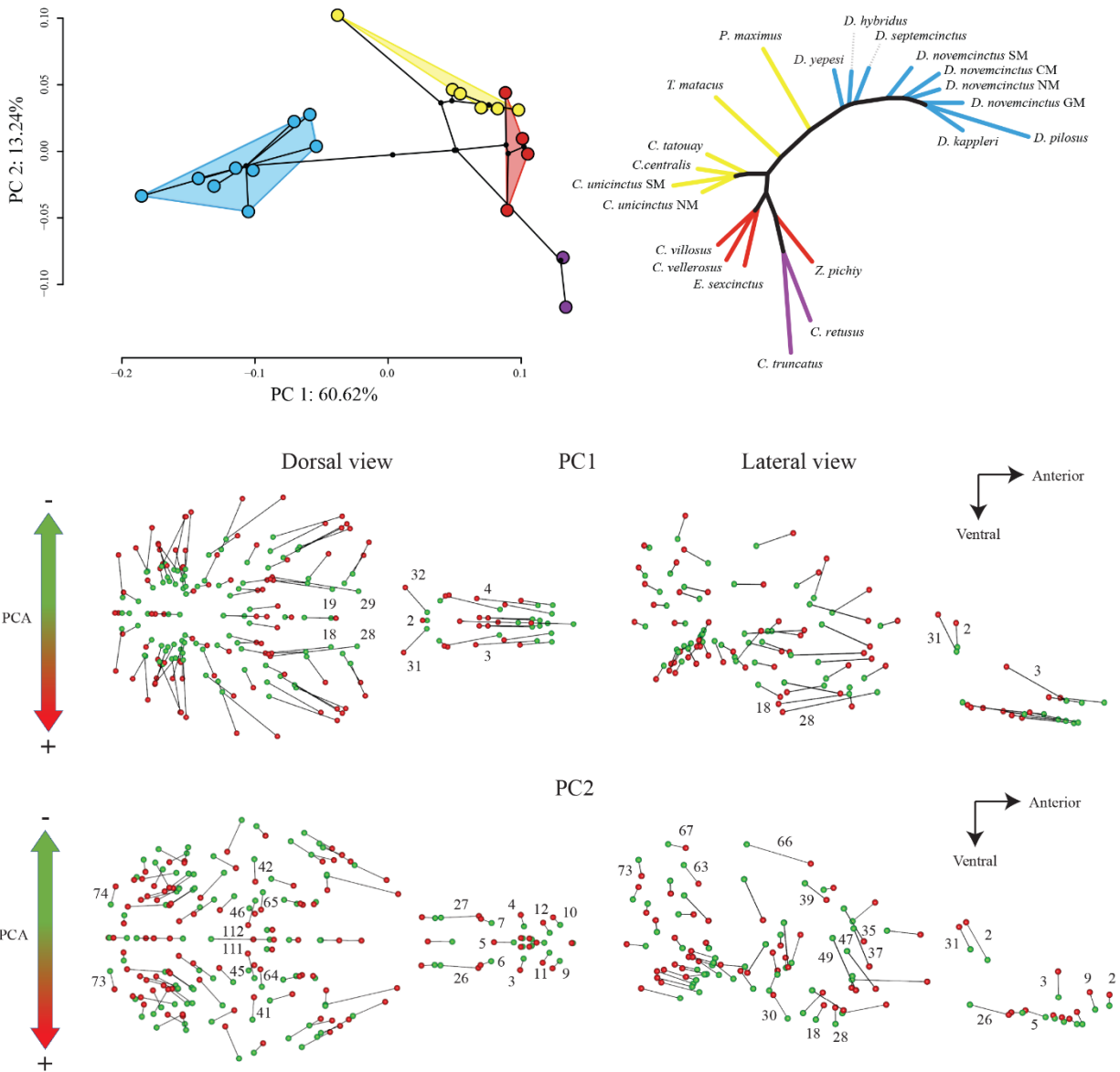


Figure 55. Principal Component Analysis on the DatasetExt with a neighbor-joining tree estimation for the total variance. Morphological shape changes on each axis are represented from the minimal (green) to the maximal (red) value of each axis. Landmarks discussed in the text are numbered for enhanced readability.

4.3.3.2. Extant and Fossils Best Sample

The three datasets incorporating extant and fossil taxa provide similar results and shape variations. For the Dataset-Lmax, the first two axes of the PCA account for 64.92% (Dataset-Tmax = 55.74%; Dataset-G = 70.54%) of the total variance (Figure 56; Figures S48 & S49). K_{mult} is low (= 0.26879; p -value = 0.0001; Dataset-Tmax: K_{mult} = 0.24397; p -value = 0.0001; Dataset-G: K_{mult} = 0.20687; p -value = 0.0001) which means that the taxa are phenotypically significantly less

CHAPTER 4: Exploration of Cranial Covariation Pattern in Cingulata

similar than expected with Brownian motion, assuming a high level of homoplasy. The first axis accounts for almost half of the total variance (48.04%; Dataset-Tmax = 37.75%; Dataset-G = 57.38%). From the minimum shape (most negative value) to the maximum shape (most positive value) along this axis, we observe a relative elongation, dorsoventral and mediolateral narrowing of the snout (#2-4; #6-7; #9-12; #31-32) accompanied by a relative reduction in the length of the dental row, especially at its posterior edge (#26-29), and a posteromedial migration of the postorbital constriction (#39-40). The anterior edges of the zygomatic arches assume a much more posteromedial relative position (#20-21; #33-38; #47-50). The posterior part of the cranial vault narrows mediolaterally. The rest of the points tend to slightly converge towards the center of the braincase. The shape variation along this first axis distinguishes glyptodonts (negative values) from dasypodines (positive values). Tolypeutines, euphractines, chlamyphorines, *Vassallia* and *Peltephilus* are more or less all grouped around the same values (Figure 56).

For the second axis (explaining 16.88% of total variance) (dataset-Tmax = 37.75%; dataset-G = 57.38%), the variation corresponds mainly to the reduction of the relative proportions of the braincase towards positive values. We also note a relative mediolateral widening of the anterodorsal part of the snout (#3-4; #9-10; #31-32). The shape variation along this second axis appears to be highly allometric. It distinguishes small taxa such as chlamyphorines (most negative values) from large taxa (most positive values) such as glyptodonts, *Vassallia*, *Priodontes* and a large proportion of dasypodines (Figure 56).

On the Neighbor Joining tree, chlamyphorines are nested within euphractines (Figure 56, Figures S48 & S49). Dasypodines show strong dissimilarity with other taxa (Figure 56, Figures S48 & S49). Tolypeutines are split and represent the extant clade most resembling fossil taxa (Figure 56, Figures S48 & S49). *Vassallia* appears close to the glyptodonts (Figure 56, Figures S48 & S49). Finally, *Peltephilus* and *Proeutatus* are close to the group formed by the latter two (Figure 56, Figures S48).

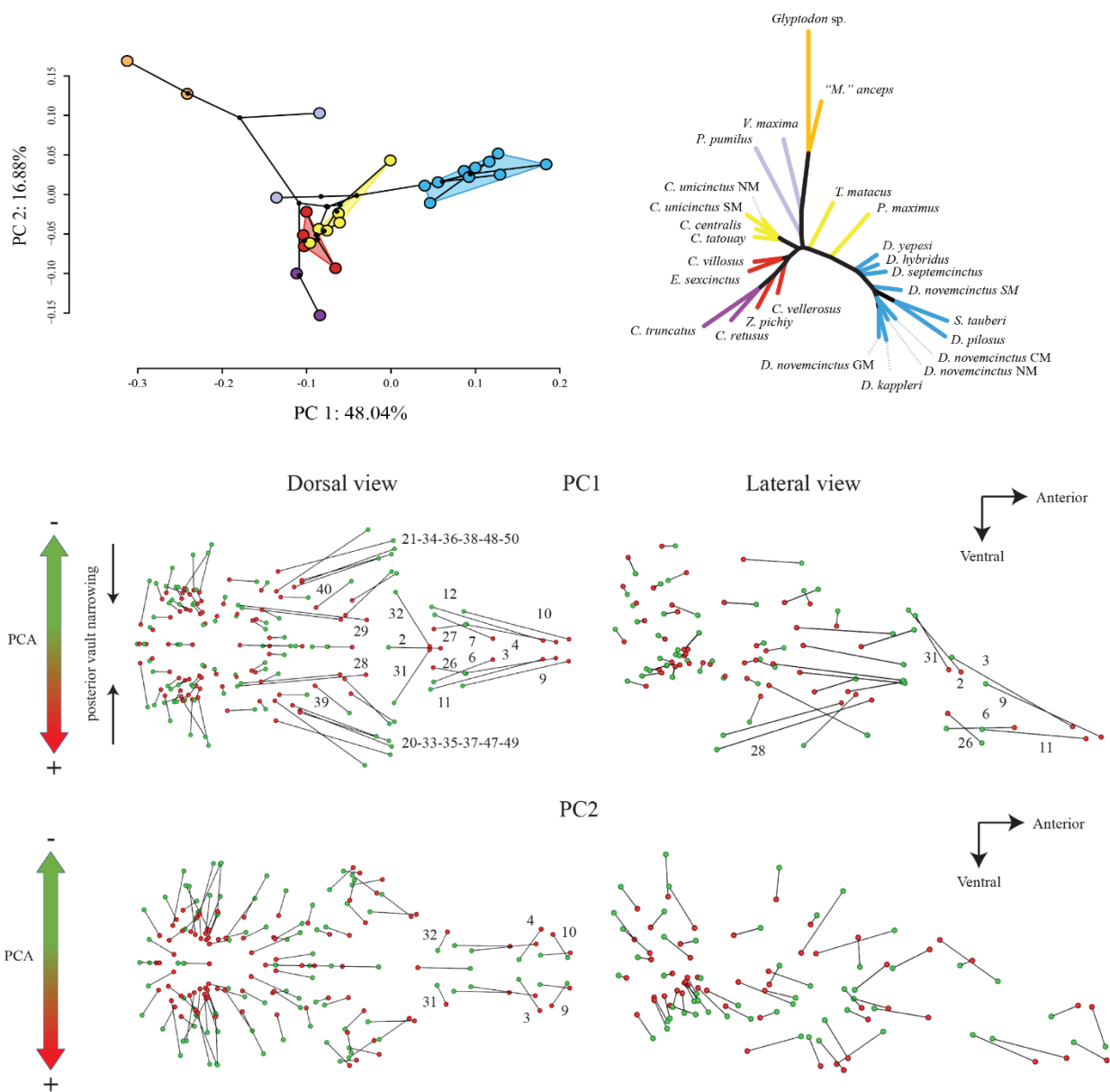


Figure 56. Principal Component Analysis on the Dataset-Lmax with a neighbor-joining tree estimation for the total variance. Morphological shape change on each axis are represented from the minimal (green) to the maximal (red) value of each axis. Landmarks discussed in the text are numbered for enhanced readability.

4.3.3.3. Intramodular Morphological variation

For the dataset-M-face, the first two axes of the PCA account for 82.72% of the total variance (Figure 57). K_{mult} is low ($= 0.54089$; p -value $= 0.0001$) which means that the taxa are phenotypically significantly less similar than expected with Brownian motion, assuming a high level of homoplasy. The first axis accounts for more than three-fifths of the total variance (64.37%). From the minimum shape (most negative value) to the maximum shape (most positive

CHAPTER 4: Exploration of Cranial Covariation Pattern in Cingulata

value) along this axis (Figure 57), the face module shows a relative shortening posteriorly due to the anterior shift of the posterior extremity of the dental row (#26-27). The anterior part of the module shows a relative broadening of the premaxillary in several directions. Ventrally, the anterior processes of the premaxillary (#11-12) take a more posterolateral and more ventral position. Dorsally, the most anterior point of the internasal is located relatively more anteriorly (#1) while the rest of the landmarks defining the anterolateral extremities of the nasal shows a strong mediolateral relative widening (#3-4; #9-10). Overall, the anterior part of the module also shows a strong relative increase in height (#3-4; #8-14). Finally, the incisive foramina (#13-16) and the anterior end of the premaxillary on the midline (#8) migrate much further posteriorly. This shape is found in dasypodines, which plot exclusively at low PC1 values. Glyptodonts, *Vassalia* and *Peltephilus* plot at positive values and thus rather exhibit the opposite shape pattern, while tolypeutines, euphractines and chlamyphorines are found at more intermediate values.

For the second axis (explaining 18.35% of total variance), from the minimum shape (most negative value) to the maximum shape (most positive value) along this axis (Figure 57), the anterior edge of the dental row (#26-27) takes a relatively more anterodorsal and lateral position. The triple contact point between premaxillary - maxillary - nasal (#3-4) is located much more posterodorsal, but also relatively more medial, while the most anterior point of the premaxillary - nasal suture (#9-10) moves anteroventrally and medially. Combined, these relative variations show a strong elongation of the dorsal part of the premaxillary. The variation of these landmarks also indicates a relative mediolateral narrowing of the front of the snout. When combined with the most anterodorsal point of the internasal suture (#1) and the most anterior points of the ventral part of the premaxillary (#8; #9-10#11-12), it also creates a slight shift in the orientation of the narial aperture anteroventrally. Finally, the anterior margin of the incisive foramina migrates anteriorly (#13-14). This shape variation distinguishes glyptodonts, corresponding to the lowest values of PC2, from euphractines, which show the highest values of PC2 (Figure 57). The other taxa are found at more intermediate values.

The NJ tree shows a good discrimination of dasypodines based on the shape of this module (Figure 57). In contrast, the distribution of the other extant clades shows less congruence with the systematics of the group (Figure 57). Fossil specimens are found closer to a subset of euphractines defined by *Euphractus* and *Chaetophractus* (Figure 57). We also note that chlamyphorines are closely linked to *Tolypeutes* in this tree (Figure 57).

CHAPTER 4: Exploration of Cranial Covariation Pattern in Cingulata

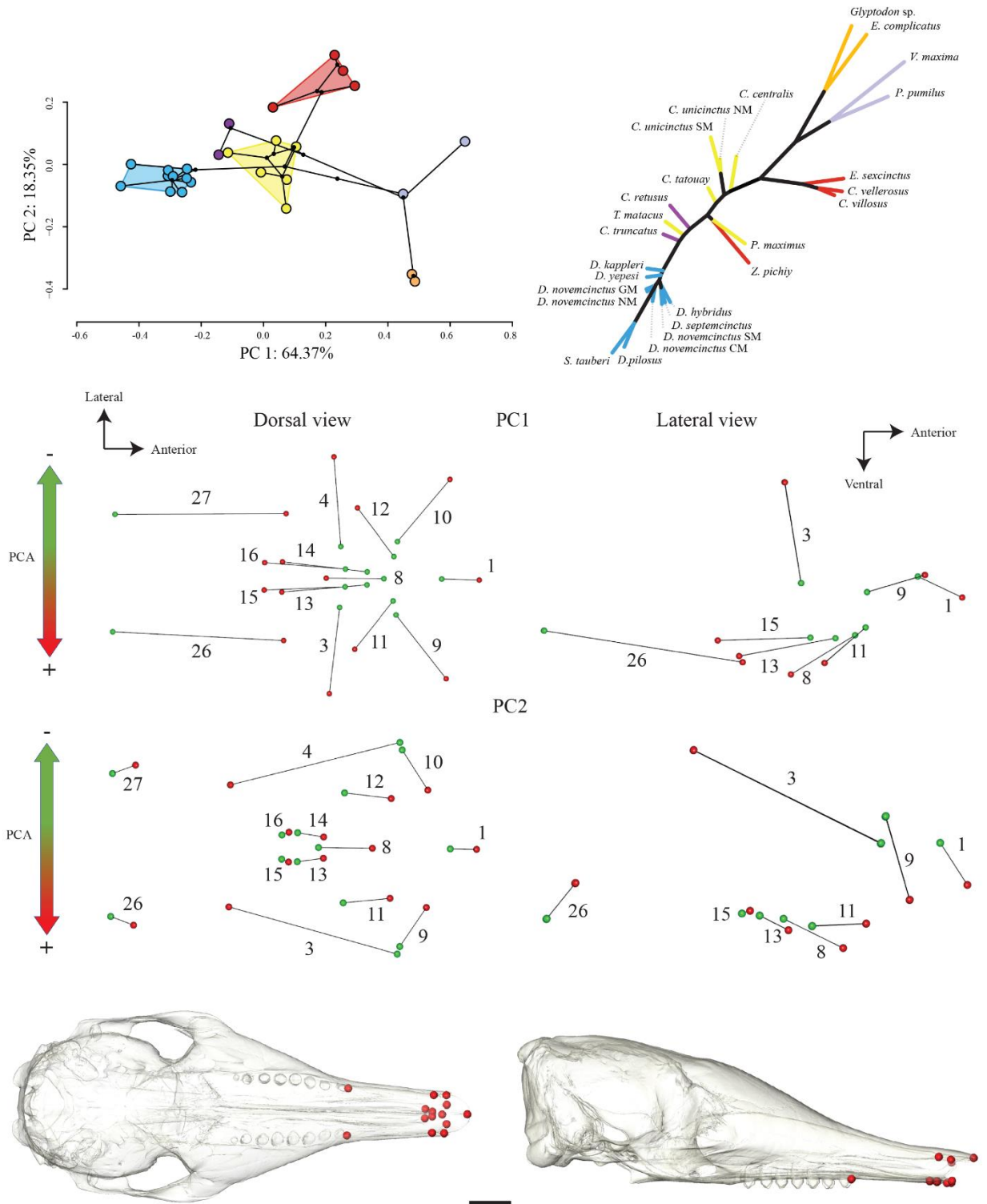


Figure 57. Principal Component Analysis on the Dataset-M-face with a neighbor-joining tree estimation for the total variance. Morphological shape changes on each axis are represented from the minimal (green) to the maximal (red) value of each axis. Landmarks discussed in the text are numbered for more readability. A skull of *Dasyptes novemcinctus* in ventral and lateral views is added to illustrate the module in each view. Scale = 1cm.

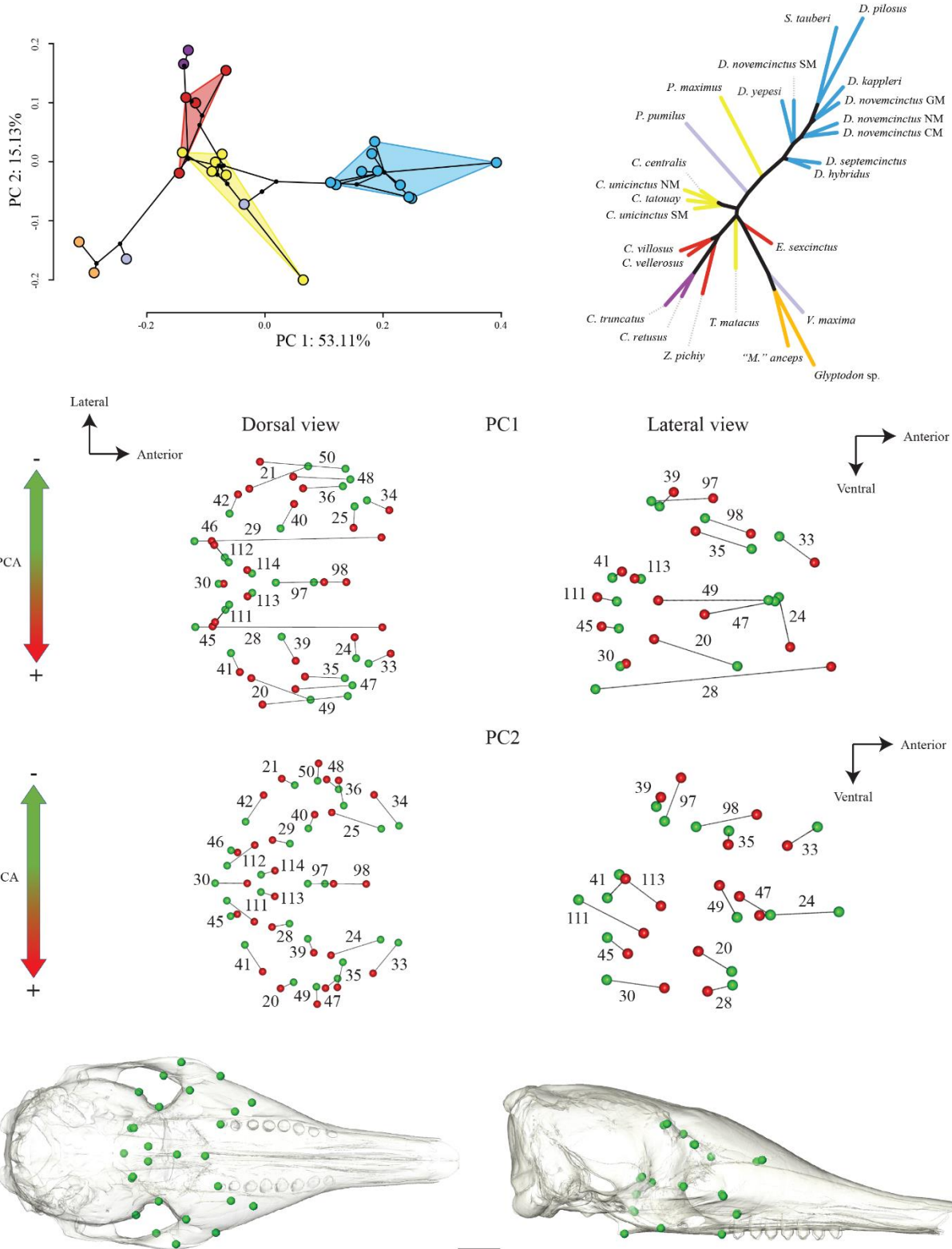
CHAPTER 4: Exploration of Cranial Covariation Pattern in Cingulata

For the dataset-M-orbit-neurocranium, the first two axes of the PCA account for 68.24% of the total variance (Figure 58). K_{mult} is low ($= 0.19177$; $p\text{-value} = 0.0001$) which means that the taxa are phenotypically significantly less similar than expected with Brownian motion, assuming a high level of homoplasy. The first axis accounts for more than half of the total variance (53.11%). From the minimum shape (most negative value) to the maximum shape (most positive value) along this axis (Figure 58), the orbit-neurocranium module shows a very strong anterodorsal migration of the posterior edge of the dental row (#28-29), whereas the most posterior point of the palatine midline (#30) hardly varies in comparison. The most dorsal point of the infraorbital foramen (#24-25) takes a much more ventromedial relative position. The intersection between jugal - maxillary suture and ventral edge of zygomatic arch (#20-21) moves more posterodorsal but also more medial. The anterior orbital edge (#35-36; 47-50) is located much more posterior, and this is accompanied by a slightly more dorsal position for the intersection between the lacrimal - frontal suture and the anterior orbital edge (#35-36) and a slightly more ventral position for the triple contact point between maxillary - jugal - lacrimal (#47-48). In contrast to the orbital edge, the rest of the anterodorsal part of the module (*i.e.*, most landmarks on the frontal bone) is shifted relatively anteriorly or anteroventrally (#33-34; #39-40; #97,98). In addition, the triple contact point between squamosal-frontal-alisphenoid extends further anterolaterally (#41-42). The most anteroventral point of the sphenorbital fissure (#45-46) and the most dorsal point of the internal posterior aperture of the optic canal (#111-112) occupy a more posterolateral position. This shape mostly corresponds to dasypodines which are included in the highest values of PC1 while glyptodonts and *Vassallia* possess the lowest values. The other taxa are found at more intermediate values. We can nevertheless note that *Priodontes* tends to more closely resemble the dasypodines on axis 1 than the other taxa.

For the second axis (explaining 15.13% of total variance), from the minimum shape (most negative value) to the maximum shape (most positive value; Figure 58), the orbit-neurocranium module shows a slightly more posteroventral relative position of the posterior edge of the dental row (#28-29) while the most posterior point of the median palatine suture (#30) moves anteriorly. The internal landmark close to the cribriform plate (#111-114) take a more anteroventral and lateral position. Overall, without describing the vectors of every single landmark on this module, the deformation towards positive values on PC2 produces an anteroposterior shortening and a mediolateral widening of the module. We also note that the proportions of the orbit are reduced

CHAPTER 4: Exploration of Cranial Covariation Pattern in Cingulata

(#35-36; #39-40; #47-50) and that the two internal landmarks present in the dorsal part of the ethmoid fossa on the midline (#97-98) show a more anterodorsal position.



CHAPTER 4: Exploration of Cranial Covariation Pattern in Cingulata

Figure 58. Principal Component Analysis on the Dataset-M-orbit-neurocranium with a neighbor-joining tree estimation for the total variance. Morphological shape changes on each axis are represented from the minimal (green) to the maximal (red) value of each axis. Landmarks discussed in the text are numbered for more readability. A skull of *Dasypus novemcinctus* in ventral and lateral views is added to illustrate the module in each view. Scale = 1cm.

This shape mostly corresponds to chlamyphorines and euphractines, which possess the highest values on PC2 while glyptodonts, *Vassallia* and *Priodontes* express the lowest values. This axis seems highly allometric, with a strong distinction between small and large taxa.

As for the face module, the NJ tree for the orbitotemporal/neurocranium module results in strong discrimination of dasypodines (**Figure 58**). In contrast, the distribution of the other extant clades shows a lesser congruence with the systematics of the group (**Figure 58**). Glyptodonts and *Vassallia* are found close to *Euphractus* and *Tolypeutes* (**Figure 58**). We also note that chlamyphorines most closely resemble *Chaetophractus* and *Zaedyus* (**Figure 58**).

For the dataset-M-vault-basicranium, the first two axes of the PCA account for 56.88% of the total variance (**Figure 59**). K_{mult} is low ($= 0.23742$; $p\text{-value} = 0.0001$) which means that the taxa are phenotypically significantly less similar than expected with Brownian motion, assuming a high level of homoplasy. The first axis accounts for more than a third of the total variance (38.42%). From the minimum shape (most negative value) to the maximum shape (most positive value) (**Figure 59**), the vault-basicranium module varies primarily in the vault area. This variation includes a relative increase in the height of the entire module, especially in the posterior part of the vault (#55-56; #67; #70-74; 99-100). A relative decrease in width of this entire module is also visible (#55-58; #70-71; #73-74). In addition, the most posterodorsal point of the zygomatic ridge of the squamosal (#55-56) is relatively more posterodorsal and medial, and is separated by an increased distance from the most dorsal point of the external acoustic meatus on the squamosal (#57-58) that shows a more posteroventral and more medial position. This suggests a strong increase in height between these two structures. This shape mostly corresponds to glyptodonts, but also to euphractines and some tolypeutines. They have the highest values on this axis, while the negative values correspond to dasypodines.

CHAPTER 4: Exploration of Cranial Covariation Pattern in Cingulata

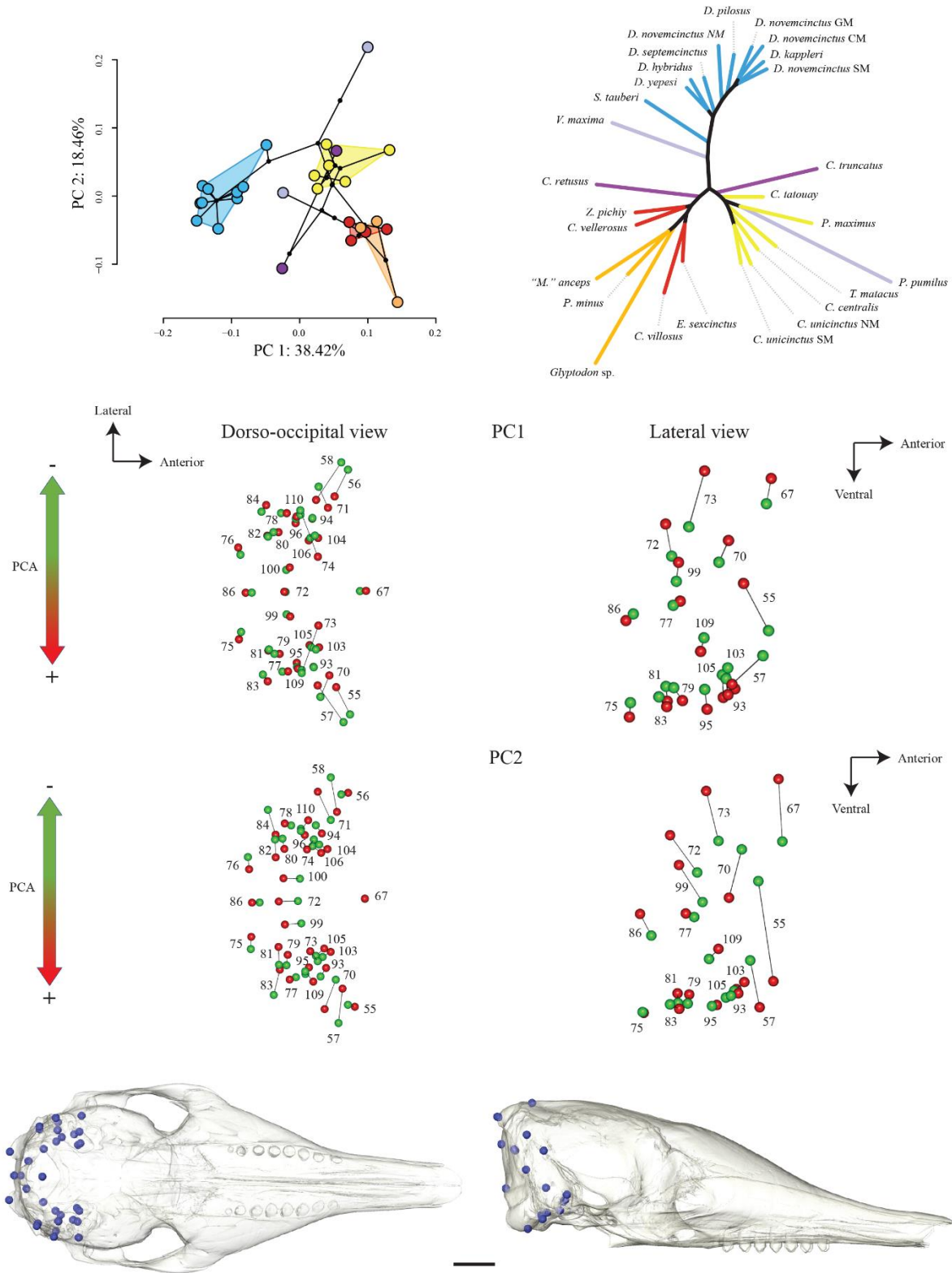


Figure 59. Principal Component Analysis on the Dataset-M- vault-basiscranium with a neighbor-joining tree estimation for the total variance. Morphological shape changes on each axis are represented from the minimal (green) to the maximal (red) value of each axis. Landmarks discussed in the text are numbered for more readability. A skull of *Dasybus novemcinctus* in ventral and lateral views is added to illustrate the module in each view. Scale = 1cm.

CHAPTER 4: Exploration of Cranial Covariation Pattern in Cingulata

For axis 2 (explaining 18.46% of total variance), from the minimum shape (most negative value) to the maximum shape (most positive value) (Figure 59), the vault-basicranium module shows variations in much the same parts as those observed on axis 1, including a strong increase in the relative height of the vault (#67; #72-74; #99-100). The most posterodorsal point of the foramen magnum (#86) is also shifted dorsally. The most distal point of the supraoccipital on the midline (#72) and the maximum points of the curvature lateral occipital ridge in the caudal cerebral fossa (#99-100) are located relatively more posteriorly. The triple contact point between the parietal - squamosal - supraoccipital (#70-71), the most posterodorsal point of the zygomatic ridge on the squamosal (#55-56) and the most dorsal point of the external acoustic meatus on squamosal (#57-58) all take a more ventral relative position (especially in #55-56). We note that the external acoustic meatus also moves medially whereas the triple contact point of parietal - squamosal – supraoccipital moves laterally. Finally, displacement of most posterior landmarks of the basicranium (#75-76; #79-84) result in a mediolateral narrowing of this region.

Contrary to the other two modules, the relative position of taxa in the morphospace shows many overlaps, and therefore a less clear distinction of clusters (Figure 59). The NJ tree shows a good discrimination of dasypodines, which are closely linked to *Vassallia* (Figure 59). Glyptodonts are found closer to euphractines and *Peltephilus* is found closer to tolpeutines (Figure 59).

As indicated in the Introduction, these results will be discussed along other results of the PhD in the [General Discussion & Conclusion](#) that follows.

GENERAL DISCUSSION & CONCLUSION

« La variation phénotypique est la matière première de la sélection naturelle, mais un siècle après Darwin, c'est un sujet presque inconnu ».

Leigh Van Valen, 1974, Translated.

“Phenotypic variation is the raw material for natural selection, yet a century after Darwin, it is an almost unknown subject”.

Leigh Van Valen, 1974.

5. General Discussion and Conclusion

5.1 *Limitation of taxonomic data and sampling*

A robust systematic framework and detailed knowledge of the taxonomic diversity generally constitute prerequisites for a multitude of biological analyses of a biological clade (*e.g.*, [Tschopp *et al.*, 2015](#)). In studies on morphological integration ([Chapters 3 & 4](#)), one needs a clear definition of the species sampled for analyses at the static and ontogenetic levels ([Klingenberg, 2014](#)). However, as we have observed in our study, the systematics of extant cingulates is often far from clear, and remains the subject of much debate in three of the four extant clades, despite their low diversity, of roughly 21 widely recognized living species (see [Chapter 1](#)).

The dasypodines (long-nosed armadillos) have been extensively investigated in recent years, and are grouped into seven extant species belonging to the single genus *Dasypus* in the latest taxonomic reports (see [Section 1](#)). Recent morphological and molecular studies suggest increasing the number of recognized species, and perhaps the number of genera as well (*e.g.*, [Castro *et al.*, 2015](#); [Feijó & Cordeira-Estrela, 2016](#); [Billet *et al.*, 2017](#); [Hautier *et al.*, 2017](#); [Feijó *et al.*, 2018](#)). The nine-banded armadillo (*i.e.*, *D. novemcinctus*) was probably the most intensively investigated species in recent years. Nine-banded armadillos have a very wide Panamerican geographical distribution ([McBee & Baker, 1982](#)) and might actually represent a complex of two to four distinct species supported by both molecular ([Huchon *et al.*, 1999](#); [Gibb *et al.*, 2016](#); [Feijó *et al.*, 2018, 2019](#); [Arteaga *et al.*, 2020](#)) and morphological evidence ([Hautier *et al.*, 2017](#); [Billet *et al.*, 2017](#)). Our study of cranial allometry in nine-banded armadillos ([Section 3.1](#)) showed similar allometric patterns in a dataset gathering three of the four potential species, as well as within the best-sampled of the four potential species, *i.e.*, the Southern Morphotype. In the rest of our analyses including *D. novemcinctus*, we considered only this best-sampled potential species, to ensure that our sample did not cover more than one species when performing analyses at the static and ontogenetic level. However, we then incorporated all four potential species in the analyses at the evolutionary level. Although we were cautious in taking into account as much as possible the potentially changing

General Discussion & Conclusion

species delimitation, a unified framework for the systematics of long-nosed armadillos remains desirable for this kind of study.

The euphractines are a less diverse clade than the dasypodines, containing 5 species of armadillos according to the latest taxonomic reports ([Chapter 1](#)). Recently, the species *Chaetophractus nationi* was challenged based on morphological and molecular arguments, and merged with the species *Chaetophractus vellerosus* (e.g., [Abba et al., 2015](#); [Gibb et al., 2016](#)). The validity of the latter is also debated in relation to its relationship with *Zaedyus pichiy*, ([Supporting Information 1](#); [Wetzel, 1985](#); [Superina & Abba, 2014](#); [Abba et al., 2015](#); [Carlini et al., 2016](#)). This taxonomic uncertainty with respect to these two species is also highlighted by molecular analyses ([Gibb et al., 2016](#); [Mitchell et al., 2016](#)). For our analyses at the static and ontogenetic level, we restricted our sample to the species *Zaedyus pichiy* because it is the most represented abundantly euphractine in museum collections, though our sample is still plagued by a large amount of missing information attached to specimens (e.g., location, sex...). Our investigation of cranial shape diversity in our sample of *Zaedyus pichiy* revealed a partitioning of the sample into two clusters ([Supporting Information 1](#)). When analyzing allometric variations in adult specimens ([Section 3.2](#)), we also observed a partitioning into two clusters, one small and one large. However, the clusters in the two analyses do not completely coincide (see [Figure 60](#) below). Although we hypothesize that the gap observed in the allometric analysis ([Figure 60](#) below and [Section 3.2](#)) corresponds, at least partly, to a difference in size between females and males (sex data almost absent for our specimens – only three females were positively identified, and these represented minimal body sizes within gp2 – [Figure 60](#), [Supporting Information 1](#)). This would be consistent with what is known about sexual dimorphism in this species ([Sidorkewicz & Casanave, 2013](#); [Superina & Abba, 2014](#)). On the other hand, the division into two clusters in the analysis of cranial shape diversity (gp1 & gp2, see [Supporting Information 1](#)) could reflect the distinction between the two known subspecies, *Zaedyus pichiy pichiy* [Desmarest, 1804](#) and *Zaedyus pichiy caurinus* [Thomas, 1928](#), which also differ in size ([Frechkop & Yepes 1949](#); [Squarcia & Casanave 1999](#); [Superina & Abba, 2014](#)). However, the geographic distributions of the two subspecies are disputed ([Wetzel et al., 2007](#); [Sidorkewicz & Casanave, 2013](#); [Superina & Abba, 2014](#)), and the recent diagnosis of the species ([Superina & Abba, 2014](#)) no longer mentions a difference in their geographic ranges. This is consistent with the distribution of our groups in the PCA in [Supporting](#)

General Discussion & Conclusion

[Information 1](#), which did not derive from distinct geographical areas. Unfortunately, no study has jointly quantified the morphological variation in *Zaedyus pichiy* regarding size, sex, subspecies, and geographical distribution. Such a study is desirable to clarify morphological variations within the species, although the frequent lack of information attached to museum specimens remains an obstacle for any allometric study.

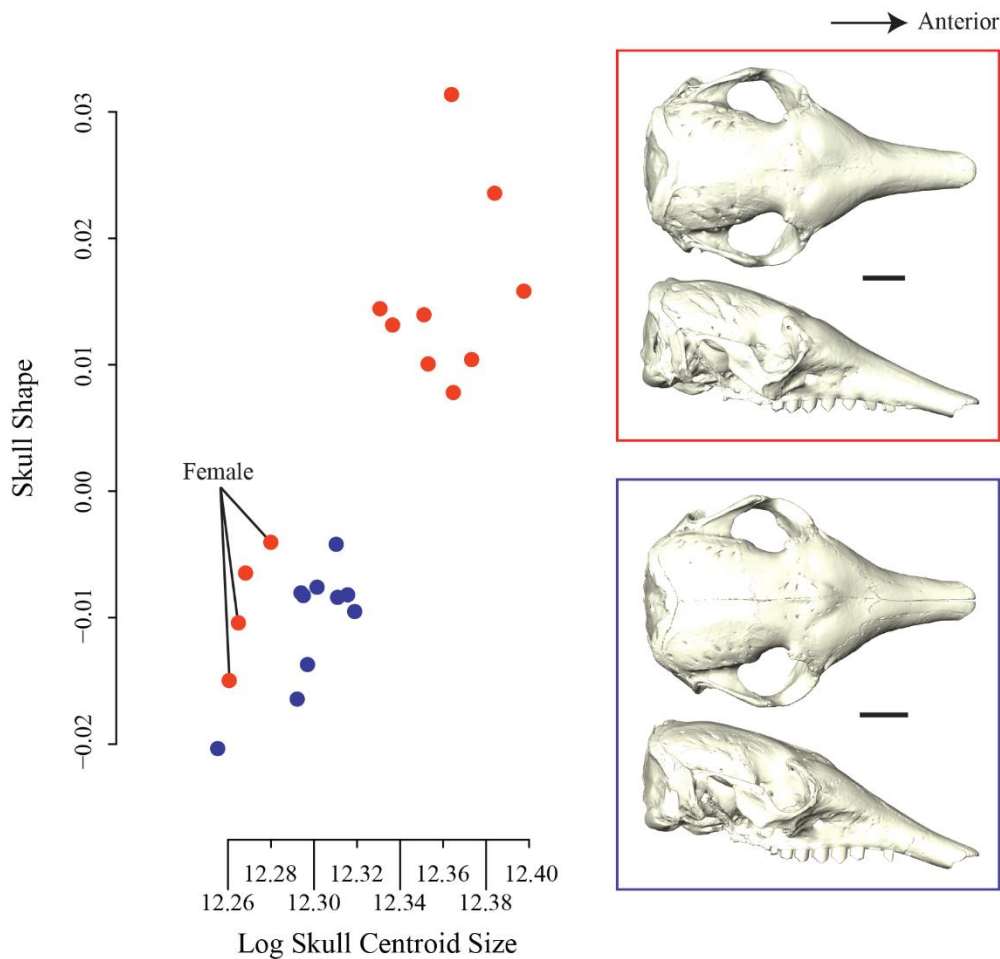


Figure 60. Plot of specimens in the analysis of static allometry on the entire skull (ES) of *Zaedyus pichiy* (Section 3.2). Specimens in blue correspond to gp1 (see Supporting Information 1) and specimens in red correspond to gp2 (see Supporting Information 1). Each group is represented by a skull in dorsal (top) and lateral (bottom) view. Sex is known for only three specimens and is reported on the figure. Scale = 1 cm.

The Tolypeutinae contains 6 currently recognized extant species (Chapter 1). Several taxonomic issues have been raised recently within the genus *Cabassous*. The first issue corresponds to the very weak molecular and morphological distinction between *Cabassous*

General Discussion & Conclusion

unicinctus and *Cabassous centralis* (Hayssen *et al.*, 2013; Hayssen, 2014; Gibb *et al.*, 2016), which calls into question the validity of these two species that are otherwise only distinguished on a geographical criterion. The second issue corresponds to the definition of the species *Cabassous unicinctus*, as revealed in our study of cranial shape diversity. This species showed an unexpectedly strong morphological distinction between specimens of *Cabassous unicinctus* from northern Brazil and those from southern Brazil (Supporting Information 1). Their geographical distribution could coincide with the two subspecies known for this species, *Cabassous unicinctus squamicaudis* Lund, 1845 which occurs north of the Amazon, and *Cabassous unicinctus unicinctus* Linnaeus, 1758, occurring south of the Amazon. These two subsets differed in cranial shape much more strongly from one another than specimens of *Cabassous centralis* differed from specimens of *Cabassous unicinctus* from northern Brazil (Supporting Information 1). For these reasons, we constructed two different datasets in *Cabassous* for our analyses at the static and ontogenetic levels, and we performed each analysis separately on the two datasets. However, as for *Dasyopus*, a clarification of the systematics within the genus *Cabassous* is urgently needed.

In this PhD dissertation, we were able to analyze a wide diversity of extant and fossil cingulate taxa. However, as explained in the previous paragraphs, the persistence of uncertainties concerning the definition of extant species constituted a limiting factor, which we tried to overcome by using several datasets. It is highly probable that these issues occur for other extant cingulate species, beyond the three that were targeted for our intraspecific analyses. Our study clearly reveals that in-depth morphological and molecular accounts of extant armadillo species are urgently needed. As regards analyses at the evolutionary level, the morphological divergence was particularly strong between the extinct and early diverging genus *Peltephilus* and other cingulates (Sections 3.2 & 4.1). A clear morphological gap often separated dasypodines from other clades as well (Section 3.2). Future workers on cranial integration in the group may wish to analyze these morphologically divergent groups separately because they may differ in their patterns of covariation as well. Despite these divergences, our analyses at the evolutionary level recovered covariation patterns similar to those found at the intraspecific level, which suggests that these patterns are pervasive in cingulates.

General Discussion & Conclusion

5.2 Potential implications of internal anatomy and morphological integration on morphological matrices in cingulates

In this PhD Dissertation, we explored the internal anatomy and the morphological integration of the cingulate skull with an aim of examining their potential implications for morphological matrices and phylogenetic relationships in the group. We discuss here our results in relation to the largest morphology-based matrix on the Cingulata, that produced by [Gaudin & Wible \(2006\)](#); abbreviated GW hereafter). We focus on some craniodental characters in this matrix and in the revised version published by [Billet *et al.* \(2011\)](#); abbreviated B hereafter). Greater attention is paid to the matrix of [Gaudin & Wible \(2006\)](#) because the modifications made by [Billet *et al.* \(2011\)](#) were not accompanied by a detailed justification. For this discussion, we have added the following taxa to the matrix: *Calyptophractus* and all glyptodonts of our sample except *Propalaehoplophorus* (see [Chapter 2](#) for coding). Potential evolutionary scenarios (reconstructed using parsimony with DELTRANS optimization) for the characters discussed are mapped below on the baseline cladogram used for [Chapter 2](#) (see [Figure S4](#)). See [Figures S50-S55](#) for plates illustrating the skulls of the cingulate taxa in our analysis in various views.

The results of our study of the internal cranial anatomy are difficult to compare with previous matrices, because no endocranial features were included in previous matrices. In addition, the few studies discussing the implication of internal structures for the phylogeny of Cingulata do not explicitly propose any characters to be included in phylogenetic matrices (*e.g.*, [Fericola *et al.*, 2012](#); [Tambusso & Fariña, 2015a, 2015b](#)). However, it is possible to evaluate the implications of our observations on the GW characters that deal with the external openings of the internal structures we have analyzed. Seven GW characters are relevant in this regard.

Character 71 from [Gaudin & Wible \(2006\)](#) (GW71) coded the relationship between the sphenopalatine foramen and caudal palatine foramen ([Figure 61](#)). In a way, this character thus codes the relationship between the sphenopalatine canal and the palatine canal at the level of their opening in the temporal fossa. Its coding indicates a clear confluence between the two foramina in most cingulates, except for *Stegotherium*, in which they are clearly separated. For several extant taxa – *i.e.*, *Dasypus*, *Chaetophractus*, *Priodontes* and *Tolypeutes* – this character is coded as polymorphic in [Gaudin & Wible \(2006\)](#). In our study (*i.e.*, [Chapter 2](#)), we analyzed the confluence between the two canals well before their opening in the temporal fossa (see character 4 – [Chapter](#)

General Discussion & Conclusion

2). A complete fusion of the two canals may distinguish chlamyphorines and glyptodonts from other cingulates (Chapter 2). Scoring this internal fusion may prove more phylogenetically informative (*i.e.*, *a posteriori* of the phylogenetic analyses) than the seemingly more variable fusion of their external openings.

GW78 deals with the absence/presence of the anterior opening of the posttemporal canal. Our study of the course of the orbitotemporal canal on the internal lateral wall of the braincase in cingulates indicated that all cingulates in our sample except for *Priodontes* had an orbitotemporal canal (or groove) (Chapter 2). *Chlamyphorus* and *Vassallia* were coded "absent" for the anterior opening of this canal in Gaudin & Wible (2006; Figure 61). Our study suggests that this canal and its anterior opening are not absent in the above-mentioned taxa and that its absence may only represent an autapomorphy of the giant armadillo *Priodontes*. In such a case, this character would become uninformative.

Four GW characters correspond to variation in the numerous foramina often present on the cranial roof or close to the posterior root of the zygomatic arch in cingulates (foramina of different origins, see below). Our study showed a high variability for most of these foramina and calls for further investigation (Chapter 2). The character GW94 describes the presence or absence of multiple foramina on the dorsal surface of the frontal bone and suggests a similarity among *Peltephilus*, extant euphractines, tolypeutines (excluding *Tolypeutes*), chlamyphorines, *Proeutatus*, *Vassallia* and some glyptodonts (Figure 61). Our study shows that some of these foramina are derived from branches of the frontal diploic vein canal (Chapter 2), whose presence remains dubious in pampatheres and glyptodonts (Chapter 2). However, some of these frontal foramina have been observed in these groups (Gaudin, 2004; Gaudin & Lyon, 2017). The high variability in their number and the doubts expressed about their presence in *Vassallia* and glyptodonts suggest that this character be abandoned until a better knowledge of these structures is gained. The same applies to characters GW95 and GW97, but this time in relation to the posttemporal and orbitotemporal canals (Figure 61). Character GW95 describes a presence of foramen in the posterolateral region of the frontal in dasypodines (with a polymorphism in *Dasypus*), *Prozaedyus*, extant euphractines, *Cabassous*, *Calyptophractus* and the crown group including *Proeutatus*, *Vassallia* and glyptodonts (excluding *Glyptodon*) (Figure 61). GW 97 describes the presence of more than 5 foramina in the temporal fossa on the parietal, which are present in all cingulates, except for *Chlamyphorus*, dasypodines and *Peltephilus*, and which are

General Discussion & Conclusion

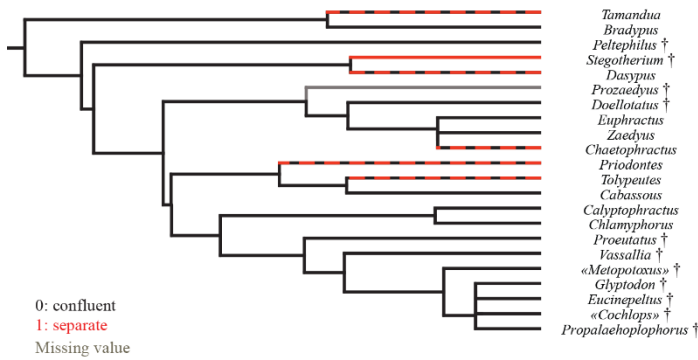
polymorphic in *Tolypeutes* and *Prozaedyus* (Figure 61). A joint revision of characters GW94, GW95 and GW97 is needed and might also focus on the varying density of *rami temporales* observed in our study (Chapter 2).

Finally, GW120 describes the presence or absence of the suprameatal foramen and accompanying accessory foramina (Figure 61). The presence/absence or number of multiple accessory foramina in this region can be variable within the same species (Chapter 2). Our examination of the internal canals has shown that these accessory foramina may correspond to ramifications originating from the posttemporal canal (and sometimes from the orbitotemporal canal), the canal for the capsuloparietal emissary vein or the region of confluence between these canals (Chapter 2). To make this distinction, we need not just endocranial data from skulls, but actual anatomical information on the vasculature housed in these canals. As for GW94, a better knowledge of the variability and homology of these structures is required. In addition, GW120 is highly polymorphic within cingulate species and its scoring also varies much within clades except for chlamyphorines (Figure 61).

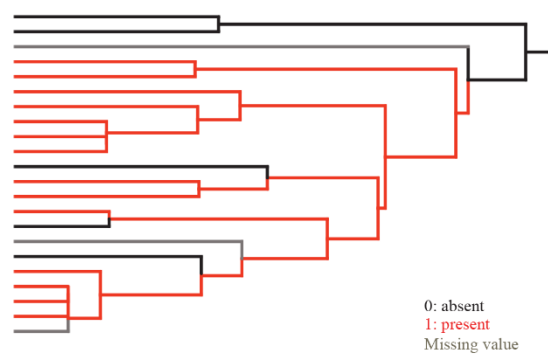
GW111 describes the presence or absence of the foramen transverse canal (Figure 61). This character was weakly informative as it only showed a resemblance between *Stegotherium* and *Chlamyphorus* (foramen absent – defined as a primitive state in Gaudin & Wible, 2006). Our investigation of the internal course of the transverse canal revealed that the *Tolypeutes* specimen in our sample did not possess this canal, which is therefore either absent in this taxon or polymorphic. More importantly, we showed that the orientation of the main branch of the transverse canal suggests a resemblance between *Proeutatus*, the pamphateres and the glyptodonts, with a loss of the canal in Pleistocene glyptodonts. This phylogenetically informative variation could be combined within a single composite character with the variation encoded by GW111 in future analyses (see Chapter 2).

General Discussion & Conclusion

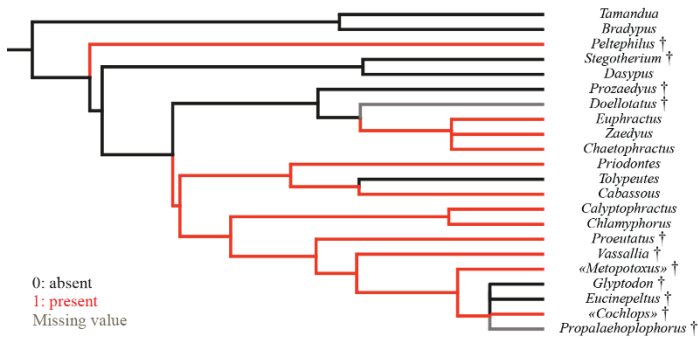
GW71: Sphenopalatine and caudal palatine foramina



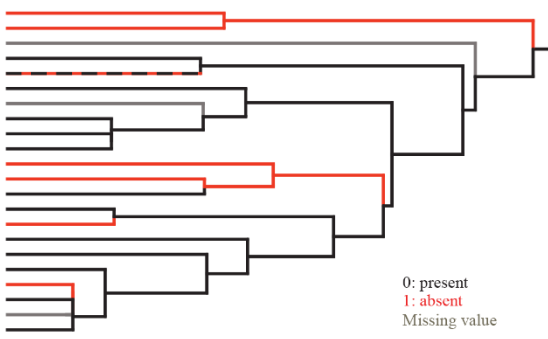
GW78: Anterior opening of orbitotemporal canal



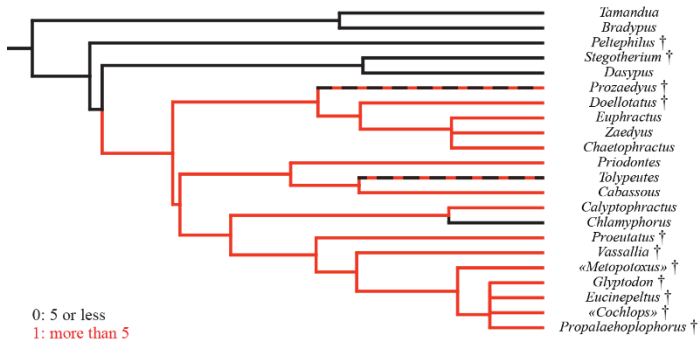
GW94: Multiple foramina on dorsal surface of frontal, around midline



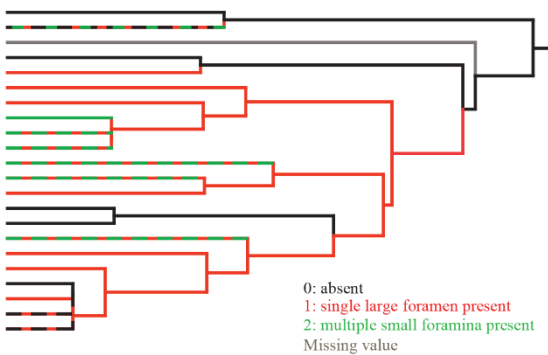
GW95: Vascular foramina situated in posterolateral region of frontal



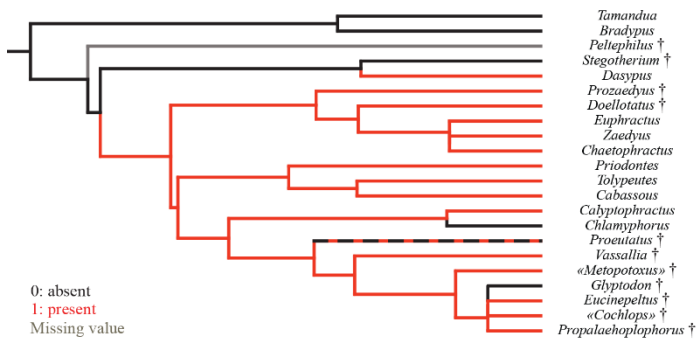
GW97: Number of foramina for rami temporales in temporal fossa of parietal



GW120: Suprameatal foramen



GW111: Large vascular foramen located immediately anterior or ventral to foramen ovale



General Discussion & Conclusion

Figure 61. Evolutionary scenarios for some characters of Gaudin & Wible (2006; GW) and Billet *et al.* (2011; B) mentioned in this Discussion (mapped on the baseline cladogram of Chapter 2). The coding follows Billet *et al.* (2011), except for the added taxa *Calyptophractus*, “*Metopotoxus*”, *Eucinepeltus*, “*Cochlops*” and *Glyptodon*, whose scores are available in Chapter 2. Branches with dots of different colors indicate polymorphism.

The second part of our work explored cranial integration patterns in relation to size with GMM methods (Chapter 3) or based on correlation among linear distances (Chapter 4), at the intraspecific and evolutionary levels. We were able to detect several allometric trends (Figure 62) and cranial covariations (Figure 63) that appear to be widespread in cingulates. Of course, none of these approaches is exhaustive, and we are surely far from having unearthed all the interesting cranial covariations in the group, which must be numerous and very complex. Nevertheless, these represent complementary approaches for an exploration of covariation patterns and their relation to morphological characters.

Considering the morphological characters present in the GW matrix, relatively few can be unambiguously connected to the strongest and most widespread covariations we found. However, there are still some aspects to be discussed in this regard, including potential implications and ways of improving some characters.

First, several GW characters quantify the variation of selective cranial distances relative to greatest skull length, which may in fact present an allometric component. For example, one could postulate that the allometric elongation of the snout and masticatory apparatus in large specimens (craniofacial allometry; CREA) detected at all levels of our analyses (Figure 62) could affect in some way the variation scored by GW36 and GW37 (Figure 64). For character 36, Gaudin & Wible (2006) describes the relative length of the rostrum starting posteriorly from the orbital rim. This character discriminates the posterior position of the orbit in dasypodines and the anteriorly shifted orbit of glyptodonts (Figure 64). In addition, it also shows a lower elongation of the snout relative to the orbit in *Calyptophractus* and *Vassallia* (Figure 64). The anteriorly shifted position of the orbit in glyptodonts contrasts with the allometric patterns we detected at the intraspecific levels or at the evolutionary level on extant species only, which rather showed a posteriorly shifted or stable position of the orbit, except for the evolutionary analysis including fossils (Chapter 3). Smaller species such as chlamyphorines also show a relatively anterior orbit position in contrast to larger forms such as certain dasypodines and *Priodontes*. At first glance, the scoring of GW36 thus seems to be incongruent with the allometric elongation of the snout found at most levels in our study and not much affected by the CREA. However, this character would be better scored with continuous

General Discussion & Conclusion

data (see below) in order to better check for a possible allometric component in its variation. Unlike the pre-orbital length, the masticatory apparatus is extremely enlarged in glyptodonts which is congruent with our results and the CREA.

Common Allometric Covariation Pattern in Cingulata

Shape variation as size increases relative to log centroid size (Entire Skull level)

Anterior snout lengthening

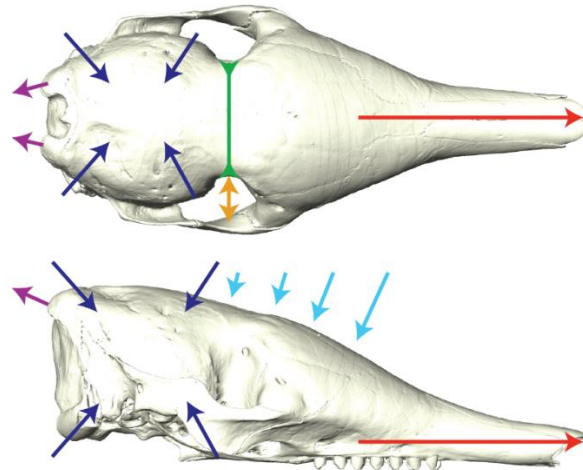
Stronger postorbital constriction

Reduction of braincase proportion

More protruding nuchal crest processes

Enlargement between zygomatic arches and postorbital constriction

Relative flattening of the cranial roof



Shape variation as size increases relative to log centroid size (Bone-By-Bone level)

Hypoglossal foramen located relatively more posterior

Relative reduction of foramen magnum

More posterior and stronger postorbital constriction

Greater separation between the annular ring and frontal roof

More protruding mastoid process

Shallower fossa subarcuata

Zygomatic arch protruding further laterally

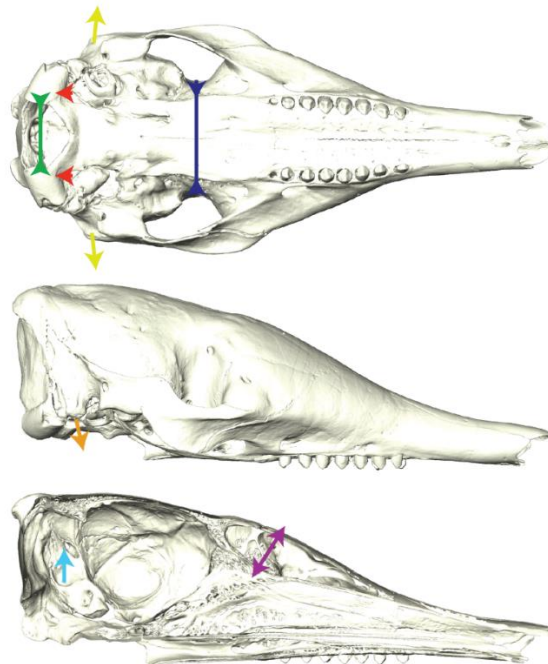
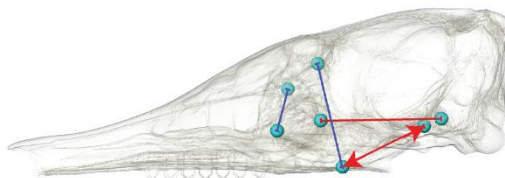


Figure 62. Summary and schematization of widespread allometric patterns in cingulates (found at the intraspecific and evolutionary levels; see [Section 3.2](#)), here represented on a *Dasyus novemcinctus* cranium (MNHN.CG.2006-565) shown (from top) in dorsal, lateral, ventral, lateral, and sagittal views.

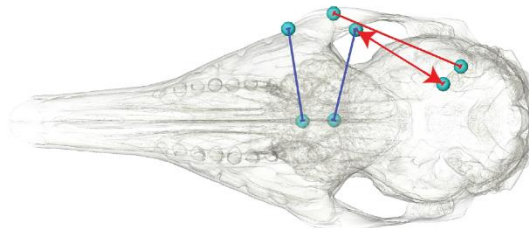
General Discussion & Conclusion

Common Covariation Pattern from Correlated Distances Pairs Selected in Cingulata

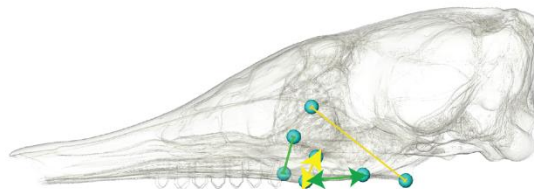
Pair n°5
Faster growth of the distance linking the anterior root of the zygomatic arch to the auditory region than the distance linking the orbital edge to the auditory region



Pair n°7
Coordinated variation of distances linking the zygomatic arch and cranial roof in the vicinity of the orbit



Pair n°10
Faster growth in width between the posterolateral edge of the palate and the ventral base of the zygomatic arch than between the central part of the palate and the anterodorsal edge of the zygomatic arch



Pair n°12
Faster growth of the distance between the posterolateral edge of the palate and the maxillary foramen than of the more dorsal distance contained between the anterior edge of the orbit and the posteromedial edge of the palate

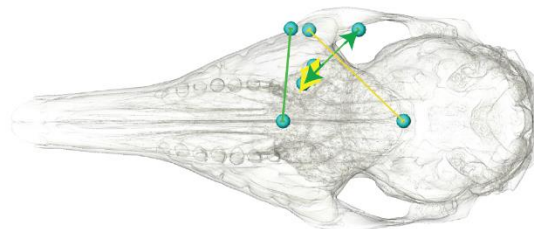


Figure 63. Summary and schematization of the selected pairs of correlated distances pairs found at the intraspecific and evolutionary levels in our samples in cingulates, represent here on a *Dasyus novemcinctus* cranium (MNHN.CG.2006-565) shown in ventral and lateral views.

GW37 describes the length of the nasal relative to the skull length. In our study, the variation of the landmark located on the nasal midline suggested an allometric shortening of the nasal in several, but not all, analyses (intraspecific *Zaedyus*, static *Dasyus*, and evolutionary analyses). The scoring of GW37 evidences no clear allometric trend as well (Figure 64), except that glyptodonts have short nasals ending posteriorly at the front of the anteriorly shifted orbits

General Discussion & Conclusion

(Fericola *et al.*, 2012). As for GW36, it would be interesting to examine more the variation of this character with quantitative data (see below).

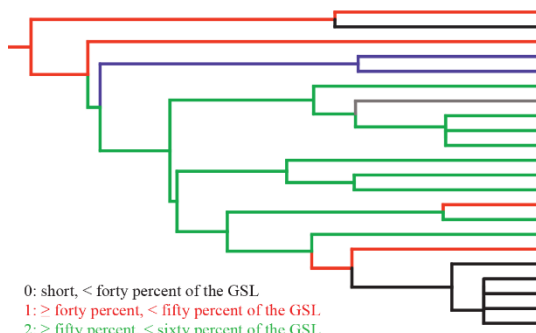
Our study also detected an allometric widening of the distance between the zygomatic arch and the postorbital constriction, creating a relatively larger temporal fenestra in large specimens (Figure 62). This allometry could influence the variation scored in GW61, which describes the maximum skull width at the zygomatic arches in relation to the greatest skull length (Figure 64). However, the scoring of GW61 only shows a resemblance between the Dasypodinae and the tolypeutines *Priodontes* and *Tolypeutes*, coded as having a transversely narrow inter-zygomatic region with all other armadillos considered wide. Thus, the binary scoring used for this character does not reflect the allometric pattern detected for these structures in our study.

Our exploration also revealed a stronger postorbital constriction as the size increases at the intraspecific and evolutionary levels in cingulates (Figure 62). This allometric pattern could affect GW62 which describes the relative width of the interorbital area compared to the greatest skull length (Figure 64). The postorbital constriction and the interorbital area may be fully confounded or very close in some taxa (*e.g.*, *Dasypus* – see Figures S50-S55), which is why we suspect a possible relationship between our allometric pattern and this character. GW62 exhibits substantial homoplasy on our baseline cladogram and is polymorphic in several clades and species (Figure 64). Its distribution on the tree seems to be partly consistent with our results, with several large taxa presenting a strong postorbital constriction (glyptodonts, pampatheres; and *Priodontes* when compared to other tolypeutines).

The variation of several of the characters discussed above may be, at least partly, impacted by allometry and would thus necessitate a revision. However, their scoring corresponds to the discretization of a ratio between two distances (*i.e.*, one length on GSL) which hides part of their variation and may partly obscure an allometric component. Alternative coding strategies may need to be used to assess more effectively their variation and to avoid an allometric signal (see Section 5.3).

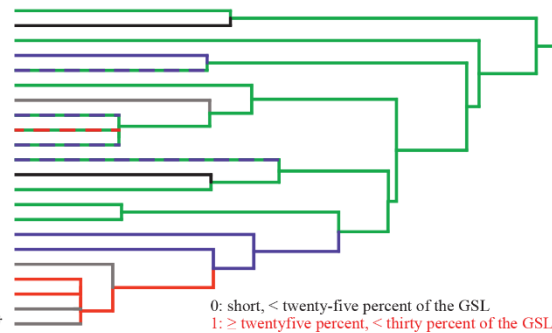
General Discussion & Conclusion

GW36: Length of rostrum to anterior orbital rim



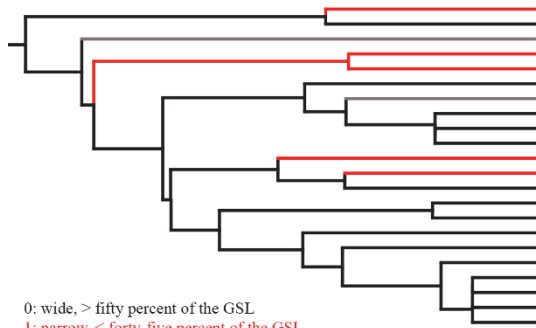
0: short, < forty percent of the GSL
 1: > forty percent, < fifty percent of the GSL
 2: ≥ fifty percent, < sixty percent of the GSL
 3: elongated, ≥ sixty percent of the GSL
 Missing value

GW37: Length of nasal bone



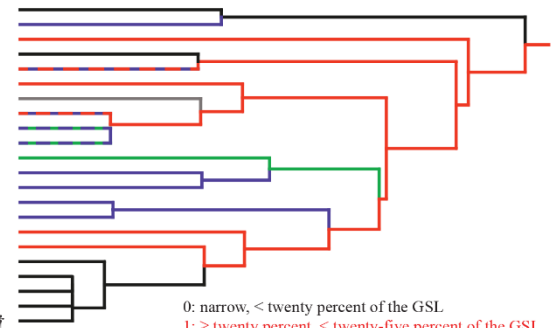
0: short, < twenty-five percent of the GSL
 1: ≥ twenty-five percent, < thirty percent of the GSL
 2: ≥ thirty percent, < thirty-five percent of the GSL
 3: elongated, ≥ thirty-five percent of the GSL
 Missing value

GW61: Maximum width of skull at zygomatic arches



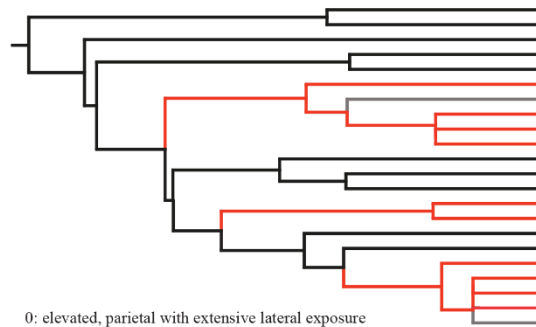
0: wide, > fifty percent of the GSL
 1: narrow, < forty-five percent of the GSL
 Missing value

GW62: Width of interorbital area



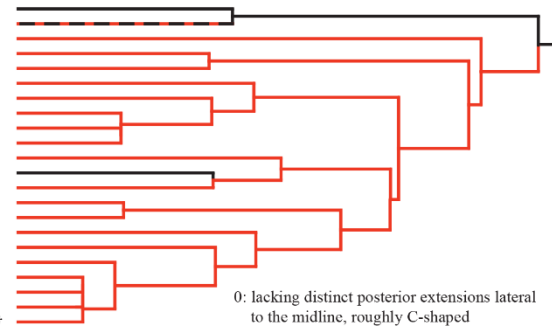
0: narrow, < twenty percent of the GSL
 1: ≥ twenty percent, < twenty-five percent of the GSL
 2: ≥ twenty-five percent, < thirty percent of the GSL
 3: wide, ≥ thirty percent of the GSL
 Missing value

GW91: Shape of braincase



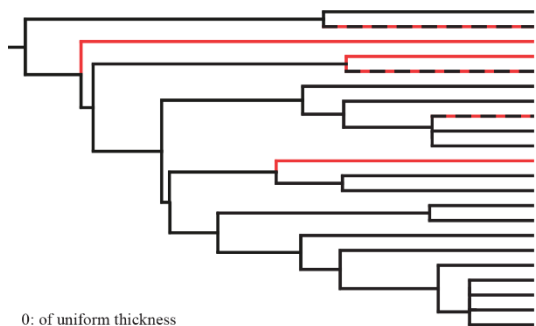
0: elevated, parietal with extensive lateral exposure
 1: dorsoventrally compressed, parietals appear relatively flat
 Missing value

GW100: Shape of nuchal crest in dorsal view



0: lacking distinct posterior extensions lateral to the midline, roughly C-shaped
 1: W-shaped, with distinct posterior extensions situated lateral to the midline

GW163: Nuchal crest



0: of uniform thickness
 1: bearing distinct, posteriorly thickened dorsal bosses
 Missing value

Tamandua
Bradypus
Peltephilus †
Stegotherium †
Dasypus
Prozaedyus †
Doellotatus †
Euphractus
Zaedyus
Chaetophractus
Priodontes
Tolypeutes
Cabassous
Calyptophractus
Chlamyphorus
Proeutatus †
Vassallia †
 «Metopotoxus» †
Glyptodon †
Eucinepeltus †
 «Cochlops» †
Propalaeohoplophorus †

Tamandua
Bradypus
Peltephilus †
Stegotherium †
Dasypus
Prozaedyus †
Doellotatus †
Euphractus
Zaedyus
Chaetophractus
Priodontes
Tolypeutes
Cabassous
Calyptophractus
Chlamyphorus
Proeutatus †
Vassallia †
 «Metopotoxus» †
Glyptodon †
Eucinepeltus †
 «Cochlops» †
Propalaeohoplophorus †

Tamandua
Bradypus
Peltephilus †
Stegotherium †
Dasypus
Prozaedyus †
Doellotatus †
Euphractus
Zaedyus
Chaetophractus
Priodontes
Tolypeutes
Cabassous
Calyptophractus
Chlamyphorus
Proeutatus †
Vassallia †
 «Metopotoxus» †
Glyptodon †
Eucinepeltus †
 «Cochlops» †
Propalaeohoplophorus †

Tamandua
Bradypus
Peltephilus †
Stegotherium †
Dasypus
Prozaedyus †
Doellotatus †
Euphractus
Zaedyus
Chaetophractus
Priodontes
Tolypeutes
Cabassous
Calyptophractus
Chlamyphorus
Proeutatus †
Vassallia †
 «Metopotoxus» †
Glyptodon †
Eucinepeltus †
 «Cochlops» †
Propalaeohoplophorus †

General Discussion & Conclusion

Figure 64. Evolutionary scenarios for some characters of Gaudin & Wible (2006; GW) and Billet *et al.* (2011; B) mentioned in this Discussion (mapped on the baseline cladogram of Chapter 2). The coding follows Billet *et al.* (2011), except for the added taxa *Calyptophractus*, “*Metopotoxus*”, *Eucinepeltus*, “*Cochlops*” and *Glyptodon*, whose scores are available in Chapter 2. Branches with dots of different colors indicate polymorphism.

In accordance with the widespread craniofacial allometry in mammals, our study also shows a reduction in braincase proportions as size increases (Figure 62). GW91 describes the shape of the braincase with a focus on the parietal (Figure 64). The scoring of GW91 suggests a resemblance between euphractines, *Prozaedyus*, chlamyphorines and glyptodonts, with a dorsoventrally compressed braincase that would distinguish them from other cingulates (Figure 64). Although this binary scoring does not reflect clearly the allometric flattening of the braincase shown in our study (small-sized chlamyphorines scored as flat), it is likely that the latter plays a role in the variation scored for this character. Large-sized glyptodonts are indeed found to have a flattened braincase (Figures S50-S55).

One of the strongest allometric patterns detected at all levels corresponds to more prominent nuchal crest processes as size increases (Figure 62). GW100 describes the shape of these crests in dorsal view, which are W-shaped in cingulates, as shown in our study. This represents a possible synapomorphy for Cingulata (Figure 64). GW163 describes differences in the posterior thickening of the nuchal crests which occur within cingulates. The scoring of GW163 suggests a resemblance between *Stegotherium*, *Priodontes* and *Peltephilus*, with posteriorly thickened dorsal bosses that would distinguish them from other cingulates (Figure 64). This scoring does not reflect the allometric pattern found in our study. The large-sized glyptodonts and pampatheres are not scored as having posteriorly thickened dorsal bosses, yet they present prominent nuchal crests (Figures S50-S55). The link between this character and our detected allometric pattern is obviously not direct, however it would be relevant to measure the correlation between the presence of these rugosities and the development of nuchal crests. As with previous characters, an alternative coding strategy could be used to accurately assess the variation of this character and avoid an allometric signal (see Section 5.3).

General Discussion & Conclusion

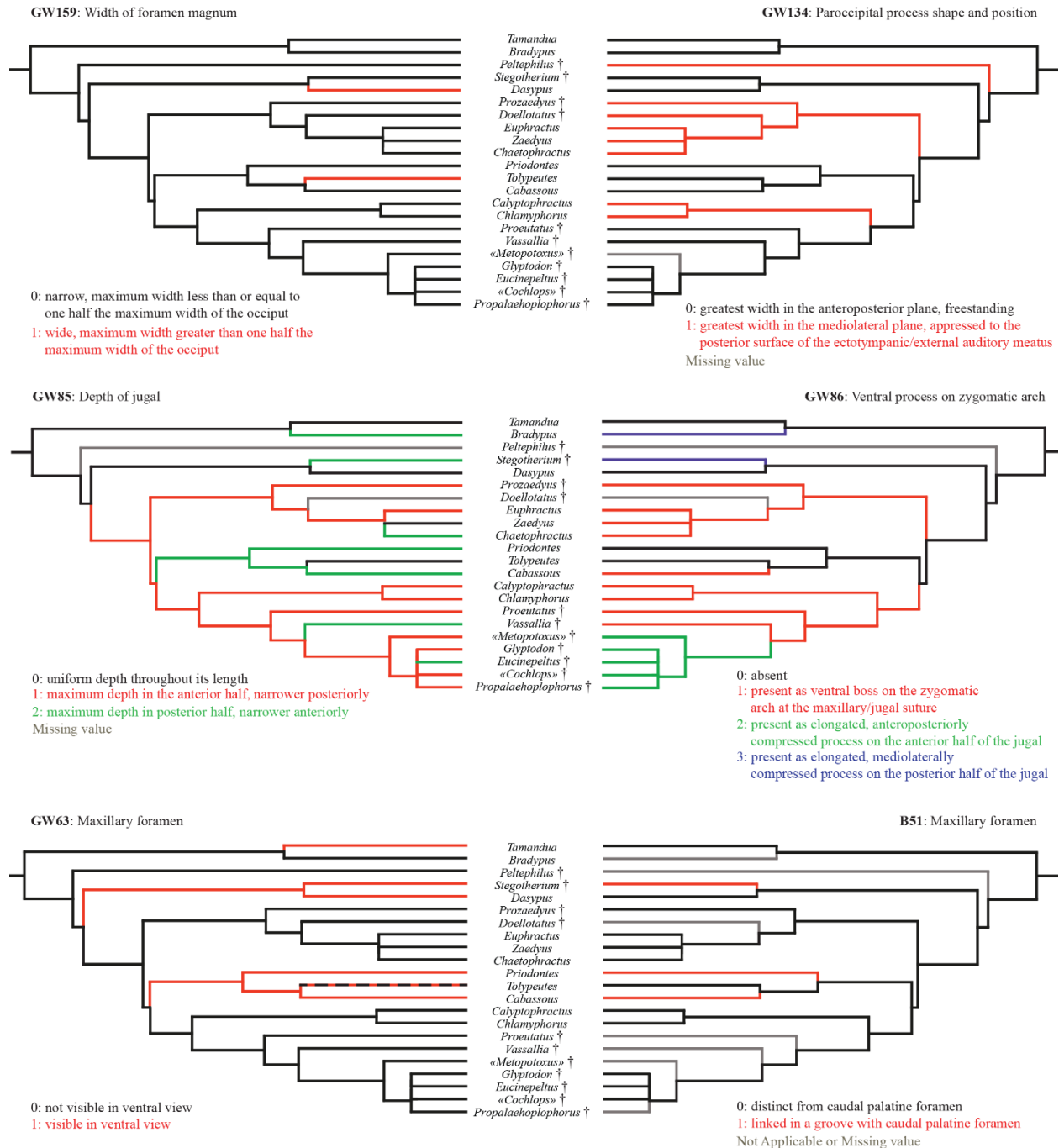


Figure 65. Evolutionary scenario for some characters of Gaudin & Wible (2006) and Billet *et al.* (2011) potentially impacted by our study with the definition and mapping of characters on the baseline cladogram of our study. The coding follows the revision of Billet *et al.* (2011) when the character is revised, otherwise it follows Gaudin & Wible (2006). Coding for *Calyptophractus*, «*Metopotoxus*», *Eucinepeltus*, «*Cochlops*» and *Glyptodon* are available in Section 2. Branches combining several states mark a polymorphism.

General Discussion & Conclusion

As demonstrated in our study, allometric pattern analysis over the entire skull (ES approach) can mask more regionalized patterns of allometry (Chapter 3). Our analyses of allometry on cranial units (3B approach) also revealed several common patterns among cingulates (Figure 62), two of which may have potential implications on GW characters.

Our 3B approach revealed an allometric reduction in the proportions of the foramen magnum as size increases (Figure 62). GW159 describes the width of the foramen magnum in relation to the width of the occiput (Figure 65). It suggests a resemblance between *Dasypus* and *Tolypeutes* as taxa with a relatively broad foramen magnum in opposition to the other cingulates (Figure 65). As for several other characters mentioned above, although the scoring of this binary character is not strongly congruent with our allometric pattern, allometry may still play a role in the variation that was scored. For this reason, alternative character constructions should be explored in the future (see Section 5.3).

Our 3B approach of cranial allometry also revealed a more salient development of the mastoid process (= paroccipital process of the petrosal in Wible & Gaudin, 2004) as size increases (Figure 62). GW134 describes the direction of the greatest width of the mastoid process and suggests a resemblance between *Peltephilus*, *Prozaedyus*, euphractines and chlamyphorines that have a process that is broader mediolaterally than anteroposteriorly (Figure 65). Only one landmark was placed on the mastoid process in our study (see Section 3.1), which did not permit examination of whether the allometric protrusion of this process could be accompanied by changes in the direction of its greatest width.

To a lesser extent, the selected pairs of correlated distances also highlight covariation patterns that need to be considered when revising phylogenetic matrices. The reduced number of selected pairs supported both at the intraspecific and evolutionary levels mainly concern the orbitotemporal region containing the anterior root of the zygomatic arch, the orbit, and the posterior part of the palate (Figure 63).

Pair n°5 suggests faster growth of the distance from the anterior root of the zygomatic arch (most ventral contact between the zygomatic process of the maxillary and the jugal) to the petrosal

General Discussion & Conclusion

than of the distance from the petrosal to a more dorsal point on the anterior edge of the orbit. This may be due to a more ventral position of the zygomatic processes of the maxillary and the jugal in larger specimens (see [Section 4.1](#)). This aspect can be compared with the variation described by at least two characters of the GW matrix.

GW 85 describes the anterior depth (height) of the jugal ([Figure 65](#)). It suggests a resemblance between *Tolypeutes*, *Zaedyus* and *Dasypus* which present a uniform depth, as opposed to *Prozaedyus*, *Euphractus*, the chlamyphorines, *Proeutatus* and glyptodonts (except *Eucinepeltus* – [Figure 65](#)) presenting a maximum depth in the anterior half of the bone, and to the other cingulates that show a maximal depth posteriorly ([Figure 65](#)). The scoring of this character cannot be directly compared to the information brought by pair n°5 but it is possible that the trend towards a more ventral position of the maxillary-jugal suture in large specimens may affect it to some extent. In addition, we were also able to note that a relatively higher jugal bone is found in larger individuals in the three species analyzed at the ontogenetic and static levels ([Chapter 3](#)). It was unclear, however, whether the jugal bone was higher anteriorly than posteriorly in large specimens, and this trend was not supported at the evolutionary level. Therefore, more research would be needed on the allometric patterns in this region (see [Section 5.3](#)) to determine if a revision of GW85 is necessary.

GW86 describes the variation of the ventral process on the anterior root of the zygomatic arch ([Figure 65](#)). It shows that glyptodonts possess a distinctive descending ventral process of the zygomatic arch ([Scott, 1903](#)) that is more marked than in other cingulates ([Figures S50-S55](#)). This is strongly reminiscent of the information provided by the pair n°5 (see above and [Section 4.1](#)) with a potentially more ventral landmark #21 in larger specimens. This suggests that the variation of this character may be influenced by an allometric pattern indicated by pair n°5 ([Section 4.1](#)), but which was not clearly detected by our GMM studies on cranial allometry ([Section 3.2](#)). Only a slightly more ventral position for this landmark was detected in intraspecific series (weak in *Zaedyus* but stronger in *Dasypus*) and at the evolutionary level incorporating fossil taxa (*i.e.*, Dataset-Lmax). In this case, like in many others, more research is needed before a revision of this character is undertaken despite the particularly extreme morphology of glyptodonts (see [Section 5.3](#)).

General Discussion & Conclusion

Finally, the pair n°12 suggests a faster growth of the distance between the posterolateral margin of the palate and the maxillary foramen than of the more dorsal distance between the anterior edge of the orbit and the posteromedial margin of the palate (Figure 63). This covariation therefore could signal an anterolateral shift of the position of the maxillary foramen with respect to the palatal edge when this area is growing, but the exact anatomical changes behind this covariation remains obscure and more research is needed (see below). Characters whose variations could be potentially related to this pattern include GW63 & B51, which both describe different aspects of the location of the maxillary foramen (Figure 65). GW63 describes the visibility of the foramen in lateral view. It suggests a resemblance between dasypodines and tolypeutines (with a polymorphism in *Tolypeutes*) which exhibit a visible foramen in lateral view (Figure 65). B51 describes the connection between this foramen and the caudal palatine foramen. The two foramina are in the same groove in *Stegotherium*, *Priodontes* and *Cabassous* (Figure 65). Curiously, the taxa gathered by these two characters correspond to taxa with a strong reduction in the height of the dental alveoli, an aspect for which we question the allometric component (see Chapter 2).

Overall, potential links between GW characters and the pairs of correlated distances selected in our work are extremely difficult to establish, more than for the results of our studies on cranial allometry. A complementary analytical method to overcome these difficulties would be to analyze the covariation between two anatomical regions each composed of several landmarks. This is a strategy that is widely used with the 2-Blocks Partial Least Squares (PLS & PGLS - Bookstein *et al.*, 2003; Klingenberg *et al.*, 2003, Monteiro *et al.*, 2005, Klingenberg & Marugán-Lobón, 2013). However, this method requires the *a priori* definition of the two regions to be analyzed. Our study now allows us to highlight these potential regions (see Section 5.3).

In summary, only a small proportion of the GW and B characters were found to have a potential link with the allometric and covariation patterns obtained in our study (20 GW characters and one additional character of B). However, this small proportion should be considered in relation to the composition of our landmark set and the definition of the characters which cannot easily compared with one another in many cases. Of the 163 GW characters, 123 could not be addressed by our analyses of cranial allometry and covariations because they cannot be represented by landmarks and because a substantial number concern the mandible (not included in our study;

General Discussion & Conclusion

Figure 66, Table 16). We have discussed above several characters (n = 13 GW characters) whose variation may have ties to patterns of allometry and covariation highlighted in our study. Additional GW characters may also be related to patterns that were supported only at the intraspecific levels (Figure 66, Table 16) and were not discussed because they were not found at the evolutionary level, or vice versa. This is, for example, the case for GW39, which describes the presence or absence of a well-defined notch on the anteroventral edge of the premaxillary. The shape of this structure was allometric in *Dasybus* and *Zaedyus* (Section 3.2). This is also the case, at the evolutionary level for GW121 which describes the contact between the petrosal and the basicranial axis, which was found to be allometric at the evolutionary level but not at the intraspecific level (Section 3.2). These aspects also warrant further research.

Table 16. Summary of the potential relationships between the analyzed morphological characters (GW) and the patterns of integration found in cingulates. Characters concerning only the mandible are not added in this table (= 24/163 GW). * common to intraspecific and evolutionary levels; ** only found at the intraspecific or evolutionary level.

	Potential link with widespread patterns of integration*	Potential link with variably supported patterns of integration**	No link found	Not applicable with our landmark dataset
Gaudin & Wible (2006)	36; 37; 51; 61; 62; 63; 84; 85; 86; 90; 91; 100; 134; 152; 159; 163.	33; 38; 39; 40; 41; 46; 52; 57; 93; 96; 121; 123; 148; 158.	8; 43; 53; 79; 89; 99; 109; 110; 122; 157.	1; 2; 3; 4; 5; 6; 7; 34; 35; 42; 44; 45; 47; 48; 49; 50; 54; 55; 56; 58; 59; 60; 64; 65; 66; 67; 68; 69; 70; 71; 72; 73; 74; 75; 76; 77; 78; 80; 81; 82; 83; 87; 88; 92; 94; 95; 97; 98; 101; 102; 103; 104; 105; 106; 107; 108; 111; 112; 113; 114; 115; 116; 117; 118; 119; 120; 124; 125; 126; 127; 128; 129; 130; 131; 132; 133; 134; 135; 136; 137; 138; 139; 140; 141; 142; 143; 144; 145; 146; 147; 149; 150; 151; 153; 154; 155; 156; 160; 161; 162.

Some of these targeted GW characters also recall some of the main variations obtained during our exploration of the 3D cranial shape variation among cingulate species (Section 4.3). In spite of many variations, probably allometric, such as the relative lengthening of the snout or the reduction of the proportions of the braincase (Section 4.3), the PCAs provided further information

General Discussion & Conclusion

on morphological variation especially when they were performed on the modules obtained in [Section 4.2](#). A good example concerns the second axis of the PCA performed on the vault-basicranium module with the posterodorsal part of the module showing a relative increase in height of the vault (#67; #72-74; #86; #99-100) while the lateral part of the module corresponding to the squamosal (#55-58; #70-71) showed a much more ventral position ([Section 4.3](#)). These co-occurring shape changes on PC2 may signal a coordinated variation which could impact several GW characters (*e.g.*, 90; 91; 99; 100). However, this pattern was only analyzed with PCA and at the evolutionary level, which does not allow us to conclude whether it really represents a covariation. Analyses focused on this region at the intraspecific level would be required to test if such a covariation is present within species. Nevertheless, three-dimensional analysis of shape diversity using PCA may represent a complementary way to detect potentially covariant regions.

In conclusion, based on our investigation of GW and B characters, we observe that links between the detected patterns of integration and the scored phylogenetic characters are hard to establish. This is mainly because the comparison between the detected pattern of integration and the definition of the GW or B characters was not straightforward in many cases, due to differing methods (*e.g.*, continuous vs discrete characters) and/or scope (*e.g.*, landmarks not covering all the variation scored with a naked eye for a character). Most of the potential implications on GW and B characters are related to allometric patterns highlighted in [Chapter 3](#) rather than with pairs of correlated distances from [Section 4.1](#), probably because the interpretation of the former is less complex. Nevertheless, covariation patterns are not restricted to allometry, and even though allometry is more easily related to morphological characters than pairs of correlated distances, both need to be taken into account in morphological phylogenetics, which appears difficult with traditional coding strategies. Other approaches are thus needed to improve our understanding of the relationship between detected covariation patterns and phylogenetic characters, and thereby improve our character constructions.

General Discussion & Conclusion

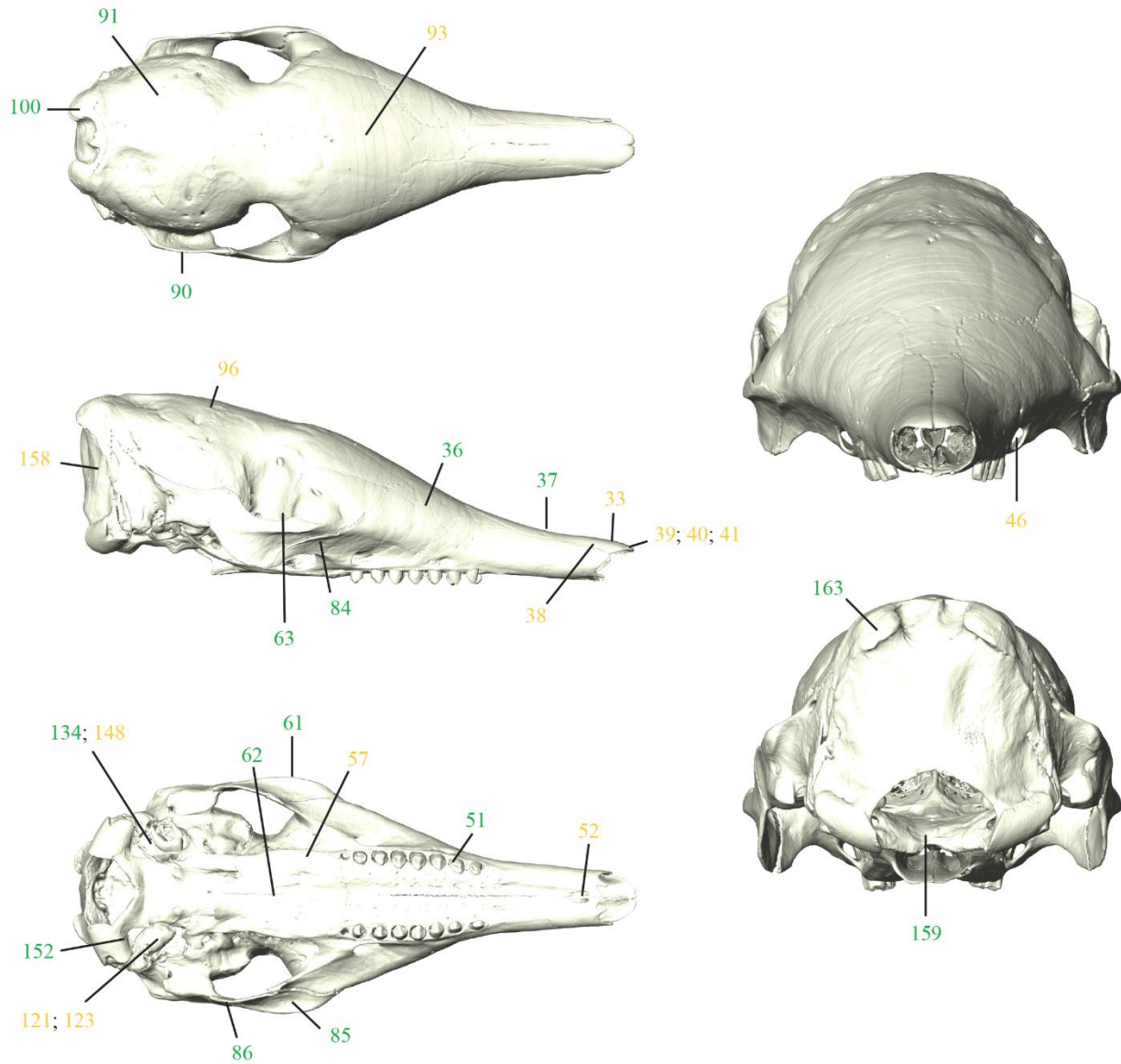


Figure 66. Skull of *Dasypus novemcinctus* (MNHN.CG.2006-565) and anatomical relocation of the GW characters potentially related to the patterns of integration found in our study (see [Table 16](#)) in dorsal (top left), lateral (middle left), ventral (bottom left), face (top right) and occipital (bottom, right) view.

General Discussion & Conclusion

5.3 Complexity of morphological variation, limitations, and prospects

Advances in analytical methods and techniques have highlighted our gross lack of sizable gaps remaining in our knowledge of morphological variation in general (Hallgrímsson & Hall, 2005). This is partly explained by the extreme complexity of this phenomenon, which has determinants that can be multiple and interconnected, acting at all levels of the biological hierarchy (Hallgrímsson & Hall, 2005). This complexity impacts all morphological studies, and in particular the studies on morphological integration and modularity which have become a major topic in evolutionary biology in recent years (Wagner & Altenberg, 1996; Klingenberg, 2008; Goswami & Polly, 2010b; Wagner *et al.*, 2007; Klingenberg, 2010). The complexity and integrated nature of morphological variation certainly represents one of the major constraints for morphological phylogenetics because the latter require independence between the characters analyzed (Felsenstein, 1973; Kluge, 1989; Emerson and Hastings, 1998; O'Keefe & Wagner, 2001; Lewis, 2001; Felsenstein, 2004). Our poor knowledge of patterns of covariation and of their complexity has potentially led authors to involuntarily leave this issue aside when scoring characters. This has led to calls for improvements in our approaches and methods relative to the issue of correlated characters (Dávalos *et al.*, 2014; Goswami *et al.*, 2014; Billet *et al.*, 2015; Billet & Bardin, 2019).

To this end, we have adopted an exploratory approach, so as not to limit the very wide field of possible morphological variations to be discovered, and to take paths that are still poorly known (Yanai & Lercher, 2020). This exploratory approach was complemented by a confirmatory approach that tested at the evolutionary level the hypotheses generated from our results at the intraspecific level, as in the case of pairs of correlated distances (Section 4.1).

Our exploratory approach extended to several biological levels (static, ontogenetic, and evolutionary) to find widespread patterns in the group (limiting the effect of ontogeny with the static level or of phylogeny with the intraspecific levels – see Klingenberg, 2014). We also looked at different scales of variation on the skull, from global (entire skull) to more local patterns (cranial subunits, pairs of distances). These different levels of analysis could be complex to interpret, especially since the approaches also varied. In the case of a strong and pervasive patterns such as those often induced by allometry, we opted for a geometric morphometrics method with a Procrustes superimposition. This superimposition can, however, be problematic for a broader approach to covariations among landmarks, *e.g.*, without depending on factors such as size

General Discussion & Conclusion

(Cardini, 2019b, 2020; Klingenberg, 2020). Therefore, we opted for the analysis of covariations among distances, although this approach also presents a high degree of complexity and the constraint of dealing with a gigantic amount of data. The relationship between distances and 3D coordinates (*i.e.*, landmarks) remains exceedingly difficult and unclear (Hubbe *et al.*, 2016) limiting our interpretations. This limitation is also one of the major impediments to the exploratory approach. By taking new paths, we had very few comparable studies in the literature on which to rely. We tried to interpret some of our covariation patterns on the basis of well-known general patterns, *e.g.*, craniofacial allometry or developmental and functional hypotheses, but we often found ourselves limited by the lack of comparable data. Nevertheless, our exploratory approach allowed us to treat a very large amount of data and generate many new hypotheses on integration patterns within the cingulate skull. We are hopeful that this will pave the way for future studies to test our hypotheses further and to extend our patchy knowledge of morphological integration with the use of other exploratory approaches.

As regards the GW characters whose variation may be partly linked to size (see above), several ways forward may exist. If several characters score evolutionary changes all related to size variation, then they are necessarily partly dependent, which is problematic for phylogenetic analyses (Felsenstein, 1973; Kluge, 1989; Emerson & Hastings, 1998; O'Keefe & Wagner, 2001; Lewis, 2001; Felsenstein, 2004). One strategy would be to simply remove these characters from phylogenetic analysis. This strategy would appear as unsatisfactory as it could lead to a loss of phylogenetic information, since a phylogenetic signal may still be contained in the variation of characters with an allometric component. The GW 36, 37, 61, and 62 characters discussed above correspond to discretized continuous characters. Numerous studies criticize the unsatisfactory nature of this type of trait, notably because of the loss of information linked to discretization, which reflects less well the morphological variation but also the subjective aspect of the definition of the intervals (Hillis & Huelsenbeck, 1992; Yang, 1998; Donoghue & Ree, 2000; Wiens, 2001; Parins-Fukuchi, 2018). In addition, several authors argue that most morphological variation is basically continuous (Thiele, 1993; Rae, 1998; Wiens, 2001; Parins-Fukuchi, 2018). A better strategy would be to treat these traits in a continuous manner (Wiens, 2001; Parins-Fukuchi, 2018) and then assess their relationship with allometry. This would greatly facilitate assessment by making it clearer to compare with only continuous variables (see below).

General Discussion & Conclusion

If two characters are covarying, one strategy could be to combine them in a single character as proposed by [Wilkinson \(1995\)](#) in his composite coding strategy ([Figure 67](#)). Although the relationship between GW characters and the detected patterns of integration remains to be clarified in many cases, this strategy can represent a promising way forward relative to the issue of character independence for phylogenies (see a different example on discrete characters in [Billet & Bardin, 2019](#); and see a concrete example below on continuous variables).

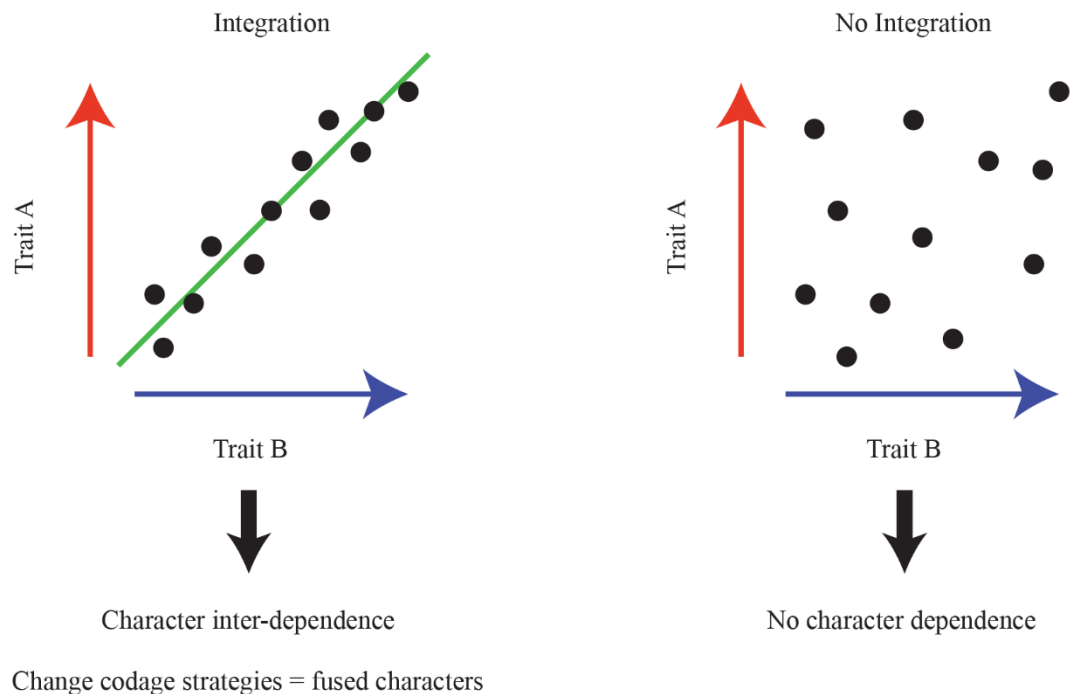


[Figure 67](#). Rationale of the composite coding strategy ([Wilkinson, 1995](#)) in the case of highly correlated continuous characters.

Our study also gives rise to other ideas of character construction and scoring regarding the evolutionary history of cingulates. The covariation patterns detected at certain levels appear as potentially discriminating elements within cingulates. For example, a well-established consensus in the literature lies in the distinction between dasypodids (containing *Dasybus*) and chlamyphorids (containing *Cabassous* and *Zaedyus*). We detected in various cases covariation patterns common to *Cabassous* and *Zaedyus* but absent in *Dasybus*, such as the relative lengthening of the frontal process of the nasal when the size increases at the intraspecific level

General Discussion & Conclusion

(Section 3.2). Further investigation in other cingulates could confirm that this covariation itself is potentially a synapomorphy of chlamyphorids, which could thus be coded as a character.

In a different way, patterns common to all three species at the intraspecific level may also be present in other cingulates and might deliver phylogenetic information as well. In this case, coding strategies could follow the suggestion to code the allometric trajectories that potentially represent biological traits under selection (Weber, 1990; Frankino *et al.*, 2005; Adams & Nistri, 2010; Wilson & Sánchez-Villagra, 2010; Klingenberg, 2010; Urošević *et al.*, 2013; Porto *et al.*, 2013; Giannini, 2014). This could be done, for instance, for the relative shortening and increase in height of the jugal when size increases, detected at the intraspecific level in *Dasyopus*, *Zaedyus* and *Cabassous* (Section 3.2). Coding the slopes of differing trajectories could thus add new characters to matrices on cingulates.

The relationship between the intra- and interspecific level can also potentially provide ideas for new coding strategies. In the case of two highly correlated traits at the two levels, the regressions could have rather similar slopes. This is what we observe in the case of pair n°5 for example (Figure 68A; and see Section 4.1). In the case of pair n°5, a quantification of the orthogonal distance of taxa from the regression line may provide phylogenetic information that could be scored as a continuous character (Strategy C1 - Figure 68B). This would represent the position of species relative to the regression line. For instance, the lower position of most euphractines (red dots; Figure 68B) relative to the line indicate that they tend to have lower values for the distance #21-108 relative to the common trend in cingulates, which could constitute interesting phylogenetic information. Similarly, one may also want to code as a continuous character the position of the taxa along the regression line once fitted (Strategy C2). It could for example distinguish the dasypodines, which have low values for these distances relative to the skull size when compared to other cingulates (Figure 68B). Ideally, these strategies could be used only if the resulting traits are not correlated with other traits and not allometric. Further investigation in this direction could be conducted based on our results but the position of taxa on regression plots suggests that it might be a promising avenue for alternative coding to incorporate the impact of covariation patterns.

General Discussion & Conclusion

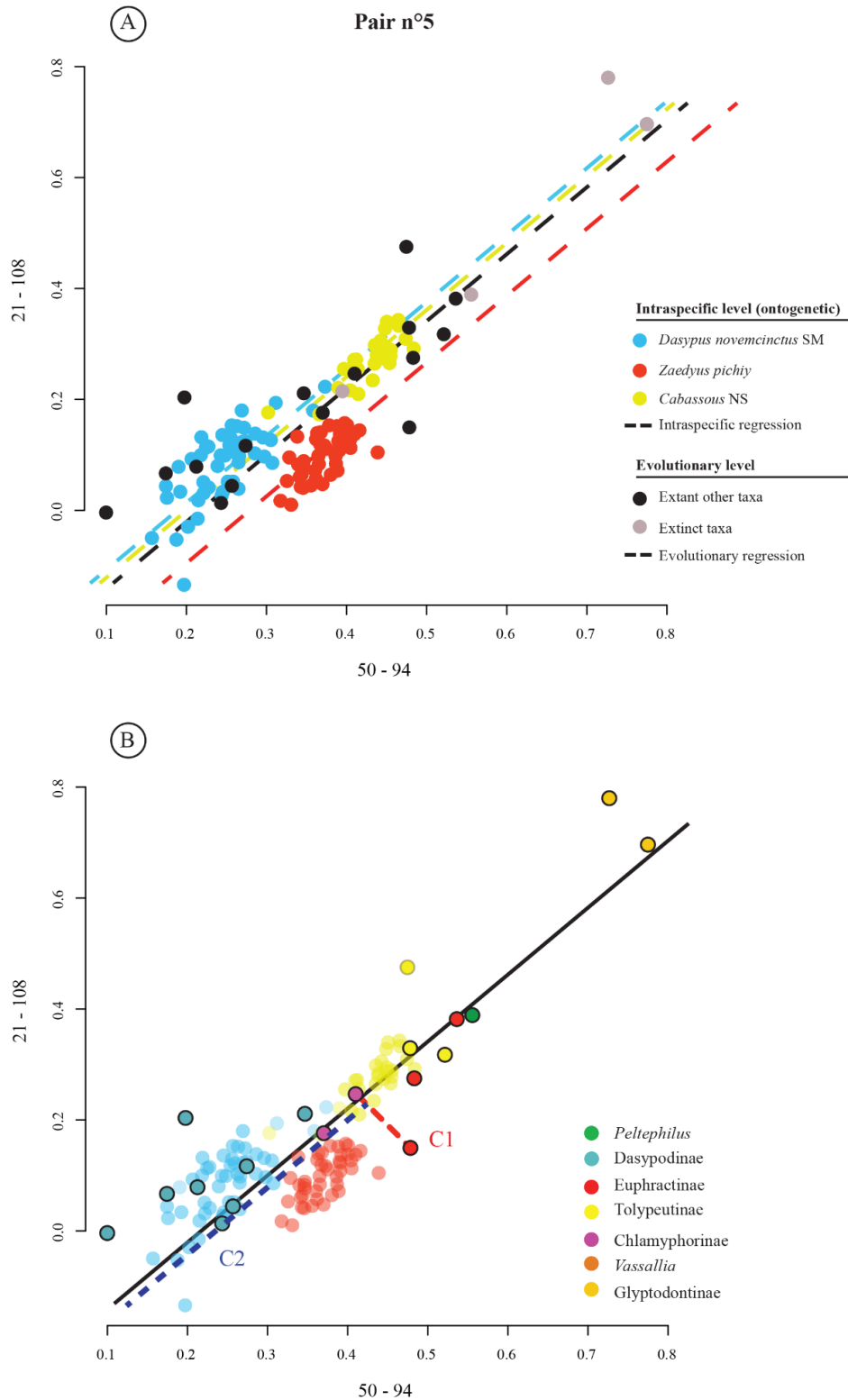


Figure 68. Covariation between the selected S-distances 50-94 and 21-18 (pair n°5) with a comparison between intraspecific and evolutionary level. A, both levels for regressions have similar slopes which suggest a widespread covariation pattern in cingulates. B, potential coding strategies C1 (quantification of the orthogonal distance of taxa relative to the regression line) and C2 (taxa position along the regression line).

General Discussion & Conclusion

Finally, the covariation patterns derived from correlated distance pairs as well as PCAs allow the targeting of potentially highly covariant regions, *e.g.*, anterior edge of orbit and ventral part of anterior root of zygomatic arches), once these regions have been identified, one way to further investigate patterns of covariation would be to conduct analyses such as 2-blocks partial least squares to improve our understanding of the 3-dimensional covariation of two regions (*e.g.*, [Bookstein *et al.*, 2003](#); [Klingenberg *et al.*, 2003](#); [Monteiro *et al.*, 2005](#); [Klingenberg & Marugán-Lobón, 2013](#)). These analyses require an a priori division into two blocks which was not possible before our study, but which could now be utilized based on the results of our study.

Beyond their phylogenetic implications, our multilevel analyses of patterns of cranial integration in cingulates may pave the way for further studies aiming at a better understanding patterns and processes of morphological covariation. In the light of our results, it would be possible to analyze more concretely the development of cranial units during ontogeny in cingulates, particularly at the prenatal level. This would be particularly relevant in the case of the development of the zygomatic arch, which appears to be developed at the prenatal level in glyptodonts ([Zurita *et al.*, 2009](#)) but also in nine-banded armadillo fetuses ([Le Verger *et al.*, unpublished data](#)). Outside cingulates, it would be also interesting to couple this kind of analysis with a study of gene expression for highly correlated regions in model organisms (*e.g.*, for the zygomatic arch - [Percival *et al.*, 2018](#)), or to examine the implication of developmental constraints on allometric patterns. A good way to complement our approach would also be to investigate muscular anatomy through dissections at different ontogenetic stages within species, as many detected covariations were found in regions of muscle insertion (*e.g.*, the nuchal crest, mastoid process, and descending process of zygomatic arch).

In conclusion, morphological covariations represent an insufficiently known and yet pervasive aspect of morphological variation. A better knowledge of this complex phenomenon is an important step for the improvement of morphological phylogenetic characters, which remain essential for the incorporation of fossils in phylogenies. The present work has allowed a deep exploration of covariation patterns in the skull of cingulates, but it was by no mean exhaustive, which again highlights the immense field of study that the analysis of morphological variation (and covariation) represents ([Hallgrímsson & Hall, 2005](#)). Our study corresponds to a preliminary

General Discussion & Conclusion

and exploratory step and argues for more in-depth analysis, including new coding strategies of covarying traits, which represents a promising new path for morphological phylogenetics. Pending further studies of this kind in cingulates, it is currently hard to state what the impact of our results could be on morphological matrices and on the reconstruction of cingulate relationships based on morphological data. Our analysis of the internal cranial anatomy has shown several resemblances between chlamyphorines and glyptodonts, as well as between the latter and the extinct pampatheres and the extinct genus *Proeutatus*. These findings are in partial agreement with molecular analyses and with previous morphological accounts (Gaudin & Wible, 2006; Billet et al., 2011; Delsuc et al., 2016; Mitchell et al., 2016) and might help to reach a more consensual vision of the phylogenetic relationships within the Cingulata in the future. In addition, our results have shown the existence of pervasive patterns of cranial integration in the group, especially allometry. This pervasiveness of allometry may imply that if morphological evidence may exist to group small-sized chlamyphorines together with giant-sized glyptodonts (Delsuc et al., 2016, Mitchell et al., 2016), then it might also be largely hidden by allometric patterns. Although allometric and other covariation patterns are difficult to compare with characters already defined in morphological matrices, alternative coding strategies must be used to evaluate their impact on such phylogenetic hypotheses in the future.

REFERENCES

- Abba AM, Cassini GH, Valverde G, Tilak MK, Vizcaíno SF, Superina M, Delsuc F.** 2015. Systematics of hairy armadillos and the taxonomic status of the Andean hairy armadillo (*Chaetophractus nationi*). *Journal of Mammalogy* 96: 673–689 p.
- Abdala F, Flores DA, Giannini NP.** 2001. Postweaning ontogeny of the skull of *Didelphis albiventris*. *Journal of Mammalogy* 82: 190–200 p.
- Abrantes EAL, Bergqvist LP.** 2006. Proposta filogenética para os Dasypodidae (Mammalia: Cingulata). In: Gallo V, Brito PM, Silva HMA, Figueirido FJ. eds. *Paleontologia Vertebrados: Grandes Temas e Contribuições Científicas*. Interciências, Rio de Janeiro, 261–274 p.
- Ackermann RR.** 2005. Ontogenetic integration in the hominoid face. *Journal of Human Evolution* 48:175–197 p.
- Acuña F, Sidorkewicz NS, Popp AI, Casanave EB.** 2017. A geometric morphometric study of sex differences in the scapula, humerus and ulna of *Chaetophractus villosus* (Xenarthra, Dasypodidae). *Iheringia, Serie Zoología* 107: e2017010.
- Adams DC.** 2014. A generalized K statistic for estimating phylogenetic signal from shape and other high dimensional multivariate data. *Systematic biology* 63: 685–697 p.
- Adams DC, Nistri A.** 2010. Ontogenetic convergence and evolution of foot morphology in European cave salamanders (Family: Plethodontidae). *BMC Evolutionary Biology* 10: 216–226 p.
- Adams DC, Collyer ML.** 2018. Phylogenetic ANOVA: Group-clade aggregation, biological challenges, and a refined permutation procedure. *Evolution* 72: 1204–1215 p.
- Adams DC, Rohlf FJ, Slice DE.** 2004. Geometric morphometrics: ten years of progress following the ‘revolution’. *Italian Journal of Zoology* 71: 5–16 p.
- Adams DC, Rohlf FJ, Slice DE.** 2013. A field comes of age: geometric morphometrics in the 21st century. *Hystrix, the Italian Journal of Mammalogy* 24: 7–14 p.
- Adams DC, Collyer ML, Kaliontzopoulou A.** 2018. Geomorph: Software for geometric morphometric analyses. *R package version 3.0.7*. R Foundation for Statistical Computing, Vienna, Austria.
- Adams DC, Collyer ML, Kaliontzopoulou A.** 2019. Geomorph: Software for geometric morphometric analyses. *R package version 3.1.1*. R Foundation for Statistical Computing, Vienna, Austria.
- Adams DC, Collyer ML, Kaliontzopoulou A.** 2020. Geomorph: Software for geometric morphometric analyses. *R package version 3.2.1*. R Foundation for Statistical Computing, Vienna, Austria.
- Aguiar JM, Da Fonseca GAB.** 2008. Conservation status of the Xenarthra. In: Vizcaíno SF, Loughry WJ. eds. *The Biology of the Xenarthra*. University Press of Florida, Gainesville, 215–231 p.
- Albrecht PW.** 1967. The cranial arteries and cranial arterial foramina of the turtle genera *Chrysemys*, *Sternotherus*, and *Trionyx*: a comparative study with analysis of possible evolutionary implications. *Tulane Studies in Zoology* 14: 81–99 p.

References

- Albrecht PW.** 1976. The cranial arteries of turtles and their evolutionary significance. *Journal of Morphology* 149: 159–182 p.
- Ameghino F.** 1884. *Filogenia: Principios de clasificación transformista basados sobre leyes naturales y proporciones matemáticas*. Lajouane F. ed. Buenos Aires, 390 p.
- Ameghino F.** 1887. Enumeración sistemática de las especies de mamíferos fósiles coleccionados por Carlos Ameghino en los terrenos eocenos de Patagonia austral y depositados en el Museo La Plata. *Boletín del Museo La Plata* 1: 1–26 p.
- Ameghino F.** 1889. Contribución al conocimiento de los mamíferos fósiles de la República Argentina. *Actas de la Academia Nacional de Ciencias en Córdoba* 6: 1–1027 p.
- Ameghino F.** 1891. Nuevos restos de mamíferos fósiles descubiertos por Carlos Ameghino en el Eoceno inferior de la Patagonia austral. Especies nuevas, adiciones y correcciones. *Revista Argentina de Historia Natural* 1: 289–328 p.
- Ameghino F.** 1902. Preliminary notes on new mammals from the Cretaceous terrains of Patagonia. *Boletín de la Academia Nacional de Ciencias de Córdoba* 17: 5–70 p.
- Anderson MJ.** 2001. A new method for non-parametric multivariate analysis of variance. *Austral ecology* 26: 32–46 p.
- Araújo R, Fernandez V, Polcyn MJ, Fröbisch J, Martins RM.** 2017. Aspects of gorgonopsian paleobiology and evolution: insights from the basicranium, occiput, osseous labyrinth, vasculature, and neuroanatomy. *PeerJ* 5: e3119.
- Armbruster WS.** 1991. Multilevel analysis of morphometric data from natural plant populations: insights into ontogenetic, genetic, and selective correlations in *Dalechampia scandens*. *Evolution* 45: 1229–1244 p.
- Armbruster WS, Gobeille RD.** 2004. Does pollen competition reduce the cost of inbreeding?. *American Journal of Botany* 91: 1939–1943 p.
- Arteaga MC, Gasca-Pineda J, Bello-Bedoy R, Eguiarte LE, Medellín RA.** 2020. Conservation Genetics, Demographic History, and Climatic Distribution of the Nine-Banded Armadillo (*Dasypus novemcinctus*): An Analysis of Its Mitochondrial Lineages. In: Ortega J, Maldonado JE. eds. *Conservation Genetics in Mammals: Integrative Research Using Novel Approaches*. Springer, Cham, 141–163 p.
- Asher RJ, Geisler JH, Sánchez-Villagra MR.** 2008. Morphology, paleontology, and placental mammal phylogeny. *Systematic Biology* 57: 311–317 p.
- Aya-Cuero C, Chacón-Pacheco J, Anacleto TCS.** 2019. *Dasypus kappleri* (Cingulata: Dasypodidae). *Mammalian Species* 51: 51–60 p.
- Baker J, Meade A, Pagel M, Venditti C.** 2015. Adaptive evolution toward larger size in mammals. *Proceedings of the National Academy of Sciences* 112: 5093–5098 p.
- Barasoain D, Contreras VH, Tomassini RL, Zurita AE.** 2020. A new pygmy armadillo (Cingulata, Euphractinae) from the late Miocene of Andean Argentina reveals an unexpected evolutionary history of the singular *Prozaedyus* lineage. *Journal of South American Earth Sciences* 100: 102589.
- Barbeito-Andrés J, Gonzalez PN, Hallgrímsson B.** 2016. Prenatal development of skull and brain in a mouse model of growth restriction. *Revista Argentina de Anthropologia Biologica* 18: 1–13 p.
- Bardin J, Rouget I, Cecca F.** 2017. Ontogenetic data analyzed as such in phylogenies. *Systematic biology* 66: 23–37 p.

References

- Bardua C, Wilkinson M, Gower DJ, Sherratt E, Goswami A.** 2019. Morphological evolution and modularity of the caecilian skull. *BMC evolutionary biology* 19: 30–52 p.
- Bardua C, Fabre AC, Bon M, Das K, Stanley EL, Blackburn DC, Goswami A.** 2020. Evolutionary integration of the frog cranium. *Evolution* 74: 1200–1215 p.
- Barone R.** 2000. *Anatomie comparée des mammifères domestiques*. Vigot. ed. Paris, 1021 p.
- Bergqvist LP, Abrantes EAL, Avilla LDS.** 2004. The Xenarthra (Mammalia) of Sao Jose de Itaboraí Basin (upper Paleocene, Itaborian), Rio de Janeiro, Brazil. *Geodiversitas* 26: 323–337 p.
- Billet G, Bardin J.** 2019. Serial Homology and Correlated Characters in Morphological Phylogenetics: Modeling the Evolution of Dental Crests in Placentals. *Systematic Biology* 68: 267–280 p.
- Billet G, Hautier L, Muizon de C, Valentin X.** 2011. Oldest cingulate skulls provide congruence between morphological and molecular scenarios of armadillo evolution. *Proceedings of the Royal Society B: Biological Sciences* 278: 2791–2797 p.
- Billet G, Hautier L, Lebrun R.** 2015a. Morphological diversity of the bony labyrinth (inner ear) in extant Xenarthrans and its relation to phylogeny. *Journal of Mammalogy* 96: 658–672 p.
- Billet G, Muizon de C, Schellhorn R, Ruf I, Ladevèze S, Bergqvist L.** 2015b. Petrosal and inner ear anatomy and allometry amongst specimens referred to Litopterna (Placentalia). *Zoological Journal of the Linnean Society* 173: 956–987 p.
- Billet G, Hautier L, Thoisy de B, Delsuc F.** 2017. The hidden anatomy of paranasal sinuses reveals biogeographically distinct morphotypes in the nine-banded armadillo (*Dasybus novemcinctus*). *PeerJ* 5: e3593.
- Bokma F, Godinot M, Maridet O, Ladevèze S, Costeur L, Solé F, Gheerbrant E, Peigné S, Jacques F, Laurin M.** 2016. Testing for Depéret's rule (body size increase) in mammals using combined extinct and extant data. *Systematic biology* 65: 98–108 p.
- Bolker JA.** 2000. Modularity in development and why it matters to evodevo. *American Zoologist* 40: 770–776 p.
- Bollback JP.** 2006. SIMMAP: stochastic character mapping of discrete traits on phylogenies. *BMC Bioinformatics* 7: 1–7 p.
- Bon M, Bardua C, Goswami A, Fabre AC.** 2020. Cranial integration in the fire salamander, *Salamandra salamandra* (Caudata: Salamandridae). *Biological Journal of the Linnean Society* 130: 178–194 p.
- Bookstein FL, Gunz P, Mitteroecker P, Prossinger H, Schaefer K, Seidler H.** 2003. Cranial integration in *Homo*: singular warps analysis of the midsagittal plane in ontogeny and evolution. *Journal of Human Evolution* 44: 167–187 p.
- Bordas AF.** 1932. Proposición de un nuevo género para “*Eutatus inornatus*”. *Physis* 11: 167–168 p.
- Boscaini A, Iurino DA, Sardella R, Tirao G, Gaudin TJ, Pujos F.** 2018. Digital cranial endocasts of the extinct sloth *Glossotherium robustum* (Xenarthra, Mylodontidae) from the late Pleistocene of Argentina: description and comparison with the extant sloths. *Journal of Mammalian Evolution* 27: 55–71 p.
- Boscaini A, Iurino DA, Mamani Quispe B, Andrade Flores R, Sardella R, Pujos F, Gaudin TJ.** 2020. Cranial anatomy and paleoneurology of the extinct sloth *Catonyx tarijensis* (Xenarthra, Mylodontidae) from the late Pleistocene of Oruro, Southwestern Bolivia. *Frontiers in Ecology and Evolution* 8: 1–16 p.

References

- Brown CM, Vavrek MJ.** 2015. Small sample sizes in the study of ontogenetic allometry; implications for palaeobiology. *PeerJ* 3: e818.
- Bubadué JM, Cáceres N, Carvalho RS, Meloro C.** 2015. Ecogeographical variation in skull shape of South-American canids: abiotic or biotic processes?. *Evolutionary Biology* 43: 145e159.
- Bulygina E, Mitteroecker P, Aiello L.** 2006. Ontogeny of facial dimorphism and patterns of individual development within one human population. *American Journal of Physical Anthropology: The Official Publication of the American Association of Physical Anthropologists* 131: 432–443 p.
- Burmeister H.** 1863. Ein neuer *Chlamyphorus*. *Abhandlungen Naturforschende Gesellschaft zu Halle* 7: 165–171 p.
- Burmeister H.** 1874. Monografía de los glyptodontes en el Museo Público de Buenos Aires. *Anales del Museo Público de Buenos Aires* 2: 1–412 p.
- Cáceres N, Meloro C, Carotenuto F, Passaro F, Sponchiado J, Melo GL, Raia P.** 2014. Ecogeographical variation in skull shape of capuchin monkeys. *Journal of Biogeography* 41: 501–512 p.
- Camacho J, Moon R, Smith SK, Lin JD, Randolph C, Rasweiler JJ, Richard R, Abzhanov A.** 2020. Differential cellular proliferation underlies heterochronic generation of cranial diversity in phyllostomid bats. *EvoDevo* 11: 1–17 p.
- Cappellini E, Prohaska A, Racimo F, Welker F, Pedersen MW, Allentoft ME, Damgaard PB, Gutenbrunner P, Dunne J, Hammann S, Roffet-Salque M, Ilardo M, Moreno-Mayar V, Wang Y, Sikora M, Vinner L, Cox J, Evershed RP, Willerslev E.** 2018. Ancient biomolecules and evolutionary inference. *Annual Review of Biochemistry* 87: 1029–1060 p.
- Cardini A.** 2019a. Craniofacial allometry is a rule in evolutionary radiations of placentals. *Evolutionary Biology* 46: 239–248 p.
- Cardini A.** 2019b. Integration and modularity in Procrustes shape data: is there a risk of spurious results?. *Evolutionary Biology* 46: 90–105 p.
- Cardini A.** 2020. Less tautology, more biology? A comment on “high-density” morphometrics. *Zoomorphology* 139: 1–17 p.
- Cardini A, O’Higgins P.** 2005. Post-natal ontogeny of the mandible and ventral cranium in *Marmota* species (Rodentia, Sciuridae): allometry and phylogeny. *Zoomorphology* 124: 189–203 p.
- Cardini A, Elton S.** 2007. Sample size and sampling error in geometric morphometric studies of size and shape. *Zoomorphology* 126: 121–134 p.
- Cardini A, Polly PD.** 2013. Larger mammals have longer faces because of size-related constraints on skull form. *Nature communications* 4: 2458.
- Cardini A, Polly PD, Dawson R, Milne N.** 2015. Why the long face? Kangaroos and wallabies follow the same ‘rule’ of cranial evolutionary allometry (CREA) as placentals. *Evolutionary Biology* 42: 169–176 p.
- Carlini AA, Zurita AE.** 2010. An introduction to cingulate evolution and their evolutionary history during the great American biotic interchange: biogeographical clues from Venezuela. In: Sánchez-Villagra M, Aguilera O, Carlini AA. eds. *Uruguay and Venezuela paleontology. The fossil record of the northern neotropics*. Indiana University Press, Bloomington, 233–255 p.

References

- Carlini AA, Vizcaíno SF, Scillato-Yane GJ.** 1997. Armored xenarthrans: a unique taxonomic and ecologic assemblage. In: Kay RF, Madden RH, Cifelli RL, Flynn JJ. eds. *Vertebrate paleontology in the Neotropics. The Miocene Fauna of La Venta, Colombia*. Smithsonian Institution Press, Washington/London, 213–226 p.
- Carlini AA, Ciancio MR, Flynn JJ, Scillato-Yané GJ, Wyss AR.** 2009. The phylogenetic and biostratigraphic significance of new armadillos (Mammalia, Xenarthra, Dasypodidae, Euphractinae) from the Tinguirirican (Early Oligocene) of Chile. *Journal of Systematic Palaeontology* 7: 489–503 p.
- Carlini AA, Soibelzon E, Glaz D.** 2016. *Chaetophractus vellerosus* (Cingulata: Dasypodidae). *Mammalian Species* 48: 73–82 p.
- Cassini GH.** 2013. Skull geometric morphometrics and paleoecology of Santacrucian (Late Early Miocene; Patagonia) native ungulates (Astrapotheria, Litopterna, and Notoungulata). *Ameghiniana* 50: 193–216 p.
- Carranza-Castañeda OC, Miller WE.** 2004. Late Tertiary terrestrial mammals from central Mexico and their relationship to South American immigrants. *Revista Brasileira de Paleontologia* 7: 249–261 p.
- Castellanos A.** 1932. Nuevos géneros de gliptodontes en relación con su filogenia. *Physis* 11: 92–100 p.
- Castellanos A.** 1946. Un nuevo gliptodontoideo del Araucanense del valle de Yocavil (Santa María) de la Provincia de Tucumán. *Publicaciones del Instituto de Fisiografía y Geología* 6: 1–19 p.
- Castellanos A.** 1959. Trascendencia de la obra de Florentino Ameghino. *Revista de la Facultad de Ciencias Naturales de Salta* 1: 35–56 p.
- Castro M, Ciancio M, Pacheco V, Salas Gismondi R, Bostelmann Torrealba E, Carlini AA.** 2015. Reassessment of the hairy long-nosed armadillo “*Dasypus*” *pilosus* (Xenarthra, Dasypodidae) and revalidation of the genus *Cryptophractus* Fitzinger, 1856. *Zootaxa* 3947: 30–48 p.
- Cheverud JM.** 1982a. Phenotypic, genetic, and environmental morphological integration in the cranium. *Evolution* 36: 499–516 p.
- Cheverud JM.** 1982b. Relationships among ontogenetic, static, and evolutionary allometry. *American Journal of Physical Anthropology* 59: 139–149 p.
- Cheverud JM.** 1984. Quantitative genetics and developmental constraints on evolution by selection. *Journal of theoretical biology* 110: 155–171 p.
- Cheverud JM.** 1995. Morphological integration in the saddle-back tamarin (*Saguinus fuscicollis*) cranium. *The American Naturalist* 145: 63–89 p.
- Chinga J, Pérez F.** 2016. Ontogenetic integration in two species of *Schizanthus* (Solanaceae): A comparison with static integration patterns. *Flora* 221: 75–81 p.
- Churchill M, Miguel J, Beatty BL, Goswami A, Geisler JH.** 2019. Asymmetry drives modularity of the skull in the common dolphin (*Delphinus delphis*). *Biological Journal of the Linnean Society* 126: 225–239 p.
- Ciancio MR, Castro MC, Galliari FC, Carlini AA, Asher RJ.** 2012. Evolutionary implications of dental eruption in *Dasypus* (Xenarthra). *Journal of Mammalian Evolution* 19: 1–8 p.
- Cione AL, Gasparini GM, Soibelzon E, Soibelzon LH, Tonni EP.** 2015. *The great American biotic interchange: a South American perspective*. Springer. ed. Dordrecht, 97 p.
- Claude J.** 2008. *Morphometrics with R*. Springer-Verlag. ed. New York, 317 p.

References

- Claude J.** 2013. Log-shape ratios, Procrustes superimposition, elliptic Fourier analysis: three worked examples in R. *Virtual Morphology and Evolutionary Morphometrics in the new millennium* 24: 94–102 p.
- Clavel J, Merceron G, Escarguel G.** 2014. Missing Data Estimation in Morphometrics: How Much is Too Much?. *Systematic Biology* 63: 203–218 p.
- Clavel J, Escarguel G, Merceron G.** 2015. mvMORPH: an R package for fitting multivariate evolutionary models to morphometric data. *Methods in Ecology and Evolution* 6: 1311–1319 p.
- Cobb SN, O'Higgins P.** 2004. Hominins do not share a common postnatal facial ontogenetic shape trajectory. *Journal of Experimental Zoology Part B: Molecular and Developmental Evolution* 302: 302–321 p.
- Codón SM, Estecondo SG, Galíndez EJ, Casanave EB.** 2001. Ultrastructure and morphometry of ovarian follicles in the armadillo *Chaetophractus villosus* (Mammalia, Dasypodidae). *Revista Brasileira de Biologia* 61: 485–499 p.
- Collyer ML, Adams DC.** 2013. Phenotypic trajectory analysis: comparison of shape change patterns in evolution and ecology. *Hystrix, the Italian Journal of Mammalogy* 24: 75–83 p.
- Collyer ML, Sekora DJ, Adams DC.** 2015. A method for analysis of phenotypic change for phenotypes described by high-dimensional data. *Heredity* 115: 357–365 p.
- Cope ED.** 1889. The Edentata of North America. *The American Naturalist* 23: 657–664 p.
- Cornette R, Tresset A, Herrel A.** 2015. The shrew tamed by Wolff's law: Do functional constraints shape the skull through muscle and bone covariation?. *Journal of Morphology* 276: 301–309 p.
- Costa FR, Clerici GP, Lobo-Ribeiro L, Rosa PS, Rocha-Barbosa O.** 2019. Analysis of the spatio-temporal parameters of gaits in *Dasypus novemcinctus* (Xenarthra: Dasypodidae). *Acta Zoologica* 100: 61–68 p.
- Coutier F, Hautier L, Cornette R, Amson E, Billet G.** 2017. Orientation of the lateral semicircular canal in Xenarthra and its links with head posture and phylogeny. *Journal of Morphology* 278: 704–717 p.
- Cozzuol MA.** 2006. The Acre vertebrate fauna: Age, diversity, and geography. *Journal of South American Earth Sciences* 21: 85–203 p.
- Curtis AA, Lai G, Wei F, Van Valkenburgh B.** 2015. Repeated loss of frontal sinuses in arctoid carnivorans. *Journal of Morphology* 276: 22–32 p.
- Cuvier G.** 1798. *Tableau élémentaire de l'histoire naturelle des animaux*. Baudouin. ed. Paris, 770 p.
- Dávalos LM, Velazco PM, Warsi OM, Smits PD, Simmons NB.** 2014. Integrating incomplete fossils by isolating conflicting signal in saturated and non-independent morphological characters. *Systematic Biology* 63: 582–600 p.
- De Esteban Trivigno S, Mendoza M, De Renzi M.** 2008. Body mass estimation in Xenarthra: A predictive equation suitable for all quadrupedal terrestrial placentals?. *Journal of Morphology* 269: 1276–1293 p.
- De Iuliis G, Bargo MS, Vizcaíno SF.** 2000. Variation in skull morphology and mastication in the fossil giant armadillos *Pampatherium* spp. and allied genera (Mammalia: Xenarthra: Pampatheriidae), with comments on their systematics and distribution. *Journal of Vertebrate Paleontology* 20: 743–754 p.
- De Iuliis G, Edmund AG.** 2002. *Vassallia maxima* Castellanos, 1946 (Mammalia: Xenarthra: Pampatheriidae), from Puerta del Corral Quemado (late Miocene to early Pliocene), Catamarca Province, Argentina. *Smithsonian contributions to paleobiology* 93: 49–64 p.

References

- Del Castillo DL, Viglino M, Flores DA, Cappozzo HL.** 2017. Skull ontogeny and modularity in two species of *Lagenorhynchus*: Morphological and ecological implications. *Journal of Morphology* 278: 203–214 p.
- Delsuc F, Scally M, Madsen O, Stanhope MJ, De Jong WW, Catzeflis FM, Springer MS, Douzery EJ.** 2002. Molecular phylogeny of living xenarthrans and the impact of character and taxon sampling on the placental tree rooting. *Molecular biology and evolution* 19: 1656–1671 p.
- Delsuc F, Stanhope MJ, Douzery EJ.** 2003. Molecular systematics of armadillos (Xenarthra, Dasypodidae): contribution of maximum likelihood and Bayesian analyses of mitochondrial and nuclear genes. *Molecular Phylogenetics and Evolution* 28: 261–275 p.
- Delsuc F, Superina M, Tilak MK, Douzery EJ, Hassanin A.** 2012. Molecular phylogenetics unveils the ancient evolutionary origins of the enigmatic fairy armadillos. *Molecular Phylogenetics and Evolution* 62: 673–680 p.
- Delsuc F, Gibb GC, Kuch M, Billet G, Hautier L, Southon J, Rouillard JM, Fernicola JC, Vizcaíno SF, MacPhee RDE, Poinar HN.** 2016. The phylogenetic affinities of the extinct glyptodonts. *Current Biology* 26: 155–156 p.
- Derrickson EM.** 1992. Comparative reproductive strategies of altricial and precocial eutherian mammals. *Functional Ecology* 6: 57–65 p.
- Desbiez ALJ, Massocato GF, Kluyber D.** 2020. Insights into giant armadillo (*Priodontes maximus* Kerr, 1792) reproduction. *Mammalia* 84: 283–293 p.
- Desmarest AG.** 1804. Tableau méthodique des mammifères. *Nouveau dictionnaire d'histoire naturelle* 24: 5–58 p.
- Donoghue MJ, Ree RH.** 2000. Homoplasy and developmental constraint: a model and an example from plants. *American Zoologist* 40: 759–769 p.
- Downing K, White R.** 1995. The cingulates (Xenarthra) of Leisey Shell Pit local fauna (Irvingtonian), Hillborough County, Florida. *Bulletin of the Florida Museum of Natural History* 37: 375–396 p.
- Drake AG, Klingenberg CP.** 2008. The pace of morphological change: historical transformation of skull shape in St Bernard dogs. *Proceedings of the Royal Society B: Biological Sciences* 275: 71–76 p.
- Drake AG, Klingenberg CP.** 2010. Large-scale diversification of skull shape in domestic dogs: disparity and modularity. *The American Naturalist* 175: 289–301 p.
- Dryden IL, Mardia KV.** 2016. *Statistical shape analysis: with applications in R*. John Wiley & Sons. ed. Chichester, 496 p.
- Dushoff J, Kain MP, Bolker BM.** 2019. I can see clearly now: reinterpreting statistical significance. *Methods in Ecology and Evolution* 10: 756–759 p.
- Edgeworth FH.** 1923. On the development of the cranial muscles of *Tatusia* and *Manis*. *Journal of Anatomy London* 57: 313–335 p.
- Edmund AG, Theodor J.** 1997. A new giant Armadillo. In: Kay RF, Madden RH, Cifelli RL, Flynn JJ. eds. *Vertebrate paleontology in the Neotropics. The Miocene Fauna of La Venta, Colombia*. Smithsonian Institution Press, Washington/London, 227–232 p.
- Emerson SB, Hastings PA.** 1998. Morphological correlations in evolution: consequences for phylogenetic analysis. *The Quarterly Review of Biology* 73: 141–162 p.

References

- Engelmann GF.** 1985. The phylogeny of the Xenarthra. In: Montgomery. ed. *The evolution and ecology of armadillos, sloths and vermilinguas*. Smithsonian Institution Press, Washington, 51–64 p.
- Esquerré D, Sherratt E, Keogh JS.** 2017. Evolution of extreme ontogenetic allometric diversity and heterochrony in pythons, a clade of giant and dwarf snakes. *Evolution* 71: 2829–2844 p.
- Esselstyn JA, Oliveros CH, Swanson MT, Faircloth BC.** 2017. Investigating difficult nodes in the placental mammal tree with expanded taxon sampling and thousands of ultraconserved elements. *Genome Biology and Evolution* 9: 2308–2321 p.
- Evans HE, De Lahunta A.** 2012. *Miller's Anatomy of the Dog*. Saunders. ed. St Louis, 850 p.
- Fabre AC, Perry JM, Hartstone-Rose A, Lowie A, BoensA, Dumont M.** 2018. Do muscles constrain skull shape evolution in Strepsirrhines?. *The Anatomical Record* 301: 291–310 p.
- Fariña RA, Vizcaíno SF.** 2001. Carved teeth and strange jaws: how glyptodonts masticated. *Acta Palaeontologica Polonica* 46: 219–234 p.
- Fariña RA, Vizcaíno, SF, De Iuliis G.** 2013. *Megafauna: giant beasts of Pleistocene South America*. Indiana University Press. ed. Bloomington, 448 p.
- Farke AA.** 2010. Evolution and functional morphology of the frontal sinuses in Bovidae (Mammalia: Artiodactyla), and implications for the evolution of cranial pneumaticity. *Zoological Journal of the Linnean Society* 159: 988–1014 p.
- Feijó A, Cordeiro-Estrela P.** 2016. Taxonomic revision of the *Dasybus kappleri* complex, with revalidations of *Dasybus pastasae* (Thomas, 1901) and *Dasybus beniensis* Lönnberg, 1942 (Cingulata, Dasypodidae). *Zootaxa* 4170: 271–297 p.
- Feijó A, Patterson BD, Cordeiro-Estrela P.** 2018. Taxonomic revision of the long-nosed armadillos, Genus *Dasybus* Linnaeus, 1758 (Mammalia, Cingulata). *PloS one* 13: e0195084.
- Feijó A, Vilela JF, Cheng J, Schetino MAA, Coimbra RTF, Bonvicino CR, Santos FR, Patterson BD, Cordeiro-Estrela P.** 2019. Phylogeny and molecular species delimitation of long-nosed armadillos (*Dasybus*: Cingulata) supports morphology-based taxonomy. *Zoological Journal of the Linnean Society* 186: 813–825 p.
- Feijó A, Patterson BD, Cordeiro-Estrela P.** 2020. Phenotypic variability and environmental tolerance shed light on nine-banded armadillo Nearctic invasion. *Biological Invasions* 22: 255–269 p.
- Felice RN, Goswami A.** 2018. Developmental origins of mosaic evolution in the avian cranium. *Proceedings of the National Academy of Sciences* 115: 555–560 p.
- Felice RN, Watanabe A, Cuff AR, Noirault E, Pol D, Witmer LM, Norell MA, O'Connor PM, Goswami A.** 2019. Evolutionary integration and modularity in the archosaur cranium. *Integrative and comparative biology* 59: 371–382 p.
- Felice RN, Watanabe A, Cuff AR, Hanson M, Bhullar BAS, Rayfield ER, Witmer LM, Norell MA, Goswami A.** 2020. Decelerated dinosaur skull evolution with the origin of birds. *PLoS biology* 18: e3000801.
- Felsenstein J.** 1973. Maximum likelihood and minimum-steps methods for estimating evolutionary trees from data on discrete characters. *Systematic Biology* 22: 240–249 p.
- Felsenstein J.** 2004. *Inferring phylogenies*. Sinauer Associates. ed. Sunderland, 664 p.
- Ferigolo J.** 1985. Evolutionary trends of the histological pattern in the teeth of Edentata (Xenarthra). *Archives of Oral Biology* 30: 71–82 p.

References

- Fernicola JC.** 2008. Nuevos aportes para la sistemática de los Glyptodontia Ameghino 1889 (Mammalia, Xenarthra, Cingulata). *Ameghiniana* 45: 553–574 p.
- Fernicola JC, Toledo N, Bargo MS, Vizcaíno SF.** 2012. A neomorphic ossification of the nasal cartilages and the structure of paranasal sinus system of the glyptodont *Neosclerocalyptus* Paula Couto 1957 (Mammalia, Xenarthra). *Palaeontologia Electronica* 15: 1–22 p.
- Fernicola, JC, Rinderknecht A, Jones W, Vizcaíno SF, Porpino K.** 2017. A new species of *Neoglyptatelus* (Mammalia, Xenarthra, Cingulata) from the late Miocene of Uruguay provides new insights on the evolution of the dorsal armor in cingulates. *Ameghiniana* 55: 233–252 p.
- Ferreira-Cardoso S, Billet G, Gaubert P, Delsuc F, Hautier L.** 2019. Skull shape variation in extant pangolins (Pholidota: Manidae): allometric patterns and systematic implications. *Zoological Journal of the Linnean Society* 188: 255–275 p.
- Fitzinger LJ.** 1856. Versammlung Deutscher Naturforscher und Ärzte in Wien. *Tageblatt* 32: 123.
- Flores DA, Giannini N, Abdala F.** 2006. Comparative postnatal ontogeny of the skull in the australidelphian metatherian *Dasyurus albopunctatus* (Marsupialia: Dasyuromorpha: Dasyuridae). *Journal of Morphology* 267: 426–440 p.
- Flores DA, Abdala F, Giannini N.** 2010. Cranial ontogeny of *Caluromys philander* (Didelphidae: Caluromyinae): a qualitative and quantitative approach. *Journal of Mammalogy* 91: 539–550 p.
- Flower WH.** 1882. On the mutual affinities of the animals composing the order Edentata. *Proceeding of the Zoological Society of London* 50: 358–367 p.
- Foley NM, Springer MS, Teeling EC.** 2016. Mammal madness: is the mammal tree of life not yet resolved?. *Philosophical Transactions of the Royal Society B: Biological Sciences* 371: 20150140.
- Frankino WA, Zwaan BJ, Stern DL, Brakefield PM.** 2005. Natural selection and developmental constraints in the evolution of allometries. *Science* 307: 718–720 p.
- Frappell PB, Boggs DF, Kilgore Jr DL.** 1998. How stiff is the armadillo? A comparison with the allometrics of mammalian respiratory mechanics. *Respiration physiology* 113: 111–122 p.
- Frechkop S, Yepes J.** 1949. Etude systématique et zoogéographique des Dasypodidés conservés à l'Institut. *Institut royal des sciences naturelles de Belgique* 25: 1–56 p.
- Frederich B, Sheets HD.** 2010. Evolution of ontogenetic allometry shaping giant species: a case study from the damselfish genus *Dascyllus* (Pomacentridae). *Biological Journal of the Linnean Society* 99: 99–117 p.
- Freidline SE, Gunz P, Hublin JJ.** 2015. Ontogenetic and static allometry in the human face: contrasting Khoisan and Inuit. *American journal of physical anthropology* 158: 116–131 p.
- Frost SR, Marcus LF, Bookstein FL, Reddy DP, Delson E.** 2003. Cranial allometry, phylogeography, and systematics of large-bodied papionins (primates: Cercopithecoinae) inferred from geometric morphometric analysis of landmark data. *The Anatomical Record Part A: Discoveries in Molecular, Cellular, and Evolutionary Biology: An Official Publication of the American Association of Anatomists* 275: 1048–1072 p.
- Gaffney ES.** 1979. Comparative cranial morphology of recent and fossil turtles. *Bulletin of the American Museum of Natural History* 164: 65–375 p.
- Galliari FC, Carlini AA, Sánchez-Villagra MR.** 2010. Evolution of the axial skeleton in armadillos (Mammalia, Dasypodidae). *Mammalian Biology* 75: 326–333 p.

References

- Gardner AL.** 2005. Order Cingulata. In: Wilson DE, Reeder DM. eds. *Mammal Species of the World: A Taxonomic and Geographic Reference*. Johns Hopkins University Press. Baltimore, 94–99 p.
- Gaudin TJ.** 1995. The ear region of edentates and the phylogeny of the Tardigrada (Mammalia, Xenarthra). *Journal of Vertebrate Paleontology* 15: 672–705 p.
- Gaudin TJ.** 2004. Phylogenetic relationships among sloths (Mammalia, Xenarthra, Tardigrada): the craniodental evidence. *Zoological Journal of the Linnean Society* 140: 255–305 p.
- Gaudin TJ, Wible JR.** 2006. The phylogeny of living and extinct armadillos (Mammalia, Xenarthra, Cingulata): a craniodental analysis. In: Carrano MT, Gaudin TJ, Blob RW, Wible JR. eds. *Amniote Paleobiology: Perspectives on the Evolution of Mammals, Birds, and Reptiles*. University of Chicago Press, Chicago, 153–198 p.
- Gaudin TJ, Croft DA.** 2015. Paleogene Xenarthra and the evolution of South American mammals. *Journal of Mammalogy* 96: 622–634 p.
- Gaudin TJ, Lyon LM.** 2017. Cranial osteology of the pampathere *Holmesina floridanus* (Xenarthra: Cingulata; Blancan NALMA), including a description of an isolated petrosal bone. *PeerJ* 5: e4022.
- Gerber S, Eble GJ, Neige P.** 2008. Allometric space and allometric disparity: a developmental perspective in the macroevolutionary analysis of morphological disparity. *Evolution: International Journal of Organic Evolution* 62: 1450–1457 p.
- Gerber S, Hopkins MJ.** 2011. Mosaic heterochrony and evolutionary modularity: the trilobite genus *Zacanthopsis* as a case study. *Evolution: International Journal of Organic Evolution* 65: 3241–3252 p.
- Giannini NP.** 2014. Quantitative developmental data in a phylogenetic framework. *Journal of Experimental Zoology Part B: Molecular and Developmental Evolution* 322: 558–566 p.
- Giannini NP, Segura V, Giannini MI, Flores D.** 2010. A quantitative approach to the cranial ontogeny of the puma. *Mammalian Biology* 75: 47–554 p.
- Gibb GC, Condamine FL, Kuch M, Enk J, Moraes-Barros N, Superina M, Poinar HN, Delsuc F.** 2016. Shotgun mitogenomics provides a reference phylogenetic framework and timescale for living xenarthrans. *Molecular Biology and Evolution* 33: 621–642 p.
- Gillette DD, Ray CE.** 1981. Glyptodonts of North America. *Smithsonian Contributions to paleobiology* 40: 1–255 p.
- Gomes Rodrigues H, Cornette R, Clavel J, Cassini G, Bhullar BAS, Fernández-Monescillo M, Moreno K, Herrel A, Billet G.** 2018. Differential influences of allometry, phylogeny and environment on the rostral shape diversity of extinct South American notoungulates. *Royal Society open science* 5: 171816.
- Gonzalez PN, Perez SI, Bernal V.** 2011. Ontogenetic allometry and cranial shape diversification among human populations from South America. *The Anatomical Record: Advances in Integrative Anatomy and Evolutionary Biology* 294: 1864–1874 p.
- González-Ruiz LR.** 2010. *Los Cingulata (Mammalia, Xenarthra) del Mioceno temprano y medio de Patagonia (edades Santacrucense y “Friasense”). Revisión sistemática y consideraciones bioestratigráficas*. Ph.D. dissertation, Universidad Nacional de La Plata, Facultad de Ciencias Naturales y Museo. La Plata. 471 p.
- González-Ruiz LR, Brandoni D, Zurita AE, Green JL, Novo NM, Tauber AA, Tejedor MF.** 2020. Juvenile Glyptodont (Mammalia, Cingulata) from the Miocene of Patagonia, Argentina: Insights into Mandibular and Dental Characters. *Journal of Vertebrate Paleontology* 40: e1768398.

References

- González-Ruiz LR, Ciancio MR, Martin GM, Zurita AE.** 2015. First record of supernumerary teeth in Glyptodontidae (Mammalia, Xenarthra, Cingulata). *Journal of Vertebrate Paleontology* 35: e885033.
- Good PI.** 2000. *Permutation tests: a practical guide to resampling methods for testing hypotheses*. Springer. ed. New York, 270 p.
- Goodall C.** 1991. Procrustes methods in the statistical analysis of shape. *Journal of the Royal Statistical Society: Series B (Methodological)* 53: 285–321 p.
- Gordon A.** 1999. *Classification (2nd edition)*. Chapman and Hall/CRC press. ed. London, 272 p.
- Goswami A.** 2006. Cranial modularity shifts during mammalian evolution. *The American Naturalist* 168: 270–280 p.
- Goswami A, Prochel J.** 2007. Ontogenetic morphology and allometry of the cranium in the common European mole (*Talpa europaea*). *Journal of Mammalogy* 88: 667–677 p.
- Goswami A, Polly PD.** 2010a. The influence of character correlations of phylogenetic analyses: a case study of the carnivoran cranium. In: Goswami A, Friscia A. eds. *Carnivoran evolution: new views on phylogeny, form, and function*. Cambridge University Press, Cambridge, 141–164 p.
- Goswami A, Polly PD.** 2010b. Methods for studying morphological integration and modularity. *The Paleontological Society Papers* 16: 213–243 p.
- Goswami A, Finarelli JA.** 2016. EMMLi: a maximum likelihood approach to the analysis of modularity. *Evolution* 70: 1622–1637 p.
- Goswami A, Smaers JB, Soligo C, Polly PD.** 2014. The macroevolutionary consequences of phenotypic integration: from development to deep time. *Philosophical Transactions of the Royal Society B: Biological Sciences* 369: 20130254.
- Goswami A, Watanabe A, Felice RN, Bardua C, Fabre AC, Polly PD.** 2019. High-density morphometric analysis of shape and integration: the good, the bad, and the not-really-a-problem. *Integrative and comparative biology* 59: 669–683 p.
- Gould SJ.** 1966. Allometry and size in ontogeny and phylogeny. *Biological Reviews* 41: 587–638 p.
- Gould SJ.** 1989. A developmental constraint in *Cerion*, with comments on the definition and interpretation of constraint in evolution. *Evolution* 43: 516–539 p.
- Gray DJE.** 1865. Revision of the genera and species of entomophagous edentata, founded on the examination of the specimens in the British Museum. *Proceedings of the Zoological Society of London* 33: 359–386 p.
- Guillerme T, Brazeau MD.** 2018. Influence of different modes of morphological character correlation on phylogenetic tree inference. *BioRxiv*: 308742.
- Gunnell GF, Rose KD.** 2008. “Edentata” summary. In: Janis CM, Gunnell GF, Uhen MD. eds. *Evolution of Tertiary Mammals of North America: Volume 2: Small Mammals, Xenarthrans, and Marine Mammals*. Cambridge University Press. Cambridge, 127–134 p.
- Hallgrímsson B, Hall BK.** 2005. *Variation: a central concept in biology*. Elsevier Academic Press. ed. Burlington, 592 p.
- Hallgrímsson, B, Willmore K, Dorval C, Cooper DM.** 2004. Craniofacial variability and modularity in macaques and mice. *Journal of Experimental Zoology Part B: Molecular and Developmental Evolution* 302: 207–225 p.

References

- Hallgrímsson B, Lieberman DE, Young NM, Parsons T, Wat S.** 2007. Evolution of covariance in the mammalian skull. In: Bock G, Goddard J. eds. *Tinkering: The Microevolution of Development: Novartis Foundation Symposium*. Wiley, New York, 164–190 p.
- Hallgrímsson B, Jammiczky H, Young NM, Rolian C, Parsons TE, Boughner JC, Marcucio RS.** 2009. Deciphering the palimpsest: studying the relationship between morphological integration and phenotypic covariation. *Evolutionary biology* 36: 355–376 p.
- Hallgrímsson B, Percival CJ, Green R, Young NM, Mio W, Marcucio R.** 2015. Morphometrics, 3D imaging, and craniofacial development. *Current topics in developmental biology* 115: 561–597 p.
- Hallgrímsson B, Katz DC, Aponte JD, Larson JR, Devine J, Gonzalez PN, Young NM, Roseman CC, Marcucio RS.** 2019. Integration and the Developmental Genetics of Allometry. *Integrative and comparative biology* 59: 1369–1381 p.
- Halliday TJ, Upchurch P, Goswami A.** 2017. Resolving the relationships of Paleocene placental mammals. *Biological Reviews* 92: 521–550 p.
- Harlan R.** 1825. Description of a New Genus of Mammiferous Quadrupeds of the Order Edentata. In: Phillips W. ed. *Zoological Journal*. London, 154–163 p.
- Harrison LB, Larsson HC.** 2015. Among-character rate variation distributions in phylogenetic analysis of discrete morphological characters. *Systematic Biology* 64: 307–324 p.
- Hautier L, Weisbecker V, Goswami A, Knight F, Kardjilov N, Asher RJ.** 2011. Skeletal ossification and sequence heterochrony in xenarthran evolution. *Evolution & development* 13: 460–476 p.
- Hautier L, Billet G, Thoisy de B, Delsuc F.** 2017. Beyond the carapace: skull shape variation and morphological systematics of long-nosed armadillos (genus *Dasybus*). *PeerJ* 5: e3650.
- Hayssen V, Ortega J, Morales-Leyva A, Martínez-Mendez N.** 2013. *Cabassous centralis* (Cingulata: Dasypodidae). *Mammalian Species* 45: 12–17 p.
- Hayssen V.** 2014a. *Cabassous unicinctus* (Cingulata: Dasypodidae). *Mammalian Species* 46: 16–23 p.
- Hayssen V.** 2014b. *Cabassous tatouay* (Cingulata: Dasypodidae). *Mammalian Species* 46: 28–32 p.
- Hayssen V.** 2014c. *Cabassous chacoensis* (Cingulata: Dasypodidae). *Mammalian Species* 46: 24–27 p.
- Heck L, Sánchez-Villagra MR, Stange M.** 2019. Why the long face? Comparative shape analysis of miniature, pony, and other horse skulls reveals changes in ontogenetic growth. *PeerJ* 7: e7678.
- Heesy CP.** 2005. Function of the mammalian postorbital bar. *Journal of Morphology* 264: 363–380 p.
- Hennekam JJ, Benson RB, Herridge VL, Jeffery N, Torres-Roig E, Alcover JA, Cox PG.** 2020. Morphological divergence in giant fossil dormice. *Proceedings of the Royal Society B* 287: 20202085.
- Hennig C.** 2007. Cluster-wise assessment of cluster stability. *Computational Statistics & Data Analysis* 52: 258–271 p.
- Herrera CM, Powell JE, Esteban GI, Del Papa C.** 2017. A new Eocene dasypodid with caniniforms (Mammalia, Xenarthra, Cingulata) from northwest Argentina. *Journal of Mammalian Evolution* 24: 275–288 p.
- Hillis D, Huelsenbeck J.** 1992. Signal, noise, and reliability in molecular phylogenetic analyses. *Journal of Heredity* 83: 189–195 p.

References

- Hoffman EA, Rowe TB.** 2018. Jurassic stem-mammal perinates and the origin of mammalian reproduction and growth. *Nature* 561: 104–108 p.
- Hoffstetter R.** 1958. Xenarthra. In: Piveteau J. ed. *Traité de Paléontologie*. Masson & Cie. Paris, 535–636 p.
- Hubbe A, Melo D, Marroig G.** 2016. A case study of extant and extinct Xenarthra cranium covariance structure: implications and applications to paleontology. *Paleobiology* 42: 465–488 p.
- Huchon D, Delsuc F, Catzeflis FM, Douzery EJ.** 1999. Armadillos exhibit less genetic polymorphism in North America than in South America: nuclear and mitochondrial data confirm a founder effect in *Dasyopus novemcinctus* (Xenarthra). *Molecular Ecology* 8: 1743–1748 p.
- Huxley TH.** 1864. II. On the osteology of the genus *Glyptodon*. *Philosophical Transactions of the Royal Society of London* 155: 31–70 p.
- Illiger JKW.** 1811. *Prodromus Systematis Mammalium et Avium: Additis Terminis Zoographicis Utriusque Classis, Eorumque Versione Germanica*. Salfeld C. ed. Berlin, 301 p.
- Izenman AJ.** 2013. Multivariate regression. In: Izenman AJ. ed. *Modern Multivariate Statistical Techniques*. Springer-Verlag, New York, 159–194 p.
- Jamniczky HA, Hallgrímsson B.** 2011. Modularity in the skull and cranial vasculature of laboratory mice: implications for the evolution of complex phenotypes. *Evolution & development* 13: 28–37 p.
- Jolicoeur P, Mosimann JE.** 1960. Size and shape variation in the painted turtle. A principal component analysis. *Growth* 24: 339–354 p.
- Jolliffe IT.** 2002. Graphical representation of data using principal components. In: Jolliffe IT. ed. *Principal component analysis*. Springer-Verlag, New York, 78–110 p.
- Kang Y, Su J, Yao B, Ji W, Hegab IM, Hanafy AM, Zhang D.** 2020. Geometric morphometric analysis of the plateau zokor (*Eospalax baileyi*) revealed significant effects of environmental factors on skull variations. *Zoology*: 125779.
- Kerr R.** 1792. *The animal kingdom or zoological system, of the celebrated Sir Charles Linnaeus. class I. Mammalia: contain a complete systematic description, arrangement, and nomenclature, of all the known species and varieties of Mammalia, or animals which give suck to their young; being a translation of that part of the Systema Naturae, as lately published, with great improvements, by Professor Gmelin of Goettingen, together with numerous additions from more recent zoological writers, and illustrated with copperplates*. Strahan A, Cadell T, Creech W. eds. London/Edinburgh, 644 p.
- Klenovšek T.** 2014. Skull modularity of the European ground squirrel *Spermophilus citellus* (Linnaeus, 1766). *Acta Biologica Slovenica* 57: 59–67 p.
- Klenovšek T, Jojić V.** 2016. Modularity and cranial integration across ontogenetic stages in Martino's vole, *Dinaromys bogdanovi*. *Contributions to Zoology* 85: 275–289 p.
- Klingenberg CP.** 1996. Multivariate allometry. In: Marcus LF, Corti M, Loy A, Naylor GJP, Slice DE. eds. *Advances in morphometrics*. Springer, Boston, 23–49 p.
- Klingenberg CP.** 2005. Developmental constraints, modules, and evolvability. In: Hallgrímsson B, Hall BK. eds. *Variation: a central concept in biology*. Elsevier Academic Press. ed. Burlington, 219–247 p.

References

- Klingenberg CP.** 2008. Morphological integration and developmental modularity. *Annual review of ecology, evolution, and systematics* 39: 115–132 p.
- Klingenberg CP.** 2010. Evolution and development of shape: integrating quantitative approaches. *Nature Reviews Genetics* 1: 623–635 p.
- Klingenberg CP.** 2013. Cranial integration and modularity: insights into evolution and development from morphometric data. *Hystrix, the Italian Journal of Mammalogy* 24: 43–58 p.
- Klingenberg CP.** 2014. Studying morphological integration and modularity at multiple levels: concepts and analysis. *Philosophical Transactions of the Royal Society B: Biological Sciences* 369: 20130249.
- Klingenberg CP.** 2016. Size, shape, and form: concepts of allometry in geometric morphometrics. *Development genes and evolution* 226: 113–137 p.
- Klingenberg CP.** 2020. How Exactly Did the Nose Get That Long? A Critical Rethinking of the Pinocchio Effect and How Shape Changes Relate to Landmarks. *Evolutionary Biology* 1–13 p.
- Klingenberg CP, Zimmermann M.** 1992. Static, ontogenetic, and evolutionary allometry: a multivariate comparison in nine species of water striders. *The American Naturalist* 140: 601–620 p.
- Klingenberg CP, McIntyre GS.** 1998. Geometric morphometrics of developmental instability: analyzing patterns of fluctuating asymmetry with Procrustes methods. *Evolution* 52: 1363–1375 p.
- Klingenberg CP, Zaklan SD.** 2000. Morphological integration between developmental compartments in the *Drosophila* wing. *Evolution* 54: 1273–1285 p.
- Klingenberg CP, Marugán-Lobón J.** 2013. Evolutionary covariation in geometric morphometric data: analyzing integration, modularity, and allometry in a phylogenetic context. *Systematic biology* 62: 591–610 p.
- Klingenberg CP, Barluenga M, Meyer A.** 2002. Shape analysis of symmetric structures: quantifying variation among individuals and asymmetry. *Evolution* 56: 1909–1920 p.
- Klingenberg CP, Mebus K, Auffray JC.** 2003. Developmental integration in a complex morphological structure: how distinct are the modules in the mouse mandible?. *Evolution & development* 5: 522–531 p.
- Klingenberg CP, Duttke S, Whelan S, Kim M.** 2012 Developmental plasticity, morphological variation and evolvability: a multilevel analysis of morphometric integration in the shape of compound leaves. *Journal of Evolutionary Biology* 25: 115–129 p.
- Kluge AG.** 1989. A concern for evidence and a phylogenetic hypothesis of relationships among *Epicrates* (Boidae, Serpentes). *Systematic Biology* 38: 7–25 p.
- Kraglievich JL, Rivas S.** 1951. *Orophodon* Amegh: representante de una nueva superfamilia orophodontoidea del suborden Xenarthra;(nota preliminar). *Ciencias Zoológicas* 2: 9–28 p.
- Krauss F.** 1862. Ueber ein neues Gürtelthier aus Surinam. *Archiv für Naturgeschichte* 28: 19–34 p.
- Krentzel D, Angielczyk K.** 2016. Why are mammals such air-heads? Porcupines and function of the frontal sinus in mammals. In: Evans RD, Cary NC. eds. *Integrative and comparative biology*. Oxford university press, USA, 56: 117–117 p.
- Krmpotic CM, Galliari FC, Barbeito CG, Carlini AA.** 2012. Development of the integument of *Dasypus hybridus* and *Chaetophractus vellerosus*, and asynchronous events with respect to the postcranium. *Mammalian Biology - Zeitschrift für Säugetierkunde* 77: 314–326 p.

References

- Laurito CA, Valerio AL.** 2012. Paleobiogeografía del arribo de mamíferos suramericanos al sur de América Central de previo al Gran Intercambio Biótico Americano: un vistazo al GABI en América Central. *Revista Geológica de América Central* 46: 123–144 p.
- Ledevin R, Koyabu D.** 2019. Patterns and constraints of craniofacial variation in Colobine monkeys: disentangling the effects of phylogeny, allometry and diet. *Evolutionary Biology* 46: 14–34 p.
- Lee MSY, Palci A.** 2015. Morphological phylogenetics in the genomic age. *Current Biology* 25: 922–929 p.
- Legg DA, Sutton MD, Edgecombe GD.** 2013. Arthropod fossil data increase congruence of morphological and molecular phylogenies. *Nature communications* 4: 1–7 p.
- Lele S, Richtsmeier JT.** 1991. Euclidean distance matrix analysis: A coordinate-free approach for comparing biological shapes using landmark data. *American journal of physical anthropology* 86: 415–427 p.
- Lewis PO.** 2001. A likelihood approach to estimating phylogeny from discrete morphological character data. *Systematic Biology* 50: 913–925 p.
- Linde-Medina M.** 2016. Testing the cranial evolutionary allometric ‘rule’ in Galliformes. *Journal of Evolutionary Biology* 29: 1873–1878 p.
- Linnaeus C.** 1758. *Systema naturae per regna tria naturæ, secundum classes, ordines, genera, species, cum characteribus, differentiis, synonymis, locis.* Tomus I. Editio decima, reformata. Homiae: Laurentii Salvii.
- Loughry WJ, Superina M, McDonough CM, Abba AM.** 2015. Research on armadillos: a review and prospectus. *Journal of Mammalogy* 96: 635–644 p.
- Lund PW.** 1845. *Conspectum dasypodum.* Det Kongelige Danske Videnskabernes Selskabs Skrifter. *Naturvidenskabelige og Mathematisk Afdeling Series* 4: 82–86 p.
- Madden RH, Guerrero J, Kay RF, Flynn JJ, Swisher CC, Walton AH.** 1997. The Laventan Stage and Laventan Age: new chronostratigraphic and geochronologic units for the Miocene of South America. In: Kay RF, Madden RH, Cifelli RL, Flynn JJ. eds. *Vertebrate Paleontology in the Neotropics. The Miocene Fauna of La Venta, Colombia.* Smithsonian Institution Press, Washington/London, 499–519 p.
- Magnus LZ, Machado RF, Cáceres N.** 2018. The environment is a major driver of shape and size variation in widespread extant xenarthrans. *Mammalian Biology* 89: 52–61 p.
- Makedonska J, Wright BW, Strait DS.** 2012. The effect of dietary adaption on cranial morphological integration in capuchins (Order Primates, Genus *Cebus*). *PloS one* 7: e40398.
- Marcy AE, Guillerme T, Sherratt E, Rowe KC, Phillips MJ, Weisbecker V.** 2020. Australian rodents reveal conserved Cranial Evolutionary Allometry across 10 million years of murid evolution. *The American Naturalist* 196: 755–768 p.
- Marr MM, MacLeod N.** 2019. Geographical variation in Eurasian red squirrel (*Sciurus vulgaris* L., 1758) mandibles and the issue of subspecies-level organization: a failure of history?. *Biological Journal of the Linnean Society* 128: 337–359 p.
- Marroig G, Cheverud JM.** 2004. Cranial evolution in sakis (Pithecia, Platyrrhini) I: interspecific differentiation and allometric patterns. *American Journal of Physical Anthropology: The Official Publication of the American Association of Physical Anthropologists* 125: 266–278 p.
- Marroig G, Shirai LT, Porto A, De Oliveira FB, De Conto V.** 2009. The evolution of modularity in the mammalian skull II: evolutionary consequences. *Evolutionary Biology* 36: 136–148 p.

References

- McBee K, Baker RJ.** 1982. *Dasypus novemcinctus*. *Mammalian species* 162: 1–9 p.
- McDonald HG.** 2003. Xenarthran skeletal anatomy: primitive or derived? (Mammalia, Xenarthra). *Senckenbergiana biologica* 83: 5–18 p.
- McDonough CM, Loughry WJ.** 2018. Family Dasypodidae (long-nosed armadillos). In: Mittermeier RA, Wilson DE. eds. *Handbook of the Mammals of the World: Insectivores, sloths and colungos*. Lynx edicions, Spain, 30–47 p.
- McKenna MC, Bell SK.** 1997. *Classification of mammals: above the species level*. Columbia University Press. ed. New York, 640 p.
- McMurtrie H.** 1831. *The animal kingdom arranged in conformity with its organization. By the Baron Cuvier, and translated from the French, with notes and additions*. G. & C. & H. Carvill, New York, 528 p.
- Meloro C, Cáceres N, Carotenuto F, Passaro F, Sponchiado J, Melo GL, Raia P.** 2014. Ecogeographical variation in skull morphometry of howler monkeys (Primates: Atelidae). *Zoologischer Anzeiger* 253: 345e359.
- Messineo PG, Politis GG.** 2009. New radiocarbon dates from the Campo Laborde site (Pampean Region, Argentina) support the Holocene survival of giant ground sloth and glyptodonts. *Current Research in the Pleistocene* 26: 5–9 p.
- Miller GS.** 1899. Notes on the naked-tailed armadillos. *Proceedings of the Biological Society of Washington* 13:1–8 p.
- Milne N, O’Higgins P.** 2012. Scaling of form and function in the xenarthran femur: a 100-fold increase in body mass is mitigated by repositioning of the third trochanter. *Proceedings of the Royal Society B: Biological Sciences* 279: 3449–3456 p.
- Milne N, Toledo N, Vizcaíno SF.** 2012. Allometric and group differences in the Xenarthran femur. *Journal of Mammalian Evolution* 19: 199–208 p.
- Milne N, Vizcaíno SF, Fernicola JC.** 2009. A 3D geometric morphometric analysis of digging ability in the extant and fossil cingulate humerus. *Journal of Zoology* 278: 48–56 p.
- Mitchell KJ, Scanferla A, Soibelzon E, Bonini R, Ochoa J, Cooper A.** 2016. Ancient DNA from the extinct South American giant glyptodont *Doedicurus sp.* (Xenarthra: Glyptodontidae) reveals that glyptodonts evolved from Eocene armadillos. *Molecular Ecology* 25: 3499–3508 p.
- Mitteroecker P, Bookstein F.** 2007. The conceptual and statistical relationship between modularity and morphological integration. *Systematic biology* 56: 818–836 p.
- Mitteroecker P, Bookstein F.** 2008. The evolutionary role of modularity and integration in the hominoid cranium. *Evolution: International Journal of Organic Evolution* 62: 943–958 p.
- Mitteroecker P, Gunz P, Weber GW, Bookstein FL.** 2004. Regional dissociated heterochrony in multivariate analysis. *Annals of Anatomy - Anatomischer Anzeiger* 186: 463–470 p.
- Mitteroecker P, Gunz P, Bookstein FL.** 2005. Heterochrony and geometric morphometrics: a comparison of cranial growth in *Pan paniscus* versus *Pan troglodytes*. *Evolution & Development* 7: 244–258 p.
- Mitteroecker P, Gunz P, Windhager S, Schaefer K.** 2013. A brief review of shape, form, and allometry in geometric morphometrics, with applications to human facial morphology. *Hystrix* 24: 59–66 p.

References

- Mitteroecker P, Bartsch S, Erking C, Grunstra NDS, Le Maître A, Bookstein FL.** 2020. Morphometric Variation at Different Spatial Scales: Coordination and Compensation in the Emergence of Organismal Form. *Systematic Biology*: syaa007
- Moeller W.** 1968. Allometrische analyse der gürteltier schädel. Ein beitrage zur phylogenie der Dasypodidae Bonaparte, 1838. *Zoologische Jahrbücher. Abteilung für Anatomie und Ontogenie der Tiere* 85: 411–528 p.
- Monson TA.** 2020. Patterns and magnitudes of craniofacial covariation in extant cercopithecids. *The Anatomical Record* 303: 3068–3084 p.
- Monteiro LR.** 1999. Multivariate regression models and geometric morphometrics: the search for causal factors in the analysis of shape. *Systematic Biology* 48:192–9 p.
- Monteiro LR, Abe AS.** 1997. Allometry and morphological integration in the skull of *Tupinambis merianae* (Lacertilia: Teiidae). *Amphibia-Reptilia* 18: 397–405 p.
- Monteiro LR, Less LG, Abe AS.** 1999. Ontogenetic variation in skull shape of *Thrichomys apereoides* (Rodentia: Echimyidae). *Journal of Mammalogy* 80: 102–111 p.
- Monteiro LR, Bonato V, Dos Reis SF.** 2005. Evolutionary integration and morphological diversification in complex morphological structures: mandible shape divergence in spiny rats (Rodentia, Echimyidae). *Evolution & Development* 7: 429–439 p.
- Morlon H, Parsons TL, Plotkin JB.** 2011. Reconciling molecular phylogenies with the fossil record. *Proceedings of the National Academy of Sciences* 108: 16327–16332 p.
- Mosimann JE.** 1970. Size allometry: size and shape variables with characterizations of the lognormal and generalized gamma distributions. *Journal of the American Statistical Association* 65: 930–945 p.
- Moyano SR, Giannini NP.** 2017. Comparative cranial ontogeny of *Tapirus* (Mammalia: Perissodactyla: Tapiridae). *Journal of Anatomy* 231: 665–682 p.
- Moyano SR, Cassini GH, Giannini NP.** 2018. Skull Ontogeny of the Hyraxes *Procavia capensis* and *Dendrohyrax arboreus* (Procaviidae: Hyracoidea). *Journal of Mammalian Evolution* 26: 317–331 p.
- Moyano SR, Morales MM, Giannini NP.** 2020. Skull ontogeny of the pronghorn (*Antilocapra americana*) in the comparative context of native North American ungulates. *Canadian Journal of Zoology* 98: 165–174 p.
- Muizon de C, Billet G, Argot C, Ladevèze S, Goussard F.** 2015. *Alcidedorbignya inopinata*, a basal pantodont (Placentalia, Mammalia) from the early Palaeocene of Bolivia: anatomy, phylogeny and palaeobiology. *Geodiversitas* 37: 397–634 p.
- Murtagh F, Legendre P.** 2014. Ward's hierarchical agglomerative clustering method: which algorithms implement Ward's criterion?. *Journal of classification* 31: 274–295 p.
- Naples VL.** 1985. Form and function of the masticatory musculature in the tree sloths, *Bradypus* and *Choloepus*. *Journal of Morphology* 183: 25–50 p.
- Naylor GJP, Adams DC.** 2001. Are the fossil data really at odds with the molecular data? Morphological evidence for cetartiodactyla phylogeny reexamined. *Systematic Biology* 50: 444–453 p.
- Nogueira MR, Peracchi AL, Monteiro LR.** 2009. Morphological correlates of bite force and diet in the skull and mandible of phyllostomid bats. *Functional Ecology* 23: 715–723 p.
- Nummela S.** 1995. Scaling of the mammalian middle ear. *Hearing research* 85: 18–30 p.

References

- O'Keefe FR, Wagner PJ.** 2001. Inferring and testing hypotheses of cladistic character dependence by using character compatibility. *Systematic Biology* 50: 657–675 p.
- Oksanen J, Blanchet FG, Friendly M, Kindt R, Legendre P, McGlinn D.** 2019. Vegan: Community Ecology Package. *R package version 2.5-4*. R Foundation for Statistical Computing, Vienna, Austria.
- O'Leary MA, Bloch JI, Flynn JJ, Gaudin TJ, Giallombardo A, Giannini NP, Goldberg SL, Kraatz BP, Luo ZX, Meng J, Ni X, Novacek M, Perini FA, Randall ZS, Rougier GW, Sargis EJ, Silcox MT, Simmons NB, Spaulding M, Velazco PM, Weksler M, Wible JR, Cirranello AL.** 2013. The placental mammal ancestor and the post-K-Pg radiation of placentals. *Science* 339: 662–667 p.
- Oliver JD, Jones KE, Hautier L, Loughry WJ, Pierce SE.** 2016. Vertebral bending mechanics and xenarthrous morphology in the nine-banded armadillo (*Dasypus novemcinctus*). *Journal of Experimental Biology* 219: 2991–3002 p.
- Olson EC, Miller RL.** 1958. *Morphological integration*. University of Chicago Press. ed. Chicago, 376 p.
- Owen R.** 1839. Description of a tooth and part of the skeleton of the *Glyptodon*, a large quadruped of the edentate order, to which belongs the tessellated bony armour figured by Mr. Clift in his memoir on the remains of the *Megatherium*, brought to England by Sir Woodbine Parish, F.G.S. *Proceedings of the Geological Society of London* 3: 108–113 p.
- Pagel M.** 1994. Detecting correlated evolution on phylogenies: a general method for the comparative analysis of discrete characters. *Proceedings of the Royal Society of London. Series B: Biological Sciences* 255: 37–45 p.
- Paradis E, Schliep K.** 2019. ape 5.0: an environment for modern phylogenetics and evolutionary analyses in R. *Bioinformatics* 35: 526–528 p.
- Parins-Fukuchi C.** 2018. Use of continuous traits can improve morphological phylogenetics. *Systematic Biology* 67: 328–339 p.
- Parr WC, Wilson LA, Wroe S, Colman NJ, Crowther MS, Letnic M.** 2016. Cranial shape and the modularity of hybridization in dingoes and dogs; hybridization does not spell the end for native morphology. *Evolutionary Biology* 43: 171–187 p.
- Parsons KJ, Son YH, Crespel A, Thambithurai D, Killen S, Harris MP, Albertson RC.** 2018. Conserved but flexible modularity in the zebrafish skull: implications for craniofacial evolvability. *Proceedings of the Royal Society B: Biological Sciences* 285: 20172671.
- Pascual R, Ortiz-Jaureguizar E, Prado JL.** 1996. Land Mammals: Paradigm for Cenozoic South American Geobiotic Evolution. *Münchener Geowissenschaftliche Abhandlungen* 30: 265–319 p.
- Patterson B, Pascual R.** 1972. The Fossil Mammal Fauna of South America. In: Keast A, Erk FC, Glass B. eds. *Evolution, Mammals, and Southern Continents*. State University of New York Press, Albany, 247–309 p.
- Patterson B, Segall W, Turnbull WD.** 1989. The ear region in xenarthrans (=Edentata, Mammalia). Part I. Cingulates. *Fieldiana Geology* 18:1–46 p.
- Paula-Couto C.** 1954. Megatérios intertropicais do Pleistoceno. *Anais da Academia Brasileira de Ciências* 26: 447–463 p.
- Pélabon C, Bolstad GH, Egset CK, Cheverud JM, Pavlicev M, Rosenqvist G.** 2013. On the relationship between ontogenetic and static allometry. *The American Naturalist* 181: 195–212 p.
- Pélabon C, Firmat CJP, Bolstad GH, Voje KL, Houle D, Cassara J, Le Rouzic A, Hansen TF.** 2014. Evolution of morphological allometry. *Annals of the New York Academy of Sciences* 1320: 58–75 p.

References

- Percival CJ, Green R, Roseman CC, Gatti DM, Morgan JL, Murray SA, Donahue LR, Nayeux JM, Pollard KM, Hua K, Pomp D, Marcucio R, Pomp D.** 2018. Developmental constraint through negative pleiotropy in the zygomatic arch. *EvoDevo* 9: 1–16 p.
- Perea D, Toriño P, Ciancio MR.** 2014. La presencia del xenartro *Palaeopeltis inornatus* Ameghino, 1894, en la Formación Fray Bentos (Oligoceno tardío), Uruguay. *Ameghiniana* 51: 254–258 p.
- Piekarski N, Gross JB, Hanken J.** 2014. Evolutionary innovation and conservation in the embryonic derivation of the vertebrate skull. *Nature Communications* 5: 5661.
- Piras P, Salvi D, Ferrara G, Maiorino L, Delfino M, Pedde L, Kotsakis T.** 2011. The role of post-natal ontogeny in the evolution of phenotypic diversity in *Podarcis* lizards. *Journal of Evolutionary Biology* 24: 2705–2720 p.
- Plateau O, Foth C.** 2020. Birds have peramorphic skulls, too: anatomical network analyses reveal oppositional heterochronies in avian skull evolution. *Communications Biology* 3: 1–12 p.
- Polini N, Camina R, Casanave EB.** 1999. Morphological and morphometrical study of the blood leukocytes from *ChaetophRACTUS villosus* (Mammalia, Dasypodidae). *Comparative Haematology International* 9:162–167 p.
- Porpino KDO, Fernicola JC, Bergqvist LP.** 2010. Revisiting the intertropical Brazilian species *Hoplophorus euphractus* (Cingulata, Glyptodontidae) and the phylogenetic affinities of *Hoplophorus*. *Journal of Vertebrate Paleontology* 30: 911–927 p.
- Porto A, De Oliveira FB, Shirai LT, De Conto V, Marroig G.** 2009. The evolution of modularity in the mammalian skull I: morphological integration patterns and magnitudes. *Evolutionary Biology* 36: 118–135 p.
- Porto A, Shirai LT, De Oliveira FB, Marroig G.** 2013. Size variation, growth strategies, and the evolution of modularity in the mammalian skull. *Evolution* 67: 3305–3322 p.
- Price SA, Hopkins SS.** 2015. The macroevolutionary relationship between diet and body mass across mammals. *Biological Journal of the Linnean Society* 115: 173–184 p.
- Pyron RA.** 2015. Post-molecular systematics and the future of phylogenetics. *Trends in Ecology and Evolution* 30: 384–389 p.
- Rae TC.** 1998. The logical basis for the use of continuous characters in phylogenetic systematics. *Cladistics* 14: 221–228 p.
- Rager L, Hautier L, Forasiepi A, Goswami A, Sánchez-Villagra MR.** 2014. Timing of cranial suture closure in placental mammals: phylogenetic patterns, intraspecific variation, and comparison with marsupials. *Journal of Morphology* 275: 125–140 p.
- Revell LJ.** 2012. phytools: an R package for phylogenetic comparative biology (and other things). *Methods in ecology and Evolution* 3: 217–223 p.
- Richtsmeier JT, Burke Deleon V, Lele SR.** 2002. The promise of geometric morphometrics. *American Journal of Physical Anthropology: The Official Publication of the American Association of Physical Anthropologists* 119: 63–91 p.
- Rohlf FJ.** 2001. Comparative methods for the analysis of continuous variables: geometric interpretations. *Evolution* 55: 2143–2160 p.
- Rohlf FJ, Slice D.** 1990. Extensions of the Procrustes method for the optimal superimposition of landmarks. *Systematic Biology* 39: 40–59 p.

References

- Rohlf FJ, Marcus LF.** 1993. A revolution morphometrics. *Trends in Ecology & Evolution* 8: 129–132 p.
- Romiguier J, Ranwez V, Delsuc F, Galtier N, Douzery EJ.** 2013. Less is more in mammalian phylogenomics: AT-rich genes minimize tree conflicts and unravel the root of placental mammals. *Molecular Biology and Evolution* 30: 2134–2144 p.
- Ross CF, Metzger KA.** 2004. Bone strain gradients and optimization in vertebrate skulls. *Annals of Anatomy-Anatomischer Anzeiger* 186: 387–396 p.
- Saitou N, Nei M.** 1987. The neighbor-joining method: a new method for reconstructing phylogenetic trees. *Molecular Biology and Evolution* 4: 406–425 p.
- Sánchez-Villagra MR.** 2012. *Embryos in deep time: the rock record of biological development*. University of California Press. San Francisco, 265 p.
- Sánchez-Villagra MR, Wible JR.** 2002. Patterns of evolutionary transformation in the petrosal bone and some basicranial features in marsupial mammals, with special reference to didelphids. *Journal of Zoological Systematics and Evolutionary Research* 40: 26–45 p.
- Sánchez-Villagra MR, Narita Y, Kuratani S.** 2007. Thoracolumbar vertebral number: the first skeletal synapomorphy for afrotherian mammals. *Systematics and Biodiversity* 5: 1–7 p.
- Santana SE, Lofgren SE.** 2013. Does nasal echolocation influence the modularity of the mammal skull?. *Journal of Evolutionary Biology* 26: 2520–2526 p.
- Sardi ML, Ventrice F, Rozzi FR.** 2007. Allometries throughout the late prenatal and early postnatal human craniofacial ontogeny. *The Anatomical Record: Advances in Integrative Anatomy and Evolutionary Biology* 290: 1112–1120 p.
- Schlager S.** 2017. Morpho and Rvcg – Shape Analysis in R: R-Packages for Geometric Morphometrics, Shape Analysis and Surface Manipulations. In: Zheng G, Li S, Székely G. eds. *Statistical Shape and Deformation Analysis*. Academic Press, London, 217–256 p.
- Schneider CA, Rasband WS, Eliceiri KW.** 2012. NIH Image to ImageJ: 25 years of image analysis. *Nature methods* 9: 671–675 p.
- Scillato-Yané GJ.** 1976. Sobre un Dasypodidae (Mammalia, Xenarthra) de edad Riochiquense (Palaeoceno superior) de Itaboraí (Brazil). *Anais da Academia brasileira de Ciências* 48: 527–530 p.
- Scillato-Yané GJ.** 1980. Catálogo de los Dasypodidae fósiles (Mammalia, Edentata) de la República Argentina, in II Congreso Argentino de Paleontología y Bioestratigrafía y I Congreso Latinoamericano de Paleontología, Buenos Aires, 1978. *Actas* 3: 7–36 p.
- Scillato-Yané GJ.** 1982. *Los Dasypodidae (Mammalia, Edentata) del Plioceno y Pleistoceno de la Argentina: La Plata, Argentina*. Ph.D. dissertation, Universidad Nacional de La Plata, Facultad de Ciencias Naturales y Museo. La Plata. 159 p.
- Scillato-Yané GJ, Krmptotic CM, Esteban GI.** 2010. Las especies del género *Chasicotatus* Scillato-Yané (Eutatini, Dasypodidae). *Revista mexicana de ciencias geológicas* 27: 43–55 p.
- Scotland RW, Olmstead RG, Bennett JR.** 2003. Phylogeny reconstruction: the role of morphology. *Systematic Biology* 52: 539–548 p.
- Scott WB.** 1903. Mammalia of the Santa Cruz beds. I. Edentata. In Scott WB. ed. *Reports of the Princeton University Expeditions to Patagonia*. Princeton University, Princeton/Stuttgart, 1–364 p.

References

- Scrucca L, Fop M, Murphy TB, Raftery AE.** 2016. mclust 5: clustering, classification and density estimation using Gaussian finite mixture models. *The R journal* 8: 289–317 p.
- Segura V, Prevosti F.** 2012. A quantitative approach to the cranial ontogeny of *Lycalopex culpaeus* (Carnivora: Canidae). *Zoomorphology* 131: 79–92 p.
- Serrano-Fochs S, De Esteban-Trivigno S, Marcé-Nogué J, Fortuny J, Fariña RA.** 2015. Finite element analysis of the Cingulata jaw: an ecomorphological approach to armadillo's diets. *PLoS One* 10: e0120653.
- Sharp AC, Rich TH.** 2016. Cranial biomechanics, bite force and function of the endocranial sinuses in *Diprotodon optatum*, the largest known marsupial. *Journal of Anatomy* 228: 984–995 p.
- Shea BT.** 1983. Allometry and heterochrony in the African apes. *American Journal of Physical Anthropology* 62: 275–289 p.
- Shea BT.** 1985. Bivariate and multivariate growth allometry: statistical and biological considerations. *Journal of Zoology* 206: 367–390 p.
- Shockey BJ, Vlachos E.** 2017. New Early Diverging Cingulate (Xenarthra: Peltephilidae) from the Late Oligocene of Bolivia and Considerations Regarding the Origin of Crown Xenarthra. *Bulletin of the Peabody Museum of Natural History* 58: 3–94 p.
- Sibly RM, Brown JH.** 2007. Effects of body size and lifestyle on evolution of mammal life histories. *Proceedings of the National Academy of Sciences* 104: 17707–17712 p.
- Sidlauskas B.** 2008. Continuous and arrested morphological diversification in sister clades of characiform fishes: a phylomorphospace approach. *Evolution: International Journal of Organic Evolution* 62: 3135–3156 p.
- Sidorkewicz NS, Casanave EB.** 2012. Morphology of the middle ear in three species of armadillos (Dasypodidae, Xenarthra) from Argentina. *International Journal of Morphology* 30: 1500–1507 p.
- Sidorkewicz NS, Casanave EB.** 2013. Morphological characterization and sex-related differences of the mandible of the armadillos *Chaetophractus vellerosus* and *Zaedyus pichiy* (Xenarthra, Dasypodidae), with consideration of dietary aspects. *Iheringia, Série Zoológica* 103: 153–162 p.
- Simons EA, Frost SR.** 2020. Ontogenetic allometry and scaling in catarrhine crania. *Journal of Anatomy* 00: 1–18 p.
- Simpson GG.** 1930. *Holmesina septentrionalis*, extinct giant armadillo of Florida. *American Museum Novitates* 422: 1–10 p.
- Simpson GG.** 1945. The principles of classification and a classification of mammals. *Bulletin of the American Museum of Natural History* 85: 1–350 p.
- Simpson GG.** 1948. The beginning of the age of mammals in South America. Part 1. Introduction. Systematics: Marsupialia, Edentata, Condylarthra, Liptopterna, and Notioprogonia. *Bulletin of the American Museum of Natural History* 91: 1–227 p.
- Simpson GG.** 1980. *Splendid isolation: the curious history of South American mammals*. Yale University Press. ed. New Haven, 266 p.
- Slater GJ, Van Valkenburgh B.** 2009. Allometry and performance: the evolution of skull form and function in felids. *Journal of evolutionary biology* 22: 2278–2287 p.
- Slijper EJ.** 1962. *Whales*. Hutchinson and Co. ed. London, 475 p.

References

- Smith FA, Boyer AG, Brown JH, Costa DP, Dayan T, Ernest SKM, Evans AR, Fortelius M, Gittleman JL, Hamilton MJ, Harding LE, Lintulaakso K, Lyons SK, McCain C, Okie JG, Saarinen JJ, Sibly RM, Stephens PR, Theodor J, Uhen MD.** 2010. The evolution of maximum body size of terrestrial mammals. *Science* 330: 1216–1219 p.
- Smith HF.** 2011. The role of genetic drift in shaping modern human cranial evolution: a test using microevolutionary modeling. *International Journal of Evolutionary Biology*: 145262.
- Smith K, Redford KH.** 1990. The anatomy and function of the feeding apparatus in two armadillos (Dasypoda): anatomy is not destiny. *Journal of Zoology* 222: 27–47 p.
- Smith P, Owen RD.** 2017. *Calyptopractus retusus* (Cingulata: Dasypodidae). *Mammalian Species* 49: 57–62 p.
- Smith TD, McMahan MJ, Millen ME, Llera C, Engel SM, Li L, Bhatnagar KP, Burrows AM, Zumpano MP, DeLeon VB.** 2017. Growth and development at the sphenothmoidal junction in perinatal primates. *The Anatomical Record* 300: 2115–2137 p.
- Soibelzon E, Mino-Boilini AR, Zurita AE, Krmpotic CM.** 2010. Los Xenarthra (Mammalia) del Ensenadense (Pleistoceno Inferior a Medio) de la Region Pampeana (Argentina). *Revista Mexicana de Ciencias Geologicas* 27: 449–469 p.
- Sousa PC, Santos EAA, Bezerra JAB, Lima GL, Castelo TS, Fontenele-Neto JD, Silva AR.** 2013. Morphology, morphometry and ultrastructure of captive six-banded armadillo (*Euphractus sexcinctus*) sperm. *Animal Reproduction Science* 140: 279–285 p.
- Springer MS, Meredith RW, Eizirik E, Teeling E, Murphy WJ.** 2008. Morphology and placental mammal phylogeny. *Systematic Biology* 57: 499–503 p.
- Springer MS, Meredith RW, Teeling EC, Murphy WJ.** 2013. Technical comment on “The placental mammal ancestor and the post-K-Pg radiation of placentals”. *Science* 341: 613–613 p.
- Squarcia SM, Casanave EB.** 1999. Discriminación entre las subespecies de *Zaedyus pichiy* (Mammalia, Dasypodidae) utilizando caracteres morfométricos craneanos. *Physis* 57: 19–24 p.
- Squarcia SM, Casanave EB, Cirone GR.** 1993. Morfología craneana de *Chaetophractus villosus* (Desmarest, 1804) (Mammalia, Dasypodidae). *Iheringia Serie Zoologia* 75: 55–61 p.
- Squarcia SM, Casanave EB, Cirone GR.** 1999. Sexual dimorphism in *Chaetophractus villosus* (Mammalia, Dasypodidae) based on craniometrical characters. *Anales del Museo de Historia Natural Valparaiso* 24: 91–94 p.
- Squarcia SM, Sidorkewicz NS, Casanave EB.** 2006. Osteología Craneana del Armadillo *Chaetophractus villosus* (Mammalia, Xenarthra, Dasypodidae). *International Journal of Morphology* 24: 541–547 p.
- Squarcia SM, Sidorkewicz NS, Casanave EB.** 2007. The hypertrophy of the tympanic bulla in three species of dasypodids (Mammalia, Xenarthra) from Argentina. *International Journal of Morphology* 25: 597–602 p.
- Squarcia SM, Sidorkewicz NS, Camina R, Casanave EB.** 2009. Sexual dimorphism in the mandible of the armadillo *Chaetophractus villosus* (Desmarest, 1804) (Dasypodidae) from northern Patagonia, Argentina. *Brazilian Journal of Biology* 69: 347–352 p.
- Strauss RE, Altig R.** 1992. Ontogenetic body form changes in three ecological morphotypes of anuran tadpoles. *Growth, Development & Aging* 56: 3–16 p.
- Superina M, Abba AM.** 2014. *Zaedyus pichiy* (Cingulata: Dasypodidae). *Mammalian Species* 46: 1–10 p.

References

- Superina M, Loughry WJ.** 2015. Why do Xenarthrans matter?. *Journal of Mammalogy* 96: 617–621 p.
- Superina M, Abba AM.** 2018. Family Chlamyphoridae (Chlamyphorid armadillos). In: Mittermeier RA, Wilson DE. eds. *Handbook of the Mammals of the World: Insectivores, sloths and colungos*. Lynx edicions, Spain, 48–73 p.
- Superina M, Pagnutti N, Abba AM.** 2013. What do we know about armadillos? An analysis of four centuries of knowledge about a group of South American mammals, with emphasis on their conservation. *Mammal Review* 44: 69–80 p.
- Suzuki TK.** 2013. Modularity of a leaf moth-wing pattern and a versatile characteristic of the wing-pattern ground plan. *BMC Evolutionary Biology* 158: 1–13 p.
- Swofford DL.** 2002. PAUP: Phylogenetic analysis using parsimony (and other methods). Version 4.0a167. Sinauer Associates, Sunderland, 522 p.
- Tamagnini D, Meloro C, Cardini A.** 2017. Anyone with a long-face? Craniofacial Evolutionary Allometry (CREA) in a family of short-faced mammals, the Felidae. *Evolutionary Biology* 44: 476–495 p.
- Tambusso PS, Fariña RA.** 2015a. Digital cranial endocast of *Pseudoplohophorus absolutus* (Xenarthra, Cingulata) and its systematic and evolutionary implications. *Journal of Vertebrate Paleontology* 35: e967853.
- Tambusso PS, Fariña RA.** 2015b. Digital endocranial cast of *Pampatherium humboldtii* (Xenarthra, Cingulata) from the Late Pleistocene of Uruguay. *Swiss Journal of Palaeontology* 134: 109–116 p.
- Tarver JE, Dos Reis M, Mirarab S, Moran RJ, Parker S, O'Reilly JE, King BJ, O'Connell MJ, Asher RJ, Warnoe T, Peterson KJ, Donoghue PCJ, Pisani D.** 2016. The interrelationships of placental mammals and the limits of phylogenetic inference. *Genome Biology and Evolution* 8: 330–344 p.
- Taulman JF, Robbins LW.** 1996. Recent range expansion and distributional limits of the nine-banded armadillo (*Dasyus novemcinctus*) in the United States. *Journal of Biogeography* 23: 635–648 p.
- Terray L, Plateau O, Abourachid A, Böhmer C, Delapré A, Bernardie de la X, Cornette R.** 2020. Modularity of the neck in birds (Aves). *Evolutionary Biology* 47: 97–110 p.
- Thewissen JGM.** 1989. Mammalian frontal diploic vein and the human foramen caecum. *The Anatomical Record* 223: 242–244 p.
- Thiele K.** 1993. The holy grail of the perfect character: the cladistic treatment of morphometric data. *Cladistics* 9: 275–304 p.
- Thomas O.** 1894. On a new species of armadillo from Bolivia. *Annals and Magazine of Natural History* 6: 70–72 p.
- Thomas O.** 1928. Size differences in the little "pichi" armadillos. *Annals and Magazine of Natural History* 10: 526–527 p.
- Tibshirani R, Walther G, Hastie T.** 2001. Estimating the number of clusters in a data set via the gap statistic. *Journal of the Royal Statistical Society: Series B (Statistical Methodology)* 63: 411–423 p.
- Tschopp E, Mateus O, Benson RB.** 2015. A specimen-level phylogenetic analysis and taxonomic revision of Diplodocidae (Dinosauria, Sauropoda). *PeerJ* 3: e857.
- Upham NS, Esselstyn JA, Jetz W.** 2019. Inferring the mammal tree: Species-level sets of phylogenies for questions in ecology, evolution, and conservation. *PLoS biology* 17: e3000494.

References

- Urošević A, Ljubisavljević K, Ivanović A.** 2013. Patterns of cranial ontogeny in lacertid lizards: morphological and allometric disparity. *Journal of Evolutionary Biology* 26: 399–415 p.
- Urošević A, Ljubisavljević K, Ivanović A.** 2019. Multilevel assessment of the lacertid lizard cranial modularity. *Journal of Zoological Systematics and Evolutionary Research* 57: 145–158 p.
- Uyeda JC, Zenil-Ferguson R, Pennell MW.** 2018. Rethinking phylogenetic comparative methods. *Systematic Biology* 67: 1091–1109 p.
- Vizcaíno SF.** 1995. Identificación específica de las “mulitas” género *Dasypus* L. (Mammalia, Dasypodidae) del noroeste Argentino. Descripción de una nueva especie. *Mastozoología Neotropical* 2: 5–13 p.
- Vizcaíno SF.** 2009. The teeth of the “toothless”: novelties and key innovations in the evolution of xenarthrans (Mammalia, Xenarthra). *Paleobiology* 35: 43–366 p.
- Vizcaíno SF, Fariña RA.** 1996. Un índice de aptitud fosorial para armadillos (Xenarthra, Cingulata) fósiles sudamericanos. *Ameghiniana* 33: 1–473 p.
- Vizcaíno SF, Fariña RA.** 1997. Diet and locomotion of the armadillo *Peltephilus*: a new view. *Lethaia* 30: 79–86 p.
- Vizcaíno SF, Bargo MS.** 1998. The masticatory apparatus of the armadillos *Eutatus* (Mammalia, Cingulata) and some allied genera. Evolution and paleobiology. *Paleobiology* 24: 371–383 p.
- Vizcaíno SF, Milne N.** 2002. Structure and function in armadillo limbs (Mammalia: Xenarthra: Dasypodidae). *Journal of Zoology* 257: 117–127 p.
- Vizcaíno SF, De Iuliis G.** 2003. Evidence for advanced carnivory in fossil armadillos (Mammalia: Xenarthra: Dasypodidae). *Paleobiology* 29: 123–138 p.
- Vizcaíno SF, Loughry WJ.** 2008. *Biology of the Xenarthra*. University Press of Florida. ed. Gainesville, 370 p.
- Vizcaíno, SF, De Iuliis G, Bargo MS.** 1998. Skull shape, masticatory apparatus, and diet of *Vassallia* and *Holmesina* (Mammalia: Xenarthra: Pamphathiidae). When anatomy constrains destiny. *Journal of Mammalian Evolution* 5: 293–321 p.
- Vizcaíno SF, Fariña RA, Mazzetta G.** 1999. Ulnar dimensions and fossoriality in armadillos and other South American mammals. *Acta Theriologica* 44: 309–320 p.
- Vizcaíno SF, Milne N, Bargo MS.** 2003. Limb reconstruction of *Eutatus seguini* (Mammalia: Xenarthra: Dasypodidae). Paleobiological implications. *Ameghiniana* 40: 89–101 p.
- Vizcaíno SF, Fariña RA, Bargo MS, De Iuliis G.** 2004. Functional and phylogenetic assessment of the masticatory adaptations in Cingulata (Mammalia, Xenarthra). *Ameghiniana* 41: 651–664 p.
- Vizcaíno SF, Bargo MS, Kay RF, Milne N.** 2006. The armadillos (Mammalia, Xenarthra, Dasypodidae) of the Santa Cruz formation (early-middle Miocene): An approach to their paleobiology. *Palaeogeography Palaeoclimatology Palaeoecology* 237: 255–269 p.
- Vizcaíno SF, Blanco RE, Bender JB, Milne N.** 2011. Proportions and function of the limbs of glyptodonts. *Lethaia* 44: 93–101 p.

References

- Vizcaíno SF, Cassini GH, Toledo N, Bargo MS.** 2012a. On the evolution of large size in mammalian herbivores of Cenozoic. In: Patterson BP, Costa LP. eds. *Bones, Clones and Biomes: an 80-million year History of Recent Neotropical Mammals*. The University of Chicago Press, Chicago/London, 76–101 p.
- Vizcaíno SF, Fernicola JC, Bargo MS.** 2012b. Paleobiology of Santacrucian glyptodonts and armadillos (Xenarthra, Cingulata). In: Vizcaíno SF, Kay RF, Bargo MS. eds. *Early Miocene paleobiology in Patagonia: high-latitude paleocommunities of the Santa Cruz Formation*. Cambridge University Press, New York, 194–215 p.
- Wagner GP, Altenberg L.** 1996. Perspective: complex adaptations and the evolution of evolvability. *Evolution* 50: 967–976 p.
- Wagner GP, Pavlicev M, Cheverud JM.** 2007. The road to modularity. *Nature Reviews Genetics* 8: 921–931 p.
- Wake DB, Wake MH, Specht CD.** 2011. Homoplasy: from detecting pattern to determining process and mechanism of evolution. *Science* 331: 1032–1035 p.
- Ward JH.** 1963. Hierarchical grouping to optimize an objective function. *Journal of the American Statistical Association* 58: 236–244 p.
- Warren M.** 2019. Move over, DNA: ancient proteins are starting to reveal humanity's history. *Nature* 570: 433–437 p.
- Warton DI, Weber NC.** 2002. Common slope tests for bivariate errors-in-variables models. *Biometrical Journal* 2: 161–174 p.
- Warton DI, Wright IJ, Falster DS, Westoby M.** 2006. Bivariate line-fitting methods for allometry. *Biological Reviews* 81: 259–291 p.
- Warton DI, Duursma RA, Falster DS, Taskinen S.** 2012. smatr 3-an R package for estimation and inference about allometric lines. *Methods in Ecology and Evolution* 3: 257–259 p.
- Watanabe A, Fabre AC, Felice RN, Maisano JA, Müller J, Herrrel A, Goswami A.** 2019. Ecomorphological diversification in squamates from conserved pattern of cranial integration. *Proceedings of the National Academy of Sciences* 116: 14688–14697 p.
- Weaver TD, Roseman CC, Stringer CB.** 2007. Were Neandertal and modern human cranial differences produced by natural selection or genetic drift?. *Journal of Human Evolution* 53: 135–145 p.
- Weber KE.** 1990. Selection on wing allometry in *Drosophila melanogaster*. *Genetics* 126: 975–989 p.
- Weidenreich F.** 1941. The brain and its role in the phylogenetic transformation of the human skull. *Transactions of the American Philosophical Society* 31: 320–442 p.
- Wesley-Hunt GD, Flynn JJ.** 2005. Phylogeny of the Carnivora: basal relationships among the carnivoramorphans, and assessment of the position of ‘Miacoidea’ relative to Carnivora. *Journal of Systematic Palaeontology* 3: 1–28 p.
- Weston EM.** 2003. Evolution of ontogeny in the hippopotamus skull: using allometry to dissect developmental change. *Biological Journal of the Linnean Society* 80: 625–638 p.
- Wetzel RM.** 1985. Taxonomy and distribution of armadillos, Dasypodidae. In: Montgomery GG. ed. *The evolution and ecology of armadillos, sloths, and vermilinguas*. Smithsonian Institution Press, Washington DC, 23–46 p.

References

- Wetzel RM, Mondolfi E.** 1979. The subgenera and species of long-nosed armadillos, genus *Dasybus* L. In: Eisenberg JF. ed. *Vertebrate ecology in the northern Neotropics*. Smithsonian Institution Press, Washington DC, 43–63 p.
- Wetzel RM, Wetzel RM.** 1980. Revision of the naked-tailed armadillos genus *Cabassous* McMurtrie. *Annals of Carnegie Museum* 49: 323–357 p.
- Wetzel RM, Gardner AL, Redford KH, Eisenberg JF.** 2007. Order cingulata. In: Gardner AL. ed. *Mammals of South America: Marsupials, Xenarthrans, Shrews, and Bats*. University of Chicago Press, Chicago, 128–156 p.
- Wible JR.** 1993. Cranial circulation and relationships of the colugo *Cynocephalus* (Dermoptera, Mammalia). *American Museum Novitates* 3072: 1–27 p.
- Wible JR.** 2010. Petrosal anatomy of the nine-banded armadillo, *Dasybus novemcinctus* Linnaeus, 1758 (Mammalia, Xenarthra, Dasypodidae). *Annals of the Carnegie Museum* 79: 1–28 p.
- Wible JR, Gaudin TJ.** 2004. On the cranial osteology of the yellow armadillo *Euphractus sexcinctus* (Dasypodidae, Xenarthra, Placentalia). *Annals of the Carnegie Museum* 73: 1–117 p.
- Wible JR, Spaulding M.** 2013. On the cranial osteology of the African palm civet, *Nandinia binotata* (Gray, 1830) (Mammalia, Carnivora, Feliformia). *Annals of the Carnegie Museum* 82: 1–114 p.
- Wible JR, Rougier GW, Novacek MJ, Asher RJ.** 2009. The eutherian mammal *Maelestes gobiensis* from the Late Cretaceous of Mongolia and the phylogeny of Cretaceous Eutheria. *Bulletin of the American Museum of Natural History* 327: 1–123 p.
- Wiens JJ.** 2001. Character analysis in morphological phylogenetics: problems and solutions. *Systematic Biology* 50: 689–699 p.
- Wiens JJ.** 2004. The role of morphological data in phylogeny reconstruction. *Systematic Biology* 53: 653–661 p.
- Wilkinson M.** 1995. A comparison of two methods of character construction. *Cladistics* 11: 297–308 p.
- Willmore KE, Leamy L, Hallgrímsson B.** 2006. Effects of developmental and functional interactions on mouse cranial variability through late ontogeny. *Evolution & development* 8: 550–567 p.
- Wilson DE, Mittermeier RA, Ruff S, Martínez-Vilalta A, Cavallini P.** 2018. In: Mittermeier RA, Wilson DE. eds. *Handbook of the Mammals of the World: Insectivores, sloths and colungos*. Lynx edicions, Spain, 1–710 p.
- Wilson LA.** 2011. Comparison of prenatal and postnatal ontogeny: cranial allometry in the African striped mouse (*Rhabdomys pumilio*). *Journal of Mammalogy* 92: 407–420 p.
- Wilson LA.** 2013. Allometric disparity in rodent evolution. *Ecology and Evolution* 3: 971–984 p.
- Wilson LA.** 2018. The evolution of ontogenetic allometric trajectories in mammalian domestication. *Evolution* 72: 867–877 p.
- Wilson LA, Sánchez-Villagra MR.** 2010. Diversity trends and their ontogenetic basis: an exploration of allometric disparity in rodents. *Proceedings of the Royal Society B: Biological Sciences* 277: 1227–1234 p.
- Woodburne MO, Goin FJ, Raigemborn MS, Heizler M, Gelfo JN, Oliveira EV.** 2014. Revised timing of the South American early Paleogene land mammal ages. *Journal of South American Earth Sciences* 54: 109–119 p.

References

- Wright AM, Lloyd GT, Hillis DM.** 2016. Modeling character change heterogeneity in phylogenetic analyses of morphology through the use of priors. *Systematic Biology* 65: 602–611 p.
- Yanai I, Lercher M.** 2020. A hypothetical is a liability. *Genome biology* 21: 231.
- Yang Z.** 1998. On the best evolutionary rate for phylogenetic analysis. *Systematic Biology* 47: 125–133 p.
- Young NM.** 2006. Function, ontogeny and canalization of shape variance in the primate scapula. *Journal of Anatomy* 209: 623–636 p.
- Young NM, Hallgrímsson B.** 2005. Serial homology and the evolution of mammalian limb covariation structure. *Evolution* 59: 2691–2704 p.
- Zachos FE.** 2020. Mammalian Phylogenetics: A Short Overview of Recent Advances. In: Hackländer K, Zachos F. eds. *Handbook of the Mammals of Europe*. Springer, Switzerland, 1–18 p.
- Zachos FE, Asher RJ.** 2018. *Mammalian evolution, diversity and systematics. Handbook of zoology, Mammalia*. De Gruyter. Berlin, 352 p.
- Zelditch ML.** 2005. Developmental regulation of variability. In: Hallgrímsson B, Hall BK. eds. *Variation: a central concept in biology*. Elsevier Academic Press. ed. Burlington, 249–276 p.
- Zelditch ML, Sheets HD, Fink WL.** 2003. The ontogenetic dynamics of shape disparity. *Paleobiology* 29: 139–156 p.
- Zelditch ML, Wood A, Swiderski D.** 2009. Building developmental integration into functional systems: function-induced integration of mandibular shape. *Evolutionary Biology* 36: 71–87 p.
- Zelditch ML, Swiderski DL, Sheets HD.** 2012. *Geometric morphometrics for biologists: a primer*. Academic Press, New York, 488 p.
- Zollikofer CP, Ponce De León MS, Schmitz RW, Stringer CB.** 2008. New insights into mid-late Pleistocene fossil hominin paranasal sinus morphology. *The Anatomical Record: Advances in Integrative Anatomy and Evolutionary Biology* 291: 1506–1516 p.
- Zumpano MP, Richtsmeier JT.** 2003. Growth-related shape changes in the fetal craniofacial complex of humans (*Homo sapiens*) and pigtailed macaques (*Macaca nemestrina*): a 3D-CT comparative analysis. *American Journal of Physical Anthropology* 120: 339–351 p.
- Zurita AE, Miño-Boilini AR, Soibelzon E, Scillato-Yané GJ, Gasparini GM, Paredes-Ríos F.** 2009. First record and description of an exceptional unborn specimen of Cingulata Glyptodontidae: *Glyptodon* Owen (Xenarthra). *Comptes Rendus Palevol* 8: 573–578 p.
- Zurita AE, Scarano AC, Carlini AA, Scillato-Yané GJ, Soibelzon E.** 2011. *Neosclerocalyptus* spp. (Cingulata: Glyptodontidae: Hoplophorini): cranial morphology and palaeoenvironments along the changing Quaternary. *Journal of Natural History* 45: 893–914 p.

References

APPENDICES

Supporting Information 1: *Cabassous* & *Zaedyus*

1. A confusing taxonomic context in extant species of cingulate

Today, 21 extant species of cingulates are recognized (McDonough & Loughry, 2018; Superina & Abba, 2018). This account might however be slightly inaccurate as recent analyses of mitochondrial genomes suggested that several species can potentially be lumped together while others should be split (Gibb *et al.*, 2016). In *Dasypus novemcinctus*, there was even a high level of congruence between new morphological and molecular data to propose that this species should be viewed as a species complex requiring further investigation (Huchon *et al.*, 1999; Gibb *et al.*, 2016; Billet *et al.*, 2017; Hautier *et al.*, 2017; Feijó *et al.*, 2018, 2019; Arteaga *et al.*, 2020). In summary, these recent examples underline that the systematics of many extant species within Cingulata may require revision. The identification of a well-defined taxonomic context is very important for the purposes of our study exploring static and ontogenetic covariation patterns within three extant species of armadillos – *Dasypus novemcinctus* (southern morphotype), *Zaedyus pichiy* (Desmarest, 1804), and *Cabassous unicinctus* (Linnæus, 1758). As mentioned above, the variation and systematics within *Dasypus novemcinctus* was recently studied at the molecular and morpho-anatomical level (Huchon *et al.*, 1999; Gibb *et al.*, 2016; Billet *et al.*, 2017; Hautier *et al.*, 2017; Feijó *et al.*, 2018, 2019; Arteaga *et al.*, 2020) and these results were considered for our specimen selection within this species complex (Chapters 2, 3 & 4).

However, the systematics of the two other selected species, *Cabassous unicinctus* and *Zaedyus pichiy*, remain unclear. For this reason, and because museal specimens in our sample might have been previously misidentified, we tried to explore in more details their specific identification based on different criterions. We determined the relative age of specimens using discrete observation of bone sutures and performed analyses on the cranial shape using landmarks to investigate how specimens were distributed in the morphospace for each species. Using existing diagnoses, the distribution of specimens in the morphospace, their ontogenetic stage, size differences and geographical origin (when available), we discuss below our final selection of specimens within these two species.

2. Taxonomic context and sampling in *Cabassous* and *Zaedyus*

2.1 *The Cabassous Case*

2.1.1 *State of the Art and Diagnosis*

The genus *Cabassous* (McMurtrie, 1831) belongs to the Tolypeutinae also composed of the genera *Priodontes* (Cuvier, 1825) and *Tolypeutes* (Illiger, 1811) with which the cranial diagnoses allow a clear differentiation. *Cabassous* is currently composed of four species, with two of them having partly overlapping geographical distributions (Figure SI.1) – *Cabassous unicinctus* and *Cabassous tatouay* (Hayssen, 2014a; Hayssen, 2014b).

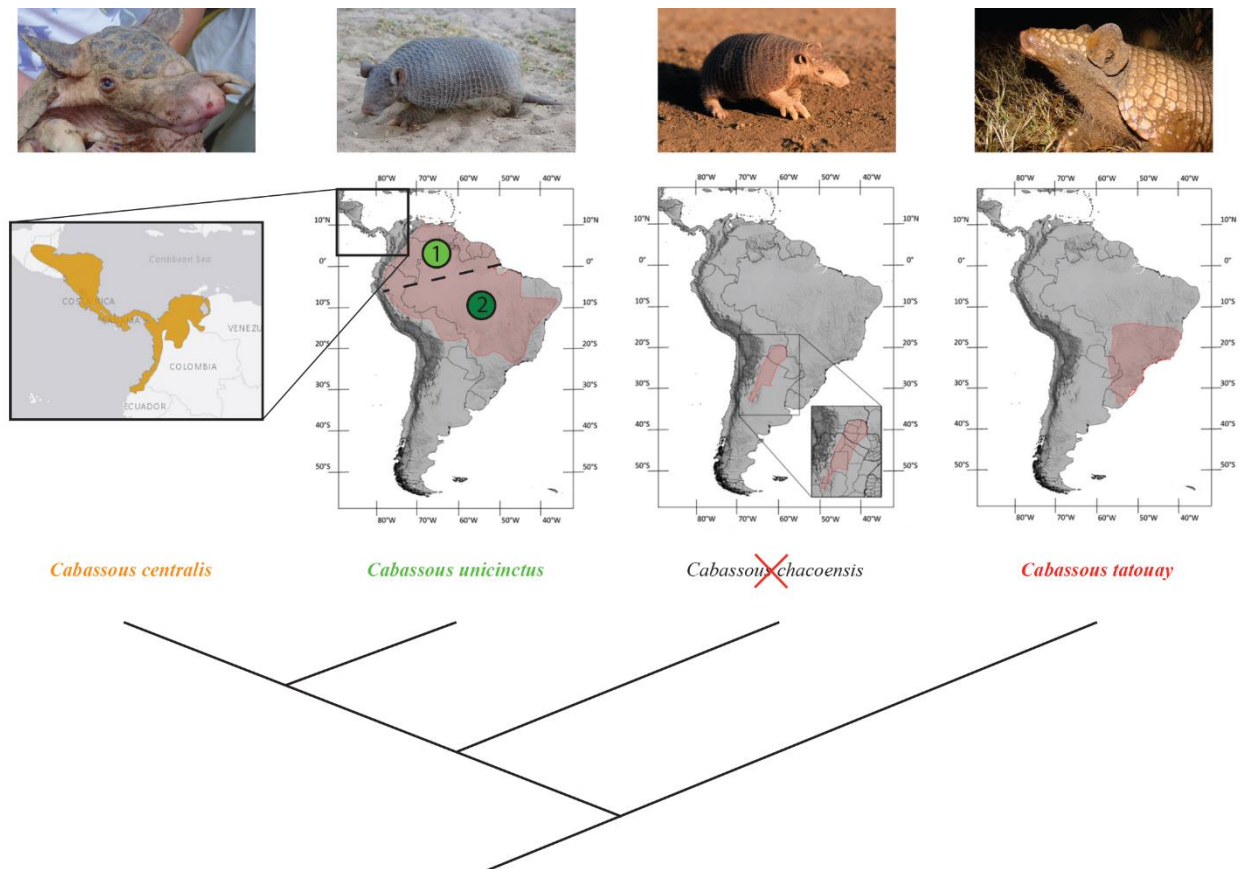


Figure SI.1. Phylogenetic relationships within the *Cabassous* clade (Gibb *et al.*, 2016) and geographical distribution of each species. 1, geographical area of *Cabassous unicinctus unicinctus*, and 2, geographical area of *Cabassous unicinctus squamicaudis* (Wetzel *et al.*, 2007). The photographs and maps are from the International Union for Conservation of Nature (= IUCN) website.

Cabassous unicinctus and *Cabassous tatouay* differ morpho-anatomically by a strong variation in size (average of greatest cranial size: 81.85 mm in *Cabassous unicinctus* and 108.5 mm *Cabassous tatouay* (Hayssen, 2014a, 2014b)) and a ratio of palate length to maxillary tooth row length longer in *C. tatouay* than in the other three species (Hayssen, 2014a). *Cabassous chacoensis* does not occur in the ranges of the other species and differs from them by a curvature of the tooth row and mandibular ramus on both dorsoventral and mediolateral axes (Wetzel, 1980) with the first and last teeth compressed anteroposteriorly rather than transversely (Hayssen, 2014c). Molecular studies suggest a clear genetic distinction between *Cabassous tatouay*, *Cabassous chacoensis* and a clade gathering *Cabassous centralis* and *Cabassous unicinctus*, but not between the latter two species (Gibb *et al.*, 2016). *Cabassous centralis* and *Cabassous unicinctus* differ in their geographical distribution position on either side of the northern range of the Andes (Hayssen, 2014b) but not clearly in their morphology, except possibly for the external surface of their pinna (Hayssen *et al.*, 2013) (Figure SI.1). Moreover, it should be noted that two subspecies are known for *Cabassous unicinctus* (Wetzel *et al.*, 2007): one distributed in the north and west of the Amazon River (*Cabassous unicinctus unicinctus* (Linnæus, 1758)) and one distributed in the south-eastern part of Brazil (*Cabassous unicinctus squamicaudis* (Lund, 1845)).

2.1.2 Sampling and a priori hypothesis

During the PhD³, digital data of 36 specimens identified as *Cabassous unicinctus* in 7 museum collections worldwide were acquired using X-ray micro-computed tomography (μ CT) (see Appendices of Chapter 3 for the table), all of which were labelled as *Cabassous unicinctus*. Among the 36 specimens, 27 have a known geographical origin (see Appendices of Chapter 3 for the table and Figure SI.2). None are present in the geographical range of *Cabassous chacoensis* and none present its distinctive dental characters (see above). Four specimens originate from the area of *Cabassous centralis*. One specimen was collected in Colombia without more precision, which could correspond to the geographical areas of *Cabassous centralis* and *Cabassous unicinctus*. Most of the remaining 22 specimens are present in areas where *Cabassous unicinctus* occurs (Appendices of Chapter 3 for the table and Figure SI.2). 15 are distributed in the area containing only *Cabassous unicinctus* and seven are distributed in the overlapping geographic region between

³ Many of the specimens were sent as scans or they were sent by mail for me to scan them. As a result, we were not able to do any verification before scanning them. This constraint also concerns the sampling of *Zaedyus pichiy*.

Cabassous unicinctus and *Cabassous tatouay* (Appendices of Chapter 3 for the table and Figure SI.2). Among them, seven specimens are large (*i.e.* > 100 mm), which is also the case for two specimens of unknown geographical origin. On this basis, we could hypothesize that the initial sampling includes nine *Cabassous tatouay*, four *Cabassous centralis*, and 15 *Cabassous unicinctus*. For the eight additional specimens, seven have unknown origins and one corresponds to the specimen collected in Colombia. There is some doubt about their taxonomic attribution between *Cabassous centralis* and *Cabassous unicinctus*.



Figure SI.2. Summary map showing the geographical distribution of *Cabassous* specimens investigated in this study. In red, *Cabassous tatouay*; in orange, *Cabassous centralis*; in light green, *Cabassous unicinctus* from Cluster B (see below); in dark green, *Cabassous unicinctus* from Cluster C (see below). 1, northern Amazon corresponding to the geographical area of *Cabassous unicinctus unicinctus*. 2, southern Amazon corresponding to the geographical area of *Cabassous unicinctus squamicaudis*. Specimens reported with a white star denote the absence of geographical information besides the country of origin.

2.2 The *Zaedyus* Case

2.2.1 State of art and Diagnosis

The monospecific genus *Zaedyus*, belongs to the Euphractinae composed of 4 species – *Euphractus sexcinctus* (Linnæus, 1758); *Chaetophractus villosus* (Desmarest, 1804); *Chaetophractus vellerosus*; and *Zaedyus pichiy*. *Chaetophractus nationi* is currently considered a synonym for *Chaetophractus vellerosus* (Abba *et al.*, 2015) (Figure SI.3).

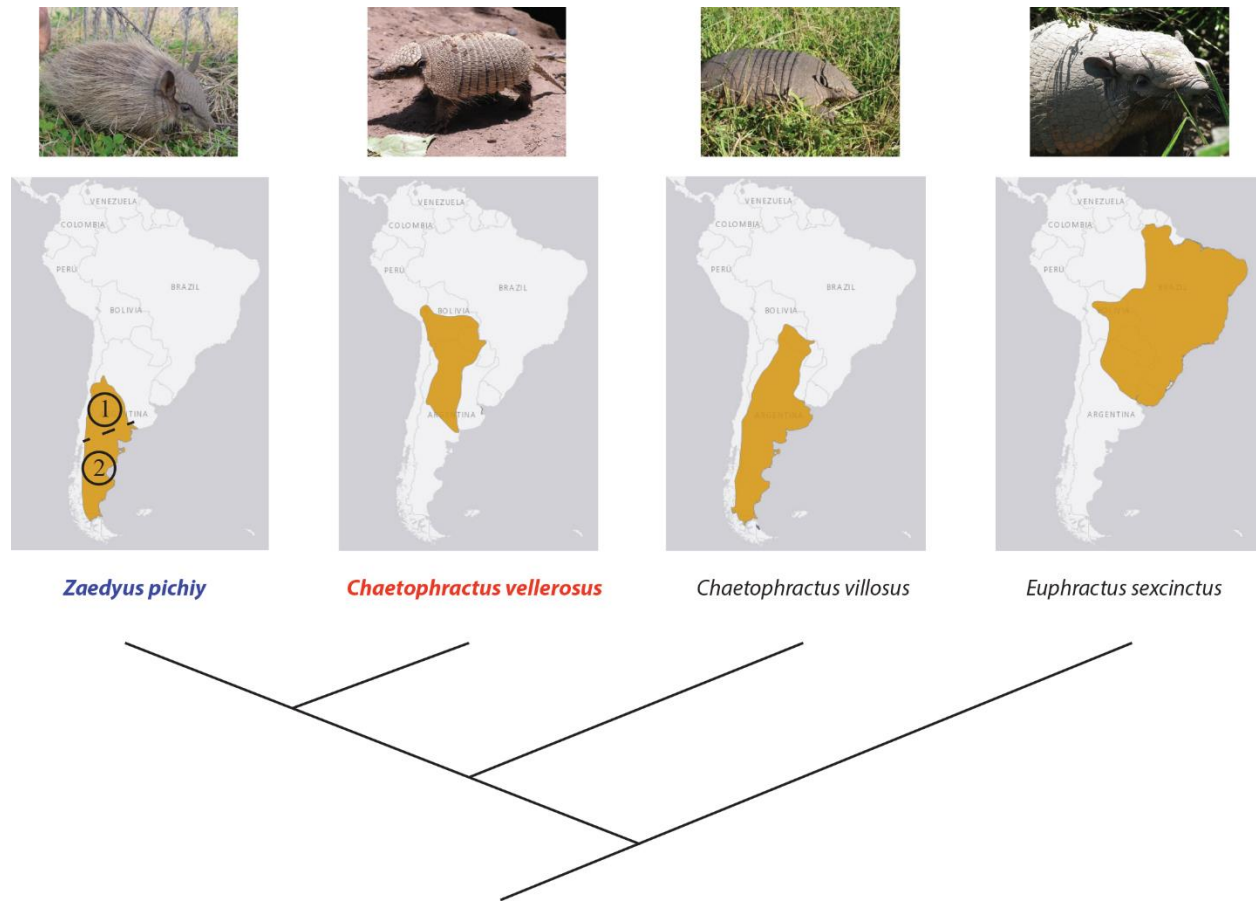


Figure SI.3. Phylogenetic relationships within the *Euphractinae* clade (Gibb *et al.*, 2016) and geographical distribution of each species. 1, potential geographical area of *Zaedyus pichiy caurinus* and, 2, potential geographical area of *Zaedyus pichiy pichiy* (Wetzel *et al.*, 2007). The photographs and maps are from the International Union for Conservation of Nature (= IUCN) website.

Genetic distances between genera leave little doubt as to the distinction between these species although the analysis of Gibb *et al.* (2016) suggests that *Chaetophractus* is a paraphyletic genus.

Euphractus sexcinctus is well differentiated from other euphractines both molecularly and morpho-anatomically (Abba *et al.*, 2015). *Chaetophractus villosus* differs quite strongly in size from the two closest species: head-and-body length averages 330 mm in *Chaetophractus villosus* (Carlini *et al.*, 2016); 245.1 mm in *Chaetophractus vellerosus* (Carlini *et al.*, 2016); 273 mm in *Zaedyus pichiy* (see details – Superina & Abba, 2014). The major difficulty therefore lies in differentiating between the two smaller species *Chaetophractus vellerosus* and *Zaedyus pichiy*. On the skull, Superina & Abba (2014), mentioned that these two species essentially differ by the presence (*Chaetophractus vellerosus*) or absence (*Zaedyus pichiy*) of a tooth on the premaxillary and a slight frontal depression present in *Zaedyus pichiy*. However, the presence of teeth on the premaxillary of *Zaedyus pichiy* has already been mentioned (*e.g.*, Gaudin & Wible, 2006). Abba *et al.* (2015) added that the snout of *Zaedyus pichiy* is thinner and more elongated than that of *Chaetophractus vellerosus*. The geographical distribution also differs between the two species with a distribution in northern Argentina and Bolivia for *Chaetophractus vellerosus* and a more southern Argentinean distribution for *Zaedyus pichiy* but with a small area of overlap in central Argentina (Figure SI.3). In addition, *Zaedyus pichiy* includes two known subspecies, *Zaedyus pichiy pichiy* Desmarest, 1804 and *Zaedyus pichiy caurinus* Thomas, 1928, which also slightly differ in size (Frechkop & Yepes 1949; Squarcia & Casanave 1999; Superina & Abba, 2014). However, some studies distinguish the geographical distribution of the two subspecies (Wetzel *et al.*, 2007; Sidorkewicz & Casanave, 2013) but the recent diagnosis of the species (Superina & Abba, 2014) no longer makes this distinction.

2.2.2 Sampling and a priori hypothesis

During the PhD, digital data of 45 specimens identified as *Zaedyus pichiy* in 6 museum collections worldwide were acquired using X-ray micro-computed tomography (μ CT) (Appendices of Chapter 3 for the table). As size is not clearly diagnostic between *Chaetophractus vellerosus* and *Zaedyus pichiy* (see above), most of the *a priori* attributions are based on the geographical origin of the specimens. Unfortunately, only a reduced proportion of the sample has a known geographical origin (17/45). Among these, sixteen originate from the distributional area of *Zaedyus pichiy*, and one specimen from Bolivia, within the area of distribution of *Chaetophractus vellerosus* (Figure SI.4). The analyses of skull shape were performed mainly to ensure that the specimens of unknown origin are *Zaedyus pichiy* and not *Chaetophractus vellerosus* (see below).



Figure SI.4. Summary map showing the geographical distribution of potential *Zaedyus* specimens investigated in this study. In red, suspected *Chaetophractus vellerosus*; in light blue, *Zaedyus* from Cluster B (see below); in dark blue, *Zaedyus* from Cluster A (see below). 1, Mendoza province corresponding to the geographical area of *Zaedyus pichiy caurinus*. 2, southern part of Argentina corresponding to the geographical area of *Zaedyus pichiy pichiy*. Specimens reported with a star denote the absence of geographical information besides the country of origin.

3. Methods

For both datasets, the same analyses were performed along considerations on the ontogeny and the geographical distribution. For the analysis of the *Zaedyus pichiy* sample, the presence or absence of teeth on the premaxillary was also taken into account in the interpretation of the results in order to consider the observations of [Superina & Abba \(2014\)](#) (see above).

3.1 Determination of ontogenetic stage

Contrary to *Dasybus novemcinctus*, in tolpeutines and euphractines there is only one functional generation of teeth ([Ciancio et al., 2012](#)). Therefore, the three dental variables used to determine ontogenetic stages in *Dasybus* ([Section 3.1](#)) cannot be used in *Zaedyus* or *Cabassous*.

Only the skull length and ossification index will be used for these genera. [Hubbe *et al.* \(2016\)](#) propose to consider as adult specimens only those xenarthran specimens (including almost all cingulate genera) in which both the supraoccipital-exoccipital and basioccipital-exoccipital contact are completely closed. They add that the basioccipital-basisphenoid suture is fused in their sample. Accordingly, we consider as strictly adult, specimens having these three bony contacts completely fused if these are consistent with the length of their skull. Their criteria work relatively well with our ossification index. (see results). Conversely, a specimen with completely unfused supraoccipital-exoccipital contact will be considered juvenile (for other more precision on timing of cranial suture closure refer to [Rager *et al.*, 2013](#)). Consequently, the degrees of intermediate ossification correspond to subadult stages. The skull length (see [Section 3.1](#)) and ossification index for each specimen in *Cabassous* and *Zaedyus* datasets are available in [Appendices of Chapter 3](#) for the table.

3.2 *Quantification and processing*

Refer to [Section 3.2](#).

3.3 *Principal Component Analysis (PCA)*

Once the data was processed, we performed a principal component analysis of shape variation to determine how our specimens are distributed in the morphospace of each dataset ([Dryden & Mardia, 1998](#)). Our aim is to quickly identify if there are one or more shape clusters on PC1 and PC2 in our sample and then perform more specific analyses. This analysis was performed using the *plotTangentspace* function in the *geomorph* R package.

3.4 *Permutational Multivariate Analysis of Variance*

After the principal component analysis, we extracted the matrix scores of the principal components in order to analyze the variance of the selected groups. With Euclidean distances, the permutational multivariate analysis of variance enables the partition of sums of squares using dissimilarities (*e.g.*, [Plateau & Foth, 2020](#)). Using a random permutation (= 10 000), the analysis allows to define if the shape variation of two groups is significantly different (*p-value* < 0.05) or not. This test is similar to a MANOVA and allows us to test the pairwise distinction of groups within the same principal

component analysis. These tests were performed with the *adonis* function in the R package *vegan* v. 2.5-6 (Oksanen *et al.*, 2019).

3.5 *Neighbour joining trees*

Using the distance matrix from the principal component scores, we performed neighbor-joining tree estimations (Saitou & Nei, 1987) for the total variance, using the function *nj* in the R package *ape* v.5.3 (Paradis & Schliep, 2019). This phenetic analysis considers the overall dissimilarities between all the specimens.

4. Results

4.1 *Cabassous sample selection*

4.1.1 *Ontogenetic stages and skull length*

A bivariate plot of ossification scores versus skull length clearly distinguishes a group of large specimens from the rest of the sample (Figure 6). This group of large specimen gathers 7 specimens whose distribution is in the *Cabassous tatouay* area and 2 of unknown origin. This supports the *a priori* hypothesis of the presence of *Cabassous tatouay* in the sampling (n=9 specimens). The ossification scores and the distinction between ontogenetic stages in this potential cluster of *Cabassous tatouay* do not seem to covary with skull length. Although sampling is low for this cluster (n = 9), this result indicates either that there is little variation in size between a juvenile and an adult in this species, or that our observations on ossification are not adapted to the determination of ontogenetic stages within this particular group. No clear geographic cluster can be seen for the rest of the *Cabassous* specimens in the sample. Their ontogenetic stages are better discriminated, and the largest specimens have relatively high ossification scores (Figure SI.6). One specimen remains problematic because it is partially deteriorated at the basicranium level which leads to a decrease in the ossification index (see Appendices of Chapter 3 for the table). However, the detectable sutures and its size tend to consider this specimen as adult (Appendices of Chapter 3 for the table). Based on these observations, the sampling may consist 2 juveniles, 2 subadults and 5 adults of *C. tatouay* and of 3 juveniles, 8 subadults and 16 adults for the remaining *Cabassous* specimens. It is summarized in Table SI.1.

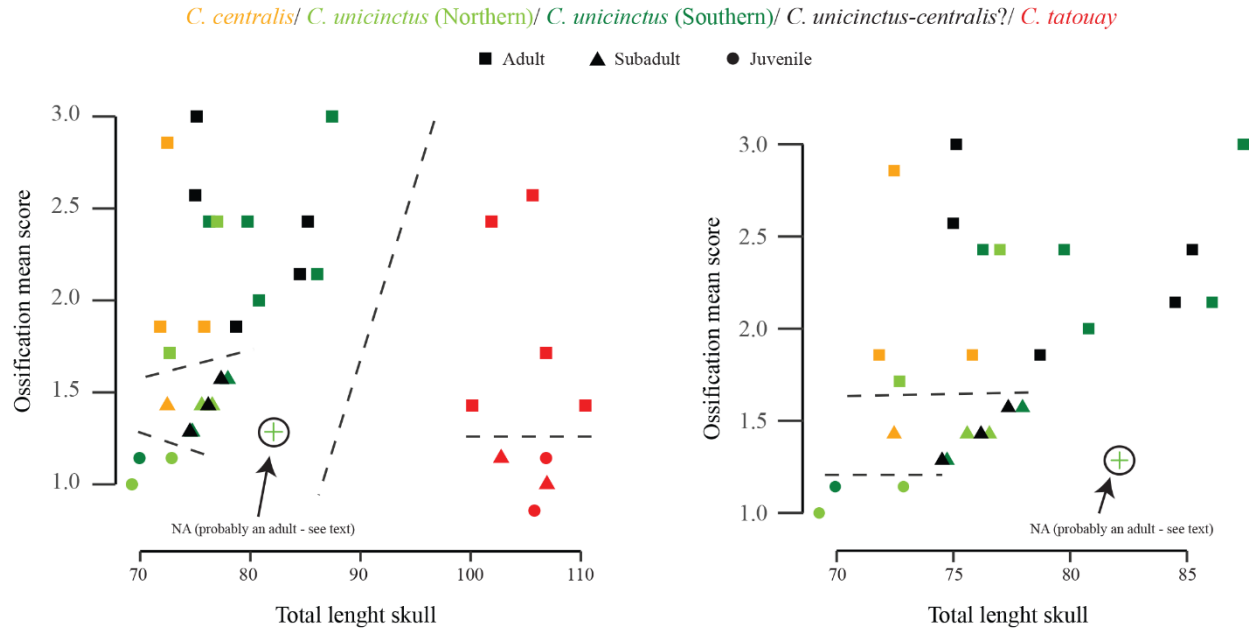


Figure SI.5. Ontogenetic stages determined based on Hubbe *et al.* (2016), as compared to the ossification score and the total length of the skull. The ontogenetic stages correspond to juvenile (circle); subadult (triangle); adult (square); specimen problematic (see text) (cross).

Table SI.1. Summary of ontogenetic stage composition by groups (see text).

	Juvenile	Subadult	Adult
<i>C. centralis</i>	0	1	3
<i>C. uncinctus</i> (northern)	1	2	6
<i>C. uncinctus</i> (southern)	2	2	2
<i>C. uncinctus-centralis</i> ?	0	3	5
Total	3	8	16
<i>C. tatouay</i>	2	2	5
Total	5	10	21

4.1.2 Principal components analysis

On the first two axes of the analysis (= 41.17% of the variance), 3 clusters are visible in the morphospace and one specimen stands out independently of these three groups (Figure SI.6). PC1 is dominated by shape variations similar to craniofacial allometry (Chapter 3). The main shape variations on PC2 corresponds to shifts in the front of the tooth row; the position of the infraorbital

foramen; the position of the posterolateral end of the nasal and that of the two posterior root of the zygomatic arches. The isolated individual corresponds to a very young specimen (lowest ossification scores – [Figure SI.5](#)) in comparison with the other specimens. Otherwise, ontogeny does not seem correlated with the distribution of groups in the morphospace defined by these two axes. Cluster A shows a clear separation between the 9 large-sized specimens (see above) and the rest of the dataset which supports their tentative attribution to *Cabassous tatouay*. The cluster B in the center of the morphospace consists of specimens originating within the northern part of the distributional area of *Cabassous unicinctus* (i.e., *Cabassous unicinctus unicinctus* in [Figure SI.1](#)), two specimens from the southern region (i.e., *Cabassous unicinctus squamicaudis* in [Figure SI.1](#)), all remaining specimens of unknown origins and specimens originating within the distributional area of *Cabassous centralis*. This cluster therefore shows no distinction between *Cabassous centralis* and *Cabassous unicinctus unicinctus*. and the cluster C corresponds to specimens originating within the distributional area of *Cabassous unicinctus squamicaudis* ([Figure SI.1](#)). This distribution in the morphospace suggests a clear distinction between two subsets in *Cabassous unicinctus* along a latitudinal gradient, which could be reminiscent of previously proposed subspecies (see above). However, the presence of 2 specimens from the southern region gathered with northern specimens shows that there is no exact correspondence between traditional subspecies and these clusters.

4.1.3 Permutational ANOVA

The pairwise distinction of the three clusters observed on PC1-2 and of other presumed taxonomic entities were tested ([Tables SI.2](#)), with the exclusion of the very young specimen (see above). Although, some groups are poorly sampled (e.g., *Cabassous centralis* area = 4), the tests are still presented as an indication. This analysis shows that all the pairwise tested groups have a statistically different shape from one another across the variance except for potential groups within the cluster B of PC1-2 (specimens of unknown origin in cluster B with *Cabassous unicinctus* specimens of cluster B and the latter with the group formed by the combination of specimens of unknown origin in cluster B with the specimens originating from the distributional area of *Cabassous centralis*) ([Tables SI.2](#)). We can therefore conclude that statistically the three clusters of PCA are well dissociated from one another but that within cluster B, it is not possible to ensure

CHAPTER 1: SUPPORTING INFORMATION

a statistical difference between specimens of known or unknown origin and between specimens originating from the distributional areas of *Cabassous centralis* or *Cabassous unicinctus*.

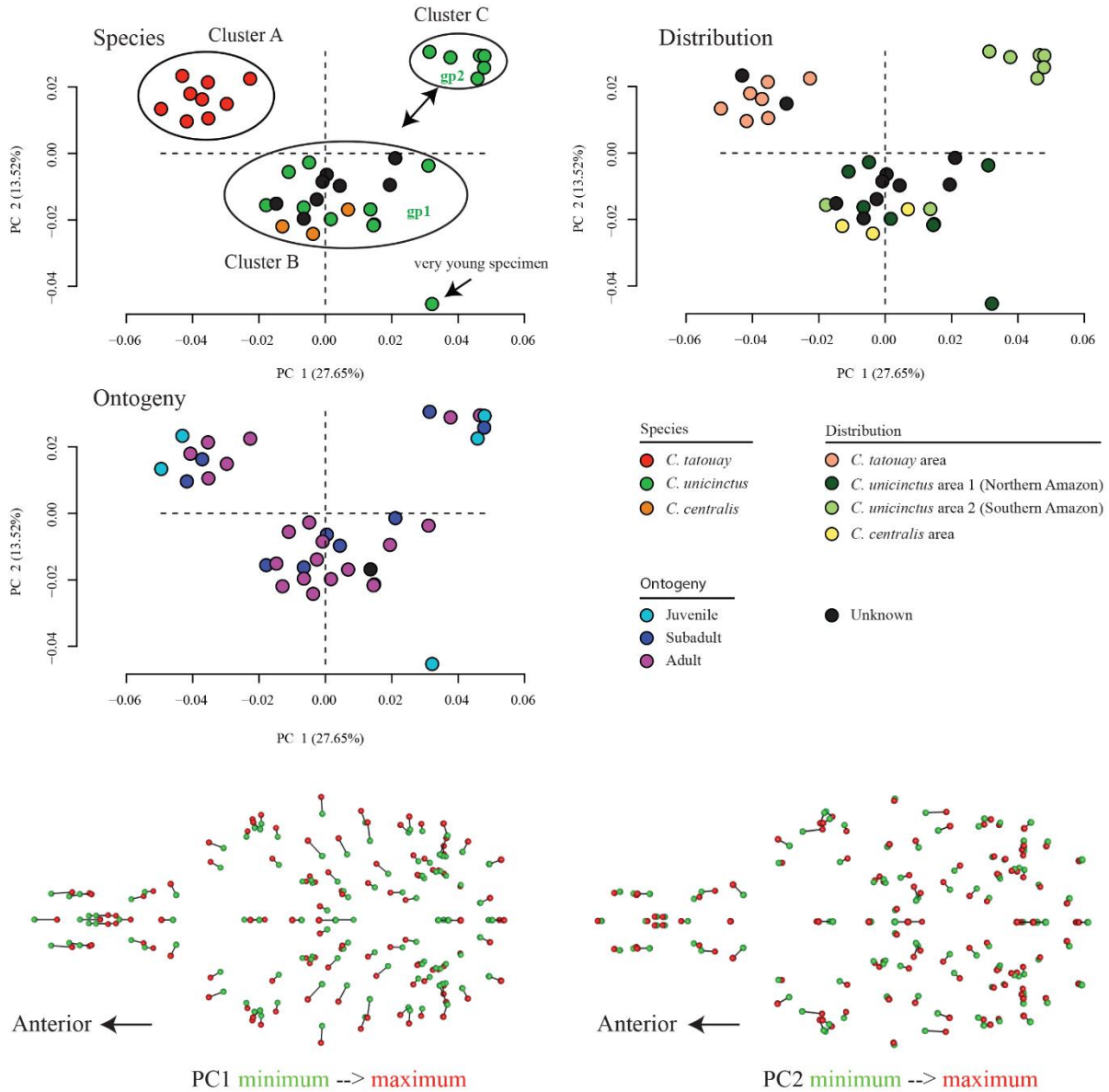


Figure SI.6. Results of the PCA performed on morphometric data in *Cabassous* with a focus on species, geographical distribution, and ontogenetic stage, distribution in the morphospace. Shape changes were visualized as vectors from the minimal shape (green) to the maximal shape (red) of each PC axes. Abbreviations: gp1, group of *Cabassous unicinctus* belonging to Cluster B; gp2, group of *Cabassous unicinctus* belonging to Cluster C.

Table SI.2. Statistical results of each permutational multivariate analysis of variance in *Cabassous*. For the symmetrical matrix, the lower triangle corresponds to the R^2 values and the upper triangle corresponds to the p -value. Each group is defined in Figure SI.6.

VS							R ²	p-value
	-	0.0008	0.0003	0.0001	0.0001	gp1 vs  + 	09.81	0.0116
	40.09	-	0.0058	0.0096	0.0023	gp1 vs  + 	09.51	0.031
	31.76	23.46	-	0.0113	0.6651	 vs gp1	24.69	0.0001
	40.77	27.84	21.15	-	0.0165	 vs gp2	53.46	0.0002
	29.20	18.70	06.84	23.91	-	 vs  + 	13.48	0.0017
						 vs  + 	07.38	0.16
						 vs  + 	17.86	0.0004
						 vs  + 	20.35	0.0017
						 vs  + 	19.20	0.0005

4.1.4 Neighbour joining

The neighbour joining (NJ) analysis allows us to visualize more precisely the phenetic distances between specimens over the whole variance. The NJ tree obtained is congruent with the permutational test and the first two PCA axes (Figure SI.7). Beside the very young specimen, two groups are very distant from other specimens (cluster B): the cluster A (*Cabassous tatouay*) and the cluster C. Specimens originating from the distributional areas of *Cabassous centralis* are found nested within the cluster B together with many specimens originating within the northern part of the distributional area of *Cabassous unicinctus*, specimens of unknown origins and 2 specimens originating within the southern part of the distributional area of *Cabassous unicinctus*. In addition, the ontogenetic stages do not seem to have a major influence on phenetic distances as they are distributed all over the NJ tree.

based on their mitogenomes (Gibb *et al.*, 2016), which is also true for their overall morphology (Hayssen *et al.*, 2013). Based on these results, specimens originating within the distributional area of *Cabassous centralis* will be included within our *Cabassous unicinctus* dataset. The case of cluster C remains problematic. It may represent a different entity within or out of *Cabassous unicinctus*. Interestingly, the geographical origins of specimens in cluster C are partly overlapping with that of subspecies *Cabassous unicinctus squamicaudis* but two other specimens originating within the distributional area of this subspecies group with cluster B instead (mainly composed of specimens originating within the distributional area of *Cabassous unicinctus unicinctus*). Therefore, the situation seems to disagree partly with current subspecific recognition within *Cabassous unicinctus* and larger-scale studies, including molecular data and more specimens from the southern region are needed to clarify this aspect. Because of this uncertainty, we decided to perform our studies on *Cabassous unicinctus* on two data sets: one dataset corresponding to cluster B (n = 21 specimens) and one dataset including cluster B and cluster C (n = 27).

4.2 *Zaedyus sample selection*

4.2.1 *Ontogenetic stages determination*

The bivariate plot of the ossification index and skull length in *Zaedyus pichiy* shows that largest specimens generally present high ossification scores (Figure SI.8). A very young specimen, suspected to be a neonate or a fetus specimen, is separated from other specimens by a large gap in the bivariate plot. As it is morphologically very divergent, it will not be added to the following analyses. For the 44 remaining specimens, the criteria of Hubbe *et al.* (2016) on ossification of the basicranium enables us to tentatively distinguish between the ontogenetic stages present in the sample. This criterion separates three distinct areas on the bivariate plot for juveniles, subadults and adults, except for two specimens which have low ossification scores while being large and identified as adults with Hubbe *et al.*'s criteria (Figure SI.8). The specimen designated as a potential *C. vellerosus* is recognized as a juvenile. Besides a rather good separation of ontogenetic stages, there are no obvious groupings related to geographical origin (compared to specimens of unknown origin) or to the presence/absence of teeth on the premaxillary.

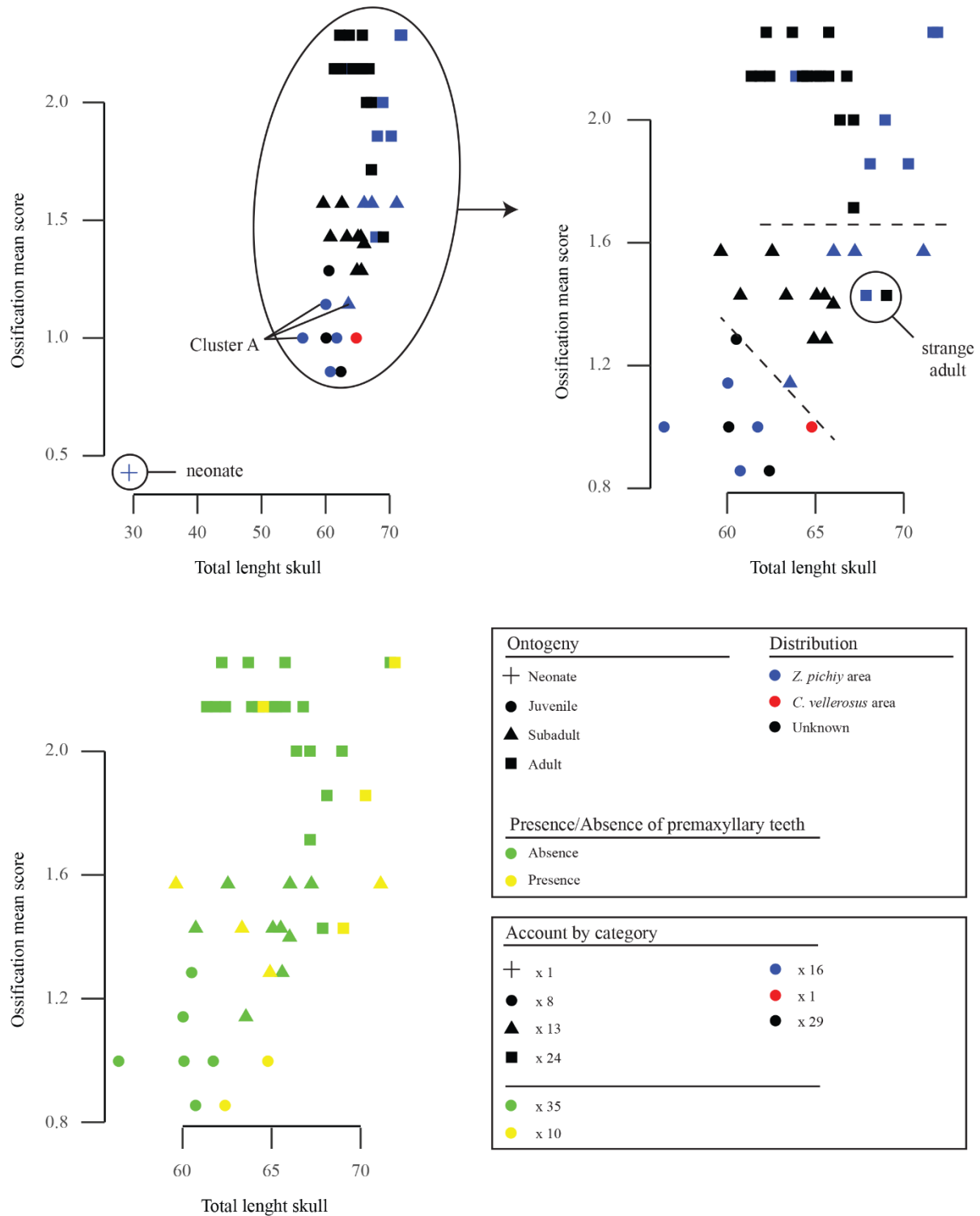


Figure SI.8. Ontogenetic stages determined based on Hubbe *et al.* (2016), as compared to the ossification score and the total length of the skull with a focus without the youngest specimen with a plot of the presence/absence of premaxillary teeth (Superina & Abba, 2014). The ontogenetic stages correspond to neonate (cross); juvenile (circle); subadult (triangle); adult (square).

4.2.2 *Principal components analysis*

On the first two axes of the analysis (= 31.48% of the variance), 2 large clusters are formed in the morphospace and two specimens stand out of these groups (Figure SI.9) (see below). The position of the zygomatic arches, the nuchal crests, and the cranial roof all vary on this axis while PC2 is mainly dominated by the variation of the nasal bone. The Bolivian specimen (*Chaetophractus vellerosus* area) takes an off-centered position in relation to the rest of the sample and this is also the case of a specimen of unknown origin. The clear separation in the morphospace of the Bolivian specimen from most of the sample seems to support its referral to *Chaetophractus vellerosus*. The status of the other off-centered specimen, of unknown origin, remains unclear (*Chaetophractus vellerosus?*) and will be further addressed in the following analyses. The separation of two large clusters in the PC1-2 morphospace, both of which contain specimens originating from the *Zaedyus pichiy* distributional area and specimens with premaxillary teeth and of all ontogenetic stages, raises questions on the existence of two large distinct entities within the sample. Interestingly, the only 2 of the three individuals in cluster A (Figure SI.9) with precisely known geographical origins come from the northern part of the *Zaedyus pichiy* distributional area. Cluster B seems to gather more southern specimens, but precise information is lacking for many specimens, including one of unknown origin in Chile.

4.2.3 *Permutational ANOVA*

The permutational analysis was performed between the two main clusters found in the PC1-2 morphospace and between specimens with a tooth on the premaxillary or not. The inclusion and exclusion of the two suspected *Chaetophractus vellerosus* specimens were also tested. The analysis indicates a statistically supported distinction between the two clusters whether cluster B includes the two suspected *Chaetophractus vellerosus* specimens or not (see Table SI.3). The analysis found no supported distinction between groups based on the presence/absence of a tooth on the premaxillary when the suspected *Chaetophractus vellerosus* specimens were excluded (Table SI.3). These analyses confirm a possible distinction between the two clusters on PC1-2, but more importantly, they invalidate the presence/absence of premaxillary teeth as a criterion for group distinction in our sample.

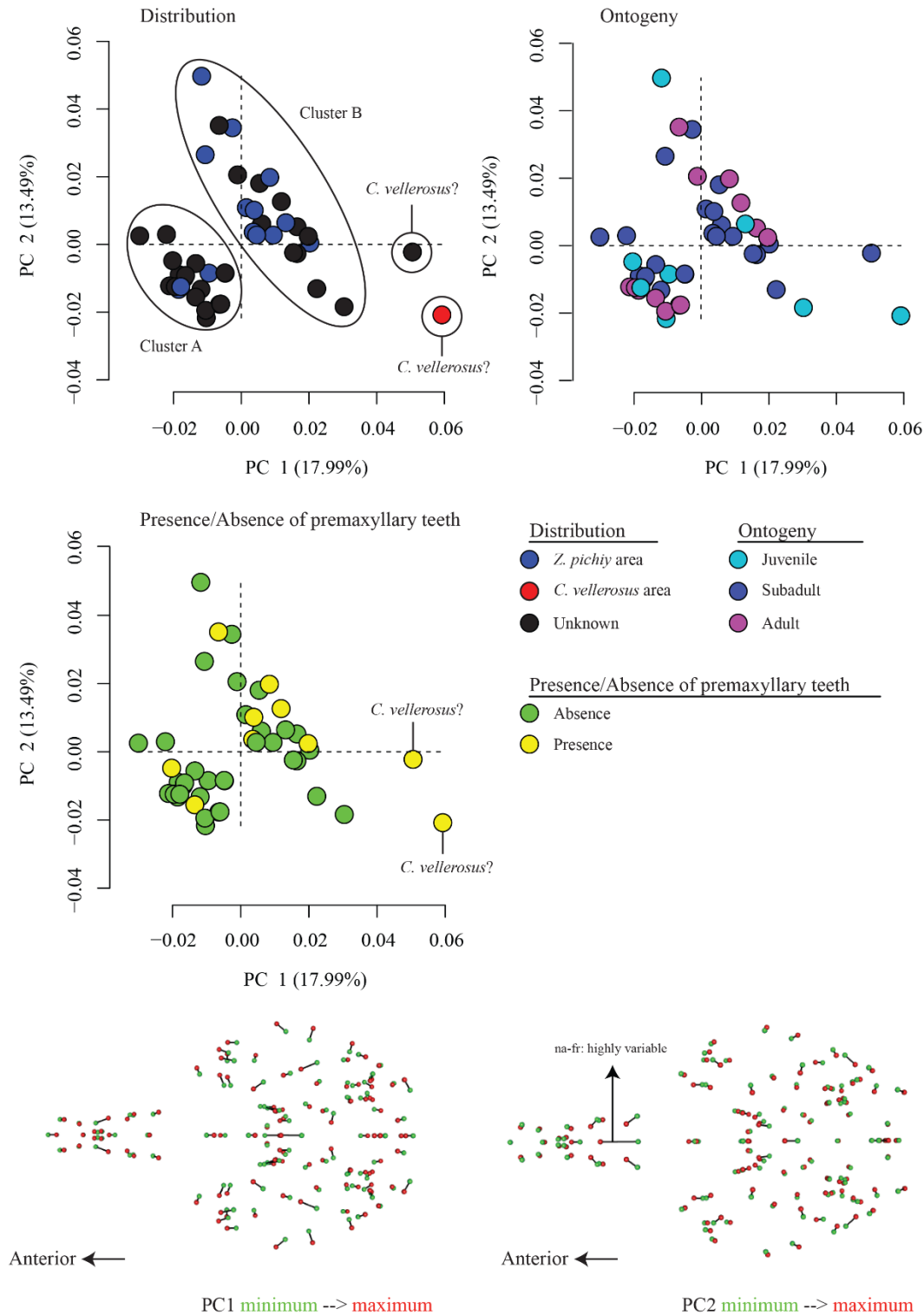


Figure SI.9. Results of the PCA performed on morphometric data in *Zaedyus* with a focus on geographical distribution, ontogenetic stage, and presence/absence of premaxillary teeth, distribution in the morphospace. Shape changes were visualized as vectors from the minimal shape (green) to the maximal shape (red) of each PC axes.

CHAPTER 1: SUPPORTING INFORMATION

Table SI.3. Statistical results of each permutational multivariate analysis of variance in *Zaedyus*. Each group is defined in [Figure SI.9](#).

Tests:	No Bolivian specimen:		with the Bolivian specimen (in Cluster B):	
	R ²	p-value	R ²	p-value
Cluster A vs Cluster B	15.41	0.0001	14.76	0.0001
Presence vs absence of premaxillary teeth	02.71	0.2716	04.06	0.0262

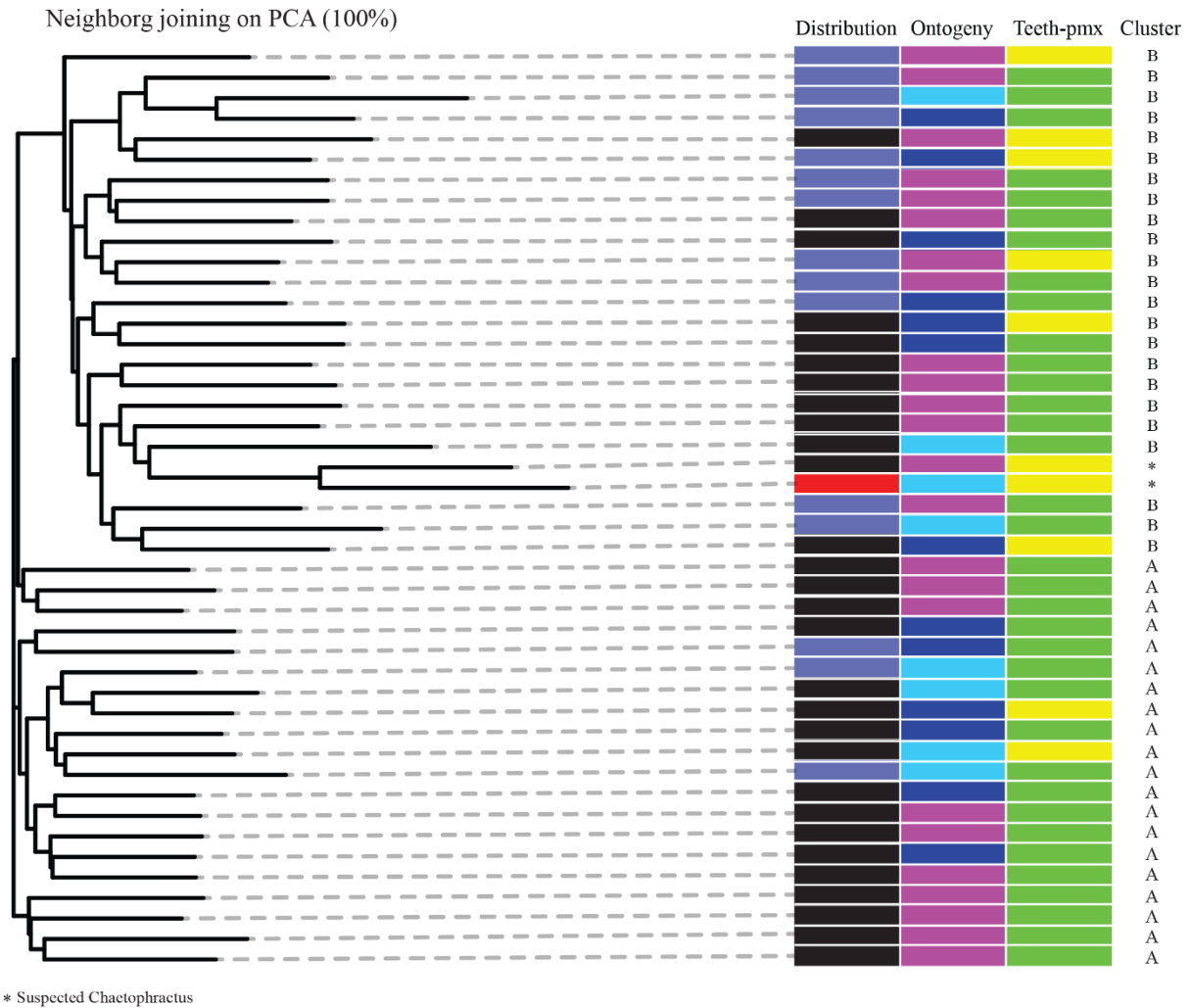


Figure SI.10. Unrooted neighbour-joining trees performed from PCA in *Zaedyus*. Each category for geographical distribution, ontogenetic stages and presence/absence of premaxillary teeth are represented in [Figure SI.9](#).

4.2.4 *Neighbour joining tree*

The reconstructed neighbour joining (NJ) tree (Figure SI.10) confirms a dissimilarity between two clusters A and B on the total variance within the sample and also underlines the stronger dissimilarity of the two suspected *Chaetophractus vellerosus* specimens relative to the rest of the sample. The ontogenetic stages as well as the presence of teeth on the premaxillary do not reflect any particular cluster in the NJ tree.

4.2.5 *Conclusion and Selection*

All the tests and analyses show a distinction of two large clusters in the sampling and the probable presence of two specimens of *Chaetophractus vellerosus* (one of which originates outside the *Zaedyus pichiy* distributional area) that separate well from those two clusters. Based on these results, we will not include in our dataset these two latter specimens. All other specimens seem to separate in two distinct entities, which might be geographically distinct, but none of which shows specimens originating outside of the distributional area of *Zaedyus pichiy*. This could well suggest different subspecies, but this does not seem to be congruent with currently accepted subspecies for this species (Wetzel *et al.*, 2007). Another possibility could correspond to the known sexual dimorphism in the species, but our dataset has too many missing data to test this hypothesis (see [General Discussion & Conclusion](#)). It would thus be premature at this stage to state on the possible status of these entities. Pending future studies on this aspect, we decided to include together clusters A and B in our *Zaedyus pichiy* series (n = 43; 44 with the very young specimen)

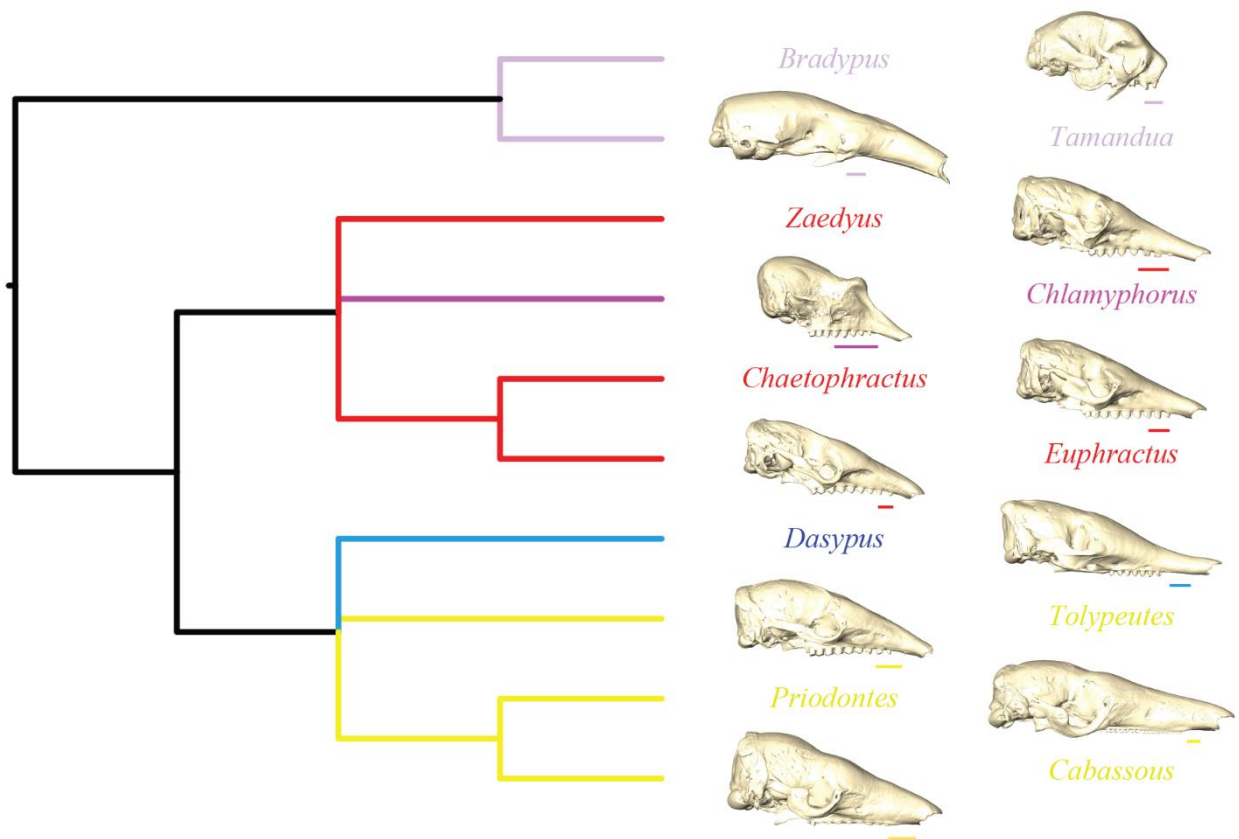


Figure S1. Morphological phylogenetic analysis of Billet *et al.* (2011) only with extant specimens. Tree length = 346 (on 5 trees of maximum parsimony), CI = 0.743, RI = 0.637. The color follows the work of Mitchell *et al.* (2016). Each taxon is illustrated by a skull in lateral view. Scale = 1 cm.

Supporting Information 2: Matrix and Analytical Parameters

For de description of each characters and the previous coded taxa see [Billet *et al.* \(2011\)](#).

Parameters:

- Dimensions ntax = 22 nchar = 125;
- Format datatype = standard;
- Gap = -;
- Missing = ?;
- States = "0 1 2 3 4 5 6".
- Heuristic search settings: Optimality criterion = parsimony;
- Character-status summary: Of 125 total characters: 27 characters are of type 'ord' (Wagner); 98 characters are of type 'unord'; All characters have equal weight; All characters are parsimony-informative; Gaps are treated as "missing"; Multistate taxa interpreted as polymorphism.
- Starting tree(s) obtained via stepwise addition;
- Addition sequence: random;
- Number of replicates = 1000;
- Starting seed = generated automatically;
- Number of trees held at each step = 10;
- Branch-swapping algorithm: tree-bisection-reconnection (TBR) with reconnection limit = 8;
- Steepest descent option not in effect;
- Initial 'Maxtrees' setting = 100;
- Branches collapsed (creating polytomies) if maximum branch length is zero;
- 'MulTrees' option in effect;
- Keeping only trees compatible with constraint-tree "kevin";
- Trees are unrooted.

Calyptophractus retusus

3210? 1???? 10611 12020 10012 01211 11010 12112 ??011 10000 0000? 00010 10221 11121 01011 111?0 00110
10111 110?0 0?10? 01011 2300? ??01 10101 10110

“*Cochlops*” *debilis*

3?1?? 2???? ????? ?????? ??0? ??201 ?0010 13113 ?0021 10000 0?00? 110?? ??121 21121
01111 111?1 01100 10210 11010 120-? 001?? 0??1? ?????1 1211? (01)0111

Eucinepeltus complicatus

3211? 21101 206?? ????? ?0?0? 10201 10010 13113 ?0021 1?000 0?0?? 110?? 1?122 21121 00111 111?1 011?0
10210 1???0 ????? 001?? ???1? ???1 12111 10111

Glyptodon sp.

3211? 21101 20601 02321 10?0? 10201 10010 13113 10021 10000 0?0?? 110?? 1?121 21121 00111 111?1 0?1?0
10210 11010 120?1 001?? 0??1? ??01 12111 10111

“*Metopotoxus*” *anceps*

3???? 2???? ????? ?????? ??0? ??20? ?0010 13??? ?0011 10000 ??00? 110?? ???21 21121 01111 111?1 1?1??
?0210 ????? ????? 0???? ?????? ???1 1211? 0011?

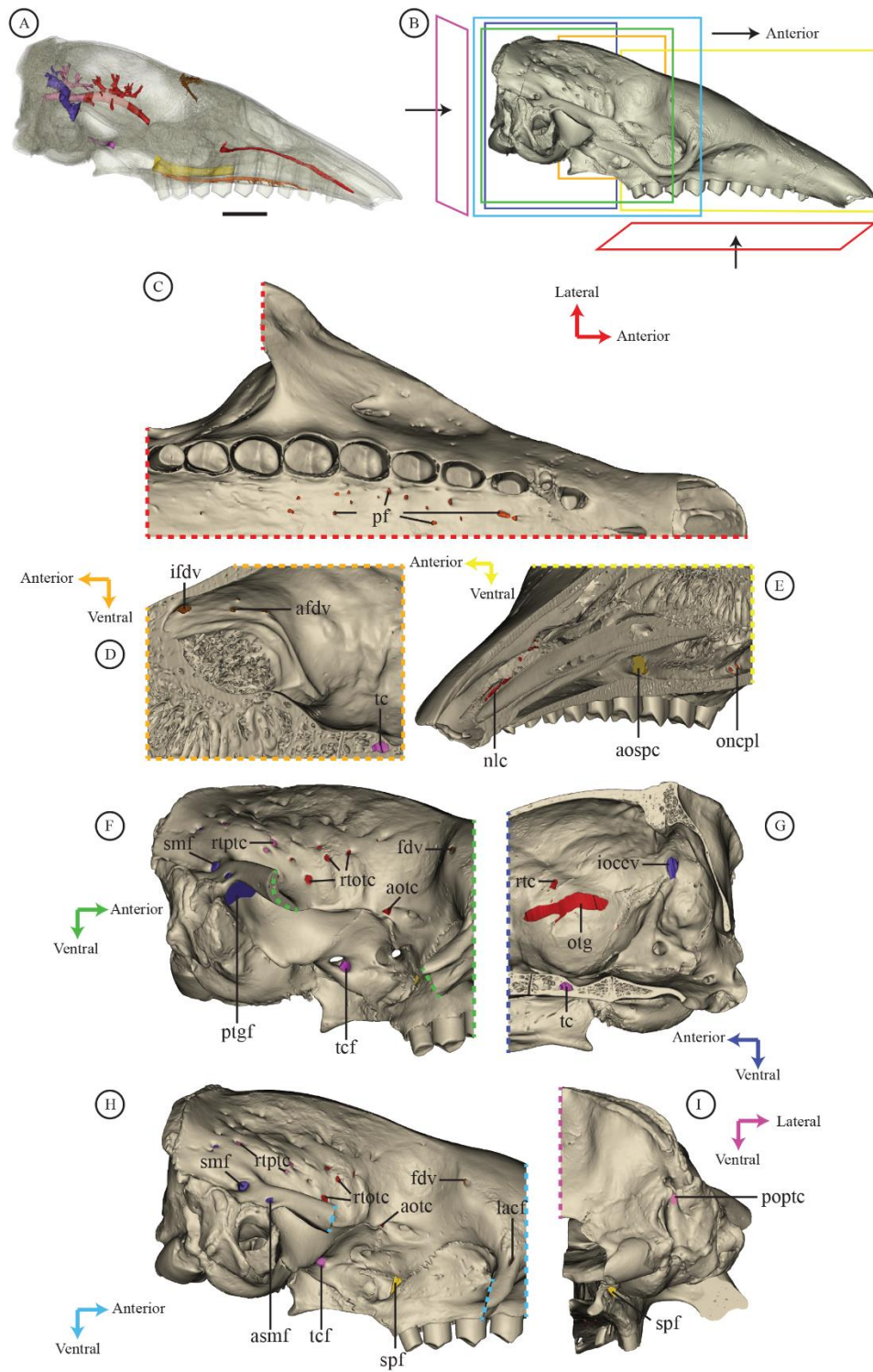


Figure S2. Illustration of the internal and external openings of each selected canal on a specimen of *Euphractus sexcinctus* (AMNH 133304) in transparent and non-transparent views. A, B, F and H, lateral view; C, ventral view; D and E, oblique internal view; G, lateral view of the braincase inner part; I, occipital view. Colors of the canals follow Figure 9. Abbreviations: **afd**v, accessory frontal diploic vein internal opening; **aospc**, anterior opening of the sphenopalatine canal; **aotc**, anterior opening of the orbitotemporal canal, **asmf**, accessory suprameatal foramen; **fdv**, foramen for the frontal diploic vein; **ifdv**, internal foramen for the frontal diploic vein; **ioccv**, internal opening of the capsuloparietal emissary vein canal; **lacf**, lacrimal foramen; **nlc**, nasolacrimal canal; **oncpl**, opening in nasopharyngeal canal of palatine canal; **otg**, orbitotemporal groove; **pf**, palatine foramina; **poptc**, posterior opening of the posttemporal canal; **ptgf**, postglenoid foramen; **ramus temporalis** canal; **rtotc**, *rami temporales* foramina from the orbitotemporal canal; **rtptc**, *rami temporales* foramina from the posttemporal canal; **smf**, suprameatal foramen; **spf**, sphenopalatine foramen; **tc**, transverse canal; **tcf**, transverse canal foramen. Scale = 1 cm.

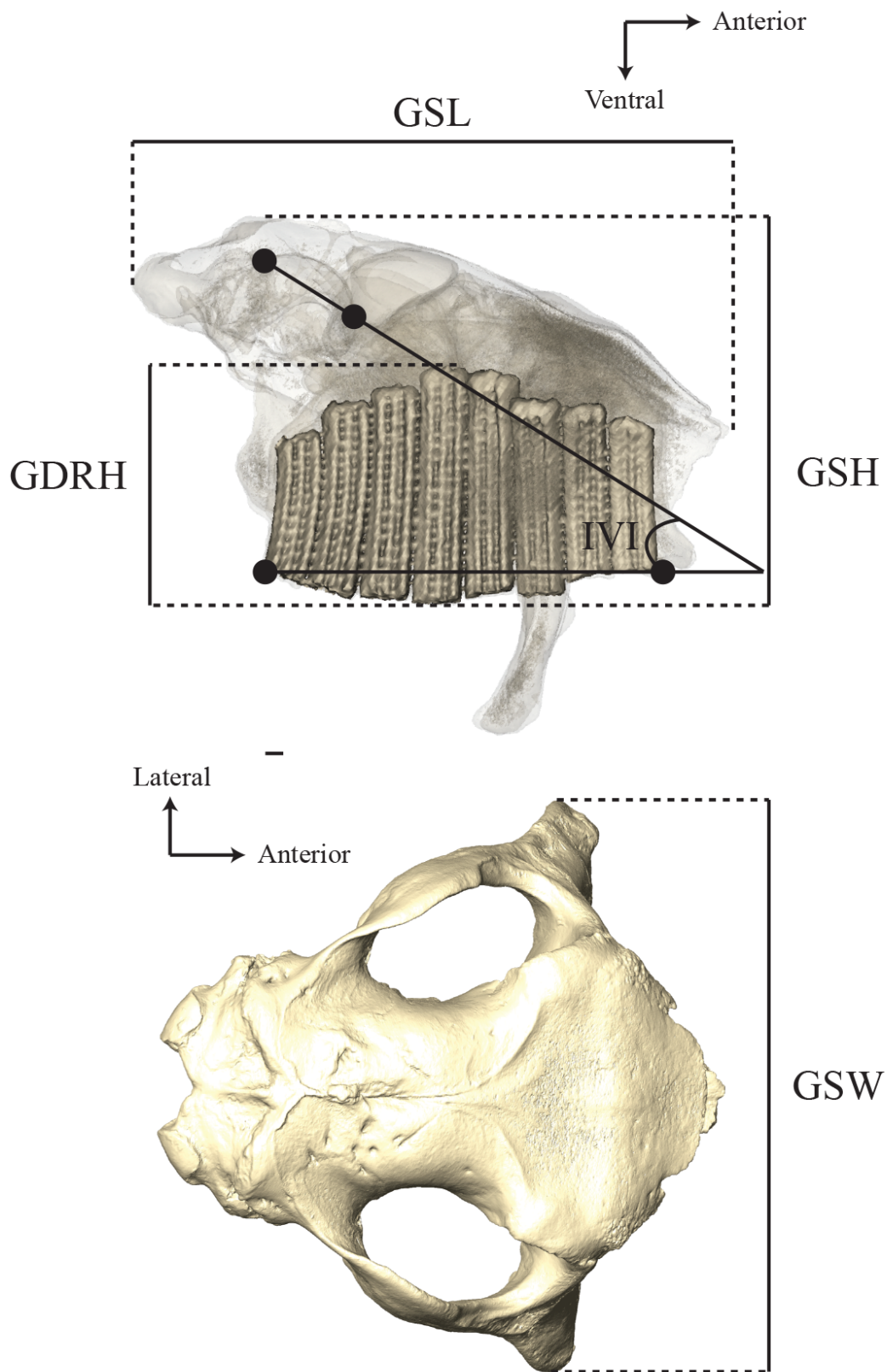


Figure S3. Cranial measurements (Table S2) illustrated on a transparent cranium in lateral (top) and dorsal (bottom) view of *Glyptodon* sp. MNHN.F.PAM 760. Abbreviations: **GDRH**, greatest dental row height; **GSH**, greatest skull height; **GSL**, greatest skull length; **GSW**, greatest skull width; **IVI**, internal vault inclination (= angle between the anteroposterior axis of the cranium (defined by the line connecting the most anterior and posterior edges of the dental row) and the straight line connecting the most dorsal point of the annular ring and the most ventral point of the tentorial process). Scale = 1 cm.

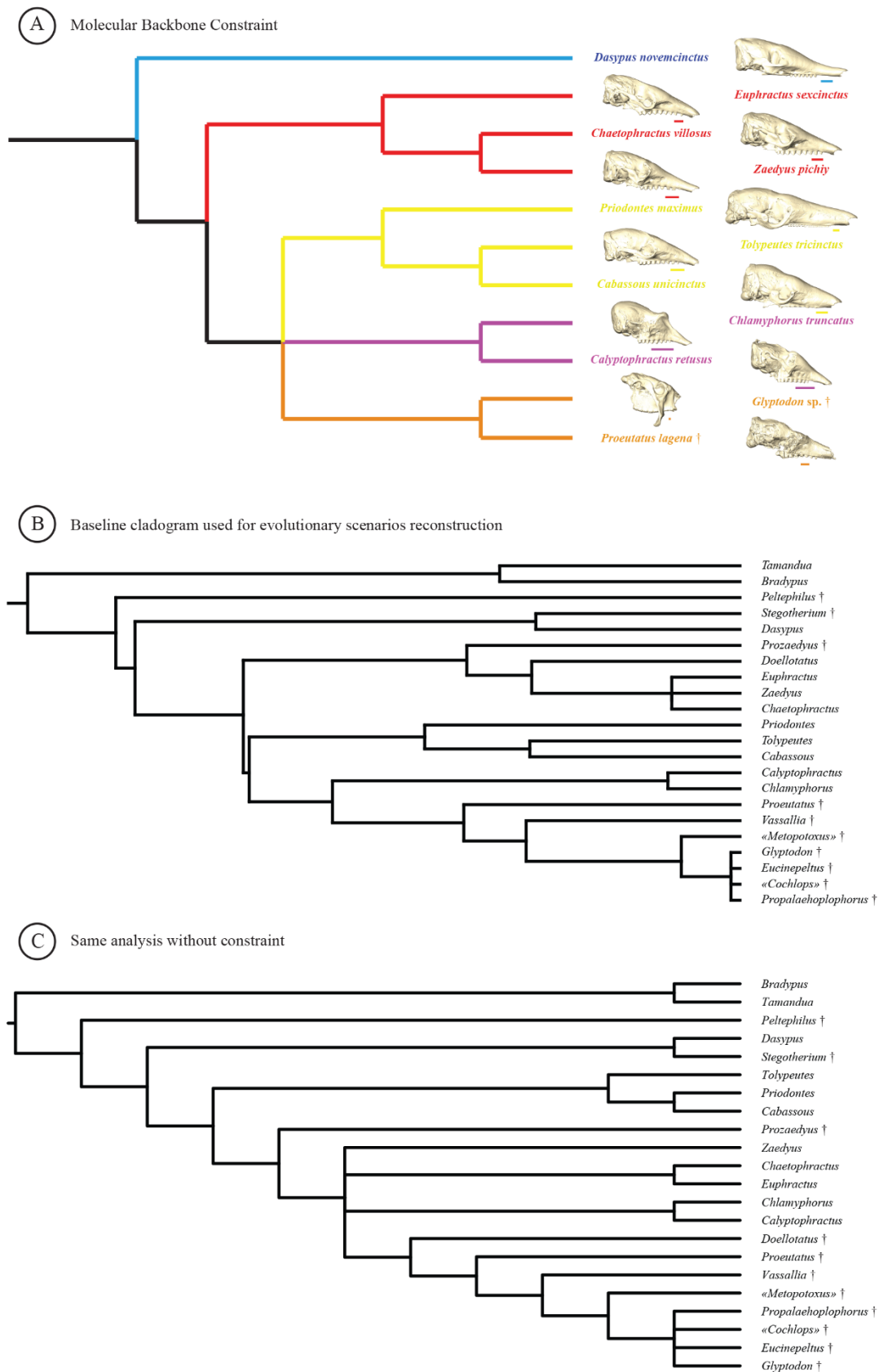


Figure S4. A, modified backbone constraint from Mitchell *et al.* (2016) used for our phylogenetic analysis (see text). *Proeutatus* is enforced as the sister group of glyptodonts in accordance with most phylogenetic analyses using morphology (Engelmann, 1985; Gaudin & Wible, 2006; Billet *et al.*, 2011; Herrera *et al.*, 2017). B. Topology of the baseline cladogram. C. Topology of the strict consensus from the same analysis without constraint. See Supporting information 2 for phylogenetic analysis.

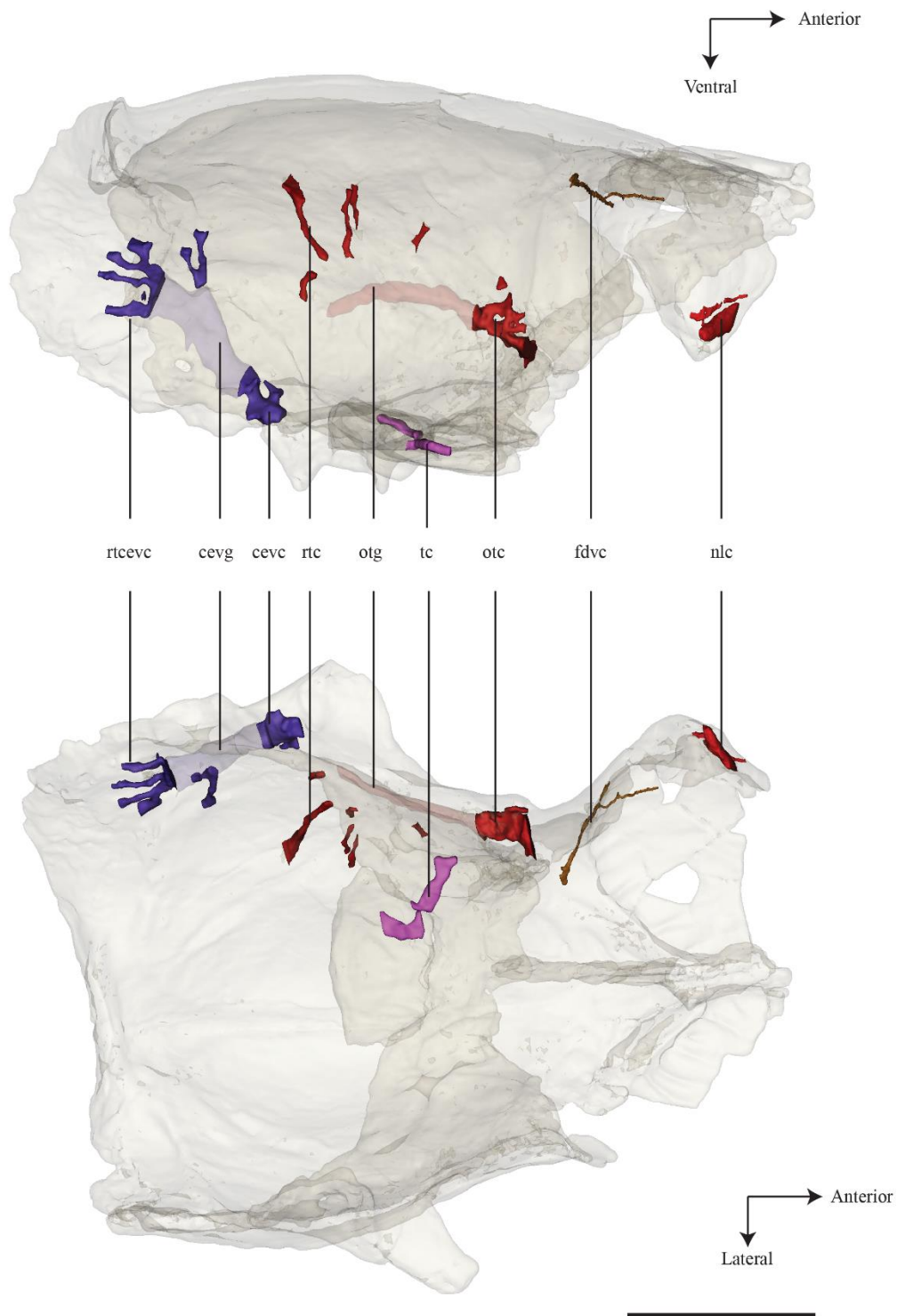
Utaetus buccatus †

Figure S5. Reconstructed canals in *Utaetus buccatus* in right lateral (top) and ventral (bottom) views. The preserved parts of the cranium (caudal cranium) are shown with transparency. Abbreviations: **cevc**, capsuloparietal emissary vein canal; **cevg**, capsuloparietal emissary vein groove; **fdvc**, frontal diploic vein canal; **nlc**, nasolacrimal canal; **otc**, orbitotemporal canal; **otg**, orbitotemporal groove; **rtc**, rami temporales canals; **rtcevc**, rami temporales from capsuloparietal emissary vein canal; **tc**, transverse canal. Scale = 1 cm.

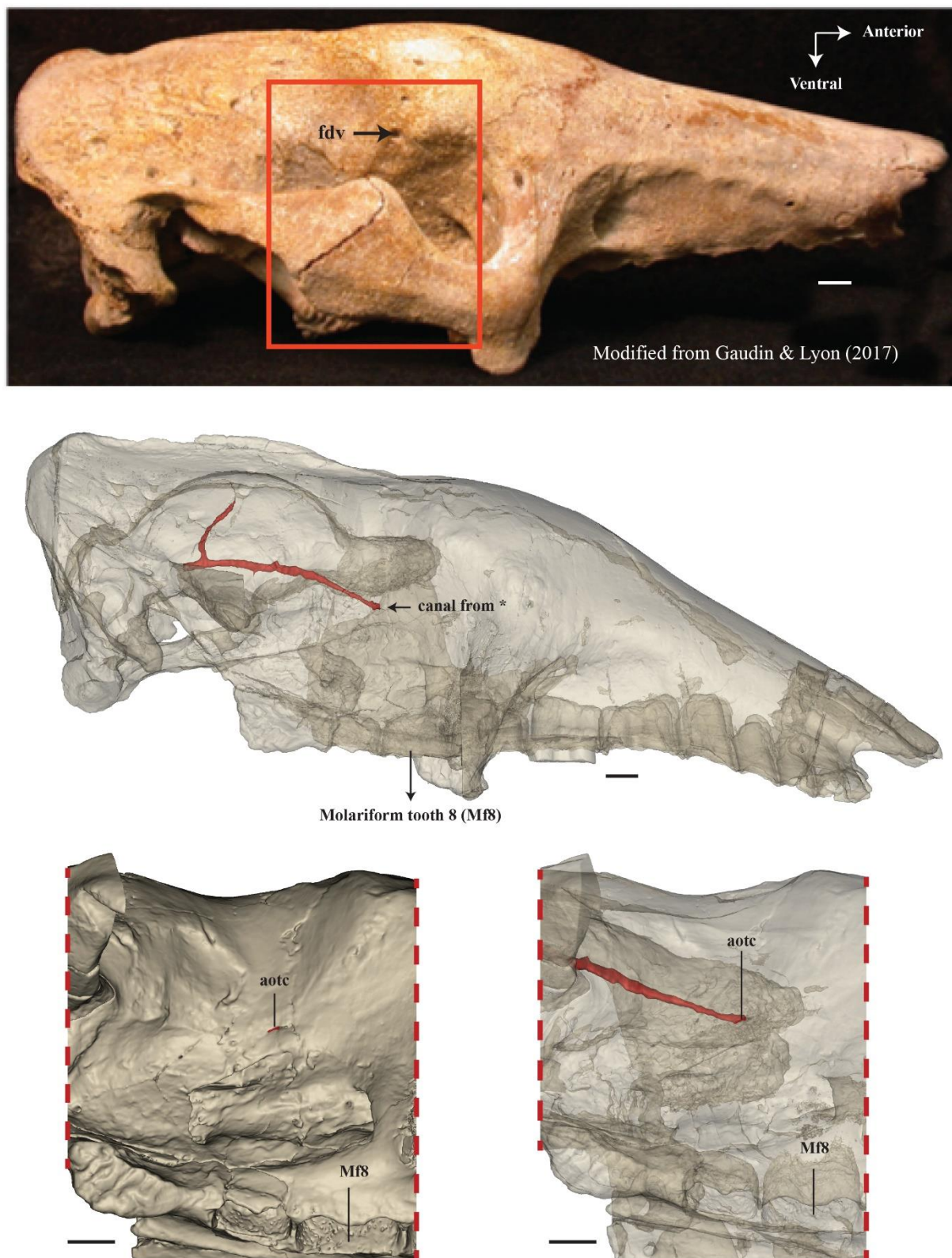


Figure S6. Illustration of the foramen for the frontal diploic vein identified in the study by [Gaudin & Lyon \(2017\)](#) on *Holmesina floridanus* (UF 191448) (A) and the anterior opening of the orbitotemporal canal in *Vassallia maxima* (FMNH P14424) in a right lateral view with transparency (B) and a view focused on the orbitotemporal region (C). Abbreviations: **aotc**, anterior opening of the orbitotemporal canal; **fdv**, foramen for the frontal diploic vein. Scale = 1 cm.

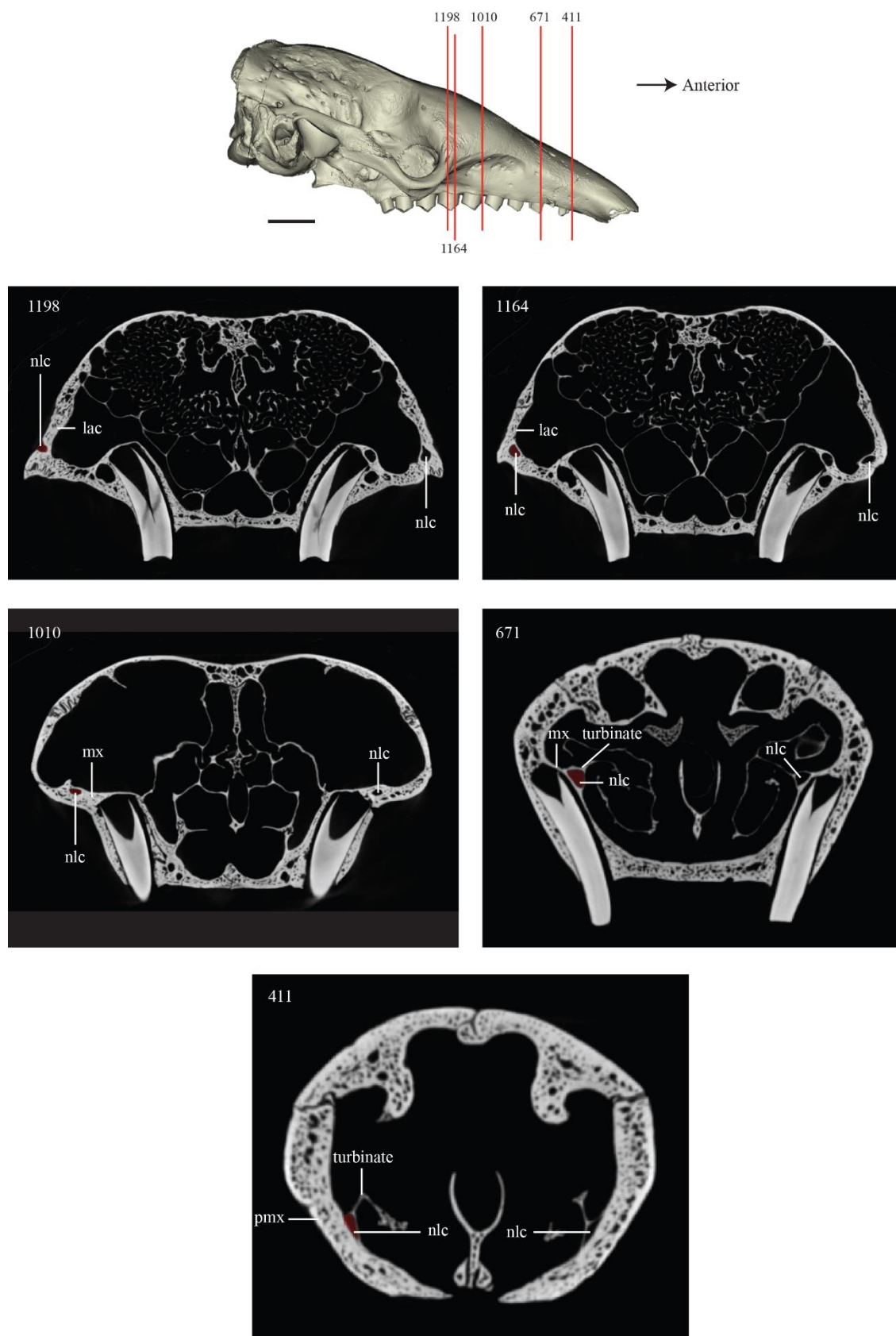


Figure S7. Identification of the bones enclosing the nasolacrimal canal in *Euphractus sexcinctus* (AMNH 133304) illustrated by a skull in right lateral view (top). The slices analyzed are indicated on the skull by their number in the image stack and illustrated below. The nasolacrimal canal is reconstructed in red on each slice, on the left side of the image. Abbreviations: **lac**, lacrimal; **mx**, maxillary; **nlc**, nasolacrimal canal; **pmx**, premaxillary. Scale = 1 cm.

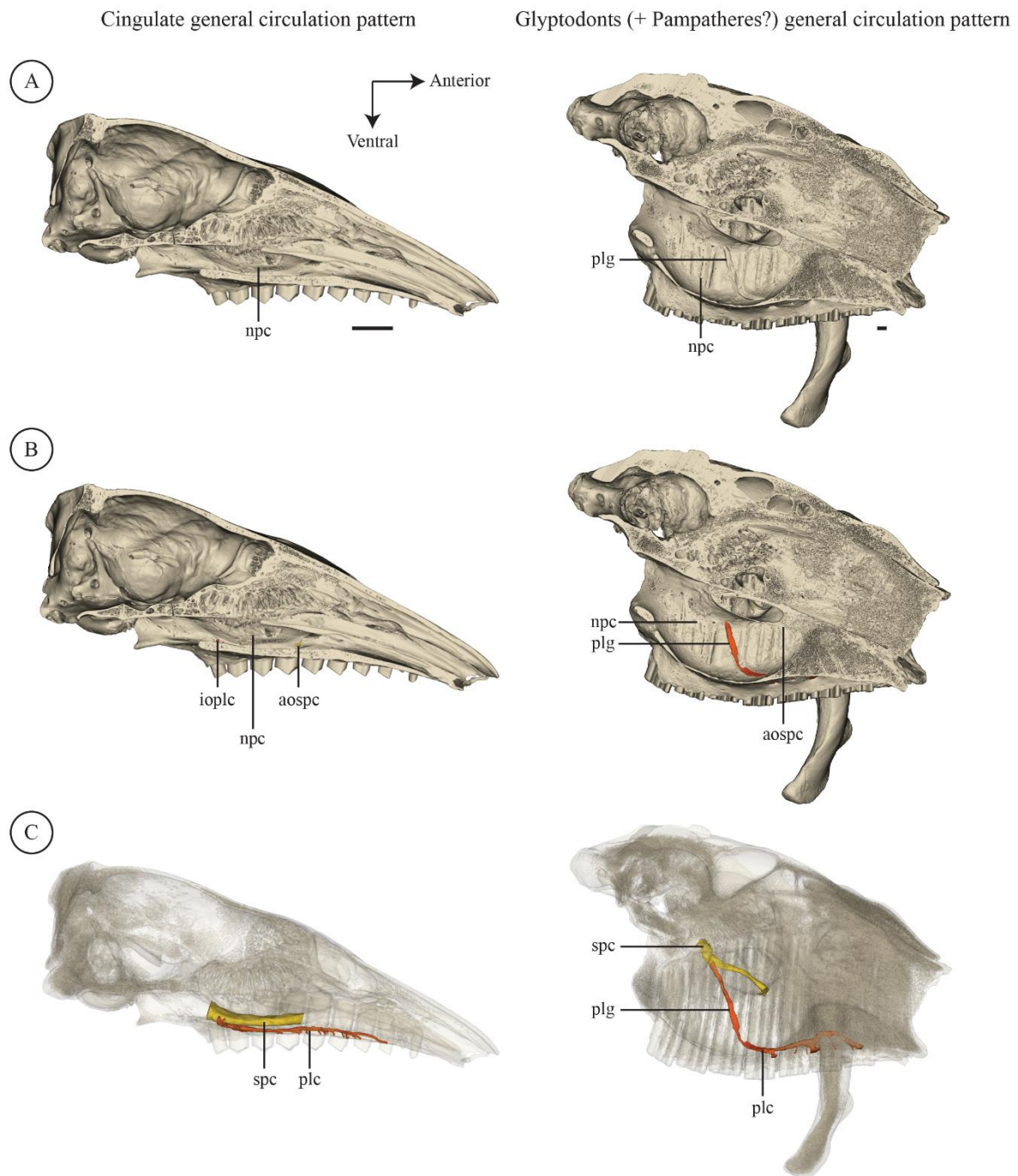


Figure S8. Comparative illustration of the trajectory of the palatine canal in glyptodonts and other cingulates (illustrated here by *Euphractus sexcinctus* (AMNH 133304)). A, lateral internal view on a skull sectioned on the midline. B, same view as A but with the palatine canal reconstructed. C, same view as A with skull transparency and with the sphenopalatine and palatine canals reconstructed. Abbreviations: **aospc**, anterior opening of the sphenopalatine canal; **iovlc**, internal opening of the palatine canal; **npc**, nasopharyngeal canal; **plg**, palatine groove; **spc**, sphenopalatine canal. Scale = 1cm.

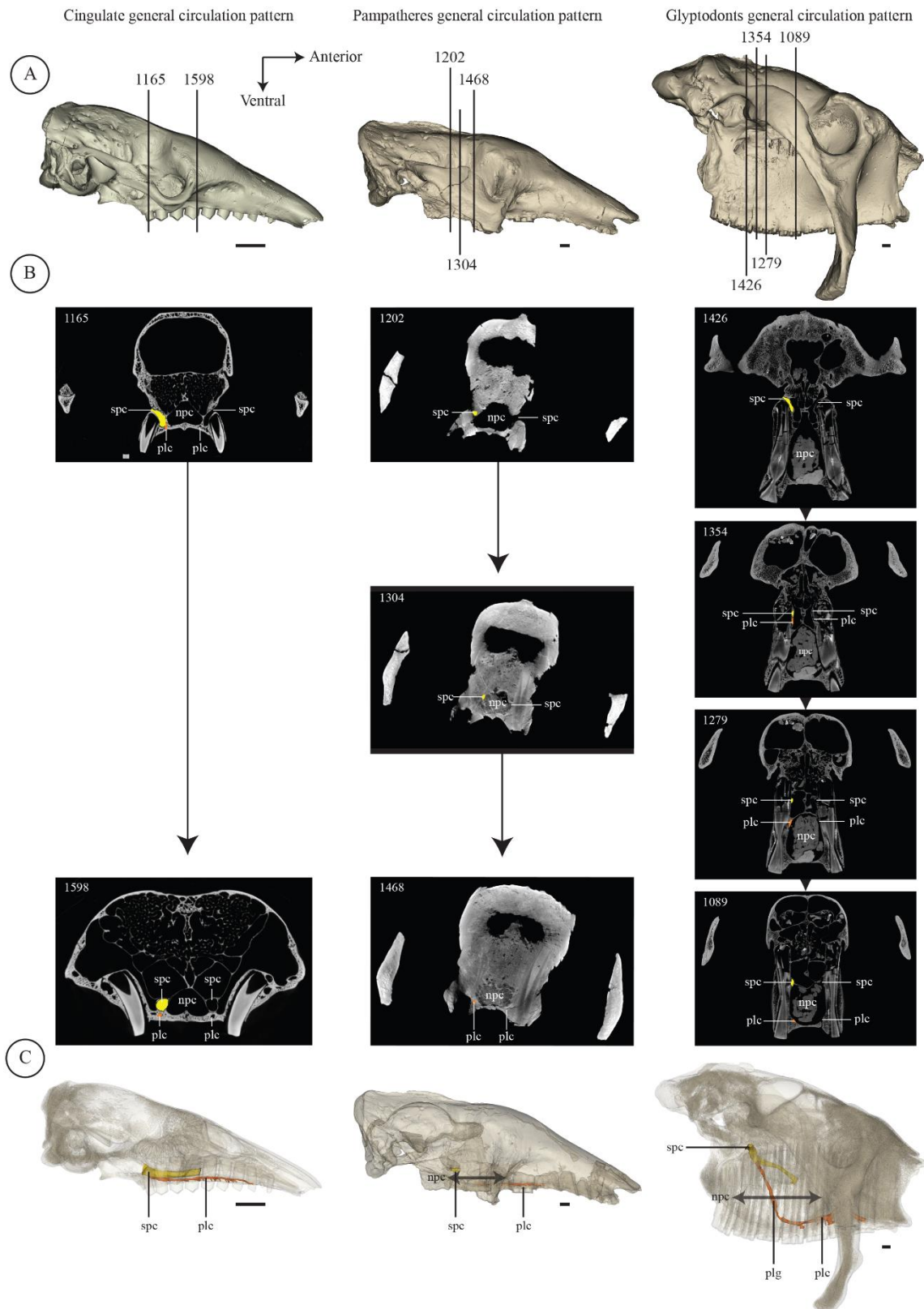


Figure S9. Illustration of the position of the sphenopalatine and palatine canals in relation to the nasopharyngeal canal in *Euphractus sexcinctus* (AMNH 133304), *Vassallia maxima* (FMNH P14424) and *Glyptodon sp.* (MNHN.F.PAM 760). A. Selected slides (numbered according to their position in the image stack) indicated on the skull in lateral view. B. Slides in coronal view. C. Canals are indicated on skull in transparency in lateral view (same as A). The same colors were used for canals: orange, palatine canal; yellow, sphenopalatine canal. Abbreviations: **npc**, nasopharyngeal canal; **plc**, palatine canal; **plg**, palatine groove; **spc**, sphenopalatine canal. Scale = 1 cm.

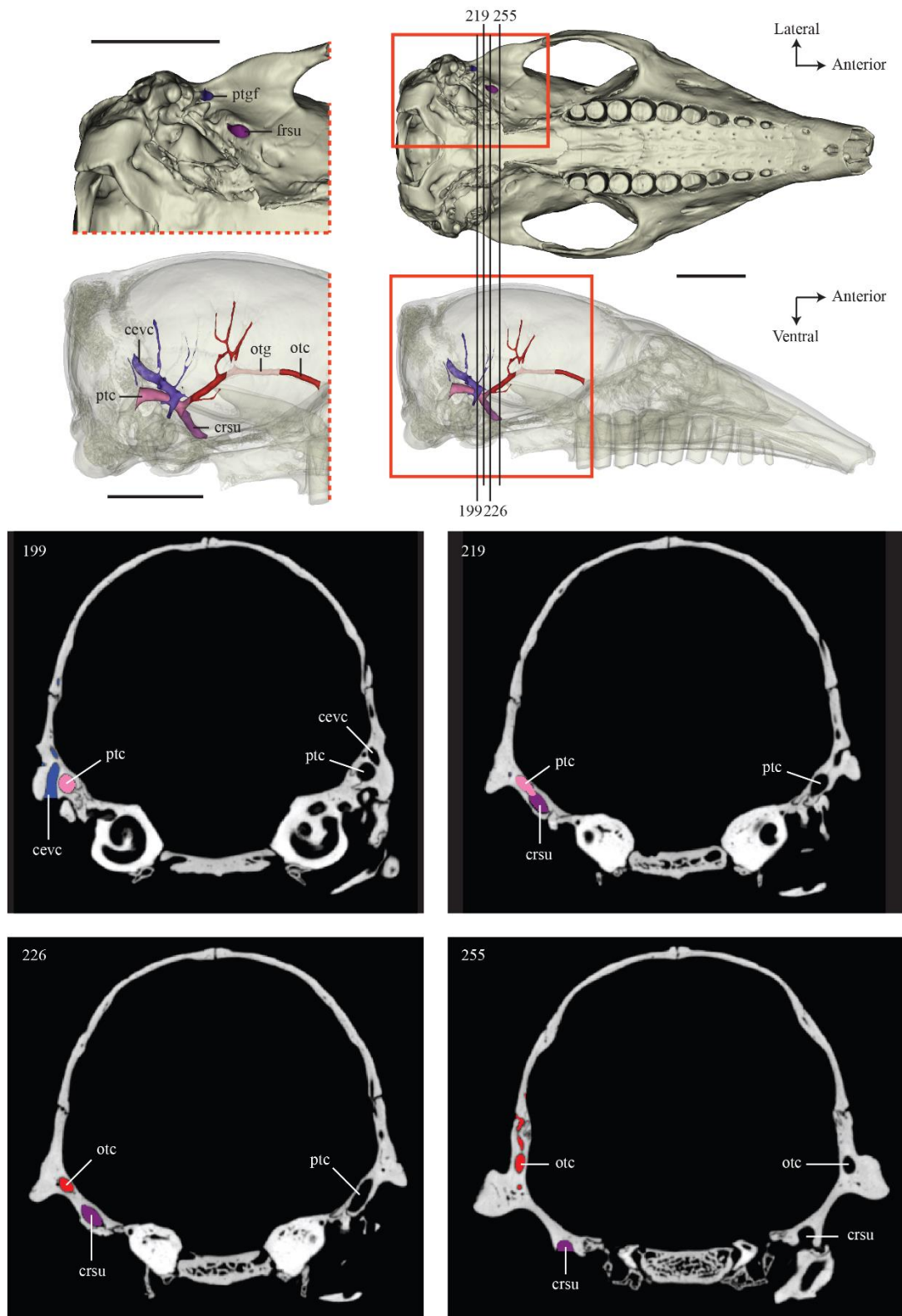


Figure S10. Identification of the canal for the ramus superior of the stapedia artery in *Tolypeutes matacus* (FMNH 28345). External opening is illustrated on a skull in ventral view with a focus on the auditory region. Canal trajectory in relation to the other braincase canals is representing on a transparent skull in lateral view with a focus on the neurocranium. Several parts of the canal (external opening, contact with the orbitotemporal and posttemporal canal, etc.) are also illustrated by numbered slides (in relation to the total number of slides) and indicated on the skulls. Abbreviations: **cevc**, capsuloparietal emissary vein canal; **crsu**, canal for the ramus superior of the stapedia artery; **otc**, orbitotemporal canal; **otg**, orbitotemporal groove; **ptc**, posttemporal canal. Scale = 1 cm.

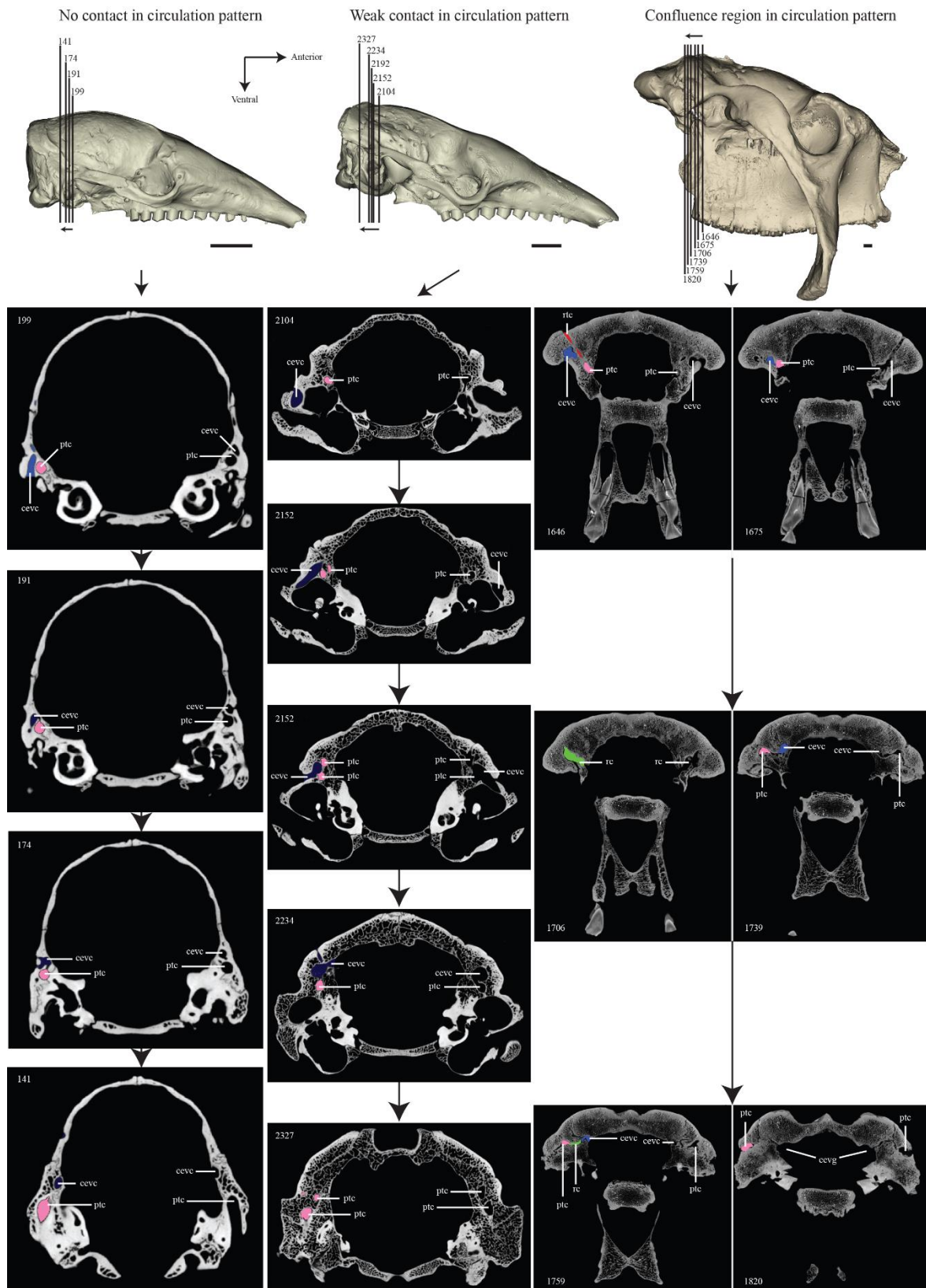


Figure S11. 3 Different cases of contact/non-contact between the three braincase canals analyzed in our study (including the region of confluence) in *Tolypeutes matacus* (FMNH 28345), *Euphractus sexcinctus* (AMNH 133304) and *Glyptodon* sp. (MNHN.F.PAM 760). Selected slides (numbered according to the total slide number) are indicated on skull in lateral view and canals are coloured on one side of each slide. Abbreviations: **cevc**, capsuloparietal emissary vein canal; **cevg**, capsuloparietal emissary vein groove; **ptc**, posttemporal canal; **rc**, region of confluence; **rtc**, ramus temporalis canal. Scale = 1 cm.

CHAPTER 2: TABLE

Table S1. List of adult specimens used for assessing the intraspecific variation in *Dasypus*, *Zaedyus* and *Cabassous*.

Family/Clade	Species	Institutional number	Locality
Dasypodinae	<i>Dasypus novemcinctus</i>	AMNH 255866	Bolivia, Beni, Cercado
Dasypodinae	<i>Dasypus novemcinctus</i>	AMNH 211668	Bolivia, Beni, Cercado, ca. 23 kilometers west of San Javier
Dasypodinae	<i>Dasypus novemcinctus</i>	AMNH 262658	Bolivia, Pando, Nicolas Suarez, 5 kilometers upstream from Cachuela
Dasypodinae	<i>Dasypus novemcinctus</i>	AMNH 263287	Bolivia, Santa Cruz, Andres Ibanez, Ayacucho
Dasypodinae	<i>Dasypus novemcinctus</i>	AMNH 205727	Uruguay, Lavalleja, Zapican, 12 kilometers west southwest of Zapican
Euphractinae	<i>Zaedyus pichiy</i>	FMNH 23810	Argentina, Chubut
Euphractinae	<i>Zaedyus pichiy</i>	AMNH 94327	Argentina, Chubut, Sarmiento, Colhue Huapi Lake
Euphractinae	<i>Zaedyus pichiy</i>	MNH 1883-158	Argentina, Santa Cruz
Euphractinae	<i>Zaedyus pichiy</i>	ZMB 46103	South America, Argentina, Puerto Jenkins, -47,75779, -65,90836
Euphractinae	<i>Zaedyus pichiy</i>	ZMB 46104	South America, Argentina, Oso Marino, -47,9237, -65,83145
Tolypeutinae	<i>Cabassous unicinctus</i>	MNH 1999-1044	French Guiana
Tolypeutinae	<i>Cabassous unicinctus</i>	MNH 1998-2255	French Guiana, Petit-Saut
Tolypeutinae	<i>Cabassous unicinctus</i>	AMNH 137196	South America, Brazil, Para, Tapajos River, Igarape Brabo
Tolypeutinae	<i>Cabassous unicinctus</i>	AMNH 74113	South America, Peru, Loreto, Maynas
Tolypeutinae	<i>Cabassous unicinctus</i>	MVZ 155192	Peru, Rio Cenepa

Table S2. Cranial measurements in mm for **GSL**, **GSW**, **GSH**, **GDRH** and Geometric mean, and in degree for **IVI** (see **Figure S3**). Symbol: ?, missing data.

Species	GSL	GSW	GSH	GDRH	IVI	Geometric mean
<i>Bradypus tridactylus</i>	75.67	49.15	42.92	13.79	3.66	54.25
<i>Tamandua tetradactyla</i>	124.82	41.56	50.71	0	11.06	64.07
<i>Peltephilus pumilus</i> †	93.9	49.04	42.17	22.76	-4.85	57.91
<i>Utaetus buccatus</i> †	?	?	?	?	?	?
<i>Dasypus novemcinctus</i> *	38.69	19.28	17.77	0.8	0.8	23.67
<i>Dasypus novemcinctus</i> **	54.14	24.89	20.04	3.02	10.26	30.00
<i>Dasypus novemcinctus</i> ***	79.36	33.52	26.28	4.61	10.18	41.19
<i>Dasypus novemcinctus</i> ****	89.04	39.07	37.65	5.78	17.73	50.78
<i>Stegotherium tauberi</i> †	138.9	49.29	46.11	3.05	20.83	68.09
<i>Prozaedyus</i> †	66.71	30.45	29.34	7.16	?	39.06
<i>Euphractus sexcinctus</i>	105.97	66.55	47.09	15.17	6.58	69.25
<i>Chaetophractus villosus</i>	89.39	58.46	37.48	14.07	3.96	58.07
<i>Zaedyus pichiy</i> *	29.31	18.31	13.86	0.55	?	19.52
<i>Zaedyus pichiy</i> **	56.43	33.47	24.76	6.39	3.04	36.03
<i>Zaedyus pichiy</i> ***	63.56	39.03	27.18	7.2	2.4	40.70
<i>Zaedyus pichiy</i> ****	71.65	42.59	29.18	8.52	1.67	44.65
<i>Doellotatus</i> sp. †	?	?	37.35	15.36	8.08	?
<i>Cabassous unicinctus</i> **	69.94	40.62	35.69	8.24	16.79	46.63
<i>Cabassous unicinctus</i> ***	77.96	38.79	34.72	6.19	12.85	47.17
<i>Cabassous unicinctus</i> ****	87.41	47.09	37.78	9.53	8.57	53.77
<i>Tolypeutes matacus</i>	69.16	31.89	28.95	8.46	-1.04	39.96
<i>Priodontes maximus</i>	189.35	80.34	53.58	7.12	-2.11	93.41
<i>Chlamyphorus truncatus</i>	36.56	24.3	20.41	6.35	18.29	26.27
<i>Calyptophractus retusus</i>	42.86	27.38	23.41	8.22	11.68	30.17
<i>Proeutatus lagena</i> †	110.98	61.64	50.89	17.86	17.92	70.35
<i>Vassallia maxima</i> †	243.85	138.42	105.18	63.82	0.08	152.55
" <i>Metopotoxus</i> " <i>anceps</i> †	138.22	98.17	76.17	38.95	19.45	101.11
<i>Propalaeophlorus minus</i> †	141.27	117.01	80.33	44.41	18.56	109.91
" <i>Cochlops</i> " <i>debilis</i> †	145.82	102.54	89.25	45.64	21.2	110.10
<i>Eucinepeltus complicatus</i> †	180.25	139.63	93.44	54.93	?	132.98
<i>Glyptodon</i> sp. †	331.59	336.88	209.27	124.07	35.84	285.93

† extinct species; * perinatal stage; ** juvenile; *** subadult; **** adult.

Supporting Information 3: Determination of Ontogenetic Stages.

To perform analyses at the ontogenetic level and then at a static level, it is necessary to determine as precisely as possible the relative ontogenetic stage of each specimen.

1. Material and methods

PROTOCOL

The determination of the developmental stage of each specimen is based on dental eruption, cranial ossification, and cranial length. Except for size, these variables are each composed of various discrete observations scored numerically (see below). The scored observations are then averaged and compiled in a dental eruption index or a cranial ossification index. The observations on dental eruption were made on CT-images and on 3D reconstructions of the skulls and correspond to the number, the class, and the generation of the teeth (deciduous premolar, dPM; permanent premolar, PM; molar, M). The genus *Dasypus* is the only known xenarthran taxon that retains two functional generations of teeth (Ciancio *et al.*, 2012). The adult upper tooththrow of *D. novemcinctus* is composed of seven premolars and one molar. The use of CT-images was critical as it permitted to detect the presence of forming tooth buds in crypts. Based on our observations of the upper dentition, we defined five dental stages: (1) dPMs starting to mineralize or erupting; (2) all dPMs well mineralized, possibly all erupted, no PM in the crypts (*i.e.*, PM not mineralized); (3) all dPMs erupted, with part of the PMs mineralized but still in the crypts (not yet reaching the alveoli); (4) part of the dPMs about to be replaced by PMs (one or several PMs has/have erupted through the alveoli, but remain(s) almost unworn); (5) all PMs erupted and no remain of dPMs left (Figure S12). As only one premolar generation was present in stages (2) and (5), we considered three measurements on the fourth premolar locus (the most represented tooth in our sampling) to discriminate between these stages: total height of the tooth, height of the alveoli, and height of the growth front (Figure S13; Table S6). We then plotted each of these variables relative to the length of the skull (LTC; see below) to delineate graphically the stages (2) and (5) (Figure S13). Cranial ossification was characterized based on suture closures (0: not in contact, 1: unfused, 2: partly fused, 3: fused). Only bones whose suture closure varies along our ontogenetic series were scored. Seven sutures were then scored, and the mean of these scores was computed to give the

ossification score for each specimen (Table S7). The cranial length value (LTC - measure taken between landmark #1 and #84) used for this analysis was taken from Hautier *et al.* (2017). All cranial length, dental eruption and cranial ossification indexes are presented in Table S5. The combination of these three variables enabled us to confirm the ontogenetic separation of specimens in five stages. It was not possible to determine the degree of ossification for four specimens out of 96 because of missing bones. In addition, eight armadillos could not be associated with a dental stage because of the absence of the P4. Twelve specimens could not be assigned to an ontogenetic stage. Specimens with missing teeth could not be allocated to a precise stage and could not be included in the ontogenetic analyses.

2. Results

POSTNATAL ONTOGENETIC STAGES IN NINE-BANDED ARMADILLOS

For each of the remaining 84 specimens, the ontogenetic division based on the dental stages is in agreement with the ossification score and the cranial length (Figure S14). Only one specimen was attributed to stage (1), which corresponds to stillborn individuals (according to a collection label). This specimen is not included in the following analyses as its shape is too extreme compared to the rest of the sample. 11 specimens correspond to stage (2), which we call juvenile stage hereafter. This juvenile stage is characterized by the presence of only deciduous teeth and represents the largest range of cranial length in our ontogenetic delineation (Figure S14). Stages (3) and (4), which comprise seven and nine specimens respectively, are close and partly overlap graphically; they were combined into a single sub-adult stage. The stage (5) is composed of 56 specimens and is here considered as the adult stage. It is noteworthy that cranial suture closure still occurs within this adult stage (see also Rager *et al.*, 2013). Based on this combination of proxies, ossification does not appear as the best marker for the determination of ontogenetic stages. However, combining these three proxies makes enabled us to make rather robust hypotheses on the ontogenetic stage of a specimen.

Supporting Information 4: allometric variation at the static level

The variations described correspond to cases where the allometric variation is different from the variation described in the main text (ontogenetic level).

Alisphenoid-Orbitosphenoid-Pterygoid-Basisphenoid complex (Figure S19.A1-A3)

Most of the allometric static variation is concentrated on the lateral edge of the bone complex. As the size increases, the entoglenoid process is more massive (#77). The most posteroventral point of the suture between the alisphenoid and squamosal is relatively more ventral (#72). The pterygoid wing is longer and oriented more laterally (#66). Otherwise, we found the same variation than at the ontogenetic level for the sphenorbital fissure (#48); the dorsal transverse ridge delimiting the ethmoidal fossa anteriorly (#130) and the contact between frontal, squamosal and alisphenoid (#44). There is no major difference when using the log centroid size of the OBU.

Frontal (Figure S19.B1-B3)

Two trends can be noted. The first corresponds to a homogeneous anterior extension of the frontal (landmarks #2; #34). The second corresponds to a relative reduction in the proportions of the rest of the structure when the size increases (= frontal parts posterior to the postorbital constriction) (#36, #38, #42; #44, #78, #81, #113, #131). This is a trend already obtained at the ontogenetic level, except that at the static level the intensity of the shape variation is practically the same for all the landmarks. There is no difference using the log centroid size of the bone at this level.

Palatine (Figure S19.C1-C3)

The allometric variation at this level is similar to the one obtained for the ontogenetic level, except for the two lateral landmarks (#21; #46) which only mark a reduction lateromedial of the bone width when size increase. As difference with the ontogenetic level, the same differences observed between the analyses with different centroid sizes are observed except that the intensity of the variations is much lower. With the log centroid size of the bone, we observe the same variation but with higher intensities.

Parietal (Figure S19.D1-D3)

The allometric variation at this level is essentially the same as for the ontogenetic level except for the tentorial process, which presents no distinct variation (#73). With the log centroid size of the bone, we observe the same variation but with higher intensities.

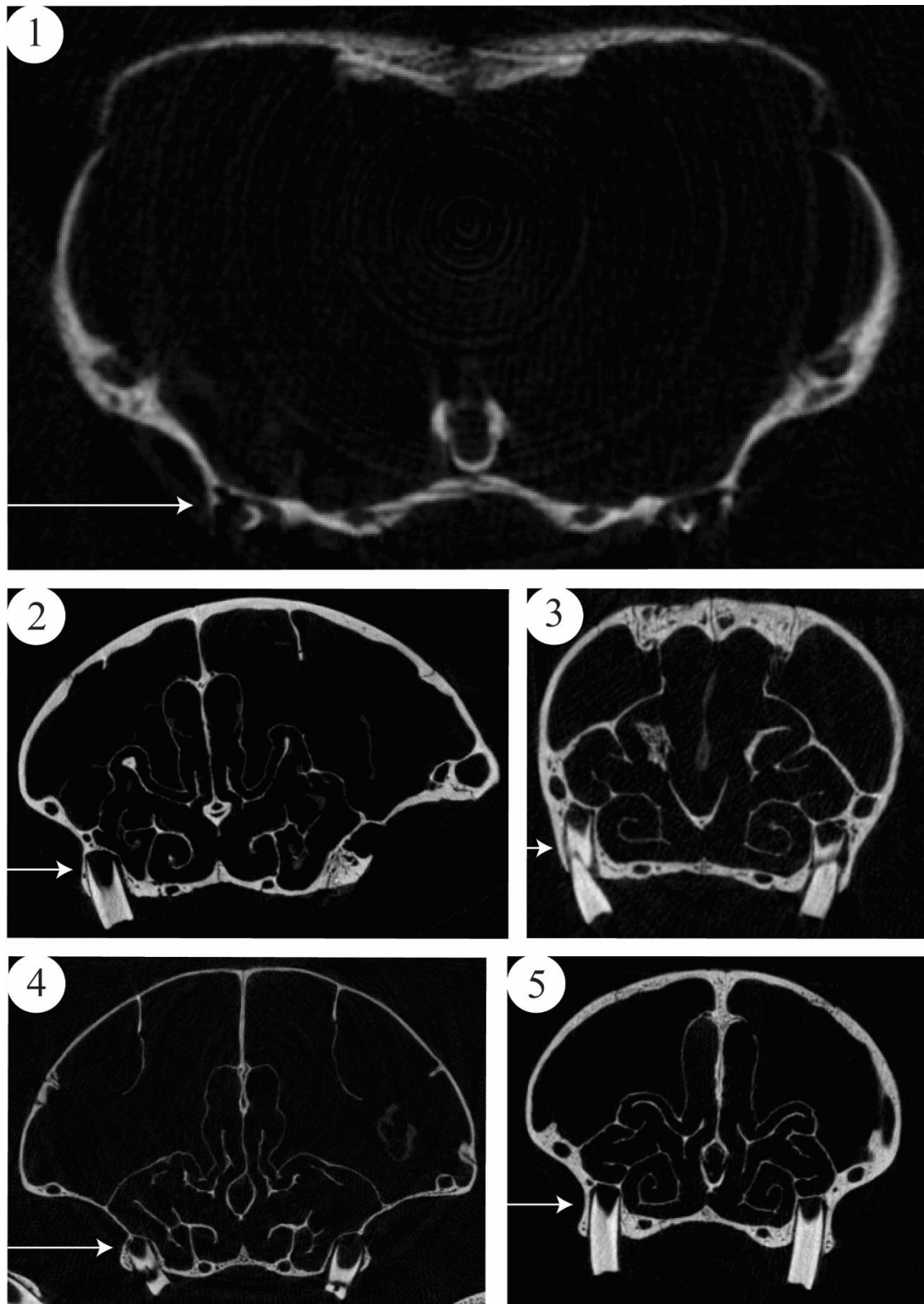


Figure S12. CT-scan sections representing the five dental stages defined in relation to the eruption of deciduous (dPM) and permanent teeth (PM). The analyzed locus always corresponds to the 4th premolar represented here by an arrow. Based on our observations of the upper dentition, we defined five dental stages: (1) dPMs starting to mineralize or erupting; (2) all dPMs well mineralized, possibly all erupted, no PM in the crypts (*i.e.*, PM not mineralized); (3) all dPMs erupted, with part of the PMs mineralized but still in the crypts (not yet reaching the alveoli); (4) part of the dPMs about to be replaced by PMs (one or several PMs has/have erupted through the alveoli, but remain(s) almost unworn); (5) all PMs erupted and no remain of dPMs left (see [Supporting Information 3](#)).

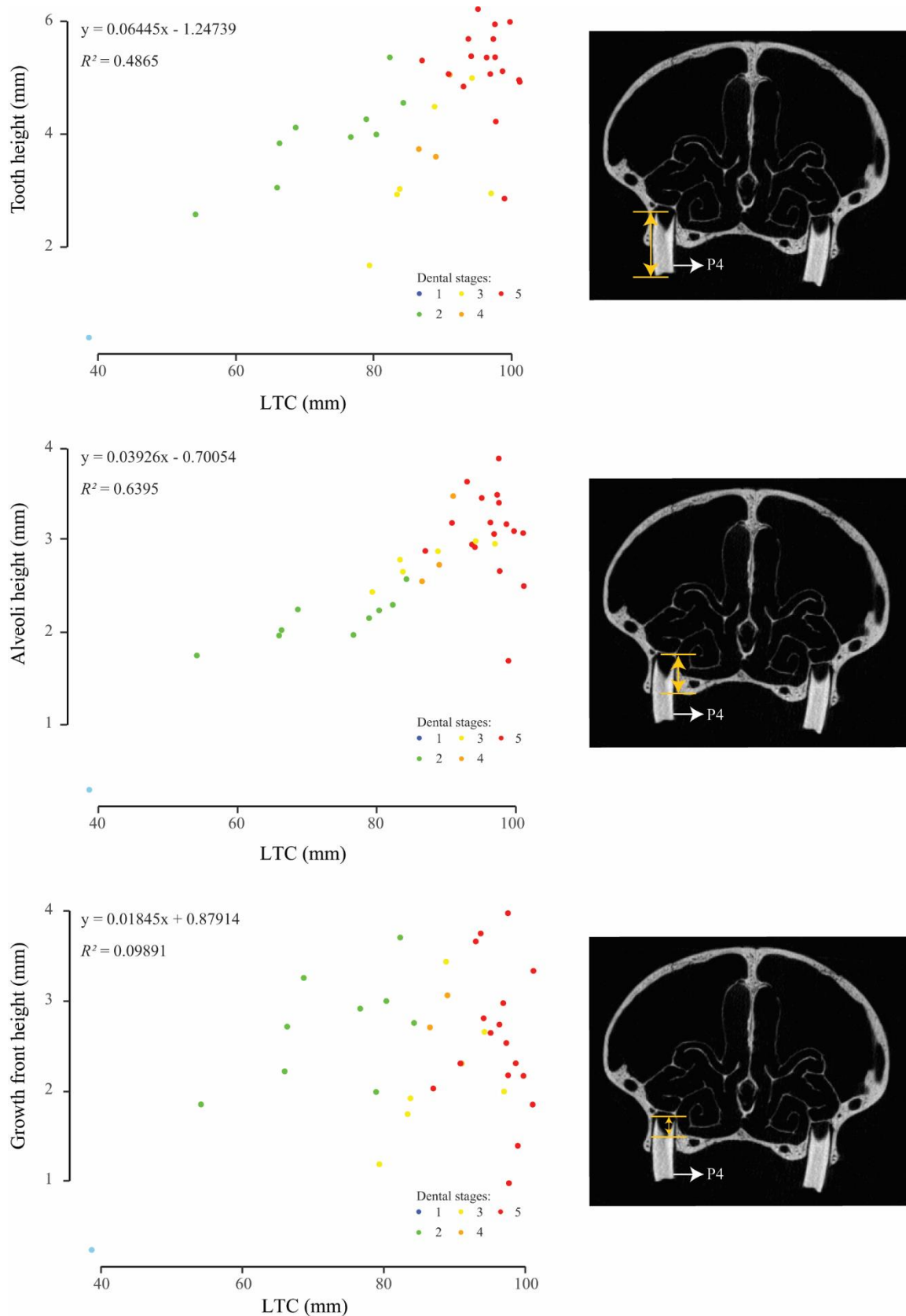


Figure S13. Bivariate linear regressions among three dentary measurements and the LTC. A. With the height of the P4/dPM4. B. With the height of the alveoli of the PM4/dPM4. C. With the height of the growth front of the P4/dPM4. Each measurement is illustrated in the section to the right of each graph. For each simple regression, the slope equation and R^2 are specified. In each case, specimens, whose dental stage (2 or 5) is unknown, were determined *a posteriori* (see [Supporting Information 3](#)).

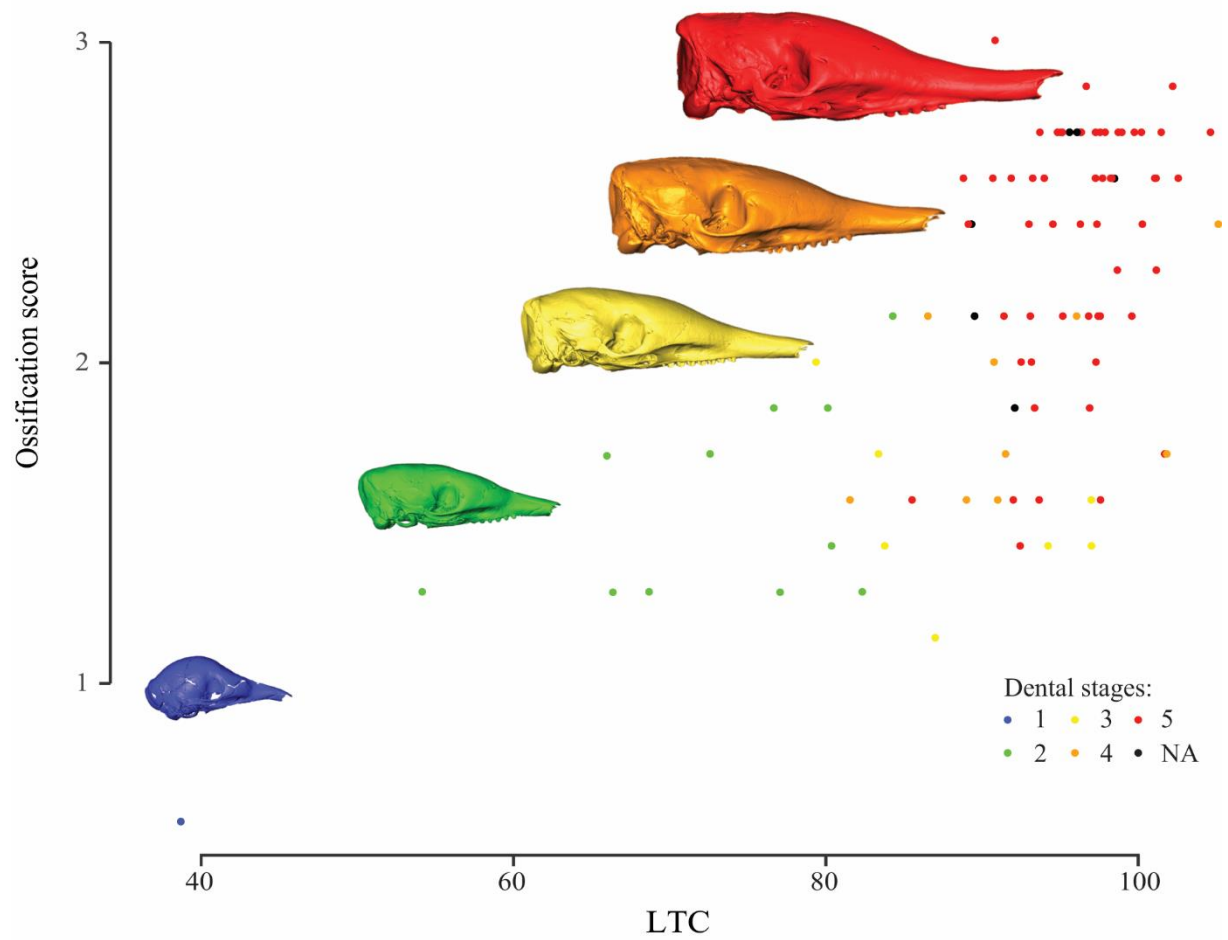


Figure S14. Ontogenetic stages determined based on dental eruption, as compared to the ossification score and the total length of the skull (LTC). The dental stages correspond here to: 1, stillborn (n = 1); 2, juvenile (n = 11); 3, subadult 1 (n = 7); 4, subadult 2 (n = 9); 5, adult (n = 56). The black dots refer to specimens (n = 12) whose dental stage could not be determined. See [Supporting Information 3](#) for more detail.

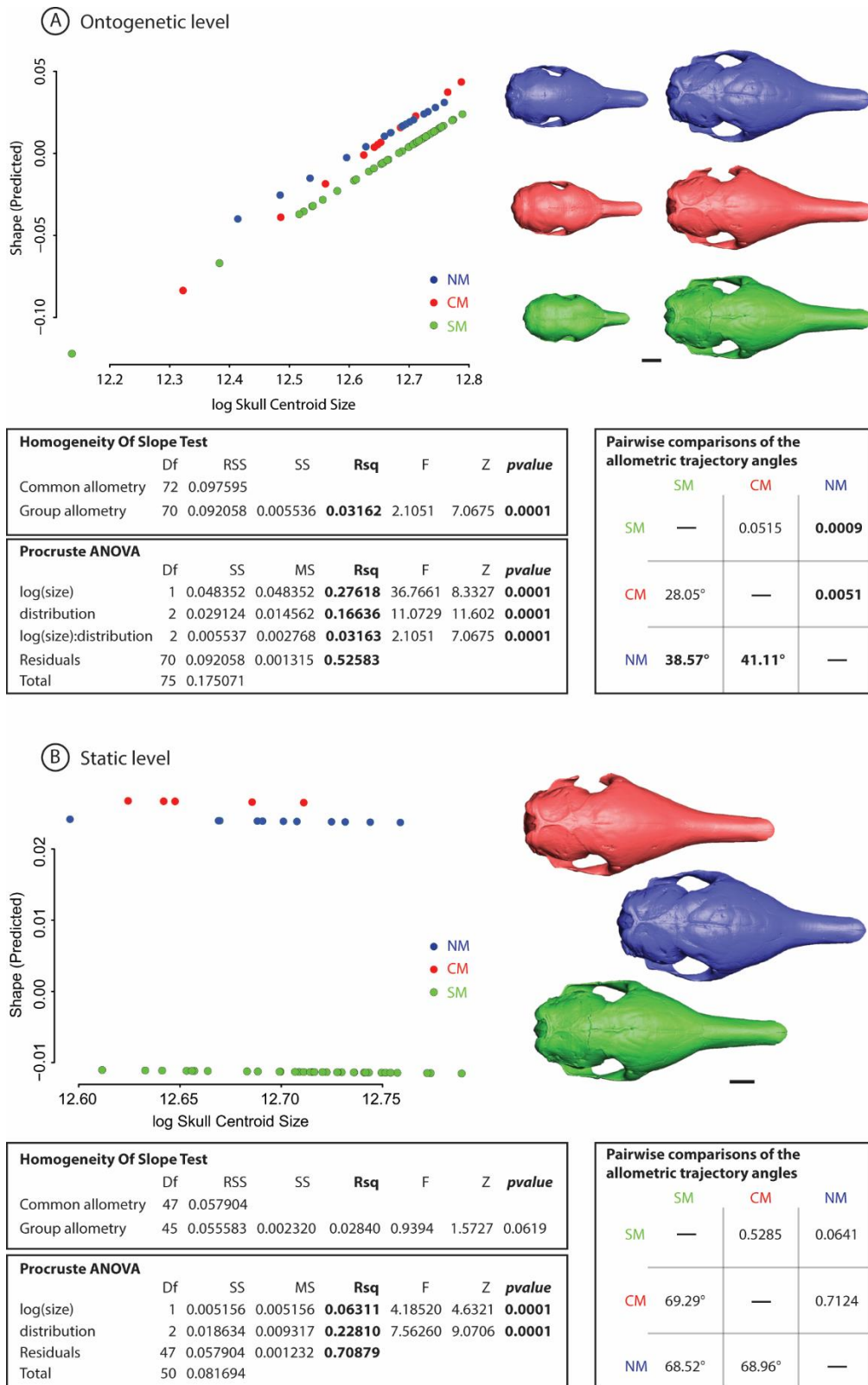


Figure S15. Allometric trajectories among three nine-banded armadillo’s morphotypes (Southern, Central and Northern) at ontogenetic (A – illustrated by juvenile and adult specimens in dorsal view) and static (B – illustrated by adult specimens in dorsal view) levels. The y-axis values are the principal component 1 of the predicted values of a multivariate regression of shape on size; the x-axis values are the log-transformed skull centroid sizes for each specimen. For each level, the HOS test, Procrustes ANOVA and Pairwise comparisons of the allometric trajectory angles results are shown (in bold, the R^2 and p -value for the first two analyses and the angles between the slope and its intercept with a significant p -value). Scale bar: 1 cm. (see [Material and Methods](#)).

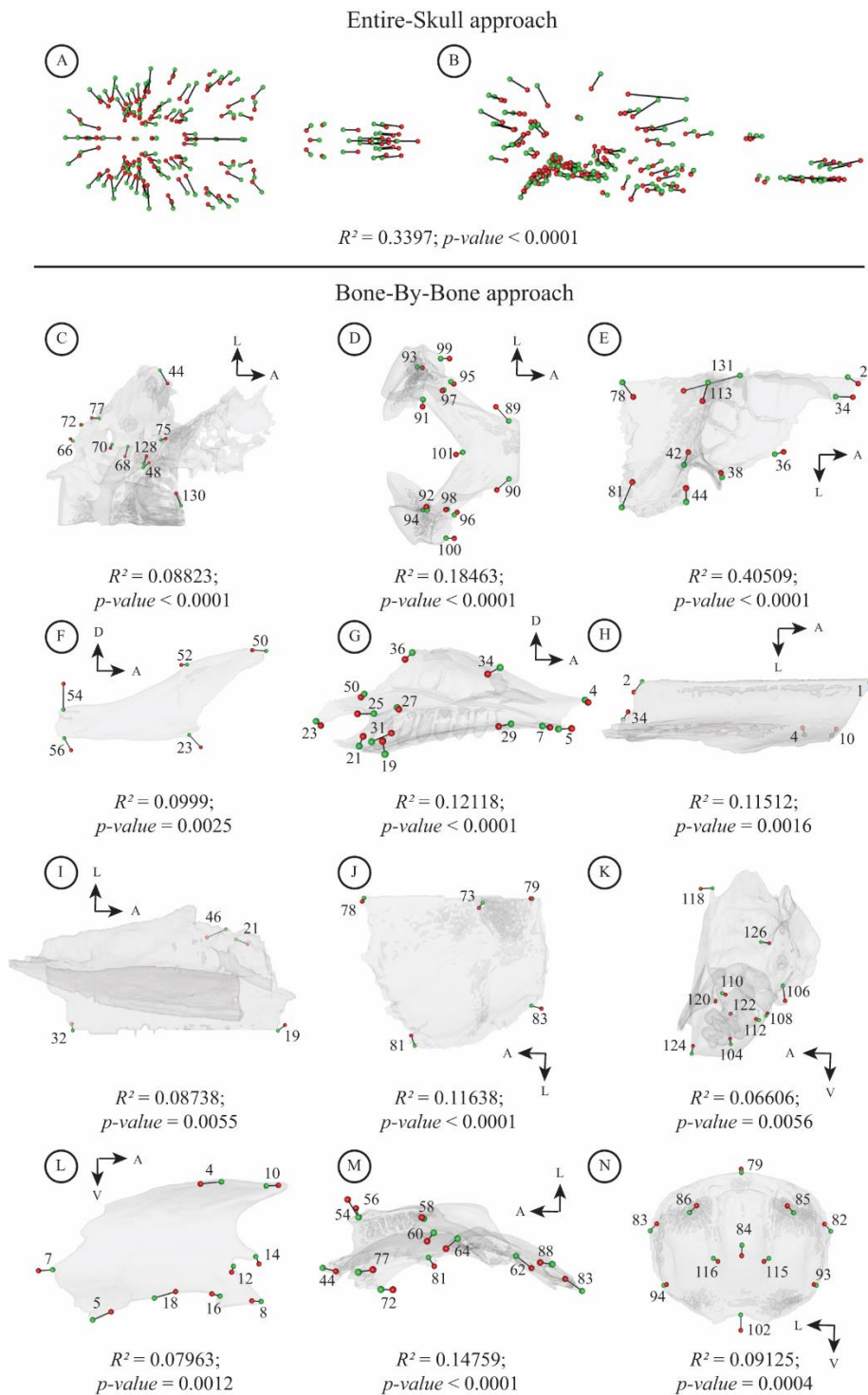


Figure S16. Vector representation in southern morphotype of the allometric shape changes detected for the entire skull and a given cranial unit (OBU), represented between its minimal (green – smaller centroid size) and maximal (red – larger centroid size) shape (see Figure 23) with the associated R^2 and p -value. Results of the analyses performed at the ontogenetic level, and with the log skull centroid size taken as the size variable (see text). For each OBU, the changes are shown in one view with vectors from minimal to maximal shape with the minimal OBU shape shown in transparency. A) Entire skull in dorsal view. B) Entire skull in lateral view. C) Alisphenoid-orbitosphenoid-pterygoid-basisphenoid complex in dorsal view. D) Basioccipital-exoccipital complex in ventral view. E) Frontal in ventral view. F) Jugal in medial view. G) Maxillary in medial view. H) Nasal in ventral view. I) Palatine in dorsal view. J) Parietal in dorsal view. K) Petrosal in lateral view. L) Premaxillary in medial view. M) Squamosal in ventral view. N) Supraoccipital in occipital view. Landmark numbers and orientation arrows were added for more readability as well as the overall representation of the unpaired bones (basioccipital and supraoccipital). Abbreviations: A, anterior; D, dorsal; L, lateral; V, ventral.

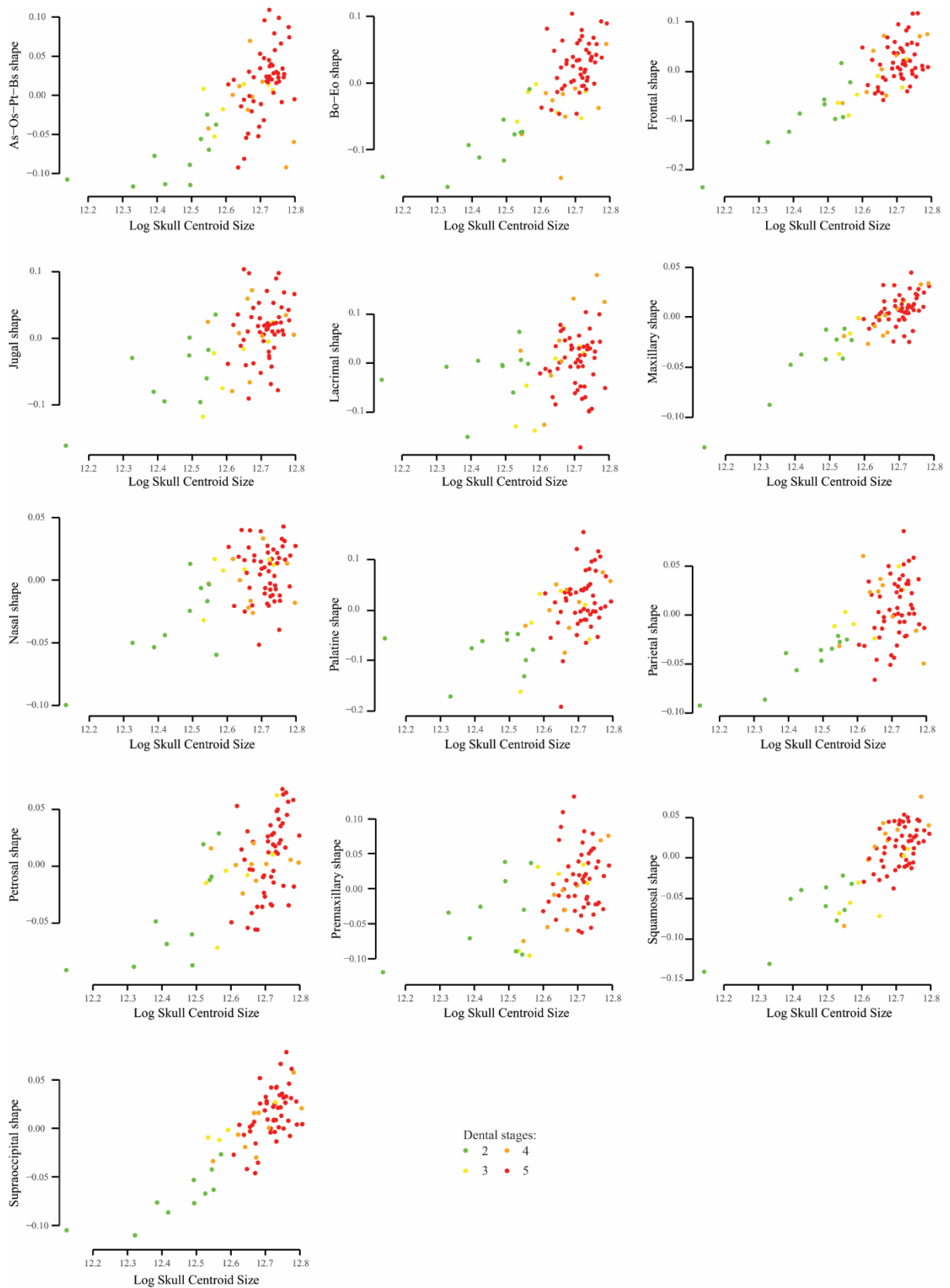


Figure S17. Multivariate regression for each OBU at the ontogenetic level using log skull centroid size.

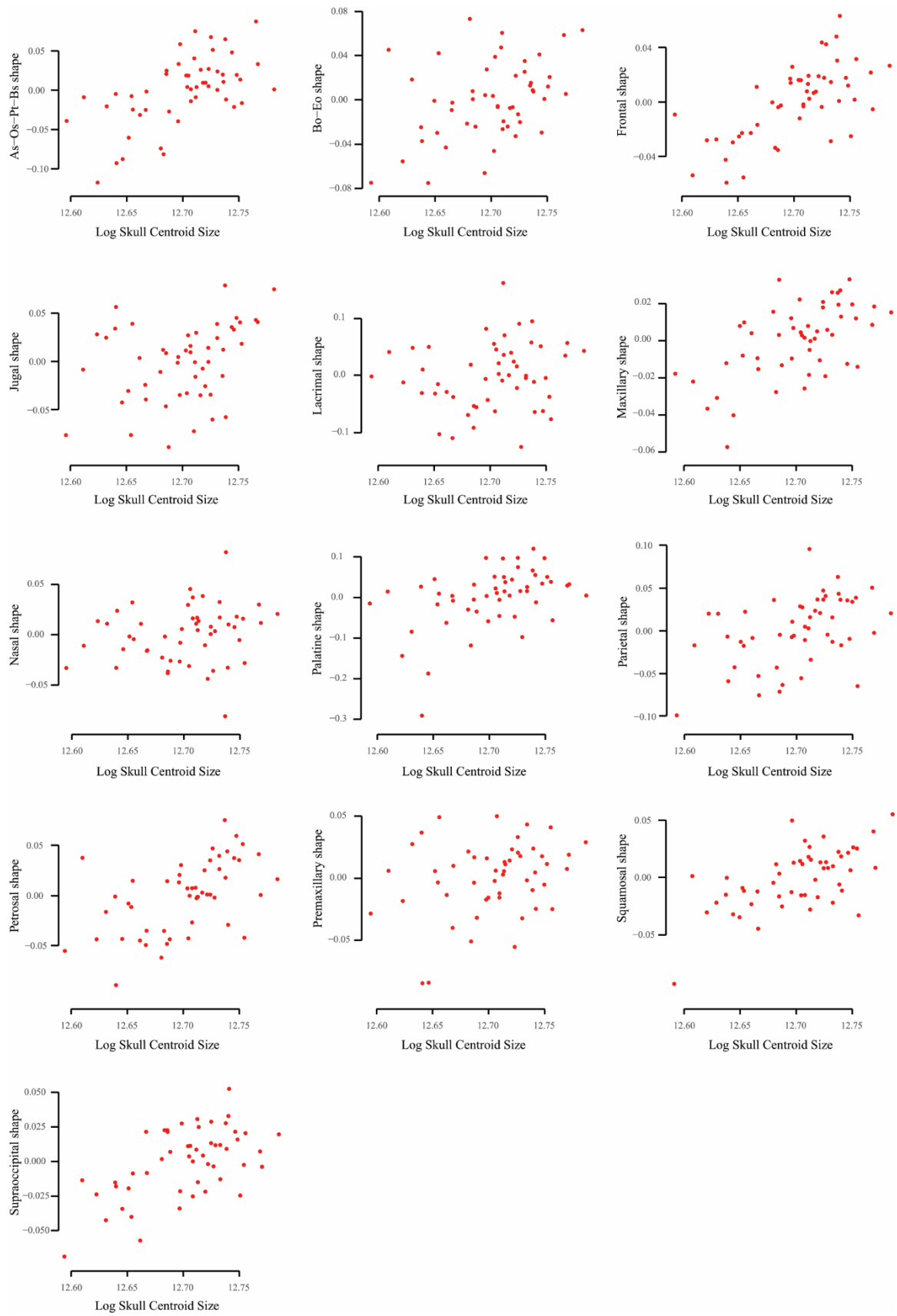


Figure S18. Multivariate regression for each OBU at the static level with log skull centroid size.

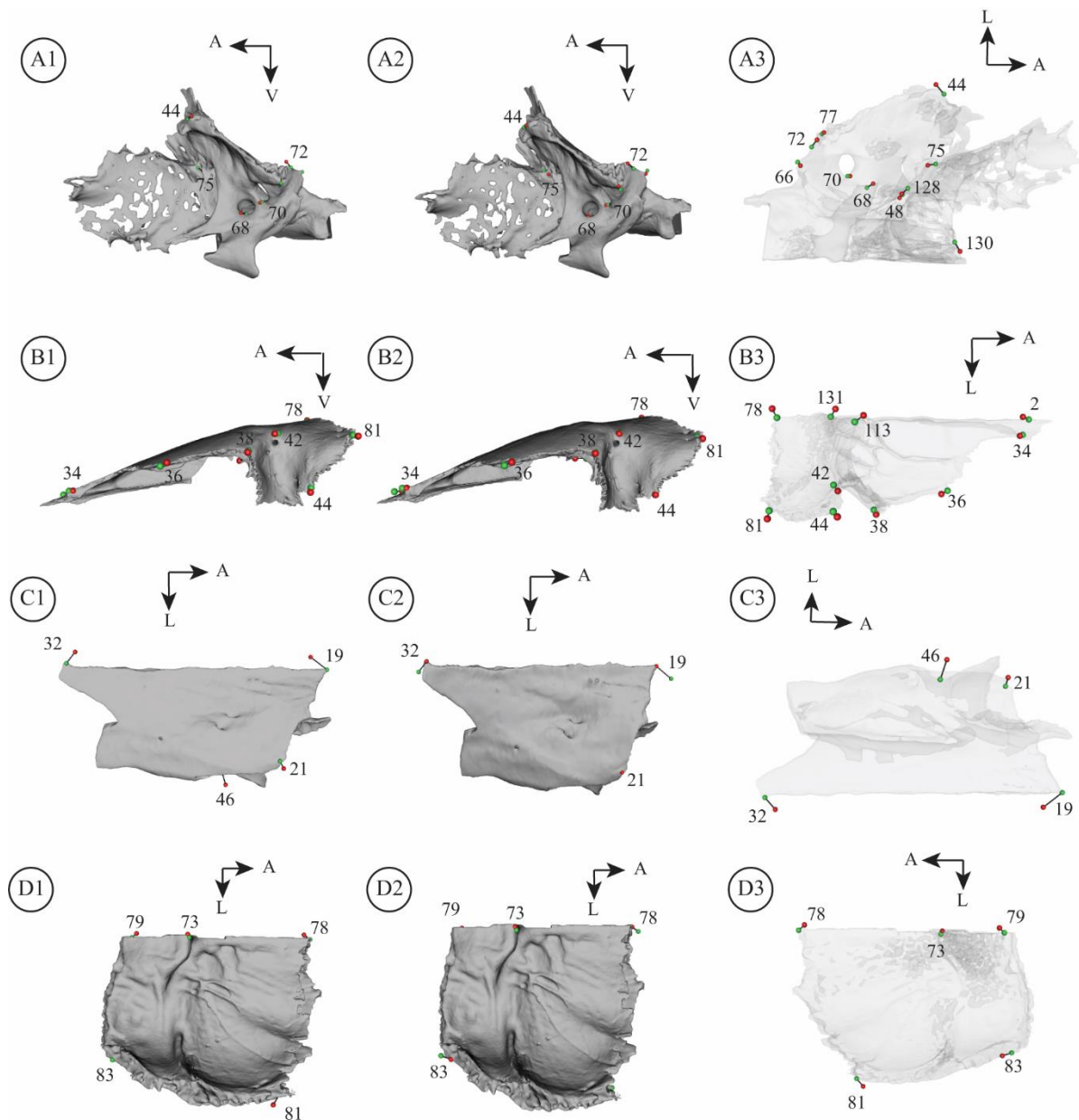


Figure S19. Vector representation of the allometric shape changes detected for a given cranial unit (OBU), represented between its minimal (green – smaller centroid size) and maximal (red – larger centroid size) shape (see [Figure 23](#)). Results of the analysis performed at the static level, and with the log skull centroid size as the size variable (see text). For each OBU, the changes are shown in three subsections organized horizontally: 1, vectors from minimal to maximal shape with minimal OBU shape; 2, same as 1) with maximal OBU shape; 3, minimal OBU shape in transparency with vectors. A) Alisphenoid-orbitosphenoid-pterygoid-basisphenoid complex; A1-A2, lateral view; A3, dorsal view. B) Frontal; B1-B2, lateral view; B3, dorsal view. C) Palatine; C1-C2, ventral view; C3, dorsal view. D) Parietal; D1-D2, ventral view; D3, dorsal view. Landmark numbers and orientation arrows were added for more readability. Abbreviations: A, anterior; L, lateral; V, ventral.

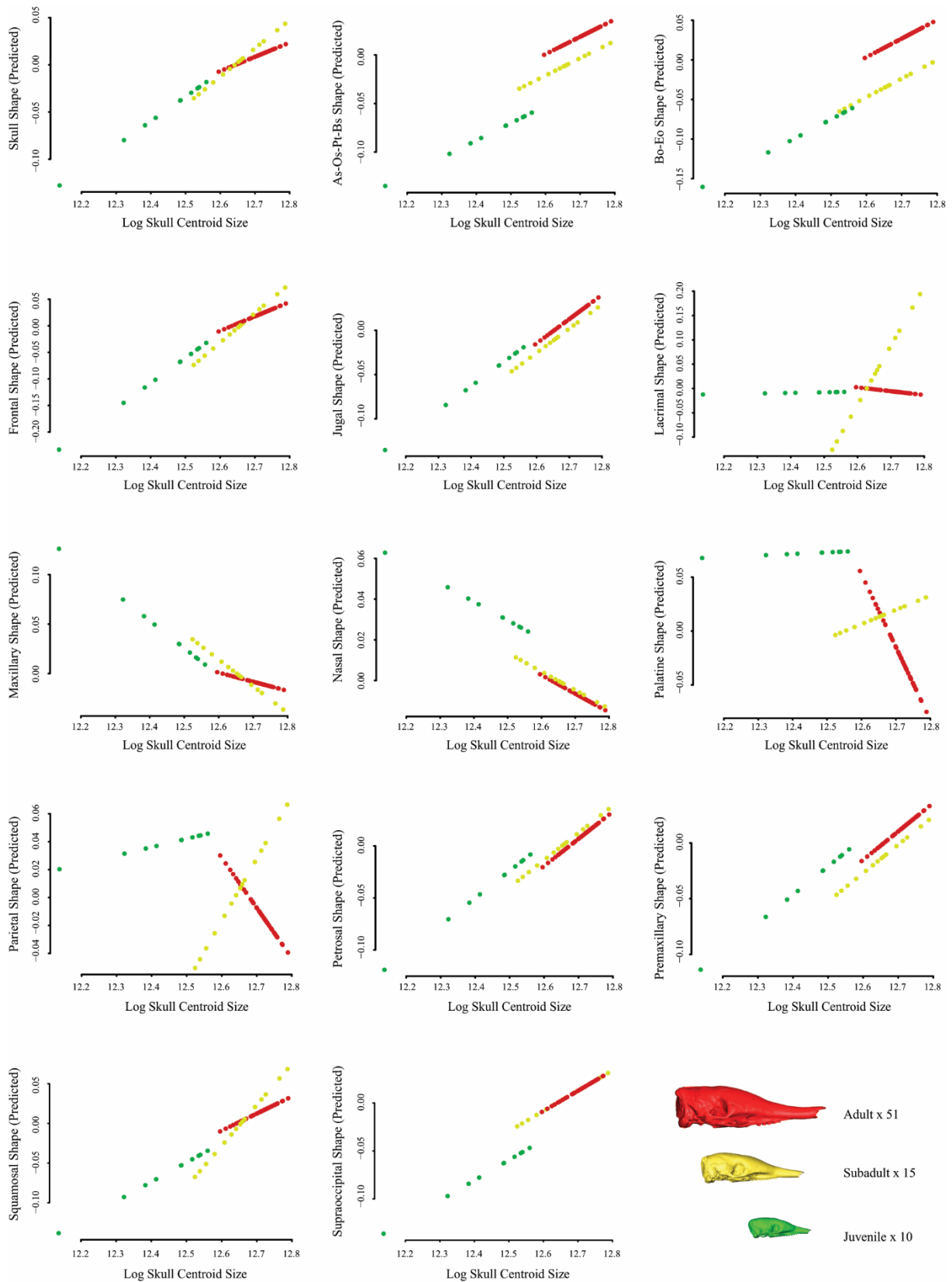


Figure S20. Common allometric analyses. Trajectories are derived from homogeneity of slope test, plotting log transformed geometric means in the x-axis (*i.e.*, log skull centroid size) and the PC1 of the predicted values of multivariate regression of shape ratios on size in the y-axis (Shape (Predicted)) (see [Material and Methods](#)).

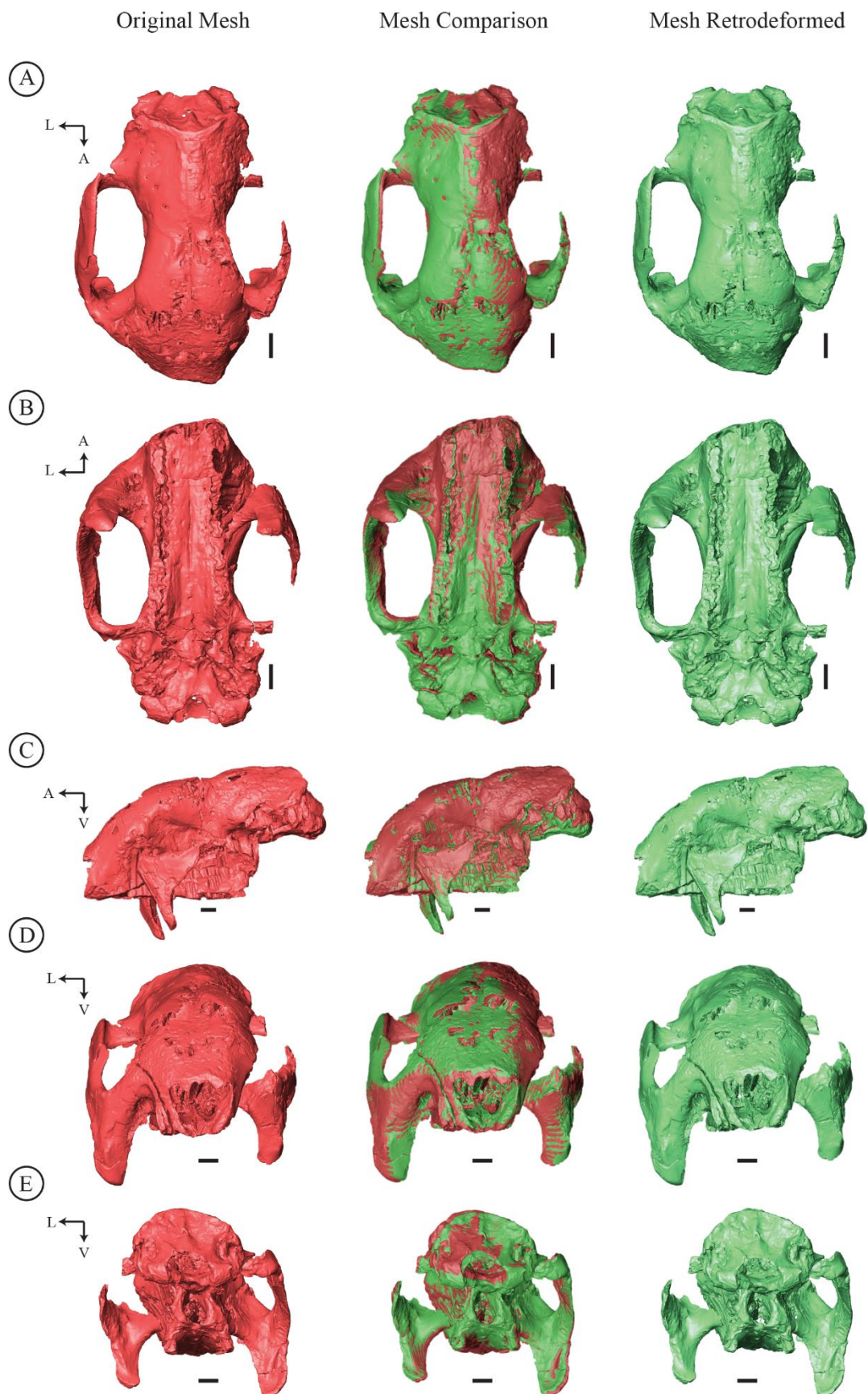


Figure S21. Retrodeformation applied on the skull of “*Metopotoxus*” *anceps* (YPM-PU 15612) with an illustration of the original specimen and a comparison between the two meshes. A, dorsal view; B, ventral view; C, lateral view; D, face view; E, occipital view. Abbreviations: A, anterior; L, lateral; V, ventral. Scale-bars = 1 cm.

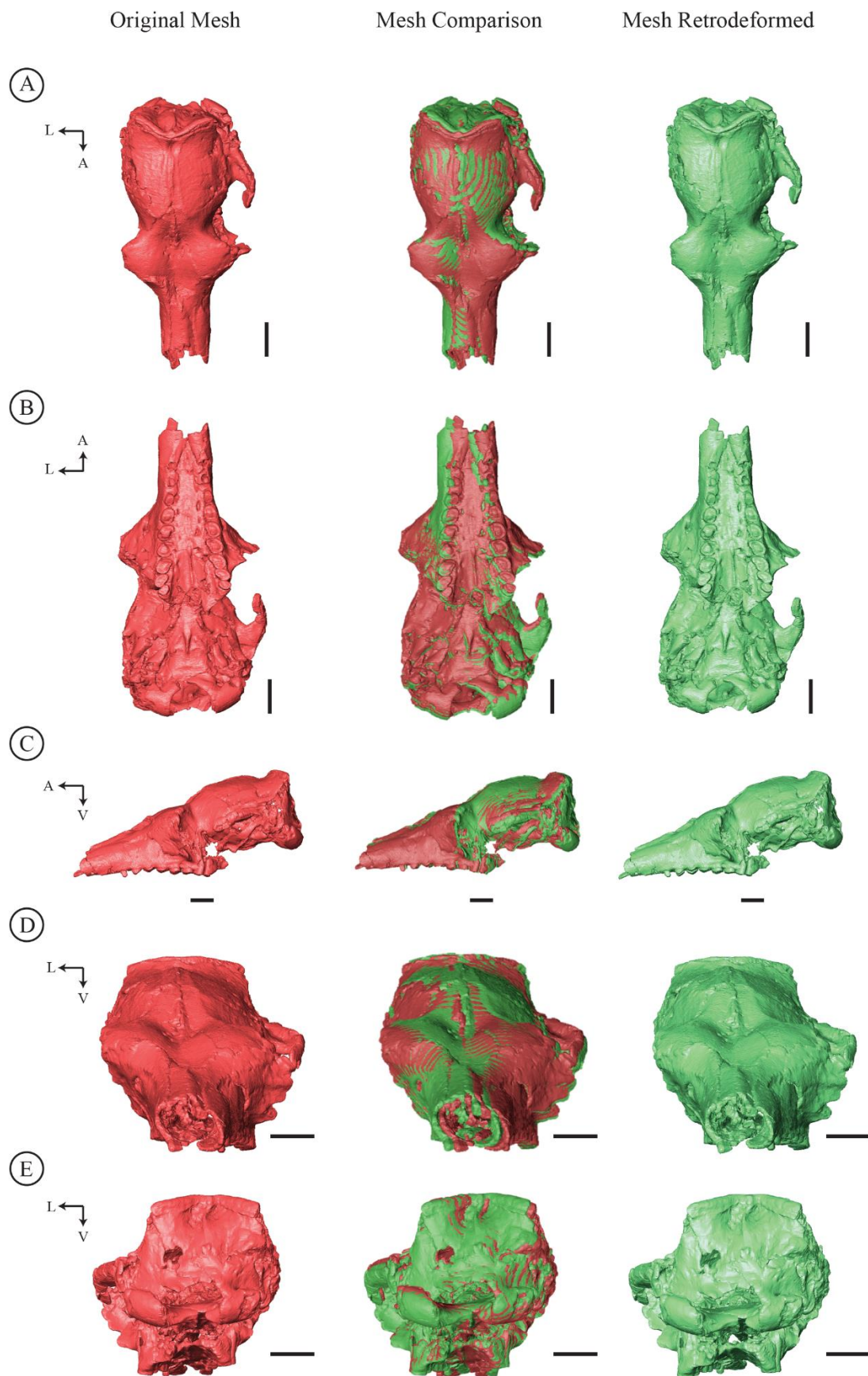


Figure S22. Retrodeformation applied on the skull of *Proeutatus lagena* (YPM-PU 15613) with an illustration of the original specimen and a comparison between the two meshes. A, dorsal view; B, ventral view; C, lateral view; D, face view; E, occipital view. Abbreviations: A, anterior; L, lateral; V, ventral. Scale-bars = 1 cm.

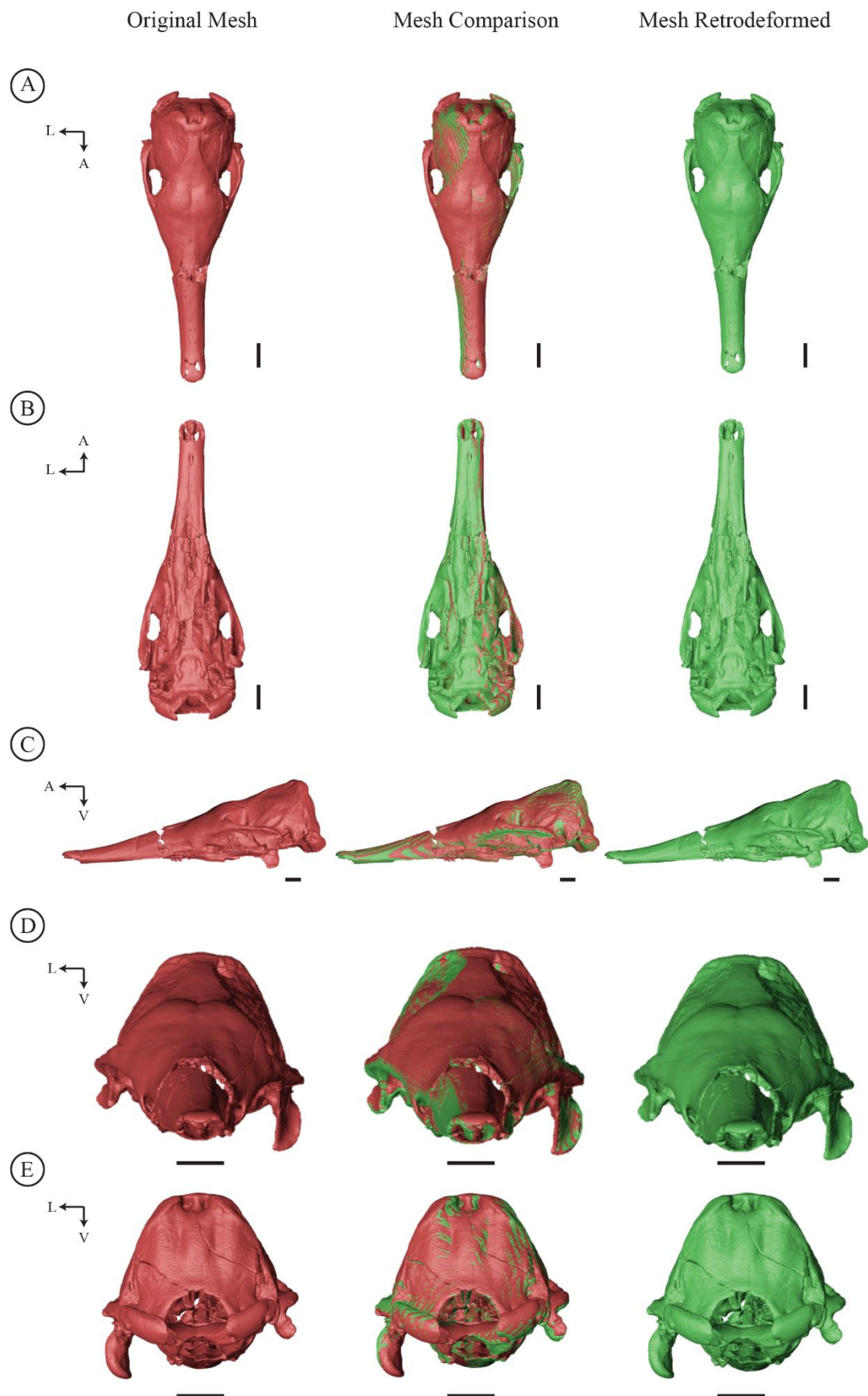


Figure S23. Retrodeformation applied on the skull of *Stegotherium tauberi* (YPM-PU 15565) with an illustration of the original specimen and a comparison between the two meshes. A, dorsal view; B, ventral view; C, lateral view; D, face view; E, occipital view. Abbreviations: A, anterior; L, lateral; V, ventral. Scale-bars = 1 cm.

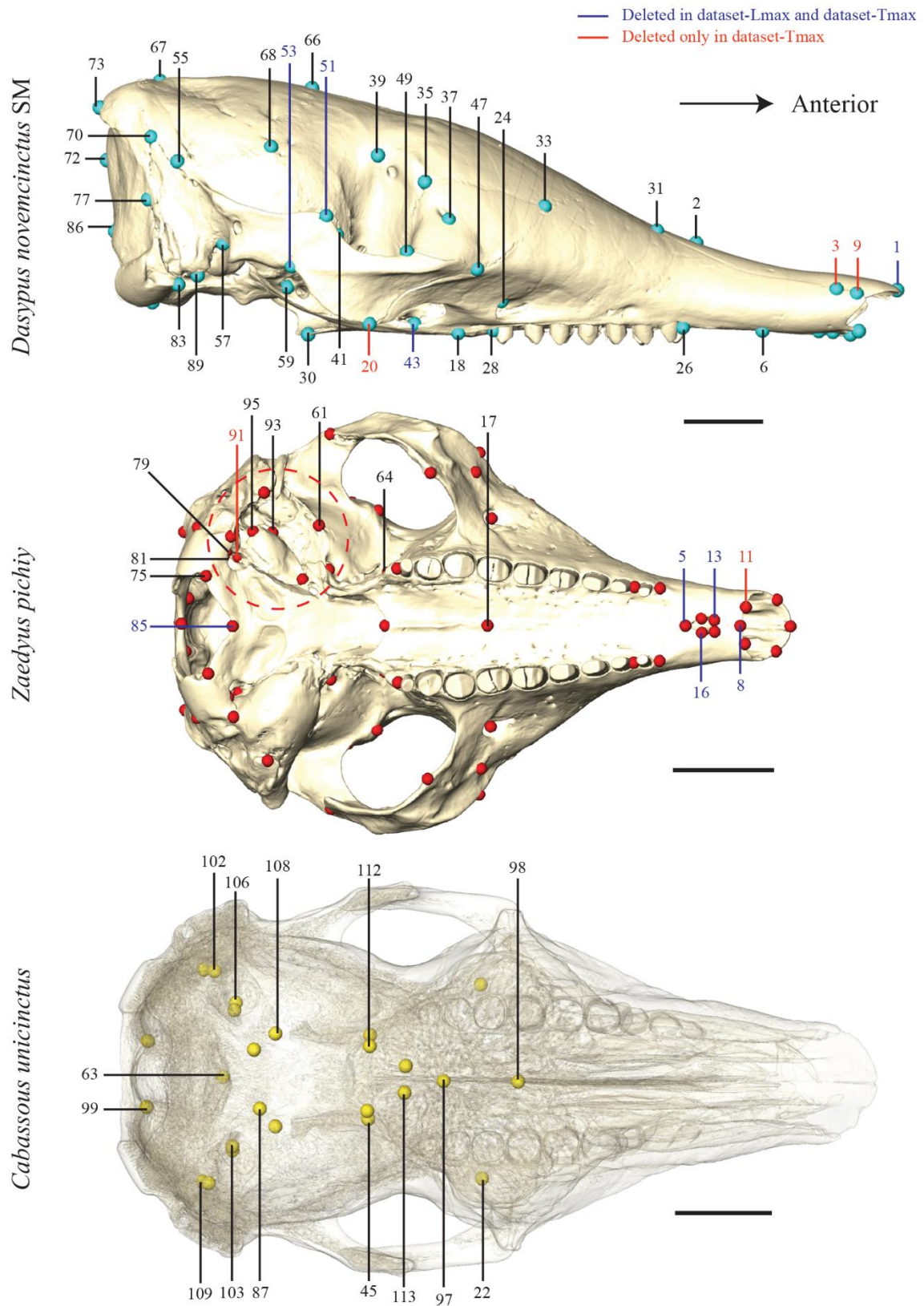


Figure S24. Landmarks digitized on the skull of *Dasypus novemcinctus* (lateral view), *Zaedyus pichiy* (ventral view) and *Cabassous unicinctus* (ventral view with bone transparency (25%)) with details on the deleted landmarks for Dataset-Lmax and Dataset-Tmax. Scale-bar = 1 cm. List of landmarks can be found in Table 13.

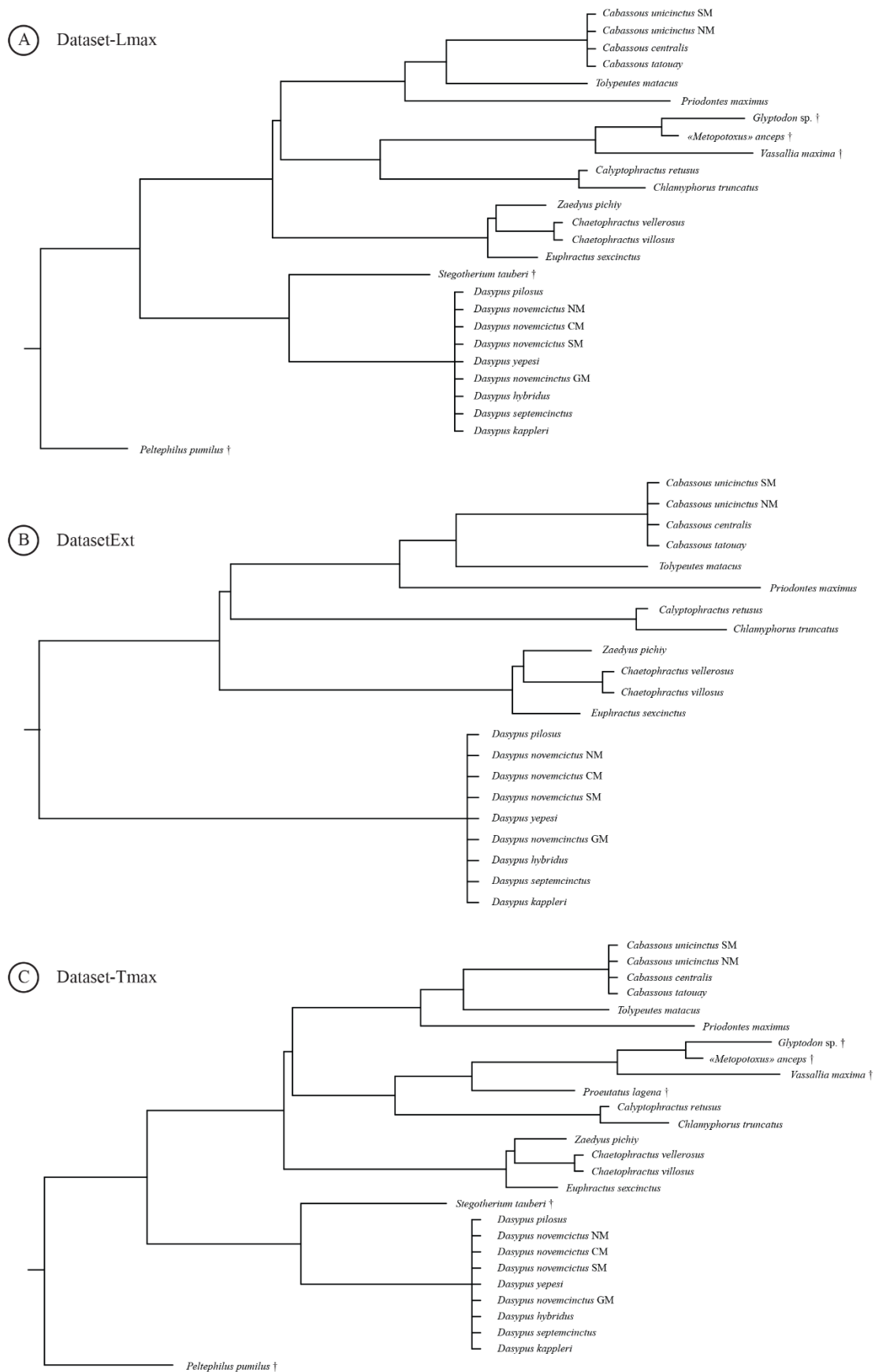


Figure S25. Topology of trees used for phylogenetic regression for each evolutionary dataset (A, B and C) (for more detail see [Material & Methods – Chapter 2 & Section 3.2](#)). CM, Central Morphotype; GM, Guianan Morphotype; NM, Northern Morphotype; SM, Southern Morphotype. †, extinct species.

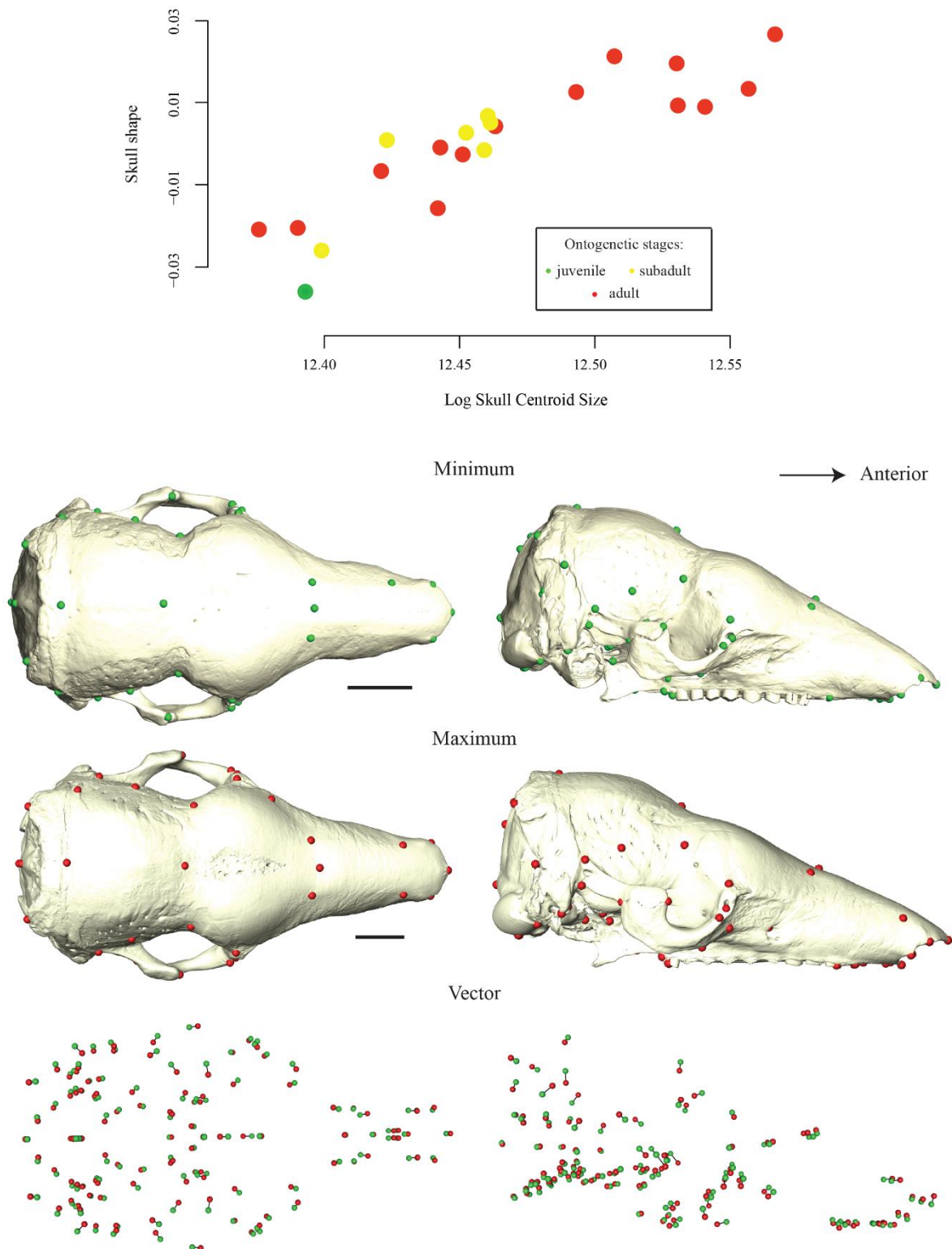


Figure S26. Ontogenetic allometry on the entire skull (ES) of *CabassousN*. Ontogenetic stages are represented with different colors (juvenile = green; subadult = yellow; adult = red; see text for more detail). For graphical display, we used the projected regression scores of the shape data to represent shape variation related to changes in log skull centroid size (Adams *et al.*, 2013). Shape changes were visualized as vectors from the minimal shape (green) to the maximal shape (red) of the shape regression scores corresponding to the projection of the data points in shape space on to an axis in the direction of the regression vector (see Drake & Klingenberg, 2008). Multivariate regression of skull shape on log skull centroid size at the ontogenetic level representing 8.80% of the total shape variation.

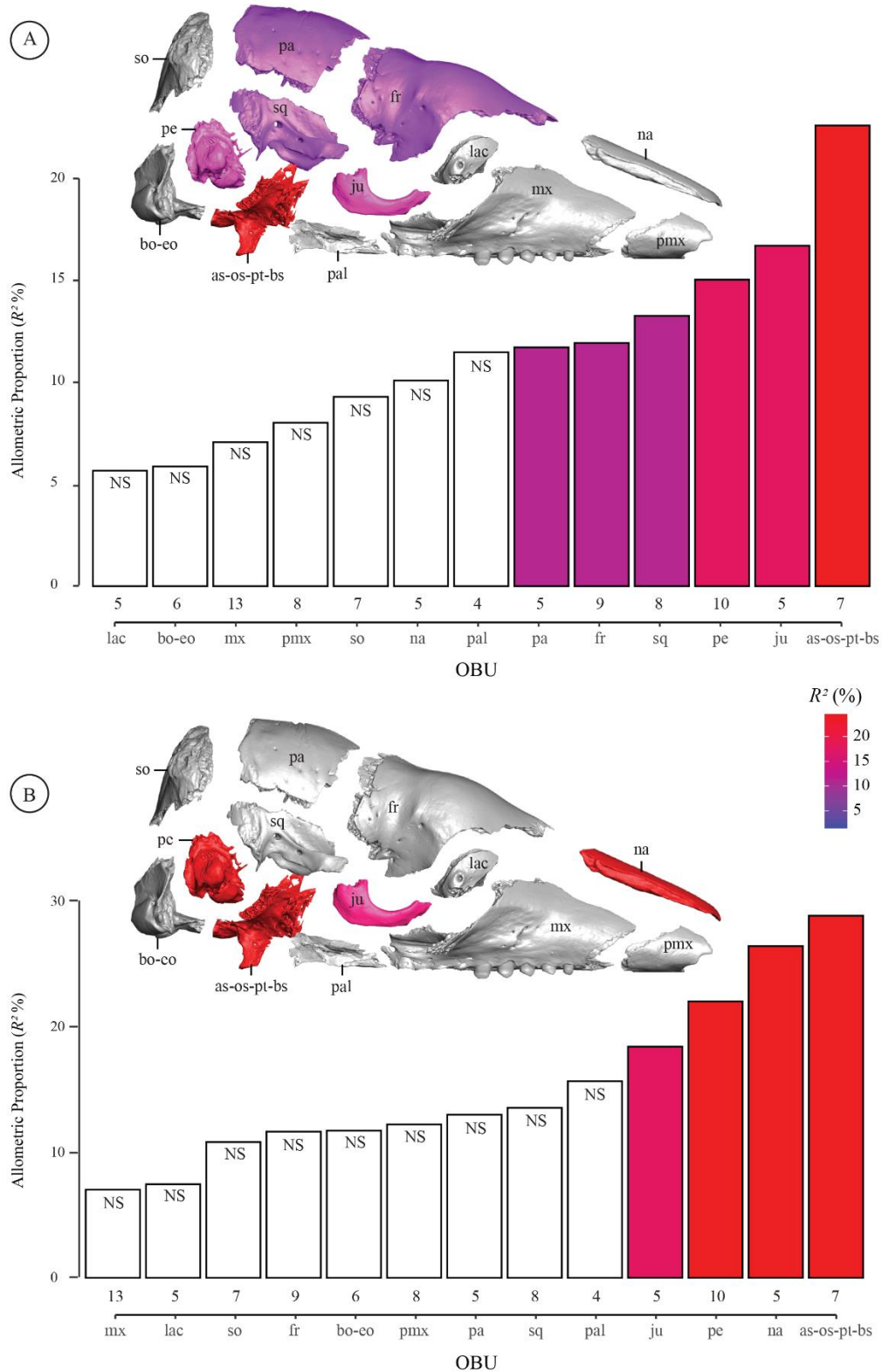


Figure S27. Bar graphs showing the allometric proportions (R^2) of each cranial unit's (OBU) total shape variation under the 3B approach (see text), at the ontogenetic (A) and static (B) levels in *CabassousN*. Allometric proportions are shown with the log skull centroid size taken as size variable. On the virtually dislocated skull (in right lateral view), the allometric proportions are reported in corresponding colors. White bars indicate a statistically unsupported (NS) allometry for a given OBU (at p -value > 0.05). Abbreviations of OBUs: as-os-pt-bs, alisphenoid-orbitosphenoid-ptyergoid-basisphenoid complex; bo-eo, basioccipital-exoccipital complex; fr, frontal; ju, jugal; lac, lacrimal; mx, maxillary; na, nasal; pa, parietal; pal, palatine; pe, petrosal; pmx, premaxillary; so, supraoccipital; sq, squamosal.

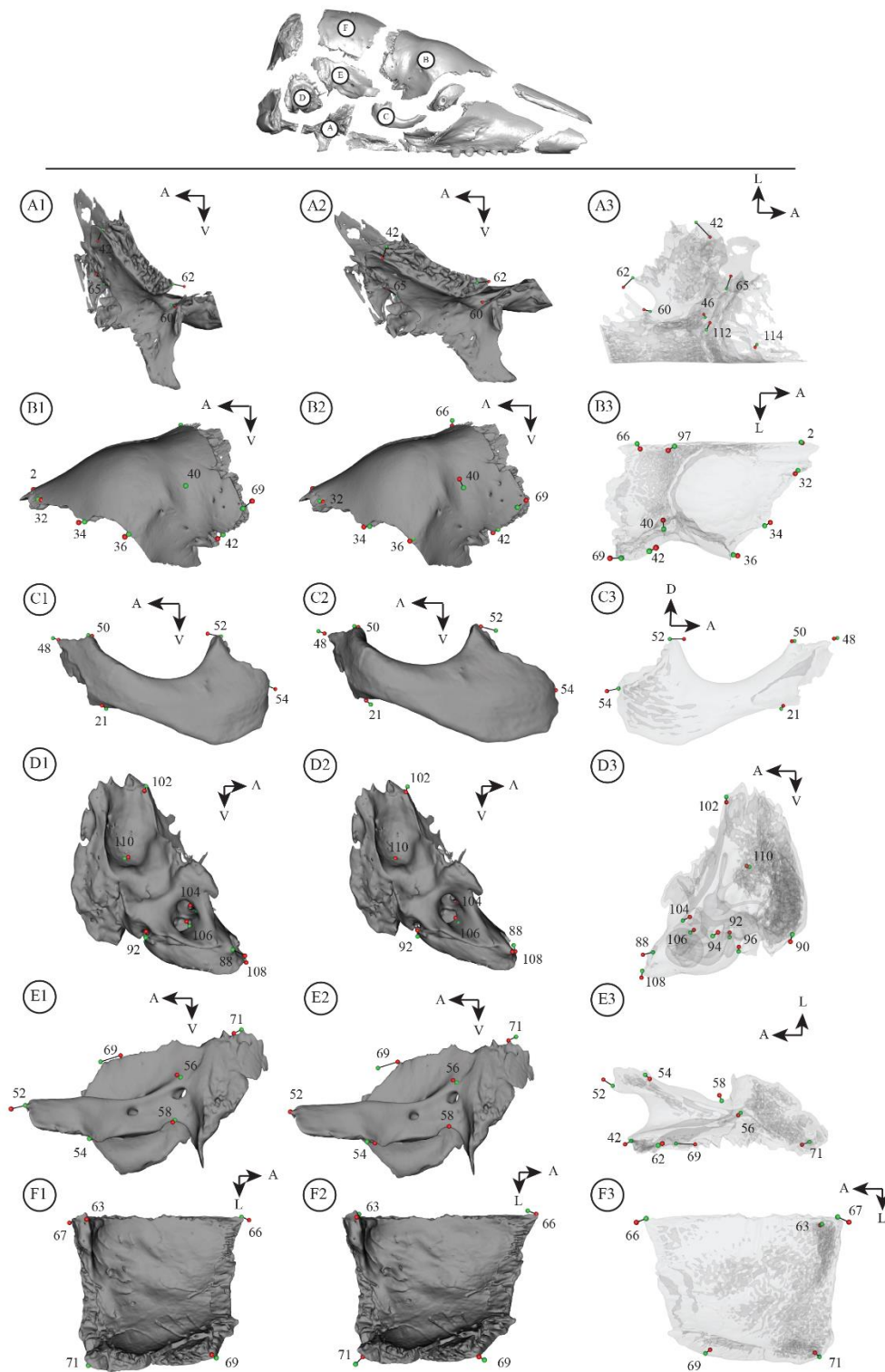


Figure S28. Vector representation of the allometric shape changes detected for a given cranial unit (OBU) in *CabassousN*, represented between its minimal (green – smaller centroid size) and maximal (red – larger centroid size) shape (see Figure 29). Results of the analysis performed at the ontogenetic level, and with the log skull centroid size taken as the size variable (see text). For each OBU, the changes are shown in three subsections organized horizontally: 1, vectors from minimal to maximal shape with minimal OBU shape; 2, same as 1) with maximal OBU shape; 3, minimal OBU shape in transparency with vectors. A) alisphenoid-orbitosphenoid-ptyergoid-basisphenoid complex; A1-A2, lateral view; A3, dorsal view. B) frontal; B1-B2, lateral view; B3, ventral view. C) jugal; C1-C2, lateral view; C3, medial view. D) petrosal; D1-D2, medial view; D3, lateral view. E) squamosal; E1-E2, lateral view; E3, ventral view. F) parietal; F1-F2, ventral view; F3, dorsal view. Landmark numbers and orientation arrows were added for more readability. Abbreviations: A, anterior; L, lateral; V, ventral.

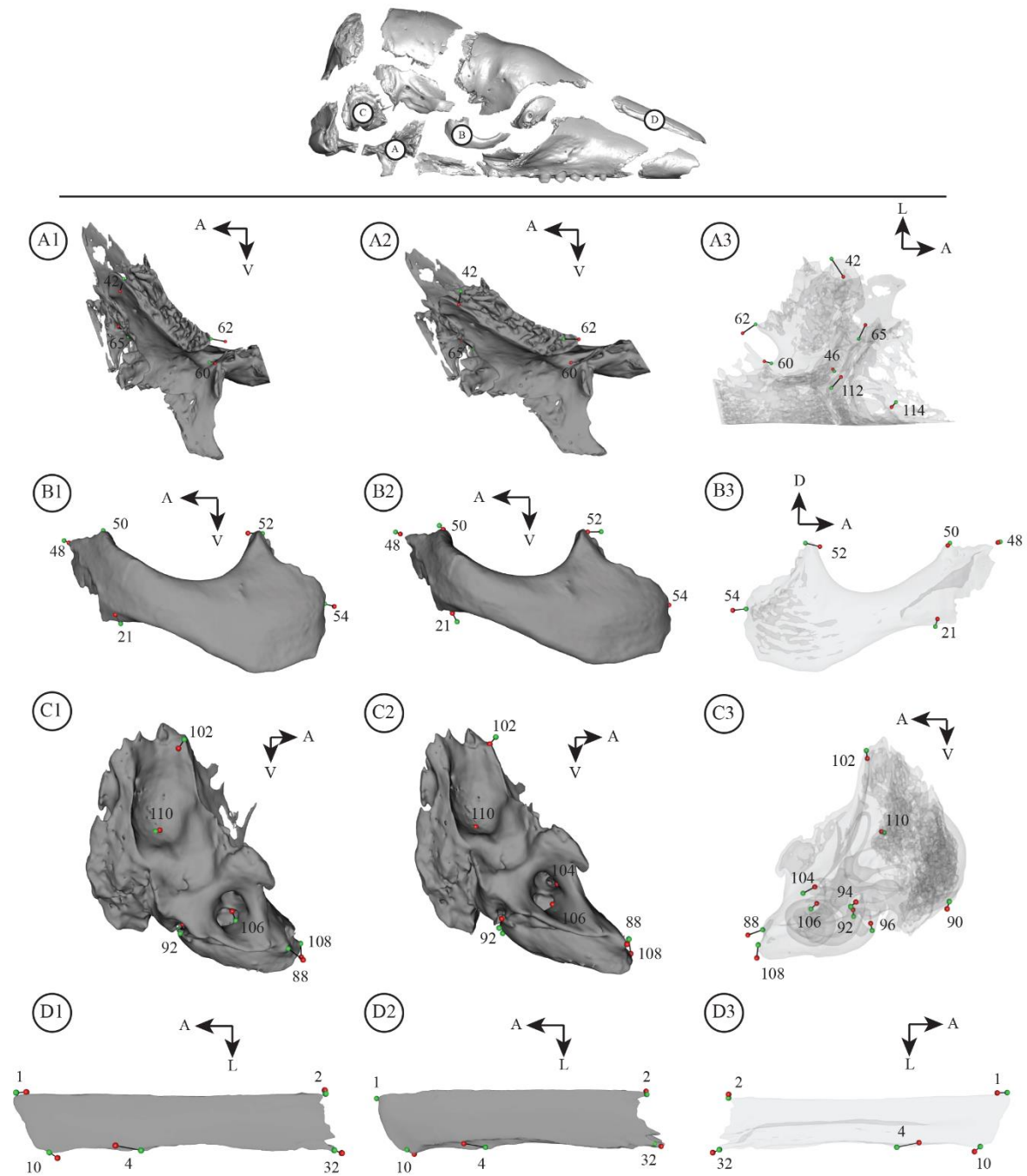


Figure S29. Vector representation of the allometric shape changes detected for a given cranial unit (OBU) in *CabassousNS*, represented between its minimal (green – smaller centroid size) and maximal (red – larger centroid size) shape (see [Figure 29](#)). Results of the analysis performed at the static level, and with the log skull centroid size taken as the size variable (see text). For each OBU, the changes are shown in three subsections organized horizontally: 1, vectors from minimal to maximal shape with minimal OBU shape; 2, same as 1) with maximal OBU shape; 3, minimal OBU shape in transparency with vectors. A) alisphenoid-orbitosphenoid-pterygoid-basisphenoid complex; A1-A2, lateral view; A3, dorsal view. B) jugal; B1-B2, lateral view; B3, medial view. C) petrosal; C1-C2, medial view; C3, lateral view. D) nasal; D1-D2, dorsal view; D3, ventral view. Landmark numbers and orientation arrows were added for more readability. Abbreviations: A, anterior; D, dorsal; L, lateral; V, ventral.

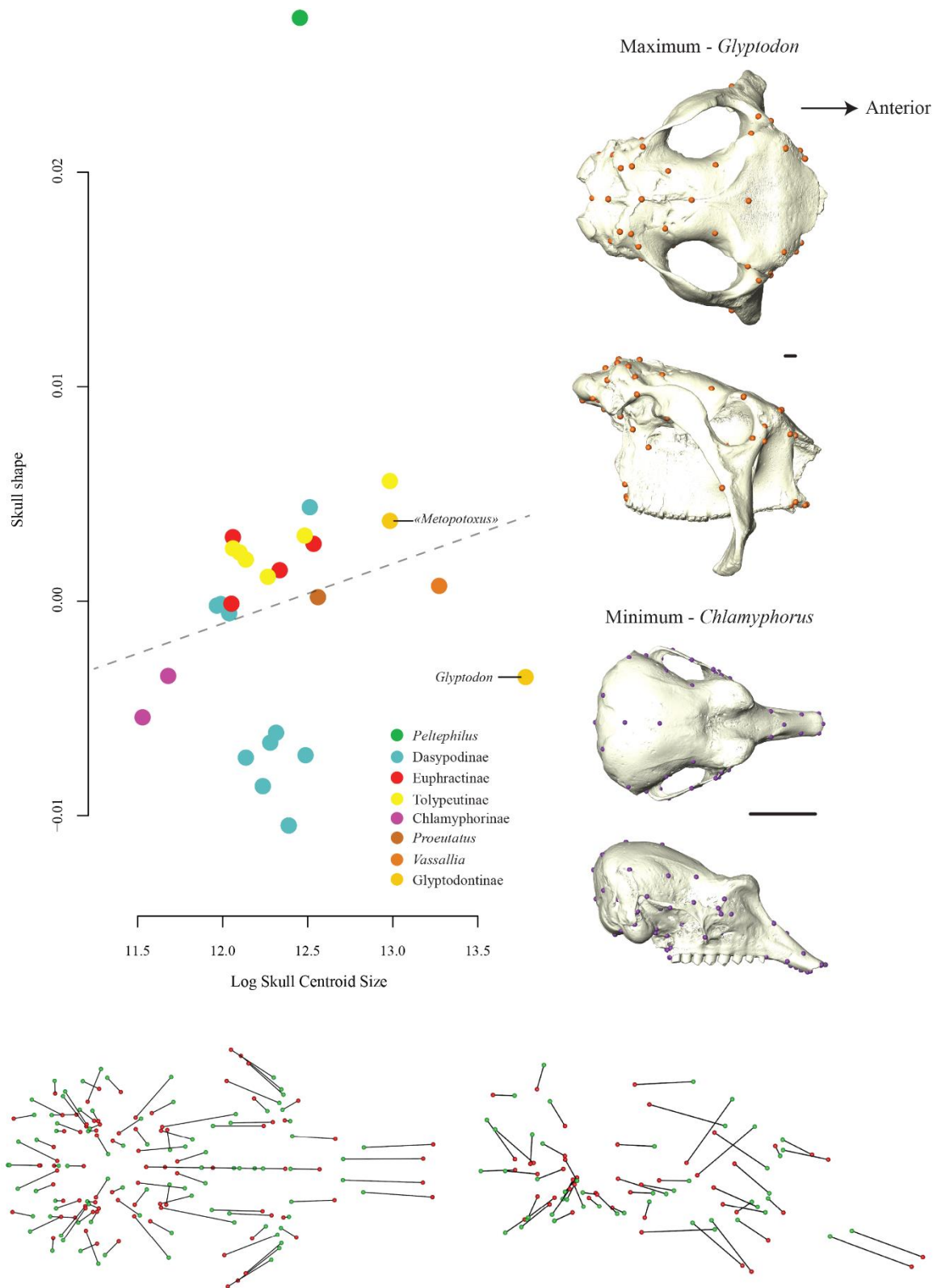


Figure S30. Evolutionary allometry on the entire skull (ES) of Dataset-Tmax. Clades and fossils taxa are represented with different colors. For graphical display, we used the projected regression scores of the shape data to represent shape variation related to changes in log centroid size (Adams *et al.*, 2013). Shape changes were visualized as vectors from the minimal shape (green) to the maximal shape (red) of the shape regression scores corresponding to the projection of the data points in shape space on to an axis in the direction of the regression vector (see Drake & Klingenberg, 2008). Phylogenetic regression of skull shape on log skull centroid size of Dataset-Tmax, representing 13.62% of the total shape variation.

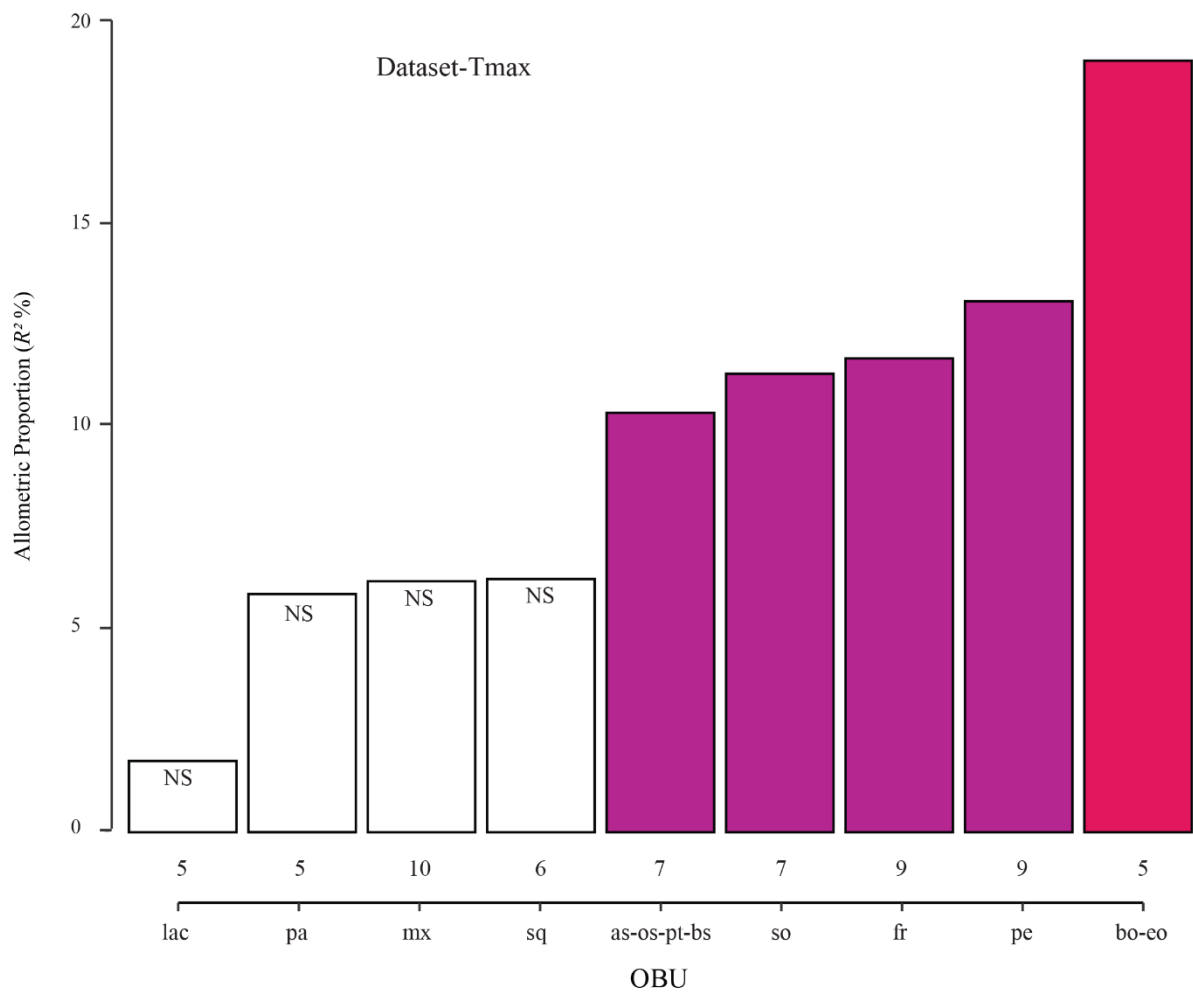


Figure S31. Bar graphs showing the allometric proportions (R^2) of each cranial unit's (OBU) total shape variation under the 3B approach (see text) for both evolutionary datasets. Allometric proportions are shown with the log skull centroid size taken as size variable. White bars indicate a statistically unsupported (NS) allometry for a given OBU (at p -value > 0.05). Abbreviations of OBUs: as-os-pt-bs, alisphenoid-orbitosphenoid-pterygoid-basisphenoid complex; bo-eo, basioccipital-exoccipital complex; fr, frontal; ju, jugal; lac, lacrimal; mx, maxillary; na, nasal; pa, parietal; pal, palatine; pe, petrosal; pmx, premaxillary; so, supraoccipital; sq, squamosal.

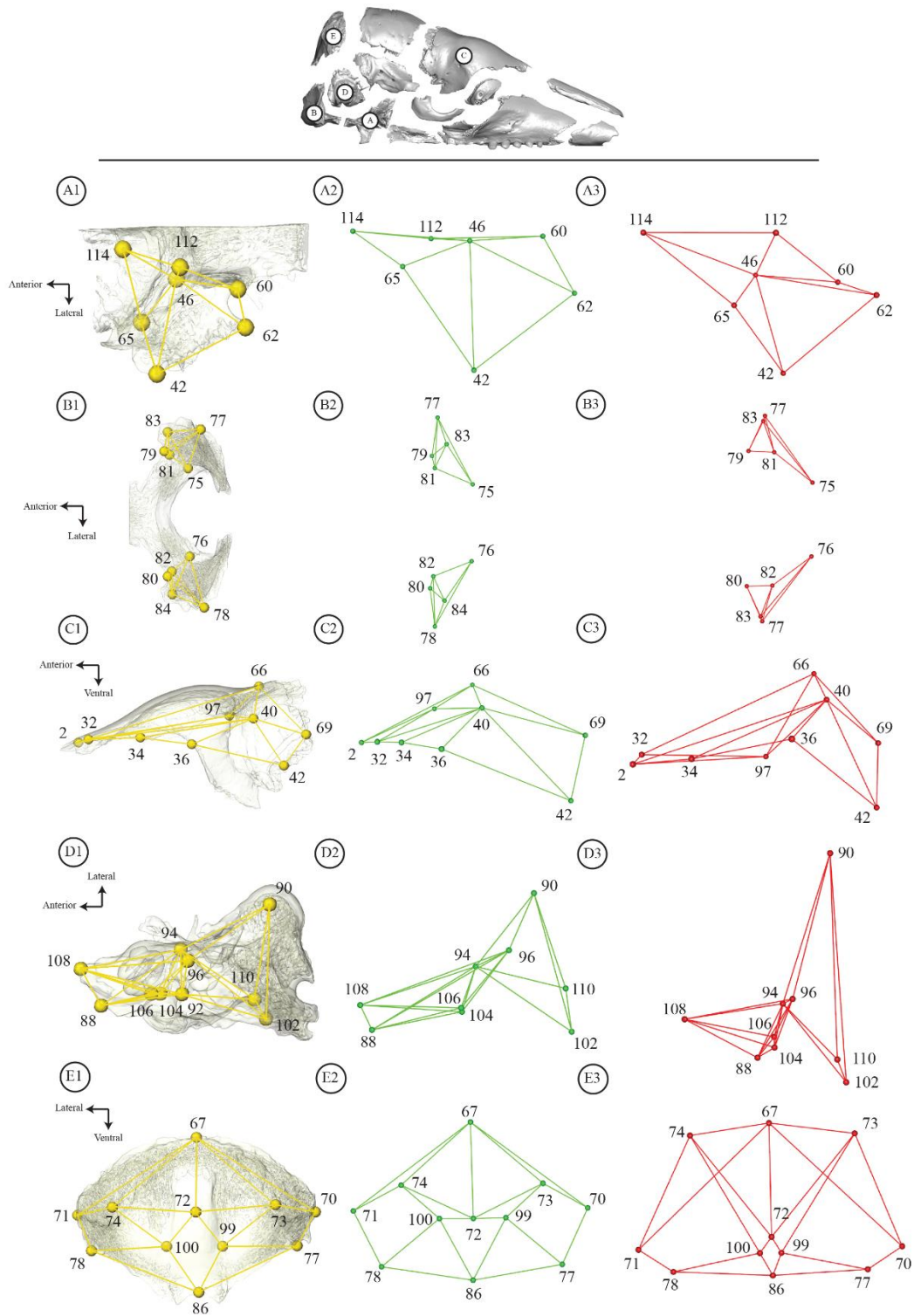


Figure S32. Shape representation of the allometric shape changes detected for a given cranial unit (OBU) in Dataset-Tmax, represented between its minimal (green – smaller centroid size) and maximal (red – larger centroid size) shape (see Figure 29). Results of the analysis performed at the evolutionary level, and with the log skull centroid size taken as the size variable (see text). Each OBU is defined in three subsections organized horizontally: 1, landmarks and wireframe on an OBU of *Cabassous* used as a reference; 2, landmarks with a wireframe representing the minimal OBU shape; 3, landmarks with a wireframe representing the maximal OBU shape. A1-A3, alisphenoid-orbitosphenoid-ptyergoid-basisphenoid complex in dorsal view. B1-B3, basioccipital-exoccipital complex in dorsal view. C1-C3, frontal in lateral view. D1-D3, petrosal in ventral view. E1-E3, supraoccipital in occipital view. Landmark numbers and orientation arrows were added for more readability as well as the overall representation of the unpaired bone (basioccipital, supraoccipital).

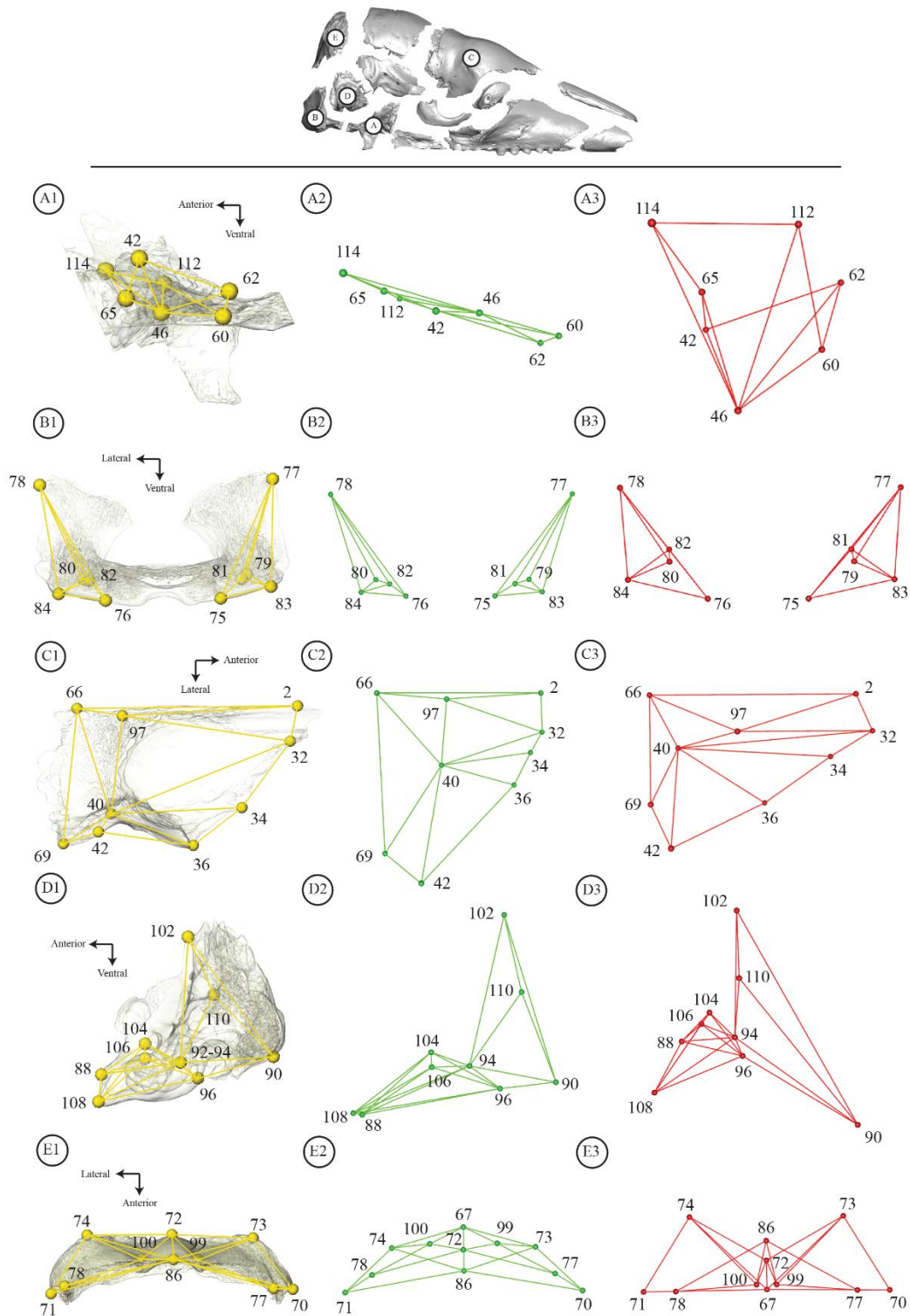


Figure S33. (continued from [Figure 38](#)). Shape representation of the allometric shape changes detected for a given cranial unit (OBU) in Dataset-Tmax, represented between its minimal (green – smaller centroid size) and maximal (red – larger centroid size) shape (see [Figure 29](#)). Results of the analysis performed at the evolutionary level, and with the log skull centroid size taken as the size variable (see text). Each OBU is defined in three subsections organized horizontally: 1, landmarks and wireframe on an OBU of *Cabassous* used as a reference; 2, landmarks with a wireframe representing the minimal OBU shape; 3, landmarks with a wireframe representing the maximal OBU shape. A1-A3, alisphenoid-orbitosphenoid-ptyergoid-basisphenoid complex in lateral view. B1-B3, basioccipital-exoccipital complex in occipital view. C1-C3, frontal in ventral view. D1-D3, petrosal in lateral view. E1-E3, supraoccipital in ventral view. Landmark numbers and orientation arrows were added for more readability as well as the overall representation of the unpaired bone (basioccipital, supraoccipital).

CHAPTER 3: TABLE

Table S3. List of specimens. Available on the HAL open archive portal.

Table S4. Landmark coordinates without treatment. Available on the HAL open archive portal.

Table S5. List of landmarks placed on each of the 76 specimens, with a precision on the estimated landmarks (in red) (see [Material & Methods – Section 3.1](#)). Available on the HAL open archive portal.

Table S6. Measurements on the location of the P4, LTC and dental stages. * Specimen assigned to a dental stage *a posteriori* (see [Figure S13](#)). Available on the HAL open archive portal.

Table S7. Ontogenetic table with the ossification score, the dental score and LTC. Available on the HAL open archive portal.

Table S8. Statistical results of the Procrustes ANOVA from the multivariate regressions at ontogenetic and static level for ES and 3B analyses with log skull centroid size (see [Table 5](#)).

	Log Skull Centroid Size													
	Ontogenetic Level							Static Level						
	Df	SS	MS	R ²	F	Z	p-value	Df	SS	MS	R ²	F	Z	p-value
Entire skull	75	0.048352	0.0483520	0.27618	28.236	7.79710	0.0001	50	0.005156	0.0051561	0.06311	3.3010	3.8848	0.0002
Premaxillary	75	0.042180	0.0421840	0.04242	3.2785	2.39370	0.0054	50	0.003260	0.0032557	0.00558	0.2749	-2.0260	0.9774
Maxillary	75	0.039450	0.0394490	0.10665	8.8338	5.19810	0.0001	50	0.006498	0.0064982	0.03148	1.5928	1.2830	0.1040
Nasal	75	0.016883	0.0168834	0.08368	6.7581	2.78840	0.0004	50	0.001321	0.0013211	0.01127	0.5586	-0.3919	0.6700
Frontal	75	0.165070	0.1650690	0.29873	31.523	5.41580	0.0001	50	0.016091	0.0160908	0.05965	3.1082	2.1868	0.0200
Lacrimal	75	0.020920	0.0209190	0.01568	1.1789	0.57448	0.2802	50	0.003540	0.0035418	0.00429	0.2112	-1.5767	0.9425
Jugal	75	0.063700	0.0637040	0.06006	4.7287	2.51260	0.0015	50	0.008480	0.0084764	0.01476	0.7341	-0.1278	0.5640
Palatine	75	0.096720	0.0967150	0.09004	7.3223	2.58230	0.0006	50	0.056860	0.0568620	0.08829	4.7450	2.1024	0.0053
Parietal	75	0.030140	0.0301386	0.06661	5.2811	2.76100	0.0005	50	0.016008	0.0160080	0.06036	3.1475	1.9868	0.0120
Squamosal	75	0.083660	0.0836610	0.11490	9.6064	5.67020	0.0001	50	0.012920	0.0129168	0.03084	1.5593	1.3391	0.0875
As-Os-Pt-Bs	75	0.090010	0.0900120	0.07351	5.8712	4.27170	0.0001	50	0.032930	0.0329280	0.04347	2.2269	2.0606	0.0178
Supraoccipital	75	0.074610	0.0746130	0.10031	8.2502	4.12040	0.0001	50	0.010060	0.0100551	0.02223	1.1140	0.4710	0.3164
Bo-Ex	75	0.131830	0.1318260	0.19612	18.053	5.38020	0.0001	50	0.009730	0.0097300	0.02801	1.4119	0.9354	0.1756
Petrosal	75	0.041650	0.0416460	0.06281	4.9591	3.81260	0.0001	50	0.018560	0.0185574	0.0427	2.1858	1.9228	0.0242

CHAPTER 3: TABLE

Table S9. Statistical results of the Procrustes ANOVA from the multivariate regressions for each ontogenetic stage for 3B approach using the log skull centroid size (see [Table S6](#)).

	Log Skull Centroid Size																				
	Juvenile (N = 10)							Subadult (N = 15)							Adult (N = 51)						
	Df	SS	MS	R ²	F	Z	p-value	Df	SS	MS	R ²	F	Z	p-value	Df	SS	MS	R ²	F	Z	p-value
Entire Skull	9	0.012341	0.0123409	0.45026	6.5522	3.4243	0.0005	14	0.011540	0.0115404	0.34846	6.9526	4.2238	0.0002	50	0.005156	0.0051561	0.06311	3.3010	3.8848	0.0002
Premaxillary	9	0.012367	0.0123670	0.07737	0.6709	-0.6599	0.7393	14	0.053930	0.0539300	0.25597	4.4723	2.6821	0.0016	50	0.003260	0.0032557	0.00558	0.2749	-2.0260	0.9774
Maxillary	9	0.014352	0.0143516	0.29837	3.4020	2.6405	0.0053	14	0.019914	0.0199143	0.24496	4.2175	3.0692	0.0008	50	0.006498	0.0064982	0.03148	1.5928	1.2830	0.1040
Nasal	9	0.007942	0.0079419	0.21065	2.1350	1.1938	0.1068	14	0.001262	0.0012626	0.05470	0.7523	-0.1102	0.5587	50	0.001321	0.0013211	0.01127	0.5586	-0.3919	0.6700
Frontal	9	0.038097	0.0380970	0.50433	8.1396	2.9802	0.0005	14	0.036748	0.0367480	0.36966	7.6237	3.2273	0.0004	50	0.016091	0.0160908	0.05965	3.1082	2.1868	0.0200
Lacrimal	9	0.006499	0.0064990	0.04779	0.4015	-0.9360	0.8327	14	0.131630	0.1316320	0.37951	7.9511	0.0023	0.0023	50	0.003540	0.0035418	0.00429	0.2112	-1.5767	0.9425
Jugal	9	0.022055	0.0220550	0.14280	1.3327	0.6379	0.2647	14	0.050156	0.0501560	0.18160	2.8846	1.6142	0.0394	50	0.008480	0.0084764	0.01476	0.7341	-0.1278	0.5640
Palatine	9	0.000801	0.0008009	0.00776	0.0626	-2.5716	0.9931	14	0.084873	0.0848730	0.37248	7.7166	2.3607	0.0031	50	0.056860	0.0568620	0.08829	4.7450	2.1024	0.0053
Parietal	9	0.010730	0.0107300	0.17248	1.6674	0.9414	0.1762	14	0.025883	0.0258828	0.29289	5.3847	2.6930	0.0014	50	0.016008	0.0160080	0.06036	3.1475	1.9868	0.0120
Squamosal	9	0.014418	0.0144170	0.13981	1.3003	0.7748	0.2253	14	0.033621	0.0336210	0.23893	4.0813	3.2314	0.0006	50	0.012920	0.0129168	0.03084	1.5593	1.3391	0.0875
As-Os-Pt-Bs	9	0.016600	0.016600	0.11073	0.9961	0.1391	0.4488	14	0.011670	0.0116700	0.05703	0.7862	-0.3946	0.6605	50	0.032930	0.0329280	0.04347	2.2269	2.0606	0.0178
Supraoccipital	9	0.007747	0.0077470	0.08856	0.7774	-0.1792	0.5530	14	0.021395	0.0213948	0.15893	2.4564	1.7216	0.0421	50	0.010060	0.0100551	0.02223	1.1140	0.4710	0.3164
Bo-Eo	9	0.019054	0.0190545	0.26473	2.8804	2.1222	0.0124	14	0.009230	0.0092305	0.09176	1.3133	0.7344	0.2475	50	0.009730	0.0097300	0.02801	1.4119	0.9354	0.1756
Petrosal	9	0.019448	0.0194481	0.24980	2.6638	2.2019	0.0071	14	0.009377	0.0093770	0.07592	1.0680	0.3282	0.3881	50	0.018560	0.0185574	0.0427	2.1858	1.9228	0.0242

Table S10. Statistical results of the homogeneity of slope test between ontogenetic stages using the log skull centroid size (see Figure S20). A significant *p-value* (< 0.05 – unshaded line) implies that at least one of the groups has a different allometric trajectory from the others.

	HOS test between ontogenetic stages using Log Skull Centroid Size						
	Df	RSS	SS	R^2	F	Z	<i>p-value</i>
Entire skull	70	0.11318	0.0081105	0.046327	2.5081	5.6213	0.0001
Premaxillary	70	0.88453	0.0377180	0.037934	1.4925	1.3684	0.0849
Maxillary	70	0.29504	0.0197750	0.053459	2.3459	3.3933	0.0001
Nasal	70	0.16745	0.0043138	0.021381	0.9017	0.3639	0.3743
Frontal	70	0.35370	0.0213300	0.038601	2.1106	2.8602	0.0022
Lacrimal	70	1.16630	0.1044800	0.078316	3.1354	2.2786	0.0111
Jugal	70	0.92418	0.0466330	0.043969	1.7661	1.5098	0.0618
Palatine	70	0.83270	0.1219600	0.113540	5.1262	3.0572	0.0001
Parietal	70	0.36319	0.0356900	0.078882	3.4393	3.0782	0.0001
Squamosal	70	0.60170	0.0242220	0.033267	1.4090	1.8926	0.0271
As-Os-Pt-Bs	70	1.05100	0.0396680	0.032396	1.3210	1.4538	0.0722
Supraoccipital	70	0.63526	0.0214840	0.028882	1.1837	0.9168	0.1822
Bo-Ex	70	0.48188	0.0119230	0.017738	0.8660	0.6395	0.2658
Petrosal	70	0.58855	0.0202500	0.030539	1.2042	1.0264	0.1520

CHAPTER 3: TABLE

Table S11. List of *Zaedyus* and *Cabassous* specimens. The material studied is stored in the collections of the *Muséum national d'Histoire naturelle* (MNHN, *collections Zoologie et Anatomie comparée, Mammifères et Oiseaux*) in Paris (France), the Natural History Museum (NHM) in London (UK), the American Museum of Natural History (AMNH) in New York (USA), the *Muséum d'Histoire Naturelle* in Geneva (MHNG, Switzerland), Naturalis Biodiversity Center (NBC) in Leiden (Netherlands), the Field Museum of Natural History (FMNH) in Chicago (USA), the Museum für Naturkunde (MfN – ZMB) in Berlin (Germany), the Museum of Vertebrate Zoology (MVZ) in Berkeley (USA), and the *Institut des Sciences de l'évolution* (ISEM) in Montpellier.

Institution	Museum-N°	Genus	species	Distribution
AMNH	25668	<i>Zaedyus</i>	<i>pichiy</i>	Argentina, Santa Cruz, Corpen Aike, Chico River
AMNH	17448	<i>Zaedyus</i>	<i>pichiy</i>	Argentina, Santa cruz, Corpen Aike, Chico River, 100 miles from coast
AMNH	94327	<i>Zaedyus</i>	<i>pichiy</i>	Argentina, Chubut, Sarmiento, Colhue Huapi Lake
AMNH	25667	<i>Zaedyus</i>	<i>pichiy</i>	Argentina, Santa Cruz, Corpen Aike, Chico River
NHM	27-6-4-56	<i>Zaedyus</i>	<i>pichiy</i>	?
NHM	90-2-20-7	<i>Zaedyus</i>	<i>pichiy</i>	?
NHM	46-5-13-17	<i>Zaedyus</i>	<i>pichiy</i>	?
NHM	99-8-5-10	<i>Zaedyus</i>	<i>pichiy</i>	?
NHM	76-9-26-14	<i>Zaedyus</i>	<i>pichiy</i>	?
NHM	22-11-23-1	<i>Zaedyus</i>	<i>pichiy</i>	?
FMNH	23810	<i>Zaedyus</i>	<i>pichiy</i>	Argentina, Chubut
FMNH	28506	<i>Zaedyus</i>	<i>pichiy</i>	Argentina, Santa Cruz, Paso Ibanez
MHNG	1276.076	<i>Zaedyus</i>	<i>pichiy</i>	Argentina, Chubut, Fofo Cahuel
MHNG	1627.053	<i>Zaedyus</i>	<i>pichiy</i>	Argentina, Chubut, Punta Ninfas
MNHN	1917-135	<i>Zaedyus</i>	<i>pichiy</i>	?
MNHN	2007-382	<i>Zaedyus</i>	<i>pichiy</i>	?
MNHN	1897-446	<i>Zaedyus</i>	<i>pichiy</i>	?
MNHN	1897-440	<i>Zaedyus</i>	<i>pichiy</i>	?
MNHN	1883-158	<i>Zaedyus</i>	<i>pichiy</i>	Argentina, Santa Cruz
MNHN	1897-445	<i>Zaedyus</i>	<i>pichiy</i>	?
MNHN	1897-472	<i>Zaedyus</i>	<i>pichiy</i>	?
MNHN	1897-456	<i>Zaedyus</i>	<i>pichiy</i>	?
MNHN	1897-450	<i>Zaedyus</i>	<i>pichiy</i>	?
MNHN	1897-468	<i>Zaedyus</i>	<i>pichiy</i>	?
MNHN	1897-470	<i>Zaedyus</i>	<i>pichiy</i>	?
MNHN	1897-447	<i>Zaedyus</i>	<i>pichiy</i>	?
MNHN	1897-442	<i>Zaedyus</i>	<i>pichiy</i>	?
MNHN	1897-449	<i>Zaedyus</i>	<i>pichiy</i>	?
MNHN	1897-457	<i>Zaedyus</i>	<i>pichiy</i>	?
MNHN	1897-454	<i>Zaedyus</i>	<i>pichiy</i>	?
MNHN	1897-1268	<i>Zaedyus</i>	<i>pichiy</i>	Argentina, Barraca Blanca
MNHN	1897-461	<i>Zaedyus</i>	<i>pichiy</i>	?
MNHN	1897-452	<i>Zaedyus</i>	<i>pichiy</i>	?
MNHN	1897-473	<i>Zaedyus</i>	<i>pichiy</i>	?
MNHN	1971-1045	<i>Zaedyus</i>	<i>pichiy</i>	Chili, L.E. Peña
MNHN	2007-369	<i>Zaedyus</i>	<i>pichiy</i>	?
MNHN	2007-375	<i>Zaedyus</i>	<i>pichiy</i>	Argentina, Patagonia
ZMB	49038	<i>Zaedyus</i>	<i>pichiy</i>	South America, Argentina, Oso Marino, -47,9237, -65,83145
ZMB	46104	<i>Zaedyus</i>	<i>pichiy</i>	South America, Argentina, Oso Marino, -47,9237, -65,83145
ZMB	85890	<i>Zaedyus</i>	<i>pichiy</i>	?
ZMB	48627	<i>Zaedyus</i>	<i>pichiy</i>	South America, Argentina, Puerto Jenkins, -47,75779, -65,90836
ZMB	48626	<i>Zaedyus</i>	<i>pichiy</i>	?
ZMB	46103	<i>Zaedyus</i>	<i>pichiy</i>	South America, Argentina, Puerto Jenkins, -47,75779, -65,90836
AMNH	133386	<i>Cabassous</i>	<i>unicinctus</i> (N)	South America, Brazil, Mato Grosso do Sul, Maracaju
AMNH	133335	<i>Cabassous</i>	<i>unicinctus</i> (S)	Brazil, Mato Grosso do Sul, Maracaju
AMNH	133336	<i>Cabassous</i>	<i>unicinctus</i> (S)	Brazil, Mato Grosso do Sul, Maracaju
AMNH	37546	<i>Cabassous</i>	<i>unicinctus</i> (S)	South America, Brazil, Mato Grosso, Diamantino
AMNH	14862	<i>Cabassous</i>	<i>centralis</i>	South America, Colombia, Magdalena, Santa Marta
AMNH	137196	<i>Cabassous</i>	<i>unicinctus</i> (N)	South America, Brazil, Para, Tapajos River, Igarape Brabo
AMNH	14863	<i>Cabassous</i>	<i>centralis</i>	South America, Colombia, Antioquia, Valparaiso
AMNH	23441	<i>Cabassous</i>	<i>centralis</i>	South America, Colombia, Magdalena, Santa Marta
AMNH	60636	<i>Cabassous</i>	<i>centralis</i>	South America, Venezuela, Zulia, Maracaibo
AMNH	74113	<i>Cabassous</i>	<i>unicinctus</i> (N)	South America, Peru, Loreto, Maynas

CHAPTER 3: TABLE

Table S11. Continued.

Institution	Museum-N°	Genus	species	Distribution
AMNH	98459	<i>Cabassous</i>	<i>unicinctus</i> (N)	South America, Peru, Loreto, Maynas
AMNH	133318	<i>Cabassous</i>	<i>unicinctus</i> (S)	South America, Brazil, Goias, Anapolis
AMNH	133334	<i>Cabassous</i>	<i>unicinctus</i> (S)	South America, Brazil, Mato Grosso do Sul, Maracaju
AMNH	136256	<i>Cabassous</i>	<i>centralis</i> or <i>unicinctus</i> (N)	Colombia
NHM	3-7-12-2	<i>Cabassous</i>	<i>centralis</i> or <i>unicinctus</i> (N)	?
NHM	7-6-15-9	<i>Cabassous</i>	<i>centralis</i> or <i>unicinctus</i> (N)	?
NHM	16-6-5-36	<i>Cabassous</i>	<i>centralis</i> or <i>unicinctus</i> (N)	?
NHM	71-2503	<i>Cabassous</i>	<i>unicinctus</i> (S)	264 km N of Xavantina, Mato Grosso, Brazil
NHM	78-12-13-1	<i>Cabassous</i>	<i>unicinctus</i> (N)	Demerara, Guyana
ISEM	V3455	<i>Cabassous</i>	<i>centralis</i> or <i>unicinctus</i> (N)	?
MNHN	2007-374	<i>Cabassous</i>	<i>centralis</i> or <i>unicinctus</i> (N)	?
MNHN	1953-457	<i>Cabassous</i>	<i>centralis</i> or <i>unicinctus</i> (N)	?
MNHN	1998-2255	<i>Cabassous</i>	<i>unicinctus</i> (N)	Petit-Saut, Guyana
MNHN	1917-159	<i>Cabassous</i>	<i>centralis</i> or <i>unicinctus</i> (N)	?
MNHN	1999-1044	<i>Cabassous</i>	<i>unicinctus</i> (N)	French Guyane
MVZ	155192	<i>Cabassous</i>	<i>unicinctus</i> (N)	Peru, Rio Cenepa
NCB	26326B	<i>Cabassous</i>	<i>unicinctus</i> (N)	Suriname

CHAPTER 3: TABLE

Table S12. List of specimens for interspecific sample. CM, Central Morphotype; GM, Guianan Morphotype; NM, Northern Morphotype; SM, Southern Morphotype.

Family/Clade	Species	Institutional number	Locality	Period	Age range	Reference
Peltephilidae	<i>Peltephilus pumilus</i> †	YPM-PU 15391	Argentina; Santa Cruz formation; Coy inlet	Santacrucian	17.5-16.3	Ameghino, 1887
Dasypodinae	<i>Dasypus hybridus</i>	AMNH 205721	Uruguay; Treinta y Tres	Extant	0	Desmarest, 1804
Dasypodinae	<i>Dasypus novemcinctus</i> SM	MNHN 2006-565	Brazil; Pará	Extant	0	Linnaeus, 1758
Dasypodinae	<i>Dasypus novemcinctus</i> CM	NHM 98-10-3-23	Colombia; Valdivia	Extant	0	Linnaeus, 1758
Dasypodinae	<i>Dasypus novemcinctus</i> NM	NMNH 565067	Guatemala; Escuintla; Finca Las Mercedes; Escuintla; 33 Km SE; Brito	Extant	0	Linnaeus, 1758
Dasypodinae	<i>Dasypus novemcinctus</i> GM	NHM 52-1183	Suriname; Zanderiyi	Extant	0	Linnaeus, 1758
Dasypodinae	<i>Dasypus kappleri</i>	NHM 82-7-26-12	South America - No more precision	Extant	0	Krauss, 1862
Dasypodinae	<i>Dasypus septemcinctus</i>	NHM 86-10-4-7	South America - No more precision	Extant	0	Linnaeus, 1758
Dasypodinae	<i>Dasypus pilosus</i>	NHM 94-10-1-13	Peru; Andes	Extant	0	Fitzinger, 1856
Dasypodinae	<i>Dasypus yepesi</i>	MLP 30.III.90.8	Argentina, Salta, Departamento de Orán, San Andrés	Extant	0	Vizcaíno, 1995
Dasypodidae	<i>Stegotherium tauberi</i> †	YPM-PU 15565	Argentina; Santa Cruz formation	Santacrucian	17.5-16.3	Ameghino, 1887
Euphractinae	<i>Euphractus sexcinctus</i>	AMNH 133304	Brazil; Goias; Anapolis	Extant	0	Linnaeus, 1758
Euphractinae	<i>Chaetophractus villosus</i>	AMNH 173546	South America - No more precision	Extant	0	Desmarest, 1804
Euphractinae	<i>Chaetophractus vellerosus</i>	MNHN 2003-461	South America - No more precision	Extant	0	Gray, 1865
Euphractinae	<i>Zaedyus pichiy</i>	FMNH 23810	Argentina; Chubut	Extant	0	Desmarest, 1804
Tolypeutinae	<i>Cabassous unicinctus</i> NM	MNHN 1999-1044	French Guiana	Extant	0	Linnaeus, 1758
Tolypeutinae	<i>Cabassous unicinctus</i> SM	NHM 71-2503	Brazil; Mato Grosso; 264 km N of Xavantina	Extant	0	Linnaeus, 1758
Tolypeutinae	<i>Cabassous centralis</i>	AMNH 23441	South America, Colombia, Magdalena, Santa Marta	Extant	0	Miller, 1899
Tolypeutinae	<i>Cabassous tatouay</i>	NHM 86-10-4-5	Brazil; Rio Grande do Sul	Extant	0	Desmarest, 1804
Tolypeutinae	<i>Tolypeutes matacus</i>	FMNH 28345	Brazil; Mato Grosso; Descalvado	Extant	0	Desmarest, 1804
Tolypeutinae	<i>Priodontes maximus</i>	AMNH 208104	Zoo - No more precision	Extant	0	Kerr, 1792
Chlamyphorinae	<i>Chlamyphorus truncatus</i>	AMNH 5487	Argentina; Mendoza	Extant	0	Harlan, 1825
Chlamyphorinae	<i>Calyptophractus retusus</i>	NMNH 283134	Bolivia; Santa Cruz	Extant	0	Burmeister, 1863
Chlamyphoridae	<i>Proeutatus lagenai</i> †	YPM-PU 15613	Argentina; Santa Cruz formation	Santacrucian	17.5-16.3	Ameghino, 1887
Pampatheriinae	<i>Vassallia maxima</i> †	FMNH P14424	Argentina; Catamarca; Corral Quemado	Montehermosan	6.8-4.0	Castellanos, 1946
Glyptodontinae	" <i>Metopotoxus</i> " <i>anceps</i> †	YPM-PU 15612	Argentina; Santa Cruz formation; Lago Pueyrredón	Santacrucian	17.5-16.3	Scott, 1903
Glyptodontinae	<i>Glyptodon</i> sp.†	MNHN PAM-759	Argentina; Buenos Aires	Pleistocene	3.0-0.011	Owen, 1839

† extinct species

CHAPTER 3: TABLE

Table S13. List of landmarks after reduction of landmark set with their definition. *, internal landmark; **, amended definition for interspecific datasets. The modifications were made because the last tooth in *Dasybus* was not always present and the minimum interorbital length was confused with postorbital constriction (see Table 3).

Number	Definition
1	Most anterodorsal point of the internasal suture
2	Intersection between internasal suture and frontal bone
3-4	Triple contact point between premaxillary/maxillary/nasal
5	Intersection between midline and premaxillary/ maxillary suture
6-7	Most posterior point of the premaxillary/maxillary suture on the palate
8	Most anterior point of the premaxillary midline suture
9-10	Most anterior point of the premaxillary/nasal suture
11-12	Most anterior point of the premaxillary anterior process
13-14	Most anterior point of incisive foramen in strict ventral view
15-16	Most posterior point of incisive foramen in strict ventral view
17	Intersection between palatine/maxillary suture and the palate midline
18-19	Intersection between maxillary/palatine suture and lateral edge of palate
20-21	Intersection between jugal/maxillary suture and ventral edge of zygomatic arch
22-23	Most dorsal point of the maxillary foramen
24-25	Most dorsal point of the infraorbital foramen
26-27	Most anterior point of the alveolar margin of the dental row
28-29	Most posterior point of the alveolus margin of the dental row **
30	Most posterior point of the palatine midline
31-32	Triple contact point between frontal/maxillary/nasal
33-34	Triple contact point between lacrimal/maxillary/frontal
35-36	Intersection between the lacrimal/frontal suture and the anterior orbital edge
37-38	Anteroventral margin of the lacrimal foramen
39-40	Point marking the maximal postorbital constriction dorsomedially **
41-42	Triple contact point between squamosal/frontal/alisphenoid
43-44	Most anteroventral point of caudal palatine foramen (in lateral view)
45-46	Most anteroventral point of the sphenorbital fissure
47-48	Triple contact point between maxillary/jugal/lacrimal
49-50	Intersection between anterior orbital edge and jugal/lacrimal suture
51-52	Most dorsal point of the jugal/squamosal suture
53-54	Most ventral point of the jugal/squamosal suture
55-56	Most posterodorsal point of the zygomatic ridge of the squamosal
57-58	Most dorsal point of the external acoustic meatus on squamosal (in lateral view)
59-60	Most anteroventral point of the foramen ovale
61-62	Most posterior point of the alisphenoid/squamosal suture in front of pyriform fenestra
63*	Anteroventral tip of the tentorial process on the midline
64-65	Most anterodorsal point of the optic foramen
66	Intersection between frontal/parietal suture and the midline
67	Intersection between parietal/supraoccipital suture and the midline
68-69	Triple contact point between the frontal/squamosal/parietal
70-71	Triple contact point between the parietal/squamosal/supraoccipital
72	Most distal point of the supraoccipital on the midline (occipital face)
73-74	Most posterior point of the nuchal process of the supraoccipital
75-76	Intersection between the anteromedial edge of occipital condyle and foramen magnum
77-78	Triple contact point between the supraoccipital/exoccipital/petrosal
79-80	Most posterolateral point of the jugular foramen
81-82	Most posterolateral point of the hypoglossal foramen

CHAPTER 3: TABLE

Table S13. Continued.

Number	Definition
83-84	Most anterolateral point of the occipital condyle (in ventral view)
85	Most anteroventral point of the foramen magnum
86	Most posterodorsal point of the foramen magnum
87-88	Most medial point of promontorium of petrosal in ventral view
89-90	Most anteroventral point of mastoid process (= paroccipital process of petrosal)
91-92	Most ventral point of external aperture of cochlear canaliculus
93-94	Most anterior point of the fenestra vestibuli
95-96	Most anteroventral point of the external aperture of cochlear fossula
97*	Dorsal intersection of annular ridge and midline
98*	Dorsal intersection between cribriform plate and median septum posterior to the latter
99-100*	Maximum curvature point of the lateral occipital ridge in caudal cerebral fossa
101-102*	Most dorsal point of the petrosal on the level of the crista tentoria transversally
103-104*	Most anteromedial point of the foramen acusticum superius
105-106*	Most anteromedial point of the foramen acusticum inferius
107-108*	Most anterior point of epitympanic wing of petrosal
109-110*	Maximum curvature point in the ventromedial area of the fossa subarcuata
111-112*	Most dorsal point of the internal posterior aperture of the optic canal
113-114*	Most ventromedial point on the annular ridge lateral to posterior median septum

Table S14. Landmark coordinates without treatment for new intra- and interspecific sample. CM, Central Morphotype; GM, Guianan Morphotype; NM, Northern Morphotype; SM, Southern Morphotype. †, extinct species. Available on the HAL open archive portal.

Table S15. Comparison of the number of landmarks between each dataset for the entire skull and each cranial unit (see also Table 3). In red, too low landmark number or not well distributed over the cranial unit - no analysis on the OBU (see Materiel & Methods - Section 3.2).

ES/OBU	Landmark Number			
	Section 3.1	<i>Zaedyus/Cabassous</i> /DatasetExt	Dataset-Lmax	Dataset-Tmax
Entire Skull	131	114	100	90
Premaxillary	9	8	4	1
Maxillary	13	13	12	10
Nasal	5	5	4	2
Frontal	10	9	9	9
Lacrimal	5	5	5	5
Jugal	5	5	3	2
Palatine	4	4	3	3
Parietal	5	5	5	5
Squamosal	12	8	6	6
As-Os-Pt-BS	10	7	7	7
Supraoccipital	7	7	7	7
Bo-Eo	7	6	5	5
Petrosal	10	10	10	9

Table S16. Landmark composition of each OBU for interspecific datasets. Green, present; Red, absent. *, internal landmark; **, amended definition for interspecific datasets. The modifications were made because the last tooth in *Dasybus* was not always present and the minimum interorbital length was confused with postorbital constriction (see [Table 3](#)). Available on the HAL open archive portal.

Table S17. List of landmarks placed on each *Zaedyus* and *Cabassous* specimens, with a precision on the estimated landmarks (in red by TPS; in orange by symmetrization) (see [Material & Methods – Section 3.2](#)). Available on the HAL open archive portal.

Table S18. List of landmarks placed on specimens for evolutionary analyses, with a precision on the estimated landmarks (in red not estimated because the specimens are too distant morphologically; in orange by symmetrization) (see [Material & Methods – Section 3.2](#)). CM, Central Morphotype; GM, Guianan Morphotype; NM, Northern Morphotype; SM, Southern Morphotype. †, extinct species. Available on the HAL open archive portal.

Table S19. Ontogenetic table with the ossification score, the dental score and LTC for *Zaedyus* and *Cabassous* specimens. Available on the HAL open archive portal.

CHAPTER 3: TABLE

Table S20. Results of the multivariate regression for ES and 3B with log skull centroid size at the ontogenetic and static levels in *Cabassous*N. Index: a, slope coefficient; Intercept; R^2 , allometric proportion of shape variation; p -value, significance following the permutation test. The shaded lines correspond to the tests with a non-significant p -value (> 0.05).

	<i>Cabassous</i> N																			
	Ontogenetic level									Static level										
	N	Df	SS	MS	R2	F	Z	P	a	b	N	Df	SS	MS	R2	F	Z	P	a	b
Entire Skull	21	20	0.004021	0.0040208	0.08798	1.833	2.3369	0.0131	0.251	-3.128	14	13	0.0030862	0.0030862	0.10763	1.4473	1.4068	0.0859	0.2501	-3.1207
Premaxillary	21	20	0.02856	0.02856	0.08014	1.6553	1.0793	0.1438	0.6689	-8.3377	14	13	0.029611	0.029611	0.12225	1.6713	1.0101	0.1665	0.7746	-9.6663
Maxillary	21	20	0.008393	0.0083927	0.07057	1.4425	1.0897	0.1371	0.3626	-4.5198	14	13	0.005318	0.0053176	0.07025	0.9067	-0.030925	0.5236	0.3282	-4.0963
Nasal	21	20	0.008648	0.0086475	0.10084	2.1307	1.3423	0.0967	0.3681	-4.5879	14	13	0.013845	0.0138445	0.26438	4.3128	2.1081	0.0211	0.5296	-6.6096
Frontal	21	20	0.012914	0.0129135	0.11924	2.5723	2.1635	0.0103	0.4498	-5.6065	14	13	0.007022	0.0070217	0.11652	1.5827	1.1544	0.1225	0.3772	-4.7071
Lacrimal	21	20	0.02541	0.025406	0.05663	1.1405	0.47507	0.3319	0.6309	-7.8638	14	13	0.019096	0.019096	0.07463	0.9678	0.25322	0.4177	0.622	-7.763
Jugal	21	20	0.027921	0.0279207	0.16691	3.8066	2.3979	0.0027	0.6614	-8.2438	14	13	0.020704	0.0207045	0.18429	2.7111	1.8066	0.0224	0.6477	-8.0829
Palatine	21	20	0.026266	0.026266	0.11466	2.4606	1.3753	0.0699	0.6415	-7.9958	14	13	0.025141	0.025141	0.15672	2.2302	1.2338	0.1031	0.7137	-8.9069
Parietal	21	20	0.015113	0.0151128	0.11705	2.5188	1.6261	0.04	0.4866	-6.0651	14	13	0.011179	0.0111786	0.13004	1.7937	1.0874	0.1368	0.4759	-5.9392
Squamosal	21	20	0.031691	0.031691	0.13255	2.9032	2.2681	0.0129	0.7046	-8.7828	14	13	0.020563	0.020563	0.13552	1.8812	1.359	0.0852	0.6455	-8.0552
As-Os-Pt-BS	21	20	0.07721	0.077212	0.22588	5.5439	3.1506	0.0001	0.4383	-13.71	14	13	0.061909	0.061909	0.28863	4.8689	2.7324	0.0016	1.12	-13.98
Supraoccipital	21	20	0.021318	0.021318	0.09282	1.9441	1.3838	0.078	0.5779	-7.2035	14	13	0.017234	0.017234	0.10819	1.4557	0.85002	0.21	0.5909	-7.3744
Bo-Eo	21	20	0.005677	0.0056768	0.05865	1.1838	0.54565	0.3058	0.2982	-3.7172	14	13	0.007925	0.0079248	0.11736	1.5955	1.1186	0.1247	0.4007	-5.0007
Petrosal	21	20	0.025862	0.0258623	0.15028	3.3603	2.9825	0.0004	0.6365	-7.9341	14	13	0.026571	0.0265709	0.22036	3.3917	3.0227	0.0002	0.7337	-9.1567

Table S21. Results of the multivariate regression for ES and 3B with log skull centroid size at the evolutionary level in Dataset-Tmax. Index: a, slope coefficient; Intercept; R^2 , allometric proportion of shape variation; p -value, significance following the permutation test. The shaded lines correspond to the tests with a non-significant p -value (> 0.05).

	Dataset-Tmax																			
	With phylogenetic correction									Without phylogenetic correction										
	N	Df	SS	MS	R2	F	Z	P	a	b	N	Df	SS	MS	R2	F	Z	P	a	b
Entire Skull	27	26	0.014259	0.0142593	0.13619	3.9414	3.5213	0.0001	0.002118	-0.026173	27	26	0.15314	0.153141	0.1721	5.197	3.2209	0.0003	0.1626	-2.0093
Premaxillary	-	-	-	-	-	-	-	-	-	-	-	-	-	-	-	-	-	-	-	-
Maxillary	27	26	0.015518	0.0155176	0.06229	1.6608	1.1795	0.1227	0.0142	-0.1755	27	26	0.23186	0.231861	0.09483	2.6192	1.6938	0.05217	0.2001	-2.4724
Nasal	-	-	-	-	-	-	-	-	-	-	-	-	-	-	-	-	-	-	-	-
Frontal	27	26	0.015061	0.0150609	0.11761	3.3323	2.6231	0.0063	0.02483	-0.30682	27	26	0.31208	0.312077	0.24034	7.9095	3.3207	0.0002	0.2321	-2.8683
Lacrimal	27	26	0.00882	0.0088156	0.01769	0.4502	-0.72294	0.7698	0.01545	-0.19095	27	26	0.17115	0.171152	0.09355	2.5801	1.6994	0.0314	0.1719	-2.1242
Jugal	-	-	-	-	-	-	-	-	-	-	-	-	-	-	-	-	-	-	-	-
Palatine	-	-	-	-	-	-	-	-	-	-	-	-	-	-	-	-	-	-	-	-
Parietal	27	26	0.007496	0.0074962	0.05912	1.5708	0.94073	0.1717	0.003698	-0.04569	27	26	0.15401	0.154014	0.19621	6.1026	2.8276	0.0005	0.1631	-2.015
Squamosal	27	26	0.015233	0.0152327	0.06286	1.6769	1.0003	0.1639	0.01403	-0.17332	27	26	0.13928	0.139276	0.10497	2.932	1.7968	0.0251	0.1551	-1.9162
As-Os-Pt-BS	27	26	0.0442	0.044205	0.10411	2.9052	1.9533	0.0289	-0.00425	0.05251	27	26	0.4001	0.4001	0.20198	6.3275	3.3434	0.0002	0.2629	-0.32478
Supraoccipital	27	26	0.022044	0.022044	0.1138	3.2102	2.4608	0.0025	-0.00446	0.05511	27	26	0.12583	0.125828	0.11033	3.1002	2.1818	0.0104	0.1474	-1.8213
Bo-Eo	27	26	0.018599	0.018599	0.19149	5.9213	3.0963	0.0001	0.004096	-0.050605	27	26	0.15271	0.152708	0.32225	11.887	3.7057	0.0001	0.1624	-2.0065
Petrosal	27	26	0.031344	0.0313443	0.13179	3.795	3.0261	0.0002	0.0007881	-0.0097381	27	26	0.4008	0.4008	0.21758	6.9519	3.1092	0.0002	0.2631	-3.2506

Supporting Information 5: R Script.

```
#####
##### Covariation Exploration Section 4.1 & 4.2 #####
#####

##### packages
library(Morpho)
library(geomorph)
library(FactoMineR)
library(igraph)
library(abind)
library(smatr)
library(ggplot2)
library(vegan)
library(ape)
library(mclust)
library(fpc)
library(cluster)
library(factoextra)
library(dendextend)

##### choose space work
setwd(choose.dir())

#####
##### SAMPLE #####
#####

##### SAMPLE Ontogenetic level
##### Dasyopus
Tatou1<-read.csv(file="/Landmarks_Dasyopus_novemcinctus_SM_AMNH-
365.pts",skip=2,header=F,sep="",row.names=1)
Tatou2<-read.csv(file="/Landmarks_Dasyopus_novemcinctus_SM_AMNH-
75896.pts",skip=2,header=F,sep="",row.names=1)
Tatou3<-read.csv(file="/Landmarks_Dasyopus_novemcinctus_SM_AMNH-
91707.pts",skip=2,header=F,sep="",row.names=1)
Tatou4<-read.csv(file="/Landmarks_Dasyopus_novemcinctus_SM_AMNH-
91710.pts",skip=2,header=F,sep="",row.names=1)
Tatou5<-read.csv(file="/Landmarks_Dasyopus_novemcinctus_SM_AMNH-
93116.pts",skip=2,header=F,sep="",row.names=1)
Tatou6<-read.csv(file="/Landmarks_Dasyopus_novemcinctus_SM_AMNH-
93118.pts",skip=2,header=F,sep="",row.names=1)
Tatou7<-read.csv(file="/Landmarks_Dasyopus_novemcinctus_SM_AMNH-
93735.pts",skip=2,header=F,sep="",row.names=1)
Tatou8<-read.csv(file="/Landmarks_Dasyopus_novemcinctus_SM_AMNH-
98515.pts",skip=2,header=F,sep="",row.names=1)
Tatou9<-read.csv(file="/Landmarks_Dasyopus_novemcinctus_SM_AMNH-
133259.pts",skip=2,header=F,sep="",row.names=1)
Tatou10<-read.csv(file="/Landmarks_Dasyopus_novemcinctus_SM_AMNH-
133261.pts",skip=2,header=F,sep="",row.names=1)
Tatou11<-read.csv(file="/Landmarks_Dasyopus_novemcinctus_SM_AMNH-
133265.pts",skip=2,header=F,sep="",row.names=1)
Tatou12<-read.csv(file="/Landmarks_Dasyopus_novemcinctus_SM_AMNH-
133266.pts",skip=2,header=F,sep="",row.names=1)
Tatou13<-read.csv(file="/Landmarks_Dasyopus_novemcinctus_SM_AMNH-
133328.pts",skip=2,header=F,sep="",row.names=1)
```

```

Tatou14<-read.csv(file="/Landmarks_Dasypus_novemcinctus_SM_AMNH-
133329.pts",skip=2,header=F,sep="",row.names=1)
Tatou15<-read.csv(file="/Landmarks_Dasypus_novemcinctus_SM_AMNH-
133330.pts",skip=2,header=F,sep="",row.names=1)
Tatou16<-read.csv(file="/Landmarks_Dasypus_novemcinctus_SM_AMNH-
133338.pts",skip=2,header=F,sep="",row.names=1)
Tatou17<-read.csv(file="/Landmarks_Dasypus_novemcinctus_SM_AMNH-
133342.pts",skip=2,header=F,sep="",row.names=1)
Tatou18<-read.csv(file="/Landmarks_Dasypus_novemcinctus_SM_AMNH-
133381.pts",skip=2,header=F,sep="",row.names=1)
Tatou19<-read.csv(file="/Landmarks_Dasypus_novemcinctus_SM_AMNH-
133397.pts",skip=2,header=F,sep="",row.names=1)
Tatou20<-read.csv(file="/Landmarks_Dasypus_novemcinctus_SM_AMNH-
136252.pts",skip=2,header=F,sep="",row.names=1)
Tatou21<-read.csv(file="/Landmarks_Dasypus_novemcinctus_SM_AMNH-
205726.pts",skip=2,header=F,sep="",row.names=1)
Tatou22<-read.csv(file="/Landmarks_Dasypus_novemcinctus_SM_AMNH-
205727.pts",skip=2,header=F,sep="",row.names=1)
Tatou23<-read.csv(file="/Landmarks_Dasypus_novemcinctus_SM_AMNH-
211665.pts",skip=2,header=F,sep="",row.names=1)
Tatou24<-read.csv(file="/Landmarks_Dasypus_novemcinctus_SM_AMNH-
211668.pts",skip=2,header=F,sep="",row.names=1)
Tatou25<-read.csv(file="/Landmarks_Dasypus_novemcinctus_SM_AMNH-
262658.pts",skip=2,header=F,sep="",row.names=1)
Tatou26<-read.csv(file="/Landmarks_Dasypus_novemcinctus_SM_AMNH-
262659.pts",skip=2,header=F,sep="",row.names=1)
Tatou27<-read.csv(file="/Landmarks_Dasypus_novemcinctus_SM_AMNH-
263287.pts",skip=2,header=F,sep="",row.names=1)
Tatou28<-read.csv(file="/Landmarks_Dasypus_novemcinctus_SM_BMNH-1-2-1-
34.pts",skip=2,header=F,sep="",row.names=1)
Tatou29<-read.csv(file="/Landmarks_Dasypus_novemcinctus_SM_BMNH-1-6-6-
84.pts",skip=2,header=F,sep="",row.names=1)
Tatou30<-read.csv(file="/Landmarks_Dasypus_novemcinctus_SM_BMNH-3-7-7-
146.pts",skip=2,header=F,sep="",row.names=1)
Tatou31<-read.csv(file="/Landmarks_Dasypus_novemcinctus_SM_BMNH-3-7-7-
150.pts",skip=2,header=F,sep="",row.names=1)
Tatou32<-read.csv(file="/Landmarks_Dasypus_novemcinctus_SM_BMNH-3-9-4-
102.pts",skip=2,header=F,sep="",row.names=1)
Tatou33<-read.csv(file="/Landmarks_Dasypus_novemcinctus_SM_BMNH-11-10-27-
3.pts",skip=2,header=F,sep="",row.names=1)
Tatou34<-read.csv(file="/Landmarks_Dasypus_novemcinctus_SM_BMNH-14-4-25-
86.pts",skip=2,header=F,sep="",row.names=1)
Tatou35<-read.csv(file="/Landmarks_Dasypus_novemcinctus_SM_BMNH-24-12-12-
73.pts",skip=2,header=F,sep="",row.names=1)
Tatou36<-read.csv(file="/Landmarks_Dasypus_novemcinctus_SM_BMNH-26-1-12-
21.pts",skip=2,header=F,sep="",row.names=1)
Tatou37<-read.csv(file="/Landmarks_Dasypus_novemcinctus_SM_BMNH-26-1-12-
22.pts",skip=2,header=F,sep="",row.names=1)
Tatou38<-read.csv(file="/Landmarks_Dasypus_novemcinctus_SM_BMNH-28-10-11-
53.pts",skip=2,header=F,sep="",row.names=1)
Tatou39<-read.csv(file="/Landmarks_Dasypus_novemcinctus_SM_BMNH-28-10-11-
54.pts",skip=2,header=F,sep="",row.names=1)
Tatou40<-read.csv(file="/Landmarks_Dasypus_novemcinctus_SM_BMNH-82-9-30-
31.pts",skip=2,header=F,sep="",row.names=1)
Tatou41<-read.csv(file="/Landmarks_Dasypus_novemcinctus_SM_BMNH-82-9-30-
32.pts",skip=2,header=F,sep="",row.names=1)
Tatou42<-read.csv(file="/Landmarks_Dasypus_novemcinctus_SM_BMNH-93-1-1-
17.pts",skip=2,header=F,sep="",row.names=1)
Tatou43<-read.csv(file="/Landmarks_Dasypus_novemcinctus_SM_LSU-
12306.pts",skip=2,header=F,sep="",row.names=1)

```

```
Tatou44<-read.csv(file="/Landmarks_Dasypus_novemcinctus_SM_LSU-
15920.pts",skip=2,header=F,sep="",row.names=1)
Tatou45<-read.csv(file="/Landmarks_Dasypus_novemcinctus_SM_MHNG-
838.081.pts",skip=2,header=F,sep="",row.names=1)
Tatou46<-read.csv(file="/Landmarks_Dasypus_novemcinctus_SM_MHNG-
964.067.pts",skip=2,header=F,sep="",row.names=1)
Tatou47<-read.csv(file="/Landmarks_Dasypus_novemcinctus_SM_MNHN-2006-
565.pts",skip=2,header=F,sep="",row.names=1)
Tatou48<-read.csv(file="/Landmarks_Dasypus_novemcinctus_SM_USNM-
406700.pts",skip=2,header=F,sep="",row.names=1)
```

```
array.lm<-bindArr(as.matrix(Tatou1),as.matrix(Tatou2),as.matrix(Tatou3),
as.matrix(Tatou4),as.matrix(Tatou5),as.matrix(Tatou6),
as.matrix(Tatou7),as.matrix(Tatou8),as.matrix(Tatou9),
as.matrix(Tatou10),as.matrix(Tatou11),as.matrix(Tatou12),
as.matrix(Tatou13),as.matrix(Tatou14),as.matrix(Tatou15),
as.matrix(Tatou16),as.matrix(Tatou17),as.matrix(Tatou18),
as.matrix(Tatou19),as.matrix(Tatou20),as.matrix(Tatou21),
as.matrix(Tatou22),as.matrix(Tatou23),as.matrix(Tatou24),
as.matrix(Tatou25),as.matrix(Tatou26),as.matrix(Tatou27),
as.matrix(Tatou28),as.matrix(Tatou29),as.matrix(Tatou30),
as.matrix(Tatou31),as.matrix(Tatou32),as.matrix(Tatou33),
as.matrix(Tatou34),as.matrix(Tatou35),as.matrix(Tatou36),
as.matrix(Tatou37),as.matrix(Tatou38),as.matrix(Tatou39),
as.matrix(Tatou40),as.matrix(Tatou41),as.matrix(Tatou42),
as.matrix(Tatou43),as.matrix(Tatou44),as.matrix(Tatou45),
as.matrix(Tatou46),as.matrix(Tatou47),as.matrix(Tatou48),along=3)
```

```
dimnames(array.lm)[[3]]<-c("Tatou1","Tatou2","Tatou3","Tatou4","Tatou5",
"Tatou6","Tatou7","Tatou8","Tatou9","Tatou10",
"Tatou11","Tatou12","Tatou13","Tatou14","Tatou15",
"Tatou16","Tatou17","Tatou18","Tatou19","Tatou20",
"Tatou21","Tatou22","Tatou23","Tatou24","Tatou25",
"Tatou26","Tatou27","Tatou28","Tatou29","Tatou30",
"Tatou31","Tatou32","Tatou33","Tatou34","Tatou35",
"Tatou36","Tatou37","Tatou38","Tatou39","Tatou40",
"Tatou41","Tatou42","Tatou43","Tatou44","Tatou45",
"Tatou46","Tatou47","Tatou48")
```

```
##### CabassousN
```

```
Tatou1<-
read.csv(file="/Landmarks_Cabassous_unicinctus_AMNH_14862.landmarkAscii.pts",skip=2,header=F,sep="",
row.names=1)
Tatou2<-
read.csv(file="/Landmarks_Cabassous_unicinctus_AMNH_14863.landmarkAscii.pts",skip=2,header=F,sep="",
row.names=1)
Tatou3<-
read.csv(file="/Landmarks_Cabassous_unicinctus_AMNH_23441.landmarkAscii.pts",skip=2,header=F,sep="",
row.names=1)
Tatou4<-
read.csv(file="/Landmarks_Cabassous_unicinctus_AMNH_136256.landmarkAscii.pts",skip=2,header=F,sep=""
,row.names=1)
Tatou5<-
read.csv(file="/Landmarks_Cabassous_unicinctus_AMNH_60636.landmarkAscii.pts",skip=2,header=F,sep="",
row.names=1)
Tatou6<-
read.csv(file="/Landmarks_Cabassous_unicinctus_AMNH_74113.landmarkAscii.pts",skip=2,header=F,sep="",
row.names=1)
```

```

Tatou7<-
read.csv(file="/Landmarks_Cabassous_unicinctus_AMNH_98459.landmarkAscii.pts",skip=2,header=F,sep="",
row.names=1)
Tatou8<-
read.csv(file="/Landmarks_Cabassous_unicinctus_AMNH_133386.landmarkAscii.pts",skip=2,header=F,sep=""
,row.names=1)
Tatou9<-
read.csv(file="/Landmarks_Cabassous_unicinctus_AMNH_137196.landmarkAscii.pts",skip=2,header=F,sep=""
,row.names=1)
Tatou10<-read.csv(file="/Landmarks_Cabassous_unicinctus_BMNH_3-7-12-
2.landmarkAscii.pts",skip=2,header=F,sep="",row.names=1)
Tatou11<-read.csv(file="/Landmarks_Cabassous_unicinctus_BMNH_7-6-15-
9.landmarkAscii.pts",skip=2,header=F,sep="",row.names=1)
Tatou12<-read.csv(file="/Landmarks_Cabassous_unicinctus_BMNH_16-6-5-
36.landmarkAscii.pts",skip=2,header=F,sep="",row.names=1)
Tatou13<-read.csv(file="/Landmarks_Cabassous_unicinctus_BMNH_78-12-13-
1.landmarkAscii.pts",skip=2,header=F,sep="",row.names=1)
Tatou14<-read.csv(file="/Landmarks_Cabassous_unicinctus_MNHN_1917-
159.landmarkAscii.pts",skip=2,header=F,sep="",row.names=1)
Tatou15<-read.csv(file="/Landmarks_Cabassous_unicinctus_MNHN_1953-
457.landmarkAscii.pts",skip=2,header=F,sep="",row.names=1)
Tatou16<-read.csv(file="/Landmarks_Cabassous_unicinctus_MNHN_1998-
2255.landmarkAscii.pts",skip=2,header=F,sep="",row.names=1)
Tatou17<-read.csv(file="/Landmarks_Cabassous_unicinctus_MNHN_1999-
1044.landmarkAscii.pts",skip=2,header=F,sep="",row.names=1)
Tatou18<-read.csv(file="/Landmarks_Cabassous_unicinctus_MNHN_2007-
374.landmarkAscii.pts",skip=2,header=F,sep="",row.names=1)
Tatou19<-
read.csv(file="/Landmarks_Cabassous_unicinctus_MVZ_155192.landmarkAscii.pts",skip=2,header=F,sep="",r
ow.names=1)
Tatou20<-
read.csv(file="/Landmarks_Cabassous_unicinctus_RMNH_26326.B.landmarkAscii.pts",skip=2,header=F,sep=""
,row.names=1)
Tatou21<-
read.csv(file="/Landmarks_Cabassous_unicinctus_V_3455.landmarkAscii.pts",skip=2,header=F,sep=""
,rownames=1)

array.lm<-bindArr(as.matrix(Tatou1),as.matrix(Tatou2),as.matrix(Tatou3),
as.matrix(Tatou4),as.matrix(Tatou5),as.matrix(Tatou6),
as.matrix(Tatou7),as.matrix(Tatou8),as.matrix(Tatou9),
as.matrix(Tatou10),as.matrix(Tatou11),as.matrix(Tatou12),
as.matrix(Tatou13),as.matrix(Tatou14),as.matrix(Tatou15),
as.matrix(Tatou16),as.matrix(Tatou17),as.matrix(Tatou18),
as.matrix(Tatou19),as.matrix(Tatou20),as.matrix(Tatou21),along=3)

dimnames(array.lm)[[3]]<-c("Tatou1","Tatou2","Tatou3","Tatou4","Tatou5",
"Tatou6","Tatou7","Tatou8","Tatou9","Tatou10",
"Tatou11","Tatou12","Tatou13","Tatou14","Tatou15",
"Tatou16","Tatou17","Tatou18","Tatou19","Tatou20",
"Tatou21")

##### CabassousNS
Tatou1<-
read.csv(file="/Landmarks_Cabassous_unicinctus_AMNH_14862.landmarkAscii.pts",skip=2,header=F,sep="",
row.names=1)
Tatou2<-
read.csv(file="/Landmarks_Cabassous_unicinctus_AMNH_14863.landmarkAscii.pts",skip=2,header=F,sep=""
,row.names=1)

```

```

Tatou3<-
read.csv(file="/Landmarks_Cabassous_unicinctus_AMNH_23441.landmarkAscii.pts",skip=2,header=F,sep="",
row.names=1)
Tatou4<-
read.csv(file="/Landmarks_Cabassous_unicinctus_AMNH_136256.landmarkAscii.pts",skip=2,header=F,sep="",
,row.names=1)
Tatou5<-
read.csv(file="/Landmarks_Cabassous_unicinctus_AMNH_60636.landmarkAscii.pts",skip=2,header=F,sep="",
row.names=1)
Tatou6<-
read.csv(file="/Landmarks_Cabassous_unicinctus_AMNH_37546.landmarkAscii.pts",skip=2,header=F,sep="",
row.names=1)
Tatou7<-
read.csv(file="/Landmarks_Cabassous_unicinctus_AMNH_74113.landmarkAscii.pts",skip=2,header=F,sep="",
row.names=1)
Tatou8<-
read.csv(file="/Landmarks_Cabassous_unicinctus_AMNH_98459.landmarkAscii.pts",skip=2,header=F,sep="",
row.names=1)
Tatou9<-
read.csv(file="/Landmarks_Cabassous_unicinctus_AMNH_133318.landmarkAscii.pts",skip=2,header=F,sep="",
,row.names=1)
Tatou10<-
read.csv(file="/Landmarks_Cabassous_unicinctus_AMNH_133334.landmarkAscii.pts",skip=2,header=F,sep="",
,row.names=1)
Tatou11<-
read.csv(file="/Landmarks_Cabassous_unicinctus_AMNH_133335.landmarkAscii.pts",skip=2,header=F,sep="",
,row.names=1)
Tatou12<-
read.csv(file="/Landmarks_Cabassous_unicinctus_AMNH_133336.landmarkAscii.pts",skip=2,header=F,sep="",
,row.names=1)
Tatou13<-
read.csv(file="/Landmarks_Cabassous_unicinctus_AMNH_133386.landmarkAscii.pts",skip=2,header=F,sep="",
,row.names=1)
Tatou14<-
read.csv(file="/Landmarks_Cabassous_unicinctus_AMNH_137196.landmarkAscii.pts",skip=2,header=F,sep="",
,row.names=1)
Tatou15<-read.csv(file="/Landmarks_Cabassous_unicinctus_BMNH_3-7-12-
2.landmarkAscii.pts",skip=2,header=F,sep="",row.names=1)
Tatou16<-read.csv(file="/Landmarks_Cabassous_unicinctus_BMNH_7-6-15-
9.landmarkAscii.pts",skip=2,header=F,sep="",row.names=1)
Tatou17<-read.csv(file="/Landmarks_Cabassous_unicinctus_BMNH_16-6-5-
36.landmarkAscii.pts",skip=2,header=F,sep="",row.names=1)
Tatou18<-read.csv(file="/Landmarks_Cabassous_unicinctus_BMNH_71-
2503.landmarkAscii.pts",skip=2,header=F,sep="",row.names=1)
Tatou19<-read.csv(file="/Landmarks_Cabassous_unicinctus_BMNH_78-12-13-
1.landmarkAscii.pts",skip=2,header=F,sep="",row.names=1)
Tatou20<-read.csv(file="/Landmarks_Cabassous_unicinctus_MNHN_1917-
159.landmarkAscii.pts",skip=2,header=F,sep="",row.names=1)
Tatou21<-read.csv(file="/Landmarks_Cabassous_unicinctus_MNHN_1953-
457.landmarkAscii.pts",skip=2,header=F,sep="",row.names=1)
Tatou22<-read.csv(file="/Landmarks_Cabassous_unicinctus_MNHN_1998-
2255.landmarkAscii.pts",skip=2,header=F,sep="",row.names=1)
Tatou23<-read.csv(file="/Landmarks_Cabassous_unicinctus_MNHN_1999-
1044.landmarkAscii.pts",skip=2,header=F,sep="",row.names=1)
Tatou24<-read.csv(file="/Landmarks_Cabassous_unicinctus_MNHN_2007-
374.landmarkAscii.pts",skip=2,header=F,sep="",row.names=1)
Tatou25<-
read.csv(file="/Landmarks_Cabassous_unicinctus_MVZ_155192.landmarkAscii.pts",skip=2,header=F,sep="",r
ow.names=1)

```

```

Tatou26<-
read.csv(file="/Landmarks_Cabassous_unicinctus_RMNH_26326.B.landmarkAscii.pts",skip=2,header=F,sep="
",row.names=1)
Tatou27<-
read.csv(file="/Landmarks_Cabassous_unicinctus_V_3455.landmarkAscii.pts",skip=2,header=F,sep="",row.na
mes=1)

array.lm<-bindArr(as.matrix(Tatou1),as.matrix(Tatou2),as.matrix(Tatou3),
as.matrix(Tatou4),as.matrix(Tatou5),as.matrix(Tatou6),
as.matrix(Tatou7),as.matrix(Tatou8),as.matrix(Tatou9),
as.matrix(Tatou10),as.matrix(Tatou11),as.matrix(Tatou12),
as.matrix(Tatou13),as.matrix(Tatou14),as.matrix(Tatou15),
as.matrix(Tatou16),as.matrix(Tatou17),as.matrix(Tatou18),
as.matrix(Tatou19),as.matrix(Tatou20),as.matrix(Tatou21),
as.matrix(Tatou22),as.matrix(Tatou23),as.matrix(Tatou24),
as.matrix(Tatou25),as.matrix(Tatou26),as.matrix(Tatou27),along=3)

dimnames(array.lm)[[3]]<-c("Tatou1","Tatou2","Tatou3","Tatou4","Tatou5",
"Tatou6","Tatou7","Tatou8","Tatou9","Tatou10",
"Tatou11","Tatou12","Tatou13","Tatou14","Tatou15",
"Tatou16","Tatou17","Tatou18","Tatou19","Tatou20",
"Tatou21","Tatou22","Tatou23","Tatou24","Tatou25",
"Tatou26","Tatou27")

##### Zaedyus
Tatou1<-
read.csv(file="/Landmarks_Zaedyus_pichiy_AMNH_17448.landmarkAscii.pts",skip=2,header=F,sep="",row.na
mes=1)
Tatou2<-
read.csv(file="/Landmarks_Zaedyus_pichiy_AMNH_25667.landmarkAscii.pts",skip=2,header=F,sep="",row.na
mes=1)
Tatou3<-
read.csv(file="/Landmarks_Zaedyus_pichiy_AMNH_25668.landmarkAscii.pts",skip=2,header=F,sep="",row.na
mes=1)
Tatou4<-
read.csv(file="/Landmarks_Zaedyus_pichiy_AMNH_94327.landmarkAscii.pts",skip=2,header=F,sep="",row.na
mes=1)
Tatou5<-read.csv(file="/Landmarks_Zaedyus_pichiy_BMNH_27-6-4-
56.landmarkAscii.pts",skip=2,header=F,sep="",row.names=1)
Tatou6<-read.csv(file="/Landmarks_Zaedyus_pichiy_BMNH_90-2-20-
7.landmarkAscii.pts",skip=2,header=F,sep="",row.names=1)
Tatou7<-read.csv(file="/Landmarks_Zaedyus_pichiy_BMNH_46-5-13-
17.landmarkAscii.pts",skip=2,header=F,sep="",row.names=1)
Tatou8<-read.csv(file="/Landmarks_Zaedyus_pichiy_BMNH_99-8-5-
10.landmarkAscii.pts",skip=2,header=F,sep="",row.names=1)
Tatou9<-read.csv(file="/Landmarks_Zaedyus_pichiy_BMNH_76-9-26-
14.landmarkAscii.pts",skip=2,header=F,sep="",row.names=1)
Tatou10<-read.csv(file="/Landmarks_Zaedyus_pichiy_BMNH_22-11-23-
1.landmarkAscii.pts",skip=2,header=F,sep="",row.names=1)
Tatou11<-
read.csv(file="/Landmarks_Zaedyus_pichiy_FMNH_1.landmarkAscii.pts",skip=2,header=F,sep="",row.names=
1)
Tatou12<-
read.csv(file="/Landmarks_Zaedyus_pichiy_FMNH_2.landmarkAscii.pts",skip=2,header=F,sep="",row.names=
1)
Tatou13<-
read.csv(file="/Landmarks_Zaedyus_pichiy_MHNG_1276.076.landmarkAscii.pts",skip=2,header=F,sep="",ro
w.names=1)

```

```

Tatou14<-
read.csv(file="/Landmarks_Zaedyus_pichiy_MHNG_1627.053.landmarkAscii.pts",skip=2,header=F,sep="",row.names=1)
Tatou15<-read.csv(file="/Landmarks_Zaedyus_pichiy_MNHN_1917-135.landmarkAscii.pts",skip=2,header=F,sep="",row.names=1)
Tatou16<-read.csv(file="/Landmarks_Zaedyus_pichiy_MNHN_2007-382.landmarkAscii.pts",skip=2,header=F,sep="",row.names=1)
Tatou17<-read.csv(file="/Landmarks_Zaedyus_pichiy_MNHN_1897-446.landmarkAscii.pts",skip=2,header=F,sep="",row.names=1)
Tatou18<-read.csv(file="/Landmarks_Zaedyus_pichiy_MNHN_1897-440.landmarkAscii.pts",skip=2,header=F,sep="",row.names=1)
Tatou19<-read.csv(file="/Landmarks_Zaedyus_pichiy_MNHN_1883-158.landmarkAscii.pts",skip=2,header=F,sep="",row.names=1)
Tatou20<-read.csv(file="/Landmarks_Zaedyus_pichiy_MNHN_1897-445.landmarkAscii.pts",skip=2,header=F,sep="",row.names=1)
Tatou21<-read.csv(file="/Landmarks_Zaedyus_pichiy_MNHN_1897-472.landmarkAscii.pts",skip=2,header=F,sep="",row.names=1)
Tatou22<-read.csv(file="/Landmarks_Zaedyus_pichiy_MNHN_1897-456.landmarkAscii.pts",skip=2,header=F,sep="",row.names=1)
Tatou23<-read.csv(file="/Landmarks_Zaedyus_pichiy_MNHN_1897-450.landmarkAscii.pts",skip=2,header=F,sep="",row.names=1)
Tatou24<-read.csv(file="/Landmarks_Zaedyus_pichiy_MNHN_1897-468.landmarkAscii.pts",skip=2,header=F,sep="",row.names=1)
Tatou25<-read.csv(file="/Landmarks_Zaedyus_pichiy_MNHN_1897-470.landmarkAscii.pts",skip=2,header=F,sep="",row.names=1)
Tatou26<-read.csv(file="/Landmarks_Zaedyus_pichiy_MNHN_1897-447.landmarkAscii.pts",skip=2,header=F,sep="",row.names=1)
Tatou27<-read.csv(file="/Landmarks_Zaedyus_pichiy_MNHN_1897-442.landmarkAscii.pts",skip=2,header=F,sep="",row.names=1)
Tatou28<-read.csv(file="/Landmarks_Zaedyus_pichiy_MNHN_1897-449.landmarkAscii.pts",skip=2,header=F,sep="",row.names=1)
Tatou29<-read.csv(file="/Landmarks_Zaedyus_pichiy_MNHN_1897-457.landmarkAscii.pts",skip=2,header=F,sep="",row.names=1)
Tatou30<-read.csv(file="/Landmarks_Zaedyus_pichiy_MNHN_1897-454.landmarkAscii.pts",skip=2,header=F,sep="",row.names=1)
Tatou31<-read.csv(file="/Landmarks_Zaedyus_pichiy_MNHN_1897-1268.landmarkAscii.pts",skip=2,header=F,sep="",row.names=1)
Tatou32<-read.csv(file="/Landmarks_Zaedyus_pichiy_MNHN_1897-461.landmarkAscii.pts",skip=2,header=F,sep="",row.names=1)
Tatou33<-read.csv(file="/Landmarks_Zaedyus_pichiy_MNHN_1897-452.landmarkAscii.pts",skip=2,header=F,sep="",row.names=1)
Tatou34<-read.csv(file="/Landmarks_Zaedyus_pichiy_MNHN_1897-473.landmarkAscii.pts",skip=2,header=F,sep="",row.names=1)
Tatou35<-read.csv(file="/Landmarks_Zaedyus_pichiy_MNHN_1971-1045.landmarkAscii.pts",skip=2,header=F,sep="",row.names=1)
Tatou36<-read.csv(file="/Landmarks_Zaedyus_pichiy_MNHN_2007-369.landmarkAscii.pts",skip=2,header=F,sep="",row.names=1)
Tatou37<-read.csv(file="/Landmarks_Zaedyus_pichiy_MNHN_2007-375.landmarkAscii.pts",skip=2,header=F,sep="",row.names=1)
Tatou38<-
read.csv(file="/Landmarks_Zaedyus_pichiy_ZMB_46103.landmarkAscii.pts",skip=2,header=F,sep="",row.names=1)
Tatou39<-
read.csv(file="/Landmarks_Zaedyus_pichiy_ZMB_46104.landmarkAscii.pts",skip=2,header=F,sep="",row.names=1)
Tatou40<-
read.csv(file="/Landmarks_Zaedyus_pichiy_ZMB_48626.landmarkAscii.pts",skip=2,header=F,sep="",row.names=1)

```

```
Tatou41<-
read.csv(file="/Landmarks_Zaedyus_pichiy_ZMB_48627.landmarkAscii.pts",skip=2,header=F,sep="",row.names=1)
Tatou42<-
read.csv(file="/Landmarks_Zaedyus_pichiy_ZMB_49038.landmarkAscii.pts",skip=2,header=F,sep="",row.names=1)
Tatou43<-
read.csv(file="/Landmarks_Zaedyus_pichiy_ZMB_85890.landmarkAscii.pts",skip=2,header=F,sep="",row.names=1)
```

```
array.lm<-bindArr(as.matrix(Tatou1),as.matrix(Tatou2),as.matrix(Tatou3),
  as.matrix(Tatou4),as.matrix(Tatou5),as.matrix(Tatou6),
  as.matrix(Tatou7),as.matrix(Tatou8),as.matrix(Tatou9),
  as.matrix(Tatou10),as.matrix(Tatou11),as.matrix(Tatou12),
  as.matrix(Tatou13),as.matrix(Tatou14),as.matrix(Tatou15),
  as.matrix(Tatou16),as.matrix(Tatou17),as.matrix(Tatou18),
  as.matrix(Tatou19),as.matrix(Tatou20),as.matrix(Tatou21),
  as.matrix(Tatou22),as.matrix(Tatou23),as.matrix(Tatou24),
  as.matrix(Tatou25),as.matrix(Tatou26),as.matrix(Tatou27),
  as.matrix(Tatou28),as.matrix(Tatou29),as.matrix(Tatou30),
  as.matrix(Tatou31),as.matrix(Tatou32),as.matrix(Tatou33),
  as.matrix(Tatou34),as.matrix(Tatou35),as.matrix(Tatou36),
  as.matrix(Tatou37),as.matrix(Tatou38),as.matrix(Tatou39),
  as.matrix(Tatou40),as.matrix(Tatou41),as.matrix(Tatou42),
  as.matrix(Tatou43),along=3)
```

```
dimnames(array.lm)[[3]]<-c("Tatou1","Tatou2","Tatou3","Tatou4","Tatou5",
  "Tatou6","Tatou7","Tatou8","Tatou9","Tatou10",
  "Tatou11","Tatou12","Tatou13","Tatou14","Tatou15",
  "Tatou16","Tatou17","Tatou18","Tatou19","Tatou20",
  "Tatou21","Tatou22","Tatou23","Tatou24","Tatou25",
  "Tatou26","Tatou27","Tatou28","Tatou29","Tatou30",
  "Tatou31","Tatou32","Tatou33","Tatou34","Tatou35",
  "Tatou36","Tatou37","Tatou38","Tatou39","Tatou40",
  "Tatou41","Tatou42","Tatou43")
```

```
##### SAMPLE Static level
```

```
##### Dasypus
```

```
Tatou1<-read.csv(file="/Landmarks_Dasypus_novemcinctus_SM_AMNH-365.pts",skip=2,header=F,sep="",row.names=1)
Tatou2<-read.csv(file="/Landmarks_Dasypus_novemcinctus_SM_AMNH-75896.pts",skip=2,header=F,sep="",row.names=1)
Tatou3<-read.csv(file="/Landmarks_Dasypus_novemcinctus_SM_AMNH-93118.pts",skip=2,header=F,sep="",row.names=1)
Tatou4<-read.csv(file="/Landmarks_Dasypus_novemcinctus_SM_AMNH-93735.pts",skip=2,header=F,sep="",row.names=1)
Tatou5<-read.csv(file="/Landmarks_Dasypus_novemcinctus_SM_AMNH-133329.pts",skip=2,header=F,sep="",row.names=1)
Tatou6<-read.csv(file="/Landmarks_Dasypus_novemcinctus_SM_AMNH-133330.pts",skip=2,header=F,sep="",row.names=1)
Tatou7<-read.csv(file="/Landmarks_Dasypus_novemcinctus_SM_AMNH-133338.pts",skip=2,header=F,sep="",row.names=1)
Tatou8<-read.csv(file="/Landmarks_Dasypus_novemcinctus_SM_AMNH-133342.pts",skip=2,header=F,sep="",row.names=1)
Tatou9<-read.csv(file="/Landmarks_Dasypus_novemcinctus_SM_AMNH-133397.pts",skip=2,header=F,sep="",row.names=1)
Tatou10<-read.csv(file="/Landmarks_Dasypus_novemcinctus_SM_AMNH-136252.pts",skip=2,header=F,sep="",row.names=1)
Tatou11<-read.csv(file="/Landmarks_Dasypus_novemcinctus_SM_AMNH-205726.pts",skip=2,header=F,sep="",row.names=1)
```

```
Tatou12<-read.csv(file="/Landmarks_Dasypus_novemcinctus_SM_AMNH-
205727.pts",skip=2,header=F,sep="",row.names=1)
Tatou13<-read.csv(file="/Landmarks_Dasypus_novemcinctus_SM_AMNH-
211668.pts",skip=2,header=F,sep="",row.names=1)
Tatou14<-read.csv(file="/Landmarks_Dasypus_novemcinctus_SM_AMNH-
262658.pts",skip=2,header=F,sep="",row.names=1)
Tatou15<-read.csv(file="/Landmarks_Dasypus_novemcinctus_SM_AMNH-
263287.pts",skip=2,header=F,sep="",row.names=1)
Tatou16<-read.csv(file="/Landmarks_Dasypus_novemcinctus_SM_BMNH-1-2-1-
34.pts",skip=2,header=F,sep="",row.names=1)
Tatou17<-read.csv(file="/Landmarks_Dasypus_novemcinctus_SM_BMNH-1-6-6-
84.pts",skip=2,header=F,sep="",row.names=1)
Tatou18<-read.csv(file="/Landmarks_Dasypus_novemcinctus_SM_BMNH-3-7-7-
146.pts",skip=2,header=F,sep="",row.names=1)
Tatou19<-read.csv(file="/Landmarks_Dasypus_novemcinctus_SM_BMNH-3-7-7-
150.pts",skip=2,header=F,sep="",row.names=1)
Tatou20<-read.csv(file="/Landmarks_Dasypus_novemcinctus_SM_BMNH-3-9-4-
102.pts",skip=2,header=F,sep="",row.names=1)
Tatou21<-read.csv(file="/Landmarks_Dasypus_novemcinctus_SM_BMNH-11-10-27-
3.pts",skip=2,header=F,sep="",row.names=1)
Tatou22<-read.csv(file="/Landmarks_Dasypus_novemcinctus_SM_BMNH-14-4-25-
86.pts",skip=2,header=F,sep="",row.names=1)
Tatou23<-read.csv(file="/Landmarks_Dasypus_novemcinctus_SM_BMNH-24-12-12-
73.pts",skip=2,header=F,sep="",row.names=1)
Tatou24<-read.csv(file="/Landmarks_Dasypus_novemcinctus_SM_BMNH-26-1-12-
21.pts",skip=2,header=F,sep="",row.names=1)
Tatou25<-read.csv(file="/Landmarks_Dasypus_novemcinctus_SM_BMNH-26-1-12-
22.pts",skip=2,header=F,sep="",row.names=1)
Tatou26<-read.csv(file="/Landmarks_Dasypus_novemcinctus_SM_BMNH-28-10-11-
53.pts",skip=2,header=F,sep="",row.names=1)
Tatou27<-read.csv(file="/Landmarks_Dasypus_novemcinctus_SM_BMNH-28-10-11-
54.pts",skip=2,header=F,sep="",row.names=1)
Tatou28<-read.csv(file="/Landmarks_Dasypus_novemcinctus_SM_BMNH-82-9-30-
31.pts",skip=2,header=F,sep="",row.names=1)
Tatou29<-read.csv(file="/Landmarks_Dasypus_novemcinctus_SM_BMNH-82-9-30-
32.pts",skip=2,header=F,sep="",row.names=1)
Tatou30<-read.csv(file="/Landmarks_Dasypus_novemcinctus_SM_BMNH-93-1-1-
17.pts",skip=2,header=F,sep="",row.names=1)
Tatou31<-read.csv(file="/Landmarks_Dasypus_novemcinctus_SM_LSU-
12306.pts",skip=2,header=F,sep="",row.names=1)
Tatou32<-read.csv(file="/Landmarks_Dasypus_novemcinctus_SM_MHNG-
838.081.pts",skip=2,header=F,sep="",row.names=1)
Tatou33<-read.csv(file="/Landmarks_Dasypus_novemcinctus_SM_MNHN-2006-
565.pts",skip=2,header=F,sep="",row.names=1)
```

```
array.lm<-bindArr(as.matrix(Tatou1),as.matrix(Tatou2),as.matrix(Tatou3),
as.matrix(Tatou4),as.matrix(Tatou5),as.matrix(Tatou6),
as.matrix(Tatou7),as.matrix(Tatou8),as.matrix(Tatou9),
as.matrix(Tatou10),as.matrix(Tatou11),as.matrix(Tatou12),
as.matrix(Tatou13),as.matrix(Tatou14),as.matrix(Tatou15),
as.matrix(Tatou16),as.matrix(Tatou17),as.matrix(Tatou18),
as.matrix(Tatou19),as.matrix(Tatou20),as.matrix(Tatou21),
as.matrix(Tatou22),as.matrix(Tatou23),as.matrix(Tatou24),
as.matrix(Tatou25),as.matrix(Tatou26),as.matrix(Tatou27),
as.matrix(Tatou28),as.matrix(Tatou29),as.matrix(Tatou30),
as.matrix(Tatou31),as.matrix(Tatou32),as.matrix(Tatou33),along=3)
```

```
dimnames(array.lm)[[3]]<-c("Tatou1","Tatou2","Tatou3","Tatou4","Tatou5",
"Tatou6","Tatou7","Tatou8","Tatou9","Tatou10",
"Tatou11","Tatou12","Tatou13","Tatou14","Tatou15",
```

```
"Tatou16", "Tatou17", "Tatou18", "Tatou19", "Tatou20",
"Tatou21", "Tatou22", "Tatou23", "Tatou24", "Tatou25",
"Tatou26", "Tatou27", "Tatou28", "Tatou29", "Tatou30",
"Tatou31", "Tatou32", "Tatou33")
```

```
##### CabassousN
```

```
Tatou1<-
read.csv(file="/Landmarks_Cabassous_unicinctus_AMNH_14862.landmarkAscii.pts",skip=2,header=F,sep="",
row.names=1)
Tatou2<-
read.csv(file="/Landmarks_Cabassous_unicinctus_AMNH_23441.landmarkAscii.pts",skip=2,header=F,sep="",
row.names=1)
Tatou3<-
read.csv(file="/Landmarks_Cabassous_unicinctus_AMNH_136256.landmarkAscii.pts",skip=2,header=F,sep="",
,row.names=1)
Tatou4<-
read.csv(file="/Landmarks_Cabassous_unicinctus_AMNH_60636.landmarkAscii.pts",skip=2,header=F,sep="",
row.names=1)
Tatou5<-
read.csv(file="/Landmarks_Cabassous_unicinctus_AMNH_74113.landmarkAscii.pts",skip=2,header=F,sep="",
row.names=1)
Tatou6<-
read.csv(file="/Landmarks_Cabassous_unicinctus_AMNH_137196.landmarkAscii.pts",skip=2,header=F,sep="",
,row.names=1)
Tatou7<-read.csv(file="/Landmarks_Cabassous_unicinctus_BMNH_7-6-15-
9.landmarkAscii.pts",skip=2,header=F,sep="",row.names=1)
Tatou8<-read.csv(file="/Landmarks_Cabassous_unicinctus_BMNH_78-12-13-
1.landmarkAscii.pts",skip=2,header=F,sep="",row.names=1)
Tatou9<-read.csv(file="/Landmarks_Cabassous_unicinctus_MNHN_1917-
159.landmarkAscii.pts",skip=2,header=F,sep="",row.names=1)
Tatou10<-read.csv(file="/Landmarks_Cabassous_unicinctus_MNHN_1953-
457.landmarkAscii.pts",skip=2,header=F,sep="",row.names=1)
Tatou11<-read.csv(file="/Landmarks_Cabassous_unicinctus_MNHN_1998-
2255.landmarkAscii.pts",skip=2,header=F,sep="",row.names=1)
Tatou12<-read.csv(file="/Landmarks_Cabassous_unicinctus_MNHN_1999-
1044.landmarkAscii.pts",skip=2,header=F,sep="",row.names=1)
Tatou13<-
read.csv(file="/Landmarks_Cabassous_unicinctus_MVZ_155192.landmarkAscii.pts",skip=2,header=F,sep="",r
ow.names=1)
Tatou14<-
read.csv(file="/Landmarks_Cabassous_unicinctus_V_3455.landmarkAscii.pts",skip=2,header=F,sep="",row.na
mes=1)
```

```
array.lm<-bindArr(as.matrix(Tatou1),as.matrix(Tatou2),as.matrix(Tatou3),
as.matrix(Tatou4),as.matrix(Tatou5),as.matrix(Tatou6),
as.matrix(Tatou7),as.matrix(Tatou8),as.matrix(Tatou9),
as.matrix(Tatou10),as.matrix(Tatou11),as.matrix(Tatou12),
as.matrix(Tatou13),as.matrix(Tatou14),along=3)
```

```
dimnames(array.lm)[[3]]<-c("Tatou1", "Tatou2", "Tatou3", "Tatou4", "Tatou5",
"Tatou6", "Tatou7", "Tatou8", "Tatou9", "Tatou10",
"Tatou11", "Tatou12", "Tatou13", "Tatou14")
```

```
##### CabassousNS
```

```
Tatou1<-
read.csv(file="/Landmarks_Cabassous_unicinctus_AMNH_14862.landmarkAscii.pts",skip=2,header=F,sep="",
row.names=1)
Tatou2<-
read.csv(file="/Landmarks_Cabassous_unicinctus_AMNH_23441.landmarkAscii.pts",skip=2,header=F,sep="",
row.names=1)
```

```

Tatou3<-
read.csv(file="/Landmarks_Cabassous_unicinctus_AMNH_136256.landmarkAscii.pts",skip=2,header=F,sep=""
,row.names=1)
Tatou4<-
read.csv(file="/Landmarks_Cabassous_unicinctus_AMNH_60636.landmarkAscii.pts",skip=2,header=F,sep=""
,row.names=1)
Tatou5<-
read.csv(file="/Landmarks_Cabassous_unicinctus_AMNH_74113.landmarkAscii.pts",skip=2,header=F,sep=""
,row.names=1)
Tatou6<-
read.csv(file="/Landmarks_Cabassous_unicinctus_AMNH_133318.landmarkAscii.pts",skip=2,header=F,sep=""
,row.names=1)
Tatou7<-
read.csv(file="/Landmarks_Cabassous_unicinctus_AMNH_137196.landmarkAscii.pts",skip=2,header=F,sep=""
,row.names=1)
Tatou8<-read.csv(file="/Landmarks_Cabassous_unicinctus_BMNH_7-6-15-
9.landmarkAscii.pts",skip=2,header=F,sep=""
,row.names=1)
Tatou9<-read.csv(file="/Landmarks_Cabassous_unicinctus_BMNH_71-
2503.landmarkAscii.pts",skip=2,header=F,sep=""
,row.names=1)
Tatou10<-read.csv(file="/Landmarks_Cabassous_unicinctus_BMNH_78-12-13-
1.landmarkAscii.pts",skip=2,header=F,sep=""
,row.names=1)
Tatou11<-read.csv(file="/Landmarks_Cabassous_unicinctus_MNHN_1917-
159.landmarkAscii.pts",skip=2,header=F,sep=""
,row.names=1)
Tatou12<-read.csv(file="/Landmarks_Cabassous_unicinctus_MNHN_1953-
457.landmarkAscii.pts",skip=2,header=F,sep=""
,row.names=1)
Tatou13<-read.csv(file="/Landmarks_Cabassous_unicinctus_MNHN_1998-
2255.landmarkAscii.pts",skip=2,header=F,sep=""
,row.names=1)
Tatou14<-read.csv(file="/Landmarks_Cabassous_unicinctus_MNHN_1999-
1044.landmarkAscii.pts",skip=2,header=F,sep=""
,row.names=1)
Tatou15<-
read.csv(file="/Landmarks_Cabassous_unicinctus_MVZ_155192.landmarkAscii.pts",skip=2,header=F,sep=""
,row.names=1)
Tatou16<-
read.csv(file="/Landmarks_Cabassous_unicinctus_V_3455.landmarkAscii.pts",skip=2,header=F,sep=""
,row.names=1)

array.lm<-bindArr(as.matrix(Tatou1),as.matrix(Tatou2),as.matrix(Tatou3),
as.matrix(Tatou4),as.matrix(Tatou5),as.matrix(Tatou6),
as.matrix(Tatou7),as.matrix(Tatou8),as.matrix(Tatou9),
as.matrix(Tatou10),as.matrix(Tatou11),as.matrix(Tatou12),
as.matrix(Tatou13),as.matrix(Tatou14),as.matrix(Tatou15),
as.matrix(Tatou16),along=3)

dimnames(array.lm)[[3]]<-c("Tatou1","Tatou2","Tatou3","Tatou4","Tatou5",
"Tatou6","Tatou7","Tatou8","Tatou9","Tatou10",
"Tatou11","Tatou12","Tatou13","Tatou14","Tatou15",
"Tatou16")

##### Zaedyus
Tatou1<-
read.csv(file="/Landmarks_Zaedyus_pichiy_AMNH_94327.landmarkAscii.pts",skip=2,header=F,sep=""
,row.names=1)
Tatou2<-read.csv(file="/Landmarks_Zaedyus_pichiy_BMNH_90-2-20-
7.landmarkAscii.pts",skip=2,header=F,sep=""
,row.names=1)
Tatou3<-read.csv(file="/Landmarks_Zaedyus_pichiy_BMNH_46-5-13-
17.landmarkAscii.pts",skip=2,header=F,sep=""
,row.names=1)
Tatou4<-read.csv(file="/Landmarks_Zaedyus_pichiy_BMNH_22-11-23-
1.landmarkAscii.pts",skip=2,header=F,sep=""
,row.names=1)

```

```

Tatou5<-
read.csv(file="/Landmarks_Zaedyus_pichiy_FMNH_2.landmarkAscii.pts",skip=2,header=F,sep="",row.names=
1)
Tatou6<-read.csv(file="/Landmarks_Zaedyus_pichiy_MNHN_1917-
135.landmarkAscii.pts",skip=2,header=F,sep="",row.names=1)
Tatou7<-read.csv(file="/Landmarks_Zaedyus_pichiy_MNHN_2007-
382.landmarkAscii.pts",skip=2,header=F,sep="",row.names=1)
Tatou8<-read.csv(file="/Landmarks_Zaedyus_pichiy_MNHN_1897-
446.landmarkAscii.pts",skip=2,header=F,sep="",row.names=1)
Tatou9<-read.csv(file="/Landmarks_Zaedyus_pichiy_MNHN_1897-
440.landmarkAscii.pts",skip=2,header=F,sep="",row.names=1)
Tatou10<-read.csv(file="/Landmarks_Zaedyus_pichiy_MNHN_1883-
158.landmarkAscii.pts",skip=2,header=F,sep="",row.names=1)
Tatou11<-read.csv(file="/Landmarks_Zaedyus_pichiy_MNHN_1897-
445.landmarkAscii.pts",skip=2,header=F,sep="",row.names=1)
Tatou12<-read.csv(file="/Landmarks_Zaedyus_pichiy_MNHN_1897-
472.landmarkAscii.pts",skip=2,header=F,sep="",row.names=1)
Tatou13<-read.csv(file="/Landmarks_Zaedyus_pichiy_MNHN_1897-
456.landmarkAscii.pts",skip=2,header=F,sep="",row.names=1)
Tatou14<-read.csv(file="/Landmarks_Zaedyus_pichiy_MNHN_1897-
468.landmarkAscii.pts",skip=2,header=F,sep="",row.names=1)
Tatou15<-read.csv(file="/Landmarks_Zaedyus_pichiy_MNHN_1897-
457.landmarkAscii.pts",skip=2,header=F,sep="",row.names=1)
Tatou16<-read.csv(file="/Landmarks_Zaedyus_pichiy_MNHN_1897-
454.landmarkAscii.pts",skip=2,header=F,sep="",row.names=1)
Tatou17<-read.csv(file="/Landmarks_Zaedyus_pichiy_MNHN_1897-
461.landmarkAscii.pts",skip=2,header=F,sep="",row.names=1)
Tatou18<-read.csv(file="/Landmarks_Zaedyus_pichiy_MNHN_1897-
452.landmarkAscii.pts",skip=2,header=F,sep="",row.names=1)
Tatou19<-read.csv(file="/Landmarks_Zaedyus_pichiy_MNHN_1971-
1045.landmarkAscii.pts",skip=2,header=F,sep="",row.names=1)
Tatou20<-
read.csv(file="/Landmarks_Zaedyus_pichiy_ZMB_46103.landmarkAscii.pts",skip=2,header=F,sep="",row.names=1)
Tatou21<-
read.csv(file="/Landmarks_Zaedyus_pichiy_ZMB_46104.landmarkAscii.pts",skip=2,header=F,sep="",row.names=1)
Tatou22<-
read.csv(file="/Landmarks_Zaedyus_pichiy_ZMB_48627.landmarkAscii.pts",skip=2,header=F,sep="",row.names=1)
Tatou23<-
read.csv(file="/Landmarks_Zaedyus_pichiy_ZMB_85890.landmarkAscii.pts",skip=2,header=F,sep="",row.names=1)

array.lm<-bindArr(as.matrix(Tatou1),as.matrix(Tatou2),as.matrix(Tatou3),
as.matrix(Tatou4),as.matrix(Tatou5),as.matrix(Tatou6),
as.matrix(Tatou7),as.matrix(Tatou8),as.matrix(Tatou9),
as.matrix(Tatou10),as.matrix(Tatou11),as.matrix(Tatou12),
as.matrix(Tatou13),as.matrix(Tatou14),as.matrix(Tatou15),
as.matrix(Tatou16),as.matrix(Tatou17),as.matrix(Tatou18),
as.matrix(Tatou19),as.matrix(Tatou20),as.matrix(Tatou21),
as.matrix(Tatou22),as.matrix(Tatou23),along=3)

dimnames(array.lm)[[3]]<-c("Tatou1","Tatou2","Tatou3","Tatou4","Tatou5",
"Tatou6","Tatou7","Tatou8","Tatou9","Tatou10",
"Tatou11","Tatou12","Tatou13","Tatou14","Tatou15",
"Tatou16","Tatou17","Tatou18","Tatou19","Tatou20",
"Tatou21","Tatou22","Tatou23")

```

```
#####
#####
##### data set treatment
#####
#####
#####

##### Landmark excess
array.lm<-array.lm[-131,,]
array.lm<-array.lm[-90,,]
array.lm<-array.lm[-89,,]
array.lm<-array.lm[-88,,]
array.lm<-array.lm[-87,,]
array.lm<-array.lm[-77,,]
array.lm<-array.lm[-76,,]
array.lm<-array.lm[-68,,]
array.lm<-array.lm[-67,,]
array.lm<-array.lm[-66,,]
array.lm<-array.lm[-65,,]
array.lm<-array.lm[-60,,]
array.lm<-array.lm[-59,,]
array.lm<-array.lm[-58,,]
array.lm<-array.lm[-57,,]
array.lm<-array.lm[-12,,]
array.lm<-array.lm[-11,,]

##### NA Estimation
array.lm2<-estimate.missing(array.lm, method="TPS")

##### Symmetrize
left<-
c(4,7,10,12,14,16,19,21,23,25,27,29,32,34,36,38,40,42,44,46,48,50,52,54,56,58,60,62,65,69,71,74,76,78,80,82,8
4,88,90,92,94,96,100,102,104,106,108,110,112,114)
right<-
c(3,6,9,11,13,15,18,20,22,24,26,28,31,33,35,37,39,41,43,45,47,49,51,53,55,57,59,61,64,68,70,73,75,77,79,81,83
,87,89,91,93,95,99,101,103,105,107,109,111,113)
pairedLM <- cbind(left,right)
sym <- symmetrize(array.lm2[,,],pairedLM)

#####
#####
##### Euclidean Distance Matrix Analysis #####
#####
#####

##### function Claude (2008)
FM<-function(M){as.matrix(dist(M))}

fm<-function(M){mat<-FM(M); mat[col(mat)<row(mat)]}

mEDMA<-function(A)
{n<-dim(A)[3];p<-dim(A)[1]; k<-dim(A)[2]
E<-matrix(NA,n,p*(p-1)/2)
for (i in 1:n){E[i,]<-(fm[A[,i]))^2}
Em<-apply(E,2,mean)
S<-((apply(t((t(E)-Em)^2),2,sum))/n)
if (k==2){omega<-(Em^2-S)^0.25}
if (k==3){omega<-(Em^2-1.5*S)^0.25}
Om<-diag(0,p)
Om[row(Om)>col(Om)]<-omega; Om<-t(Om)}
```

```
Om[row(Om)>col(Om)]<-omega
Om}
```

```
MDS<-function(mat, k)
{p<-dim(mat)[1]
C1<-diag(p)-1/p*matrix(1,p,p)
B<- -0.5*C1%*%mat^2%*%C1
eC<-eigen(B)
eve<-eC$eigenvectors
eva<-eC$values
MD<-matrix(NA, p, k)
for (i in 1:k)
{MD[,i]<-sqrt(eva[i])*eve[,i]}
MD}
```

```
mEDMA2<-function(A)
{k<-dim(A)[2]
Eu<-mEDMA(A)
M<-MDS(Eu,k)
list("M"=M, "FM"=FM(M))}
```

```
vEDMA<-function(A){
p<-dim(A)[1]
k<-dim(A)[2]; n<-dim(A)[3]
Bs<-array(NA, dim=c(p,p,n))
for (i in 1:n){
Cc<-apply(A[,i],2,mean)
Ac<-t(t(A[,i])-Cc)
Bs[,i]<-Ac%*%t(Ac)}
B<-apply(Bs, 1:2,mean)
M<-mEDMA2(A)$M
Ek<-(B-M%*%t(M))/k
Ek}
```

```
##### Problematic landmarks caused by weak distance
```

```
sym<-sym[-38,,]
sym<-sym[-37,,]
sym<-sym[-23,,]
sym<-sym[-22,,]
sym<-sym[-19,,]
sym<-sym[-18,,]
sym<-sym[-7,,]
sym<-sym[-6,,]
```

```
##### Eigenvector scaling and covar matrix from the Cheverud (1982) strategy
```

```
vcv_Pha_tri<-vEDMA(sym)
pca_Pha_tri<-eigen(vcv_Pha_tri)
loadings_Pha_tri<-pca_Pha_tri$eigenvectors
scaled_loadings_Pha_tri<-t(t(pca_Pha_tri$eigenvectors[,1:77]) * sqrt(pca_Pha_tri$values[1:77]))# take only positive
eigenvalues
scaled_euc_Pha_tri<-dist(scaled_loadings_Pha_tri)
fit_Pha_tri<-hclust(scaled_euc_Pha_tri,method="ward.D2")
plot(fit_Pha_tri)
Gap<-clusGap(x=scaled_loadings_Pha_tri, FUNcluster=hcut, K.max=20, B=9999, hc_method="ward.D2",
hc_func="hclust")
plot(Gap)
```

```
##### tree customization
```

```
fviz_dend(fit_Pha_tri, k = 3,cex = 0.5,
k_colors = c("#FF0000", "#FF6600", "#00FF00", "#FFFF33",
```

CHAPTER 4: SUPPORTING INFORMATION

```
"#33FFFF", "#0000FF", "#CC33CC", "#FF00CC"),
color_labels_by_k = TRUE,
ggtheme = theme_gray()) # change k from the Gap statistic

##### Check how the number of modules fit the tree
d_clust_Pha_tri <- Mclust(scaled_euc_Pha_tri, G=3)
d_clust_Pha_tri$classification # percentage in accordance with the tree

##### Find the modules on the tree using k and compute bootstrap
fit_boot_4_Pha_tri <-
clusterboot(scaled_euc_Pha_tri, B=9999, clustermethod="disthclustCBI", method="ward.D2", k=8)
rect.hclust(fit_Pha_tri, k = 8, border = "red")

#####
###
##### Distance Linear Analysis #####
#####
###

##### Define side (depending of the landmark dataset - use only one side and center reduce the amount of
regression)
left <-
c(4,7,10,12,14,16,19,21,23,25,27,29,32,34,36,38,40,42,44,46,48,50,52,54,56,58,60,62,65,69,71,74,76,78,80,82,8
4,88,90,92,94,96,100,102,104,106,108,110,112,114)
right <-
c(3,6,9,11,13,15,18,20,22,24,26,28,31,33,35,37,39,41,43,45,47,49,51,53,55,57,59,61,64,68,70,73,75,77,79,81,83
,87,89,91,93,95,99,101,103,105,107,109,111,113)
center <- c(1,2,5,8,17,30,63,66,67,72,85,86,97,98)
intersect(right, center)
length(c(left, center))

##### Distance Matrix
distArray <- array(NA, c(114, 114, 48)) # Matrix built with sample size
i=1
n=1
j=1
for(j in 1:48){ # Specimen number
  for(n in 1:nrow(sym[,j])){
    for(i in 1:nrow(sym[,j])){
      d <- sqrt(((sym[n,1,j]-sym[i,1,j])^2)+((sym[n,2,j]-sym[i,2,j])^2)+((sym[n,3,j]-sym[i,3,j])^2)) # compute each
distance with landmark coordinates
      distArray[n,i,j] <- d
    }
  }
}

##### Define couple list
listofcouple <- array(NA, c(2016, 2)) # 2016 = (length(c(left, center)) * (length(c(left, center)) - 1)) / 2
listofdistance <- array(NA, c(1, 2016, 48))
listofdistancegeo <- array(NA, c(1, 2016, 48))
k=1
geosize <- NA
for(k in 1:48){ # Specimen number
  adjacencymatrix <- graph_from_adjacency_matrix(distArray[c(left, center), c(left, center), k], mode = "lower",
weighted = T,
          diag = FALSE, add.colnames = NULL, add.rownames = NA)
  listedge <- get.edgelist(adjacencymatrix, names=TRUE)
  weightofedge <- E(adjacencymatrix)$weight
  listofdistance[,k] <- weightofedge
}
```

CHAPTER 4: SUPPORTING INFORMATION

```
listofdistancegeo[,k]<-listofdistance[,k]^(1/length(listofdistance[,1])) # Be careful for large data set, apply
power before product as in this study
geosize[k]<-prod(listofdistancegeo[,k]) # Otherwise use Claude's original function (2008)
}

adjacencymatrix2<-graph_from_adjacency_matrix(distArray[,1], mode = "lower", weighted = T,
      diag = FALSE, add.colnames = NULL, add.rownames = NA)
listedge2<-get.edgelist(adjacencymatrix2, names=TRUE)
listofcouple<-listedge2
listofcouplesub<-listofcouple[ listofcouple[,1]%in%c(left,center) & listofcouple[,2]%in%c(left,center), ]

##### Apply log shape ratio equation for standardization of distance list
listofdistanceStand<-array(NA,c(1,2016,48)) # Sample number
for(i in 1:48) {
  listofdistanceStand[,i]<-log(listofdistance[,i]/ geosize[i])
}

##### distarray log shape ratio
distanceStand<-array(NA,c(114,114,48)) # Sample number
k=1
for(k in 1:48){
  distanceStand[,k]<-log(distArray[,k]/geosize[k])
}

##### couple bind
listofcouplesimple<-listofcouplesub
couples<-NA
for(i in 1:nrow(listofcouplesimple)) {
  couples[i]<-paste(listofcouplesimple[i,1],"-",listofcouplesimple[i,2],sep="")
}
indexcouples<-combn(1:length(couples),2)

##### function for pre-computation of correlation indice r
varcouples<-function (y,x) {
  abs(cor(y,x))
}

##### r computation for each pair of distance
ldm1<-NA;ldm2<-NA;ldm3<-NA;ldm4<-NA;r<-NA
for(i in 1:2031120) {#ncol(indexcouples)} {
  indx<-listofcouplesimple[indexcouples[1,i],]
  indy<-listofcouplesimple[indexcouples[2,i],]
  indcouple1<-indexcouples[1,i]
  indcouple2<-indexcouples[2,i]
  #poslink<-gregexpr("-",couples[i])
  #ldm1[i]<-as.numeric(substr(couples[i],1,poslink[[1]]-1))
  #ldm2[i]<-as.numeric(substr(couples[i],poslink[[1]]+1,nchar(couples[i])))
  ldm1[i]<-indx[1];ldm2[i]<-indx[2]
  ldm3[i]<-indy[1];ldm4[i]<-indy[2]
  r[i]<-varcouples(listofdistanceStand[indcouple1,],listofdistanceStand[indcouple2,])
}

##### data frame with landmarks and r
res.ratios<-data.frame(ldm1,ldm2,ldm3,ldm4,r)

##### function for number of different landmarks
alldiff<-function (x) {length(unique(x))}

##### compute number of all different landmarks
lengthsldms<-apply(res.ratios[,1:4],1, alldiff)
```

```
##### select all landmarks and different r
only4<-res.ratios[lengthsldms==4,]

##### correction of r because there is an issue in the previous calculation, I don't know where is the issue
e=1
for(e in 1:length(only4[,1])){
  only4[e,5]<-
  varcouples(distanceStand[only4$ldm1[e],only4$ldm2[e],],distanceStand[only4$ldm3[e],only4$ldm4[e],])
}

hist(only4$r) # compute histogram

##### landmark selection
ldmselection<-c(left,center)

##### Linear Distance
##### function with threshold return list of pdf regression selected (need to be cleaned)
procedure <- function (ldmselection=ldmselection, thresholdr=0.71, thresholdpval=0.05) {

  allpossibilities<-only4[apply(  only4,1, function(x) (all(x[1:4]%in%ldmselection))),]
  sup4<-allpossibilities[(allpossibilities[,5]>thresholdr),]
  allpossibilities<-sup4

  if(nrow(allpossibilities)==0) { stop("no couples of landmarks with the given thresholds") }
  ### All regression, keep only regression with a significant p-value
  i=1
  siglist<-NA
  for (i in 1:length(allpossibilities[,1])){
    dist1<-c(allpossibilities[i,1],allpossibilities[i,2])
    dist2<-c(allpossibilities[i,3],allpossibilities[i,4])
    a<-distanceStand[dist1[1],dist1[2],]
    b<-distanceStand[dist2[1],dist2[2],]
    df<-data.frame(x=a,y=b)
    mod<- sma(x ~ y, data=df, method="SMA")
    siglist[i]<-mod$groupsummary$pval
    #if (mod$groupsummary$pval<thresholdSMA){
    # siglist[i]<-mod$groupsummary$pval
    #} else {
    # siglist[i]<-NA
    #}
  }

  # Combine in one list only couples with significant p-value
  # Squamosal
  allpossibilities_only_pval<-allpossibilities[siglist<thresholdpval,]
  sup4<-allpossibilities_only_pval

  ##### Second selection, keep only regression where couples get a r threshold.
  #dim(allpossibilities_only_pval)
  #sup4<-allpossibilities_only_pval[(allpossibilities_only_pval[,5]>0.4),]
  #sup4<-allpossibilities_only_pval
  #dim(sup4)

  ##### make regression one by one (by default)
  rsquared<-NA;pvalue<-NA;slope<-NA;slopeinf<-NA;slopesup<-NA
  for(i in 1:nrow(sup4)) {
    dist1<-c(sup4[i,1],sup4[i,2])
    dist2<-c(sup4[i,3],sup4[i,4])
    a<-distanceStand[dist1[1],dist1[2],]
```

```

b<-distanceStand[dist2[1],dist2[2,]]
df<-data.frame(x=a,y=b)

mod<- sma(y ~ x, data=df, method="SMA")
pdf(paste(sup4[i,1],"-",sup4[i,2]," VS ",sup4[i,3],"-",sup4[i,4],".pdf",sep=""))
plot(mod,xlab=paste(sup4[i,1],"-",sup4[i,2],sep=""),ylab=paste(sup4[i,3],"-",sup4[i,4],sep=""),pch=20)
title(main=paste(sup4[i,1],"-",sup4[i,2]," VS ",sup4[i,3],"-",sup4[i,4],sep=""))
meanx<-mean(df$x);meany<-mean(df$y)
abline(a=meany-mod$coef[[1]][2,2]*meanx ,b=mod$coef[[1]][2,2],col="blue",lty=3)
abline(a=meany-mod$coef[[1]][2,3]*meanx ,b=mod$coef[[1]][2,3],col="blue",lty=3)
abline(a=mod$coef[[1]][2,1],b=mod$coef[[1]][1,2],col="blue",lty=3)
abline(a=mod$coef[[1]][2,1],b=mod$coef[[1]][1,3],col="blue",lty=3)
rsquared[i]<-mod$R2[[1]]
pvalue[i]<-mod$pval[[1]]
slope[i]<-mod$coef[[1]][2,1];slopeinf[i]<-mod$coef[[1]][2,2];slopesup[i]<-mod$coef[[1]][2,3]
text(min(df$x),max(df$y),pos=4,labels=paste("R2=",round(rsquared[i],3),"\\n","P-
value=",round(pvalue[i],3),sep=""))
dev.off()
##### Save R2, p-value, slope, slope min and slope max (to know if there is isotropy or allometry)
}
resultssma<-data.frame(sup4[,1:4],rsquared,pvalue,slope,slopeinf,slopesup)
colnames(resultssma)<-c("ldm1","ldm2","ldm3","ldm4","rsquared","pvalue","slope","slopeinf","slopesup")
return(resultssma)
write.table(resultssma, file="Regression_rX_pvalX.txt", row.names=FALSE, col.names=FALSE)
}

##### Analysis
result<-procedure(ldmselection=ldmselection, thresholdr=0.71, thresholdpval=0.05)
str(result)
summary(result)
res.procedure<-
data.frame(result$ldm1,result$ldm2,result$ldm3,result$ldm4,result$rsquared,result$pvalue,result$slope,result$sl
opeinf,result$slopesup)
hist(res.procedure$result.rsquared)

##### Export table from funcion procedure
write.table(res.procedure, file="Regression_rX_pvalX.txt", row.names=FALSE, col.names=FALSE)

```

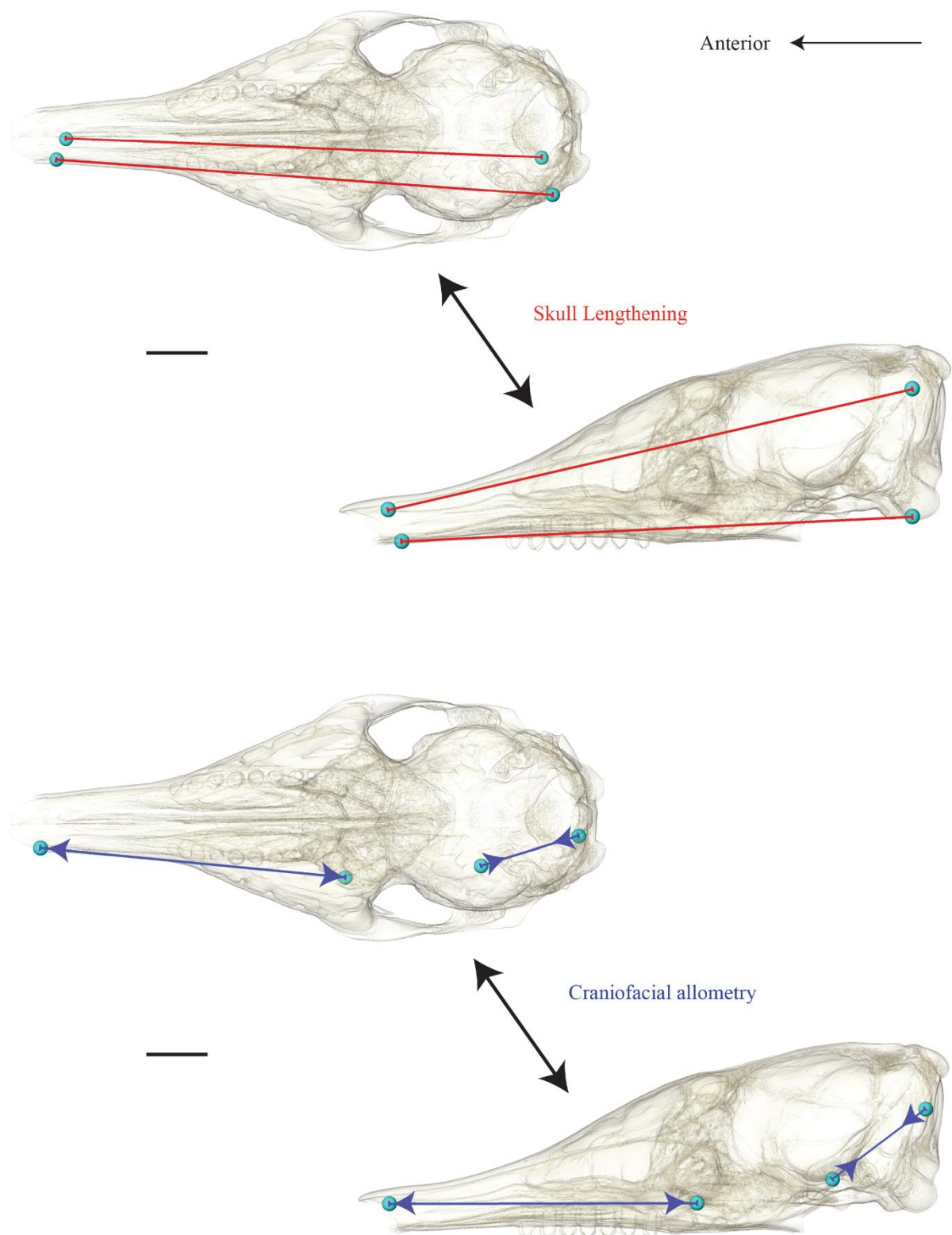


Figure S34. Examples of non-selected pairs of correlated distances illustrated on a skull of *Dasypus novemcinctus* SM. In red, a pair of covarying distances related to a lengthening of the skull (*i.e.*, long, and parallel distances covering the skull anteroposteriorly). Other pairs of this nature (long, parallel and overlapping) in different directions (*e.g.*, skull height) did not appear among the pairs above the threshold criteria. In blue, a pair of covarying distances that signaled an increase in the length of the snout relative to a decrease in the proportions of the neurocranium (= craniofacial allometry – negative correlation) already well-known in nine-banded armadillos (Chapter 3). Scale = 1 cm.

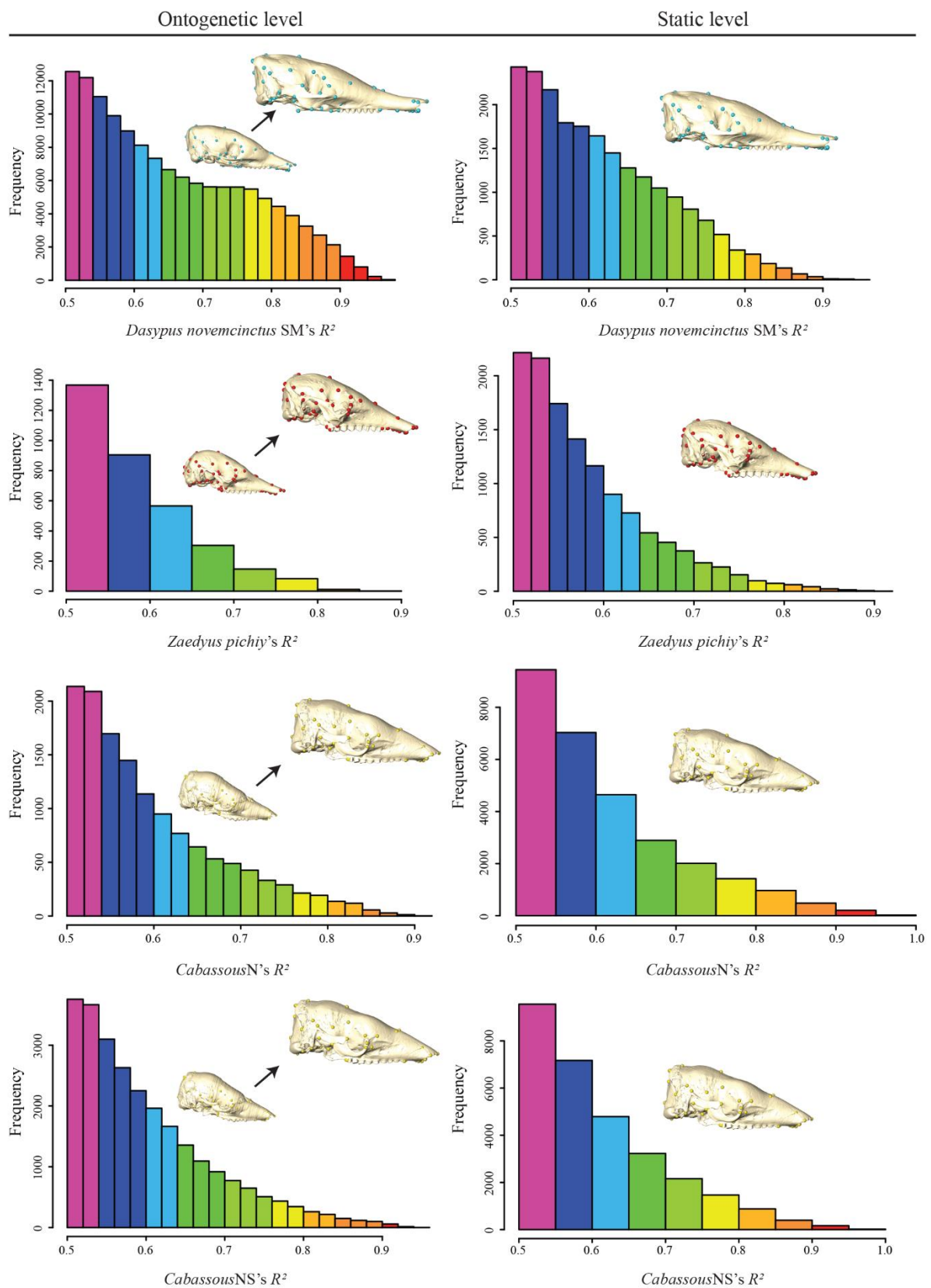


Figure S35. Frequencies of the pairs of correlated distances according to the values of R^2 (i.e., the square of correlation coefficient r) for each species at the ontogenetic level (represented by a juvenile and an adult specimen in lateral view) and at the static level (represented by an adult specimen in lateral view). The color gradient from purple to red represents the detected R^2 values from 0.5 to 1.

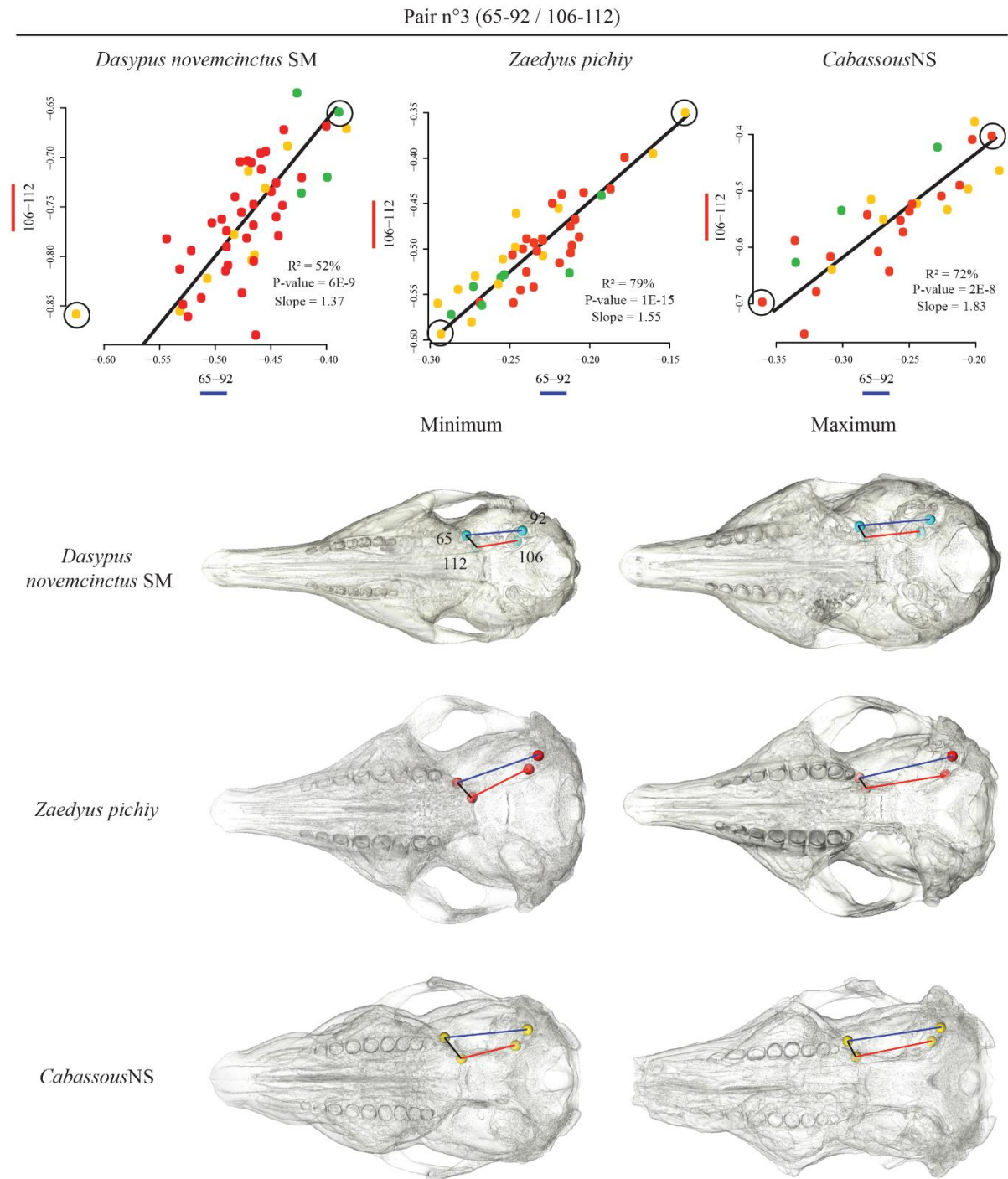


Figure S36. Covariation in the selected pair n°3 (65 - 92 / 106 - 112) illustrated by the SMA plot (see [Material & Methods](#)) for each species (green = juvenile; yellow = subadult; red = adult). Extreme specimens are identified by a circle on the plots and presented in ventral view for each species with the distances illustrated.

Pair n°4 (38-80 / 50-92) - Extreme points

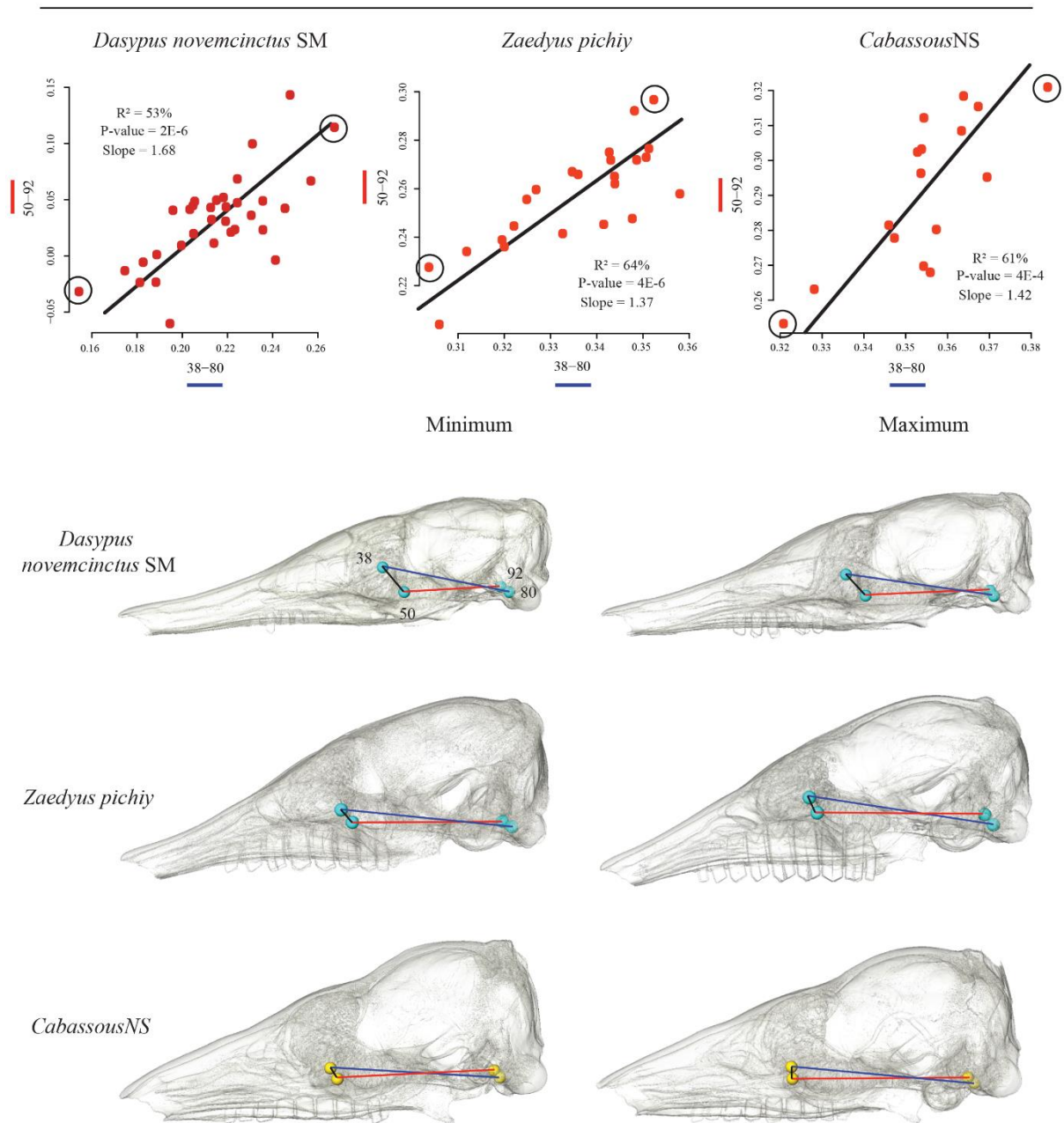


Figure S37. Covariation in the selected pair n°4 (38 - 80 / 50 - 92) illustrated by the SMA plot (see [Material & Methods](#)) for each species. Extreme specimens are identified by a circle on the plots and presented in lateral view for each species with the distances illustrated.

Pair n°5 (50-94 / 21-108) - Extreme points

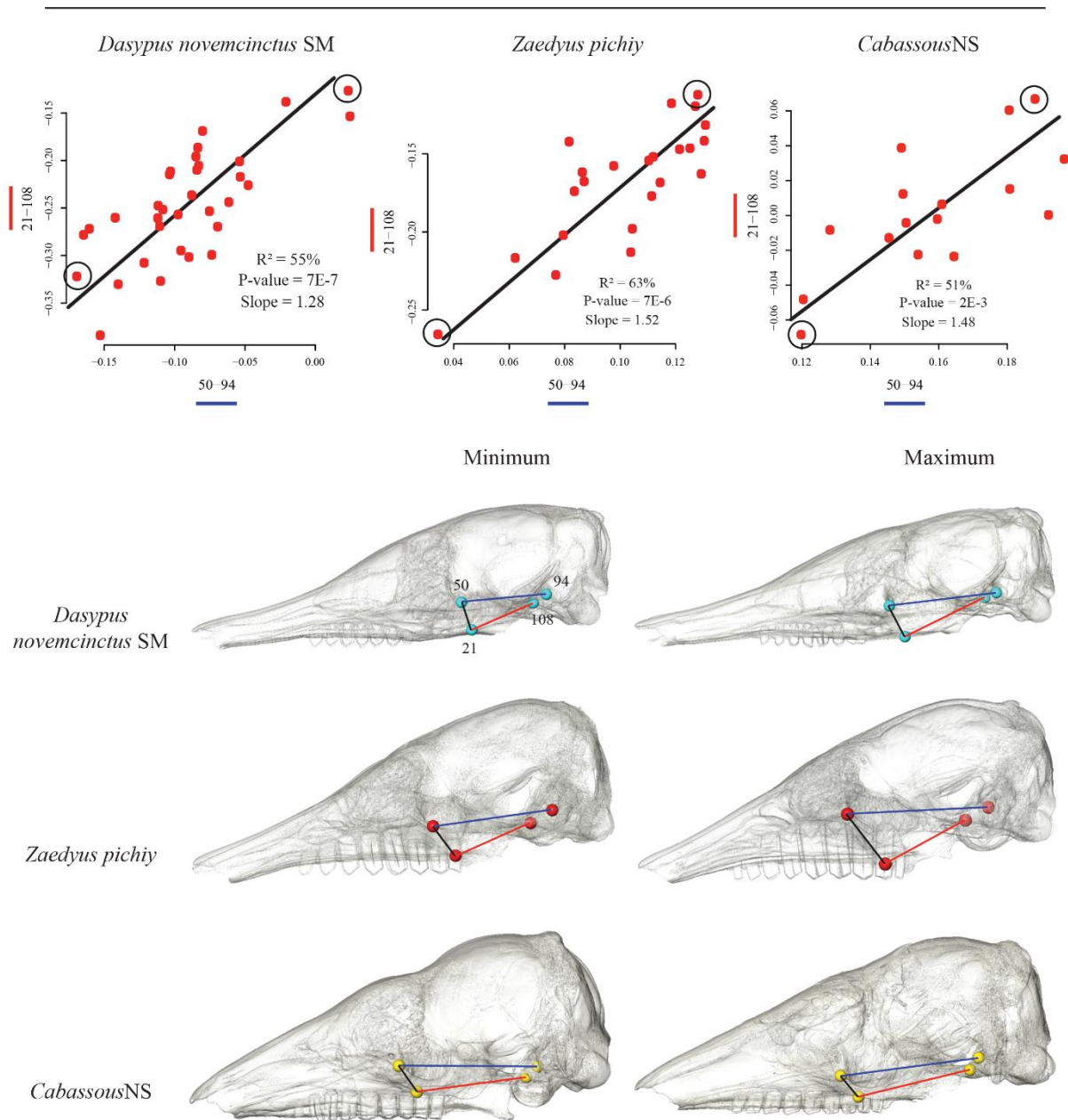


Figure S38. Covariation in the selected pair n°5 (50 - 94 / 21 - 108) illustrated by the SMA plot (see [Material & Methods](#)) for each species. Extreme specimens are identified by a circle on the plots and presented in lateral view for each species with the distances illustrated.

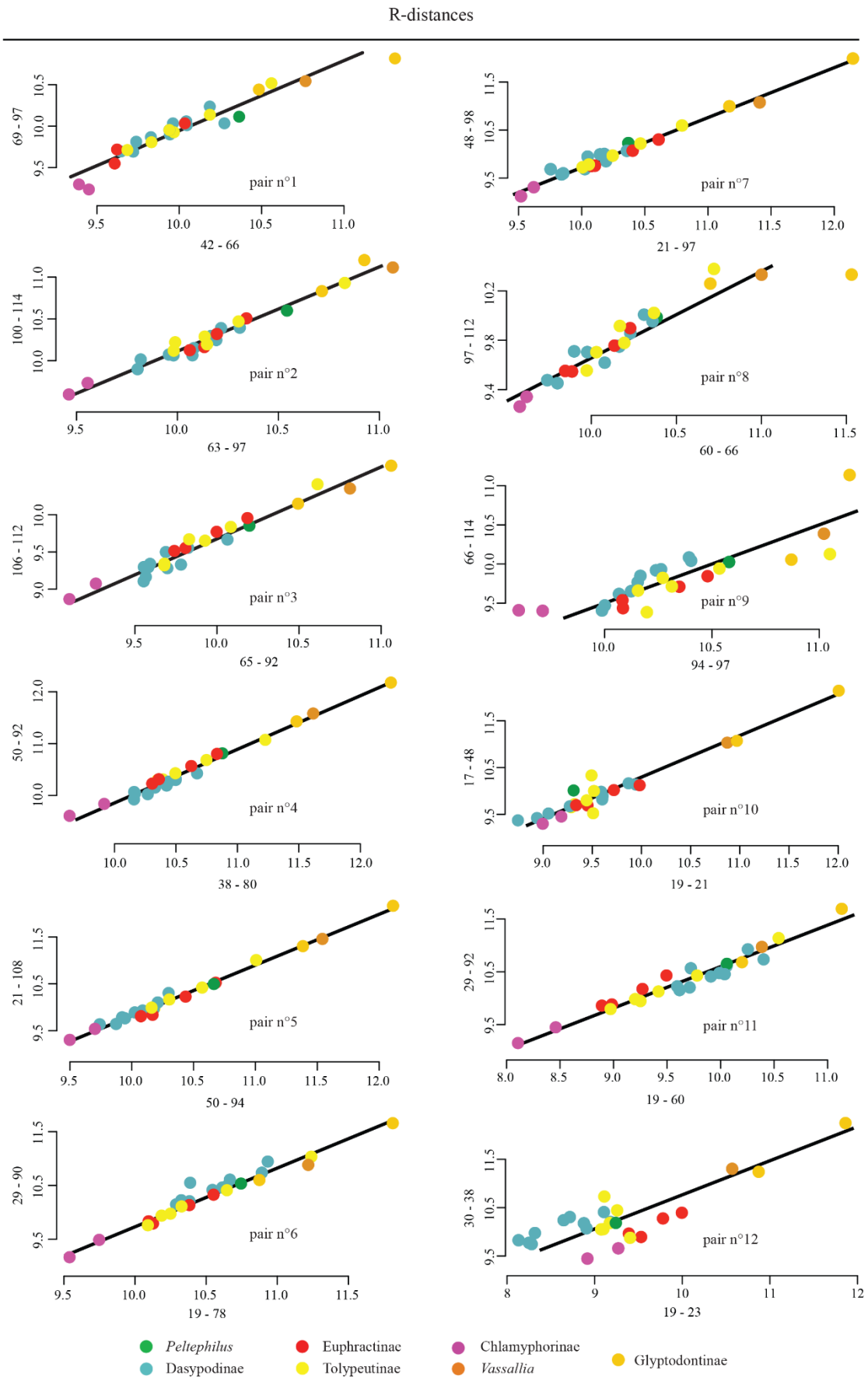


Figure S39. SMA plot of $\log(R\text{-distances})$ pairs selected (see [Material & Methods](#)) for the evolutionary level.

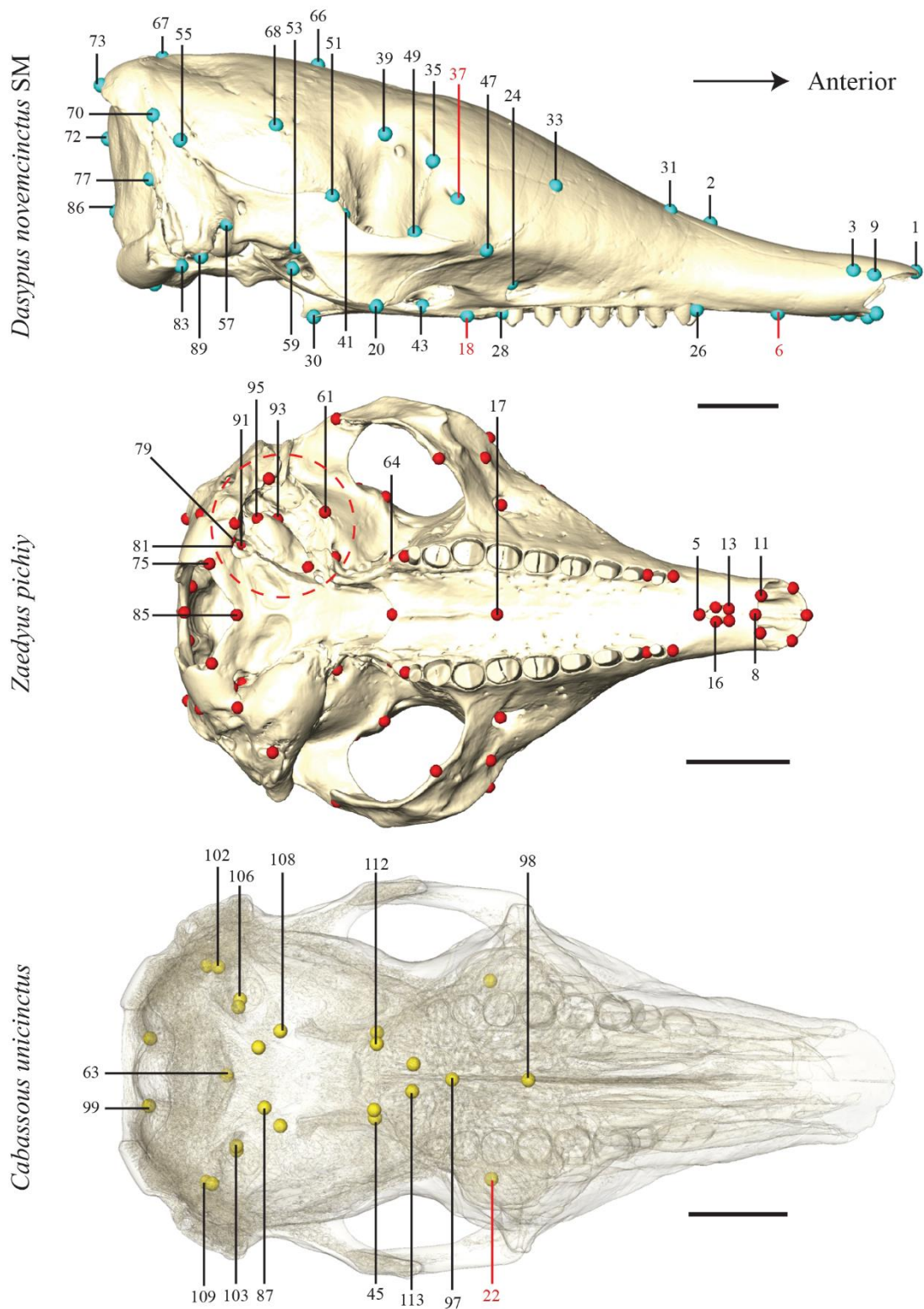


Figure S40. Landmarks digitized on the skull of *Dasyurus novemcinctus* (lateral view), *Zaedyus pichiy* (ventral view) and *Cabassous unicinctus* (dorsal view, with transparency). The red dotted circle marks the area corresponding to the tympanic bulla that was virtually cleared in *Zaedyus pichiy*. The red landmark numbers correspond to the landmarks not selected for EDMA (see text). Scale-bar = 1 cm.

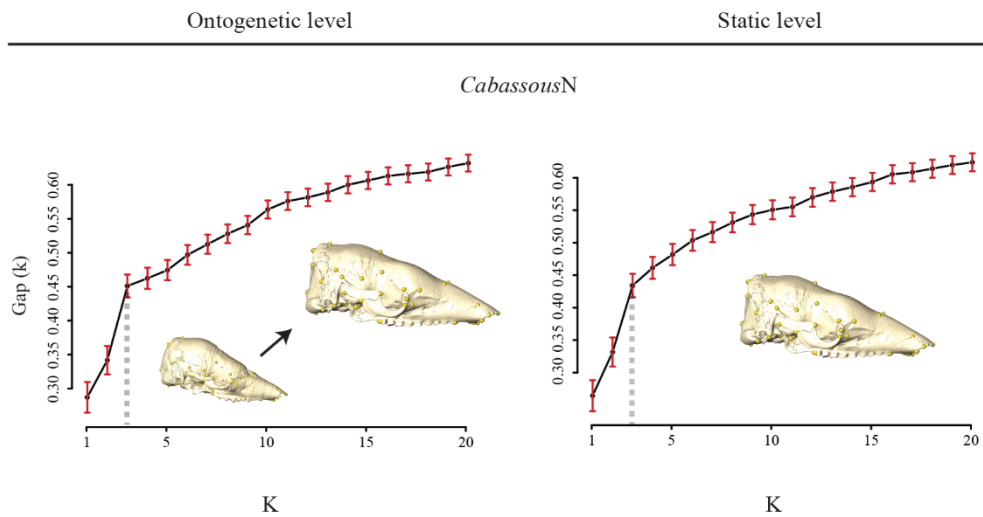


Figure S41. Selection of the number of stable modules using the gap statistic for *CabassousN* at the ontogenetic level (represented by a juvenile and an adult specimen in lateral view, with landmarks) and at the static level (represented by an adult only). The slope break showing the number of statistically stable modules (see text) is marked by a dotted grey line.

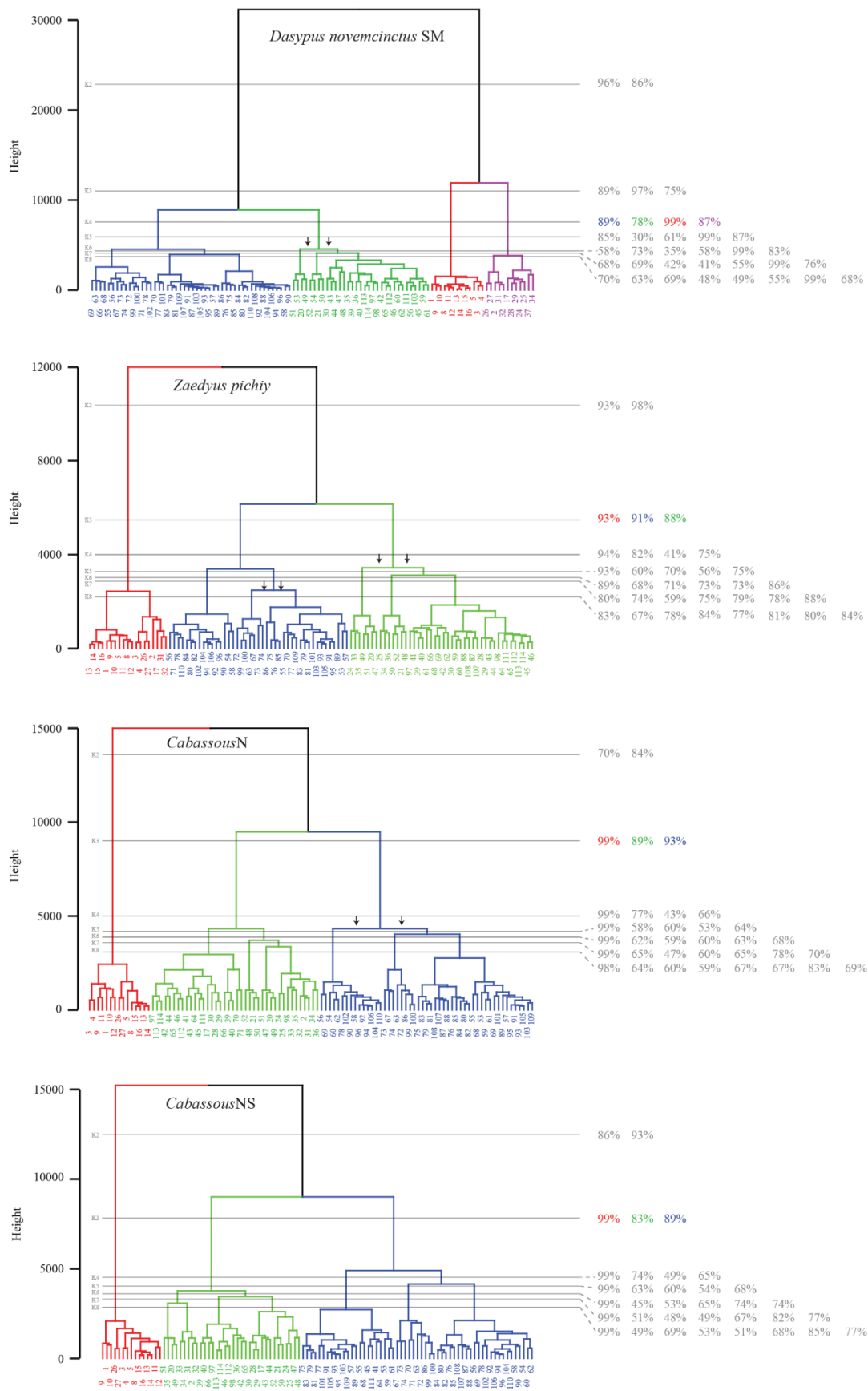


Figure S42. Dendrogram obtained following the hierarchical clustering applied to the EDMA results for each species at the ontogenetic level, with bootstrap values. In red, anterior-face or face module; in purple, mid-face module; in green, orbit-neurocranium module; in blue, vault-basicranium module.

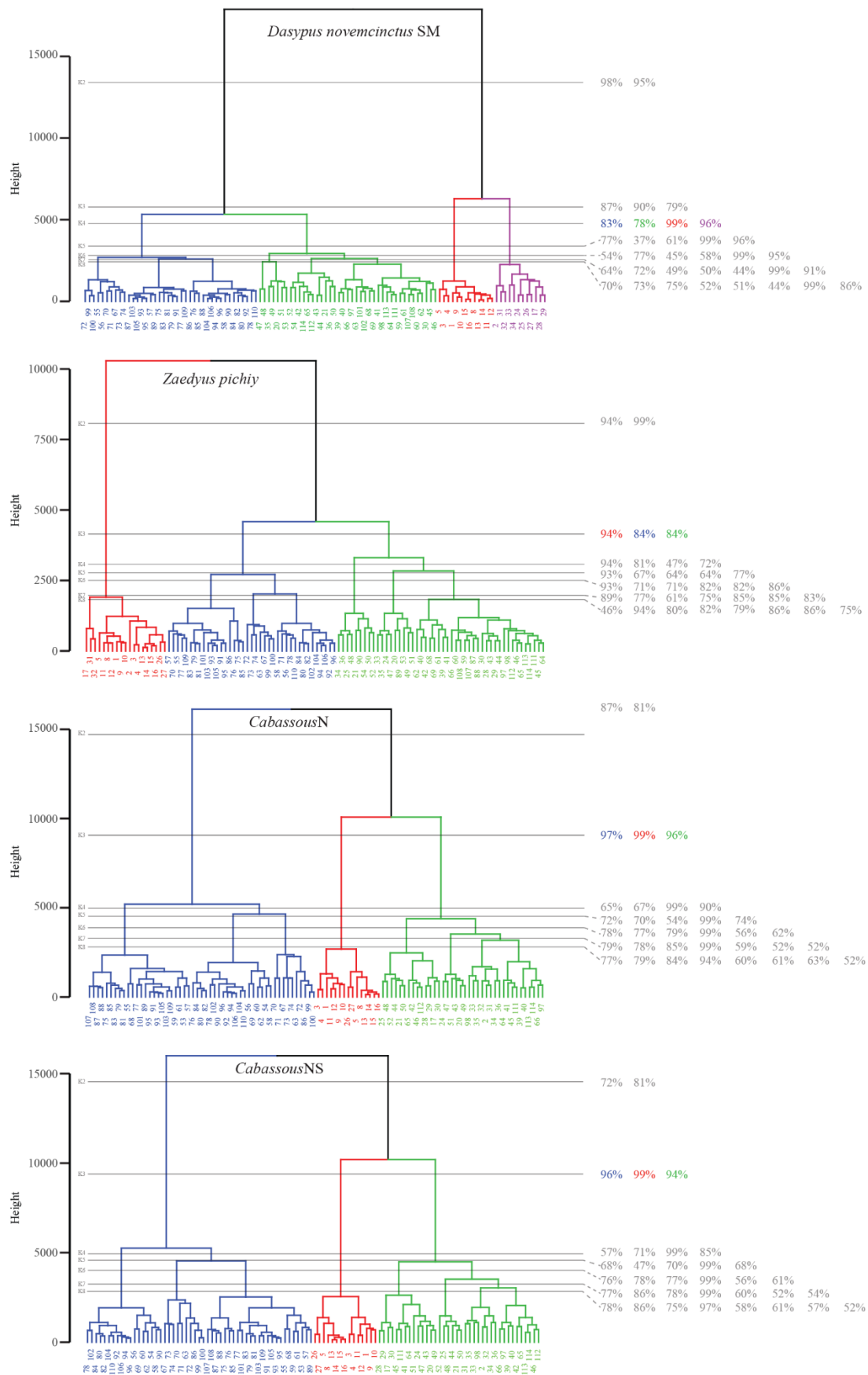


Figure S43. Dendrogram obtained following the hierarchical clustering applied to the EDMA results for each species at the static level, with bootstrap values. In red, anterior-face or face module; in purple, mid-face module; in green, orbit-neurocranium module; in blue, vault-basicranium module.

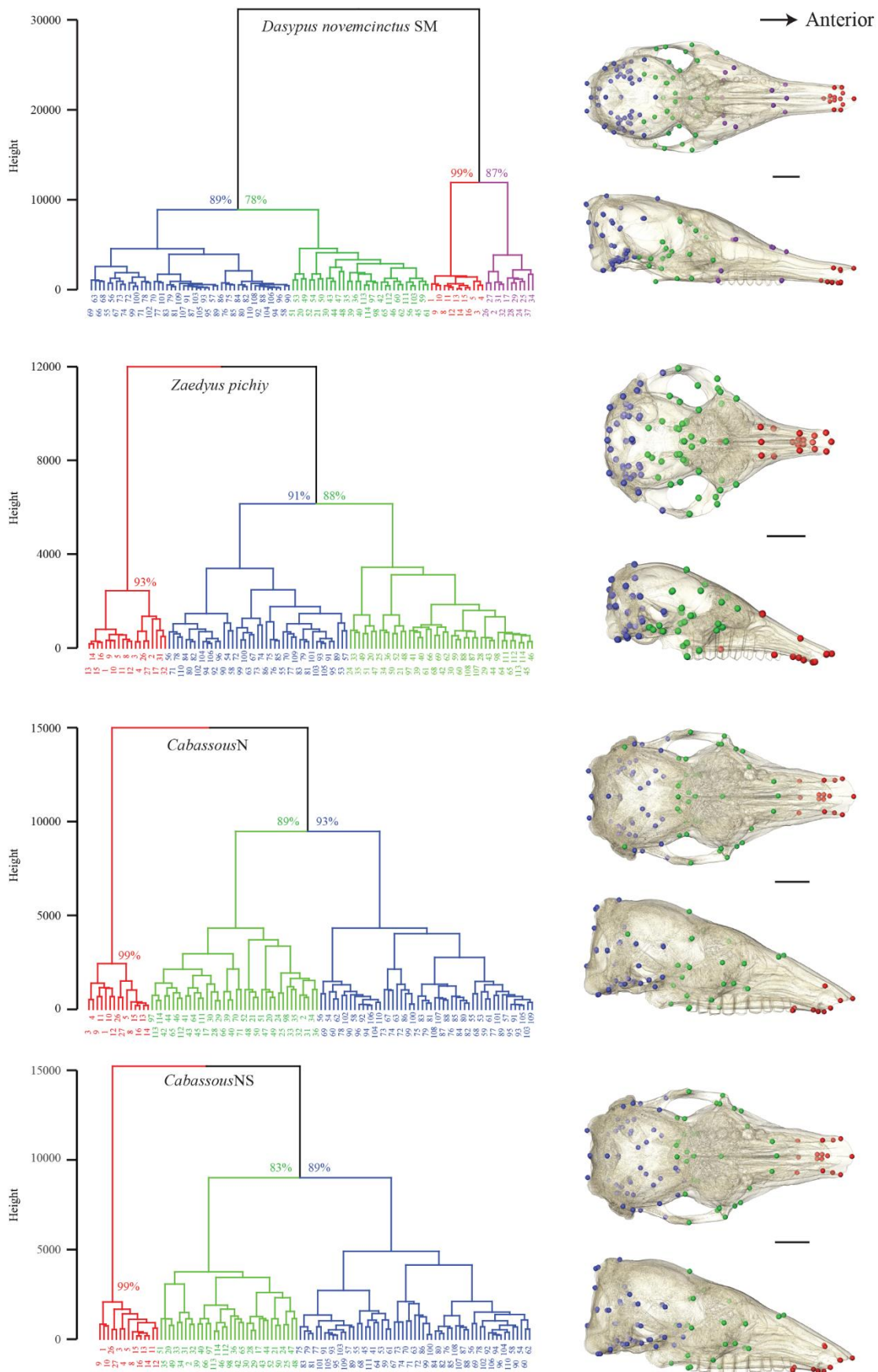


Figure S44. Dendrogram obtained following the hierarchical clustering applied to the EDMA results for each species at the ontogenetic level, with a mapping on skull. In red, anterior-face or face module; in purple, mid-face module; in green, orbit-neurocranium module; in blue, vault-basiscranium module.

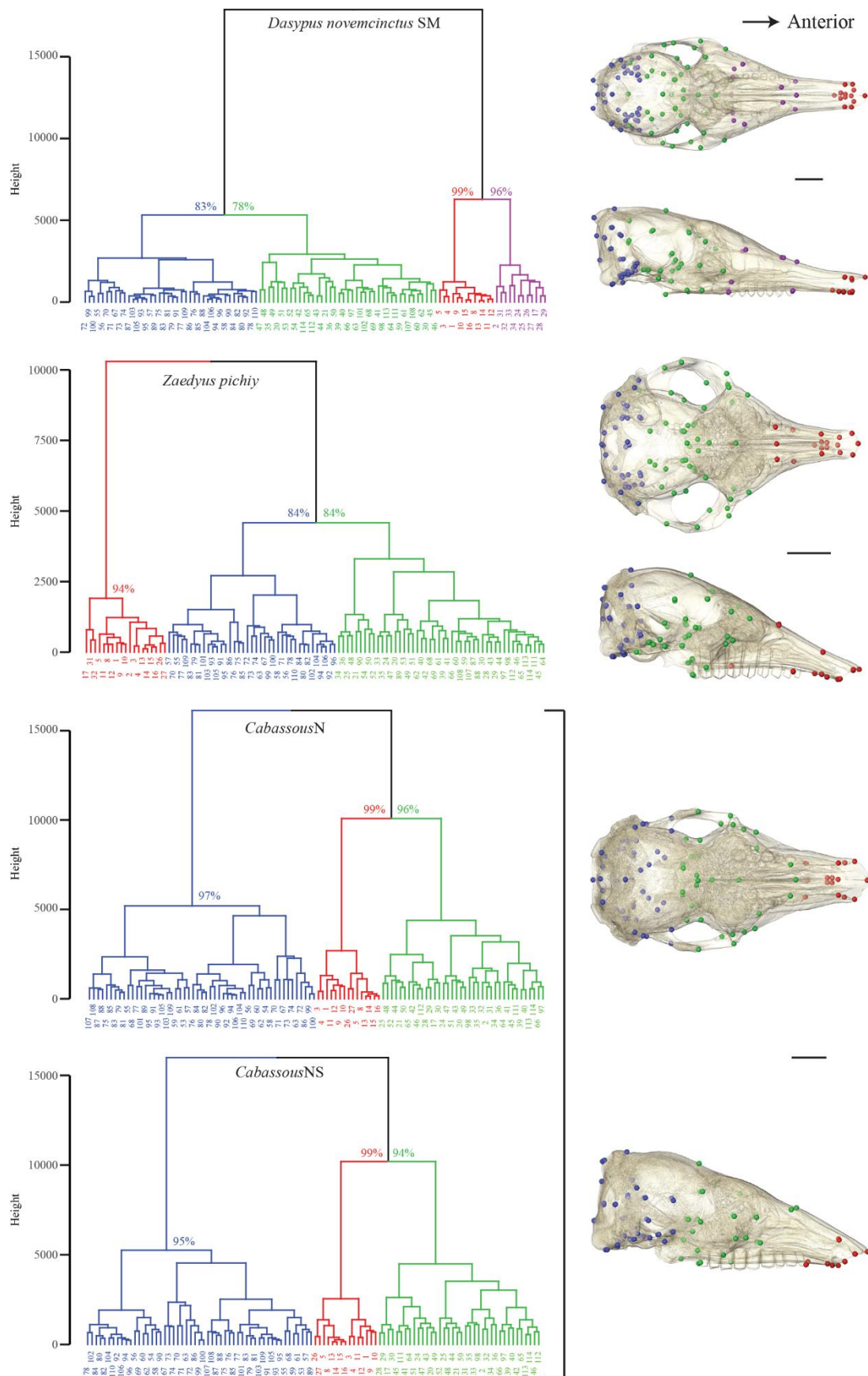


Figure S45. Dendrogram obtained following the hierarchical clustering applied to the EDMA results for each species at the static level, with a mapping on skull. In red, anterior-face or face module; in purple, mid-face module; in green, orbit-neurocranium module; in blue, vault-basiscranium module.

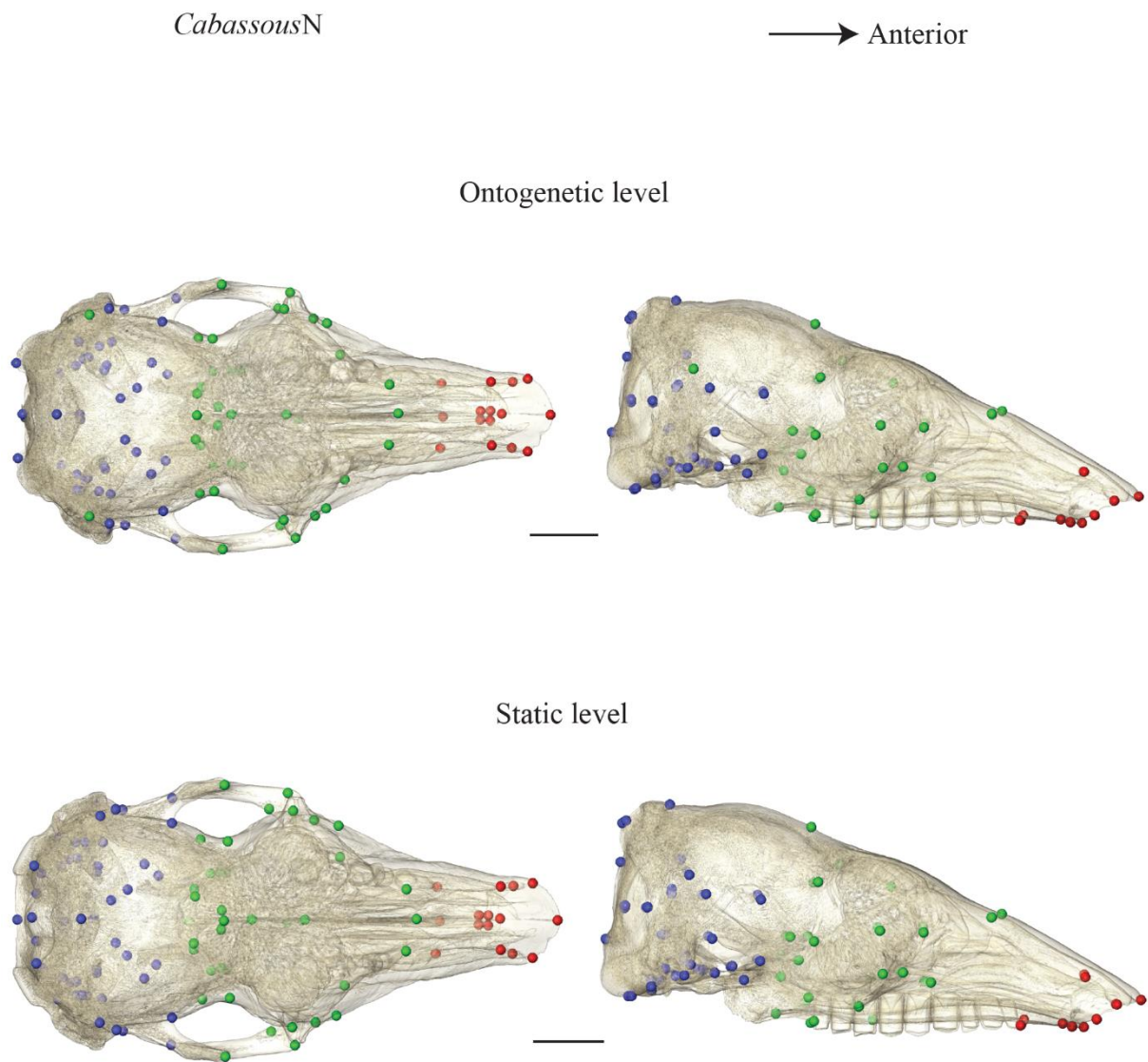


Figure S46. Mapping of the modules obtained for *Cabassous*N at the ontogenetic, and static levels. In red, anterior-face or face module; in purple, mid-face module; in green, orbit-neurocranium module; in blue, vault-basiscranium module.

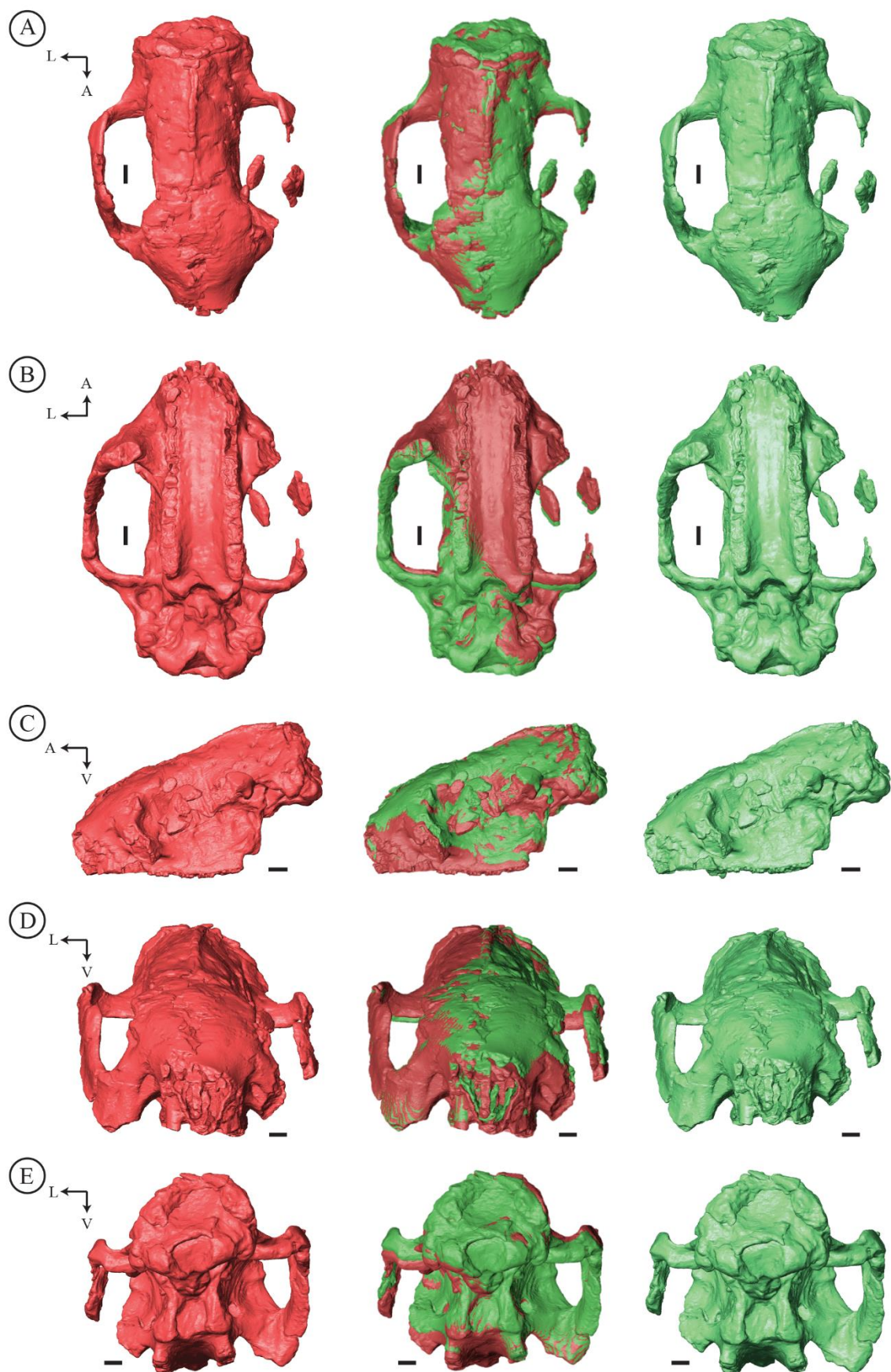


Figure S47. Retrodeformation applied on the skull of “*Metopotoxus*” *anceps* (YPM-PU 15612) with an illustration of the original specimen and a comparison between the two meshes. A, dorsal view; B, ventral view; C, lateral view; D, face view; E, occipital view. Abbreviations: A, anterior; L, lateral; V, ventral. Scale-bars = 1 cm.

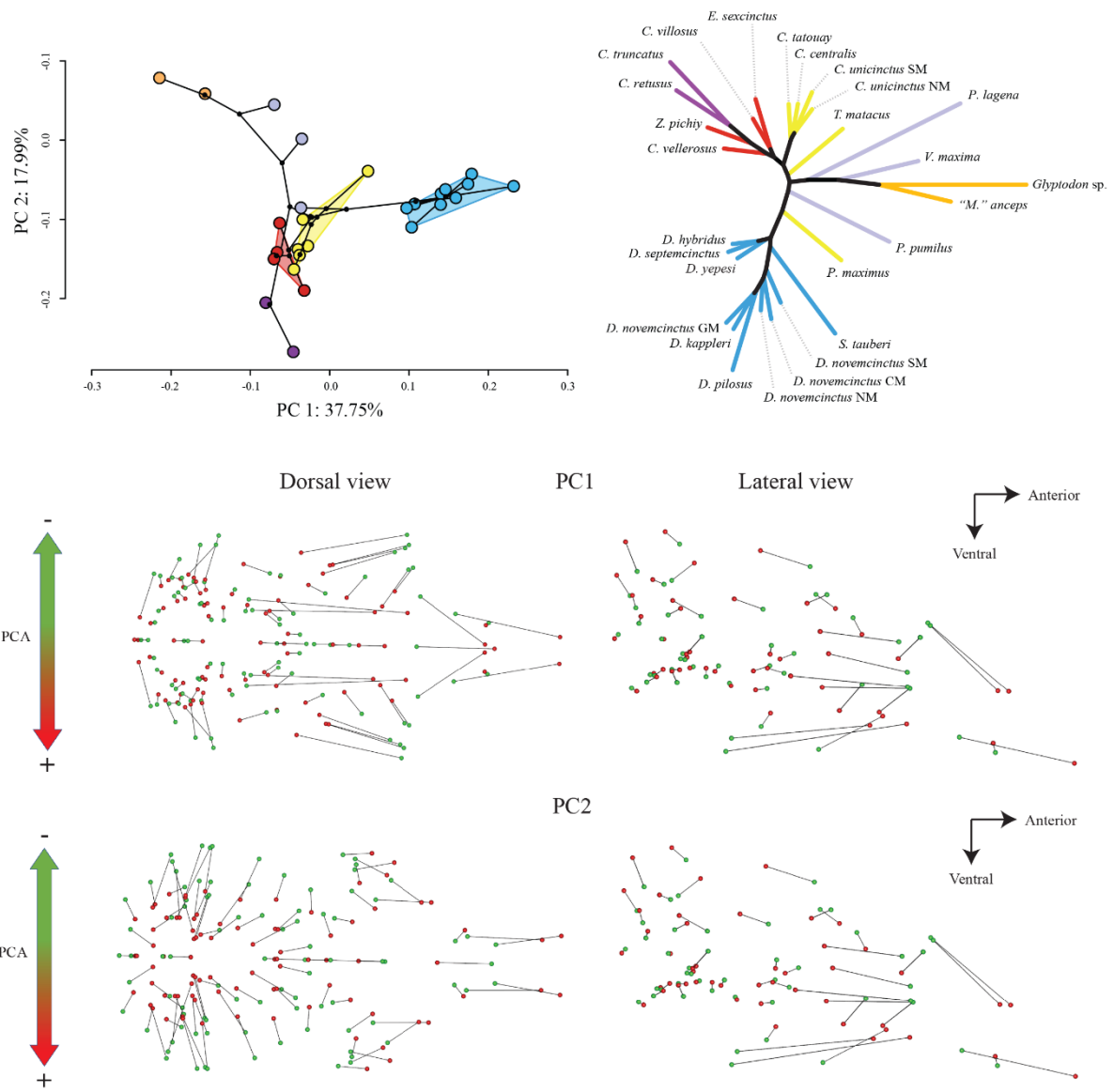


Figure S48. Principal Component Analysis on the Dataset-Tmax with a neighbor-joining tree estimation for the total variance. Morphological shape change on each axis are represented from the minimal (green) to the maximal (red) value of each axis.

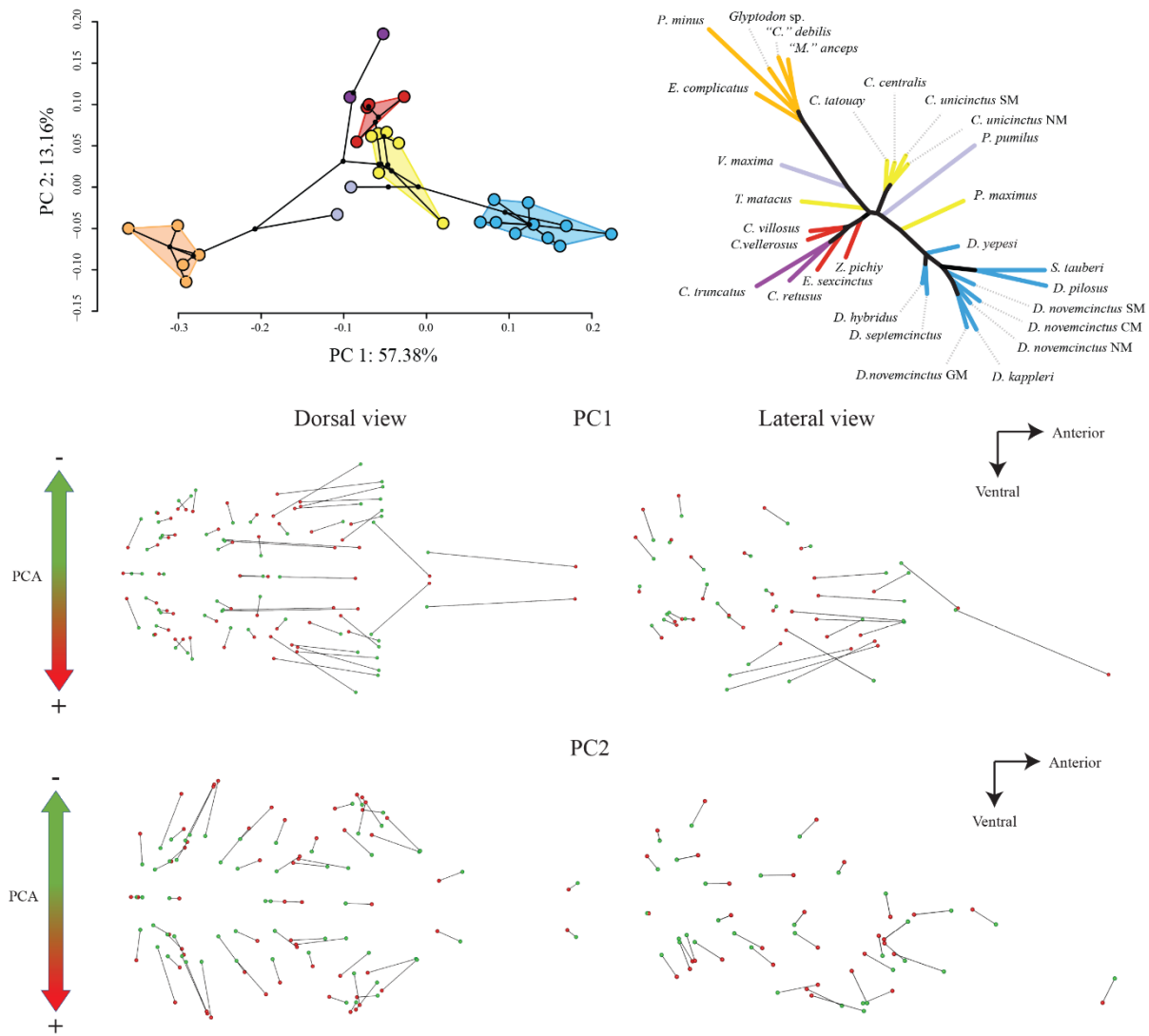


Figure S49. Principal Component Analysis on the Dataset-G with a neighbor-joining tree estimation for the total variance. Morphological shape change on each axis are represented from the minimal (green) to the maximal (red) value of each axis.

Table S22. List of specimens for intraspecific sample. Available on the HAL open archive portal.

Table S23 List of linear S-distance pairs selected according to our threshold criteria at the ontogenetic level in the 3 species (DZC). Each distance is indicated by the landmarks that define it. For a given *Cabassous* dataset, results are shaded when they are below the threshold level. The numbering of pairs follows the text. Available on the HAL open archive portal.

Table S24. List of linear S-distance pairs selected according to our threshold criteria at the static level in the 3 species (DZC). Each distance is indicated by the landmarks that define it. For a given *Cabassous* dataset, results are shaded when they are below the threshold level. The numbering of pairs follows the text. Available on the HAL open archive portal.

Table S25. List of linear S-distance pairs selected according to our threshold criteria at the ontogenetic level in the 2 species (ZC). Each distance is indicated by the landmarks that define it. For a given *Cabassous* dataset, results are shaded when they are below the threshold level. The numbering of pairs follows the text. Available on the HAL open archive portal.

Table S26. List of linear S-distance pairs selected according to our threshold criteria at the static level in the 2 species (ZC). Each distance is indicated by the landmarks that define it. For a given *Cabassous* dataset, results are shaded when they are below the threshold level. The numbering of pairs follows the text. Available on the HAL open archive portal.

Table S27. Summary statistics of the standard major axis regression (SMA) for all the pairs of correlated S-distances obtained according to our threshold criteria at the ontogenetic level in each of the 3 species. Each distance is indicated by the landmarks that define it. Available on the HAL open archive portal.

Table S28. Summary statistics of the standard major axis regression (SMA) for all the pairs of correlated S-distances obtained according to our threshold criteria at the static level in each of the 3 species. Each distance is indicated by the landmarks that define it. Available on the HAL open archive portal.

Table S29. Correspondence between the EDMA and Mclust dendograms for each module (in %). The evaluation limit is fixed at the level of 4 modules following the results of the statistical gap (Figure S41).

		Mclust Compatibility			
		Module 1	Module 2	Module 3	Module 4
Ontogenetic level	<i>Dasybus novemcinctus</i> SM	100%	100%	85%	98%
	<i>Zaedyus pichiy</i>	84%	-	82%	100%
	<i>Cabassous</i> N	100%	-	95%	100%
	<i>Cabassous</i> NS	100%	-	100%	93%
Static level	<i>Dasybus novemcinctus</i> SM	100%	100%	86%	100%
	<i>Zaedyus pichiy</i>	84%	-	79%	100%
	<i>Cabassous</i> N	100%	-	100%	100%
	<i>Cabassous</i> NS	100%	-	100%	100%

Table S30. Assignment of each landmark to each module for each species at each level (*i.e.*, ontogenetic and static) and calculation of the percentage assignment of a landmark to a module for each level (*i.e.*, ontogenetic and static) as a result of concatenation between each species. In red, anterior-face or face module; in purple, mid-face module; in green, orbit-neurocranium module; in blue, vault-basicranium module. Available on the HAL open archive portal.

Table S31. Taxonomic composition of each dataset. CM, Central Morphotype; GM, Guianan Morphotype; NM, Northern Morphotype; SM, Southern Morphotype. † extinct species. Available on the HAL open archive portal.

Table S32. Landmark composition of each dataset. CM, Central Morphotype; GM, Guianan Morphotype; NM, Northern Morphotype; SM, Southern Morphotype. † extinct species. Available on the HAL open archive portal.

Table S33. Landmark coordinates of *Propalaeohoplophorus minus*, “*Cochlops*” *debilis* and *Eucinepeltus complicatus*. † extinct species. Available on the HAL open archive portal.

Table S34. List of landmarks placed of *Propalaeohoplophorus minus*, “*Cochlops*” *debilis* and *Eucinepeltus complicatus*, with a precision on the estimated landmarks (in orange by symmetrization; red, deleted landmarks). Available on the HAL open archive portal.

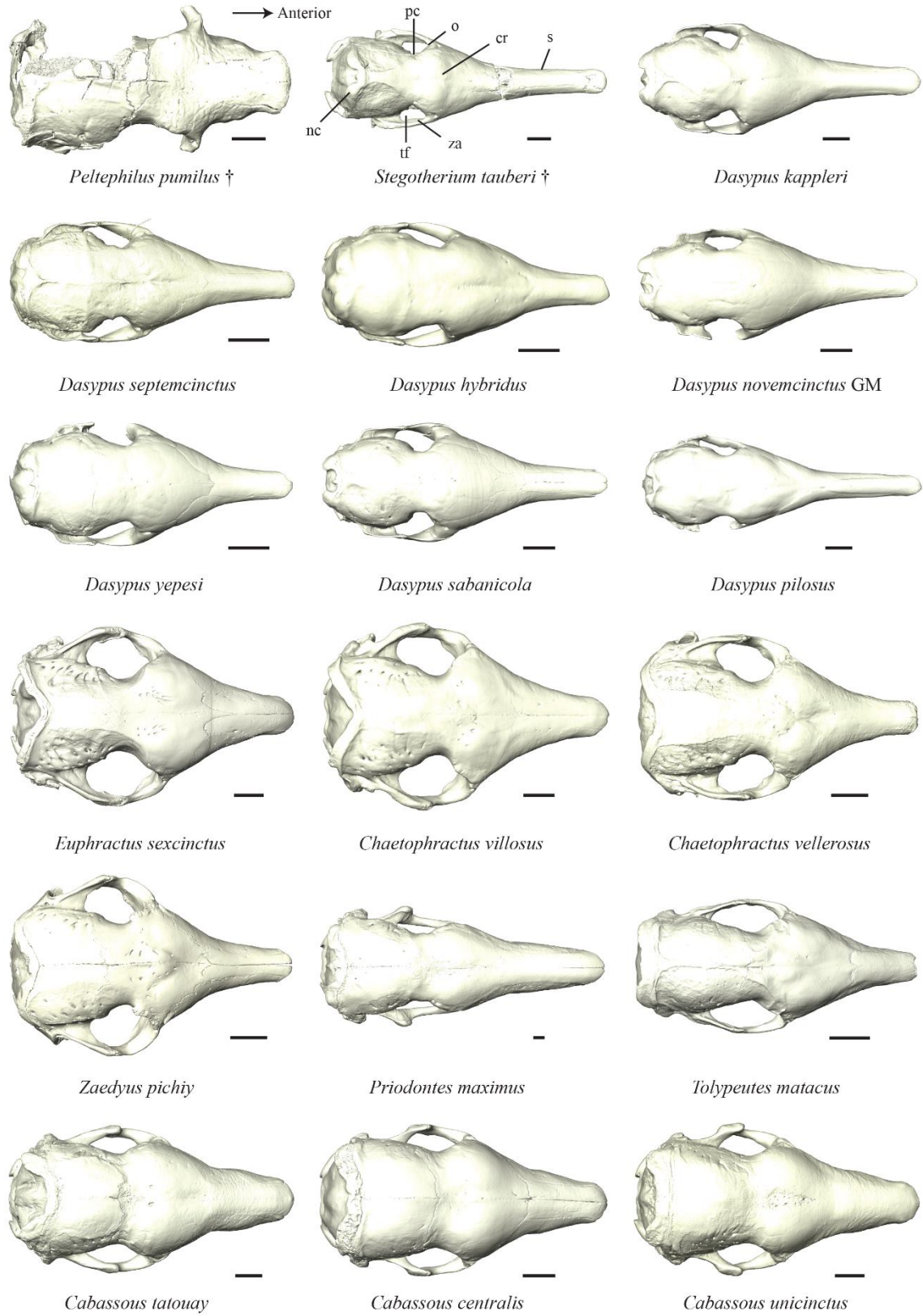


Figure S50. Plate of cingulate craniums in dorsal view. Abbreviations: cr, cranial roof; nc, nuchal crest; o, orbit; pc, postorbital constriction; s, snout; tf, temporal fossa; za, zygomatic arch. Scale = 1cm.

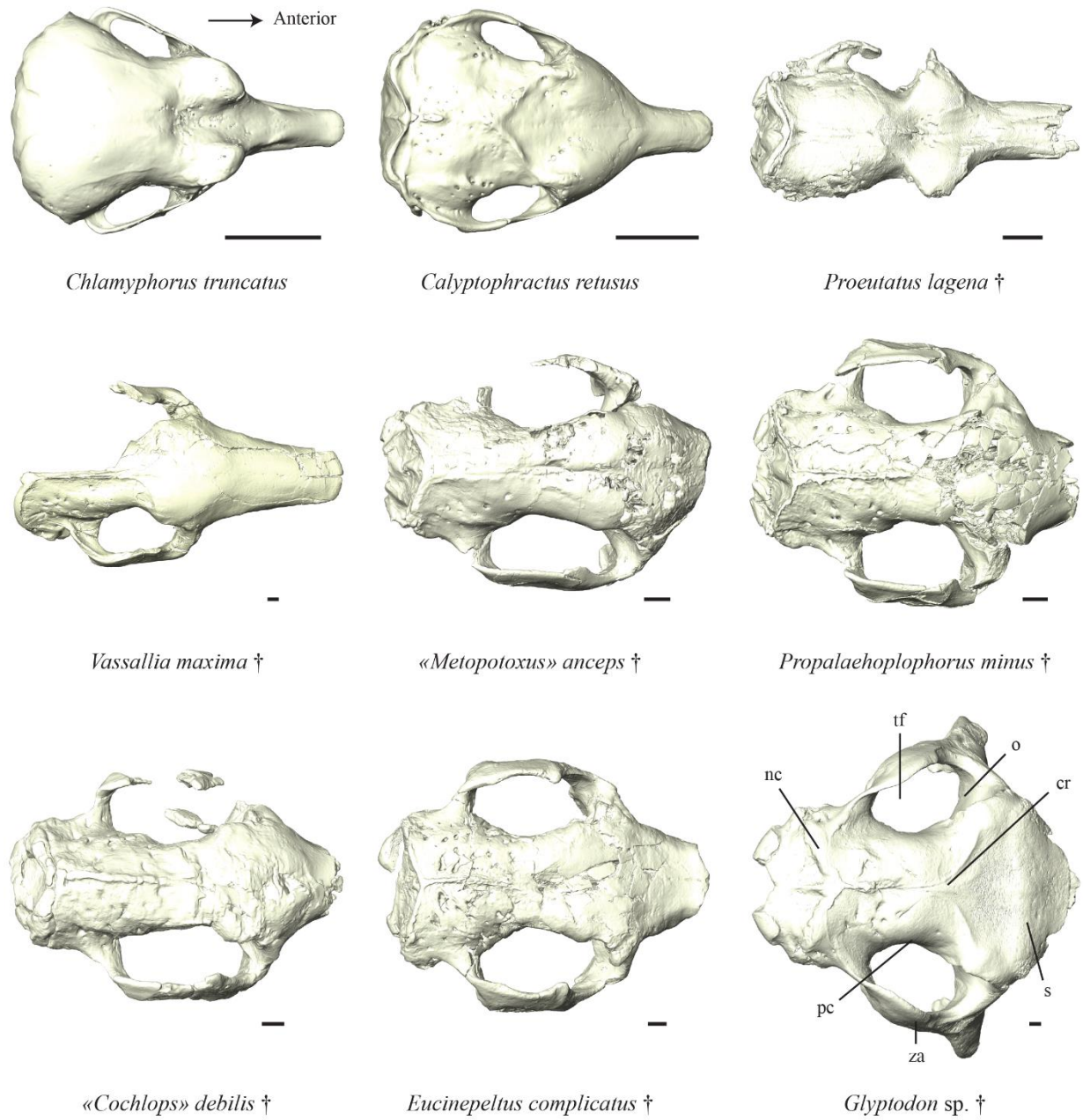


Figure S51 (continued from Figure S50). Plate of cingulate craniums in dorsal view. Abbreviations: cr, cranial roof; nc, nuchal crest; o, orbit; pc, postorbital constriction; s, snout; tf, temporal fossa; za, zygomatic arch. Scale = 1cm.

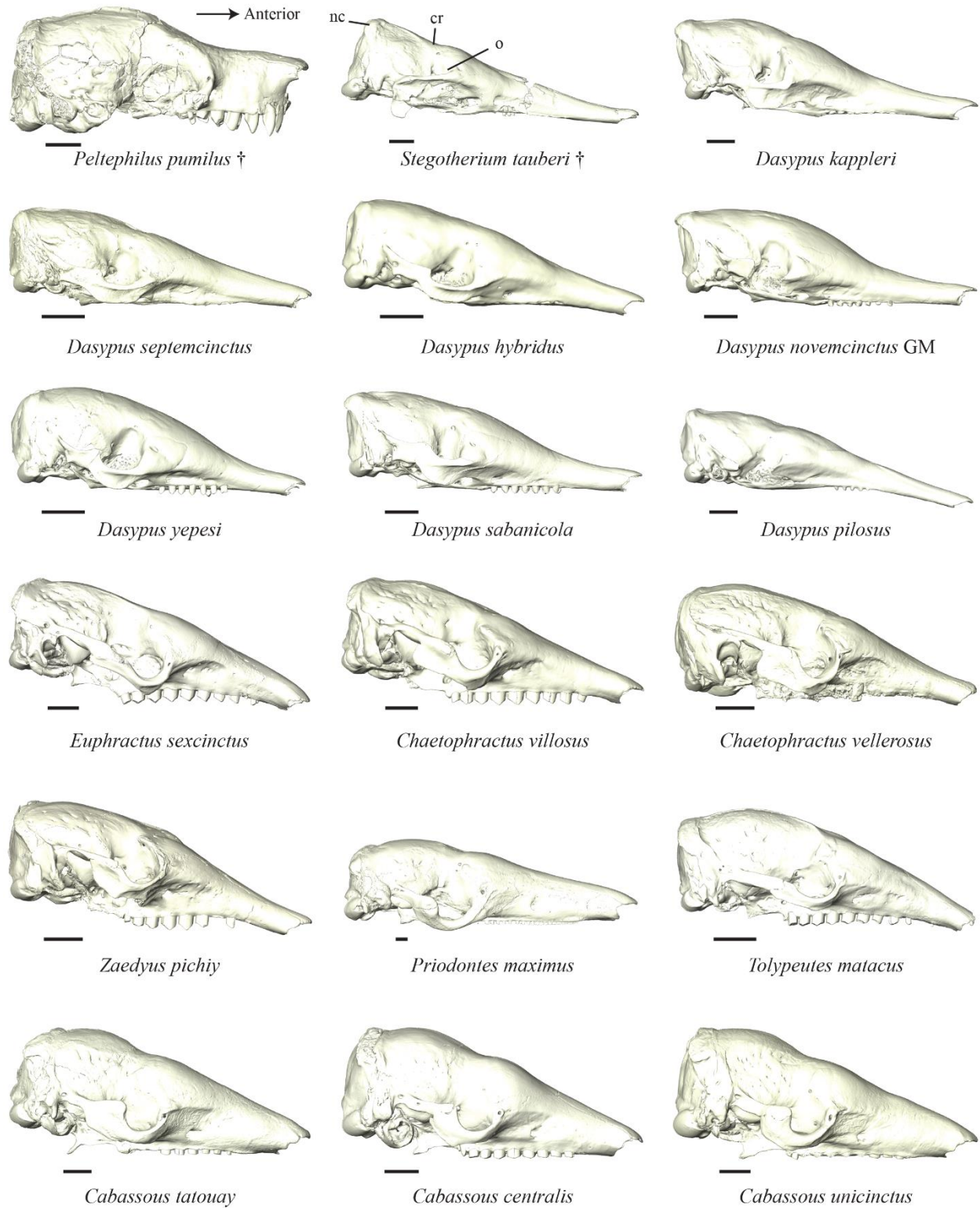


Figure S52. Plate of cingulate craniums in lateral view. Abbreviations: cr, cranial roof; nc, nuchal crest; o, orbit. Scale = 1cm.

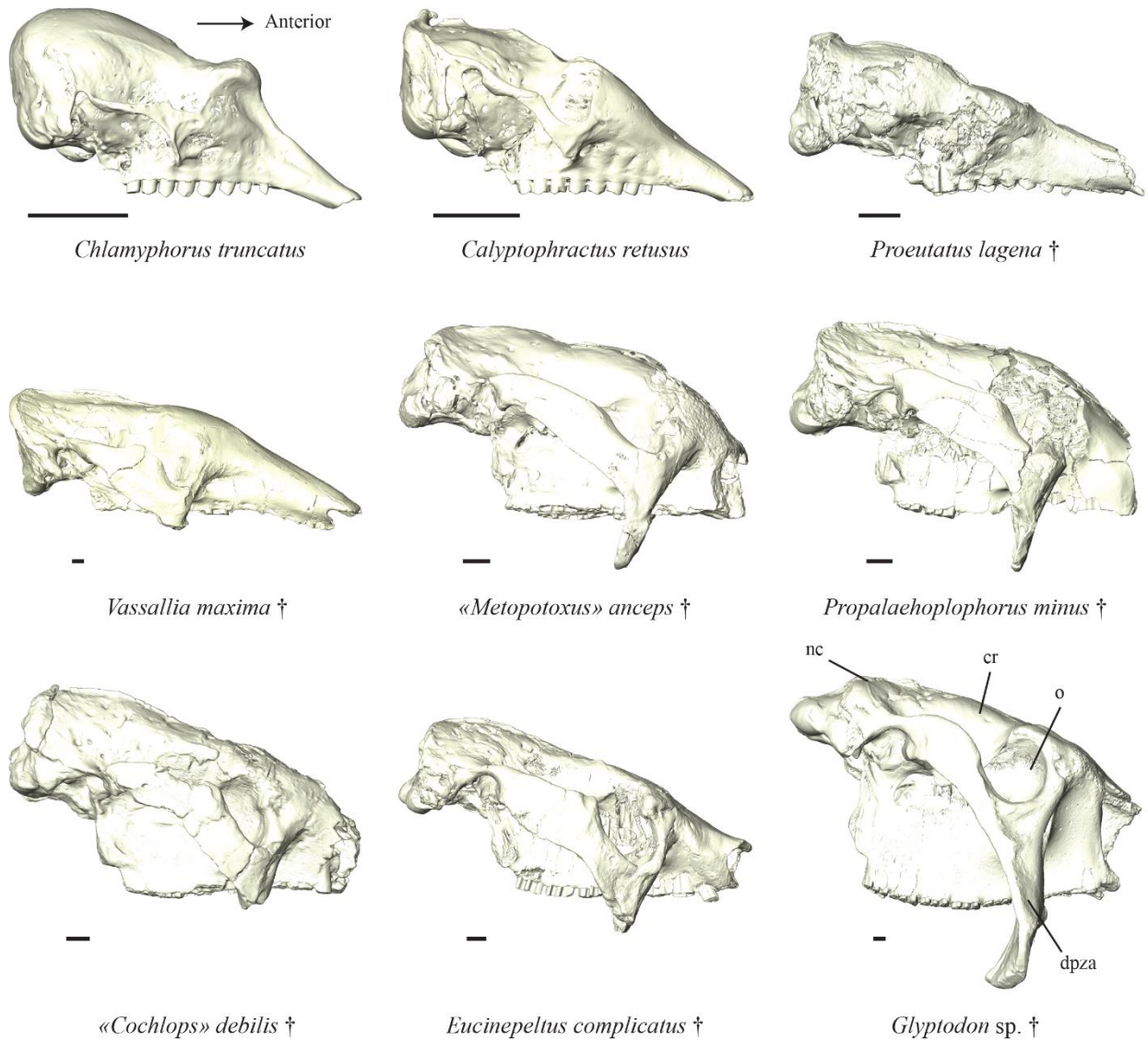


Figure S53 (continued from Figure S52). Plate of cingulate craniums in lateral view. Abbreviations: cr, cranial roof; dpza, descending process of zygomatic arch; nc, nuchal crest; o, orbit. Scale = 1cm.

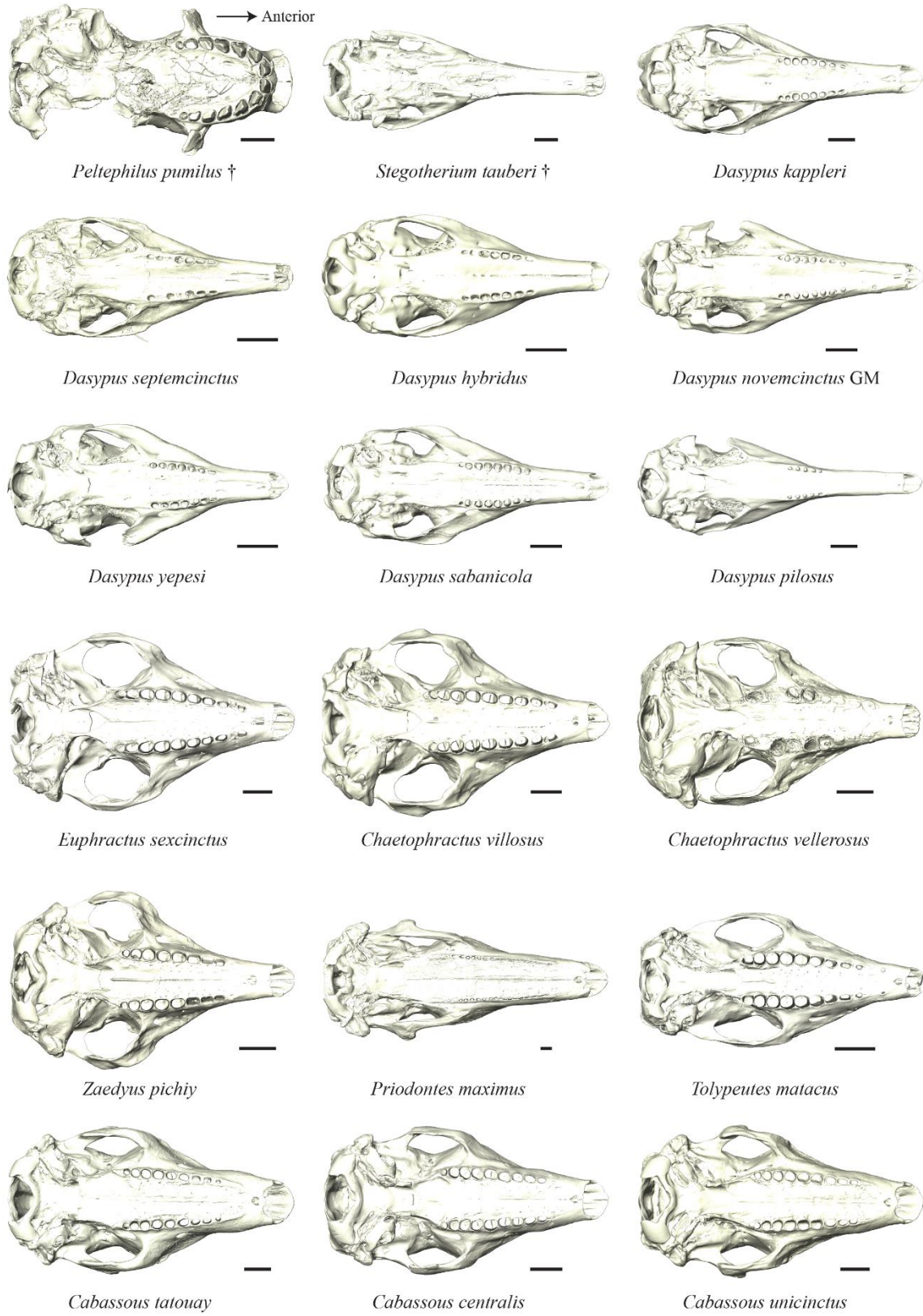


Figure S54. Plate of cingulate craniums in ventral view. Scale = 1cm.

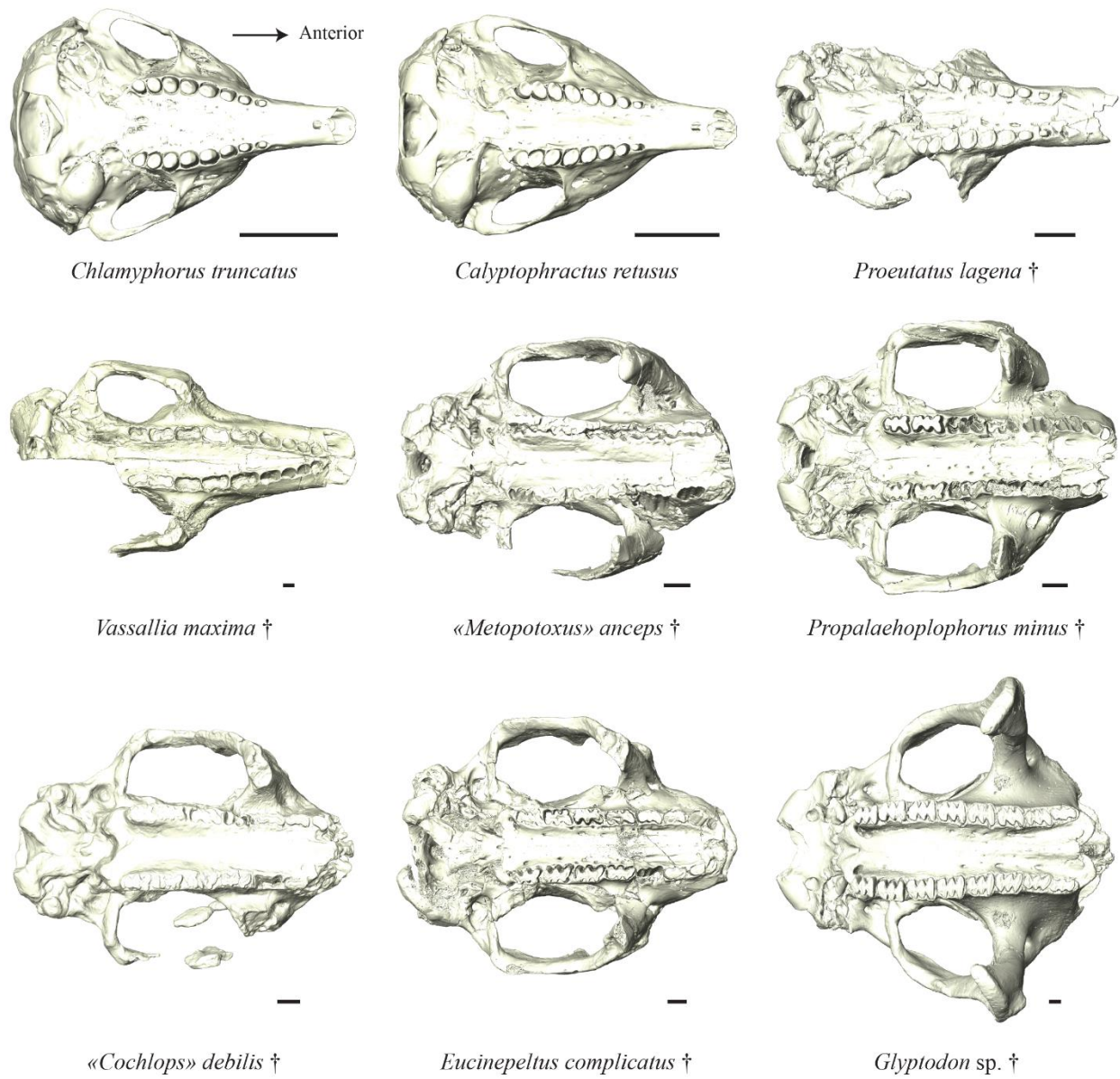


Figure S55. (continued from Figure S54). Plate of cingulate craniums in ventral view. Scale = 1cm.

ABSTRACT

Extended Abstract:

Morphological variation is a pervasive phenomenon, which has long inspired naturalists and led them to propose classifications of organisms based on observed similarities and differences. However, the more we examine morphological variation, the more we discover its extreme complexity. In recent decades, the use of morphological variation as a source of characters for phylogenetic analyses has been strongly questioned despite the primacy of these data for the study of extinct taxa inaccessible to molecular analyses. The prime importance of morphological data for reconstructing relationships of extinct forms is hampered by critical assessments of its performance, particularly for analyses within placental mammals. This observation is in line with the fact that many studies have called for an improvement of our phylogenetic methods using morphology, especially for broader exploration of patterns of morphological variation and a better identification of the covariation among traits.

Cingulates are a group of placental mammals that belong to the superorder Xenarthra together with anteaters and sloths. The Cingulata includes the extant armadillos and extinct taxa such as glyptodonts. This clade represents an ideal case study for the exploration of morphological variation in a phylogenetic context. Their modest extant diversity permits a detailed exploration of the entire group, while their past diversity, showing cranial shapes very unusual in mammals, offers a wide range of investigations. The major interest of this group for the subject treated in the present work lies in the lack of congruence between phylogenetic analyses using morphological or molecular data. In this work, we first highlight the lack of consensus between these hypotheses and point out the existing gaps in our morphological knowledge of the group, more specifically concerning the internal cranial anatomy and the integration patterns (= tendency of traits to covary) on the skull. We show that an exploration of these two aspects will be useful to complete morphological matrices but also to better understand the existing covariations among several anatomical structures and characters that can mislead morphological phylogenetics.

Our work starts with an in-depth study of the internal anatomy of the skull in a diverse sample of Cingulata, assuming that these poorly known structures can deliver new phylogenetic information. The virtual 3D reconstruction (using X-ray microtomography) of selected canals and cavities related to cranial vascularization, innervation or tooth insertion allowed us to compare the locations, trajectories and shape of these structures and to discuss their potential interest for cingulate systematics. We tentatively reconstructed evolutionary scenarios for eight selected traits on these structures, which often showed a greater resemblance of glyptodonts with pampatheres, with the genus *Proeutatus* and/or with chlamyphorines. This latter aspect was partly congruent with recent molecular hypotheses, but more research is needed on these resemblances and on the potential effects of development and allometry on the observed variations. Overall, these comparisons enable us to highlight new anatomical variation that may be of great interest to further explore the evolutionary history of cingulates and the origins of glyptodonts on a morphological basis.

Then, our work explores patterns of morphological integration on the skull of cingulates in two steps. We first focus on one of the most powerful integration factors known in mammals - allometry - in order to target cranial covariation patterns related to size variation. Our work on this aspect starts with an exploratory approach on one of the best sampled cingulate species, the nine-banded armadillo. It enables us to identify allometric patterns in this species at two scales - the entire skull and cranial units - and at two levels of integration - the static and ontogenetic levels. Based on this exploratory study, we test with the same approach the existence of similar allometric patterns in two other extant and distantly related species of cingulates (in the genera *Cabassous* and *Zaedyus*). All these patterns are then compared to an evolutionary analysis of allometry gathering most extant cingulate species and most of the emblematic fossil groups (with a focus on glyptodonts). This comparison makes it possible to determine if certain allometric patterns detected at the species level were at play during the evolution of cingulates. It highlights several covariations between the size and shape of the skull that seem to be present across the whole group. One of the strongest allometric patterns detected corresponds to the craniofacial allometry, i.e., a more elongated face in larger crania, which is already well known in mammals. In addition, strong and widespread allometric changes were also detected for the postorbital constriction, the zygomatic arch, the nuchal crests, the mastoid process of the petrosal, the cranial roof or the foramen magnum.

The second step on morphological integration corresponds to an in-depth study of the strongest covariations within cranial linear distances in the three species of armadillos initially sampled for allometry. Our selective exploration of pairs of covarying distances highlight additional strong cranial correlations not detected in our previous

ABSTRACT

study on allometry. The patterns obtained in the three species are then analyzed at the evolutionary level to identify whether these covariations were also present in the morphological evolution of the group. The supported evolutionary correlations concern in particular the anterior root of zygomatic arch, a region particularly rich in muscular insertions. In a complementary way, we perform the very first exploration of cranial modularity in cingulates at the intraspecific level and of their diversity in cranial shape at the evolutionary level. They reveal a partitioning of the integration into three anteroposteriorly distributed modules on the skull and identified potential cranial regions for further research of covariation patterns.

Finally, we discuss the implications of these studies regarding the already existing phylogenetic hypotheses and the cranial characters used in the matrices. Our results on cranial integration are compared with existing matrices and phylogenetic analyses in order to identify possible groups of traits that may covary and to discuss their potential impact on the phylogenetic reconstruction within the group. Although it hints at a necessary revision of some characters, the comparison of the detected covariation patterns with morphological matrices proves difficult. We argue that alternative coding strategies (such as the use of continuous characters) need to be further explored for a better evaluation of the covariation and allometry among scored characters and for an overall improvement of our character constructions. Our exploratory work emphasizes again the great complexity of morphological variation and the resulting challenge of scoring independent morphological characters for phylogenetic analysis.

Résumé Étendu:

La variation morphologique est un phénomène omniprésent, qui a longtemps inspiré les naturalistes et les a amenés à proposer des classifications d'organismes basées sur les similitudes et les différences observées. Cependant, plus on examine la variation morphologique, plus on découvre son extrême complexité. Au cours des dernières décennies, l'utilisation de la variation morphologique comme source de caractères pour les analyses phylogénétiques a été fortement remise en question malgré la primauté de ces données pour l'étude de taxons éteints inaccessibles aux analyses moléculaires. L'importance primordiale des données morphologiques pour la reconstitution des relations de parentés des formes éteintes est entravée par les évaluations critiques de leurs performances, en particulier pour les analyses au sein des mammifères placentaires. Cette observation est conforme au fait que de nombreuses études ont appelé à une amélioration de nos méthodes phylogénétiques utilisant la morphologie, en particulier pour une exploration plus large des modèles de variation morphologique et une meilleure identification de la covariation entre les traits.

Les cingulés sont un groupe de mammifères placentaires qui appartiennent au superordre Xenarthra avec les fourmiliers et les paresseux. Les cingulata comprennent les tatous actuels et des taxons éteints tels que les glyptodontes. Ce clade représente un cas d'étude idéal pour l'exploration de la variation morphologique dans un contexte phylogénétique. Leur modeste diversité actuelle permet une exploration détaillée de l'ensemble du groupe, tandis que leur diversité passée, montrant des formes crâniennes très inhabituelles chez les mammifères, offre un large éventail d'investigations. L'intérêt majeur de ce groupe pour le sujet traité dans le présent travail réside dans le manque de congruence entre les analyses phylogénétiques utilisant des données morphologiques ou moléculaires. Dans ce travail, nous mettons d'abord en évidence le manque de consensus entre ces hypothèses et signalons les lacunes existantes dans notre connaissance morphologique du groupe, plus particulièrement en ce qui concerne l'anatomie crânienne interne et les schémas d'intégration (= tendance des traits à covarier) sur le crâne. Nous montrons qu'une exploration de ces deux aspects sera utile pour compléter les matrices morphologiques mais aussi pour mieux comprendre les covariations existantes entre plusieurs structures et caractères anatomiques qui peuvent induire en erreur la phylogénie morphologique.

Notre travail commence par une étude approfondie de l'anatomie interne du crâne dans un échantillon varié de Cingulata, en supposant que ces structures mal connues puissent fournir de nouvelles informations phylogénétiques. La reconstruction virtuelle en 3D (par microtomographie aux rayons X) de certains canaux et cavités liés à la vascularisation crânienne, à l'innervation ou à l'insertion de dents nous a permis de comparer les emplacements, les trajectoires et la forme de ces structures et de discuter de leur intérêt potentiel pour la systématique des Cingulata. Nous avons provisoirement reconstitué des scénarios évolutifs pour huit caractères sélectionnés sur ces structures, qui présentaient souvent une plus grande ressemblance des glyptodontes avec les pampatheres, avec le genre *Proeutatus* et/ou avec les chlamyphorines. Ce dernier aspect était en partie conforme aux récentes hypothèses moléculaires, mais des recherches supplémentaires sont nécessaires sur ces ressemblances et sur les effets potentiels du développement et de l'allométrie sur les variations observées. Dans l'ensemble, ces comparaisons nous permettent de mettre en évidence de nouvelles variations anatomiques qui pourraient être d'un grand intérêt pour explorer davantage l'histoire évolutive des cingulés et les origines des glyptodontes sur une base morphologique.

ABSTRACT

Ensuite, notre travail explore les patrons d'intégration morphologique sur le crâne des cingulés en deux étapes. Nous nous concentrons d'abord sur l'un des plus puissants facteurs d'intégration connus chez les mammifères - l'allométrie - afin de cibler les patrons de covariation crânienne liés à la variation de taille. Notre travail sur cet aspect commence par une approche exploratoire sur l'une des espèces de cingulés les mieux échantillonnées, le tatou à neuf bandes. Elle nous permet d'identifier les patrons allométriques de cette espèce à deux échelles - l'ensemble du crâne et des unités crâniennes - et à deux niveaux d'intégration - les niveaux statique et ontogénétique. Sur la base de cette étude exploratoire, nous testons avec la même approche l'existence de patrons allométriques similaires chez deux autres espèces de cingulés actuelles distantes phylogénétiquement (dans les genres *Cabassous* et *Zaedyus*). Tous ces patrons sont ensuite comparés à une analyse évolutive de l'allométrie rassemblant la plupart des espèces de cingulés actuelles et la plupart des groupes de fossiles emblématiques (dont les glyptodontes). Cette comparaison permet de déterminer si certains patrons allométriques détectés au niveau intraspécifique ont été en jeu lors de l'évolution des cingulés. Elle met en évidence plusieurs covariations entre la taille et la forme du crâne qui semblent être présentes dans l'ensemble du groupe. Un des patrons allométriques les plus forts détectés correspond à l'allométrie cranio-faciale, c'est-à-dire une face plus allongée dans les grands crânes, ce qui est déjà bien connu chez les mammifères. En outre, des patrons allométriques forts et étendus ont également été détectés pour la constriction postorbitale, l'arc zygomatique, les crêtes nucales, le processus mastoïdien du pétreux, le toit crânien ou le foramen magnum.

La deuxième étape sur l'intégration morphologique correspond à une étude approfondie des covariations les plus fortes au sein des distances linéaires crâniennes chez les trois espèces de tatous initialement échantillonnées pour l'allométrie. Notre exploration sélective de paires de distances covariantes met en évidence de fortes corrélations crâniennes supplémentaires non détectées dans notre précédente étude sur l'allométrie. Les modèles obtenus chez les trois espèces sont ensuite analysés au niveau évolutif pour déterminer si ces covariations étaient également présentes dans l'évolution morphologique du groupe. Les corrélations évolutives soutenues concernent notamment la racine antérieure de l'arc zygomatique, une région particulièrement riche en insertions musculaires. De manière complémentaire, nous effectuons la toute première exploration de la modularité crânienne des cingulés au niveau intraspécifique et de leur diversité de forme crânienne au niveau évolutif. Ils révèlent une partition de l'intégration en trois modules répartis antéro-postérieurement sur le crâne et identifient des régions crâniennes potentielles pour une recherche plus approfondie des patrons de covariation.

Enfin, nous discutons des implications de ces études concernant les hypothèses phylogénétiques déjà existantes et les caractères crâniens utilisés dans les matrices. Nos résultats sur l'intégration crânienne sont comparés aux matrices et aux analyses phylogénétiques existantes afin d'identifier les groupes possibles de caractères susceptibles de covarier et de discuter de leur impact potentiel sur la reconstruction phylogénétique au sein du groupe. Bien qu'elle laisse entrevoir une révision nécessaire de certains caractères, la comparaison des patrons de covariation détectés avec les matrices morphologiques s'avère difficile. Nous soutenons que des stratégies de codage alternatives (telles que l'utilisation de caractères continus) doivent être explorées plus avant pour une meilleure évaluation de la covariation et de l'allométrie parmi les caractères notés et pour une amélioration globale de nos constructions de caractères. Nos travaux exploratoires soulignent à nouveau la grande complexité de la variation morphologique et le défi qui en résulte de formaliser et coder des caractères morphologiques indépendants pour l'analyse phylogénétique.

Abstract:

Morphological variation is a complex phenomenon whose use in phylogenetic analyses is often criticized. Many studies have called for a broader exploration of patterns of morphological variation and a better identification of the covariation among traits to improve morphological phylogenetics. Cingulates represent an ideal case study for this objective since they illustrate a typical case of conflict between morphological and molecular phylogenetic reconstructions, especially for the origins of the extinct glyptodonts. In this work, we first highlight this incongruence and point out the existing gaps concerning our knowledge of the internal cranial anatomy and the patterns of integration on the skull of cingulates. An exploration of these two aspects is relevant to the enrichment of morphological matrices and to a better understanding of the existing covariations among characters, which can mislead morphological phylogenetics. Our work starts with an in-depth study of the internal anatomy of the skull (focused on selected canals and cavities related to cranial vascularization, innervation or tooth insertion) in a diverse sample of Cingulata. We tentatively reconstruct the evolutionary scenarios of eight selected traits on these structures. These suggest a greater resemblance of glyptodonts with pampatheres, with the genus *Proeutatus* and/or with chlamyphorines, which is partly congruent with molecular phylogenies. Then, we explore patterns of cranial integration within several species of extant armadillos and test if the patterns found at the intraspecific level are also supported at the evolutionary level, i.e., among species, using a rich sample of extant and extinct cingulates. We first focus on one of the most powerful integration factors known in mammals - allometry - in order to target cranial covariation patterns related to size variation. Our analysis of cranial allometry enabled us to highlight several cranial allometric patterns that are widespread in cingulates. One of the strongest allometric patterns detected corresponds to the craniofacial allometry (relatively long face in large crania), but strong and widespread allometric changes were also detected for the postorbital constriction, the zygomatic arch, the nuchal crests, the mastoid process of the petrosal, the cranial roof and the foramen magnum. Second, we perform a selective exploration of pairs of strongly covarying distances in the same samples which enable us to highlight additional strong cranial correlations. The correlations supported at both the intraspecific and evolutionary levels concern in particular the anterior root of zygomatic arch, a region particularly rich in muscular insertions. Third, we present the very first exploration of cranial modularity in cingulates at the intraspecific level that reveals a partitioning of the integration into three anteroposteriorly distributed modules on the skull. Our results are finally compared with existing morphological matrices and phylogenetic hypotheses. Although it hints at a necessary revision of several characters, the comparison of the detected patterns of integration with morphological matrices proves difficult. This highlights the necessity to further explore alternative coding strategies for a better evaluation of the covariation and allometry among scored characters and for an overall improvement of our character constructions.

Résumé :

La variation morphologique est un phénomène complexe dont l'utilisation dans les analyses phylogénétiques est souvent critiquée. De nombreuses études ont appelé à une exploration plus large des modèles de variation morphologique et à une meilleure identification de la covariation entre les traits pour améliorer les phylogénies morphologiques. Les cingulés représentent un cas d'étude idéale pour cet objectif car ils illustrent un cas typique de conflit entre les reconstructions phylogénétiques morphologiques et moléculaires, en particulier pour l'origine des glyptodontes (éteints). Dans ce travail, nous mettons d'abord en évidence cette incongruence et soulignons les lacunes existantes concernant notre connaissance de l'anatomie crânienne interne et des patrons d'intégration sur le crâne des cingulés. L'exploration de ces deux aspects est pertinente pour l'enrichissement des matrices morphologiques et pour une meilleure compréhension des covariations existantes entre les caractères, qui peuvent induire en erreur les phylogénies morphologiques. Notre travail commence par une étude approfondie de l'anatomie interne du crâne (axée sur certains canaux et cavités liés à la vascularisation et l'innervation crânienne, ou à l'insertion de dents) dans un échantillon diversifié de Cingulata. Nous reconstruisons provisoirement les scénarios évolutifs de huit traits sélectionnés sur ces structures. Ceux-ci suggèrent une plus grande ressemblance des glyptodontes avec les pampatheres, le genre *Proeutatus* et/ou avec les chlamyphorines, ce qui est en partie congruent avec les phylogénies moléculaires. Ensuite, nous explorons les patrons d'intégrations crâniens au sein de plusieurs espèces de tatous actuels et nous testons si les modèles trouvés au niveau intraspécifique sont également soutenus au niveau évolutif, c'est-à-dire entre les espèces, en utilisant un riche échantillon de cingulés actuels et éteints. Nous nous concentrons d'abord sur l'un des facteurs d'intégration les plus puissants connus chez les mammifères - l'allométrie - afin de cibler les patrons de covariations crâniens liés à la variation de taille. Notre analyse de l'allométrie crânienne nous a permis de mettre en évidence plusieurs patrons allométriques crâniens très répandus chez les cingulés. Les patrons allométriques détectés les plus forts correspondent à l'allométrie crânio-faciale (une face relativement longue pour les crânes de grandes tailles), mais des patrons allométriques forts et étendus ont également été détectés pour la constriction postorbitale, l'arc zygomatique, les crêtes nucales, le processus mastoïdien du pétrosal, le toit crânien et le foramen magnum. Ensuite, nous effectuons une exploration sélective de paires de distances fortement covariantes dans les mêmes échantillons, ce qui nous permet de mettre en évidence d'autres fortes corrélations crâniennes. Les corrélations supportées tant au niveau intraspécifique qu'au niveau évolutif concernent notamment la racine antérieure de l'arc zygomatique, une région particulièrement riche en insertions musculaires. Puis, nous présentons la toute première exploration de la modularité crânienne des cingulés au niveau intraspécifique qui révèle une partition de l'intégration en trois modules répartis antéro-postérieurement sur le crâne. Nos résultats sont enfin comparés aux matrices morphologiques existantes et aux hypothèses phylogénétiques. Bien qu'elle laisse entrevoir une révision nécessaire de plusieurs caractères, la comparaison des patrons d'intégrations détectés avec les matrices morphologiques s'avère difficile. Cela souligne la nécessité d'explorer davantage des stratégies de codage alternatives pour une meilleure évaluation de la covariation et de l'allométrie parmi les caractères notés et pour une amélioration globale de nos constructions de caractères.